



*applied sciences*

# Achievements and Prospects of Functional Pavement Materials and Structures

---

Edited by

Jian-long Zheng, Zhanping You and Xueyan Liu

Printed Edition of the Special Issue Published in *Applied Sciences*

# **Achievements and Prospects of Functional Pavement: Materials and Structures**





# Achievements and Prospects of Functional Pavement: Materials and Structures

Editors

**Jian-long Zheng**

**Zhanping You**

**Xueyan Liu**

MDPI • Basel • Beijing • Wuhan • Barcelona • Belgrade • Manchester • Tokyo • Cluj • Tianjin





*Editors*

Jian-long Zheng  
School of Traffic and  
Transportation Engineering  
Changsha University of  
Science and Technology  
Changsha  
China

Zhanping You  
Department of Civil,  
Environmental, and  
Geospatial Engineering  
Michigan Technological  
University  
Houghton  
United States

Xueyan Liu  
Faculty of Civil Engineering  
and Geosciences  
Delft University of  
Technology  
Delft  
Netherlands

*Editorial Office*

MDPI  
St. Alban-Anlage 66  
4052 Basel, Switzerland

This is a reprint of articles from the Special Issue published online in the open access journal *Applied Sciences* (ISSN 2076-3417) (available at: [www.mdpi.com/journal/applsci/special-issues/Functional.Pavement](http://www.mdpi.com/journal/applsci/special-issues/Functional.Pavement)).

For citation purposes, cite each article independently as indicated on the article page online and as indicated below:

LastName, A.A.; LastName, B.B.; LastName, C.C. Article Title. <i>Journal Name</i> <b>Year</b> , Volume Number, Page Range.
--

**ISBN 978-3-0365-5542-3 (Hbk)**

**ISBN 978-3-0365-5541-6 (PDF)**

Cover image courtesy of Zhanping You

© 2022 by the authors. Articles in this book are Open Access and distributed under the Creative Commons Attribution (CC BY) license, which allows users to download, copy and build upon published articles, as long as the author and publisher are properly credited, which ensures maximum dissemination and a wider impact of our publications.

The book as a whole is distributed by MDPI under the terms and conditions of the Creative Commons license CC BY-NC-ND.

# Contents

<b>About the Editors</b> . . . . .	vii
<b>Jian-long Zheng, Zhanping You and Xueyan Liu</b> Achievements and Prospects of Functional Pavement: Materials and Structures Reprinted from: <i>Appl. Sci.</i> <b>2020</b> , <i>10</i> , 7720, doi:10.3390/app10217720 . . . . .	1
<b>Haiping Yuan, Weiqiang Li, Yixian Wang, Hang Lin and Yan Liu</b> Resilient Modulus—Physical Parameters Relationship of Improved Red Clay by Dynamic Tri-Axial Test Reprinted from: <i>Appl. Sci.</i> <b>2019</b> , <i>9</i> , 1155, doi:10.3390/app9061155 . . . . .	5
<b>Wentong Huang, Duanyi Wang, Peiyong He, Xiang Long, Bing Tong and Jun Tian et al.</b> Rheological Characteristics Evaluation of Bitumen Composites Containing Rock Asphalt and Diatomite Reprinted from: <i>Appl. Sci.</i> <b>2019</b> , <i>9</i> , 1023, doi:10.3390/app9051023 . . . . .	23
<b>Shi Xu, Amir Tabaković, Xueyan Liu, Damian Palin and Erik Schlangen</b> Optimization of the Calcium Alginate Capsules for Self-Healing Asphalt Reprinted from: <i>Appl. Sci.</i> <b>2019</b> , <i>9</i> , 468, doi:10.3390/app9030468 . . . . .	37
<b>Chundi Si, Hang Cao, Enli Chen, Zhanping You, Ruilan Tian and Ran Zhang et al.</b> Dynamic Response Analysis of Rutting Resistance Performance of High Modulus Asphalt Concrete Pavement Reprinted from: <i>Appl. Sci.</i> <b>2018</b> , <i>8</i> , 2701, doi:10.3390/app8122701 . . . . .	49
<b>Changhong Zhou, Xueyan Liu, Panos Apostolidis, A. (Tom) Scarpas and Liang He</b> Induction Heating-Assisted Compaction in Porous Asphalt Pavements: A Computational Study Reprinted from: <i>Appl. Sci.</i> <b>2018</b> , <i>8</i> , 2308, doi:10.3390/app8112308 . . . . .	67
<b>Ruxin Jing, Xueyan Liu, Aikaterini Varveri, Athanasios Scarpas and Sandra Erkens</b> The Effect of Ageing on Chemical and Mechanical Properties of Asphalt Mortar Reprinted from: <i>Appl. Sci.</i> <b>2018</b> , <i>8</i> , 2231, doi:10.3390/app8112231 . . . . .	83
<b>Dingbang Wei, Bo Li, Zhengwei Zhang, Feng Han, Xingjun Zhang and Man Zhang et al.</b> Influence of Surface Texture Characteristics on the Noise in Grooving Concrete Pavement Reprinted from: <i>Appl. Sci.</i> <b>2018</b> , <i>8</i> , 2141, doi:10.3390/app8112141 . . . . .	95
<b>Yazhen Sun, Ting Yan, Changyu Wu, Xiaofang Sun, Jinchang Wang and Xuezhong Yuan</b> Analysis of the Fatigue Crack Propagation Process of the Stress-Absorption Layer of Composite Pavement Based on Reliability Reprinted from: <i>Appl. Sci.</i> <b>2018</b> , <i>8</i> , 2093, doi:10.3390/app8112093 . . . . .	105
<b>Hui Wang, Ke Jin, Xinyu Dong, Shihao Zhan and Chenghu Liu</b> Preparation Technique and Properties of Nano-TiO <sub>2</sub> Photocatalytic Coatings for Asphalt Pavement Reprinted from: <i>Appl. Sci.</i> <b>2018</b> , <i>8</i> , 2049, doi:10.3390/app8112049 . . . . .	127
<b>Hong-xin Guan, Hao-qing Wang, Hao Liu, Jia-jun Yan and Miao Lin</b> The Effect of Intermediate Principal Stress on Compressive Strength of Different Cement Content of Cement-Stabilized Macadam and Different Gradation of AC-13 Mixture Reprinted from: <i>Appl. Sci.</i> <b>2018</b> , <i>8</i> , 2000, doi:10.3390/app8102000 . . . . .	143



<b>Hui Wang, Zhen Yang, Shihao Zhan, Lei Ding and Ke Jin</b> Fatigue Performance and Model of Polyacrylonitrile Fiber Reinforced Asphalt Mixture Reprinted from: <i>Appl. Sci.</i> <b>2018</b> , <i>8</i> , 1818, doi:10.3390/app8101818 . . . . .	155
<b>Haopeng Wang, Xueyan Liu, Panos Apostolidis and Tom Scarpas</b> Non-Newtonian Behaviors of Crumb Rubber-Modified Bituminous Binders Reprinted from: <i>Appl. Sci.</i> <b>2018</b> , <i>8</i> , 1760, doi:10.3390/app8101760 . . . . .	167
<b>Ran Zhang, Qingli Dai, Zhanping You, Hainian Wang and Chao Peng</b> Rheological Performance of Bio-Char Modified Asphalt with Different Particle Sizes Reprinted from: <i>Appl. Sci.</i> <b>2018</b> , <i>8</i> , 1665, doi:10.3390/app8091665 . . . . .	181
<b>Songtao Lv, Shuangshuang Wang, Tong Guo, Chengdong Xia, Jianglong Li and Gui Hou</b> Laboratory Evaluation on Performance of Compound-Modified Asphalt for Rock Asphalt/Styrene-Butadiene Rubber (SBR) and Rock Asphalt/Nano-CaCO <sub>3</sub> Reprinted from: <i>Appl. Sci.</i> <b>2018</b> , <i>8</i> , 1009, doi:10.3390/app8061009 . . . . .	197
<b>Wei Guo, Xuedong Guo, Xing Chen and Wenting Dai</b> Properties Analysis of Oil Shale Waste as Partial Aggregate Replacement in Open Grade Friction Course Reprinted from: <i>Appl. Sci.</i> <b>2018</b> , <i>8</i> , 1626, doi:10.3390/app8091626 . . . . .	215
<b>Lijun Sun, Gang Wang, Hongchao Zhang and Liping Liu</b> Initiation and Propagation of Top-Down Cracking in Asphalt Pavement Reprinted from: <i>Appl. Sci.</i> <b>2018</b> , <i>8</i> , 774, doi:10.3390/app8050774 . . . . .	237
<b>Songtao Lv, Chaochao Liu, Jingting Lan, Hongwei Zhang, Jianlong Zheng and Zhanping You</b> Fatigue Equation of Cement-Treated Aggregate Base Materials under a True Stress Ratio Reprinted from: <i>Appl. Sci.</i> <b>2018</b> , <i>8</i> , 691, doi:10.3390/app8050691 . . . . .	251
<b>Danhua Wang, Xunhao Ding, Tao Ma, Weiguang Zhang and Deyu Zhang</b> Algorithm for Virtual Aggregates' Reconstitution Based on Image Processing and Discrete-Element Modeling Reprinted from: <i>Appl. Sci.</i> <b>2018</b> , <i>8</i> , 738, doi:10.3390/app8050738 . . . . .	269
<b>Weiguang Zhang, Tao Ma, Gang Xu, Xiaoming Huang, Meng Ling and Xiao Chen et al.</b> Fatigue Resistance Evaluation of Modified Asphalt Using a Multiple Stress Creep and Recovery (MSCR) Test Reprinted from: <i>Appl. Sci.</i> <b>2018</b> , <i>8</i> , 417, doi:10.3390/app8030417 . . . . .	285
<b>Nader Nciri, Taesub Shin, Haksoo Lee and Namjun Cho</b> Potential of Waste Oyster Shells as a Novel Biofiller for Hot-Mix Asphalt Reprinted from: <i>Appl. Sci.</i> <b>2018</b> , <i>8</i> , 415, doi:10.3390/app8030415 . . . . .	299

# About the Editors

## **Jian-long Zheng**

Dr. Zheng is a member of the Chinese Academy of Engineering. He is a highway engineering expert, professor, and doctoral supervisor of Changsha University of Science and Technology, director of the National Engineering Laboratory of Highway Maintenance Technology, director of the Key Laboratory of Highway Engineering of the Ministry of Education, the vice director of Teaching Guiding Committee for Civil Engineering of the Ministry of Education, the vice chairman of China Highway & Transportation Society and the executive director of the International Road Federation. Dr. Zheng has been long engaged in developing and practicing the technology of highway and geotechnical engineering, with over 200 articles and seven academic books published. He holds 35 national patents in inventions. He led a well know project on the Technology of Highway Construction in Expansive Soil Area, and he received the First Prize of National Science and Technology Progress Award in 2009 due to this achievement. His effort on the Technology of Asphalt Pavement State Design Method and Structural Performance Improvement Technology made him receive the Second Prize of National Science and Technology Progress Award in 2012. Meanwhile, he has won a number of special awards. He won a Second Prize of National Teaching Achievement and two First Provincial Level Prizes. He was also awarded the Outstanding Achievement Award in Transportation Technology from the Ministry of Transport among his numerous key awards.

## **Zhanping You**

Dr. Zhanping You earned his Ph.D. in Civil Engineering from the University of Illinois at Urbana - Champaign in 2003. Dr. You is a Distinguished Professor at Michigan Technological University. In his capacity as a Professor, he has completed research projects related to road materials, pavement engineering, and sustainable building materials. His contribution to pavement and materials research has led to journal articles, book chapters, and advances in engineering practice. He has led research projects from engineering practices of roads to pavement science with funding from federal, state, and local agencies. His contribution to pavement and materials research has been featured in newspapers, magazines, and other media. Dr. You has published over 400 papers in peer reviewed journals and conference proceedings. Dr. You has received numerous recognitions. He was awarded the U.S. Department of Transportation's Dwight David Eisenhower Transportation Fellowship in 2001. In both 2004 and 2005, he was awarded the Dwight David Eisenhower Transportation Faculty Fellowship. He earned the prestigious Michigan Tech Research Award in 2019 and University Distinguished Professorship. He was named a Fellow of ASCE and a Fellow of the EMI. Dr. You served as the Chair of ASCE Engineering Mechanics Institute's Pavements Committee and CI's Bituminous Materials Committee. He is also the guest editor for other journals.




**Xueyan Liu**

Dr. Liu is currently an Associate Professor in the Section of Pavement Engineering of the Faculty of Civil Engineering & Geosciences of TU Delft. He works in the areas of constitutive modeling, numerical modelling and material experimental characterization. Within the research program of the Section Pavement Engineering, his research topics mostly relate to the development and implementation of constitutive models for the simulation of the static and dynamic response of various pavement engineering materials like soils, asphalt concrete, liner and reinforcing systems and sustainable development technologies, i.e., multiscale modelling of asphaltic materials, warm/cold asphalt concrete technology, the durability of asphalt surfacings on orthotropic steel deck bridge, accelerated pavement test, pavement continuous monitoring and sustainable development technologies. Dr. Liu was granted his doctoral thesis in 2003. During the same period, Dr. Liu also participated in the team that developed the ACR<sub>e</sub> model for Asphalt Concrete Response currently implemented in 3D Computer Aided Pavement Analysis system (CAPA-3D). Dr. Liu has published more than 100 technical and journal papers on the mechanics and the finite element modelling of granular, concrete and asphaltic materials. Dr. Liu is a member of RILEM Technical Committee of Cracking in Asphalt Pavements WG3 and a member of Delft Centre for Materials (DCMat). He is also a member of ISAP, AAPT, APSE and IACMAG. Dr. Liu is an Editorial Board Member of Geomaterials (GM). Dr. Liu was appointed as a Board member of the International Association of Chinese Infrastructure Professionals (IACIP) and a member of the Academic Committee of the Key Laboratory of Road Structure and Materials Transportation Industry of the China Ministry of Transport. He is also actively involved in organizing inter/national workshops and conferences and was invited as a Scientific/Technical committee member of several international conferences.

Editorial

# Achievements and Prospects of Functional Pavement: Materials and Structures

Jian-long Zheng <sup>1</sup>, Zhanping You <sup>2,\*</sup>  and Xueyan Liu <sup>3</sup>

<sup>1</sup> School of Traffic and Transportation Engineering, Changsha University of Science and Technology (CSUST), Changsha 410004, China; zjl@csust.edu.cn

<sup>2</sup> Department of Civil and Environmental Engineering, Michigan Technological University, 1400 Townsend Drive, Houghton, MI 49931, USA

<sup>3</sup> Pavement Engineering Section, Department of Engineering Structures, Faculty of Civil Engineering and Geosciences, Delft University of Technology, 2628CN Delft, The Netherlands; x.liu@tudelft.nl

\* Correspondence: zyou@mtu.edu

Received: 8 September 2020; Accepted: 8 September 2020; Published: 31 October 2020

**Abstract:** In order to further promote the development of functional pavement technology, a Special Issue of “Achievements and Prospects of Functional Pavement” has been proposed by a group of guest editors. To reach this objective, articles included in this Special Issue are related to different aspects of functional pavement, including green roads to decrease carbon emission, noise, and pollution, safety pavement to increase skid resistance by water drainage and snow removal, intelligent roads for monitoring, power generation, temperature control and management, and durable roads to increase service life with new theory, new design methods, and prediction models, as highlighted in this editorial.

**Keywords:** functional pavement; green road; safety pavement; intelligent road; durable road; pavement materials; asphalt pavements

---

A Special Issue of "Achievements and Prospects of Functional Pavement: Materials and Structures" has been proposed and organized to present the recent achievement of functional pavement, and to promote the development of functional pavement technology. This Special Issue contains 20 technical articles [1–20], which have been peer-reviewed under the journal's rigorous review criteria. The collection includes invited papers from experts in international communities and articles that have been selected from the 2019 World Transport Convention (WTC) held in June 2019 in Beijing, the 4th International Conference on Transportation Infrastructure and Materials in Jinan, Shandong, China in 2019, and the 5th Chinese-European Workshop on Functional Pavements in 2019 in Changsha, China.

Research institutions in pavement research, such as Changsha University of Science & Technology (5 papers), Delft University of Technology (4 papers), Michigan Technological University (3 papers), Southeast University, Khalifa University of Science and Technology, Nanjing Institute of Technology, Tongji University, Dongguan University of Technology, Hefei University of Technology, Korea University of Technology and Education, Jilin University, Lanzhou Jiaotong University, Shijiazhuang Tiedao University, Shenyang Jianzhu University, and Technological University Dublin, have contributed their research achievements to this Special Issue. A summary of the articles is given in this editorial.

Research on the application of waste material in pavement construction is considered to be one of the most economical ways to achieve sustainable, designed green pavements. Nader et al. [1] investigated the use of waste oyster shells as a novel bio-filler in pavement, which is not only able to improve the quality of pavements but also to reduce the cost of their construction and solve the waste problem. Wang et al. [2] studied the complex interaction between bitumen and crumb rubber as well as the addition of warm-mix additives, and proposed a second-order polynomial function to



characterize the viscosity–temperature dependence. Guo et al. [3] developed a new modified open grade friction course (OGFC) by replacing the fine aggregate below 4.75 mm in OGFC with oil shale waste, and a silane coupling agent modifier was used to assist modification. The modified OGFC preparation is an effective technique for improving the strength and stiffness of the OGFC and reducing environmental degradation.

Materials modification technologies are thus widely used in pavement engineering to improve the performance of pavement materials. In this Special Issue, rock asphalt (RA) [4,5], diatomite [4], Styrene-Butadiene Rubber (SBR) [5], nano-CaCO<sub>3</sub> [5], and Bio-Char [6] were used as modifiers for bitumen and were evaluated in detail. The viscoelastic properties, fatigue properties, rutting resistance, anti-cracking properties, and microstructure of bitumen are presented in this Special Issue.

High technologies are applied in intelligent pavement construction, which improves the functions or endows new functions to pavements. Zhou et al. [7] studied induction heating-assisted compaction of pavement structure, which appeared to be an effective way to improve mix compaction and compatibility at low temperature. Xu et al. [8] applied calcium alginate microcapsules encapsulating an asphalt bitumen rejuvenator to improve the self-healing of bitumen once a crack initiates in the asphalt mixture. Wang et al. [9] studied the nano-TiO<sub>2</sub> photocatalytic coating on the surface of pavement, which endows the pavement with air-purifying and self-cleaning abilities. Wei et al. [10] explored the relationship between concrete pavement texture characteristics and tire/pavement noise of grooving concrete pavement, which helps to reduce the noise of the pavement. Wang et al. [11] proposed an algorithm for two-dimensional virtual aggregates modelling for the reconstitution of virtual aggregates and specimen.

Characterization research on pavement materials is important for durable pavement design and construction. The fatigue performance of asphalt mixture was investigated by Sun et al. [12], Wang et al. [13], and Zhang et al. [14]. Sun's study [15] focused on fatigue cracking resistance of a high viscous asphalt sand stress-absorption layer and rubber asphalt stress-absorption layer, and the fatigue cracking resistance of the different layer materials were evaluated by force-controlled fatigue crack propagation tests. Wang's research [13] reported on fatigue performance and a model of polyacrylonitrile fiber-reinforced asphalt mixture produced with different fiber contents and asphalt contents. Zhang et al. [14] investigated the possibility of using multiple stress creep and recovery tests to evaluate the fatigue performance of bitumen binders. Besides fatigue performance, rutting performance is also important for asphalt pavement. Si et al. [16] investigated the dynamic response of rutting resistance of high modulus asphalt concrete pavement, which provided a foundation for the performance research and further engineering practice of high modulus asphalt concrete. Top-down cracking is also a common distress phenomenon for asphalt pavement. Sun et al. [12] proposed new initiation and propagation mechanisms of top-down cracking, and validated the mechanisms through both accelerated pavement testing in the field and uniaxial repeated loading penetration tests in the laboratory at different temperatures. Asphalt aging also has a significant impact on the performance of pavement. Jing et al. [17] investigated the evolution of the chemical and mechanical properties of asphalt mortar during aging and found a higher aging level for mortars produced by first mixing and then aging, compared to the mortars produced by mixing aged bitumen with filler and sand.

Apart from the surface layer of pavement, several other researchers have characterized the mechanical properties of the aggregate base and subgrade. Guang et al. [18] and Lv et al. [19] characterized the mechanical properties of cement-treated aggregate base materials. More specifically, Guang et al. [18] developed a proprietary true triaxle apparatus to simulate the spatial status of principal stresses to conduct compressive strength tests, and the strength model analysis results suggested that the Double-Shear-Corner Model is more suitable to characterize cement-stabilized macadam's strength performance. In the research of Lv et al. [19], a fatigue equation was established based on the true stress ratio for cement-treated aggregate base materials, which provided a theoretical method and basis for unifying the mix design parameters and the construction quality control parameters. Finally, the subgrade is the natural material underneath constructed road layers, which provides the foundation

to support the pavement. In the research of Yuan et al. [20], characteristics of resilient modulus of the improved red clay at different additive content were studied through conducting laboratory repeated load triaxial tests, and they developed a comprehensive prediction model, which can be utilized to reflect the influence of compactness, moisture content, additive content, and stress state on resilient modulus.

**Acknowledgments:** This Special Issue would not be possible without the contributions of the above authors, hundreds of dedicated volunteer reviewers, and the editorial team of Applied Science.

**Conflicts of Interest:** The authors declare no conflict of interest.

## References

1. Nciri, N.; Shin, T.; Lee, H.; Cho, N. Potential of Waste Oyster Shells as a Novel Biofiller for Hot-Mix Asphalt. *Appl. Sci.* **2018**, *8*, 415. [CrossRef]
2. Wang, H.; Liu, X.; Apostolidis, P.; Scarpas, T. Non-Newtonian Behaviors of Crumb Rubber-Modified Bituminous Binders. *Appl. Sci.* **2018**, *8*, 1760. [CrossRef]
3. Guo, W.; Guo, X.; Chen, X.; Dai, W. Properties Analysis of Oil Shale Waste as Partial Aggregate Replacement in Open Grade Friction Course. *Appl. Sci.* **2018**, *8*, 1626. [CrossRef]
4. Huang, W.; Wang, D.; He, P.; Long, X.; Tong, B.; Tian, J.; Yu, P. Rheological Characteristics Evaluation of Bitumen Composites Containing Rock Asphalt and Diatomite. *Appl. Sci.* **2019**, *9*, 1023. [CrossRef]
5. Lv, S.; Wang, S.; Guo, T.; Xia, C.; Li, J.; Hou, G. Laboratory Evaluation on Performance of Compound-Modified Asphalt for Rock Asphalt/Styrene-Butadiene Rubber (SBR) and Rock Asphalt/Nano-CaCO. *Appl. Sci.* **2018**, *8*, 1009. [CrossRef]
6. Zhang, R.; Dai, Q.; You, Z.; Wang, H.; Peng, C. Rheological Performance of Bio-Char Modified Asphalt with Different Particle Sizes. *Appl. Sci.* **2018**, *8*, 1665. [CrossRef]
7. Zhou, C.; Liu, X.; Apostolidis, P.; Scarpas, T.; He, L. Induction Heating-Assisted Compaction in Porous Asphalt Pavements: A Computational Study. *Appl. Sci.* **2018**, *8*, 2308. [CrossRef]
8. Xu, S.; Tabaković, A.; Liu, X.; Palin, D.; Schlangen, E. Optimization of the Calcium Alginate Capsules for Self-Healing Asphalt. *Appl. Sci.* **2019**, *9*, 468. [CrossRef]
9. Wang, H.; Jin, K.; Dong, X.; Zhan, S.; Liu, C. Preparation Technique and Properties of Nano-TiO<sub>2</sub> Photocatalytic Coatings for Asphalt Pavement. *Appl. Sci.* **2018**, *8*, 2049. [CrossRef]
10. Wei, D.; Li, B.; Zhang, Z.; Han, F.; Zhang, X.; Zhang, M.; Li, L.; Wang, Q. Influence of Surface Texture Characteristics on the Noise in Grooving Concrete Pavement. *Appl. Sci.* **2018**, *8*, 2141. [CrossRef]
11. Wang, D.; Ding, X.; Ma, T.; Zhang, W.; Zhang, D. Algorithm for Virtual Aggregates' Reconstitution Based on Image Processing and Discrete-Element Modeling. *Appl. Sci.* **2018**, *8*, 738. [CrossRef]
12. Sun, L.; Wang, G.; Zhang, H.; Liu, L. Initiation and Propagation of Top-Down Cracking in Asphalt Pavement. *Appl. Sci.* **2018**, *8*, 774. [CrossRef]
13. Wang, H.; Yang, Z.; Zhan, S.; Ding, L.; Jin, K. Fatigue Performance and Model of Polyacrylonitrile Fiber Reinforced Asphalt Mixture. *Appl. Sci.* **2018**, *8*, 1818. [CrossRef]
14. Zhang, W.; Ma, T.; Xu, G.; Huang, X.; Ling, M.; Chen, X.; Xue, J. Fatigue Resistance Evaluation of Modified Asphalt Using a Multiple Stress Creep and Recovery (MSCR) Test. *Appl. Sci.* **2018**, *8*, 417. [CrossRef]
15. Sun, Y.; Yan, T.; Wu, C.; Sun, X.; Wang, J.; Yuan, X. Analysis of the Fatigue Crack Propagation Process of the Stress-Absorption Layer of Composite Pavement Based on Reliability. *Appl. Sci.* **2018**, *8*, 2093. [CrossRef]
16. Si, C.; Cao, H.; Chen, E.; You, Z.; Tian, R.; Zhang, R.; Gao, J. Dynamic Response Analysis of Rutting Resistance Performance of High Modulus Asphalt Concrete Pavement. *Appl. Sci.* **2018**, *8*, 2701. [CrossRef]
17. Jing, R.; Liu, X.; Varveri, A.; Scarpas, T.; Erkens, S. The Effect of Ageing on Chemical and Mechanical Properties of Asphalt Mortar. *Appl. Sci.* **2018**, *8*, 2231. [CrossRef]
18. Guan, H.-X.; Wang, H.-Q.; Liu, H.; Yan, J.-J.; Lin, M. The Effect of Intermediate Principal Stress on Compressive Strength of Different Cement Content of Cement-Stabilized Macadam and Different Gradation of AC-13 Mixture. *Appl. Sci.* **2018**, *8*, 2000. [CrossRef]
19. Lv, S.; Liu, C.; Lan, J.; Zhang, H.; Zheng, J.-L.; You, Z. Fatigue Equation of Cement-Treated Aggregate Base Materials under a True Stress Ratio. *Appl. Sci.* **2018**, *8*, 691. [CrossRef]

20. Yuan, H.; Li, W.; Wang, Y.; Lin, H.; Liu, Y. Resilient Modulus—Physical Parameters Relationship of Improved Red Clay by Dynamic Tri-Axial Test. *Appl. Sci.* **2019**, *9*, 1155. [CrossRef]

**Publisher’s Note:** MDPI stays neutral with regard to jurisdictional claims in published maps and institutional affiliations.



© 2020 by the authors. Licensee MDPI, Basel, Switzerland. This article is an open access article distributed under the terms and conditions of the Creative Commons Attribution (CC BY) license (<http://creativecommons.org/licenses/by/4.0/>).

Article

# Resilient Modulus—Physical Parameters Relationship of Improved Red Clay by Dynamic Tri-Axial Test

Haiping Yuan <sup>1</sup>, Weiqiang Li <sup>1</sup>, Yixian Wang <sup>1,2,\*</sup> , Hang Lin <sup>3</sup>  and Yan Liu <sup>4</sup>

<sup>1</sup> School of Civil Engineering, Hefei University of Technology, Hefei 230009, China; seapie@163.com (H.Y.); lwq2015@hfut.edu.cn (W.L.)

<sup>2</sup> State Key Laboratory of Geomechanics and Geotechnical Engineering, Institute of Rock and Soil Mechanics, Chinese Academy of Sciences, Wuhan 430071, China

<sup>3</sup> School of Resources and Safety Engineering, Central South University, Changsha 410083, China; linhangabc@126.com

<sup>4</sup> State Key Laboratory of Explosion Science and Technology (Beijing Institute of Technology), Beijing 100081, China; liuyan@bit.edu.cn

\* Correspondence: wangyixian2012@hfut.edu.cn

Received: 4 January 2019; Accepted: 7 March 2019; Published: 19 March 2019

**Abstract:** As one of the important parameters used in the analysis and design of subgrade, resilient modulus is directly related to the safety, economic and life time of subgrade structure. In this paper, the characteristics of resilient modulus of improved red clay at different additive content were studied through conducting laboratory repeated load tri-axial tests. The influence of stress state, moisture content, compactness, additive types, and content on resilient modulus were analyzed. In addition, the regression analysis of resilient modulus, was carried out referencing three existing prediction models. The results showed that the Andrei model can better fit the resilient modulus of red clay and have a higher determination coefficient. However, the Andrei model and other existing prediction models, reflect only the influence of stress state on resilient modulus, without considering the influence of moisture content, compactness and additive content. Therefore, based on the Andrei model, a comprehensive prediction model, which can reflect the influence of compactness, moisture content, additive content, and stress state on resilient modulus was introduced. Good agreement between the regression results and the measured ones demonstrated the integrative ability of the introduced model.

**Keywords:** red clay; additive; resilient modulus; prediction models; new comprehensive prediction model

---

## 1. Introduction

With the development of the national economy, high speed and heavy loads are inevitably the developing trend of the traffic line. In this context, static design methods will not be able to meet the increasing requirements of subgrade and pavement materials for strength and deformation. Therefore, more attention should be paid to dynamic and creep characteristics [1–8]. Soils and rocks are natural subgrade and pavement materials in the flood plain. When these are stressed, they go through stages of deformation such as elastic deformation, ductile deformation and fracture [9–20]. As a special soil, red clay is widespread in China and mainly located in the humid and rainy southern region. At present, land use is becoming more and more serious. It is the development direction and inevitable trend to make full use of the local red clay to fill the subgrade. However, the stability of the clay subgrade is particularly prominent because of the adverse factors, such as rainy weather and heavy load [21–24].

In addition, red clay should not be directly used as subgrade filling, due to the high natural moisture content and poor stability. It is necessary to include additives to improve the mechanical properties of red clay, so as to meet the filling requirements. At present, there have been some research on the mechanical properties of the improved red clay with additives, but the stability of the red clay subgrade, under dynamic loading is seldom involved [25–29].

The concept of dynamic resilient modulus of subgrade soil was introduced by Seed et al. [30], who studied the relationship between the resilient (elastic and reversible) characteristics of subgrade soil and the fatigue damage of asphalt pavement. In fact, the tensile stress and cracks, caused by the accumulation of permanent strains are the major cause of the damage of the subgrade and pavement materials [31–35]. Therefore, flexible pavement and resilient modulus values can replace compaction degree (CD) and California bearing ratio (CBR) values to reflect the stress-strain relationship of pavement structures under repeated vehicle load. A resilient modulus is one of the main parameters characterizing the mechanical properties of subgrade soils and can well-reflect the stability of subgrade soil [32]. However, it is difficult to apply and popularize a resilient modulus in practical engineering because of the test operation's complexity and high cost of tests. Therefore, it is necessary to establish models for the prediction of resilient modulus. Moreover, the prediction models can provide a reliable basis for the selection of material parameters in the structure design [36–41]. For a long time, many scholars at home and abroad have deeply explored the main factors affecting the resilient modulus of subgrade soil and established many prediction models, based on different factors, such as stress state and basic physical properties of soil [42–47]. According to the different stress variables, prediction models can be divided into three categories: Single factor model related to mass stress, a composite model related to shear stress and mass stress, and a composite model related to shear stress and confining pressure [48–60]. However, most of existing prediction models only consider the influence of stress state on the resilient modulus [42], and rarely consider the influence of compactness, moisture content, and additive content. They are generally linear fitting [35–38], or combine a single physical parameter to predict the resilient modulus [43,44].

In the design of subgrade structure, the resilient modulus is different, according to the subgrade grade. In this paper, the red clay in Anhui, China was chosen to be improved by two types of additives. Through laboratory repeated load tri-axial tests, the influence of stress state, moisture content, compactness, additive type, and content on resilient modulus were analyzed. According to the research experience [61–66], based on existing prediction models, which fail to incorporate the influence of moisture content, compactness and additive content, a comprehensive prediction model which can reflect the influence of compactness, moisture content, additive content and stress state on resilient modulus was introduced. To conclude the performance of the introduced model, the predicted and the measured resilient modulus were paralleled. The parallel found the introduced model capable of capturing the characteristics of the measured resilient modulus [54]. By comparison and verification, it was found that the proposed model predicts the modulus of resilience of the improved clay with additives of various contents, indicating that it has some potential in engineering applications.

## **2. Material Properties and Testing Method**

### *2.1. Materials*

The basic properties of the red clay used in the test are shown in Table 1. In order to analyze the influence of stress state, moisture content, compactness, additive type and content on the resilient modulus of red clay, samples prepared at different moisture content (OMC minus 3%, OMC, OMC plus 3%), different compactness of P (91%, 93%, 95%), different additive types (ordinary Portland cement, lime) and content (3%, 6%, 9%) were tested.

**Table 1.** Basic properties of red clay.

Samples	Grain Density	Natural Dry Density	Maximum Dry Density	Optimum Moisture Content	Liquid Limit	Plastic Limit	<0.075mm Grain Size
	/(g/cm)	/(g/cm)	/(g/cm)	/%	/%	/%	Soil particle content/%
Red clay	2.72	1.28	1.73	27.8	52.6	30.7	90

The chemical and mineral compositions of the red clay, obtained from X-ray diffraction measurements, are summarized in Table 2, and Table 3, respectively. It is indicated that the mineral compositions include mainly kaolinite (i.e.,  $\text{Al}_2\text{Si}_2\text{O}_5(\text{OH})_4$ ), goethite (i.e.,  $\text{FeO}(\text{OH})$ ), and diasporite (i.e.,  $\text{SiO}_2$ ). The amount of kaolinite is 60.87%. Therefore, kaolinite dominates the mineral compositions of the red clay.

**Table 2.** Chemical compositions of red clay.

Constituents	$\text{SiO}_2$	$\text{Al}_2\text{O}_3$	$\text{Fe}_2\text{O}_3$	$\text{K}_2\text{O}$	$\text{MgO}$	$\text{CaO}$	$\text{Na}_2\text{O}$	LOI
Content(%)	40.27	32.65	18.52	2.51	0.91	0.72	0.24	4.18

**Table 3.** Mineral composition of red clay.

Mineral	Mineral Compositions/(%)				
	$\text{Al}_2\text{Si}_2\text{O}_5(\text{OH})_4$	$\text{Al}(\text{OH})_3$	$\text{FeO}(\text{OH})$	$\text{SiO}_2$	Deviation
Content(%)	60.87	11.72	13.13	11.96	-2.32

Proctor compaction tests were carried out to determine maximum dry densities and optimum moisture contents of the improved red clay samples which are presented in Table 4. Based on the compaction test results, the samples were prepared at the targeted compactness and moisture content.

**Table 4.** Proctor compaction test results on samples with different additive contents.

Cement Content/%	Optimum Moisture Content/%	Maximum Dry Density/(g/cm <sup>3</sup> )	Lime Content/%	Optimum Moisture Content/%	Maximum Dry Density/(g/cm <sup>3</sup> )
3	25.6	1.75	3	26.2	1.74
6	24.3	1.76	6	25.1	1.75
9	23.2	1.78	9	24.2	1.76

The samples were prepared according to China highway geotechnical test code (JTGE40-2007). The samples were prepared as follows: Drying, grinding, mixing with additive, curing, and preparation. Three parallel samples were prepared for each group with different admixtures. The samples were placed in a standard curing room with  $25 \pm 2^\circ\text{C}$  for 7 days. For each sample, the difference between the actual and the targeted moisture contents is less than 1%, and that difference is less than 2% for compactness.

## 2.2. Testing Method

In the test, the resilient modulus values were measured by the dynamic servo system UTM400. The loading waveform is half-sine waveform and the load frequency is 1 Hz. The holding time and interval time are 0.1 s, and 0.9 s, respectively. The repeated load and resilient strain were measured by load sensor and displacement sensor respectively in the dynamic tri-axial chamber. The adopted stress loading sequence of subgrade soil was obtained from the international research results [67–70]. It is necessary to preload the samples before the test to simulate the history of subgrade stress during construction, eliminate the influence of load difference factors, such as initial loading and repeated loading and reduce the variability of test results. In addition, preloading can eliminate the possible bad contact between the bottom of the samples and the pressure plate to improve the accuracy of the

test [70]. A dynamic resilient modulus is defined as the ratio of repeated axial deviatoric stress to the recoverable axial strain as Figure 1. The cyclic number of loading is 100, and the average resilient deformation during the last 5 cycles, for each magnitude of repeated loading, was recorded. The dynamic resilient modulus of samples was calculated according to Equation (1).

$$M_r = \frac{\Delta\sigma_d}{\Delta\varepsilon_{axial}} \tag{1}$$

where  $\Delta\sigma_d$  = deviatoric stress ( $= \sigma_1 - \sigma_3$ ),  $\sigma_1$  and  $\sigma_3$  = major and minor principal stresses, and  $\Delta\varepsilon_{axial}$  = recoverable axial strain.

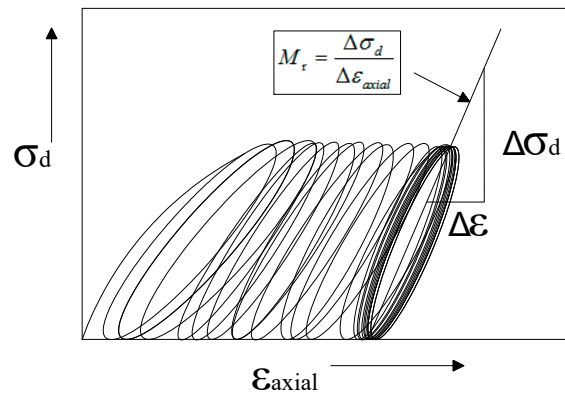


Figure 1. Definition of dynamic resilient modulus (Hopkins et al., 2001 [51]).

### 3. Analysis of Results

#### 3.1. Influence of Stress State on Resilient Modulus

Figure 2 shows the variation of resilient modulus with deviatoric stress and bulk stress of the improved red clay. It can be seen from Figure 2 that for the improved red clay, when the confining pressure is constant, the resilient modulus decreases with an increase in deviatoric stress; when the deviatoric stress is constant, the resilient modulus increases with an increase in confining pressure. At the same time, in the repeated load triaxial test,  $\sigma_2 = \sigma_3 =$  confining pressure,  $3\sigma_3 + \sigma_d =$  bulk stress, octahedral shear stress is  $\tau_{oct} = \sqrt{2}\sigma_d/3$ . Therefore, the effects of confining pressure and deviatoric stress on the resilient modulus need to be discussed. The results of the two-factor variance analysis of resilient modulus of the improved red clay, with 3% cementor 3% lime, are presented in Table 5. It can be seen from Table 5 that the effects of confining pressure and deviatoric stress on the resilient modulus are remarkable.

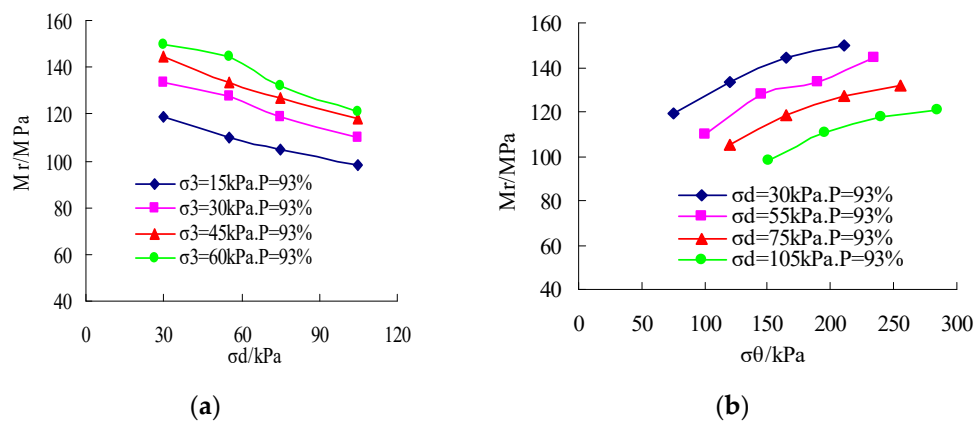
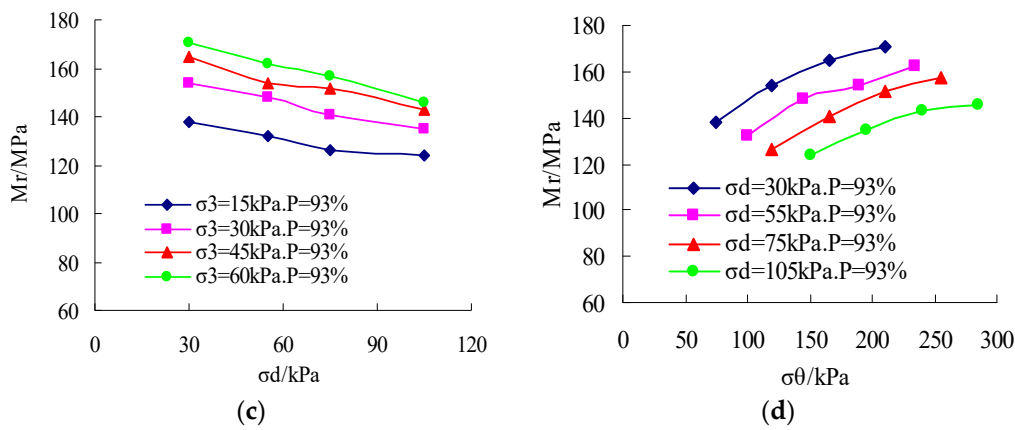


Figure 2. Cont.





**Figure 2.** Variation of resilient modulus with deviatoric stress and bulk stress. (a) Lime 3% OMC  $M_r - \sigma_d$ ; (b) Lime 3% OMC  $M_r - \sigma_\theta$ ; (c) Cement 3% OMC  $M_r - \sigma_d$ ; (d) Cement 3% OMC  $M_r - \sigma_\theta$ .

**Table 5.** Two-factor variance analysis of resilient modulus.

<b>(a) Improved red clay with 3% cement</b>						
Source of Variation	Variance Sum	Degree of Freedom	Mean Square Error	F Value	Critical Value $\alpha = 0.05$	Significance
Deviatoric stress	2397.41	3	799.136	134.39	3.86	Significant
Confining pressure	1832.63	3	610.877	102.73	3.86	Significant
Error	53.52	9	5.946			
Sum	4283.56	15				
<b>(b) Improved red clay with 3% lime</b>						
Source of Variation	Variance Sum	Degree of Freedom	Mean Square Error	F Value	Critical Value $\alpha = 0.05$	Significance
Deviatoric stress	1853.83	3	617.942	178.36	3.86	Significant
Confining pressure	1870.63	3	623.544	179.98	3.86	Significant
Error	31.18	9	3.465			
Sum	3755.64	15				

### 3.2. Prediction Models of Resilient Modulus

The concept of a resilient modulus has been used to represent the non-linear stress-strain characteristics of subgrade soils. From the above analysis, it can be concluded that the resilient modulus of improved red clay has a strong dependence on the stress state. Several prediction models have been developed in the past to express the relationship between resilient modulus and stress state. The prediction models of non-linear resilient modulus mainly include the single factor model related to bulk stress or deviatoric stress [36], the composite model related to deviatoric stress, and mass stress [38], the composite model related to shear stress and confining pressure [40], and the composite model related to confining pressure and deviatoric stress [41]. In this paper, three prediction models frequently cited were chosen to analyze the influence of deviatoric stress and confining pressure on the resilient modulus of the improved red clay.

#### 3.2.1. Uzan-Witczak Model

Uzan-witczak [38] introduced deviatoric stress and bulk stress to characterize the influence of stress state on the resilient modulus, and established the nonlinear constitutive model, as shown in Equation (2).

$$M_R = k_1 \theta^{k_2} \sigma_d^{k_3} \tag{2}$$

where  $\sigma_d$  is the deviatoric stress and  $k_1, k_2$  and  $k_3$  are regression coefficients.

$\theta$  is the bulk stress that is given as

$$\theta = \sigma_1 + \sigma_2 + \sigma_3$$

where  $\sigma_1$  is the major principal stress;  $\sigma_2$  is the intermediate principal stress, and  $\sigma_3$  is the minor principal stress or confining pressure (=  $\sigma_2$  for  $M_R$  test in triaxial test)

However, this prediction model has some limitations: when  $\sigma_d$  equals 0, the result of Equation (2) tends to infinity. When  $\sigma_1$  and  $\sigma_3$  equal 0, the result is  $0 \cdot \infty$ .

### 3.2.2. Andrei Model

In the practical problem, the intermediate and the minor principal stresses are not equal. In order to consider the influence of both of them on the resilient modulus, Andrei model [40] introduced the octahedral shear stress to replace the deviatoric stress in the May and Witczak model [71]. This operation provides a better explanation of the stress state of the materials, and further generalize the nonlinear constitutive model, as shown in Equation (3).

$$M_R = k_1 P_a \left( \frac{\theta}{P_a} \right)^{k_2} \left( \frac{\tau_{oct}}{P_a} + 1 \right)^{k_3} \quad (3)$$

where  $\tau_{oct}$  is the octahedral shear stress,  $P_a$  = atmospheric pressure and  $k_1, k_2$  and  $k_3$  are regression coefficients.

$\theta$  is the mass stress that is given as

$$\theta = \sigma_1 + \sigma_2 + \sigma_3$$

$\tau_{oct}$  is given as

$$\tau_{oct} = \frac{1}{3} \sqrt{(\sigma_1 - \sigma_3)^2 + (\sigma_1 - \sigma_2)^2 + (\sigma_2 - \sigma_3)^2}$$

where  $\sigma_1$  is the major principal stress;  $\sigma_2$  is the intermediate principal stress and  $\sigma_3$  is the minor principal stress or confining pressure.

In this prediction model, the influence of bulk stress and octahedral shear stress on the resilient modulus was fully taken into account. Compared with Equation (2), the Andrei model is essentially consistent with the Uzan-Witczak model. The difference between them is that the term  $\frac{\tau_{oct}}{P_a}$  in the Andrei model is followed by an additional constant of 1, eliminating the existing problems of the Uzan-Witczak model.

### 3.2.3. Ni Model

Based on testing results, Ni et al. [41] found that the resilient modulus was very sensitive to confining pressure, because of this, they introduced confining pressure and deviatoric stress to the prediction model to eliminate the existing problems included in the above Uzan-Witczak model. The following prediction model was given (Equation (4)):

$$M_R = k_1 P_a \left( \frac{\sigma_3}{P_a} + 1 \right)^{k_2} \left( \frac{\sigma_d}{P_a} + 1 \right)^{k_3} \quad (4)$$

where  $\sigma_3$  is the minor principal stress or confining pressure,  $\sigma_d$  is the deviatoric stress,  $P_a$  = atmospheric pressure, and  $k_1, k_2$  and  $k_3$  are regression coefficients.

Due to the difference in the physical properties of red clay in different regions, the selected prediction models were different from each other. In this paper, the above-mentioned prediction models of the resilient modulus were selected for red clay in Anhui province.

### 3.3. Regression Analysis Results

The fitting performance of a regression model is frequently evaluated by the determination coefficient,  $R^2$ , defined as the ratio of regression sum of squares (SSR) to total sum of square (SST), that is  $R^2 = SSR/SST$ .

$$SSR = \sum_{i=1}^n (y_i - \hat{y}_i)^2 \quad (5)$$

$$SST = \sum_{i=1}^n (y_i - \bar{y}_i)^2 \quad (6)$$

In Equations (5) and (6),  $y_i$  is actual value,  $\hat{y}_i$  is predicted value,  $\bar{y}_i$  is sample mean, SSR is regression sum of squares, SST is total sum of square.

Regression analysis of the test data was conducted for various conditions, and the results are shown in Table 6. From the regression results, a high coefficient of determination between the three prediction models, and the test results, is observed. For the Uzan-Witczak model, NI model and Andrei model, the coefficient of determination  $R^2$  was greater than 0.80, 0.934, and 0.937, respectively. By comparing the coefficients of determination for the three prediction models, it can be concluded that the regression results, generated by the Andrei model and the NI model, are better than the regression results generated by the Uzan-Witczak model. In particular, the Andrei model can fit the test data better than the NI model does.

In the above three prediction models of the resilient modulus,  $k_1$  is used to characterize the stiffness of the subgrade soil and is proportional to the resilient modulus. The value of  $k_1$  increases with an increase in effective stress, additive content and compactness, and decreases with an increase in moisture content.  $k_2$  reflects the influence of confining pressure (bulk stress) on resilient modulus and is positively associated with confining pressure. The value of  $k_2$  as a whole decreases with an increase in moisture content, and increases with an increase in additive content and compactness. The value of  $k_3$  is negative, indicating that a negative correlation between the resilient modulus and the deviatoric stress (octahedral shear stress).  $k_3$  shows that the dynamic resilient modulus of subgrade soils decreases with an increase in shear stress, and its value is not obviously related to the moisture content and the compactness.

**Table 6.** Parameters required in different prediction models of resilient modulus.

Additive Content	Compactness/%	Moisture Content/%	Uzan-Witzak Model			NI Model			Andrei Model					
			k1	k2	k3	R2	k1	k2	k3	R2	k1	k2	k3	R2
C6%	93	OMC minus 3%	139.6	0.2047	-0.2176	0.9260	1791.6	0.5045	-0.3637	0.9556	2033.8	0.1974	-0.9476	0.9618
		OMC	148.88	0.1953	-0.2225	0.9146	1733	0.5054	-0.4431	0.9421	1960.5	0.1999	-1.0855	0.9569
		OMC plus 3%	152.38	0.1083	-0.1391	0.9191	1585	0.2844	-0.2882	0.9669	1697.6	0.1116	-0.6782	0.9739
L6%		OMC minus 3%	123.97	0.2168	-0.2198	0.9375	1578.1	0.5632	-0.4147	0.9718	1816.1	0.2214	-1.0717	0.9812
		OMC	149.13	0.1901	-0.2585	0.934	1513	0.5253	-0.5224	0.9782	1716.3	0.2016	-1.2226	0.9721
		OMC minus 3%	129.48	0.1445	-0.1667	0.9182	1439.2	0.3776	-0.3333	0.9662	1579.2	0.1489	-0.8169	0.9788
C6%			155.61	0.1811	-0.2402	0.8621	1667.8	0.4873	-0.5172	0.9342	1874.8	0.189	-1.1987	0.9434
			148.88	0.1953	-0.2225	0.9146	1733	0.5054	-0.4431	0.9421	1960.5	0.1999	-1.0855	0.9569
		OMC	165.93	0.198	-0.2418	0.8084	1851.3	0.5399	-0.5119	0.9005	2112.9	0.2086	-1.2227	0.909
L6%			115.10	0.2107	-0.2136	0.9266	1446.8	0.557	-0.3953	0.962	1664	0.2123	-1.0225	0.9374
			149.13	0.1901	-0.2585	0.934	1513	0.5253	-0.5224	0.9782	1716.3	0.2016	-1.2226	0.9721
		OMC	144.19	0.2147	-0.244	0.8937	1708	0.5644	-0.4923	0.945	1961.7	0.2216	-1.2071	0.96
C3%		94.43	0.2335	-0.1859	0.9596	1405	0.5954	-0.2959	0.9664	1637.3	0.236	-0.8898	0.9753	
C6%		148.88	0.1953	-0.2225	0.9146	1733	0.5054	-0.4431	0.9421	1960.5	0.1999	-1.0855	0.9569	
C9%		107.73	0.2577	-0.2073	0.9224	1655.5	0.6738	-0.3373	0.9656	1969.8	0.2615	-1.0027	0.9514	
L3%	93	86.24	0.2671	-0.2462	0.9399	1241.3	0.6923	-0.4427	0.9681	1477.3	0.2719	-1.1974	0.974	
L6%		149.13	0.1901	-0.2585	0.934	1513	0.5253	-0.5224	0.9782	1716.3	0.2016	-1.2226	0.9721	
L9%		155.61	0.1885	-0.2449	0.9156	1658.2	0.4997	-0.5133	0.9545	1868.9	0.1928	-1.1943	0.9543	

Table 7 and Figure 3 show that predicted resilient modulus versus measured resilient modulus for the improved red clay prepared at 93% compactness and 6% additive (cement and lime). It can be seen that the maximum errors, between the measured and the predicted resilient modulus, by using the Andrei model, NI model and Uzan-Witczak model are, respectively, 4.533%, 3.934%, and 6.133%. In addition, the average error and variance of Andrei, NI and Uzan-Witczak models are  $1.70\% \pm 1.14\%$ ,  $2.11\% \pm 1.07\%$ , and  $2.32\% \pm 1.75\%$ , respectively. It can be concluded that the fitting performance of Andrei model is better than that of NI model and Uzan-Witczak model.

**Table 7.** Test data and forecast data of different prediction models.

Mass Stress $\sigma/kPa$	Octahedral Shear Stress/kPa	Measured Data/Mpa	Resilient Modulus					
			Andrei Model		NI Model		Uzan-Witczak Model	
			Predicted Value/Mpa	Error/%	Predicted Value/Mpa	Error/%	Predicted Value/Mpa	Error/%
75	14.14	160	160.3371	0.2102	165.572	3.3653	162.302	1.4184
100	25.93	150	152.6465	1.7338	153.1579	2.0618	150.0214	0.0143
120	35.36	144	146.379	1.6252	145.1393	0.785	145.0932	0.7534
150	49.5	132	137.405	3.9336	135.3122	2.4479	140.6242	6.1328
120	14.14	180	176.1317	2.1962	176.1559	2.1822	177.9052	1.1775
145	25.93	167.4	164.4161	1.8148	162.9482	2.732	161.3126	3.7736
165	35.36	158	156.0003	1.2819	154.4171	2.3203	154.4036	2.3292
195	49.5	145.9	144.8037	0.7571	143.9618	1.3463	148.0175	1.4306
165	14.14	187	187.7086	0.3775	186.1511	0.456	189.3211	1.226
190	25.93	180	173.5441	3.7201	172.194	4.5333	170.0567	5.847
210	35.36	165.3	163.705	0.9743	163.1788	1.2999	161.8498	2.1317
240	49.5	153.5	150.9406	1.6956	152.1303	0.9003	154.1433	0.4173
210	14.14	190.5	196.9794	3.2894	195.6467	2.6306	198.4513	4.0067
235	25.93	182.7	181.077	0.8963	180.9776	0.9517	177.2649	3.0661
255	35.36	166	170.1836	2.4583	171.5026	3.2084	168.1048	1.2521
285	49.5	155.9	156.2159	0.2022	159.8905	2.4958	159.4045	2.1985

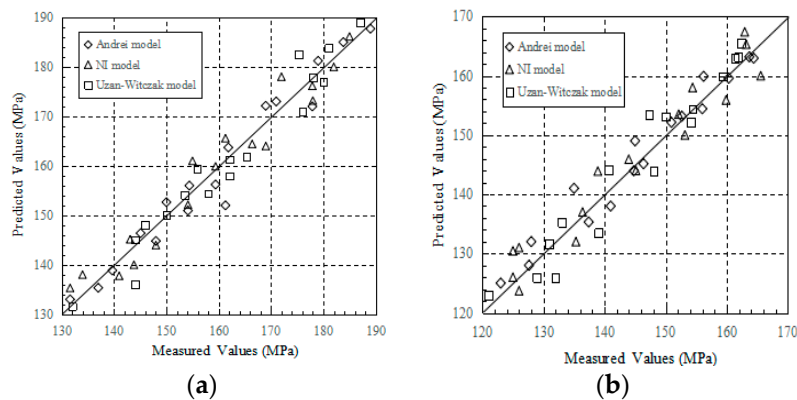


**Figure 3.** Predicted resilient modulus versus measured resilient modulus by three prediction models (Andrei model, NI model and Uzan-Witczak model). (a) 93% compactness and 6% cement; (b) 93% compactness and 6% lime.

#### 4. The Dependence of Resilient Modulus on Material Properties

##### 4.1. The Influence of Moisture Content and Compactness on Resilient Modulus

The improved red clay samples, prepared at 93% compactness and 6% cement (C6%), and prepared at 93% compactness and 6% lime (L6%), were selected to study the influence of different moisture content on the dynamic resilient modulus of the improved red clay. As can be seen from Figure 4, the resilient modulus of the improved red clay is greatly affected by moisture content, and its value decreases with an increase in moisture content. For the improved red clay with 6% cement, when the confining pressure is 15 kPa and the deviatoric stress is 30 kPa, the resilient modulus for the optimum moisture content (OMC) of 21.5% (OMC minus 3%), 24.3% (OMC), 27.1% (OMC plus 3%) is 171.2 MPa, 158.0 MPa, 147.7 MPa, respectively. Compared with the moisture content of 21.5% (OMC

minus 3%), the resilient modulus for moisture content of 24.3%, and 27.1% (OMC plus 3%) decreases by 7.71%, and 14.1%, respectively. In addition, when the moisture content is invariable, the resilient modulus of improved red clay decreases with an increase in deviatoric stress, and increases with an increase in mass stress.

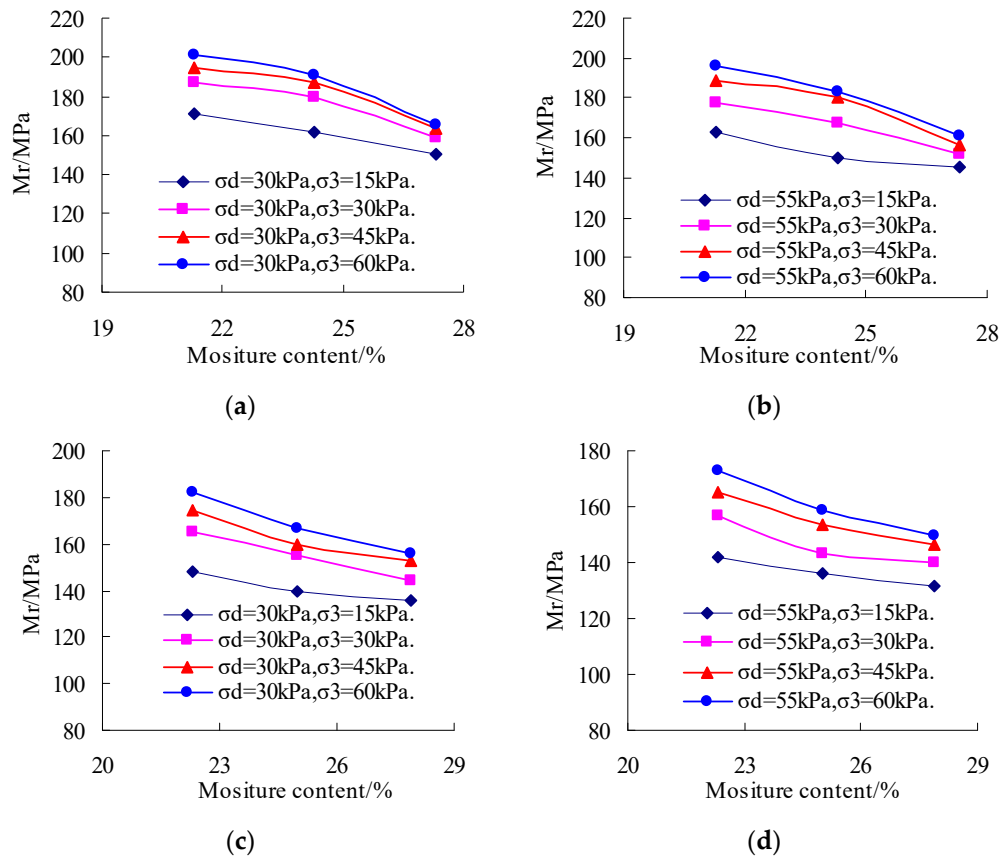


**Figure 4.**  $M_R - w$  relation curve at different stress states. (a)  $C6\%$ ,  $P93\%$ ,  $\sigma_d = 30$  kPa; (b)  $C6\%$ ,  $P93\%$ ,  $\sigma_d = 55$  kPa; (c)  $L6\%$ ,  $OMC$ ,  $\sigma_d = 30$  kPa; (d)  $L6\%$ ,  $P93\%$ ,  $\sigma_d = 55$  kPa.

The improved red clay samples, prepared at optimum moisture content and 6% cement, and prepared at OMC and 6% lime ( $L6\%$ ), were selected to study the influence of different compactness on the dynamic resilient modulus. As can be seen from Figure 5, when the moisture content is invariable, the resilient modulus of the improved red clay increases with an increase in compactness. For the improved red clay with 6% cement, when the confining pressure is 60 kPa and the deviatoric stress is 30 kPa, the resilient modulus for the red clay samples, when prepared at a compactness of 91%, 93%, and 95% is 177.89 MPa, 190.5 MPa, and 204.67 kPa, respectively. Compared with 91% compactness, the resilient modulus for compactness of 93%, and 95% increases by 7.08%, and 15.05%, respectively. In addition, when the compactness is invariable, the resilient modulus of the improved red clay decreases with an increase in deviatoric stress and increases with an increase in bulk stress.

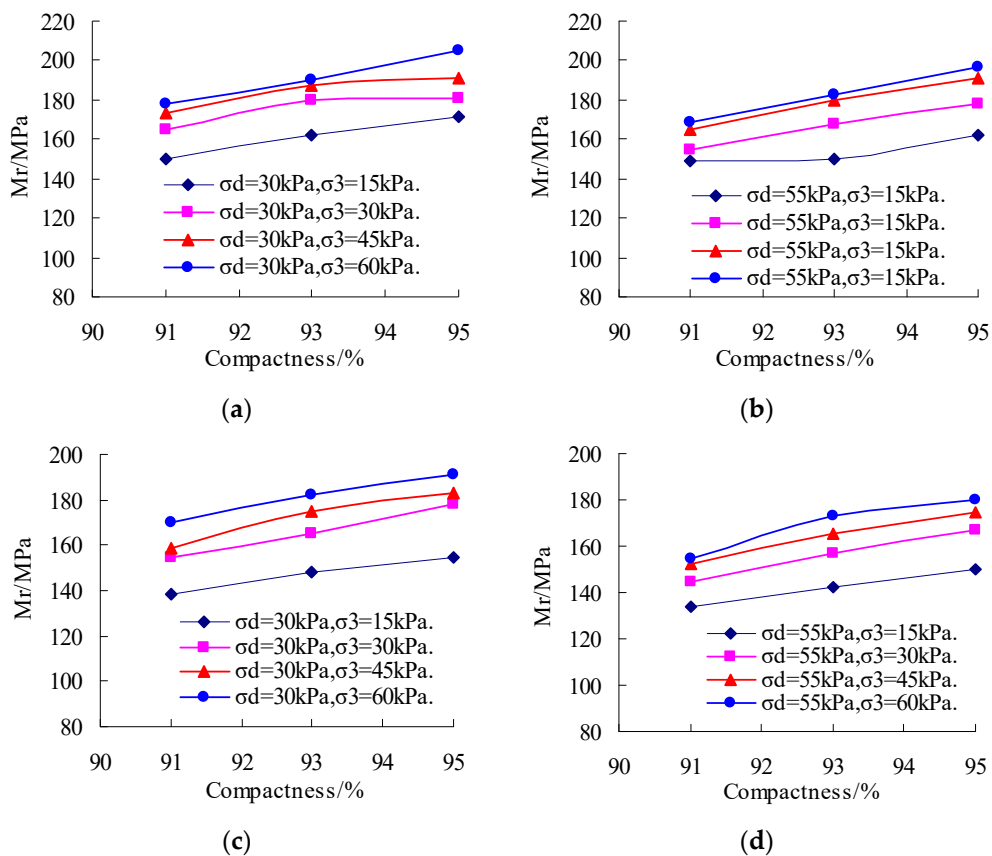


**Figure 5.**  $M_R - P$  curve at different stress states. (a) C6%, OMC,  $\sigma_d = 30$  kPa; (b) C6%, OMC,  $\sigma_d = 55$  kPa; (c) L6%, OMC,  $\sigma_d = 30$  kPa; (d) L6%, OMC,  $\sigma_d = 55$  kPa.

#### 4.2. The Influence of Additive Content on Resilient Modulus

The improved red clay prepared at optimum moisture content and 93% compactness were selected to study the influence of different additives on the dynamic resilient modulus of the improved red clay. As can be seen from Figures 6 and 7, both cement and lime (3–9%) can significantly improve the dynamic resilient modulus of the red clay. In Figure 6, when the confining pressure is 60 kPa and the deviatoric stress is 30 kPa, the resilient modulus of red clay samples, prepared at a lime content of 3%, 6%, and 9% is 149.9 MPa, 166 MPa, and 180.6 MPa, respectively. Compared with 3% lime, the resilient modulus for lime content of 6%, 9% increases by 10.75%, and 20.4%, respectively. In Figure 7, when the confining pressure is 60 kPa and the deviatoric stress is 30 kPa, the resilient modulus of red clay with cement content of 3%, 6%, and 9% is 170.4 MPa, 190.5 MPa, and 202 MPa, respectively. Compared with 3% cement, the resilient modulus for cement content of 6%, and 9% increases by 11.8%, and 18.54%, respectively. By comparing Figure 6a with Figure 7a, it can be concluded that when the confining pressure is 60 kPa and the deviatoric stress is 30 kPa, an increase of 12% in the dynamic resilient modulus was observed for 3% cement, compared with that of 3% lime. By comparing other data, it can be also seen that, when the contents of cement and lime are the same, cement can significantly improve the resilient modulus of red clay.



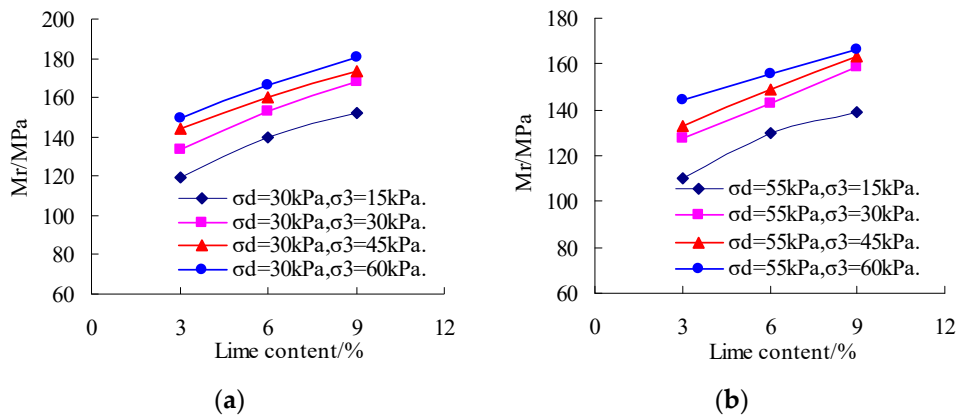


**Figure 6.** Relationship between resilient modulus ( $M_r$ ) and lime content for various stress states. (a) OMC, P93%,  $\sigma_d = 30$  kPa; (b) OMC, P93%,  $\sigma_d = 55$  kPa.

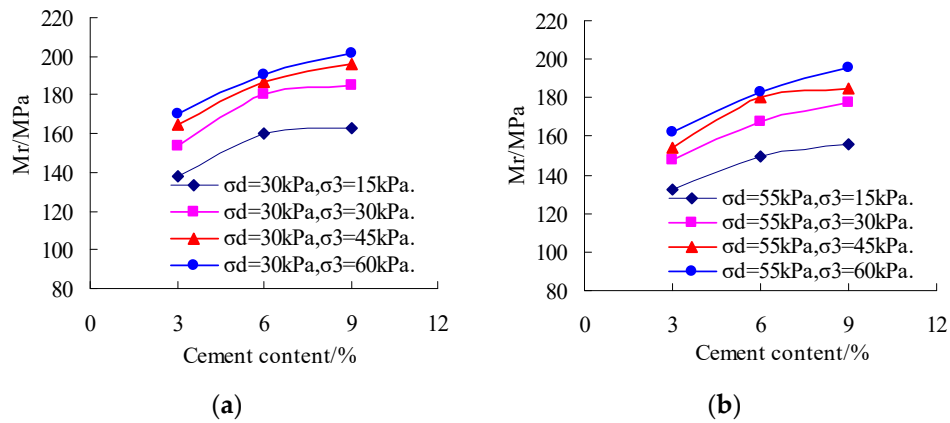


**Figure 7.** Relationship between resilient modulus ( $M_r$ ) and cement content for various stress states. (a) OMC, P93%,  $\sigma_d = 30$  kPa; (b) OMC, P93%,  $\sigma_d = 55$  kPa.

#### 4.3. New Comprehensive Prediction Model

From the analysis of the existing prediction models, it can be concluded that the Andrei model can better predict the resilient modulus of the red clay chosen for this test. However, the Andrei model and other existing prediction models reflect only the influence of the stress state on resilient modulus, but the influence of moisture content, compactness, and additive content were not considered. Lu et al. proposed a new methodology to convert the band shaped drain into an annular instead of a circle to keep the sectional area or perimeter of the band shaped drain unchanged before and after the conversion [72]. From Figure 4 through 7, it can be seen that the resilient modulus is correlated negatively with moisture content, meaning that the higher the moisture content, the smaller the resilient modulus. Additionally, the resilient modulus is correlated positively with the compactness and the additive content, which means that the greater the compactness and the additive content, the larger the resilient modulus. It can be concluded that the influence of compactness, moisture content, and additive content on the resilient modulus is remarkable.

In this paper, considering the above factors affecting the resilient modulus, the relationship between moisture content ( $W$ ), compactness ( $P$ ), additive content ( $C$ ), octahedral shear stress ( $\tau_{oct}$ ), bulk stress ( $\theta$ ), atmospheric pressure ( $P_a$ ) and resilient modulus ( $M_R$ ) are established, which is expressed as a Equation (7).

$$F(W, P, C, \tau_{oct}, \theta, P_a, M_R) = 0 \tag{7}$$

As the resilient modulus is correlated positively with the compactness and the additive content, and negatively with the moisture content, based on dimensional analysis [73], Equation (7) can be transformed into Equation (8).

$$F(P/W, C/W, \tau_{oct}/P_a, \theta/P_a, M_R) = 0 \tag{8}$$

On this basis, combined with the above existing prediction models, to eliminate the influence of dimension, the compactness and the additive content were normalized by the moisture content, respectively. The following prediction model was given (Equation (9)). In Equation (9), to eliminate the problem that the predicted value of resilient modulus is 0,  $\frac{C}{W}$  and  $\frac{\tau_{oct}}{P_a}$  add 1, respectively.

$$M_R = k_1 P_a \left(\frac{P}{W}\right)^{k_2} \left(\frac{C}{W} + 1\right)^{k_3} \left(\frac{\theta}{P_a}\right)^{k_4} \left(\frac{\tau_{oct}}{P_a} + 1\right)^{k_5} \tag{9}$$

where  $\tau_{oct}$  is the octahedral shear stress,  $P_a$  = atmospheric pressure,  $k_1, k_2, k_3, k_4$  and  $k_5$  are regression coefficients,  $\theta$  is the bulk stress,  $P$  is compactness,  $C$  is additive content,  $W$  is moisture content, and  $P_a$  is atmospheric pressure.

Regression analysis of the testing results on the red clay samples improved with cement and/or lime was carried out by using Equation (9). Presented in Table 8 are the parameters that the proposed prediction model requires, the determination coefficient of improved red clay samples prepared at different moisture content, and the compactness and additive content. For prediction models, the greater the determination coefficient,  $R^2$ , the better the regression effect, indicating a higher rationality and reliability of the prediction model. The determination coefficient of the proposed comprehensive prediction model for the additive of cement and lime is 0.84, and 0.86, respectively.

**Table 8.** Comprehensive prediction model regression equation for two additives.

Additive	Comprehensive Prediction Model Regression Equation	R <sup>2</sup>
Cement	$M_R = 0.6896P_a \left(\frac{P}{W}\right)^{0.5197} \left(\frac{C}{W} + 1\right)^{1.2702} \left(\frac{\theta}{P_a}\right)^{0.2042} \left(\frac{\tau_{oct}}{P_a} + 1\right)^{-0.9383}$	0.84
Lime	$M_R = 0.8096P_a \left(\frac{P}{W}\right)^{0.4186} \left(\frac{C}{W} + 1\right)^{0.9594} \left(\frac{\theta}{P_a}\right)^{0.2191} \left(\frac{\tau_{oct}}{P_a} + 1\right)^{-1.1321}$	0.86

The comparison between the predicted and the measured values are presented in Figures 8 and 9. As shown in Figures 8 and 9, the maximum error between the predicted and the testing results for different cement and lime contents is 8.67%, and 8.70%, respectively. In addition, the average error and variance of the new comprehensive prediction model for different cement and lime contents are, respectively,  $3.18\% \pm 4.03\%$ , and  $3.06\% \pm 3.94\%$ . The new comprehensive prediction model, which reflects the influence of compactness, moisture content, additive content, and stress state on resilient modulus has good regression performance.

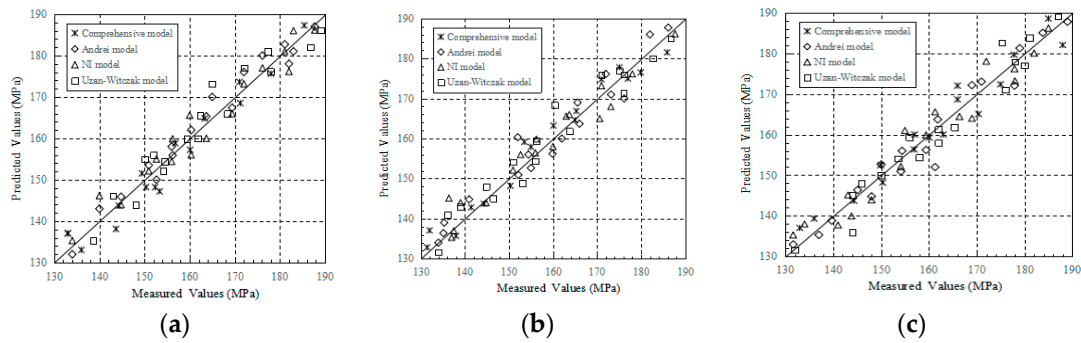


**Figure 8.** Predicted resilient modulus versus measured resilient modulus at different optimum moisture content, compactness and cement by four prediction models (comprehensive model, Andrei model, NI model & Uzan-Witczak model). (a) 93% compactness and 6% cement; (b) optimum moisture content (OMC) and 6% cement; (c) 93% compactness and OMC.

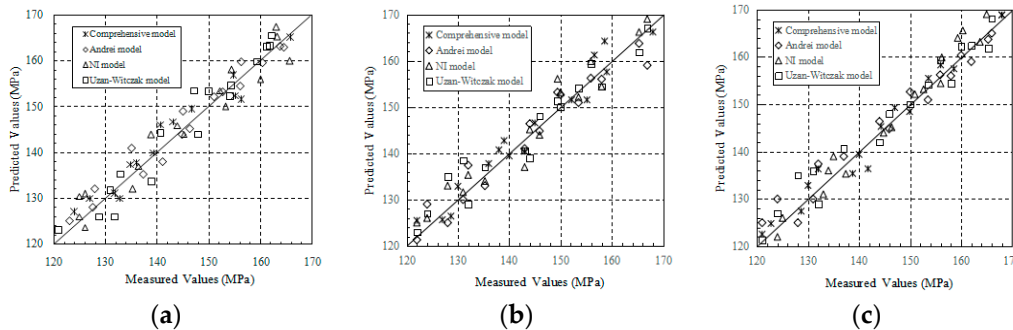


**Figure 9.** Predicted resilient modulus versus measured resilient modulus at different optimum moisture content, compactness and lime by four prediction models (Comprehensive model, Andrei model, NI model and Uzan-Witczak model). (a) 93% compactness and 6% lime; (b) OMC and 6% lime; (c) 93% compactness and OMC.

## 5. Conclusions

Due to the great difference in the physical properties of red clay in different regions, it is necessary to point out that the above predicted results are only applicable to the prediction of resilient modulus and improvement of red clay in Anhui province.

1. The testing results showed that the dynamic resilient modulus of red clay can be obviously increased by adding cement or lime (3–9%). In addition, the dynamic resilient modulus increases with an increase in compactness and additive content, and decreases with an increase in moisture content. Testing results also showed that, when the contents of cement and lime in red clay samples were the same, the dynamic resilient modulus of red clay improved with cement was slightly higher compared to that improved with lime.

2. Through a variance analysis of stress state, it can be concluded that the influence of deviatoric stress, and bulk stress on dynamic resilient modulus are significant, but the influence of deviatoric stress are more obvious. The dynamic resilient modulus of red clay increases with an increase in confining pressure. In addition, it decreases with an increase in deviatoric stress when the confining pressure is invariable, and increases with an increase in bulk stress when the deviatoric stress is invariable.

3. Three existing prediction models were used to predict the resilient modulus of the improved red clay. A comparison of the predicted results, using these prediction models, indicated that the fitting performance of the Andrei model was the best. The resilient modulus is not only affected by the stress state, but also by the compactness, moisture content, and additive content. Therefore, based on the Andrei models, a new comprehensive prediction model was proposed to reflect the influence of compactness, moisture content, additive content and stress state on resilient modulus.

By comparing the regression values with the measured values, it can be concluded that the new comprehensive prediction model has a good regression performance. The good performance applies to various additive contents, demonstrating a good potential of engineering application for the proposed prediction model.

**Author Contributions:** H.Y. and Y.W. conceived and designed the experiments; W.L. performed the experiments; H.L. and Y.L. analyzed the data; W.L. wrote the paper.

**Acknowledgments:** This research was funded by the National Natural Science Foundation of China (51874112;51774107), the Open Research Fund of State Key Laboratory of Geo-mechanics and Geotechnical Engineering, Institute of Rock and Soil Mechanics, Chinese Academy of Sciences (Z013010), the Opening Project of State Key Laboratory of Explosion Science and Technology, Beijing Institute of Technology (No. KFJJ19-02M). All financial support is gratefully acknowledged.

**Conflicts of Interest:** The authors declare no conflict of interest.

## References

1. Li, Z.Y.; Dong, C.; Zou, J.R.; Zou, W.L. Research on experiment and prediction model of dynamic resilient modulus of laterite soil in Southern Hunan. *Rock Soil Mech.* **2015**, *36*, 1840–1846.
2. Wang, Y.X.; Lin, H.; Zhao, Y.L.; Li, X.; Guo, P.P.; Liu, Y. Analysis of fracturing characteristics of unconfined rock plate under edge on impact loading. *Eur. J. Environ. Civ. Eng.* **2019**. [CrossRef]
3. Wu, F.; Chen, J.; Zou, Q.L. A nonlinear creep damage model for salt rock. *Int. J. Damage Mech.* **2018**, 1–14. [CrossRef]
4. Zhao, Y.L.; Zhang, L.Y.; Wang, W.J.; Wan, W.; Ma, W.H. Separation of elastoviscoplastic strains of rock and a nonlinear creep model. *Int. J. Geomech.* **2018**, 04017129. [CrossRef]
5. Zhao, Y.L.; Zhang, L.Y.; Wang, W.J.; Wan, W.; Li, S.Q.; Ma, W.H.; Wang, Y.X. Creep behavior of intact and cracked limestone under multi-level loading and unloading cycles. *Rock Mech. Rock Eng.* **2017**, *50*, 1409–1424. [CrossRef]
6. Qiu, X.; Yang, Q.; Wang, B.R.; Luo, X.H. Prediction Model of Dynamic Resilient Modulus of Cohesive Subgrade Soil Based on Triaxial Test System. *Key Eng. Mater.* **2013**, 579–580, 873–876. [CrossRef]
7. Lin, H.; Wang, H.; Fan, X.; Cao, P.; Zhou, K. Particle size distribution effects on deformation properties of graded aggregate base under cyclic loading. *Eur. J. Environ. Civ. Eng.* **2018**. [CrossRef]
8. Zheng, H.; Li, T.; Shen, J.; Xu, C.; Sun, H.; Lü, Q. The effects of blast damage zone thickness on rock slope stability. *Eng. Geol.* **2018**, *246*, 19–27. [CrossRef]
9. Zhang, C.Y.; Pu, C.Z.; Cao, R.H.; Jiang, T.T.; Huang, G. The stability and roof-support optimization of roadways passing through unfavorable geological bodies using advanced detection and monitoring methods, among others, in the Sanmenxia Bauxite Mine in China's Henan Province. *Bull. Eng. Geol. Environ.* **2019**. [CrossRef]
10. Zhao, Y.L.; Zhang, L.Y.; Wang, W.J.; Tang, J.Z.; Lin, H.; Wan, W. Transient pulse test and morphological analysis of single rock fractures. *Int. J. Rock Mech. Min. Sci.* **2017**, *91*, 139–154. [CrossRef]
11. Cao, R.H.; Cao, P.; Lin, H.; Ma, G.; Chen, Y. Failure characteristics of intermittent fissures under a compressive-shear test: Experimental and numerical analyses. *Theor. Appl. Fract. Mech.* **2018**, *96*, 740–757. [CrossRef]
12. Chen, Y.; Lin, H. Consistency analysis of Hoek-Brown and equivalent Mohr-coulomb parameters in calculating slope safety factor. *Bull. Eng. Geol. Environ.* **2018**. [CrossRef]
13. Zhao, Y.L.; Tang, J.Z.; Chen, Y.; Zhang, L.Y.; Wang, W.J.; Liao, J.P. Hydromechanical coupling tests for mechanical and permeability characteristics of fractured limestone in complete stress-strain process. *Environ. Earth Sci.* **2017**, *76*, 1–18. [CrossRef]
14. Zhao, Y.L.; Luo, S.L.; Wang, Y.X.; Wang, W.J.; Zhang, L.Y.; Wan, W. Numerical Analysis of Karst Water Inrush and a Criterion for Establishing the Width of Water-resistant Rock Pillars. *Mine Water Environ.* **2017**, *36*, 508–519. [CrossRef]
15. Zhao, Y.L.; Zhang, L.Y.; Wang, W.J.; Pu, C.Z.; Wan, W.; Tang, J.Z. Cracking and Stress-Strain Behavior of Rock-Like Material Containing Two Flaws Under Uniaxial Compression. *Rock Mech. Rock Eng.* **2016**, *49*, 2665–2687. [CrossRef]

16. Zhao, Y.L.; Wang, Y.X.; Wang, W.J.; Wan, W.; Tang, J.Z. Modeling of non-linear rheological behavior of hard rock using triaxial rheological experiment. *Int. J. Rock Mech. Min. Sci.* **2017**, *93*, 66–75. [CrossRef]
17. Fan, X.; Lin, H.; Lai, H.P.; Cao, R.H.; Liu, J. Numerical analysis of the compressive and shear failure behavior of rock containing multi-intermittent joints. *C. R. Méc.* **2019**, *347*, 33–48. [CrossRef]
18. Wang, Y.X.; Guo, P.P.; Li, X.; Lin, H.; Liu, Y.; Yuan, H.P. Behavior of Fiber-Reinforced and Lime-Stabilized Clayey Soil in Triaxial Tests. *Appl. Sci.* **2019**, *9*, 900. [CrossRef]
19. Fan, X.; Li, K.H.; Lai, H.P.; Xie, Y.L.; Cao, R.H. Internal stress distribution and cracking around flaws and openings of rock block under uniaxial compression: A particle mechanics approach. *Comput. Geotech.* **2018**, *102*, 28–38. [CrossRef]
20. Zhou, J.; Li, X.; Mitri, H.S. Evaluation method of rockburst: State-of-the-art literature review. *Tunn. Undergr. Space Technol.* **2018**, *81*, 632–659. [CrossRef]
21. Wang, Y.X.; Guo, P.P.; Ren, W.X.; Yuan, B.X.; Yuan, H.P.; Zhao, Y.L.; Shan, S.B.; Cao, P. Laboratory Investigation on Strength Characteristics of Expansive Soil Treated with Jute Fiber Reinforcement. *Int. J. Geomech.* **2017**, *17*, 04017101. [CrossRef]
22. Wang, Y.X.; Guo, P.P.; Dai, F.; Li, X.; Zhao, Y.L.; Liu, Y. Behavior and modeling of fiber-reinforced clay under triaxial compression by combining the superposition method with the energy-based homogenization technique. *Int. J. Geomech.* **2018**, *18*, 04018172. [CrossRef]
23. Liu, B.C.; Li, C.J.; Pan, Z.Y.; Zhang, B.H. Laboratory test for mechanical properties of Guilin red clay mixed with cement. *J. Eng. Geol.* **2012**, *20*, 633–638.
24. Wang, D.; Wang, H.; Jiang, Y. Water immersion-induced strength performance of solidified soils with reactive MgO—A green and low carbon binder. *J. Test. Eval. (ASTM)* **2019**, *47*. [CrossRef]
25. Lin, H.; Xiong, W.; Cao, P. Stability of soil nailed slope using strength reduction method. *Eur. J. Environ. Civ. Eng.* **2013**, *17*, 872–885. [CrossRef]
26. Tan, Y.Z.; Zheng, A.; Wu, P.; Fu, W. Effect of aggregate soil size on California bearing ratio values of laterite soil. *Rock Soil Mech.* **2013**, *34*, 1242–1246.
27. Wang, D.; Du, Y.; Xiao, J. Shear properties of stabilized loess using novel reactive magnesia-bearing binders. *J. Mater. Civ. Eng. (ASCE)* **2019**. [CrossRef]
28. Meng, J.; Cao, P.; Huang, J.; Lin, H.; Chen, Y.; Cao, R. Second-order cone programming formulation of discontinuous deformation analysis. *Int. J. Numer. Methods Eng.* **2019**, 1–15. [CrossRef]
29. Wang, H.; Nie, W.; Cheng, W.M.; Liu, Q.; Jin, H. Effects of air volume ratio parameters on air curtain dust suppression in a rock tunnel's fully-mechanized working face. *Adv. Powder Technol.* **2018**, *29*, 230–244. [CrossRef]
30. Seed, H.B.; Chan, C.K.; Lee, C.E. Resilience characteristics of subgrade soils and their relation to fatigue failures in asphalt pavements. In Proceedings of the International Conference on Structural Design of Asphalt Pavement, Ann Arbor, MI, USA, 20–24 August 1962; pp. 611–636.
31. Ba, M.; Fall, M.; Samb, F.; Sarr, D.; Ndiaye, M. Resilient Modulus of Unbound Aggregate Base Courses from Senegal (West Africa). *Open J. Civ. Eng.* **2011**, *1*, 1–6. [CrossRef]
32. AASHTO. *Guide for Design of Pavement Structures*; American Association of State Highway and Transportation Officials: Washington, DC, USA, 2002.
33. Shen, J.; Wan, L.; Zuo, J. Non-linear shear strength model for Coal Rocks. *Rock Mech. Rock Eng.* **2019**. [CrossRef]
34. Huang, F.; Shen, J.; Cai, M.; Xu, C. An empirical UCS model for anisotropic blocky rock masses. *Rock Mech. Rock Eng.* **2019**. [CrossRef]
35. Shen, J.; Jimenez, R. Predicting the shear strength parameters of sandstone using genetic programming. *B Eng. Geol. Environ.* **2018**, *77*, 1647–1662. [CrossRef]
36. Seed, H.B.; Mitry, F.G.; Monismith, C.L.; Chan, C.K. *Prediction of Flexible Pavement Deflections from Laboratory Repeated Load Tests*; National Academy of Sciences National Academy of Engineering: Washington, DC, USA, 1967.
37. Uzan, J. *Characterization of Granular Materials*; Transportation Research Record 1022; National Research Council: Washington, DC, USA, 1985; pp. 52–59.
38. Witczak, M.; Uzan, J. *The Universal Airport Design System, Report I of IV. Granular Material Characterization*; University of Maryland: College Park, MD, USA, 1988.

39. Uzan, J. *Characterization of Clayey Subgrade Materials for Mechanistic Design of Flexible Pavements*; Transportation Research Record 1629; Transportation Research Board: Washington, DC, USA, 1998; pp. 188–196.
40. Andrei, D. Development of a Harmonized Test Protocol for the Resilient Modulus of Unbound Materials Used in Pavement Design. Master's Thesis, University of Maryland, College Park, MD, USA, 1999.
41. Ni, B.; Hopkins, T.C.; Sun, L.; Beckham, T.L. Modeling the resilient modulus of soils. In Proceedings of the 6th International Conference on the Bearing Capacity of Roads, Railways and Airfields, Lisbon, Portugal, 24–26 June 2002; pp. 1131–1142.
42. Ozel, M.R.; Mohajerani, A. Resilient Modulus of a Stabilised Fine-grained Subgrade Soil. *Aust. Geomech. J.* **2011**, *36*, 75–86.
43. Li, Z.Y.; Zou, J.R.; Dong, C. Study on Prediction Model of Dynamic Resilient Modulus of Cohesive Subgrade Soils Considering Moisture Variation. *Appl. Mech. Mater.* **2014**, *488–489*, 411–416. [CrossRef]
44. Bao, T.N.; Mohajerani, A. Resilient Modulus of Fine-grained Soil and a Simple Testing and Calculation Method for Determining an Average Resilient Modulus Value for Pavement Design. *Transp. Geotech.* **2016**, *7*, 59–70.
45. Wang, H.; Lin, H.; Cao, P. Correlation of UCS Rating with Schmidt Hammer Surface Hardness for Rock Mass Classification. *Rock Mech. Rock Eng.* **2017**, *50*, 195–203. [CrossRef]
46. Liu, Q.; Nie, W.; Yun, H.; Peng, H.T.; Liu, C.Q.; Wei, C.H. Research on tunnel ventilation systems: Dust diffusion and pollution behavior by air curtains based on CFD technology and field measurement. *Build. Environ.* **2019**, *147*, 444–460. [CrossRef]
47. Hua, Y.; Nie, W.; Cai, P.; Liu, Y.H.; Peng, H.T.; Liu, Q. Pattern characterization concerning spatial and temporal evolution of dust pollution associated with two typical ventilation methods at fully mechanized excavation faces in rock tunnels. *Powder Technol.* **2018**, *334*, 117–131. [CrossRef]
48. Wang, Y.X.; Guo, P.P.; Lin, H.; Li, X.; Zhao, Y.L.; Yuan, B.X.; Liu, Y.; Cao, P. Numerical Analysis of Fiber-Reinforced Soils based on the Equivalent Additional Stress Concept. *Int. J. Geomech.* **2019**, in press.
49. Chen, R.; Ge, Y.H.; Chen, Z.K.; Liu, J.; Zhao, Y.R.; Li, Z.H. Analytical Solution for One-dimensional Contaminant Diffusion through Unsaturated Soils Beneath. *Geomembrane. J. Hydrol.* **2019**, *568*, 260–274. [CrossRef]
50. Chen, R.; Huang, J.W.; Chen, Z.K.; Xu, Y.; Liu, J.; Ge, Y.H. Effect of Root Density of Wheat and Okra on Hydraulic Properties of an Unsaturated Compacted Loam. *Eur. J. Soil Sci.* **2019**. [CrossRef]
51. Lu, M.M.; Jing, H.W.; Zhou, A.N.; Xie, K.H. Analytical models for consolidation of combined composite ground improved by impervious columns and vertical drains. *Int. J. Numer. Anal. Methods Geomech.* **2018**, *42*, 871–888. [CrossRef]
52. Lu, M.M.; Sloan, S.W.; Indraratna, B.; Jing, H.W.; Xie, K.H. A new analytical model for consolidation with multiple vertical drains. *Int. J. Numer. Anal. Methods Geomech.* **2016**, *40*, 1623–1640. [CrossRef]
53. Yang, S.B.; Nie, W.; Lv, S.S.; Liu, Z.Q.; Peng, H.T.; Ma, X.; Cai, P.; Xu, C.W. Effects of spraying pressure and installation angle of nozzles on atomization characteristics of external spraying system at a fully-mechanized mining face. *Powder Technol.* **2019**, *343*, 754–764. [CrossRef]
54. Lu, M.M.; Jing, H.W.; Zhou, Y.; Xie, K.H. General analytical model for consolidation of stone columns-reinforced ground and combined composite ground. *Int. J. Geomechan. (ASCE)* **2017**, *17*, 04016131. [CrossRef]
55. Cai, P.; Nie, W.; Chen, D.W.; Yang, S.B.; Liu, Z.Q. Effect of air flowrate on pollutant dispersion pattern of coal dust particles at fully mechanized mining face based on numerical simulation. *Fuel* **2019**, *239*, 623–635. [CrossRef]
56. Bao, Q.; Nie, W.; Liu, C.Q.; Liu, Y.H.; Zhang, H.H.; Wang, H.K.; Jin, H. Preparation and Characterization of a Binary-Graft-Based, Water-Absorbing Dust Suppressant for Coal Transportation. *J. Appl. Polym. Sci.* **2019**, 135. [CrossRef]
57. Jin, H.; Nie, W.; Zhang, H.H.; Liu, Y.H.; Bao, Q.; Wang, H.K. The Preparation and Characterization of a Novel Environmentally-Friendly Coal Dust Suppressant. *J. Appl. Polym. Sci.* **2019**. [CrossRef]
58. Wang, Y.X.; Shan, S.B.; Zhang, C.S.; Guo, P.P. Seismic response of tunnel lining structure in a thick expansive soil stratum. *Tunn. Undergr. Space Technol.* **2019**, *88*, 250–259. [CrossRef]
59. Yuan, B.X.; Sun, M.; Wang, Y.X.; Zhai, L.H.; Luo, Q.Z. A full 3D displacement measuring system for 3D displacement field of soil around a laterally loaded pile in transparent soil. *Int. J. Geomech.* **2019**. [CrossRef]

60. Yuan, B.X.; Xu, K.; Wang, Y.X.; Chen, R.; Luo, Q.Z. Investigation of deflection of a laterally loaded pile and soil deformation using the PIV technique. *Int. J. Geomech.* **2017**, *17*, 04016138. [CrossRef]
61. Wang, D.; Wang, H.; Di, S. Mechanical properties and microstructure of magnesia-fly ash pastes. *Road Mater. Pavement Des.* **2019**. [CrossRef]
62. Wang, D.; Zentar, R.; Abriak, N.E. Durability and swelling of solidified/stabilized dredged marine soils with class F fly ash, cement and lime. *J. Mater. Civ. Eng. (ASCE)* **2018**, *30*, 04018013. [CrossRef]
63. Wang, D.; Zentar, R.; Abriak, N.E.; Di, S.J. Long-term mechanical performance of marine sediments solidified with cement, lime and fly ash. *Mar. Georesour. Geotechnol.* **2018**, *36*, 123–130. [CrossRef]
64. Wang, M.; Shi, X.; Zhou, J.; Qiu, X. Multi-planar detection optimization algorithm for the interval charging structure of large-diameter long hole blasting design based on rock fragmentation aspects. *Eng. Optim.* **2018**, *50*, 2177–2191. [CrossRef]
65. Peng, H.; Nie, W.; Cai, P.; Liu, Q.; Liu, Z.Q. Development of a novel wind-assisted centralized spraying dedusting device for dust suppression in a fully mechanized mining face. *Environ. Sci. Pollut. Res.* **2018**, 1–16. [CrossRef]
66. Cao, R.; Cao, P.; Lin, H.; Fan, X.; Zhang, C.; Liu, T. Crack Initiation, Propagation, and Failure Characteristics of Jointed Rock or Rock-Like Specimens: A Review. *Adv. Civ. Eng.* **2019**, *2019*, 6975751. [CrossRef]
67. Liu, Z.Q.; Nie, W.; Peng, H.T.; Yang, S.B.; Chen, D.W.; Liu, Q. The effects of the spraying pressure and nozzle orifice diameter on the atomizing rules and dust suppression performances of an external spraying system in a fully-mechanized excavation face. *Powder Technol.* **2019**, in press.
68. Lekarp, F.; Isacsson, U.; Dawson, A. Resilient Response of Unbound Aggregates. *J. Transp. Eng.* **2000**, *126*, 66–75. [CrossRef]
69. Hopkins, T.C.; Beckham, T.L.; Sun, C. *Resilient Modulus of Compacted Crushed Stone Aggregate Bases*; Research Report KTC-05-27/SPR-229-01-1F; Kentucky Transportation Center, College of Engineering, University of Kentucky: Lexington, KY, USA, 2001; p. 89.
70. Ba, M.; Fall, M.; Sall, O.A.; Samb, F. Effect of Compaction Moisture Content on the Resilient Modulus of Unbound Aggregates from Senegal (west Africa). *Geomaterials* **2012**, *2*, 19–23. [CrossRef]
71. May, R.W.; Witczak, M.W. *Effective Granular Modulus to Model Pavement Response*; Transportation Research Record 810; Transportation Research Board: Washington, DC, USA, 1981; pp. 1–9.
72. Lu, M.M.; Li, D.X.; Jing, H.W.; Deng, Y.B. Analytical solution for consolidation of band-shaped drain based on an equivalent annular drain. *Int. J. Geomech.* **2019**. [CrossRef]
73. Butterfield, R. Dimensional analysis for geotechnical engineers. *Geotechnique* **1999**, *49*, 357–366. [CrossRef]



© 2019 by the authors. Licensee MDPI, Basel, Switzerland. This article is an open access article distributed under the terms and conditions of the Creative Commons Attribution (CC BY) license (<http://creativecommons.org/licenses/by/4.0/>).

Article

# Rheological Characteristics Evaluation of Bitumen Composites Containing Rock Asphalt and Diatomite

Wentong Huang <sup>1,\*</sup>, Duanyi Wang <sup>2</sup>, Peiyong He <sup>3</sup>, Xiang Long <sup>3</sup>, Bing Tong <sup>1</sup>, Jun Tian <sup>1,4</sup> and Peng Yu <sup>1</sup>

<sup>1</sup> School of Environment and Civil Engineering, Dongguan University of Technology, Dongguan 523808, China; tongb@dgut.edu.cn (B.T.); tianjun@dgut.edu.cn (J.T.); yupeng@dgut.edu.cn (P.Y.)

<sup>2</sup> School of Civil Engineering and Transportation, South China University of Technology, Guangzhou 510640, China; tcdywang@scut.edu.cn

<sup>3</sup> Yuexiu Transport Infrastructure Co., Ltd., Hong Kong 999077, China; he.peiyong@yuexiutransport.com (P.H.); winny66@163.com (X.L.)

<sup>4</sup> Key Laboratory of Transport Industry of Bridge Detection Reinforcement Technology, Chang'an University, Xi'an 710064, China

\* Correspondence: huangwt@dgut.edu.cn

Received: 13 January 2019; Accepted: 6 March 2019; Published: 12 March 2019

**Abstract:** Previous studies have showed that rock asphalt (RA) or diatomite were used to modify the petroleum bitumen. This paper presents the findings from a study conducted to evaluate the potential impact of RA and diatomite on the rheological characteristics of bitumen composites. RA and diatomite with three different dosages were added into the petroleum bitumen: 18% RA, 13% RA+7% diatomite, and 16% RA+9% diatomite by weight. The rheological characteristics of the RA and diatomite modified bitumens were evaluated in this study. The tests conducted included temperature sweep and frequency sweep tests with a dynamic shear rheometer (DSR), a Brookfield rotation viscosity test, and a scanning electron microscope test. The research showed that the addition of RA and diatomite to petroleum bitumen considerably increased the apparent viscosity, dynamic shear modulus, and rutting resistance in bitumen specimens. However, the DSR test indicated a slight reduction in the fatigue performance of composites made of RA and diatomite modified bitumens. Overall, RA and diatomite are good modifiers for petroleum bitumen for a performance improvement.

**Keywords:** rock asphalt; diatomite; rheological characteristics; high temperature performance; fatigue performance; low temperature performance

## 1. Introduction

The types of asphalt pavement damage mainly include ruts, pits, cracks, potholes, and surface shedding [1]. After several years of service, some asphalt pavements are faced with early damage. The use of high-quality bitumen materials can solve or alleviate the early problems of highway pavement [2–4]. Therefore, modified asphalt has been widely used in asphalt pavements in the past ten years. SBS-modified (Styrene-Butadiene-Styrene Block Copolymer) asphalt is the most widely used, but the production equipment of SBS-modified asphalt is very expensive and the production and transportation costs are high [5]. As a result, it is urgent to find some modified asphalt with excellent road performance, simple construction, and low costs. Rock asphalt and diatomite are good choices among many asphalt modifiers [6,7].

Rock asphalt is a natural bitumen. Its color is dark brown in micronized powder. Rock asphalt is mined in underground shafts. Rock asphalt was added into mixtures as a modifier additive [8]. Rock asphalt is made up of very high molecular weight, oligomeric, polar polynuclear hydrocarbons [9,10]. Rock asphalt



has stable and durable properties. It can change the ratio of asphaltic oil and asphaltenes [11,12]; can increase the high-temperature hardness of petroleum bitumen; and can help delay the occurrence of early defects such as potholes, ruts, and cracks on asphalt pavements [13,14].

Therefore, the fatigue performance of rock asphalt-modified bitumens was studied [15–17]. The results showed that the reduced dissipated energy ratio was a good evaluation index and that the fatigue performance of rock asphalt-modified bitumen depended on the loading mode of the test. Further, researchers studied the influence of Buton rock asphalt on the high-temperature rheological properties of asphalt and mineral filler mortar and concluded that the Buton rock asphalt could significantly improve the high temperature rheological properties of the mortar. The Buton rock asphalt mortar at an additional 20% concentration had the same anti-rutting performance as SBS-modified bitumen mortar [18–21]. Gilsonite could improve the Marshall stability and elastic modulus parameters of the mixture, but its flexibility was significantly reduced by using two gradations of Gilsonite-modified bitumen. The Marshall stability, dynamic creep, and elastic modulus test results showed that Gilsonite could improve the Marshall stability and elastic modulus parameters of the mixture and improve the rutting resistance, but the flexibility of the mixture was significantly reduced [22,23].

Moreover, a laboratory evaluation on the performance of compound-modified asphalt for rock asphalt/SBR, rock asphalt/Nano-CaCO<sub>3</sub>, rock asphalt/Nano-silica, and Nano-silica/rock asphalt/SBS have also been studied by researchers. The anti-rutting performance of 10% BRA/Nano-CaCO<sub>3</sub> compound-modified asphalt was the best. The thermal cracking performance of 5% BRA/SBR-modified asphalt has been effectively improved, and that of nano-CaCO<sub>3</sub> was not obvious. Compound-modified asphalt mixtures have higher temperature stability, low-temperature cracking resistance, moisture susceptibility, and durability than 5% SBS modified asphalt [24–26].

Diatomite is a biogenic siliceous sedimentary rock and a type of nonmetallic mineral, which is mainly composed of diatom remains and soft mud, and its main chemical composition is silica (SiO<sub>2</sub>). Diatomite has the characteristics of a high porosity, a low density, a large specific surface area, a strong adsorption capacity, stable chemical properties, and a high melting point [27,28]. Li et al. carried out a dynamic temperature scanning test of diatomite modified bitumen mortar. They compared the performance of modified bitumen mortar by adding spherical and rod-shaped diatomite [29]. The results showed that the high temperature performance of the rod-shaped diatomite bitumen mortar was better than that of the spherical diatomite. Although, diatomite can reduce the fatigue performance of modified bitumen mortar, it can significantly improve the high-temperature performance and moisture stability of the bitumen mixture. The properties of a diatomite and basalt fiber composite-modified bitumen mortar were studied [30]; the results showed that the high-temperature and low-temperature performance of the bitumen were improved. Davar et al. studied the 20 °C four-point bending fatigue life test and 5 °C indirect tensile test of a composite modified bitumen with diatomite and basalt fiber [31] and concluded that the fatigue life of the diatomite and basalt fiber modified bitumen increased and that the simultaneous use of diatomite and basalt fiber could make up for the weakness of the bitumen mixture at low temperatures.

Diatomite can play an active and effective role in bitumens and bitumen mixtures. The addition of diatomite to asphalt can increase the softening point and viscosity of bitumen and can decrease the needle penetration. Diatomite-modified bitumen has good thermal stability and adhesion. The high-temperature performance and moisture damage resistance of a diatomite-modified bitumen mixture were improved significantly but not the low-temperature performance [32,33]. Li et al. evaluated the pavement performance of a rock asphalt and diatomite-modified bitumen mixture and reported that the dynamic stability of bitumen mixture was improved the most; moisture stability is superior when the mixed diatomite content is 20% [34].

The research of bitumen mixture-modified by rock asphalt or single diatomite shows that the two types of materials are effective for improving the pavement performance of bitumen concrete, but there are still many shortcomings in improving bitumen concrete by a single material. Combining

the two types of materials can overcome their shortcomings and makes full use of the adsorption function of diatomite and the high-temperature performance of rock asphalt. Previous studies focus on the middle- and high-temperature rheological properties of bitumen, but a few of them focus on the low-temperature rheological characteristics, particularly the low-temperature fatigue properties of bitumen. Therefore, the high- and low-temperature rheological characteristics of North American rock asphalt composite diatomite-modified bitumen are investigated in this study.

## 2. Materials and Preparation

### 2.1. Materials

The petroleum bitumen used in the study was produced in Foshan, Guangdong Province, China. The petroleum bitumen was in accordance of the penetration grading of bitumen. Some physical properties of the petroleum bitumen are shown in Table 1. The RA used in this study was sourced from Utah, USA. Some physical properties of the rock asphalt are shown in Table 2. It can be speculated from Table 2 that the asphalt content of rock asphalt was about 90% and that the main component of the rest was ash. The diatomite used in this study was sourced from Xundian, Yunnan Province, China. Some physical properties of the diatomite are shown in Table 3. Diatomite’s main chemical composition is SiO<sub>2</sub>. The mineral filler used in this study was sourced from Foshan, Guangdong Province, China. Some physical properties of the mineral filler are shown in Table 4. The physical properties of petroleum bitumen, rock asphalt, diatomite, and mineral filler were normal.

**Table 1.** The physical properties of petroleum bitumen; RTFOT: Rolling Thin Film Oven Test.

Properties	Virgin Bitumen				RTFOT Residue			
	Penetration Grade at 25 °C (0.1 mm)	Softening Point (°C)	Ductility at 10 °C (cm)	Viscosity at 60 °C (Pa·s)	Mass Change (%)	Residual Penetration Ratio at 25 °C (%)	Residual Ductility at 10 °C (cm)	Softening Point (°C)
Requirement	60–80	≥46	≥15	≥180	±0.8	≥61	≥6	—
Results	71	47	33	210	−0.2	72	9	53

**Table 2.** The physical properties of rock asphalt.

Properties	Solubility in C <sub>2</sub> HCl <sub>3</sub> (%)	Specific Gravity at 25 °C (kg/m <sup>3</sup> )	Flash Point (°C)	Moisture (%)	ASH (%)	1.18 mm Percentage Passing Sieves (%)
Results	91	1153	298	0.6	7.0	100

**Table 3.** The physical properties of diatomite.

Properties	SiO <sub>2</sub>	Al <sub>2</sub> O <sub>3</sub>	Fe <sub>2</sub> O <sub>3</sub>	CaO	MgO	TiO <sub>2</sub>	K <sub>2</sub> O	Loss on Ignition (%)
Requirement	≥75	—	—	—	—	—	—	—
Results	85.2	3.6	2.3	0.6	1.6	0.2	0.4	5.2

**Table 4.** The physical properties of mineral filler.

Properties	Specific Gravity at 25 °C (g/cm <sup>3</sup> )	Hydrophilic Coefficient	Size Range (%)		
			<0.6 mm	<0.15 mm	<0.075 mm
Requirement	≥2.50	<1	100	90–100	75–100
Results	2.723	0.57	100	95.3	80.9

### 2.2. Sample Preparation

Four different dosages of modifiers were added into the petroleum bitumen: 10% mineral filler, 18% RA, 13% RA+7% diatomite, and 16% RA+9% diatomite by weight. The control bitumen binder

without modifier was also investigated for a comparison. The modified bitumens were prepared by blending a certain amount of mineral filler, RA, and RA and diatomite into the petroleum bitumen. In detail, the petroleum bitumen was preheated to 150 °C. The mineral, RA, and RA and diatomite were added into the petroleum bitumen at room temperature. The mixture was heated and maintained at a temperature of 175 °C for one hour. Afterward, the mixture was blended with a high shear mixer for 30 min at 3000 rpm.

### **3. Experimental Methods**

#### *3.1. SEM Tests*

The SEM tests applied explored the surface morphology and microstructure of bitumen binders. The SEM tests were conducted with a Zeiss field emission scanning electron microscope (SEM) produced by Carl Zeiss AG, Oberkochen, Germany. The RA and diatomite had particle sizes of 500 mesh. In this study, the SEM tests were conducted at 5000× magnification.

#### *3.2. Rotation Viscosity Test*

The apparent viscosities of the petroleum bitumen and composite modified asphalt were measured by a DV-II rotary viscometer made by the Brookfield Company, Middleboro, MA, America. The temperatures for rotational viscosity measurements were 135 °C and 175 °C. Three different dosages of modifiers were added into the petroleum bitumen: 18% RA, 13% RA+7% diatomite, and 16% RA+9% diatomite by weight.

#### *3.3. Dynamic Shear Rheometer (DSR) Test*

The temperature and frequency sweep tests were conducted to evaluate the linear rheological characteristics of composite-modified asphalt with different RA and diatomite. The commonly obtained rheological indices from the DSR test were the dynamic shear modulus ( $G^*$ ), phase angle ( $\delta$ ), and loss tangent ( $\tan\delta$ ). These indices were used to evaluate the viscosity and elasticity of the composite modified asphalt. The rutting factor ( $G^*/\sin\delta$ ) was used to evaluate the anti-rutting ability of composite-modified asphalt as a high-temperature performance index, and the fatigue factor ( $G^*\cdot\sin\delta$ ) was used to evaluate the anti-fatigue performance. The asphalt samples were 25 mm in diameter and 1 mm in thickness.

##### **3.3.1. Temperature Sweep Tests**

In this study, the temperature sweep tests were conducted at nine different temperatures: 30, 35, 40, 45, 50, 55, 60, 65, and 70 °C. The strain was controlled at 5%, and the angular velocity was 10 rad/s. Five different dosages of modifiers were added into the petroleum bitumen to evaluate the viscoelastic property of bitumen binders: 0%, 10% mineral filler, 18% RA, 13% RA+7% diatomite, and 16% RA+9% diatomite by weight. Among them, the mineral content in 16% RA+9% diatomite was equivalent to that in 10% mineral filler.

##### **3.3.2. Frequency Sweep Tests**

Under traffic loads, the asphalt pavement structure showed a dynamic loading effect, and the bitumen material exhibited different viscoelastic properties under different load frequencies. The frequency sweep test can simulate the speed of a vehicle running on the road. The loading frequency of 10 Hz simulates the speed of 60 km/h, and the loading frequency of 15 Hz simulates the speed of 90 km/h. The frequency sweep tests were conducted while changing the load frequency from 1 Hz to 25 Hz. The test temperature was 60 °C. In this study, three different dosages of modifiers were added into the petroleum bitumen to evaluate the viscoelastic property of the bitumen binders: 0%, 13% RA+7% diatomite, and 16% RA+9% diatomite by weight.

### 3.4. Bending Beam Rheometer (BBR) Test

The BBR test was used to evaluate the low-temperature performance of bitumen binders. The creep stiffness and m-value could be obtained from the BBR test at 60 s under three different temperatures ( $-6$ ,  $-12$ , and  $-18$  °C). The Superpave binder specification sets a maximum value of 300 MPa for the creep stiffness and a minimum value of 0.3 for m-value [11]. The m-value indicated a bitumen stiffness sensitivity with time and stress relaxation ability. The BBR tests were carried out at  $-6$ ,  $-12$ , and  $-18$  °C. Three different dosages of modifiers were added into the petroleum bitumen to obtain the creep stiffness and m-value of the bitumen binders: 0%, 13% RA+7% diatomite, and 16% RA+9% diatomite by weight. All samples were subjected to RTFOT (Rolling Thin Film Oven Test) aging and PAV (Pressure Ageing Vessel) aging.

## 4. Results and Discussion

### 4.1. SEM Tests

Figure 1 shows the SEM test result of RA. It can be seen from Figure 1 that the surface of the large particles is smooth, clear, and dispersed in all directions and that the fine particles are adhered to the larger particles. Previous studies have reported that RA contained highly polar functional groups with high free energy and strong absorbability [15]. Under high temperature conditions, the RA particles reach a molten state and rapidly fuse with the petroleum bitumen, improving the anti-stripping capability of the aggregate and improving the water stability of the asphalt mixture.

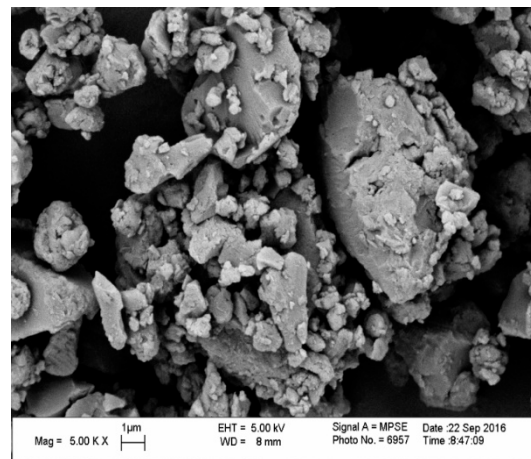


**Figure 1.** A SEM image of rock asphalt (RA).

As shown in Figure 2, the diatomite has a unique porous structure, a high porosity, a large specific surface area, and an active surface on both the inner and outer surfaces, presenting great adhesion ability and adhesion strength. Since the diatomite is mixed with the petroleum bitumen, the petroleum bitumen is absorbed on the surface of diatomite particles, and the light oil in the petroleum bitumen is also drawn into the pores of the micro-cavity to form a mechanical locking force. The surface of the diatomite shows a strong polar asphaltene layer, which greatly improves the cohesive force with the aggregate and improves the water stability of the asphalt mixture.

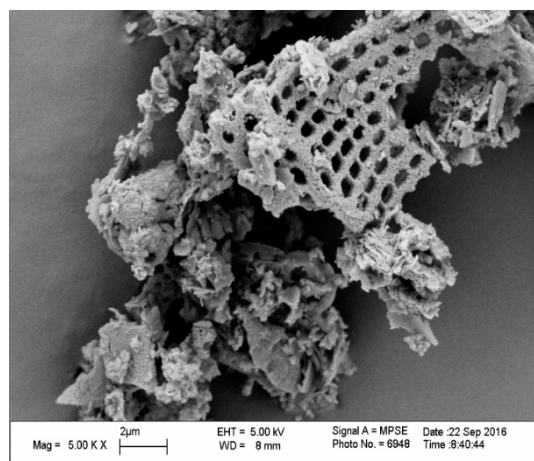


Figure 2. A SEM image of diatomite.

#### 4.2. Rotational Viscosity Test

Table 5 displays the rotational viscosity test for the control (0% RA+0% diatomite) and the modified bitumen of RA and diatomite. With an increase of RA and diatomite dosage, the apparent viscosity increases significantly at the two tested temperatures. Obviously, the RA and diatomite are also beneficial for the high-temperature performance of the bitumen. The apparent viscosity with the same dosage of RA and diatomite increases more at the lower tested temperatures. When the test temperature was 135 °C, the apparent viscosity of 16% RA+9% diatomite composite-modified asphalt reached 3.78 Pa·S, which exceeded the specification that the apparent viscosity of modified asphalt should not be greater than 3 Pa·S. Therefore, the dosage of diatomite should not exceed 9% when RA is 16% added into the petroleum bitumen by weight. Similarly, the dosage of RA should not exceed 16% when diatomite is 9%.

Table 5. The rotation viscosity test.

Component	Apparent Viscosity (Pa·S)	
	135 °C	175 °C
control	0.41	0.08
18% RA+0% diatomite	2.55	0.18
13% RA+7% diatomite	1.84	0.25
16% RA+9% diatomite	3.78	0.41

#### 4.3. Dynamic Shear Rheometer (DSR) Test

##### 4.3.1. Temperature Sweep Tests

The temperature sweep test results are summarized in Figure 3. As expected and seen in Figure 3a, all of the modified bitumens showed higher values of dynamic shear modulus  $G^*$  as compared to the control bitumen, showing the trend of elastic enhancement as well as the significant improvement in its high-temperature performance. By comparison, the dynamic shear modulus  $G^*$  was 16% RA+9% diatomite > 13% RA+7% diatomite > 18% RA > 10% mineral filler > petroleum bitumen. For example, at a temperature of 60 °C, the dynamic shear modulus of 10% mineral filler, 18% RA, 13% RA+7% diatomite, and 16% RA+9% diatomite modified bitumen increased 71.9%, 439.0%, 554.5%, and 2278.6% more than that of the control bitumen, respectively. The dynamic shear modulus  $G^*$  of the 16% RA+9% diatomite composite-modified bitumen was the largest, and the curve was flatter, indicating that the higher the content of RA and diatomite, the better the sensitivity of modified bitumen. The dynamic shear modulus  $G^*$  of 13% RA+7% diatomite modified bitumen was similar to that of 18% RA-modified bitumen, which meant that the 13% RA+7% diatomite-modified bitumen reached the dynamic shear

modulus of 18% RA modified bitumen, both of which have similar high-temperature performances. These results indicate that RA and diatomite could significantly increase the stiffness of the bitumen.

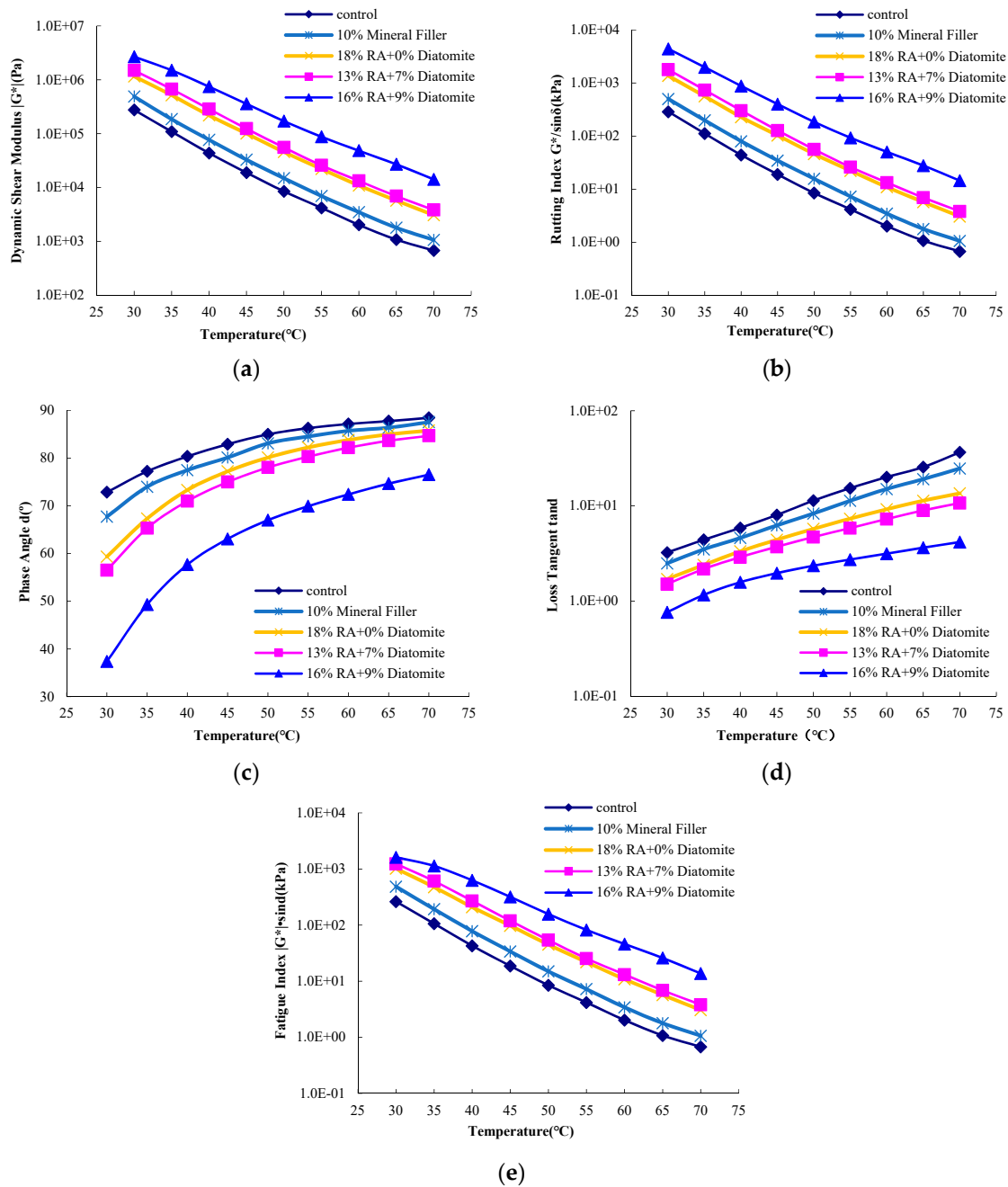


**Figure 3.** The temperature sweep results: (a) dynamic shear modulus; (b) rutting index; (c) phase angle; (d) loss tangent; and (e) fatigue index.

Figure 3b presents the rutting index  $G^*/\sin\delta$  of petroleum bitumen and four modified bitumens. The trend of the rutting index  $G^*/\sin\delta$  is overall similar to that of the dynamic modulus. In this study, the rutting index  $G^*/\sin\delta$  of the 18% RA-modified bitumen and 13% RA+7% diatomite-modified bitumen were extremely close. The rutting index  $G^*/\sin\delta$  of the 16% RA + 9% diatomite composite-modified bitumen was approximately four times that of the 18% RA-modified bitumen. The rutting index  $G^*/\sin\delta$  of the 16% RA+9% diatomite-modified bitumen was approximately 10 times that of 10% mineral filler-modified bitumen. The rutting index  $G^*/\sin\delta$  of the 16% RA+9% diatomite-modified bitumen was approximately 20 times that of the petroleum bitumen,

which indicated that both RA and diatomite could significantly increase the rutting performance. Further, the rutting performance improved with a higher RA and diatomite dosage.

Phase angle  $\delta$  is the lag of the strain with respect to the stress. The phase angle  $\delta$  for a pure elastic material is  $0^\circ$ , while for a pure plastic material is  $90^\circ$  [11]. Bitumen is a typical viscoelastic material, so the phase angle  $\delta$  should be between  $0^\circ$  and  $90^\circ$ . Under periodic loading, the peak strain falls behind the peak stress significantly, forming the phase angle  $\delta$ . Figure 3c shows the phase angle test results of petroleum bitumen and four modified bitumens. According to Figure 3c, the phase angle of the bitumen vary from  $37^\circ$  to  $89^\circ$ , within the theoretical range ( $0-90^\circ$ ). Figure 3c shows that a higher temperature results in a longer strain hysteresis, a higher phase angle, and a higher viscosity of bitumen. The phase angle of the petroleum bitumen is significantly larger than that of the modified bitumen, which indicates that the modifier constrains the movement of the bitumen molecule, enhances the elastic part of the bitumen, and improves the stability and resistance to the deformation of the modified asphalt.

Figure 3d illustrates the loss tangent  $\tan\delta$  of petroleum bitumen and four modified bitumens. The order of the magnitude of the loss tangent is the same as that of the phase angle, and the phase angle of different bitumens is getting increasingly closer with a higher temperature and tends to be the same. By contrast, the loss tangent of different bitumens is increasingly diverging with higher temperature, and the difference is becoming greater.

The fatigue index  $|G^*| \cdot \sin\delta$  test results of the petroleum bitumen and four modified bitumens are showed in Figure 3e. It can be obviously seen that the trend of the fatigue index  $|G^*| \cdot \sin\delta$  is overall similar to that of the dynamic shear modulus. The amount of work consumed by bitumen under constant strain per load cycle is proportional to the fatigue index  $|G^*| \cdot \sin\delta$ . The smaller the fatigue index  $|G^*| \cdot \sin\delta$  value, the lesser the energy consumed. The more elastic the bitumen binder, the greater the capability to restore the deformation after multiple loadings and the lower the likelihood of fatigue cracking. At different temperatures, the fatigue factor  $|G^*| \cdot \sin\delta$  of petroleum bitumen is lower than that of the modified bitumens, which indicates that the fatigue performance of the petroleum bitumen is better compared to that of the modified bitumens. The petroleum bitumen shows a better fatigue resistance because the modified bitumens contain minerals, which reduce the fatigue performance of the bitumen mortar.

The RA and diatomite-modified bitumen shows an excellent high-temperature stability and rutting performance. Further, a higher RA and diatomite dosage brings a better high-temperature performance, indicating RA and diatomite can enhance the high resistance against the permanent deformation of petroleum bitumen.

#### 4.3.2. Frequency Sweep Tests

The frequency sweep test results are summarized in Figure 4. Figure 4a illustrates the dynamic shear modulus  $G^*$  of petroleum bitumen and two modified bitumens at a frequency from 1 Hz to 25 Hz. At the same frequency, two modified bitumens show higher values of dynamic shear modulus  $G^*$  as compared to the control bitumen, indicating that RA and diatomite can significantly increase the high-temperature performance of the bitumen. Further, a higher dosage of the composite modifier of RA and diatomite results in a higher value of dynamic shear modulus  $G^*$ . As shown in Figure 4b, the rutting index  $G^*/\sin\delta$  increases gradually with frequency. The rutting index  $G^*/\sin\delta$  increases faster when the sweep frequency is lower than 5 Hz. Contrastively, the rutting index  $G^*/\sin\delta$  increases slowly and gradually and tends to be stable when the sweep frequency is higher than 5 Hz. Moreover, a higher dosage of RA and diatomite results in a better anti-rutting performance of the modified bitumen. The results show that the dynamic shear modulus  $G^*$  and rutting factor  $G^*/\sin\delta$  of petroleum bitumen are improved by incorporating RA and diatomite, which significantly improves the deformation resistance. In addition, the anti-rutting performance is improved gradually with the higher dosage of RA and diatomite.

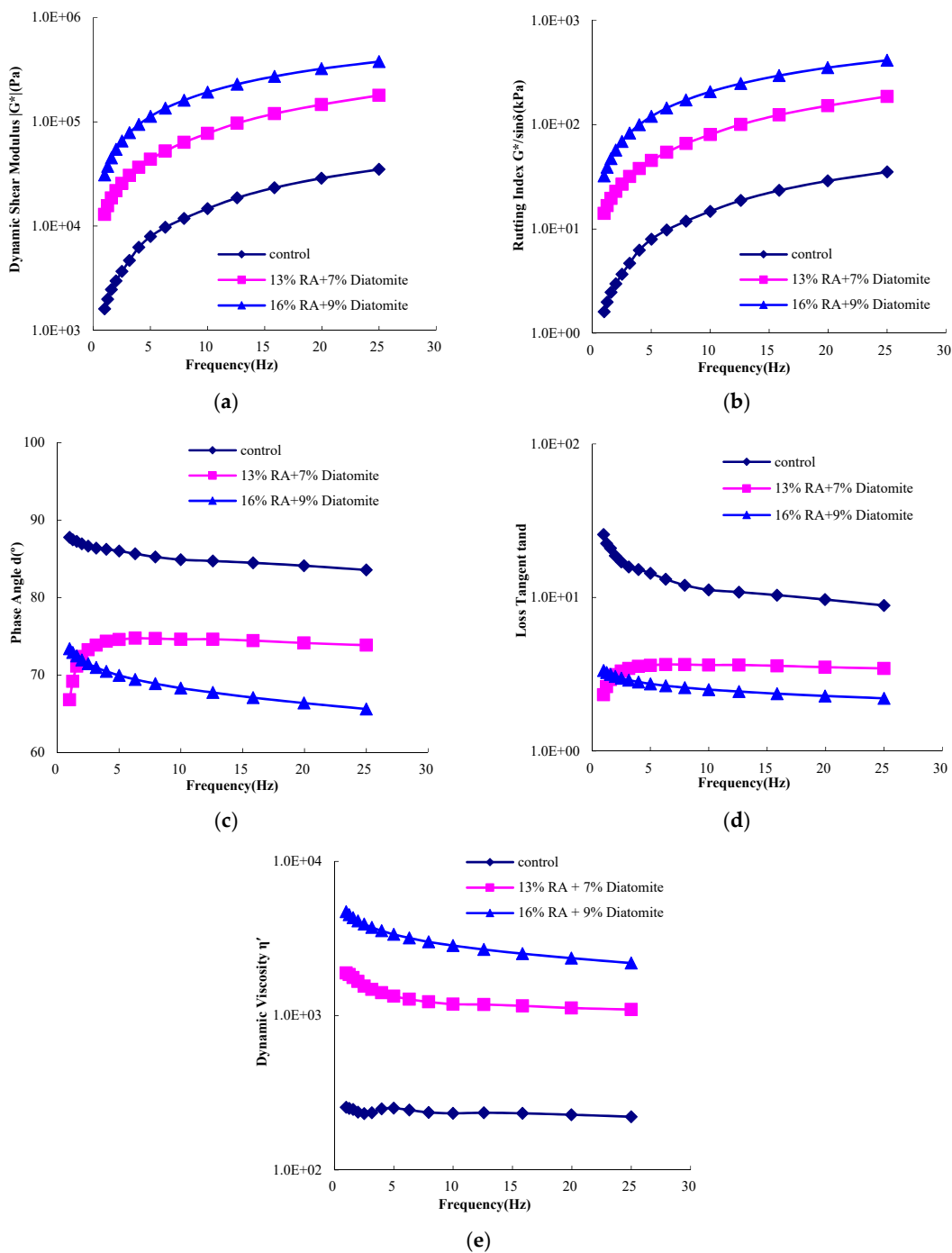


**Figure 4.** The frequency sweep results: (a) dynamic shear modulus; (b) rutting index; (c) phase angle; (d) loss tangent; and (e) fatigue index.

Figure 4c presents the phase angle  $\delta$  of petroleum bitumen and two modified bitumens. It can be seen that the phase angle  $\delta$  overall decreases with an increase in the RA and diatomite dosage. In detail, the phase angle  $\delta$  for the control, 13% RA+7% diatomite-, and 16% RA+9% diatomite-modified bitumens are  $84.9^\circ$ ,  $74.6^\circ$ , and  $68.3^\circ$ , respectively at 10 Hz. However, the phase angle  $\delta$  of 13% RA+7% diatomite-modified asphalt shows different characteristics. The phase angle  $\delta$  rises sharply when the frequency is less than 6 Hz, and it decreases gradually after 6 Hz. This indicates that the phase angle  $\delta$  of RA and diatomite-modified asphalt shows a completely different behavior at low frequency and high frequency with a low dosage of RA and diatomite. Therefore, it is suggested that a higher dosage of compound RA and diatomite be used. By comparison, the phase angle  $\delta$  of the petroleum bitumen



is close to  $90^\circ$ , indicating that the petroleum bitumen is going to lose its elasticity and enter into viscous flow. The phase angle  $\delta$  of two modified bitumens are no more than  $75^\circ$ , indicating that RA and diatomite constrain the free movement of bitumen molecules, ensuring the bitumen maintains a good overall structure, and performing a resistance to permanent deformation. As shown in Figure 4d, the change rule of the loss tangent  $\tan\delta$  is the same as that of the phase angle  $\delta$ .

The fatigue index  $|G^*| \cdot \sin\delta$  of each bitumen increases with an increase in frequency, as shown in Figure 4e. The fatigue index  $|G^*| \cdot \sin\delta$  increases sharply when the frequency is less than 5 Hz. Correspondingly, the fatigue factor  $|G^*| \cdot \sin\delta$  increases gradually when the frequency exceeds 5 Hz. In detail, the fatigue index  $|G^*| \cdot \sin\delta$  of two modified bitumens is larger than that of control bitumen at the same frequency. According to this, the modified bitumen mortar with RA and diatomite contains a certain amount of minerals and reduces its fatigue performance.

#### 4.4. BBR Test

Figure 5 presents the creep stiffness and m-value for all bitumen binders at 60 s under  $-6$ ,  $-12$ , and  $-18$  °C. Obviously, with a decrease in temperature from  $-6$  to  $-18$  °C, the creep stiffness increases and the m-value decreases for all bitumen binders. The creep stiffness of the RA+diatomite bitumens was obviously higher than that of the control bitumen, while the m-value of the RA+diatomite bitumens was slightly lower than that of the control bitumen. In detail, we failed to obtain the test results of the 16% RA+9% diatomite-modified bitumen at  $-18$  °C, but the 13% RA+7% diatomite-modified bitumen had a high creep stiffness of 573 MPa, so we could predict a higher value of the 16% RA+9% diatomite-modified bitumen. A higher stiffness corresponds to a smaller creep compliance; a greater stress was required to produce a unit strain of bitumen binder. A higher m-value indicated a better stress relaxation ability and a better cracking resistance. Therefore, the addition of RA and diatomite can weaken the low temperature performance of petroleum bitumen.

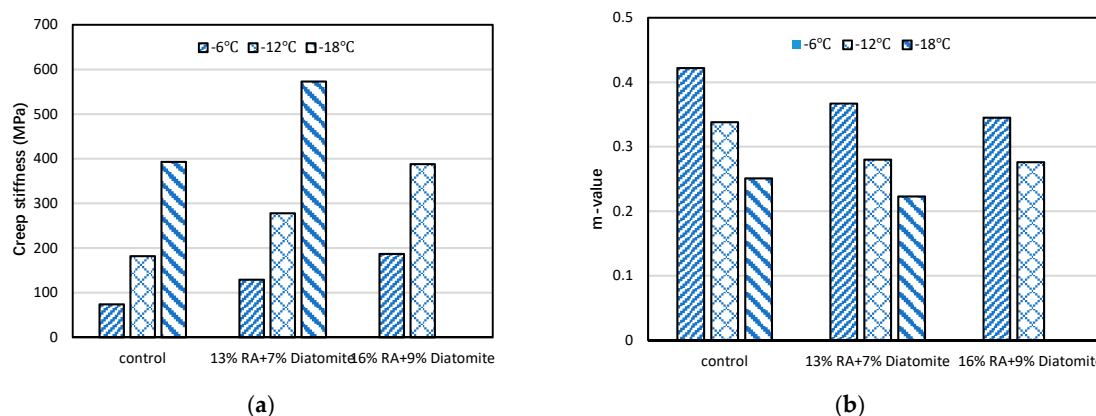


Figure 5. The BBR test results: (a) creep stiffness and (b) m-value.

## 5. Conclusions

In this study, a series of tests were conducted in order to evaluate the rheological characteristics of petroleum bitumen modified by rock asphalt (RA) and diatomite. Based on the results and discussion, some conclusion can be drawn as follows.

(1) The addition of RA and diatomite significantly improved the apparent viscosity of petroleum bitumen binders. When the test temperature was  $175$  °C, the apparent viscosity of 13% RA+7% diatomite composite-modified asphalt was 212.5% higher than that of petroleum bitumen.

(2) The master curves indicated that the addition of RA and diatomite significantly increased the dynamic shear modulus of petroleum bitumen binders. Further, a higher dosage of RA and diatomite resulted in a higher dynamic shear modulus. This increase was desirable for an improved

high-temperature performance of bitumen. The dynamic shear modulus of the 13% RA+7% diatomite composite-modified asphalt was 427.0% higher than that of petroleum bitumen at 60 °C and 10 Hz.

(3) The master curves indicated that the addition of RA and diatomite effectively enhanced the rutting performance and deformation resistance of petroleum bitumen binders. The rutting index  $G^*/\sin\delta$  of the 16% RA+9% diatomite-modified asphalt was approximately 20 times that of the petroleum bitumen in the temperature sweep tests.

(4) At different temperatures, the fatigue factor  $|G^*| \cdot \sin\delta$  of petroleum bitumen was 5 times lower than that of the modified bitumens, which indicated that the fatigue performance of bitumen binders decreased with the addition of RA and diatomite.

(5) At  $-12$  °C, the m-value of the 13% RA+7% diatomite composite-modified asphalt was 20.7% lower than that of petroleum bitumen. The low-temperature performance of bitumen binders weakened with the addition of RA and diatomite.

**Author Contributions:** Conceptualization, W.H., Data curation, W.H., J.T. and P.Y.; Formal analysis, W.H., D.W., X.L. and B.T.; Investigation, J.T. and P.Y.; Methodology, D.W., P.H. and B.T.; Project administration, P.H. and X.L.; Writing—original draft, W.H.

**Funding:** This research was funded by National Natural Science Foundation of China (Grant number [51578248, 51809046]); Research Start-up Funds of Dongguan University of Technology [ZJ20170428, GC300502-29, GC300502-32]; The Science and Technology Planning Project of Guangdong Provincial Department of Transportation [2014-02-004]; and Open Fund of Key Laboratory of Transport Industry of Bridge Detection Reinforcement Technology (Chang’an University) [300102219527, 300102219528].

**Acknowledgments:** This work is supported by Higher Education Teaching Reform Project of Department of Education of Guangdong Province [2018-180], Production-University Cooperation and Education Project of Higher Education Department of Ministry of Education [201801317027], Higher Education Research Project of Dongguan University of Technology [2017GJYB06]. The authors gratefully acknowledge their financial support.

**Conflicts of Interest:** The authors declare no conflict of interest.

## References

1. Widyatmoko, I.; Elliott, R. Characteristics of elastomeric and plastomeric binders in contact with natural asphalts. *Constr. Build. Mater.* **2008**, *22*, 239–249. [CrossRef]
2. Liao, M.; Chen, J.; Airey, G.D.; Wang, S. Rheological behavior of bitumen mixed with Trinidad lake asphalt. *Constr. Build. Mater.* **2014**, *66*, 361–367. [CrossRef]
3. Xin, C.; Lu, Q.; Ai, C.; Rahman, A.; Qiu, Y. Optimization of hard modified asphalt formula for gussasphalt based on uniform experimental design. *Constr. Build. Mater.* **2017**, *136*, 556–564. [CrossRef]
4. Xu, G.; Wang, H.; Zhu, H. Rheological properties and anti-aging performance of asphalt binder modified with wood lignin. *Constr. Build. Mater.* **2017**, *151*, 801–808. [CrossRef]
5. Kök, B.V.; Yilmaz, M.; Guler, M. Evaluation of high temperature performance of SBS + Gilsonite modified binder. *Fuel* **2011**, *90*, 3093–3099. [CrossRef]
6. Huang, W.; Xu, G. Experimental investigation on the pavement performance of Buton rock asphalt mixtures. *J. South China Univ. Technol. (Nat. Sci. Ed.)* **2012**, *40*, 87–91.
7. Galzerano, B.; Capasso, I.; Verdolotti, L.; Lavorgna, M.; Vollaro, P.; Caputo, D.; Iannace, S.; Liguori, B. Design of sustainable porous materials based on 3D-structured silica exoskeletons, *Diatomite: Chemico-physical and functional properties*. *Mater. Des.* **2018**, *145*, 196–204. [CrossRef]
8. Jahanian, H.R.; Shafabakhsh, G.H.; Divandari, H. Performance evaluation of hot mix asphalt (HMA) containing bitumen modified with Gilsonite. *Constr. Build. Mater.* **2017**, *131*, 156–164. [CrossRef]
9. Li, K.; Vasiliu, M.; McAlpin, C.R.; Yang, Y.; Dixon, D.A.; Voorhees, K.J.; Batzle, M.; Liberatore, M.W.; Herring, A.M. Further insights into the structure and chemistry of the Gilsonite asphaltene from a combined theoretical and experimental approach. *Fuel* **2015**, *157*, 16–20. [CrossRef]
10. Sun, D. A study on xinjiang asphaltite as an asphalt modifier. Part I: Composition, structure, and thermal behavior. *Pet. Sci. Technol.* **2012**, *30*, 307–315. [CrossRef]

11. Helms, J.R.; Kong, X.; Salmon, E.; Hatcher, P.G.; Schmidt-Rohr, K. Structural characterization of gilsonite bitumen by advanced nuclear magnetic resonance spectroscopy and ultrahigh resolution mass spectrometry revealing pyrrolic and aromatic rings substituted with aliphatic chains. *Org. Geochem.* **2012**, *44*, 21–36. [CrossRef]
12. Zhong, K.; Yang, X.; Luo, S. Performance evaluation of petroleum bitumen binders and mixtures modified by natural rock asphalt from Xinjiang China. *Constr. Build. Mater.* **2017**, *154*, 623–631. [CrossRef]
13. Huang, W.; Xu, G.; Liu, Y.; Wang, D. Study on modification mechanism of North American rock asphalt based on microstructure. *Funct. Mater.* **2015**, *46*, 12082–12086. (In Chinese)
14. Zhang, C.; Li, Y.; Cheng, X.; Liang, S.; Guo, X.; Zhao, H. Effects of plasma-treated rock asphalt on the mechanical properties and microstructure of oil-well cement. *Constr. Build. Mater.* **2018**, *186*, 163–173. [CrossRef]
15. Wang, M.; Lin, F.; Liu, L. Dynamic rheological properties and microscopic characteristics of ash mastics. *J. Tongji Univ. (Nat. Sci. Ed.)* **2016**, *44*, 567–571.
16. AASHTO. *Standard Method of Test for Determining the Rheological Properties of Asphalt Binder Using a Dynamic Shear Rheometer (DSR)*; American Association of State Highway and Transportation Officials: Washington, DC, USA, 2009.
17. Li, Y.; Chen, J.; Yan, J.; Guo, M. Influence of Buton rock asphalt on the physical and mechanical properties of asphalt binder and asphalt mixture. *Adv. Mater. Sci. Eng.* **2018**, 1–7. [CrossRef]
18. Yin, Y.; Zhang, X. Effect of Buton rock asphalt on rheological properties of asphalt mortar at high temperature. *J. Wuhan Univ. Technol.* **2010**, *32*, 85–89.
19. Li, R.; Karki, P.; Hao, P.; Bhasin, A. Rheological and low temperature properties of asphalt composites containing rock asphalts. *Constr. Build. Mater.* **2015**, *96*, 47–54. [CrossRef]
20. Lv, S.; Fan, X.; Yao, H.; You, L.; You, Z.; Fan, G. Analysis of performance and mechanism of Buton rock asphalt modified asphalt. *J. Appl. Polym. Sci.* **2018**, 1–8. [CrossRef]
21. Mahyuddin, A.; Tjaronge, M.W.; Ali, N.; Ramli, M.I. Experimental analysis on stability and indirect tensile strength in asphalt emulsion mixture containing Buton granular asphalt. *Int. J. Appl. Eng. Res.* **2017**, *12*, 3162–3169.
22. Wang, C.; Wang, H.; Zhao, L.; Cao, D. Experimental study on rheological characteristics and performance of high modulus asphalt binder with different modifiers. *Constr. Build. Mater.* **2017**, *155*, 26–36. [CrossRef]
23. AASHTO. *Standard Method of Test for Determining the Flexural Creep Stiffness of Asphalt Binder Using the Bending Beam Rheometer (BBR)*; American Association of State Highway and Transportation Officials: Washington, DC, USA, 2016.
24. Shi, X.; Cai, L.; Xu, W.; Fan, J.; Wang, X. Effects of nano-silica and rock asphalt on rheological properties of modified bitumen. *Constr. Build. Mater.* **2018**, *161*, 705–714. [CrossRef]
25. Lv, S.; Wang, S.; Guo, T.; Xia, C.; Li, J.; Hou, G. Laboratory evaluation on performance of compound-modified asphalt for rock asphalt/SBR and rock asphalt/Nano-CaCO. *Appl. Sci.* **2018**, *8*, 1009. [CrossRef]
26. Cai, L.; Shi, X.; Xue, J. Laboratory evaluation of composed modified asphalt binder and mixture containing nano-silica/rock asphalt/SBS. *Constr. Build. Mater.* **2018**, *172*, 204–211. [CrossRef]
27. Acurio, K.; Chico-Proano, A.; Martinez-Gomez, J.; Avila, C.F.; Avila, A.; Orozco, M. Thermal performance enhancement of organic phase change materials using spent diatomite from the palm oil bleaching process as support. *Constr. Build. Mater.* **2018**, *192*, 633–642. [CrossRef]
28. Yin, H. Study on the Mechanism of Diatomite Modification and Its Application in Dry Mixing of Asphalt Mixture. Master's Thesis, Chongqing Jiaotong University, Chongqing, China, 2012. Unpublished.
29. Li, X.; Zhang, X.; Li, Z. Dynamic viscoelastic characteristics of diatomite modified asphalt mortar. *Highway* **2006**, *10*, 145–148.
30. Cheng, Y.; Zhu, C.; Tan, G.; Lv, Z.; Yang, J.; Ma, J. Laboratory study on properties of diatomite and basalt fiber compound modified asphalt mastic. *Adv. Mater. Sci. Eng.* **2017**, *2017*, 4175167. [CrossRef]
31. Davar, A.; Tanzadeh, J.; Fadaee, O. Experimental evaluation of the basalt fibers and diatomite powder compound on enhanced fatigue life and tensile strength of hot mix asphalt at low temperatures. *Constr. Build. Mater.* **2017**, *153*, 238–246. [CrossRef]
32. Guo, Q.; Li, L.; Cheng, Y.; Jiao, Y.; Xu, C. Laboratory evaluation on performance of diatomite and glass fiber compound modified asphalt mixture. *Mater. Des.* **2015**, *66*, 51–59. [CrossRef]

33. Wei, H.; He, Q.; Jiao, Y.; Chen, J.; Hu, M. Evaluation of anti-icing performance for crumb rubber and diatomite compound modified asphalt mixture. *Constr. Build. Mater.* **2016**, *107*, 109–116. [CrossRef]
34. Li, J.; Zhao, X. Study on test performance of rock asphalt composite diatomite modified asphalt mixture. *Road Traffic Technol. (Appl. Technol. Ed.)* **2016**, *4*, 66–68.



© 2019 by the authors. Licensee MDPI, Basel, Switzerland. This article is an open access article distributed under the terms and conditions of the Creative Commons Attribution (CC BY) license (<http://creativecommons.org/licenses/by/4.0/>).



Article

# Optimization of the Calcium Alginate Capsules for Self-Healing Asphalt

Shi Xu <sup>1,\*</sup>, Amir Tabaković <sup>1,2,3</sup>, Xueyan Liu <sup>1</sup>, Damian Palin <sup>1,4</sup> and Erik Schlangen <sup>1</sup>

<sup>1</sup> Civil Engineering and Geosciences, Delft University of Technology, Delft 2628CN, The Netherlands; amir.tabakovic@dit.ie (A.T.); x.liu@tudelft.nl (X.L.); D.Palin@tudelft.nl (D.P.); Erik.Schlangen@tudelft.nl (E.S.)

<sup>2</sup> Research Enterprise and Innovation, Technological University Dublin, Dublin D07EWW4, Ireland

<sup>3</sup> School of Civil Engineering, University College Dublin, Dublin D04K3H4, Ireland

<sup>4</sup> Materials Science and Engineering, Cornell University, Ithaca, NY 14853, USA

\* Correspondence: xushi891011@gmail.com; Tel.: +31(0)-15-27-85944

Received: 3 December 2018; Accepted: 28 January 2019; Published: 30 January 2019

**Featured Application:** This self-healing technology for asphalt pavements has the potential to greatly disrupt asphalt production methods (which have been stable over the past 100 years). This paper presents a development process of ‘calcium-alginate microcapsules encapsulating an asphalt bitumen rejuvenator’. The encapsulated rejuvenator is released when required (on demand) which rejuvenates the aged binder. Once crack is initiated and starts propagating it encounters a microcapsule, energy at tip of the crack opens the microcapsule, releasing the rejuvenator (healing agent). The rejuvenator will infuse into the aged binder soften it, allowing to flow, two broken edges to get into a contact and seal the crack, i.e., repair the damage. This self-healing system has the potential to double the life span of roads, greatly improving road performance while reducing costs. By advancing self-healing technology and applying it to the road industry, the self-healing technology presents an opportunity to revolutionise road design and costs, both financial and environmental, associated with the road construction and maintenance processes.

**Abstract:** It has been demonstrated that calcium alginate capsules can be used as an asphalt healing system by pre-placing rejuvenator (healing agent) into the asphalt mix and releasing the rejuvenator on demand (upon cracking). This healing mechanism relies on the properties of capsules which are determined by the capsule preparation process. In this study, to optimize the calcium alginate capsules, capsules are prepared using varying Alginate/Rejuvenator (A/R) ratios. Light microscope microscopy and Environmental Scanning Electron Microscope (ESEM) are employed to characterize the morphology and microstructure of these capsules. Thermal stability and mechanical property are investigated by thermogravimetric analysis (TGA) and compressive tests. The testing results indicate that higher alginate content results in smaller diameter and lower thermal resistance, but higher compressive strength. The optimum A/R ratio of calcium alginate capsules is found to be 30/70. To prove the effectiveness of the optimized capsules, the capsules are embedded in asphalt mortar beams and a bending and healing program is carried out. The effect of capsule shell material on the mechanical response of asphalt mixture is evaluated through three-point bending on the mortar beams embedded with blank capsules (without the healing agent). Aged mortar beams containing alginate capsules encapsulating rejuvenator demonstrate a higher strength recovery after bending tests, which indicates effective healing due to the release of the rejuvenators from the capsules.

**Keywords:** asphalt; rejuvenation; alginate; capsules

## 1. Introduction

Asphalt concrete is widely used for pavement construction throughout the world. During its service life, the asphalt concrete ages due to environmental effects including oxidation, UV light irradiation and moisture damage, which make it become stiffer with time and gradually lose its original properties [1–4]. As a result, ageing of asphalt leads to an increase of stiffness and brittleness which make it prone to premature failures like cracking and raveling [5].

Although the phenomenon of ageing deteriorates the performance of asphalt pavement, an asphalt rejuvenator, including industrial rejuvenator and oil [5,6], can be used to reverse this process by restoring the lost properties of aged asphalt, i.e., stiffness and self-healing capacity [7]. The asphalt rejuvenator has been successfully used in asphalt recycling [8] and surface course rejuvenation [9]. However, the surface course rejuvenation allows the asphalt rejuvenator to reach no more than 2 cm of the pavement structure, which means microcracks inside the pavement cannot be healed. Moreover, all these procedures require onsite construction work which leads to traffic restrictions, use of fresh materials and an increase of CO<sub>2</sub> emission [10].

As an emerging self-healing technology in asphalt pavement, the capsule healing method provides a solution to the ageing problem, thus prolong the service life of asphalt pavement [5]. Researchers have shown that the inclusion of encapsulated asphalt rejuvenator in an asphalt mix is a promising method to improve the self-healing capacity in asphalt pavement [5]. The intention of the embedded capsules is to deliver encapsulated healing agent into the asphalt pavement, when a crack occurs, the healing agent is released into the microcrack, wets the crack surfaces, diffuses into the aged bitumen, and softens the aged binder, allowing it to flow and eventually heal the crack [10]. The concept of using embedded capsules was first reported by White et al. [11]. White's self-healing concept has been applied to many other materials, including asphalt. Research has been carried out to explore effective rejuvenator delivery system for asphalt pavement, and some encapsulation methods have been investigated, such as epoxy capsules [12] and Melamine-formaldehyde (MMF) capsules [13]. Recently, alginate, a low-cost and environmentally friendly biopolymer that is largely stored in brown algae, has been used as an encapsulation material for asphalt rejuvenator to achieve self-healing in asphalt pavement [14–17]. As an anionic polysaccharide, alginate cross-polymerizes when exposed to a solution containing divalent cations such as Ca<sup>2+</sup> [18].

Tabaković et al. [15] successfully used compartmented alginate fibers to encapsulate rejuvenator and proved the effectiveness of this self-healing system on micro-crack healing. However, the rejuvenator content in the alginate fiber compartments was very limited. To improve this situation, Xu et al. [16] developed a more efficient rejuvenator delivery system using calcium alginate capsules. The prepared capsules had the rejuvenator content of 56% by volume. These capsules were proved to be able to survive during the asphalt production process and showed a significant healing effect on asphalt mastic samples. The previous research demonstrated that alginate is a positive material for rejuvenator encapsulation thus application in self-healing asphalt [16]. However, the healing mechanism of this capsule healing system relies on the properties of the capsules. A change in diameter, microstructure or rejuvenator content of calcium alginate capsules would result in different thermal and mechanical properties, which largely affect the healing capacity of this capsule healing system. Thus, an optimization of this healing system is needed.

The main objective of this research is to optimize the calcium alginate capsules for the application in self-healing asphalt. In this study, the calcium alginate capsules are prepared with varying A/R ratios, and the thermal stability and mechanical property have been studied through thermogravimetric analysis (TGA) and compression testing. Depending on thermal stability and mechanical property, 30/70 has been found to be the optimum A/R ratio. Microscopy is used for the structural and volumetric study of the capsules. To prove the effectiveness (healing efficiency) of the capsules in an asphalt mortar mix, capsules are embedded in asphalt mortar beams and a bending and healing program is carried out. To demonstrate that the improvement of healing is from the rejuvenator

rather than the capsule shell material, blank capsules without rejuvenator are used as references in the bending and healing program.

## 2. Experimental Method

### 2.1. Materials and Preparation

#### 2.1.1. Capsule Preparation Process

As shown in Figure 1, the rejuvenator (healing agent) within the capsule structure was created by calcium alginate crosslinks inside the calcium alginate capsules [16]. Firstly, 6 wt.% sodium alginate solution was prepared in demineralized water. Then 2.5 wt.% solution of poly ethylene-alt-maleic-anhydride (PEMA) was mixed with the rejuvenator with a ratio of 40% PEMA and 60% healing agent, forming a healing agent solution. The PEMA was used to coat the rejuvenator and prevent the diffusion of rejuvenator into alginate shell. Subsequently, the sodium alginate solution and healing agent solution (rejuvenator and PEMA) were mixed. The sodium alginate and healing agent solution was prepared in varying A/R ratios: 100/0, 60/40, 50/50, 40/60, 30/70, 20/80 and 10/90. To remove any trapped air in the blend, the blend was vacuumed in a vacuum chamber for 60 min. After that, the blend was pumped through a needle dropwise into the  $\text{CaCl}_2$  solution to allow capsule formation. The  $\text{CaCl}_2$  solution was stirred at a low speed for the full duration of the capsule production process. This process prevented capsules from amalgamating. After a full capsule batch was produced, capsules were drained from the  $\text{CaCl}_2$  bath and gently washed using demineralized water. Then the calcium alginate capsules were left to dry in a drying oven for 48 h at 30 °C. Around 113.2 g of capsules can be produced based on 100 g of rejuvenator.

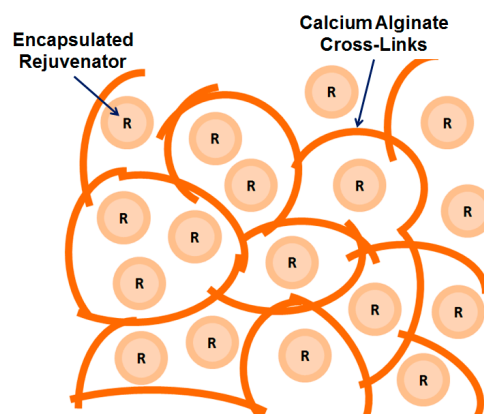


Figure 1. Rejuvenator encapsulated by the calcium alginate crosslinks.

The healing agent used in this research is an industrially produced asphalt rejuvenator 'R20' supplied from Latexfalt, Koudekerk aan den Rijn, Netherlands. All other chemicals used in the capsule preparation process were supplied from Sigma Aldrich, St. Louis, MO, USA.

#### 2.1.2. Asphalt Mortar Components

According to a porous asphalt aggregate skeleton study, the bituminous mortar in the top layer of a porous asphalt mixture contains sand fractions smaller than 0.5 mm [19,20]. Based on the RAW specification for porous asphalt [21], the mortar composition is derived. Two types of capsules were used in the mortar mix preparation, including capsules with rejuvenator (A/R ratio at 30/70) and blank capsules (A/R ratio at 100/0). As a result, three types of mortar mix were prepared, including the control mix (without capsules), 2.6 wt.% capsules mix and 2.6 wt.% blank capsules mix. The mix compositions of the asphalt mortar are shown in Table 1. The sand used in this study is sieved from the Bestone sand, Bontrup, Amsterdam, Netherlands. The filler is type wigro 60k, which consists of



25~35% calcium hydroxide, provided from Bontrup, Amsterdam, Netherlands. The 70/100 bitumen was provided by Latexfalt, Koudekerk aan den Rijn, Netherlands.

**Table 1.** Mix composition of asphalt mortar.

Mix Constituent	Percentage by Weight		
	Without Capsules	2.6% Capsules	2.6% Blank Capsules
Sand <0.5mm	34.8	34.8	34.8
Filler (Wigro60k)	32.6	32.6	32.6
Bitumen (70/100)	32.6	30.0	30.0
Capsules	0	2.6	0
Blank Capsules	0	0	2.6

Prior to mixing, all of the asphalt mix constituents were preheated in an oven for 2 h at 160 °C. Then, sand, filler and bitumen were mixed using a Hobart Mixer forming a mortar. The capsules were gradually added to the mortar. Subsequently, the mortar mixture was compacted by a roller cylinder in a mold to form the beam test samples. The length, width and height of the beams are 125 mm, 15 mm and 25 mm, respectively. A ‘v’ notch at the center of the beam was made during the casting process in order to achieve controlled crack propagation [16].

### 2.1.3. Ageing on Asphalt Mortar Mix

The aim of the capsule healing system is to achieve self-healing by restoring the lost properties of aged asphalt. The healing effect of the capsules is illustrated when applied in aged asphalt mixture. Hence, except the fresh mortar mix mentioned in Section 2.1.2, some aged asphalt mortar mix were prepared by ageing of the asphalt mortar mix based on a laboratory ageing procedure which was used by Shi et al. [16] and Tabaković et al. [15]: the asphalt mix was cured at 135 °C for 4 h and then 85 °C for 4 days.

### 2.2. Characterization of Capsules

The morphology of calcium alginate capsules was characterized using a Leica MZ 6 light microscope (Leica Microsystems B.V., Amsterdam, Netherlands) Philips XL30 ESEM (Philips, Eindhoven, Netherlands) was employed to evaluate the microstructure inside the capsule. The ESEM was operated at 20 kV accelerating voltage and the magnification was 1000×. The scanning capsules were pre-coated with epoxy and polished until the cross sections were reached; in this way, the inner structure of capsules can be investigated by scanning the cross-sectional area using ESEM.

The temperature dependent mass changes of the calcium alginate capsules were evaluated with NETZSCH STA 449 F3 Jupiter TGA system (NETZSCH, Wormerveer, Netherlands). The analysis was performed in an argon (Ar) atmosphere. As shown in Figure 2, a temperature control program was employed, and the mass changes were recorded with time.

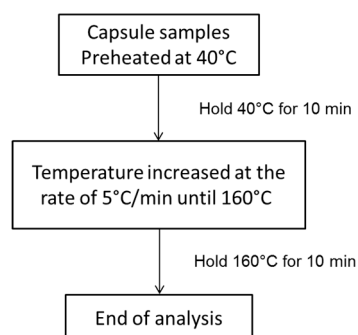


**Figure 2.** Thermogravimetric analysis (TGA) temperature control program.

The mechanical resistance of the calcium alginate capsules was evaluated by compressive strength using a micro tensile strength testing machine (TSTM) developed by Microlab (Figure 3a) [16]. The tests were performed under 20 °C with displacement control at a speed of 0.01 mm/s. A video camera was used to record the capsule deformation during the compression process. Prior to the compressive test, capsules were cured for 15 min at 10 different temperatures (at 20 °C increments from −20 °C to 160 °C) to study the mechanical property of capsules considering the multi-temperature effect. At least five capsules were studied for each condition.

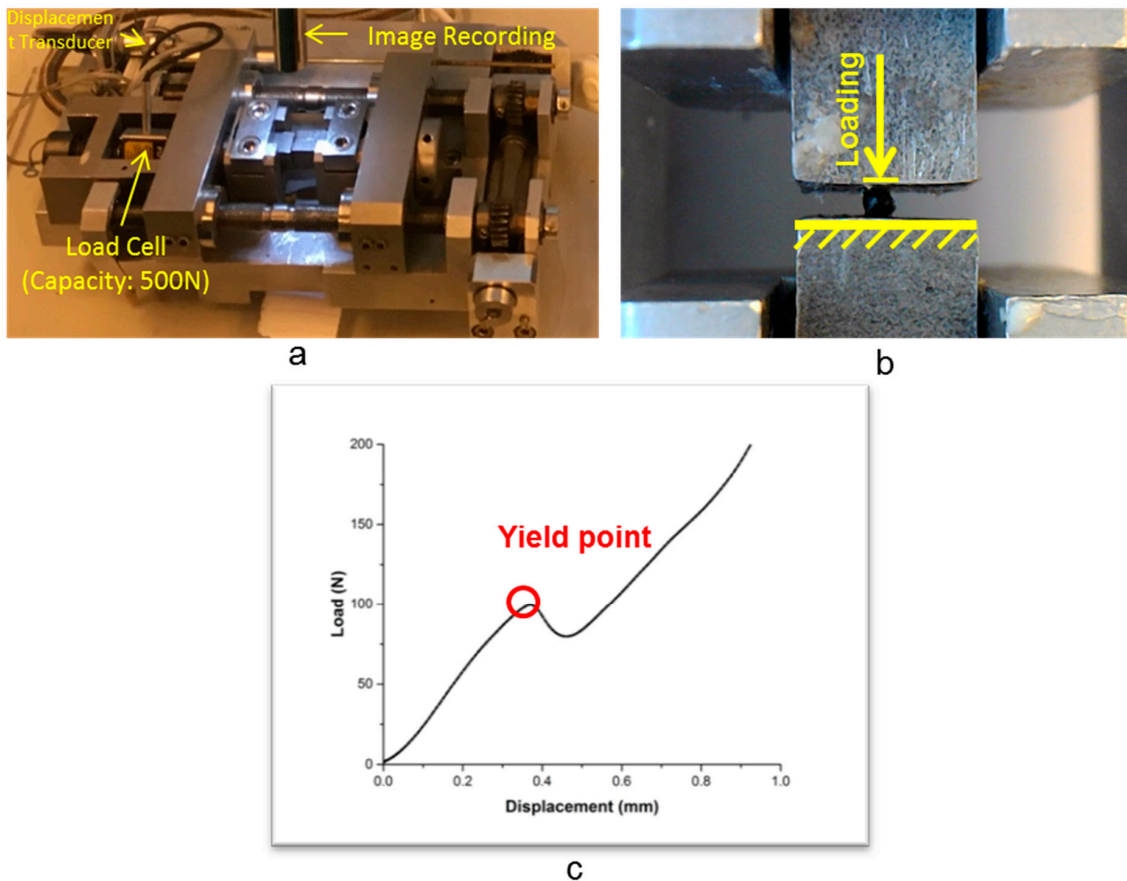


**Figure 3.** Compressive test on calcium alginate capsules using tensile strength testing machine (TSTM): (a) TSTM testing setup; (b) a capsule sample during compression; and (c) a load and displacement curve from compressive test.

In this research, the yield strength of the tested capsule (Figure 3b) was used as the compressive strength. Below this yield point (see Figure 3c) a capsule showed elastic behavior. When the stress went higher, permanent deformation was created and the capsule gradually ruptured, along with a leaking out of the rejuvenator.

### 2.3. Three-Point-Bending Test and the Healing Efficiency of the Asphalt Mortar

The 3PB test was chosen to determine the healing efficiency of the calcium alginate capsules on the asphalt mortar. By using a Universal Testing Machine (UTM) (Industrial process controls LTD, Melbourne, Australia). The 3PB tests were performed at the loading speed of 0.01mm/s under −10°C to create a brittle fracture in the mortar sample. The beam height, support span and beam width used in this study are 25 mm, 100 mm and 15 mm, respectively. During 3PB tests, the notch allowed cracks to initiate at the center of the beams and propagating throughout the cross section of the beams.

The healing efficiency of these asphalt mortar beams was evaluated through a bending and healing program. At first, 3PB tests were performed to allow crack formation and acquire the initial strength of beam specimens. Then, the fractured beams were healed back in the mold at 20 °C for 4 h and followed by 3PB tests to acquire the bending strength after the first healing. Subsequently, the fractured beams were healed again for 12 h in the mold and followed by another 3PB test to acquire the bending strength after second healing.

The Healing Index (HI) was used to characterize the healing efficiency, which was calculated using the formula below [16]:

$$HI = \frac{C_x}{C_1} \times 100\% \quad (1)$$

where HI is the healing index of asphalt mortar beam,  $C_1$  is original bending strength (MPa) of the beam sample and  $C_x$  is the bending strength (MPa) after x cycles of healing.

### 3. Results and Discussion

#### 3.1. Capsule Morphology

Figure 4 presents the optical images of the capsule with different A/R ratios. Without rejuvenator, the calcium alginate capsule has a transparent brown color and ellipsoid shape.

With encapsulated rejuvenator, the calcium alginate capsules become black, and increasing the amount of rejuvenator results in a more spherical morphology. Table 2 summarizes the diameter and morphology information of capsules fabricated with different A/R ratios. At least 12 capsules were measured for each A/R ratio type and since the well-controlled manufacture process, the capsules had the same diameters for each A/R ratio type. The results indicate that the diameter of capsules increases with rejuvenator content. When the A/R ratio is beyond 40%, the fabricated capsules become ellipsoids. This change in morphology might be due to dehydration of the hydrated alginate. During the drying process, higher alginate content would result in more dehydration and greater deformation.

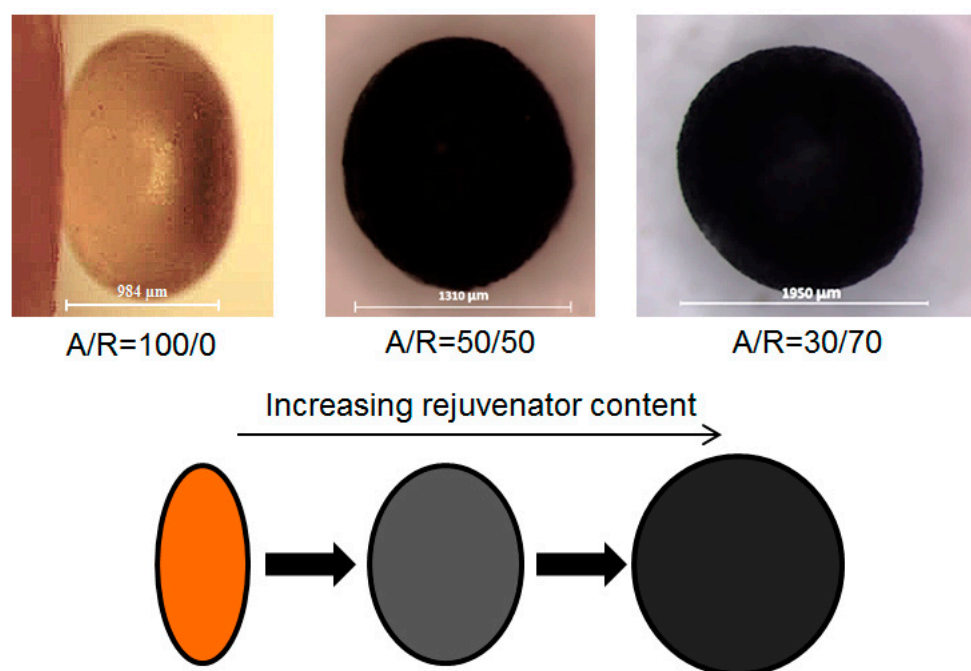


Figure 4. Microscopic images of capsules and the trend with alginate/rejuvenator (A/R) ratio.

**Table 2.** Calcium alginate capsules with different alginate/rejuvenator ratios.

Alginate/Rejuvenator Ratio (%)	Diameter ( $\mu\text{m}$ )	Minor Axis ( $\mu\text{m}$ )	Morphology
100/0	1500	980	Ellipsoid
60/40	1920	1670	
50/50	1640	1310	
40/60	1740	1600	
30/70	1950	1950	
20/80	2170	2170	Sphere
10/90	2450	2450	

### 3.2. Capsule Microstructure

The cross-sectional ESEM images of capsules fabricated with A/R ratios of 60/40, 50/50, 40/60, 30/70, 20/80 and 10/90 are shown in Figure 5. In these images, the bright pixels are recognized as alginate, while the rest are rejuvenator. These ESEM images indicate an existence of alginate network inside of the capsules, which means the capsules have the rejuvenator encapsulated in the porous media instead of the traditional capsule' core-shell structure. From the image in Figure 5a to Figure 5f, an increasing rejuvenator volume and decreasing alginate network can be seen, which matches the applied amount of rejuvenator in each capsule.

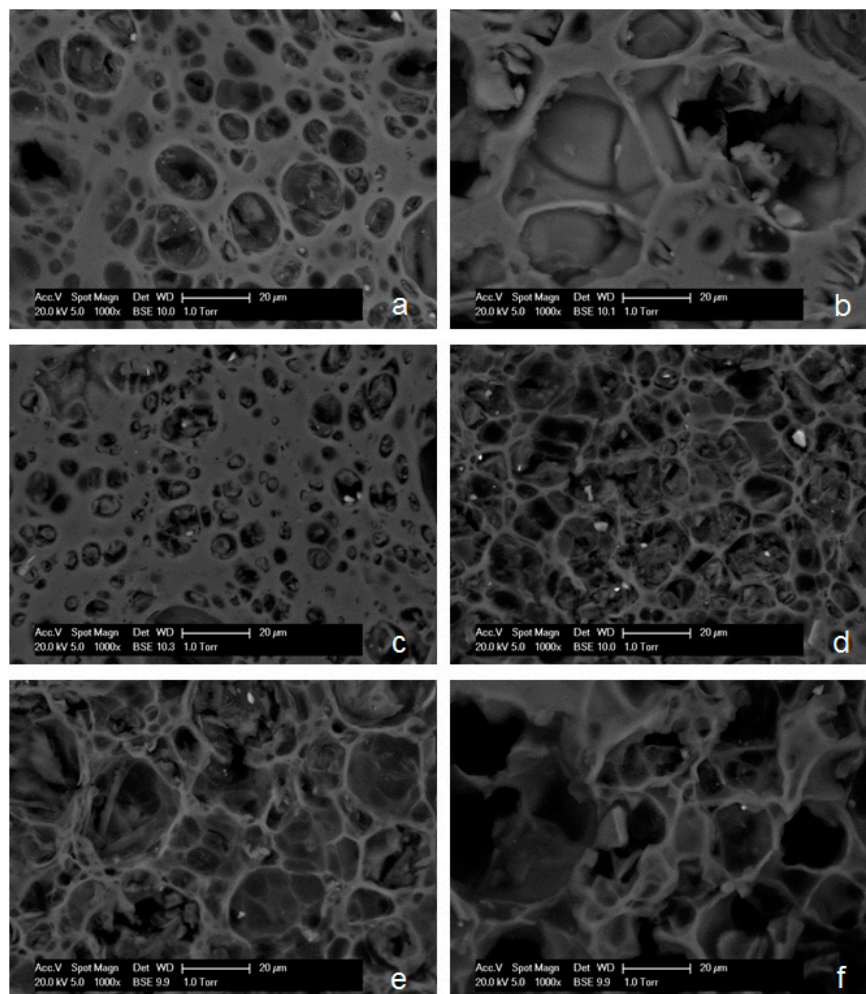


**Figure 5.** The cross-sectional ESEM images of calcium alginate capsules fabricated with A/R ratios of: (a) 60/40, (b) 50/50, (c) 40/60, (d) 30/70, (e) 20/80 and (f) 10/90.

As stated in the previous research [16], this honeycomb-like structure provides a structural reinforcement that allows the capsule to possess higher thermal and mechanical resistance. Meanwhile, the compartmented rejuvenator storage in porous media could even have multi-healing function on micro cracks.

### 3.3. Thermogravimetric Analysis

Figure 6 shows the TGA results for capsules fabricated with varying A/R ratios. When the testing temperature is below 100 °C (before 25 min), all of the capsules show less than 2% weight loss. When the testing temperature exceeds 100 °C, linear increasing weight loss trends can be observed for capsules with different A/R ratios. Weight loss of capsules in this region is most likely due to the dehydration of calcium alginate gels. Among all the analyzed capsules, capsules with an A/R ratio of 10/90 show the lowest weight loss during the tests, and the weight loss trend increases with the alginate contents. As the temperature reaches 160 °C (referred as the asphalt mixing temperature) and is held for 15 min, the weight loss of the capsules retains a linear trend, and the final weight loss percentages of capsules with A/R ratios of 60/40, 50/50, 40/60, 30/70, 20/80 and 10/90 are 10.5%, 7.9%, 5.6%, 4.9%, 3.8% and 2.2%, respectively. This indicates that the capsules, except surface moisture evaporation, do not experience any significant degradation at 160 °C. Meanwhile, when the A/R ratio is lower than 40/60, the final weight loss is lower than 5%, which means capsules with these ratios are relatively more stable and are capable of surviving the asphalt mixing temperature.

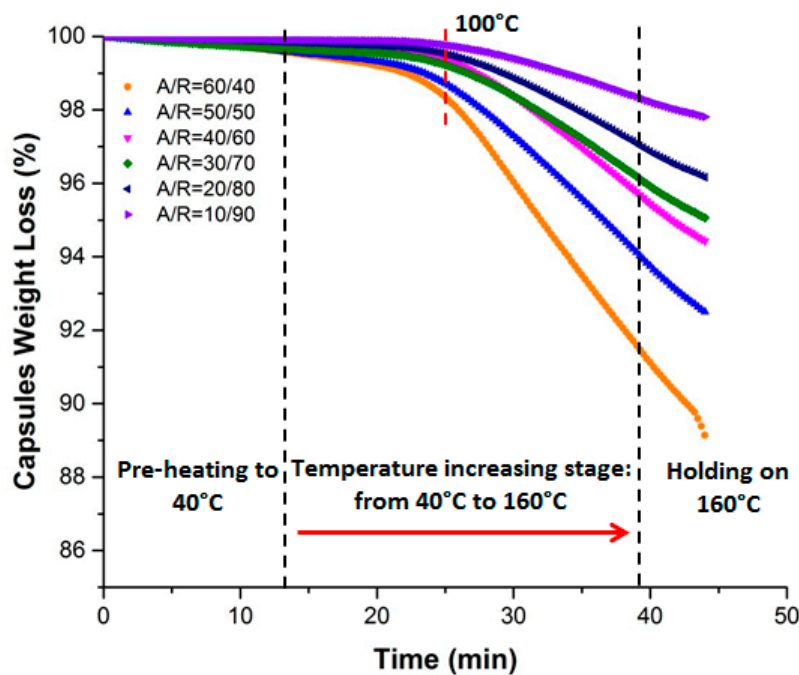


Figure 6. TGA results of capsules fabricated with varying A/R ratios.

### 3.4. Compressive Tests on Capsules

Figure 7 shows the compressive testing results for different A/R ratios of capsules. In general, with the increase of curing temperature, especially from 100 °C to 160 °C, a decrease of compressive strength can be found. It can also be seen that higher rejuvenator content results in lower compressive strength on capsules, especially under higher curing temperatures. The compressive testing results indicate that the dehydration of the alginate gel results in degradation of some of the calcium alginate chains and a decrease in the compressive strength of calcium alginate capsules.

The corresponding compression for the mastic mix is about 1.8 MPa, and the vehicle loading pressure is less than 1 MPa [22,23]. After curing at 160 °C, capsules with A/R ratios of 20/80 and



10/90 show a compressive strength less than 0.4 MPa, which is insufficient to survive the asphalt production process. Meanwhile, for the capsules with a ratio of 30/70, at the curing temperature of 160 °C, the lowest compressive strength in the curve remains 3.27 MPa. Hence, the capsules fabricated with A/R ratio of 30/70 are expected to show elastic behavior and survive the asphalt mixing process and dynamic vehicle loading during the asphalt pavement service life. Although capsules with other A/R ratios also have applicable compressive strength, they contain less rejuvenator. According to the compressive tests as well as the TGA test results, 30/70 is determined to be the optimum A/R ratio.

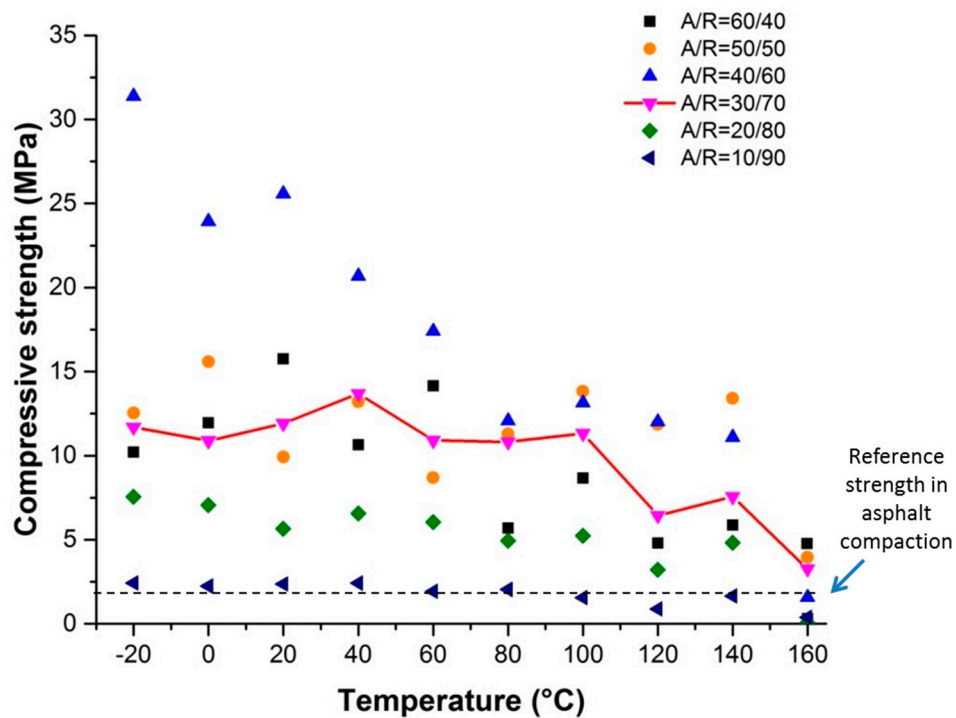


Figure 7. Compressive strength of capsules fabricated with varying A/R ratios cured under different temperatures.

### 3.5. 3PB Tests

Calcium alginate capsules prepared with the optimum A/R ratio (30/70) were applied in the asphalt mortar mix. Figure 8 shows the bending strength of the asphalt mortar beams made with fresh material. As shown in Figure 8, for all mortar beam types, the bending strength decreases after each bending and healing cycle, which indicates that the self-healing effect of the asphalt mortar beams cannot achieve full recovery of strength since the fractured area is prone to crack even after the healing process. During each testing cycle, the bending strengths of all three types of beams are very similar, and the mortar beams still have strengths about 4 MPa after 2 testing cycles, even without capsules or with blank capsules. This means that the healing capacity of the fresh material itself plays the main role in crack healing (strength recovery). It also demonstrates that the presence of calcium alginate capsules, containing rejuvenator or not, does not significantly affect the initial bending strength of the mortar beams. Hence, when the bituminous material possesses sufficient healing capacity, like in fresh bitumen, the capsule healing system could hardly improve the healing efficiency.

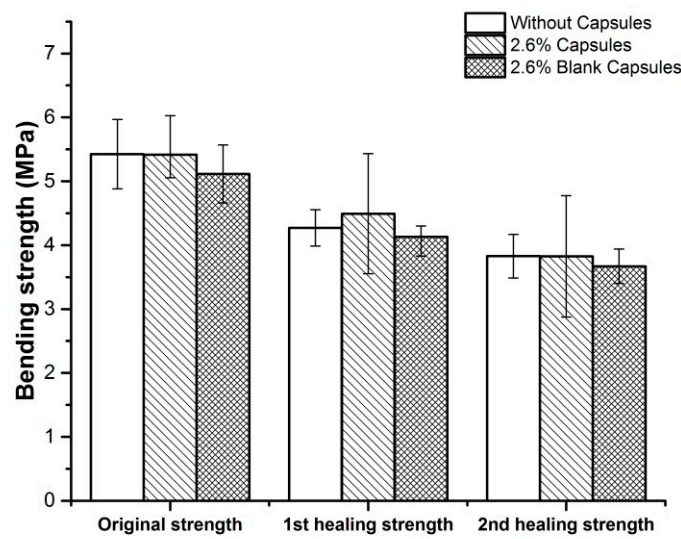


Figure 8. Bending strength of asphalt mortar beams.

Ageing of the asphalt mixture could not only increase its stiffness, but also decrease its healing capacity. As shown in Figures 8 and 9a, without capsules, the initial bending strength of aged asphalt mortar beams is 4.7 MPa, which is lower than the strength of fresh ones (5.4 MPa). This indicates that the laboratory ageing process decreases the bending strength of asphalt mortar beams. Figure 9 shows that after ageing, the asphalt mortar mix loses most of its healing capacity as the mortar beams without capsules only regain a strength of 0.2 MPa (4% of the original strength) during the first healing period. Nevertheless, with calcium alginate capsules encapsulating rejuvenator, the beams recover a strength of 1.7 MPa (40% of the original strength) during first healing (Figure 9b). This might be because the ageing of asphalt mortar greatly decreases its healing capacity, and the aged material could not provide a sufficient bond between the fracture surfaces. However, with capsules, the encapsulated asphalt rejuvenator can be released when the crack propagates through the capsules which allows localized healing around the broken capsules on the fracture surfaces. Thus, more strength can be regained during the healing process on mortar beams with capsules.

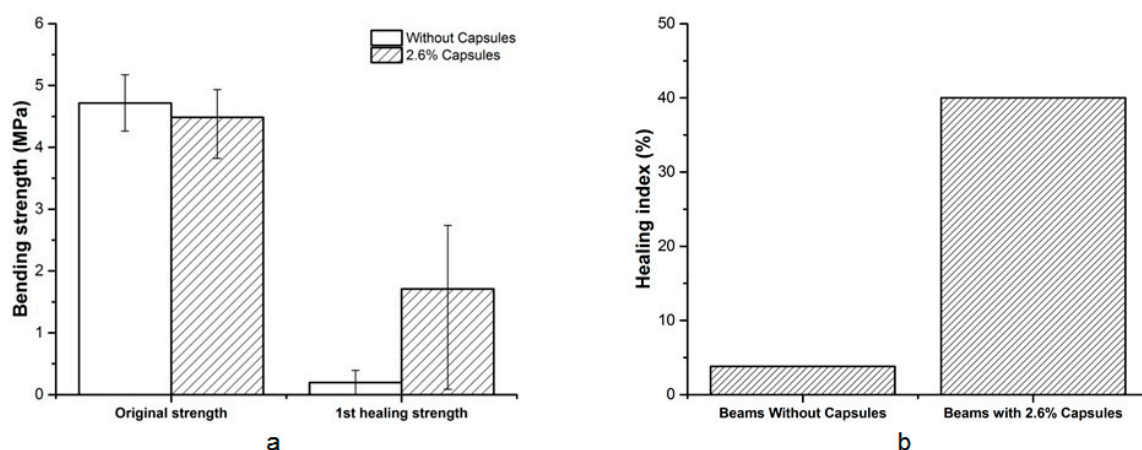


Figure 9. Testing of aged asphalt mortar beams in bending and healing program: (a) Bending strength and (b) healing efficiency.

#### 4. Conclusions

In this study, the thermal and mechanical properties of the prepared calcium alginate capsules for self-healing asphalt applications have been studied and optimized by changing the A/R ratio.

The bending tests on asphalt mortar samples further demonstrate the healing mechanism of the calcium alginate capsules healing system. The following conclusions can be drawn:

- The A/R ratios used in the capsule production process greatly influence the morphology, structure and performance of calcium alginate capsules. In principle, a higher rejuvenator content (lower A/R ratio) results in a larger diameter, larger inside pores, higher thermal resistance and less compressive strength;
- The optimum A/R ratio is 30/70, as the prepared capsules not only have sufficient thermal and mechanical resistance to survive the asphalt mixing and compaction process, but also contain as much rejuvenator as possible;
- The asphalt mortar beams with capsules, with blank capsules and without capsules demonstrated similar bending strengths for all testing cycles, which indicates that the intrinsic healing capacity of the asphalt mortar is relatively high and plays the main role in the healing process of asphalt mortar samples;
- The asphalt mortar beams with blank capsules do not showed significant difference initial bending strength than the other two mixes, which means calcium alginate, the encapsulation material of these capsules, hardly has any contribution to the bending strength of asphalt mortar beams;
- In the aged asphalt mortar beams, the samples with capsules showed a healing index of 40%, which is much higher than those without capsules (4%). This indicates that the encapsulated asphalt rejuvenator can be released upon cracking and rejuvenate the aged material to heal the crack.

The ultimate goal of self-healing asphalt is to produce a road that possesses autonomic healing ability, greatly prolonging its service life. Optimization of the calcium alginate capsules healing system helps the development of this self-healing technology and moves one step closer to this goal.

**Author Contributions:** S.X., A.T., X.L., D.P. and E.S. conceived and designed the experiments; S.X. performed the experiments and analyzed the data; S.X. wrote the paper; A.T., X.L., D.P. and E.S. reviewed the paper.

**Acknowledgments:** The authors would like to acknowledge the scholarship from the China Scholarship Council (No. 201506950066). The authors also wish to thank Bert Jan Lommerts, Irina Catiugă and Sayeda Nowrozon Nahar, Latexfalt BV, for their support to the project. In addition, the technicians from Microlab and the Section of Pavement Engineering of TU Delft are greatly appreciated for their technical support.

**Conflicts of Interest:** The authors declare no conflict of interest.

## References

1. Airey, G.D. State of the art report on ageing test methods for bituminous pavement materials. *Int. J. Pavement Eng.* **2003**, *4*, 165–176. [CrossRef]
2. Pasetto, M.; Baldo, N. Fatigue performance of asphalt concretes with RAP aggregates and steel slags. In *7th RILEM International Conference on Cracking in Pavements*; Springer: Dordrecht, The Netherlands, 2012; pp. 719–727.
3. Morea, F.; Zerbino, R. Improvement of asphalt mixture performance with glass macro-fibers. *Construct. Build. Mater.* **2018**, *164*, 113–120. [CrossRef]
4. Sun, Y.; Fang, C.; Wang, J.; Yuan, X.; Fan, D. Method of Fatigue-Life Prediction for an Asphalt Mixture Based on the Plateau Value of Permanent Deformation Ratio. *Materials* **2018**, *11*, 722. [CrossRef] [PubMed]
5. Xu, S.; García, A.; Su, J.; Liu, Q.; Tabaković, A.; Schlangen, E. Self-Healing asphalt review: From idea to practice. *Adv. Mater. Interf.* **2018**, *5*, 1800536. [CrossRef]
6. Shirzad, S.; Hassan, M.M.; Aguirre, M.A.; Mohammad, L.N.; Cooper, S.; Negulescu, I.I. Microencapsulated Sunflower Oil for Rejuvenation and Healing of Asphalt Mixtures. *J. Mater. Civ. Eng.* **2017**, *29*, 04017147. [CrossRef]
7. Tabaković, A.; Schlangen, E. Self-healing technology for asphalt pavements. *Self-Healing Mater.* **2016**, 285–306.
8. Xiao, F.; Yao, S.; Wang, J.; Li, X.; Amirkhanian, S. A literature review on cold recycling technology of asphalt pavement. *Construct. Build. Mater.* **2018**, *180*, 579–604. [CrossRef]



9. Wang, F.; Wang, Z.; Li, C.; Xiao, Y.; Wu, S.; Pan, P. The rejuvenating effect in hot asphalt recycling by mortar transfer ratio and image analysis. *Materials* **2017**, *10*, 574. [CrossRef] [PubMed]
10. Ayar, P.; Moreno-Navarro, F.; Rubio-Gámez, M.C. The healing capability of asphalt pavements: A state of the art review. *J. Cleaner Prod.* **2016**, *113*, 28–40. [CrossRef]
11. White, S.R.; Sottos, N.R.; Geubelle, P.H.; Moore, J.S.; Kessler, M.; Sriram, S.R.; Brown, E.N.; Wiswanathan, S. Autonomic healing of polymer composites. *Nature* **2001**, *409*, 794. [CrossRef] [PubMed]
12. García, Á.; Schlangen, E.; Van de Ven, M. Properties of capsules containing rejuvenators for their use in asphalt concrete. *Fuel* **2011**, *90*, 583–591. [CrossRef]
13. Su, J.; Qiu, J.; Schlangen, E. Stability investigation of self-healing microcapsules containing rejuvenator for bitumen. *Polym. Degrad. Stab.* **2013**, *98*, 1205–1215. [CrossRef]
14. Prajer, M.; Wu, X.; Garcia, S.J.; van der Zwaag, S. Direct and indirect observation of multiple local healing events in successively loaded fibre reinforced polymer model composites using healing agent-filled compartmented fibres. *Compos. Sci. Technol.* **2015**, *106*, 127–133. [CrossRef]
15. Tabaković, A.; Post, W.; Cantero, D.; Copuroglu, O.; Garcia, S.; Schlangen, E. The reinforcement and healing of asphalt mastic mixtures by rejuvenator encapsulation in alginate compartmented fibres. *SmMaS* **2016**, *25*, 084003. [CrossRef]
16. Xu, S.; Tabaković, A.; Liu, X.; Schlangen, E. Calcium alginate capsules encapsulating rejuvenator as healing system for asphalt mastic. *Construct. Build. Mater.* **2018**, *169*, 379–387. [CrossRef]
17. Xu, S.; Liu, X.; Tabaković, A.; Schlangen, E. Investigation of the Potential Use of Calcium Alginate Capsules for Self-Healing in Porous Asphalt Concrete. *Mater.* **2019**, *12*, 168. [CrossRef]
18. Draget, K.I.; Skjåk-Bræk, G.; Smidsrød, O. Alginate based new materials. *Int. J. Biol. Macromol.* **1997**, *21*, 47–55. [CrossRef]
19. Muraya, P.M. *Permanent Deformation of Asphalt Mixes*; Delft University of Technology: Delft, The Netherlands, 2007.
20. Woldekidan, M.F. *Response Modelling of Bitumen, Bituminous Mastic and Mortar*; Delft University of Technology: Delft, The Netherlands, 2011.
21. CROW, I. *Standaard RAW Bepalingen*; CROW: Ede, The Netherlands, 2005.
22. Brown, E.R.; Kandhal, P.S.; Zhang, J. *Performance Testing for Hot Mix Asphalt*; National Center for Asphalt Technology at Auburn University: Auburn, AL, USA, 2001.
23. Tabaković, A.; Karač, A.; Ivanković, A.; Gibney, A.; McNally, C.; Gilchrist, M.D. Modelling the quasi-static behaviour of bituminous material using a cohesive zone model. *Eng. Fract. Mech.* **2010**, *77*, 2403–2418. [CrossRef]



© 2019 by the authors. Licensee MDPI, Basel, Switzerland. This article is an open access article distributed under the terms and conditions of the Creative Commons Attribution (CC BY) license (<http://creativecommons.org/licenses/by/4.0/>).

Article

# Dynamic Response Analysis of Rutting Resistance Performance of High Modulus Asphalt Concrete Pavement

Chundi Si <sup>1,2,\*</sup>, Hang Cao <sup>1</sup>, Enli Chen <sup>1</sup>, Zhanping You <sup>2</sup> , Ruilan Tian <sup>1,\*</sup>, Ran Zhang <sup>2,3</sup> and Junfeng Gao <sup>3</sup> 

<sup>1</sup> Institute of Transportation Environment and Safety Engineering, Shijiazhuang Tiedao University, Shijiazhuang 050043, Hebei, China; schundi@mtu.edu (H.C.); chenenl@stdu.edu.cn (E.C.)

<sup>2</sup> Department of Civil and Environmental Engineering, Michigan Technological University, Houghton, MI 49931, USA; zyou@mtu.edu (Z.Y.); ranzhang@mtu.edu (R.Z.)

<sup>3</sup> School of Highway, Chang'an University, South Erhuan Middle Section, Xi'an 710064, Shaanxi, China; junfengg@mtu.edu

\* Correspondence: sichundi@stdu.edu.cn (C.S.); tianrl@stdu.edu.cn (R.T.)

Received: 21 October 2018; Accepted: 12 December 2018; Published: 19 December 2018

**Featured Application:** This study of the dynamic response of rutting resistance of high modulus asphalt concrete pavement will lay a foundation for the performance research and further engineering practice of high modulus asphalt concrete.

**Abstract:** In order to systematically study the rutting resistance performance of High-Modulus Asphalt Concrete (HMAC) pavements, a finite element method model of HMAC pavement was established using ABAQUS software. Based on the viscoelasticity theory of asphalt, the stress and deformation distribution characteristics of HMAC pavement were studied and compared to conventional asphalt pavement under moving loads. Then, the pavement temperature field model was established to study the temperature variation and the thermal stress in HMAC pavement. Finally, under the condition of continuous temperature variation, the creep behavior and permanent deformation of HMAC pavement were investigated. The results showed that under the action of moving loads, the strain and displacement generated in HMAC pavement were lower than those in conventional asphalt pavement. The upper surface layer was most obviously affected by outside air temperature, resulting in maximum thermal stress. Lastly, under the condition of continuous temperature change, HMAC pavement could greatly reduce the deformation of asphalt material in each surface layer compared to conventional asphalt pavement.

**Keywords:** HMAC; dynamic response; moving load; temperature field; rutting resistance; the permanent deformation

---

## 1. Introduction

Due to the heavy-duty vehicle traffic and frequency of hot weather, rutting damage of pavement has become increasingly prominent. In recent years, road researchers have explored many approaches to prevent rutting effectively. High-modulus asphalt concrete (HMAC) was first used in France to improve the modulus of pavement, and has gained increasing application in the road industry. In 1980, HMAC was first applied to road reinforcement and maintenance [1]. After that, with the fuel crisis, HMAC was applied more to both the base and surface layers of new roads. The standard for construction and design of the high modulus asphalt pavement was proposed by the French researchers in 1992. During the 1990s, the French P.R. INDUSTRI Co. developed the PR-module

type high modulus admixture for asphalt pavement. Due to the convenience of application and the favorable impact on road performance, the PR-type high-modulus admixture has been widely applied. In 1999, a French researcher conducted a long-term monitoring of the performance of asphalt pavement with low-grade asphalt binder. It was found that the use of a high-modulus admixture along with low-grade asphalt binder is a cost-effective method to enhance the rutting resistance of pavement. The low-grade asphalt binder with high-modulus admixture has been widely applied as the lower surface layer of pavement [2]. Since 2004, a lot of studies have been performed on the HMAC by the LCPC (Laboratoire Central des Ponts et Chaussées) organization of France [3].

After decades of development, high-modulus asphalt mixtures have been divided into two types in French: the high-modulus asphalt mixture surface layer (EME) and the high-modulus asphalt mixture base layer (BBME). According to the quality requirement for the high-modulus asphalt mixture, the standards NF-P98-140 (1992) [4], NF-P98-141(1993) [5], and NF EN13108-1-2007 [6] for high-modulus asphalt mixture were built by French research scholars. The applied layer and related performance requirement for the high-modulus asphalt mixture have been identified. These standards were built based on the field application, and provide technical guidance for pavement construction.

Various researchers have investigated the HMAC for field application. England investigated the high modulus asphalt binder and the related mixture based on field applications of test roads. A long-term project was conducted that determined that the anti-aging performance and moisture susceptibility of HMAC are inferior. The project was conducted by Scott Wilson Engineering Consultants Ltd. and the University of Nottingham; then, a designed standard for England was proposed based on this project [7]. In Italy, the road performance and effect of HMAC was analyzed, and the benefits of HMAC as a base layer were identified [8]. Some Portuguese researchers studied the rutting resistance of the high-modulus asphalt mixture based on the high-temperature climate [9]. Some researchers in United States (USA) also studied the design methods and analyzed the cost analysis of the HMAC [10,11]. After long-term and meticulous research, the Transportation Research Board (TRB) of the US proposed a long-life asphalt pavement design theory. In this theory, the HMAC was used in the middle surface layer of the long-life pavement structure, and the modified asphalt was used to increase the modulus [12].

Lee et al. [13] prepared the HMAC by using the SBS (Styrene-Butadiene-Styrene) modified asphalt binder and high softening point oil, and found that the HMAC has better rutting resistance. European research on the high-modulus asphalt mixture test section showed that there was an insignificant correlation between pavement cracking and the grade of asphalt. The low-grade asphalt has little impact on cracking phenomena, while it significantly contributes to the improvement of rutting resistance [14]. Rodrigo et al. [15] analyzed the strength modulus, adhesion, stability, rutting resistance, and anti-aging performance of the mixture. Espersson et al. [16] studied the influence of temperature on the performance of high-modulus asphalt mixture. It was found that under the condition of high temperatures, HMAC could reduce the required pavement thickness.

Compared with foreign countries, the research on HMAC pavement in China is still in its infancy. The cooperation between Jiangsu Transportation Research Institute and the Cooper Co. proposed three key topics during the meeting in 2009: the origin, development, and current status of the high-modulus asphalt binder; the design methods and performance of the high-modulus asphalt mixture; and the process of how England adopt the high-modulus asphalt binder [17]. In addition, some scientific research institutes also studied the high-modulus asphalt mixture. In early 2007, Liaoning Academy of Transportation Sciences carried out the research on the application technology of HMAC, and paved a test HMAC surface road on Liaofeng highway in Liaoyang City [18]. The Liaoning transportation research institute proposed the standard 'Construction Technical Specification of High Modulus Asphalt Mixture (DB 21/T1754-2009)' [19], which has provided technical support for the actual application of HMAC in Liaoning province. AiminSha et al. [20] improved the performance of HMAC by adjusting the gradation of mixture design, especially the dosage of mine powder, and adding high-molecular additives. As a result, the resilient modulus at 20 °C of HMAC increased by

about 45%. Jianlong Zheng, et al. [21] studied the pavement material design and the construction technique of HMAC under heavy traffic loading condition, and revealed the mechanical mechanism that could improve the road performance of HMAC. Ouyang Wei et al. [22] developed HMAC materials through experiments, and applied them to the middle surface layer, which has the greatest impact on pavement rutting, thus greatly improving the rutting resistance of asphalt pavement. Guangdong Road and Bridge Construction Development Corporation, in cooperation with South China University of Technology, built a HMAC pavement test section of about 1.4 km on the Beijing-Zhuhai highway. After two years of operation, the test road was exposed to high-temperature conditions, and remained in good condition [23]. Analyzing the force behavior of the conventional road structure with a HMAC layer is still necessary in order to understand rutting resistance performance of the high-modulus asphalt concrete.

In this study, the stress and temperature fields of HMAC pavement compared to conventional asphalt pavement under moving load were analyzed in ABAQUS (Rhode Island, RI, USA). Then, under the condition of continuous temperature variation, the creep and permanent behavior were studied to show the characteristics of rutting deformation resistance in the HMAC pavement structure.

## 2. Materials and HMAC Pavement Model

### 2.1. Materials

The pavement structure is from a HMAC pavement test section of a highway in Baoding city of Hebei Province, China. Two different middle surface layers, AC-20 and HMAC-20, were compared. The gradations of AC-20 and HMAC-20 were the same, as shown in Table 1. The aggregates with particle sizes between 10–15mm were basalt, and the aggregates with other particle sizes were limestone. The matrix asphalt used in AC-20 was 70#, while in HMAC-20 it was 20#; the basic properties of asphalt 70# and 20# are shown in Tables 2 and 3, respectively. The asphalt–aggregate ratios were determined as 4.4% in AC-20 and 3.8% in HMAC-20 by the Chinese specifications JTG E20-2011 [24] and JTG D50-2006 [25]. The pavement structure and corresponding material parameters based on test are shown in Table 4.

**Table 1.** Gradation of AC-20 and high-modulus asphalt concrete (HMAC)-20.

Sieve Size (mm)	26.5	19.0	16.0	13.2	9.5	4.75	2.36	1.18	0.6	0.3	0.15	0.075
Rate of Passing (%)	100	97.5	86.0	74.0	64.0	44.0	30.0	20.5	15.0	11.0	8.0	6.0

**Table 2.** Basic properties of 20# matrix asphalt.

Index	Measured Value	Requirement
Penetration at 25 °C (0.1 mm)	19.9	15~25
Dynamic viscosity at 60 °C (Pa·s)	2918	≥550
Softening point (°C)	64.6	55~71

**Table 3.** Basic properties of 70# matrix asphalt.

Index	Measured Value	Requirement
Penetration at 25 °C (0.1 mm)	66	60~80
Penetration index	−0.3	−1.5~1.0
Softening point (°C)	47.5	≥46
Flash point (°C)	322	≥260

**Table 4.** Material parameters of HMAC pavement.

Structural Layer	Thick-Ness (mm)	Density (kg·m <sup>-3</sup> )	Compressive Resilient Modulus (MPa)	Poisson's Ratio	Damping Coefficient $\alpha$
AC-13	4	2500	1 200	0.35	0.8
HMAC-20	6	2500	2 000	0.30	0.8
ATB-25	8	2450	800	0.30	0.8
Cement treated base (CTB)	34	2400	1 400	0.25	0.8
Lime fly ash treated base (LFTB)	20	1800	600	0.25	0.8
Soil	-	1850	40	0.40	0.8

Note: 1. The compressive resilient moduli are from the uniaxial compressive test based on the standard JTG D50-2006 at 20 °C. 2. ATB-25 means Asphalt-Stabilized Macadam.

### 2.2. HMAC Pavement Model

A finite element model based on the software ABAQUS(TM) V6.13 (2013) by Dassault Systèmes® (Rhode Island, RI, USA) was established (ABAQUS is one of the most powerful numerical simulation tools in the world. It can simulate the performance of most typical engineering materials and can be used to solve the problems in the field of road engineering) [26,27]. The assumptions about the road model were made as follows [28,29]. (1) The asphalt pavement surface was made of viscoelastic materials, and the remaining layers were made of linear elastic materials. (2) Structural layers were of uniform thickness, as well as isotropic and continuous without considering the influence of gravity. (3) The surface of the road was considered to be a horizontal plane, regardless of its roughness and the influence of the horizontal and vertical slopes. (4) The structural layers were completely continuous, and the displacement was continuous in the vertical direction.

In order to accurately simulate the viscoelasticity of asphalt materials, the viscoelastic parameters based on the Burgers model that were measured in the actual experiment were converted to Prony series [30]. These parameters, which were used in ABAQUS software, are shown in Table 5.

**Table 5.** Prony parameters in the Burgers model.

Structural Layer	Prony Series			
	$g_1$	$g_2$	$\tau_1$	$\tau_2$
AC-13	0.38	0.62	1 596.17	36.78
HMAC-20	0.18	0.82	24 526.03	170.58
ATB-25	0.39	0.61	1 015.55	43.04

The three-dimensional structure of the asphalt pavement was established by using ABAQUS. Due to the symmetry of the pavement structure and load, the 1/2 model was taken for analysis, and the following dimensions of the pavement model were established: length (z-direction) was eight meters, width (x-direction) was six meters, and thickness (y-direction) was three meters. The C3D8R element was used in the grid-drawing process. The gridding of the mobile zone was refined across a section of the width and along the length and thickness of the model. Gradual refinement of the grid structure was made from the base to the surface of the pavement model, as shown in Figure 1.

The boundary conditions were set as follows: (1) the fully fixed constraint was applied to the subgrade of the road; (2) displacement of the four sides of the model was constrained; and (3) symmetrical constraints were applied to the symmetrical planes.

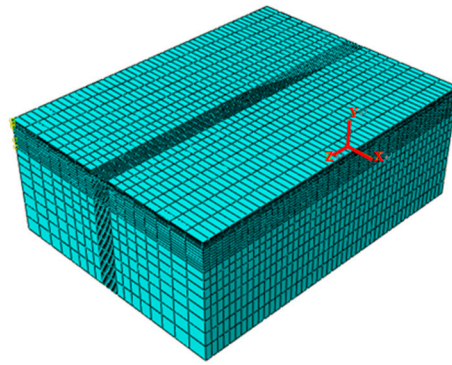


Figure 1. Finite element model of pavement structure.

### 2.3. Distribution and Application of Moving Loads

The standard axle load BZZ-100 was adopted, and the equivalent ground contact area of the load was  $0.213\text{ m} \times 0.167\text{ m}$  with the axle load of 100 kN, which is the vertical uniform rectangular load. Due to the symmetry of the wheels on both sides of the vehicle and the negligible influence they had on each other during driving, only the left side of the axle was analyzed during the simulation. The loading regions (between the tires and the roadway) are shown in Figure 2. Measurements were taken under three points: point A, between the loading regions; point B, in the center of one of the loading regions; and point C, at the outer edge of one of the loading regions. FORTRAN language was used to program an ABAQUS external subroutine, VDLOAD, to move the vehicle load 60 km/h along the moving belt [31].

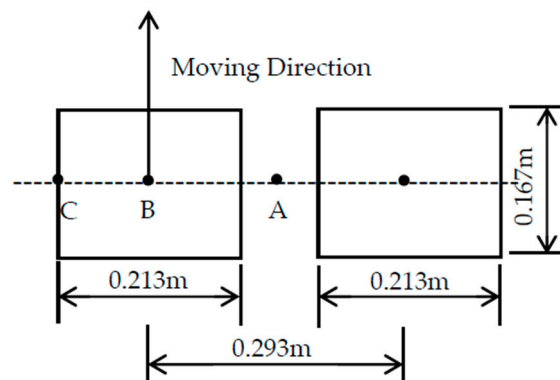


Figure 2. Diagram of loading regions.

### 3. Comparison of Mechanical Properties of HMAC and Conventional Asphalt Pavement

The structure of the conventional asphalt pavement that was used in this study was identical to the structure of HMAC pavement, except for the middle surface layer. The high-modulus structural layer in HMAC pavement was located in the middle surface layer, while the middle surface layer in the conventional asphalt pavement was composed of the ordinary material, AC-20. The specific parameters of these materials were determined by referring to literature [32], as shown in Table 6.

Table 6. Comparison of material parameters in the middle surface layer.

The Middle Surface Layer	Thickness (mm)	Density ( $\text{kg}\cdot\text{m}^{-3}$ )	Resilient Modulus (MPa)	Poisson's Ratio	Damping Coefficient $\alpha$	$g_1$	$g_2$	$\tau_1$	$\tau_2$
AC-20	6	2 500	1 000	0.35	0.8	0.37	0.63	621.07	20.45
HMAC-20	6	2 500	2 000	0.30	0.8	0.18	0.82	24 526.03	170.58

The vertical stress, vertical strain, and vertical displacement at the upper surface layer were analyzed, as well as the shear stress and the shear strain at the middle surface layer. These measurements were taken underneath point B in Figure 2: that is, underneath the center of the leftmost tire of the vehicle. This data was compared to the conventional asphalt pavement. The dynamic response comparison results are shown in Figures 3–7.

Figures 3–7 show the following results:

Under the action of moving loads, the pattern variations of the five parameters were essentially the same between the two types of pavement. Compared to conventional asphalt pavement, the vertical stress and vertical shear stress in HMAC pavement were larger, while the vertical strain, vertical shear strain, and vertical displacement were smaller. This is consistent with the conclusion of reference [33,34], which argued that the vertical stress of the upper surface layer of HMAC pavement is greater than that of conventional asphalt pavement.

The difference in the mechanical properties of HMAC pavement compared to conventional asphalt pavement are summarized as follows: the maximum vertical stress increased 7.96% from 326.11 kPa to 352.07 kPa; the strain value decreased 24.5% from  $-25.02 \mu\epsilon$  to  $-18.89 \mu\epsilon$ ; and the vertical displacement decreased 18.8% from 0.16 mm to 0.13 mm. It can be seen that the HMAC pavement has good resistance to vertical deformation.

Both the shear stress and the shear strain changed abruptly before and after the load passed the point of interest. Before the vehicle moved over the loading point, the maximum vertical shear stress of the middle surface layer compared to the conventional surface layer increased from 117.96 kPa to 132.51 kPa, while the vertical shear strain decreased from  $45.81 \mu\epsilon$  to  $30.80 \mu\epsilon$ . These relationships show that HMAC can be used to reduce the strain deformation caused by shear stress and effectively prevent the shear damage of the pavement.

Although the use of HMAC increased the stress in the surface layers, the strain decreased, which indicated that the rutting resistance ability of the asphalt pavement improved.

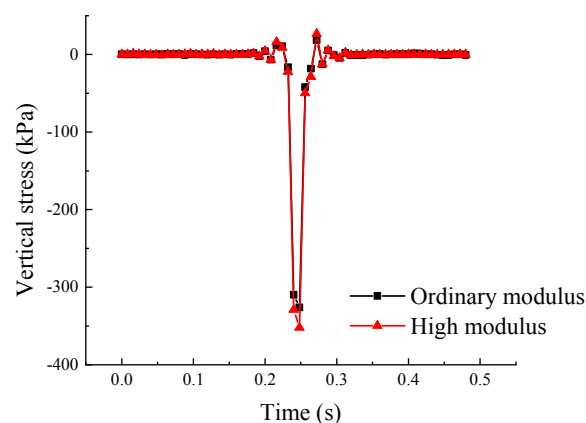


Figure 3. Comparison of vertical stress in the upper surface layer.

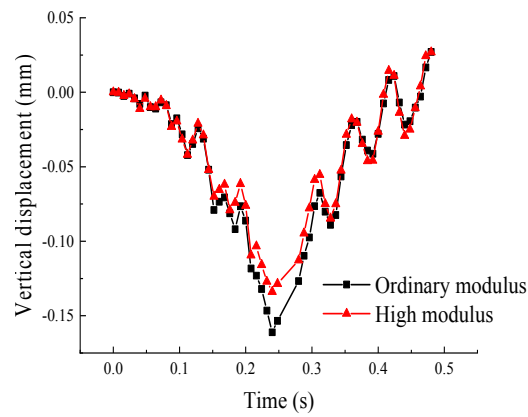


Figure 4. Comparison of vertical displacement in the upper surface layer.

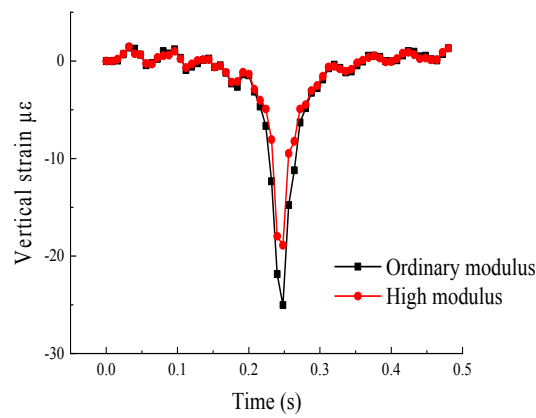


Figure 5. Comparison of vertical strain in the upper surface layer.

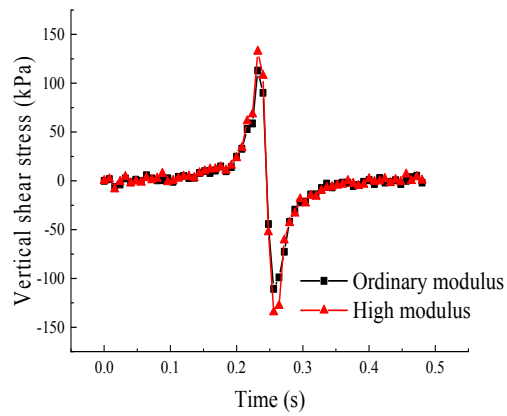


Figure 6. Comparison of vertical shear stress in the middle surface layer.



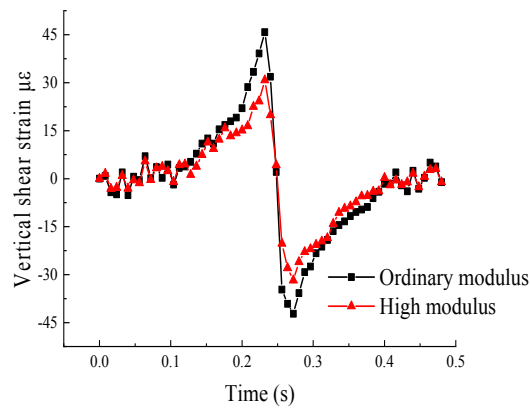


Figure 7. Comparison of vertical shear strain in the middle surface layer.

#### 4. Simulation of Temperature Field and Thermal Stress in HMAC Pavement

##### 4.1. Analysis of Temperature Field

The following assumptions were made in the establishment of the temperature field model: (1) the pavement layers were homogeneous and isotropic continua; (2) the temperature gradient in the horizontal direction was zero, and only the transfer of heat flow in the vertical direction was considered; and (3) there was continuous contact between the layers of the pavement, and the temperature and heat flow between the layers was continuous.

The temperature parameters of each layer of pavement materials were obtained from related literature [35–39]. The results are shown in Table 7.

Table 7. Temperature parameters of HMAC pavement.

Structural Layer	Depth (cm)	Density (kg·m <sup>-3</sup> )	Thermal Conductivity (J·(m·h·°C) <sup>-1</sup> )	Heat Capacity (J·(kg·°C) <sup>-1</sup> )	Solar Absorption Coefficient $\alpha_s$	Road Surface Emissivity $\epsilon$	Absolute Zero $T_Z$ (°C)
AC-13	4	2 500	3 600	900	0.9	0.81	-273
HMAC-20	10	2 500	4 680	925	0.9	0.81	-273
ATB-25	18	2 450	3 600	800	0.9	0.81	-273
CTB	52	2 400	5 600	910	0.9	0.81	-273
LFTB	72	1 800	5 200	940	0.9	0.81	-273
Soil	-	1 850	5 600	1 000	0.9	0.81	-273

Air temperature data over a 24-h span in summer, as shown in Table 8, was applied in ABAQUS to calculate the temperature field of HMAC pavement. The temperature changes of each structural layer over the 24-h period are shown in Figure 8.

Table 8. Air temperature per hour over a 24-h span in summer.

Time (h)	Air Temperature (°C)	Time (h)	Air Temperature (°C)	Time (h)	Air Temperature (°C)
1	24.5	9	29.2	17	33.7
2	23.7	10	31.8	18	32.1
3	23.1	11	33.8	19	30.1
4	22.6	12	35.6	20	29.8
5	23.5	13	36.5	21	29.2
6	24.0	14	38.1	22	27.5
7	26.2	15	36.9	23	26.9
8	27.2	16	34.7	24	25.2

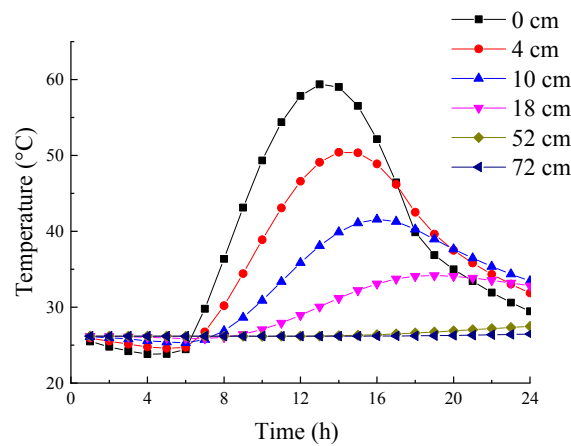


Figure 8. Temperature in each structural layer over 24 h.

It can be seen from Figure 8 that the temperature changes varied with different depths in the pavement structure. From this data, several conclusions were made.

The upper and middle surface layers were most affected by the outside air temperature, which was essentially the same as the variations of the air temperature. With increasing depth, the influence of outside air temperature gradually decreased. The temperature in the LFTB layer, which was least affected by the outside air temperature, always stayed at approximately 27 °C. When the outside air temperature reached its highest point, 38.1 °C at 14:00, the upper surface layer also reached the maximum value of approximately 59 °C. Due to the time delay of heat transfer, each structural layer reached the maximum temperature according to its depth beneath the surface, with the upper highest layer reaching the maximum temperature first. After 14:00, the temperature of each structural layer gradually decreased after reaching the maximum value. The road surface had the greatest overall change in temperature.

#### 4.2. Analysis of Thermal Stress

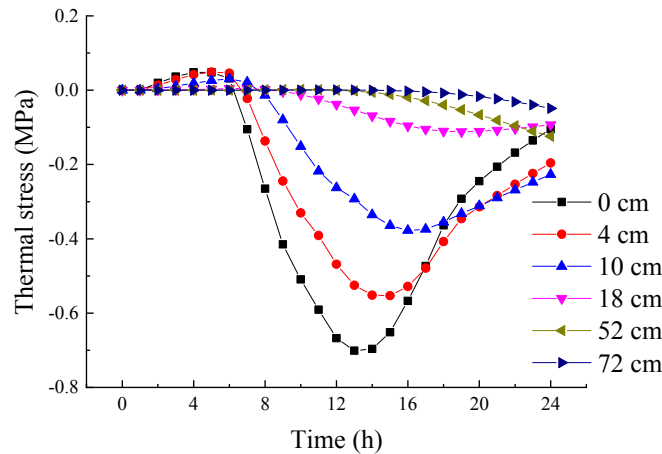
With the periodic change in temperature, the stress due to thermal expansion and contraction in the pavement structure was calculated. In the calculation of the thermal stress, the temperature coefficients and elastic moduli were different at different temperatures, and the corresponding parameters of pavement materials were determined by the related literature [40–44], as shown in Tables 9 and 10. These parameters of the materials were automatically interpolated in ABAQUS according to the actual temperature at each point. The simulated thermal stress in different layers is shown in Figure 9.

Table 9. Thermal expansion coefficients of pavement materials.

Structural Layer	Thermal Expansion Coefficient at Different Temperatures ( $10^{-5} \cdot ^\circ\text{C}^{-1}$ )				
	20 °C	30 °C	40 °C	50 °C	60 °C
AC-13	2.0	2.2	2.4	2.5	2.7
HMAC-20	1.4	1.6	1.7	1.8	1.9
ATB-25			1.2		
CTB			1.0		
LFTB			30		
Soil			20		

**Table 10.** Material elastic parameters at different temperatures.

Structural Layer	Compressive Resilient Modulus $E$ (MPa)					Poisson's Ratio $\mu$				
	20 °C	30 °C	40 °C	50 °C	60 °C	20 °C	30 °C	40 °C	50 °C	60 °C
AC-13	1 200	960	850	730	660	0.35	0.40	0.40	0.45	0.45
HMAC-20	2 000	1 650	1 210	1 080	870	0.30	0.30	0.35	0.40	0.45
ATB-25	800	690	510	420	350	0.30	0.35	0.40	0.45	0.45



**Figure 9.** Thermal stress of each structural layer over 24 h.

As shown in Figure 9, because of the decreasing of air temperature, tensile stress was generated by the shrinkage of pavement materials and reached its peak at about 4:00 from 0:00 to 6:00. In contrast, the pavement material began to expand, and generated compressive stress with the gradual increasing of air temperature after 6:00. The maximum compressive stress was reached at the same time as the maximum temperature.

Since the surface layers were most affected by the outside air temperature, the temperature field in these layers had the greatest change over the time period; therefore, the thermal stress in the surface layers had the greatest range of values. The maximum thermal stress appeared on the surface of the pavement and had a value of  $-0.7$  MPa. As the depth of the pavement increased, the thermal stress decreased continuously to approximately 0 in the base and sub-base layers. In hot summer, the maximum difference between tensile stress and compressive stress on the road surface within a day was about 0.75 MPa; the fatigue damage was easy accrued under the repeated action of thermal expansion and contraction.

Therefore, high temperature had a great impact on asphalt pavement, especially in the summer afternoon, during which the maximum temperature of the pavement surface almost reached 60 °C. Such temperatures will lead to the softening of asphalt pavement and the change of material properties; coupled with the repeating and heavy loading, fatigue damage could occur easily, which is also an important factor for rutting in the high-temperature season.

### 5. Anti-Rutting Analysis of HMAC Pavement under Continuous Temperature Variation

Rutting is generated by the combination of driving load and external environment. Based on a time-hardening creep model, the previously generated temperature field was introduced to analyze the formation process of rutting, and the rutting model was established under the condition of continuous temperature variation. By comparing the creep and permanent deformation of HMAC pavement with those of conventional asphalt pavement under moving loads, the rutting resistance characteristics of HMAC pavement were studied.

### 5.1. The Establishment of Rutting Calculation Model

The deformation of asphalt pavement includes creep deformation and elastic deformation. Rutting is a severe road distress that is mainly caused by the creep deformation [45]. In this study, the time-hardening creep model was used to simulate the rutting.

The creep deformation of pavement ( $\epsilon_{cr}$ ) is related to the temperature ( $T$ ), stress ( $q$ ), and time ( $t$ ), and was obtained from Equation (1):

$$\epsilon_{cr} = f(T, q, t) \tag{1}$$

In this study, the Norton Bailey creep law was applied to simulate the creep characteristics of asphalt mixture under loading conditions. In the analysis process, the stress is assumed to be constant; as a result, the above equation can be expressed as:

$$\epsilon_{cr} = C_1 q^{C_2} t^{C_3} \tag{2}$$

where  $q$  and  $t$  refer to the stress and time, respectively; meanwhile,  $C_1$ ,  $C_2$ , and  $C_3$  are the temperature-dependent model parameters, and were determined based on the lab tests.

Furthermore, Equation (2) can be expressed as:

$$\epsilon_{cr} = A q^n t^m \tag{3}$$

Equation (3) is the time–stress–creep model of ABAQUS, in which  $A$ ,  $m$ , and  $n$  are the model parameters:

$$A = C_1 C_3, \quad n = C_2, \quad m = C_3 - 1 \tag{4}$$

In order to simulate road rutting, the creep parameters of the asphalt surface layers were used in the model. The selected parameter values are shown in Table 11, based on references [45–49].

**Table 11.** Creep parameters of asphalt mixture at different temperatures.

Structural Layer	Temperature (°C)	Creep Parameter		
		$A$	$n$	$m$
AC-13	20	6.54E-11	0.937	−0.592
	30	3.33E-09	0.862	−0.587
	40	1.45E-08	0.792	−0.577
	50	1.39E-06	0.414	−0.525
	60	1.46E-05	0.336	−0.502
HMAC-20	20	1.46E-12	0.962	−0.601
	30	5.80E-10	0.896	−0.599
	40	5.85E-09	0.823	−0.598
	50	6.10E-07	0.415	−0.532
	60	6.50E-06	0.350	−0.522
ATB-25	20	4.59E-11	0.922	−0.581
	30	3.46E-09	0.859	−0.576
	40	1.96E-08	0.83	−0.562
	50	1.20E-06	0.322	−0.522
	60	3.76E-05	0.21	−0.418

In the analysis step module, 24 analysis steps, step-1 h through step-24 h, were set. These step represented 24 hours in a day. In order to simulate the formation of rutting of asphalt pavement during a continuous temperature change in one day, the cumulative loading time of the pavement structure needed to be input into each analysis step. The cumulative loading time of the wheel load was calculated as follows:

$$t = \frac{0.36NP}{n_w p B v} \tag{5}$$

where  $t$  (s) is the cumulative loading time of the wheel load;  $N$  is the number of wheel-loading cycles;  $P$  (kN) is the axle weight of the vehicle;  $n_w$  is number of tires on the axle;  $p$  (MPa) is the tire contact pressure;  $B$  (cm) is the width of tire-ground contact; and  $v$  (km/h) is driving speed.

According to the above formula, the required calculation parameters were determined, as shown in Table 12.

**Table 12.** Calculation parameters of rutting model.

Calculation Parameters	$P$ (kN)	$n_w$	$B$ (cm)	$N$ ( $\times 10^4$ )	$p$ (MPa)	$V$ ( $\text{km}\cdot\text{h}^{-1}$ )
Value	100	4	21.3	50	0.7	60

Substituting the above parameters into Formula (5), it can be calculated that the time during which a one-wheel load acts on the road surface is 0.01006 s, and the cumulative loading time for 500,000-axle loads is 5030 s. A traffic volume distribution of a certain section of road over 24 hours was selected, and an approximated value of the segmented cumulative loading time of each hour in one day was obtained, as shown in Table 13.

**Table 13.** Accumulated axial load time of at different time periods.

Time (h)	Proportion (%)	Accumulated Time (s)	Time (h)	Proportion (%)	Accumulated Time (s)	Time (h)	Proportion (%)	Accumulated Time (s)
1	1.027	51.65	9	2.874	144.60	17	9.034	454.40
2	0.821	41.30	10	4.517	227.20	18	7.802	392.45
3	0.739	37.15	11	5.749	289.15	19	6.981	351.10
4	0.411	20.65	12	7.391	371.80	20	4.927	247.85
5	0.587	29.55	13	7.802	392.45	21	4.106	206.55
6	0.821	41.30	14	6.57	330.45	22	3.696	185.90
7	1.150	57.85	15	7.391	371.80	23	2.874	144.60
8	2.053	103.25	16	8.623	433.75	24	2.053	103.25

Two load belts were installed in the middle of the road surface to apply the moving load. In order to calculate the road rutting, the previously calculated temperature field data were introduced in each analysis step by editing the INP file in ABAQUS.

### 5.2. Analysis of Creep Deformation at Different Depths of Pavement Structure

Rutting is mainly caused by the internal compaction and deformation of the asphalt pavement structure. Therefore, in order to further study the deformation of each structural layer, the distribution of transverse and vertical creep strain at different depths underneath the wheel center point (because of symmetry, the leftmost wheel was selected) and the point directly between the left-side wheels (hereafter: “dual-wheel center”) were studied. These points were referred to in Figure 2 as point B and point A, respectively. The results are shown in Figures 10 and 11.

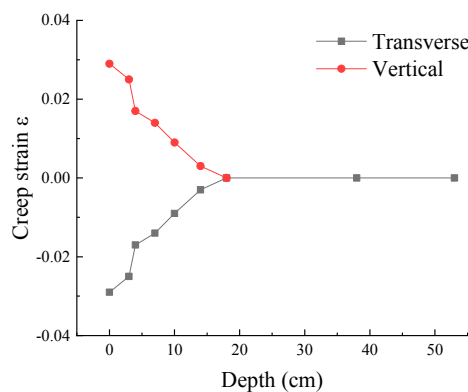


**Figure 10.** Distribution of creep strain at different depths under the center of the leftmost wheel.

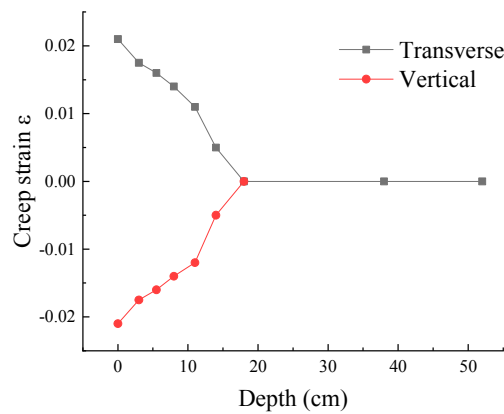


Figure 11. Distribution of creep strain at different depths under the left dual-wheel center.

As shown in Figures 10 and 11, the lateral and vertical creep strain of the structural layers underneath the road surface decreased with increasing depth, and were reduced to zero at 18 cm. This means that the creep deformation only occurred in the surface layers. The maximum vertical and transverse creep strains were almost the same, and both appeared on the road surface. The maximum creep strain underneath the center of the leftmost wheel and the dual-wheel center were 0.021 and 0.028 respectively, and the pattern variations were consistent throughout the depth of the road.

At each reference point, the vertical creep and transverse creep had opposite signs. The vertical creep strain on the road surface below the leftmost wheel center was negative, which means compressive strain; meanwhile, the horizontal creep strain was positive, which means tensile strain. In contrast, the vertical creep strain on the road surface below the dual-wheel center was tensile strain, and the horizontal creep strain was a compressive strain.

### 5.3. Comparison of Rutting Resistance between HMAC and Conventional Asphalt Pavement

#### 5.3.1. Comparison of Permanent Deformation of Surface Layers

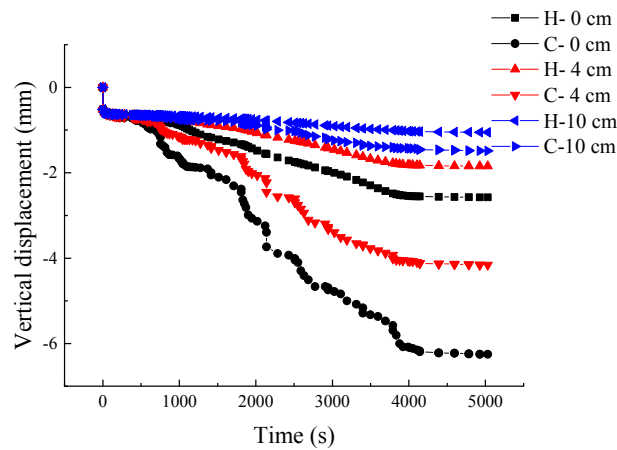
In order to further analyze the rutting resistance performance of HMAC, the permanent deformation was simulated for both HMAC and conventional asphalt pavement. The material parameters of the middle surface layer in conventional asphalt pavement are shown in Table 14. The permanent deformations are shown in Table 15 and Figures 12–14.

Table 14. Material parameters of middle surface layer of conventional asphalt pavement.

Material	Temperature (°C)	Elastic Parameters		Creep Parameters		
		Compressive Resilient Modulus E (MPa)	Poisson's Ratio $\mu$	A	n	m
AC-20	20	1 000	0.35	4.58E-11	0.944	-0.596
	30	830	0.35	2.46E-09	0.796	-0.585
	40	670	0.40	3.67E-08	0.773	-0.570
	50	530	0.45	4.80E-06	0.595	-0.532
	60	440	0.45	7.78E-05	0.384	-0.441

**Table 15.** Material parameters of middle surface layer of conventional asphalt pavement.

Pavement Type	Depth (cm)	Deformation under Point B (mm)	Deformation under Point A (mm)	Maximum Relative Deformation (mm)
HMAC Pavement	0	-2.57	1.14	3.71
	4	-1.84	0.35	2.19
	10	-1.05	-0.36	1.05
Conventional Asphalt Pavement	0	-6.25	4.59	10.84
	4	-4.16	3.24	7.4
	10	-1.47	0.12	1.59



**Figure 12.** Comparison of vertical deformation at different depths underneath the center of the leftmost wheel.

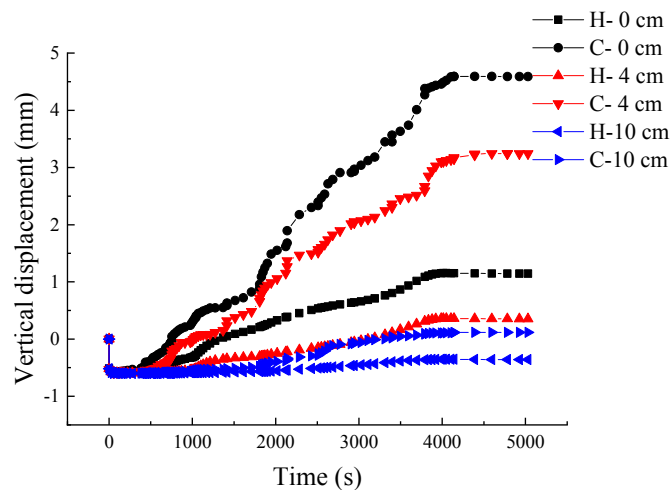


**Figure 13.** Comparison of vertical deformation at different depths underneath the dual-wheel center.

As shown in Figures 12 and 13, the internal deformation of conventional asphalt pavement changed with the increase of cumulative vehicle loading time, and its pattern variations were consistent with HMAC pavement. However, in the continuous temperature changing condition, the deformation curve of HMAC pavement fluctuated less with time and temperature, which was due to the low sensitivity of high modulus asphalt materials to temperature fluctuations. Therefore, the use of HMAC can reduce damage to the road surface caused by temperature changes.

Under continuous loading, with increasing depth, the difference in vertical displacement between HMAC pavement and conventional asphalt pavement decreased. The internal deformation of the conventional asphalt pavement increased at a faster rate, resulting in a larger difference with the

permanent deformation of the HMAC pavement, and the deformation value of both permanent tended to be stable after 4000 s.

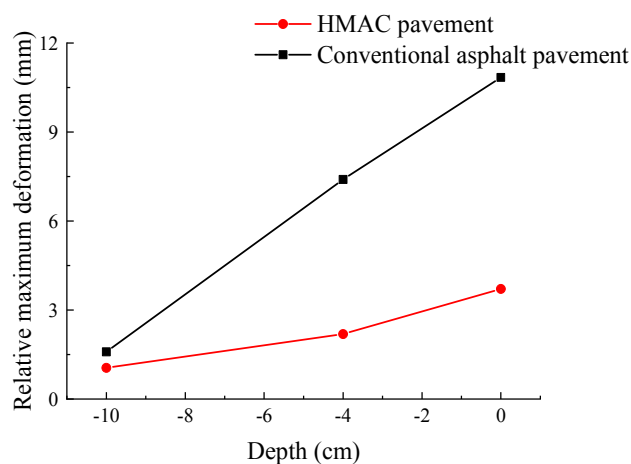


**Figure 14.** Comparison of the relative maximum deformation of two types of pavement at different depths.

From Table 15 and Figure 14, it can be seen that the deformation values of the conventional asphalt pavement at different depths were much higher than those of the HMAC pavement. At the road surface, the maximum relative deformation of conventional asphalt pavement was 10.84 mm, which was 7.13 mm higher than that of HMAC, and the difference in deformation values was the largest. The second-highest difference in deformation was 5.21 mm at the bottom of the upper surface layer. At a depth of 10 cm, although the vertical deformation was small, the maximum relative deformation of the conventional asphalt pavement was 1.59 mm. This was an increase of 51.4% compared to the HMAC pavement. Therefore, the HMAC material can significantly reduce the permanent deformation of pavement.

In the conventional asphalt pavement, the maximum relative deformation generated in the middle surface layer was the largest, at 5.81 mm. Therefore, the HMAC layer that was located in the middle surface layer could effectively reduce the relative deformation. Simultaneously, the deformation rate of the upper surface layer was also greatly reduced, thereby reducing the permanent deformation of the entire pavement.

To summarize, the permanent deformation of the two pavement structures mainly occurred in the upper and middle surface layers, while the settlement of HMAC in middle surface layer could effectively decrease the permanent deformation.

### 5.3.2. Comparison of Permanent Pavement Deformation under Heavy Traffic

Heavy traffic is a main cause for permanent deformation and the rutting distress of asphalt pavement. In order to further study the rutting resistance performance of HMAC pavement, a series of vehicle loads were applied to analyze the deformation of the two types of pavement. The result of this test is shown in Figure 15.

From Figure 15, it can be seen that as the tire contact pressure increased from 0.7 MPa to 1.5 MPa, the maximum relative deformation in both HMAC pavement and conventional asphalt pavement significantly increased; however, the maximum relative deformation of conventional asphalt pavement increased faster. When the tire contact pressure was 0.7 MPa, the maximum deformation of the conventional asphalt pavement was 7.13 mm higher than that of HMAC, and this value increased to 11.4 mm when the tire contact pressure was 1.5 MPa. Therefore, a heavy load is more harmful to the conventional pavement structure; HMAC pavement can effectively resist road deformation caused by heavy-duty loading and hot weather.



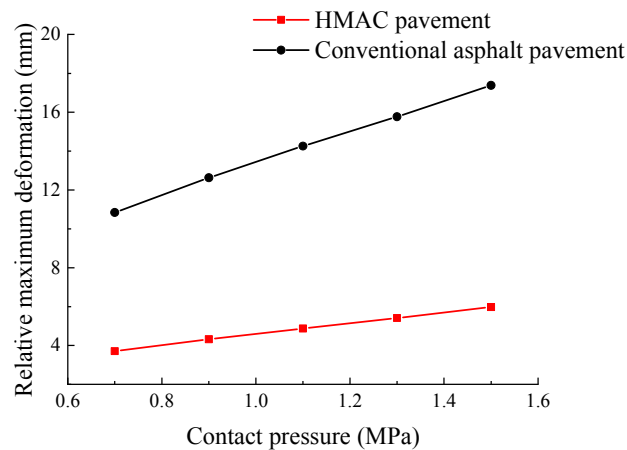


Figure 15. Comparison of maximum relative deformation at different tire contact pressure.

## 6. Summary and Conclusions

Based on the viscoelastic theory of asphalt, the finite element model in software ABAQUS was established according to the pavement structure and the material properties of the HMAC, the stress field and the temperature field was analyzed; then, the creep behavior and permanent deformation of the HMAC pavement was achieved. The following conclusions were obtained:

1. Compared to conventional asphalt pavement, vertical stress and shear stress generated in HMAC pavement increased, while the vertical strain, shear strain, and vertical displacement decreased. The vertical strain and the shear strain decreased by 24.5% and 32.8% respectively. The vertical displacement that was generated in the HMAC road surface also reduced from 0.16 mm to 0.13 mm; this is an 18.8% reduction, which improved the evenness of the road surface.

2. The pattern variations of the temperature field and the thermal stress were consistent. When the surface temperature reached the maximum of 59 °C, the maximum thermal stress of −0.7 MPa was found. As the depth increased, the influence of outside air temperature on the pavement structural layers gradually decreased.

3. In both the HMAC pavement and conventional asphalt pavement, the creep deformation only occurred in the asphalt surface layers. At the road surface, the maximum relative deformation of conventional asphalt pavement reached 10.84 mm, which was 7.13 mm higher compared to that of HMAC pavement. Therefore, the HMAC layer could effectively reduce the relative deformation of pavement.

4. With the increase of tire contact pressure from 0.7 MPa to 1.5 MPa, the maximum relative deformation increased by 2.27 mm and 6.54 mm in HMAC pavement and conventional asphalt pavement, respectively. This suggested that HMAC pavement had better resistance to road deformation and rutting.

**Author Contributions:** Conceptualization, C.S.; methodology, E.C.; software and formal analysis, H.C.; validation, R.T.; writing—original draft preparation, H.C.; writing—review and editing, R.Z., Z.Y.; visualization, J.G.

**Funding:** This work was supported by the National Natural Science Foundation of China (No. 11202142, 11302138, and 11872253), Princlal Project of Hebei Province Department of Transportation (No. Y-2010021, No 2013-2-5), Youth Talent Support Program of Hebei Province and Distinguished Young Scientists Foundation of Hebei Provincial Education Department (YQ2014038), Hebei science and technology project(18242219G).

**Conflicts of Interest:** The authors declare no conflict of interest.

## References

1. Hermansson, A. Mathematical model for paved surface summer and winter temperature, comparison of calculated and measured temperatures. *J. ColdReg. Sci. Technol.* **2004**, *40*, 1–17.

2. Transportation Research Circular. *Perpetual Bituminous Pavements: TRB Committee on General Issues in Asphalt Technology*; Number 503; Transportation Research Circular: Washington, DC, USA, 2001; pp. 12–31.
3. Kargarnovin, M.H.; Younesian, D. Response of beams on nonlinear viscoelastic foundations to harmonic moving loads. *J. Comput. Struct.* **2005**, *83*, 1865–1877. [CrossRef]
4. *Couches Dassisées: Enrobés à Module Élevé (EME)*; (NFP98-140); Renmin Communication Press: Paris, France, 1999.
5. Jean-Franeois, C. *Development and Uses of Hard Grade Asphalt and of High Modulus Asphalt Mixes in France*; Transportation Research Circular NO. 503; National Research Council: Washington, DC, USA, 2003; pp. 12–30.
6. *Bituminous Mixtures—Material Specification—Part1: Asphalt Concrete*; (NFEN13108-1:2007); Association Française de Normalisation: Paris, France, 2007.
7. Richard, E.; Scott, W. Implementing high modulus asphalt technology in the UK. In *Proceedings of the International Seminar Maintenance Techniques to Improve Pavement Performance*, Cancun, Mexico, 25–26 August 2009.
8. Pasetto, M.; Baldo, N. Permanent deformation of road and airport high performance asphalt concrete base courses. *Adv. Mater. Res.* **2013**, *723*, 494–502. [CrossRef]
9. Capitaio, S.D.; Picado-Santos, L. Assessing permanent deformation resistance of high modulus asphalt mixtures. *J. Transp. Eng.* **2006**, *132*, 394–401. [CrossRef]
10. Sanders, P.J.; Nunn, M. *The Application of Enrobe a Module Eleve in Flexible Pavements*; Transport Research Laboratory: Crowthorne, UK, 2005.
11. Rys, D.; Judycki, J.; Pszczola, M.; Jaczewski, M.; Mejlun, L. Comparison of low-temperature cracks intensity on pavements with high modulus asphalt concrete and conventional asphalt concrete bases. *Constr. Build. Mater.* **2017**, *147*, 478–487. [CrossRef]
12. Zhao, Y.Q.; Ni, Y.B. Viscoelastic response solutions of multilayered asphalt pavements. *J. Eng. Mech.* **2014**, *140*, 04014080. [CrossRef]
13. Lee, H.J.; Lee, J.H.; Park, H.M. Performance evaluation of high modulus asphalt mixtures for long life asphalt pavements. *Constr. Build. Mater.* **2007**, *21*, 1079–1081. [CrossRef]
14. Maupin, G.W.; Diefenderfer, B.K. Design of a High-Binder-High-Modulus Asphalt Mixture. *Princ. Res. Sci.* **2007**, *26*, 42–48.
15. Miró, R.; Valdés, G.; Martínez, A.; Segura, P.; Rodríguez, C. Evaluation of high modulus mixture behaviour with high reclaimed asphalt pavement (RAP) percentages for sustainable road construction. *Constr. Build. Mater.* **2011**, *25*, 3854–3862. [CrossRef]
16. Espersson, M. Effect in the high modulus asphalt concrete with the temperature. *J. Constr. Build. Mater.* **2014**, *71*, 638–643. [CrossRef]
17. Peng, Y. *Characteristic Behavior of High Modulus Asphalt and High Modulus Asphalt Mixtures*. Master's Thesis, South China University of Technology, Guangzhou, China, 2012.
18. Yang, W.T. *Research on the Technical performance with High Modulus Asphalt Concrete*. Master's Thesis, Hebei University of Technology, Tianjin, China, 2011.
19. *Construction Specification for High Modulus Asphalt Mixture*; (DB21/T1754-2009); Renmin Communication Press: Shenyang, China, 2009.
20. Sha, A.M.; Zhou, Q.H.; Yang, Q. Material composition design method for high modulus asphalt concrete. *J. Chang'an Univ. Nat. Sci. Ed.* **2009**, *3*, 1–5.
21. Ma, J. *Research on Characters of High Modulus Asphalt Concrete Pavement in Heavy Traffic Condition*. Master's Thesis, Changsha University of Science and Technology, Changsha, China, 2011.
22. Ouyang, W. *Study on Application Technology of High Modular Asphalt Concrete*. Master's Thesis, Northeastern University, Shenyang, China, 2010.
23. Luo, L. *Pavement Performance Study on the Hard Asphalt and Its Mixture*. Master's Thesis, Changsha University of Science and Technology, Changsha, China, 2009.
24. *Standard Test methods of Bitumen and Bituminous Mixtures for Highway Engineering*; (JTGE20-2011); Ministry of Transport: Beijing, China, 2011.
25. *Specifications for Design of Highway Asphalt Pavement*; (JTGD50-2006); Ministry of Transport: Beijing, China, 2006.

26. Zhuang, Z. *Finite Element Analysis and Application Based on ABAQUS*; Tsinghua University Press: Beijing, China, 2009.
27. Si, C.D.; Chen, E.L.; Fan, X.; Wang, Y.; Yu, S. Finite element simulation model of asphalt pavement based on ABAQUS. *J. Graph.* **2014**, *35*, 131–137.
28. Sousa, J.; Lysmer, J.; Monismtte, C.L. Eyelets of dynamic loads on performance of asphalt concrete pavements. *J. Transp. Res. Rec.* **1998**, *13*, 15–28.
29. White, T.D.; Zaghoul, S.M. Pavement analysis for moving aircraft load. *J. Transp. Eng.* **1997**, *123*, 436–446. [CrossRef]
30. Xu, L.; Zhao, Y.J. Finite elements analogy method for viscoelasticity of asphalt pavement. *J. North. Transp.* **2010**, *6*, 1–4.
31. Si, C.D.; Chen, E.L.; Yang, S.P.; Wang, Y.; Yu, S.W. Dynamic response of asphalt pavement considering coupling between fluid flow and stress under moving vehicle loads. *J. Vib. Shock* **2014**, *33*, 91–97.
32. Wang, F.S. A 3D fem analysis of creep deformation law of asphalt pavement based on burgers viscoelastic model. *J. Ind. Build.* **2014**, *44*, 104–109.
33. He, L.; Ling, T.Q. The influence of high modulus structure layer on fatigue performance of asphalt pavement. *J. Traffic Sci. Technol. West* **2016**, *3*, 6–11.
34. Yang, P. Study on the Properties of High Modulus Asphalt and Its Mixture. Ph.D. Thesis, South China University of Technology, Guangzhou, China, 2012.
35. Ren, D.B.; Su, B. Finite element analysis of temperature stress of asphalt pavement. *J. Shenyang Jianzhu Univ.* **2010**, *26*, 699–703.
36. Zhang, X.J.; Bai, C.L. Finite element analysis of temperature field and temperature stress of asphalt pavement. *J. East China Highw.* **2006**, *5*, 83–86.
37. Yan, Z.R. Temperature field analysis of layered pavement system. *J. Tongji Univ.* **1984**, *3*, 76–85.
38. Wu, G.C. *Temperature Stress Analysis of Semi-Rigid Pavement*; Science Press: Beijing, China, 1995.
39. Song, C.N. A survey of nonlinear temperature fields in layered pavement structures. *J. Highw.* **2005**, *1*, 49–54.
40. Wang, Z.F.; Zuo, L.; Mu, Y. Study on performance index of high modulus asphalt concrete and its application. *J. Road Mach. Constr. Mech.* **2017**, *34*, 64.
41. Qian, G.P.; Guo, Z.Y.; Zheng, J.L. Calculation of thermal viscoelastic temperature stress of asphalt pavement under environmental condition. *J. Tongji Univ.* **2003**, *31*, 150–155.
42. Zheng, M.; Li, P.; Yang, J.; Li, H.; Qiu, Y.; Zhang, Z. Fatigue life prediction of high modulus asphalt concrete based on the local stress-strain method. *J. Appl. Sci.* **2017**, *7*, 305. [CrossRef]
43. Li, P.; Zheng, M.; Wang, F.; Che, F.; Li, H.; Ma, Q.; Wang, Y. Laboratory performance evaluation of high modulus asphalt concrete modified with different additives. *J. Adv. Mater. Sci. Eng.* **2017**, *2017*, 7236153. [CrossRef]
44. Lv, S.T.; Fan, X.Y.; Xia, C.D.; Zheng, J.L.; Chen, D.; You, L.Y. Characteristics of moduli decay for the asphalt mixture under different loading conditions. *J. Appl. Sci.* **2018**, *8*, 840. [CrossRef]
45. Li, H.; Huang, X.M. Analysis of Analysis of asphalt rutting based on continuous temperature variation. *J. Southeast Univ.* **2007**, *37*, 916–920.
46. Zhang, Y.; Li, J.J. Numerical analysis of rut on high modulus asphalt pavement. *J. Highw. Traffic Technol.* **2010**, *12*, 53–55.
47. Yu, R.Y.; Yang, Y. Rutting analysis of new paved asphalt pavement considering heavy traffic vehicle restriction. *J. China Foreign Highw.* **2016**, *1*, 54–57.
48. Hu, L.L.; Lu, H.; Zhang, X.N. Comparison of module modulus of high modulus asphalt mixture. *J. Highw.* **2009**, *7*, 308–311.
49. Hua, J.F. Finite Element Modeling and Analysis of Accelerated Pavement Testing Devices and Rutting Phenomenon. Ph.D. Thesis, Purdue University, West Lafayette, Indiana, 2000.



© 2018 by the authors. Licensee MDPI, Basel, Switzerland. This article is an open access article distributed under the terms and conditions of the Creative Commons Attribution (CC BY) license (<http://creativecommons.org/licenses/by/4.0/>).

Article

# Induction Heating-Assisted Compaction in Porous Asphalt Pavements: A Computational Study

Changhong Zhou <sup>1,2</sup>, Xueyan Liu <sup>2,\*</sup>, Panos Apostolidis <sup>2</sup>, A. (Tom) Scarpas <sup>2</sup> and Liang He <sup>3</sup>

<sup>1</sup> School of Transportation and Logistics, Dalian University of Technology, Dalian 116024, China; czhou@dlut.edu.cn

<sup>2</sup> Civil Engineering and Geosciences, Delft University of Technology, 2628 CD Delft, The Netherlands; P.Apostolidis@tudelft.nl (P.A.); A.Scarpas@tudelft.nl (A.(T.)S.)

<sup>3</sup> School of Civil Engineering, Chongqing Jiaotong University, Chongqing 400074, China; heliangf1@163.com

\* Correspondence: x.liu@tudelft.nl; Tel.: +31-15-278-7918

Received: 29 September 2018; Accepted: 1 November 2018; Published: 20 November 2018

## Featured Application: Discontinuous numerical modeling of asphalt mix.

**Abstract:** Low temperature asphalt (LTA) technologies, such as warm-mixed asphalt mixes, are utilized in the paving industry to lower energy demands and greenhouse gas emissions during asphalt mixing and pavement construction. However, the asphalt mixes developed that incorporate LTA additives are more sensitive than hot-mixed asphalts to temperature reduction during compaction, which leads to inadequate compaction and subsequent poor pavement performance. The induction heating-assisted compaction of pavement structures appears to be an effective way to ameliorate such issues and to improve mix compactability at lower temperatures. Considering that induction-assisted compaction is a complex process, a computational methodology is proposed in this paper. A porous asphalt concrete mix was considered as case material. For the pavement compaction analyses after induction, the temperature field generated by electromagnetic induction was predicted and the material parameters of asphalt mortar were adjusted. The effect of induction heating on asphalt compaction effectiveness, the tendency of mix density changing, the increase in compactor passes, and the influence of temperature on compaction at different locations in the pavement were studied as well.

**Keywords:** Induction heating; pavement compaction; porous asphalt mixes; computational tools

## 1. Introduction

### 1.1. Development of Low Temperature Asphalt

Asphalt concrete mix is a combination of asphalt binder and mineral particles of various sizes (i.e., filler and aggregates). The minerals and the binder act as the structural skeleton and glue of the asphalt mix, respectively. Conventional asphalt mixes are produced and compacted at temperatures higher than 150 °C because the viscosity of asphalt binder impedes its workability at ambient temperatures. However, working with mixes at such high temperatures, greenhouse gas emissions and fumes are produced. For this reason, the asphalt industry is constantly looking for solutions to lower energy demands and reduce emissions, and the utilization of technologies that can reduce the in-plant mixing and in-field compaction temperatures of asphalt pavements are under evaluation. These technologies are named low temperature asphalt (LTA) [1–3] technologies, and the asphaltic materials developed incorporating these technologies are produced at temperatures 30 °C lower (or more) than temperatures typically used in the production of hot-mixed asphalt (HMA).

There are important environmental and health benefits associated with lower production temperatures, including lower fuel consumption and greenhouse gas emissions and reduced exposure of workers to asphalt fumes. Lower production temperatures can also potentially improve pavement performance by providing added time to mix compaction and allowing improved compaction during cold weather paving conditions. Porous Asphalt (PA) concrete is taken as case material in this research to study the construction process of low temperature porous asphalt pavement, and thus named LTPA hereinafter.

### *1.2. Development of Porous Asphalt*

A lot of effort has been spent worldwide and in the Netherlands on developing new materials and design specifications for durable PA pavement layers [4,5]. PA concrete mixes are mainly used as surface courses [6,7], and it is well known that these mixes have been developed as a material solution to increase skid resistance as well as to reduce splash during a rainstorm. Typically, an asphalt surface layer is placed, which has high air void contents, to absorb tire-pavement noise and provide good riding smoothness to reduce vehicle vibration-related noise. Factors such as aggregate characteristics, mix design, construction variables, and environment play crucial roles in the performance of PAs.

The compaction process of PAs differs from those of the conventional dense-graded mixes, which involve both static steel wheel rollers and pneumatic-tired rollers [8]. PAs are typically compacted only by a static steel roller with a few passes over the surface [9,10]. However, a serious problem in the compaction process of PAs is the aggregate segregation during laying down and the quick reduction of laying temperature when the continuity of material supply to the construction site is irregular [11]. The aggregate segregation causes unevenness in asphalt pavement surface and texture, whereas the rapid temperature reduction mainly causes inadequate compaction. All the before-mentioned leads to poor PA performance.

### *1.3. Induction Heating-Assisted Asphalt Compaction*

Asphalt compaction enhances interlocking of the aggregate-sized particles that increase the internal friction of the mix and this, in turn, provides a material with adequate stiffness and strength. However, inadequate compaction results in low mix density, high air void content, and a reduction of mix fatigue life [9]. Moreover, temperature is an important factor in mix compaction. As temperature drops, the viscosity of asphalt mix is increased and hence coated aggregate mobilization reduction will result to diminished air-void content of mix and the time required to obtain the same degree of compaction increases [9,12].

Within this framework, in order to control the temperature profile of laid asphalt mix during compaction and consequently improve the mix compactability, the implementation of induction heating (IH) technology is proposed. IH is a technique recently introduced in pavement engineering [13–16]. When an alternating electrical current is applied across an induction coil, an alternating magnetic field is developed. If the coil is placed in the vicinity of a material with inductive particles (e.g., asphalt including inductive fibers or filler-sized particles), then eddy currents are induced in the particles and heat is generated through Joule's law. The heat generated by electromagnetic induction increases the temperature of the mix and enables viscosity reduction through local melting of the binder. In this paper, a continuous IH compaction process, which consists of a continuously moving induction coil system and a roller compactor (Figure 1), was applied in LTPA-type mixes.

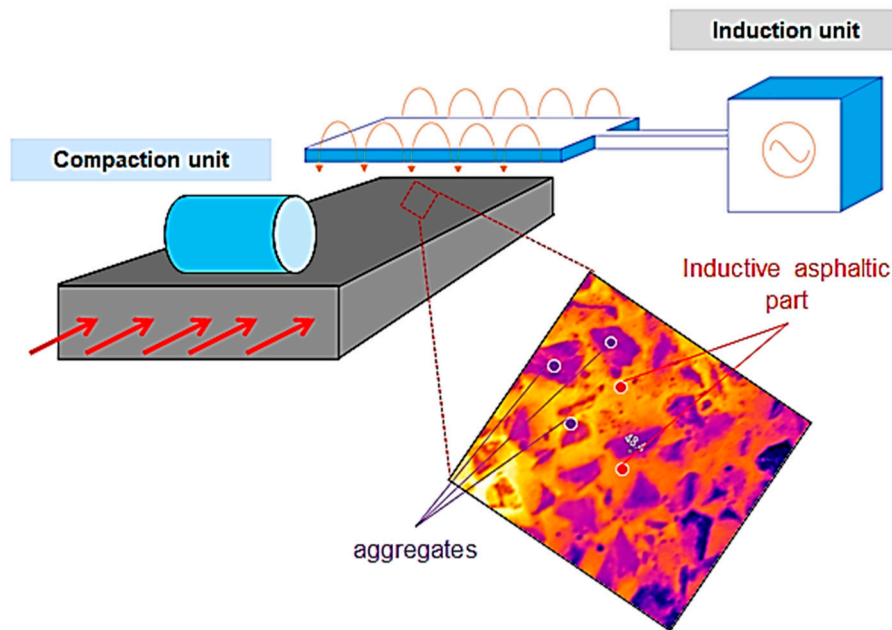


Figure 1. Induction heating-assisted pavement compaction process [17].

## 2. Objectives

The IH compaction process is complicated, and involves three coupled physics: (i) Electromagnetic induction, (ii) heat conduction, and (iii) viscoelastic mechanics. Due to the complex composition of the asphalt mix, the nonlinear mechanical behavior, and the interaction between different physics, this compaction of pavement structures can be optimized through experiments. However, the experimental studies are both expensive and time-consuming. Numerical simulations can avoid the shortcomings faced by experimental studies and provide an efficient way for this kind of research.

In the past, the finite element method (FEM) has been used to analyze the heating performance of inductive asphalt mortar under static [15] and moving [16] electromagnetic sources, but the compaction characteristics of asphalt mixtures have not been discussed. Considering that asphalt mix is a kind of granular material, and the FEM faces many difficulties in solving large deformation problems, some scholars have used the discrete element method (DEM) to simulate the indoor asphalt compaction process, but without electromagnetic heating [18,19].

The highlight of this paper is to combine these three physics together and study the on-site compaction process of asphalt mix through continuous and discontinuous mechanical computation approaches. Specifically, the COMSOL Multiphysics (V5.3, COMSOL Inc., Stockholm, Sweden, 2017) FEM and PFC3D (V5.0, Itasca Consulting Ltd., Minneapolis, MN, USA, 2017) DEM were employed in this study to simulate the IH compaction process. FEM performs well in simulating electromagnetic heating and the evolution of temperature fields, whereas DEM has the advantage in analyzing the large deformation and complex mechanical behavior of asphalt pavement caused by particle reorganization.

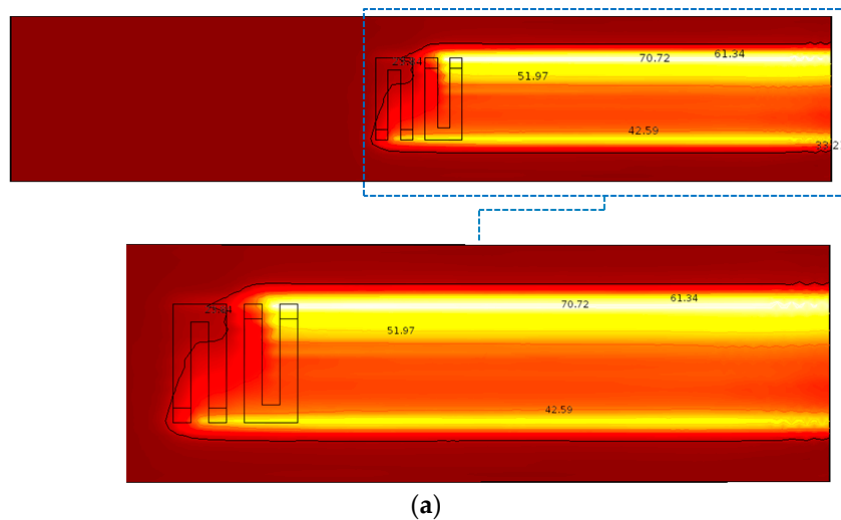
The analyses have been divided into three sequential steps: (i) The prediction of temperature field during IH, (ii) the adjustment of the material parameters of asphalt mortar, and (iii) the execution of the corresponding compaction analysis. The main objectives were to (i) demonstrate the impact of induction technology on the heat generation on the pavement surface by coupling and solving electromagnetic and heat transfer phenomena under a continuously moving induction coil, and (ii) simulate the compaction process using the discrete element method and predict the effect of induction technology on this process in different compaction environments.

### 3. Simulation of Induction Heating-Assisted Compaction in Porous Asphalt

#### 3.1. Modeling of Asphalt Induction Heating

Multiphysics modeling of electromagnetic heating provides a quick framework of analysis that is especially suited for the study of complex composite materials such as asphalt mixes. A model for inductive pavement structures has been developed elsewhere [16]. In this research, the governing equations of induction heating with continuously moving coils and the material parameters implemented in the current model are given as well. Herein, two single-turn coils were utilized with a 0.01 m height and 0.2 m width. The selected operational conditions for this IH analysis were 70 kHz and 4 kV at 20 °C, considering the convenient induction examination at room temperature. The temperature development was studied with the same speed as the moving speed of the roller compactor, at 1 m/s (~3.6 km/h). An inductive pavement and the air domain above the pavement surface were designed in such a way that the induction coils were located in the center. To simplify the response of the heated material, it was assumed to be a homogeneous continuum medium with isotropic properties.

The temperature development and the heat pattern of inductive pavement layer were predicted, and the results after 120 s of induction are shown in Figure 2. In Figure 2a, the contour lines show the evolution of the temperature gradient at the asphalt surface, and the maximum generated temperatures appeared close to the coil's gates where the concentration of magnetic fields was higher. However, apart from the highest reached temperature of the surface of the asphalt layer, increased IH efficiency (the temperature after 120 s of induction) resulted also within the asphalt layer (Figure 2b). The temperature distribution from the top to the bottom of the inductive asphalt layer is illustrated in Figure 2c. This distribution inside the layer shows the advantage of utilizing the induction technology as a heating technique to minimize temperature reduction phenomena during asphalt compaction. Thus, the viscosity of asphalt mixes could be maintained, increasing the time required for adequate compaction under low temperature conditions.



(a)  
Figure 2. Cont.



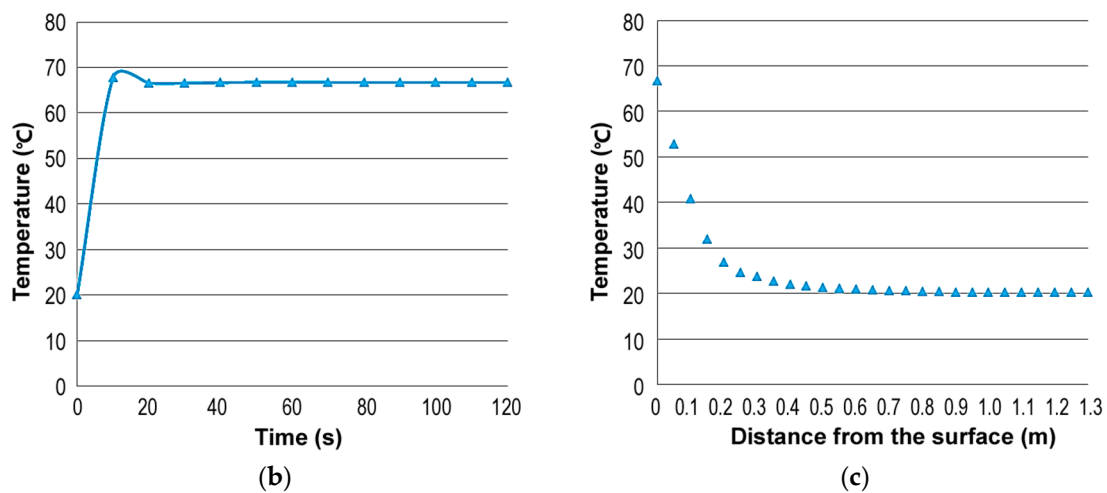


**Figure 2.** Finite element method (FEM) results of induction heating on pavement: (a) thermal field distribution on the pavement surface, (b) surface temperature development of the pavement, and (c) temperature distribution in the pavement after 120 s of induction.

### 3.2. Modeling of Asphalt Mix

DEM modeling is a computational approach in which the discontinuous materials are modeled as individual elements, and it was introduced by Cundall et al. [20,21]. This approach allows the simulation of complex and heterogeneous materials, taking into account the contacts and the interaction of particles within the aggregate skeleton. Wang et al. studied the compaction mechanics of asphalt concrete through DEM modeling [18]. Chen developed a viscoelastic contact model and applied DEM to simulate three commonly used compaction methods for hot-mix asphalt gyratory compaction, asphalt vibratory compaction, and kneading compaction [19]. Even so, the simulation of roller compaction of asphalt pavement remains to be carried out.

#### 3.2.1. Material Selection

During the years, Dutch authorities and contractors have tried to address the issues of surface pavement layers by developing PA mixes. Two characteristic examples of surface layers commonly used in the Netherlands are (i) two-layer PA with a 0/16 and 0/8 aggregate matrix in the bottom and top layer, respectively, and (ii) single-layer PA with a 0/16 aggregate matrix [10], which was used in this study (Table 1). In the PA with a 0/16 aggregate gradation, steel slag particles (finer fraction 2 mm) were added as low-cost inductive agents by replacing mineral aggregates of the same fraction.

**Table 1.** Aggregate gradation of porous asphalt (PA) 0/16 mix based on the Dutch standard (RAW 2005).

Sieving Size (mm)	22.4–16.0	16.0–11.2	11.2–8.0	8.0–5.6	5.6–2.0	2.0–0.063	<0.063
Cum. ret. (%)	4	25	57	80	85	95.5	100
% ret. by weight	4	21	32	23	5	10.5	4.5

#### 3.2.2. Micromechanical Modeling of Asphalt Mix

To simplify the micromechanical modeling of LTPAs, the mix was divided into three different individual constituents: (i) Coarse aggregate particles larger than 2.0 mm, (ii) asphalt mortar, and (iii) air voids. Considering that the shape of the coarse aggregates, which formed the aggregate skeleton in the mix, has a major impact on mix compaction and performance [22–24], five different particles with complex geometries (Figure 3) were developed to compose the PA 0/16 material. The shape of each aggregate particle was randomly chosen from these five shapes. The values of  $L:W:H$  denoted the ratio of the particle’s length, width, and height, respectively, and they were used to control the flatness and elongation of particles (Figure 3).



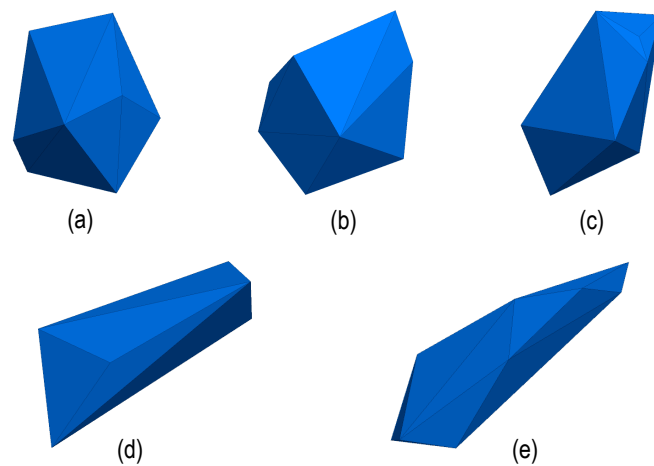


**Figure 3.** Generated coarse aggregate particles: (a,b)  $L:W:H = 1:1:1$ , (c,d)  $L:W:H = 1:0.8:0.6$ , and (e)  $L:W:H = 1:0.5:0.25$ .

For the DEM modeling, asphalt mortar (i.e., asphalt binder, mineral filler, and fine sand), which was added as the bond between the generated coarse aggregate particles in the analyses, was considered to be a continuum and homogeneous. The bond was envisioned as a pie made by many elastic springs and viscous dashpots lying on the contact plane and centered at the contact point of two particles, as seen in Figure 3. When the pie was bonded, it could resist the tensile force and the relative rotation moment until the tensile strength or shear strength limit of the spring was exceeded. After the break of contact bonds, only compressive forces were active.

Due to the fact that when two aggregates are covered by mortar, they are easily glued together during movement, the broken bond may be reglued again when the particles are close enough. This is the biggest different between compaction simulation and the common mechanical analysis for asphalt mix. This mechanism could be realized through continually judging and generating new bonds when necessary but keeping the state of old bonds unchanged during the cycle.

The pie-shaped bond model was determined by five key parameters related to asphalt mortar. These parameters were (i) the normal stiffness, (ii) the shear stiffness  $\bar{k}_s$ , (iii) the tensile strength  $\bar{\sigma}_c$ , (iv) the shear strength  $\bar{\tau}_c$  (calculated by cohesion  $c$  and angle of internal friction  $\phi$ ), and (v) the pie radius  $r_c$ . Parameters such as the gap between the particles  $g_s$ , the viscosity of contact  $\eta_n$ , and the friction of contact  $\mu$  should also be taken into account in the model development, as seen in Figure 4. The particle contact behavior was governed by Kelvin–Voigt constitutive laws, and tension was determined through the Mohr–Coulomb failure criterion.

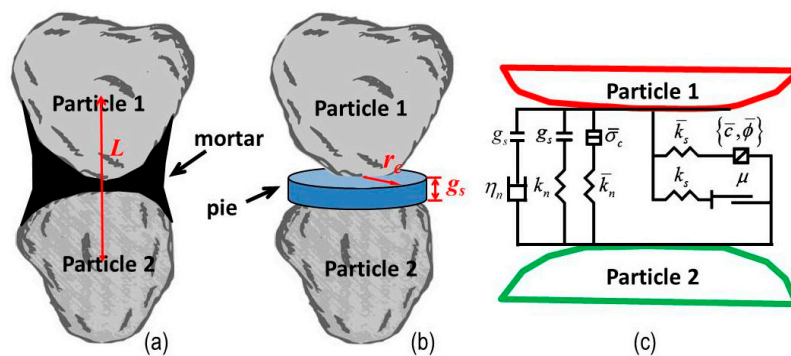


**Figure 4.** Schematic of contact conditions between the coarse aggregate particles: (a) asphalt mortar, (b) pie-shaped bond, and (c) physical model of the bond.

### 3.2.3. Model Parameters Determination

The previously mentioned five parameters had a great influence on the degree of asphalt compaction and were determined by the mix temperature. However, the compactability of the mix, which was influenced by the temperature as well, was determined by the air void content. Research [25] has shown that the air void content is linearly related to the coordination number. The coordination number of a particle is defined as the total number of particles which are in contact with it. In this paper, the air void content of the mix was changed by compressing the same pavement DEM model, and the relationship was obtained as shown in Figure 5:

$$n = n_0 + A\bar{n}_c, \tag{1}$$

where  $n$  is the air void content,  $\bar{n}_c$  is the average coordination number of aggregates, and  $n_0$  and  $A$  are coefficients.

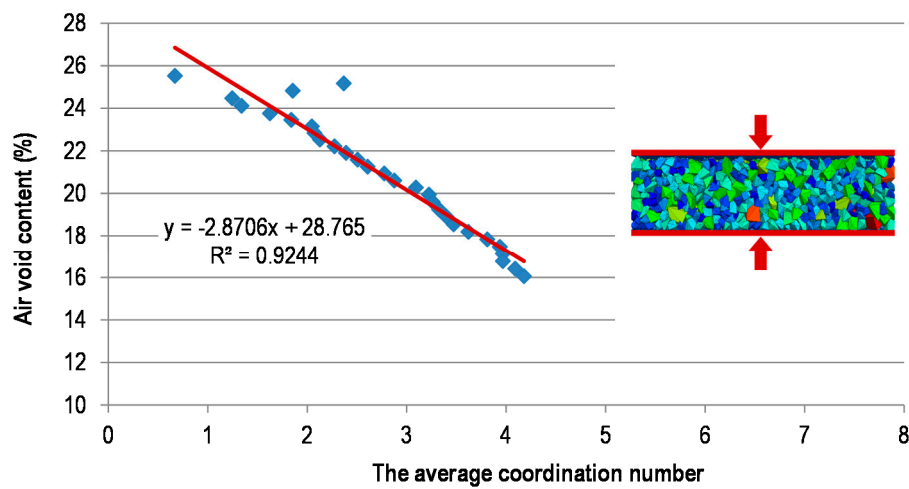


**Figure 5.** Determination of model parameters: The relationship between air void content and the average coordination number.

### Stiffness of Asphalt Mortar

The relationship of the dynamic module of asphalt mortar under different temperatures was investigated by Fernandes et al. [26], and it was expressed as shown in Equation (2),

$$E^* = E_0 e^{-\alpha T}, \tag{2}$$

where  $E^*$  is the dynamic modulus of the mortar (MPa),  $T$  is the temperature, and  $E_0$  and  $\alpha$  are the complex parameters.

In this bond model, the stiffness of asphalt mortar was only produced by a cluster of springs. The dynamic modulus was replaced by the stiffness, and the relation is given in Equation (3),

$$K = \frac{E^*}{L}, \tag{3}$$

where  $K$  is the stiffness of the bond (MPa/m) and  $L$  is the distance between the centroid of two particles that are bonded. This relationship shows that the value of stiffness is reduced when two particles are moving away and by keeping dynamic modulus constant.

In this research, the dynamic modulus of LTPA mortar was assumed to obey the curve shown in Figure 6, and the stiffness in normal direction was kept the same as that in shear direction.

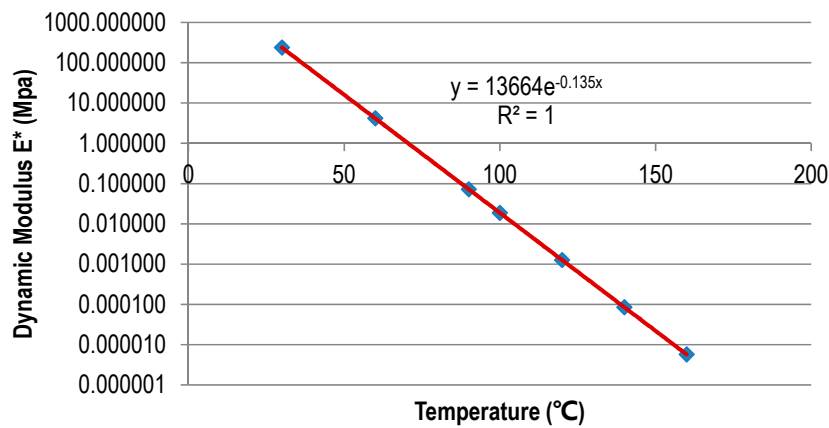


Figure 6. Determination of model parameters: Dynamic modulus of low temperature porous asphalt (LTPA) mortar.

### Strength of Asphalt Mortar

Since the asphalt mortar was assumed to be a viscoelastic material, a peak value of stress and permitted strain existed. When a bond exceeds any one of these limits, the bond can be treated as broken and the rheological property of mortar is easily reflected. The tensile and shear strength of asphalt mortar have been investigated and the obtained results demonstrate that the strength is exponentially related to temperature [27–30] (Figure 7 and Equation (4)):

$$\sigma_c = \sigma_0 e^{-\beta T}, \tag{4}$$

where  $\sigma_c$  is the tensile strength and  $\sigma_0$  and  $\beta$  are the corresponding parameters.

The elastic energy stored in the springs of the bond could not be released, as it was obviously not consistent with the purpose of simulation. Therefore, a critical strain should be applied onto the model. Then the effective strength of mortar can be written as

$$\bar{\sigma}_c = \min(\sigma_c, \bar{\epsilon}_r E^*), \tag{5}$$

where  $\bar{\sigma}_c$  is the effective strength and  $\bar{\epsilon}_r$  is the critical strain. In this research,  $\bar{\epsilon}_r$  is given by Equation (6),

$$\bar{\epsilon}_r = 0.017 e^{-0.018 T}. \tag{6}$$

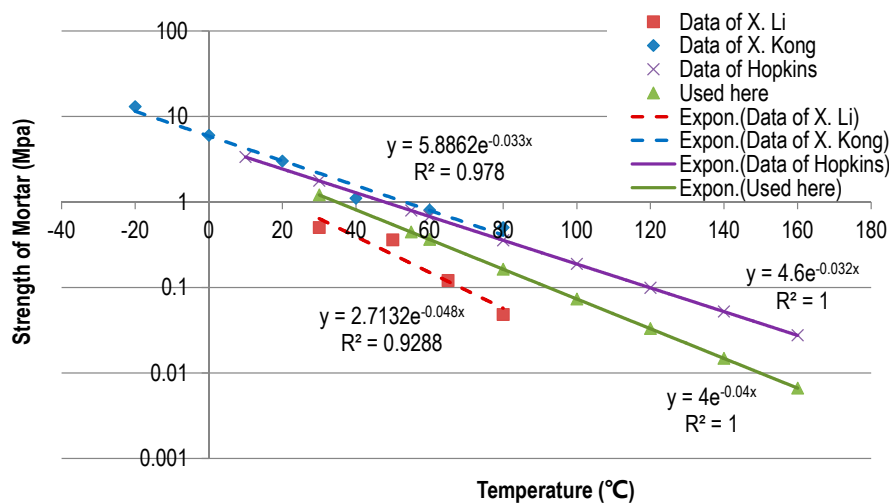


Figure 7. Determination of model parameters: Strength curves of asphalt mortar from the literature.

### Angle of Internal Friction

Since the failure mode of asphalt mortar was controlled by the Mohr–Coulomb strength criterion, the shear strength of the mortar was determined by the normal stress  $\sigma$ , the cohesion  $c$ , and the internal friction angle  $\varphi$  [31]. Herein, only the angle of internal friction is discussed, which was influenced by the temperature and the compactability of the mix [29,30]. This parameter referred not only to the attribution of asphalt mortar but also to the whole interaction of contacted particles. In Hopkins et al.’s research [29], the angle of internal friction was given by Equation (7) as a function of temperature:

$$\varphi_t = 20.7 + \frac{6.792}{(1.8T + 32)} + \frac{494.466}{(1.8T + 32)^2}. \quad (7)$$

As shown in Tinoco et al.’s report [30], the internal friction angle reduces with an increase in the air void content of the mix. The obtained data are listed in Table 2. Based on these results, the angle was determined by the following function,

$$\varphi = \gamma_n \cdot \varphi_t = \gamma_{nc} \cdot \varphi_t, \quad (8)$$

where  $\varphi$  is the internal friction angle of the bond,  $\varphi_t$  is the friction angle based on the temperature,  $\gamma_n$  is the coefficient caused by the variation in air void content, and  $\gamma_{nc}$  is the corresponding expression of  $\gamma_n$  in the form of a coordinate number, which is given by Table 2 as well.

**Table 2.** Internal friction angle as a function of air void content and the used coefficient  $\gamma_{nc}$ .

Air Void Content (%)		22	21.5	21	20.5	20	19	18	17		
Angle of internal friction $\varphi$ (°)		47.5	51.0	52.0	52.5	52.7	53.0	53.4	53.5		
Coord. Number	0	1	2	3	4	5	6	7	8	9	10
$\gamma_{nc}$	0.000	0.543	0.826	0.913	0.946	0.961	0.967	0.978	0.989	0.996	1.000

### Bond Radius

The bond radius greatly influenced the bond damage in the asphalt mortar. An easy way to obtain this parameter was to calculate it through the total effective volume of the asphalt mortar. Moreover, it was assumed that the bond radius ratio  $\zeta$  was defined as the ratio of bond radius  $r_c$  to the minimal radius  $\bar{R}$  of equivalent sphere with the same volume as the bonded particles. The total effective volume of mortar and the radius ratio  $\zeta$  could be estimated by Equations (9) and (10):

$$V_m = \sum_{i=1}^{N_b} [\pi(\zeta \bar{R}_i)^2 \cdot L] = \zeta^2 \pi \sum_{i=1}^{N_b} [\bar{R}_i^2 \cdot L], \quad (9)$$

$$\zeta = \sqrt{\frac{V_m}{\pi \sum_{i=1}^{N_b} [\bar{R}_i^2 \cdot L]}}, \quad (10)$$

where  $V_m$  is the total volume of mortar,  $N_b$  is the total number of bonds at a given time, and  $L$  is the distance of two bonded particles, as in Equation (3).

When asphalt mortar becomes denser, the bond radius obviously becomes larger. However, it is difficult to give an explicit equation between them. Here,  $L$  is assumed to be lineally related to the air void content within a short content range. Thus, distance  $L$  can be described using coordination numbers as

$$L = L_0 + bn_c, \quad (11)$$

where  $n_c$  is the particle’s coordination number and  $L_0$  and  $b$  are the corresponding coefficients.

Also, by substituting Equation (11) into Equation (10), Equation (12) is formulated:

$$\varepsilon^2 = 1 + sn_c, \quad (12)$$

where  $\epsilon$  is the enlargement multiplier of bond radius ratio  $\zeta$ , and  $s$  is the coefficient related to the coordination number.

### 3.3. Modeling of Pavement Compaction

Before simulating the compaction process of LTPA, a new model had to be created. Since there is not a mature approach to create such models directly with the required air void content, in order to make full use of the DEM mechanics and to keep the gradation distribution of the mix unchanged, the following procedure ensued: (i) Calculation of the total volume of particles according to the pavement model size and the required and initial air void content, (ii) calculation of the particle numbers of different sizes on the basis of the mix gradation, (iii) random generation of these particles (where the particles may have overlapped each other), (iv) shrinkage of all the particles by 50 times, for example, and (v) enlargement of the particles step by step (between each step, the overlaps were eliminated through DEM simulation). If each particle enlarged  $\sqrt[10]{50}$  times per step, all the particles would change back to their original size again after 10 steps, and meanwhile, the air void content of the pavement model would reach the value that was set (Figure 8). Note that, in this process, a pie-shaped bond model would be unnecessary and an elastic contact model would be enough.

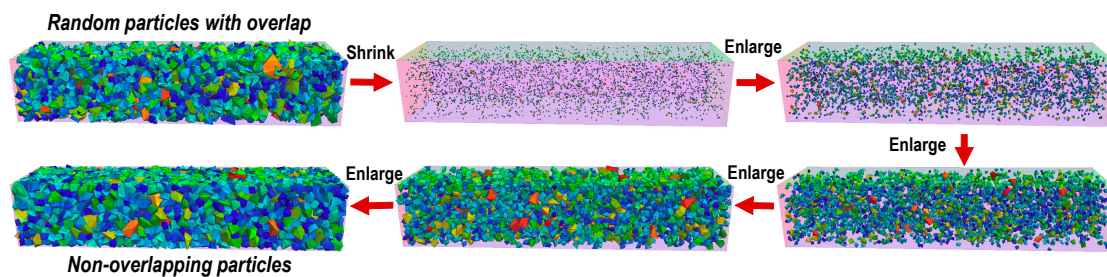


Figure 8. Generation process of pavement model.

The compaction procedure was achieved by a rigid wheel (roller wheel), which was modeled by a polyhedral shell with many small facets and rolls on the pavement model with a given weight. When the roller moved close to the border of the pavement model, one pass finished. Then the roller would go back to its original location and repeat this procedure until the end, as seen in Figure 9.

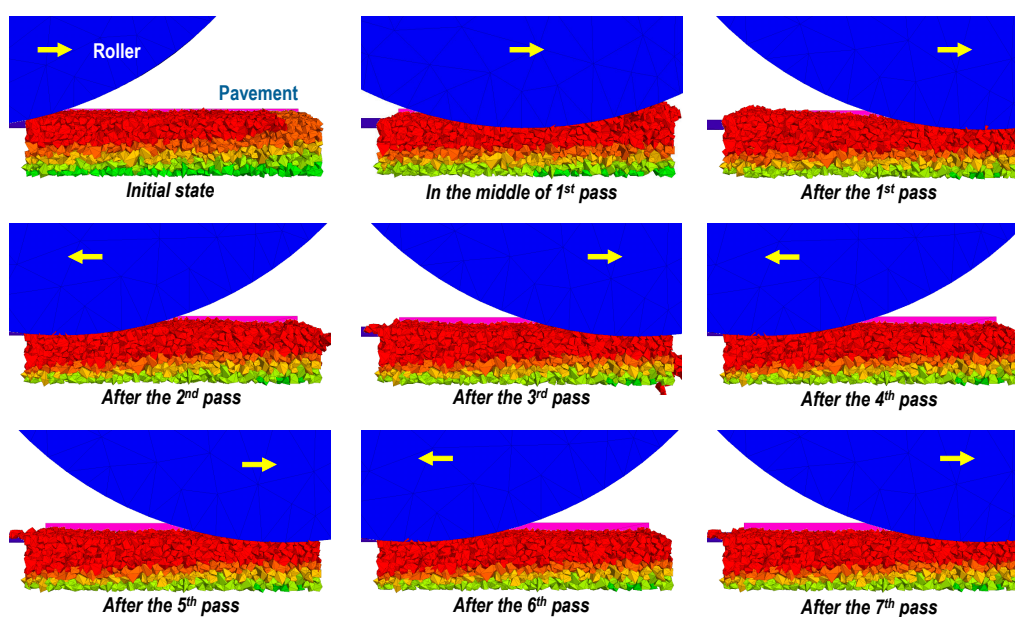


Figure 9. Simulation of pavement compaction process (due to space limitations, only part of the wheel is retained in the picture).

A schematic flow diagram of the coupling methodology is demonstrated in Figure 10, which explains how the two modeling methods combined together. As can be seen from this figure, three key relations of the process were used, (i) to adjust the temperature field according to the position of the roller, (ii) to modify the bond parameters between the particles according to the temperature and mechanical state of the investigation point, and (iii) to update the open and closed states for the particles according to the force and displacement relationship between them.

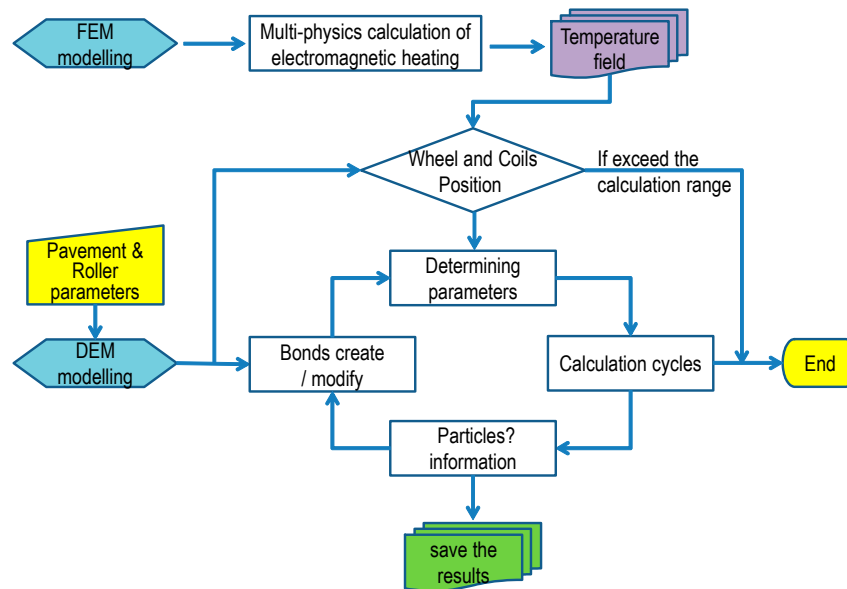


Figure 10. Schematic flow diagram of the overall coupling methodology.

#### 4. Results and Main Findings

The asphalt pavement compaction model was created by taking into account the effect of IH and its generated temperature field, which was calculated before. It was assumed that the generated heat for asphalt pavements of an initial temperature of 20 °C was also valid for higher initial temperatures. All the parameters of the asphalt compaction process are shown in Table 3.

Table 3. Parameters used in the discrete element method (DEM) analysis.

Parameters	Values
<i>Pavement model</i>	
model size	50 cm (length) × 50 cm (width) × 8 cm (thickness)
particles size	2–22.4 mm (PA 0/16)
<i>Roller Parameters</i>	
wheel size	100 cm (diameter) × 200 cm (width)
wheel weight	5 tons (one wheel)
<i>Mortar parameters</i>	
air void content estimated	$n = -2.8706 + 28.765\bar{n}_c$
dynamic modulus (MPa)	$E^* = 13664.0e^{-0.135T}$
critical strain	$\bar{\epsilon}_r = 0.017e^{-0.018T}$
effective strength (MPa)	$\bar{\sigma}_c = 232.29e^{-0.153T}$
initial bond radius ratio	$\zeta_0 = 0.06$
enlargement multiplier of bond radius	$\epsilon = \sqrt{1 + 0.06\bar{n}_c}$

The relation of asphalt compactability or air void content to the roller passes are shown in Figure 11. Four cases were considered.

Low temperature group:

- Case 1: Mix temperature  $T_0 = 60\text{ }^\circ\text{C}$  without IH.
- Case 2: Mix temperature  $T_0 = 60\text{ }^\circ\text{C}$  with IH (surface temperature of  $T_f = \sim 90\text{ }^\circ\text{C}$ ).

High temperature group:

- Case 3: Mix temperature  $T_0 = 120\text{ }^\circ\text{C}$  without IH.
- Case 4: Mix temperature  $T_0 = 120\text{ }^\circ\text{C}$  with IH (surface temperature of  $T_f = \sim 142\text{ }^\circ\text{C}$ ).

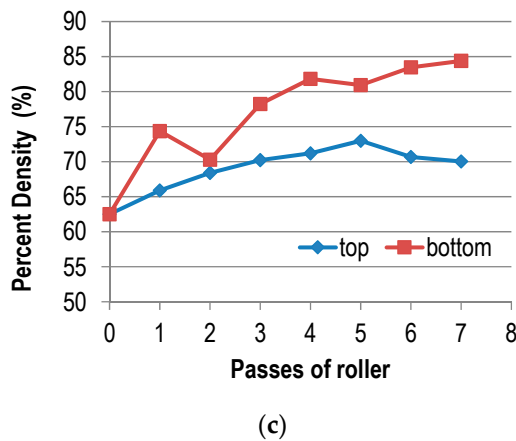
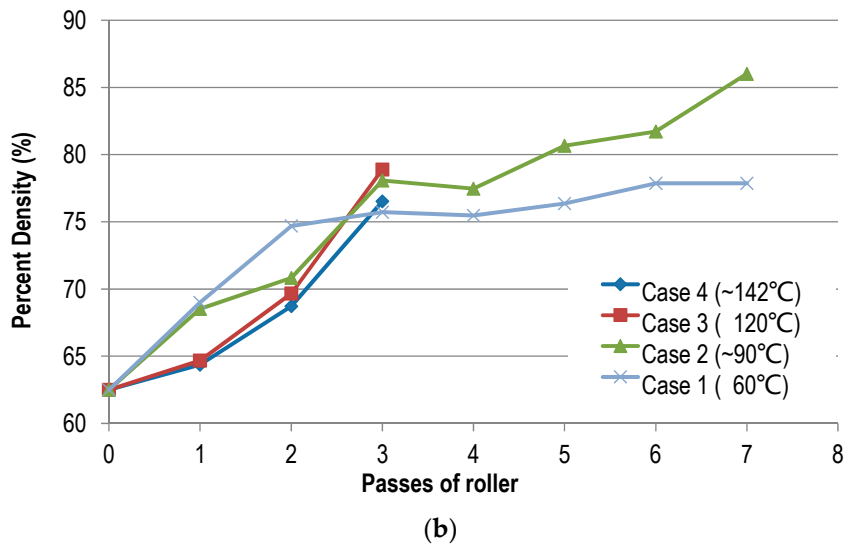
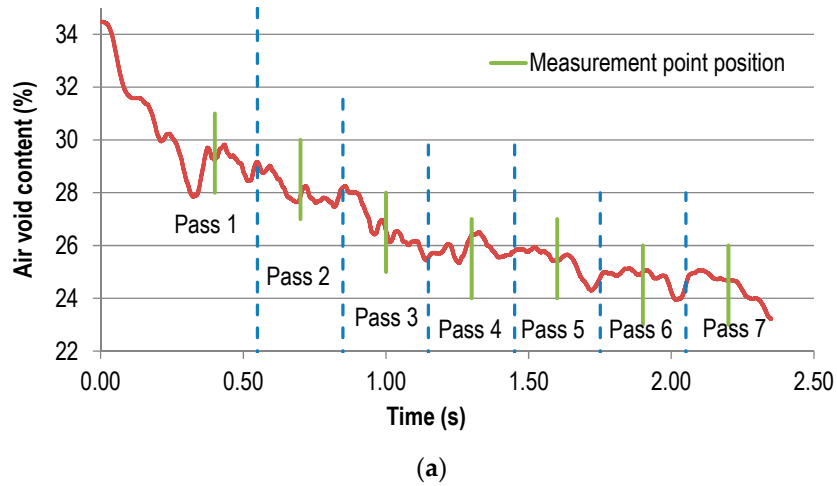
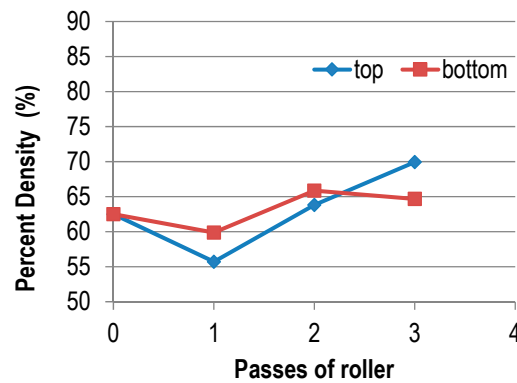


Figure 11. Cont.





(d)

**Figure 11.** Simulation results: (a) The air void content changed as passes increased at 60 °C with induction heating; and (b) a comparison of compaction effects for different cases and percent densities at different depths for (c) Case 2 (~90 °C) and (d) Case 4 (~142 °C).

In Figure 11a, it was found that during the first pass (initial compaction), the air void content fluctuated dramatically and the mix was easily flown. If taking the studied point (the midpoint of the model) as a reference, when the compactor came close to it, the mix air void content declined because of the aggregates' pushing movement. When the roller moved to the right above the point, many bonds were broken, caused by tensile stress, and the air void content showed a slight increase. When the roller moved off this point, the air void content went down again and the mix recompacted. With passes increased, the air void content continually declined, whereas fluctuation started to be stable and the variation amplitude of porosity reduced.

Figure 11b shows that the entire compaction process could be divided into two distinct stages, the early stage (passes < 3) and the late stage (passes > 3). In the early stage, the mix density during compaction could be sorted in descending order as Case 1 > Case 2 > Case 3 > Case 4. That is to say, (i) relative to the high temperature group (Case 3 and Case 4), the low temperature group (Case 1 and Case 2) showed much higher density in the early stage, and (ii) regardless of the high temperature group or low temperature group, the density of the mix without IH was higher than that with IH in the early stage (i.e., Case 1 > Case 2, Case 3 > Case 4).

In the late stage of compaction, the mix density at higher temperatures eventually exceeded the density at low temperatures (i.e., Case 2 > Case 1). The phenomenon happened mainly due to the fact that higher temperatures do not always increase the mix density, but they can increase the mobility of particles, leading to bad mix compactability. Further, IH operated efficiently in the late compaction stage when the mix density reached a certain value, rather than at the very beginning. Also, the effect of IH on the asphalt compaction process was not obvious at higher temperatures.

Figure 11c,d demonstrates the change of density at different depths (top and bottom) with increasing roller passes. These curves in Figure 11c show that the density of the bottom layer changed considerably compared to that of the top layer when the mix was at low temperature. This might have been caused by two reasons. One was the boundary conditions, and the other was the change of stiffness balance due to IH. Since the bottom layer had much stronger border restrictions than the top layer, for such a granular material, the density would obviously be larger. Furthermore, the stiffness of the top mix was also reduced more than that of the bottom mix since being heated. According to the law shown in Figure 11b, the compaction effect of the bottom layer would be higher than that of the top layer. But for high temperature cases, Figure 11d shows that the difference in density in different layers was not distinct because the balance of stiffness changed little when the mix was at high temperature.



## 5. Conclusions and Recommendations

This paper introduced a computational method combining two modeling tools to simulate asphalt pavement compaction assisted by induction heating. The proposed method allowed the dynamic change of microstructural parameters of asphalt mortar in a DEM tool according to the moving temperature field predicted by an FEM tool.

Additionally, based on the analyses, the asphalt compaction process could be divided into the early and late stages. In the early stage, the density of the mix compacted, with induction technology remaining the same. In the late stage, the mix density was larger when induction heating was applied. Thus, induction heating was more suitable at lower temperatures. Furthermore, induction heating mostly influenced the balance of stiffness at different pavement depths. For high temperatures, the effect of induction was minimal. However, for lower temperatures, heating always led to a higher density at the bottom of the pavement than at the top.

Although the objective of this paper was mainly to discuss induction heating-assisted compaction technology and the developed numerical approach, it is very necessary to carry out lab-scale tests to obtain the required parameters in further research and then to verify the results of these analyses.

**Author Contributions:** Conceptualization, X.L. and A.(T.)S.; methodology, C.Z. and P.A.; modelling, C.Z. and P.A.; writing original draft preparation, C.Z. and P.A.; writing review and editing, X.L. and L.H.; supervision, A.(T.)S.

**Funding:** This research received no external funding.

**Acknowledgments:** The first author would like to acknowledge the financial support of Sino-Dutch Bilateral Exchange Scholarship and EP-Nuffic of the Netherlands.

**Conflicts of Interest:** The authors declare no conflicts of interest.

## References

1. CROW. *Low Temperature Asphalt for a Sustainable Pavement*; CROW Publication 319; CROW: Ede, The Netherlands, 2013; ISBN 978 90 6628 613 9. (In Dutch)
2. European Asphalt Pavement Association. *The Use of Warm Mix Asphalt*; EAPA-Position Paper; EAPA: Brussels, Belgium, 2014.
3. Hanz, A.J.; Faheem, A.; Mahmoud, E.; Bahia, H.U. Measuring Effects of Warm-mix Additives: Use of Newly Developed Asphalt Binder Lubricity Test for the Dynamic Shear Rheometer. In *Transportation Research Record: Journal of the Transportation Research Board*; Transportation Research Board: Washington, DC, USA, 2010; Volume 2180, pp. 85–92.
4. Smith, H.A. *Performance Characteristics of Open-Graded Friction Courses*; NCHRP Synthesis of Highway Practice, No. 180; Transportation Research Board, National Research Council: Washington, DC, USA, 1992.
5. Van Der Zwan, J.T.; Goeman, T.; Gruis HJA, J.; Swart, J.H.; Oldenburger, R.H. Porous Asphalt Wearing Courses in the Netherlands: State of the Art Review. In *Transportation Research Record: Journal of the Transportation Research Board*; Transportation Research Board: Washington, DC, USA, 1990; pp. 95–110.
6. Kandhal, P.S.; Mallick, R.B. *Open Graded Friction Course: State of the Practice*; Transportation Research Board, National Research Council: Washington, DC, USA, 1998.
7. Hagos, E.T. The Effect of Aging on Binder Properties of Porous Asphalt Concrete. Ph.D. Thesis, TU Delft, Delft, The Netherlands, 2008.
8. Austroads. *The Influence of Compaction on the Performance of Dense Graded Asphalt*; Austroads Project TT1353; Austroads: Sydney, Australia, 2011.
9. Lu, Q.; Harvey, J.T. Laboratory Evaluation of Open-Graded Asphalt Mixes with Small Aggregates and Various Binders and Additives. In *Transportation Research Record: Journal of the Transportation Research Board*; Transportation Research Board: Washington, DC, USA, 2011; pp. 61–69.
10. Alvarez, A.E.; Martin, A.E.; Estakhri, C.K.; Button, J.W.; Glover, C.J.; Jung, S.H. *Synthesis of Current Practice on the Design, Construction, and Maintenance of Porous Friction Courses*; Technical Report. No. FHWA/TX-06/0-5262-1; Texas Transportation Institute: Houston, TX, USA, 2006.

11. Molenaar, A.A.A.; Meerkerk, A.J.J.; Miradi, M.; Van der Steen, T. Performance of Porous Asphalt concrete. *J. Assoc. Asphalt Paving Technol.* **2006**, *75*, 1053–1094.
12. Kragh, J.; Goudert, L.; Sandberg, U. *OPHTHINAL: Optimization of Thin Asphalt Layers. ERA-NET Road; Final Report*, Project No. VV 2009/40520; Danish Road Institute (DRI): Hedehusene, Denmark, 2011.
13. García, Á.; Schlangen, E.; van de Ven, M.F.C.; Liu, Q. Electrical Conductivity of Asphalt Mortar Containing Conductive Fibers and Fillers. *Constr. Build. Mater.* **2009**, *23*, 3175–3181. [CrossRef]
14. Liu, Q.; Schlangen, E.; García, Á.; van de Ven, M.F.C. Induction Heating of Electrically Conductive Porous Asphalt Concrete. *Constr. Build. Mater.* **2010**, *24*, 1207–1213. [CrossRef]
15. Apostolidis, P.; Liu, X.; Scarpas, A.; Kasbergen, C.; van de Ven, M.F.C. Advanced Evaluation of Asphalt Mortar for Induction Healing Purposes. *Constr. Build. Mater.* **2016**, *126*, 9–25. [CrossRef]
16. Apostolidis, P.; Liu, X.; Kasbergen, C.; Scarpas, A.; van de Ven, M.F.C. Toward the Design of an Induction Heating System for Asphalt Pavements with the Finite Element Method. In *Transportation Research Record*; 2633-16 TRB; National Research Council: Washington, DC, USA, 2017; pp. 136–146.
17. Apostolidis, P. Induction Healing of Asphalt Mixes with Steel Slag: The Case of Motorway A31, North Holland. In *Presentation to Rijkswaterstaat: Ministerie van Infrastructuur en Waterstaat; Rijkswaterstaat*: Utrecht, The Netherlands, 2017.
18. Wang, L.; Zhang, B.; Wang, D.; Yue, Z. Fundamental Mechanics of Asphalt Compaction through FEM and DEM Modeling. In *Analysis of Asphalt Pavement Materials and Systems: Engineering Methods*; American Society of Civil Engineers: Reston, VA, USA, 2007; pp. 45–63.
19. Chen, J. Discrete Element Method (DEM) Analyses for Hot-Mix Asphalt (HMA) Mixture Compaction. Ph.D. Thesis, University of Tennessee, Knoxville, TN, USA, 2011.
20. Cundall, P.A. A Computer Model for Simulating Progressive, Large-scale Movements in Block Rock Systems. *Proc. Symp. Int. Soc. Rock Mech.* **1971**, *2*, 129–136.
21. Cundall, P.A.; Strack, O.D. A Discrete Numerical Model for Granular Assemblies. *Geotechnique* **1979**, *29*, 47–65. [CrossRef]
22. Dondi, G.; Simone, A.; Vignali, V.; Manganelli, G. Numerical and Experimental Study of Granular Mixes for Asphalts. *Powder Technol.* **2012**, *232*, 31–40. [CrossRef]
23. Dondi, G.; Simone, A.; Vignali, V.; Manganelli, G. Discrete element modelling of influences of grain shape and angularity on performance of granular mixes for asphalts. *Procedia-Soc. Behav. Sci.* **2012**, 399–409. [CrossRef]
24. Zhou, C.; Zhang, M.; Li, Y.; Lu, J.; Chen, J. Influence of Particle Shape on Aggregate Mixture's Performance: DEM results. *Road Mater. Pavement Des.* **2017**. [CrossRef]
25. Huang, Q.; Zhan, M.; Sheng, J.; Sheng, J.-C.; Zhang, X. Numerical Method to Generate Granular Assembly with any Desired Relative Density based on DEM. *Chin. J. Geotech. Eng.* **2015**, *37*, 537–543.
26. Fernandes, M.R.S.; Forte, M.M.C.; Leite, L.F.M. Rheological Evaluation of Polymer-modified Asphalt Binders. *Mater. Res.* **2008**, *11*, 381–386. [CrossRef]
27. Li, X.; Zhang, X.; Wang, S. Study of High Temperature Performance of Asphalt Mastic Based on Dynamic Viscoelastic Mechanics. *J. Highw. Transp. Res. Dev.* **2007**, *2*, 16–20. [CrossRef]
28. Kong, X.; Liu, Y.; Zhang, Y.; Zhang, Z.; Yan, P.; Bai, Y. Influences of Temperature on Mechanical Properties of Cement Asphalt Mortars. *Mater. Struct.* **2014**, *47*, 285–292. [CrossRef]
29. Hopkins, T.C.; Sun, L.; Slepak, M.E.; Slepak, M.E. *Bearing Capacity Analysis and Design of Highway Base Materials Reinforced with Geofabrics*; Research Report KTC-05-21/SPR-238-02-1F; Kentucky Transportation Center: Lexington, KY, USA, 2005.
30. Tinoco, F.H.; Handy, R.L.; Hoover, J.M. Void Ratio and Shear Strength of Two Compacted Crushed Stones. In *Proceedings of the Iowa Academy of Science*; Iowa Academy of Science: Cedar Falls, IA, USA, 1966; Volume 73, pp. 219–233.
31. Mohr-Coulomb Theory. Available online: [https://en.wikipedia.org/wiki/Mohr%E2%80%93Coulomb\\_theory](https://en.wikipedia.org/wiki/Mohr%E2%80%93Coulomb_theory) (accessed on 27 October 2018).





Article

# The Effect of Ageing on Chemical and Mechanical Properties of Asphalt Mortar

Ruxin Jing <sup>1,\*</sup>, Xueyan Liu <sup>1</sup>, Aikaterini Varveri <sup>1</sup>, Athanasios Scarpas <sup>1,2</sup> and Sandra Erkens <sup>1</sup>

<sup>1</sup> Pavement Engineering, Delft University of Technology, 2628 CN Delft, The Netherlands;

x.liu@tudelft.nl (X.L.); a.varveri@tudelft.nl (A.V.); a.scarpas@tudelft.nl (A.S.); s.m.j.g.erkens@tudelft.nl (S.E.)

<sup>2</sup> Civil Infrastructure and Environmental Engineering Department, Khalifa University, Abu Dhabi 127788, UAE

\* Correspondence: r.jing@tudelft.nl; Tel.: +31-061-879-9589

Received: 8 October 2018; Accepted: 9 November 2018; Published: 13 November 2018

**Abstract:** Asphalt mortar is a mixture of bitumen, filler, and sand. Mortar plays an important role in asphalt mixtures as it serves as the adhesive between the coarser aggregates. Due to the effect of bitumen ageing, the chemical and mechanical properties of asphalt mortar evolve with time. The mortar becomes more brittle and prone to cracking, thus leading to inferior pavement performance. In this study, Fourier transform infrared (FTIR) spectrometry was used to quantify changes in the chemical functional groups related to ageing and to calculate the carbonyl and sulfoxide indices. In addition, frequency sweep tests and uniaxial tension tests were performed by means of dynamic shear rheometer (DSR) tests to determine evolution of the stiffness and strength due to ageing. Two different oven ageing protocols were used to evaluate the effect of fine mineral particles on bitumen ageing. The protocols differed with respect to the order of ageing and mixing of the constituents. The results showed that both the chemical and mechanical properties of mortars significantly changed with ageing. Specifically, the carbonyl index, stiffness, and strength of the mortar increased. Under the same ageing conditions, a higher ageing level was observed for mortars produced by first mixing and then ageing compared to the mortars produced by mixing aged bitumen with filler and sand. This could be due to the presence of sand and filler particles, which resulted in an increased length of diffusion paths and consequently a slower ageing process.

**Keywords:** asphalt mortar; ageing; FTIR; stiffness; strength

## 1. Introduction

Ageing of bitumen is believed to be a major contributor to many pavement distresses, such as raveling, cracking, and fatigue [1–6]. Ageing occurs during the process of storage, mixing, transportation, construction, and service. Studies have demonstrated that ductility and penetration of bitumen diminish as a result of ageing, while softening point and ignition temperature increase in the process [7–9]. Moreover, the viscosity increases and bitumen becomes stiffer.

Asphalt mortar, commonly known as fine aggregate matrix, is a mixture of bitumen, filler, and sand. It is the binding medium that holds the aggregates of an asphalt mixture together, and it plays an important role as the link between bitumen properties and mixture performance. Past studies have shown that the testing of bituminous mortar is an efficient and repeatable approach to predict the performance of asphalt mixture [10–12]. The ageing of bitumen, through the asphalt mortar as an intermediate medium, causes the mixture to become excessively hard and brittle and consequently more susceptible to producing pavement distress [13]. For this reason, some studies have considered asphalt mortar ageing. For instance, Cui et al. investigated the effect of laboratory long-term ageing on the rheological properties of asphalt mortar. The long-term ageing test is a combination of

ultraviolet ageing, thermal ageing, and humidity [14]. Molenaar et al. studied the effects of ageing on the mechanical characteristics of bituminous binders in porous asphalt (PA) concrete. The results showed that ageing increased the tensile strength of the bituminous binders but decreased the strain at break [15]. In addition, the fatigue results showed that the adhesive zone between stone and mortar tended to be the weakest link because there was a bitumen-rich interlayer [16]. Tong et al. evaluated the moisture and ageing damage of asphalt mortar using the repeated direct tensional test method. The results showed that fatigue crack growth of asphalt mortar increased substantially after ageing [17]. Zhang et al. quantified the ageing effect on the rheological characteristics of two types of asphalt mortar and applied the results to evaluate the raveling resistance of PA wearing courses in finite element simulations. It was found that ageing had more influence on the complex shear modulus of the base mortar compared to the SBS (Styrene-Butadiene-Styrene) mortar, but its effects on fatigue resistance were the opposite [18]. These studies proved that mortar ageing had a negative influence on pavement performance, such as fatigue and raveling. However, the studies were limited in considering the rheological changes of asphalt mortar subject to various conditions.

The main objective of this study was to investigate the effect of filler and sand on ageing and determine the evolution of mortar properties due to ageing. To achieve this, two different ageing conditions were applied on mortar by an oven. The ageing method differed with respect to the order of ageing and mixing of the constituents. The chemical composition of asphalt mortar was evaluated by means of Fourier transform infrared (FTIR) spectrometer. Cylindrical mortar samples were then prepared and tested using dynamic shear rheometer (DSR) tests. In addition, the original bitumen was tested after the same ageing conditions as that of asphalt mortar.

## 2. Materials and Methods

### 2.1. Materials and Asphalt Mortar Mix Design

The PEN 70/100 bitumen, which is one of the most commonly used bitumen in the Netherlands, was used in this study. Table 1 shows the main physical and rheological properties of the PEN 70/100 bitumen. The mortars were prepared using river sand, which is a type of sand with quartz, with a nominal maximum size of 2 mm and Wigro 60K filler, which is a type of filler with hydroxide that contains 25% hydrated lime (density is 2780 kg/cm<sup>3</sup>).

**Table 1.** Specifications of PEN 70/100 at fresh (unaged) state.

Property	Unit	PEN 70/100
Penetration at 25 °C	0.1 mm	70–100
Softening point	°C	43–51
Dynamic viscosity at 60 °C	Pa s	160
Complex shear modulus at 1.6 Hz and 60 °C	kPa	1.8
Phase angle at 1.6 Hz and 60 °C	°	88

The mortar was designed based on the mix design of two types of asphalt mixtures—porous asphalt (PA) 16 and stone mastic asphalt (SMA) 16—which represent an open and a dense-graded asphalt mixture, respectively, and are widely used in the Netherlands. Both PA 16 and SMA 16 consist of crushed stones with a nominal maximum aggregate size of 16 mm, river sand, Wigro 60K filler, and PEN 70/100 bitumen. The binder contents were 5.0% and 6.4% for the PA and the SMA mixture, respectively. The aggregate gradations of PA16 and SMA 16 mixtures are shown in Figure 1.

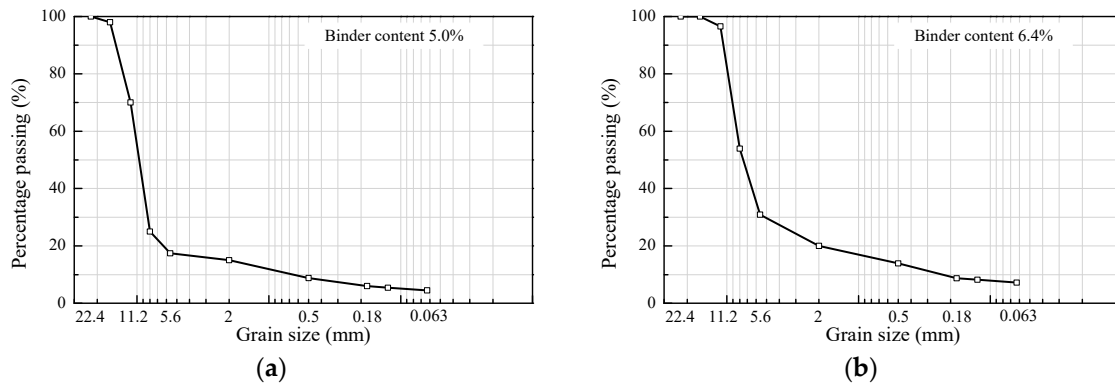


**Figure 1.** Aggregate gradation and physical properties of mixture: (a) porous asphalt (PA) 16; (b) stone mastic asphalt (SMA) 16.

The asphalt mortar used in this study contained sand with size smaller than 2 mm. On the basis of gradations of PA 16 and SMA 16 in Figure 1, the mass ratios of bitumen, filler, and sand of each mixture were calculated and are presented in Table 2. Specifically, it was 1:0.9:2.1 for the mortar in PA 16 and 1:1.25:2 for the mortar in SMA 16. Therefore, considering an average between the mortars in PA 16 and SMA 16, the mass ratio of each composition in the designed mortar was selected as 1:1:2. This mortar composition was employed in the lab investigation.

**Table 2.** Asphalt mortar recipe.

Mix Design	Bitumen	Filler	Sand
Mortar in PA 16	1	0.9	2.1
Mortar in SMA 16	1	1.125	2
Designed Mortar	1	1	2

### 2.2. Ageing Program

First, the mortar samples were tested without applying any ageing protocol so as to define their properties at unaged (fresh) conditions. Then, two oven ageing protocols that were different in the order of ageing and mixing of the constituents were applied. Specifically, in the first method, the mortar constituents—bitumen, filler, and sand—were mixed after they were aged separately in the oven (denoted as AM); this method is commonly used as laboratory ageing protocol. In contrast, the second method involved first mixing the constituents to prepare the mortar and then subjecting the mortar samples to ageing (denoted as MA); this method is close to the ageing condition in the field. The purpose of having two different protocols was to identify the effect of filler and sand on ageing. Table 3 summarizes the ageing protocols that were considered. Specifically, the temperature was selected as 100 °C for all ageing tests, and the time varied from 20 to 160 h. In addition, bitumen samples after the application of various ageing times were studied.

**Table 3.** Ageing program.

Ageing Temperature (°C)	Ageing Time (h)	Mortar_AM	Mortar_MA	Bitumen
100	20	✓		✓
	40	✓	✓	✓
	80	✓		✓
	160	✓	✓	✓

### 2.3. Sample Preparation

As the studied mortar samples were composed using fractions of aggregates up to 2 mm, the parallel-plates configuration could no longer be applied. Instead of the parallel-plates configuration,

a special set-up with clamps for cylindrical mortar sample was used for the DSR tests [19,20] (Figure 2a). The preparation procedure of the mortar samples was adopted from a previous study at TU Delft [21]. Initially, the PEN 70/100 bitumen, filler, and sand were separately heated to 150 °C. Then, the three compounds were mixed manually for 10–15 min. After the mixing process, asphalt mortar was poured into a silicone mold (Figure 2b). Two metal rings were prefixed on the top and bottom side of the mold. These metal rings ensured load transfer from the DSR into the samples (Figure 2c). After filling the mold with mortar, the mold was placed in the oven at 150 °C for 5 min to allow the suppression of possible air pockets that were formulated during pouring of the mix into the mold. Afterwards, the mold was cooled down to ambient temperature and then placed in a refrigerator at –15 °C for at least 2 h. Finally, the mortar samples were removed from the mold and checked visually for air voids at the surface of the sample. The accepted samples were placed in a special silicone mold and stored in the refrigerator at –15 °C before testing (Figure 2d).

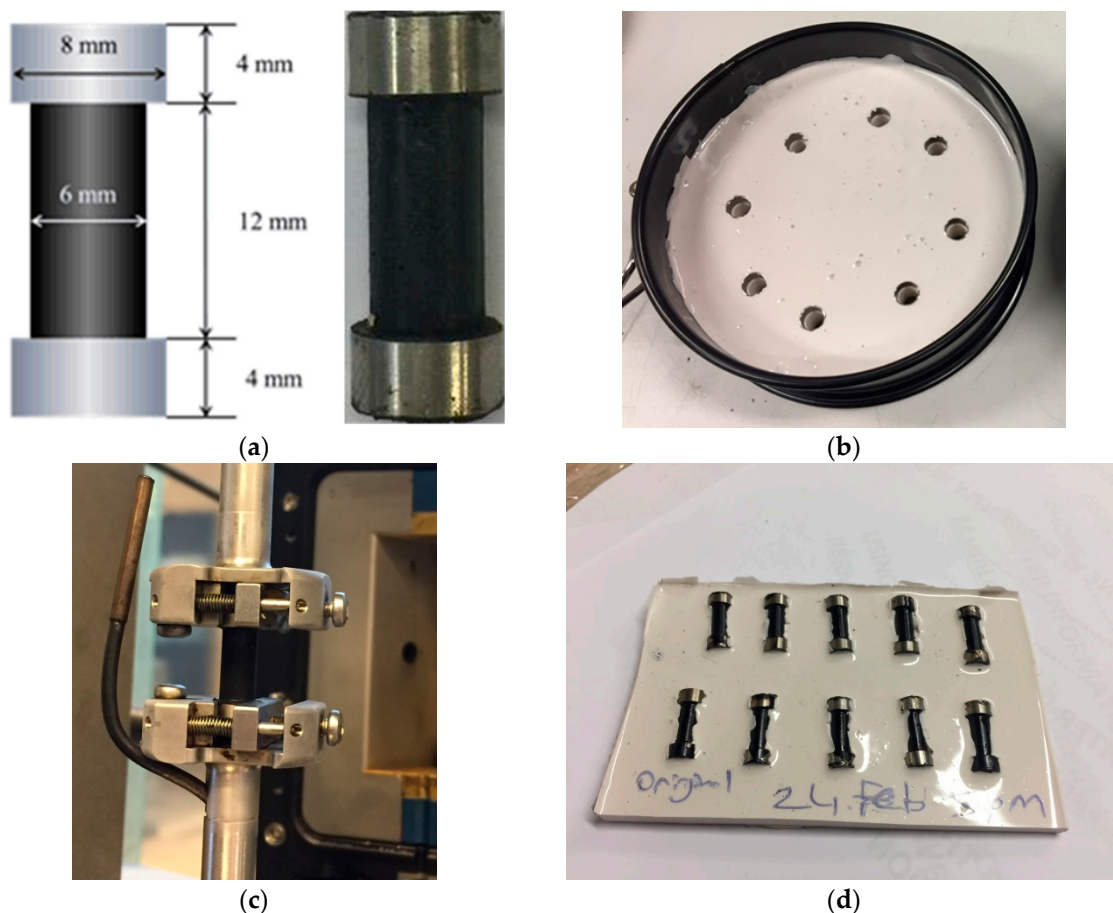


**Figure 2.** Asphalt mortar sample: (a) geometry of sample; (b) silicone mold for sample preparation; (c) measuring system for cylinder sample; (d) silicone mold for sample storage.

#### 2.4. Experimental Methods

As an efficient, convenient, and inexpensive tool, the FTIR is widely used to determine the chemical characteristics of bituminous materials. In the infrared spectrogram of bitumen, the absorbance bands corresponding to carbonyls and sulfoxides show a significant increase with ageing [22–24]. The chemical characterization in this study was performed using the Spectrum 100 FT-IR spectrometer from PerkinElmer. A single-beam configuration was used. The sample was scanned 20 times with a fixed instrument resolution of 4 cm<sup>-1</sup>. The wavenumbers were set to vary from 600 to 4000 cm<sup>-1</sup>. At least three repetition tests were performed for each ageing condition.

DSR is commonly used to investigate the rheological properties of bituminous materials [25–27]. In this study, the linear viscoelastic (LVE) strain range of the bitumen and asphalt mortar samples were initially determined using amplitude sweep tests. Within the LVE strain range, frequency sweep tests were performed at four different temperatures (0, 10, 20, and 30 °C). During the tests, the frequency varied in a logarithmic manner from 50 Hz to 0.01 Hz. Uniaxial tensile tests were performed at 0 °C with 0.2% (0.024 mm/s) tensile rate. The load and deformation in the testing process were automatically collected with a frequency of two measurements per second.

### 3. Results and Discussion

#### 3.1. Fourier Transform Infrared Spectrometer

##### 3.1.1. FTIR Spectra

The FTIR spectra were obtained in a wavenumber range from 4000 to 600  $\text{cm}^{-1}$ . However, the changes caused by ageing could be found at wavenumbers lower than 2000  $\text{cm}^{-1}$ , as shown in Figure 3. These wavenumbers corresponded to functional groups related to the oxidation processes. It showed that the carbonyl (left, red part) and sulfoxide functional (right, blue part) groups changed considerably after laboratory ageing, i.e., they both increased with ageing.

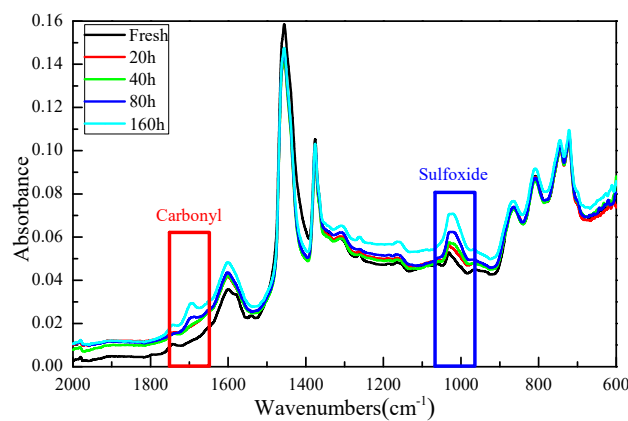


Figure 3. FTIR spectra of PEN 70/100 at different ageing hours.

The FTIR spectra of fresh mortar sample and each component (fresh bitumen, filler, and sand) are shown in Figure 4. It can be observed that the mortar—a mixture of bitumen, filler, and sand—had all functional groups as its three component materials. Figure 4 clearly shows that the carbonyl group that was present in the mortar originated only from the presence of bitumen, whereas sulfoxides can be present in all three components.

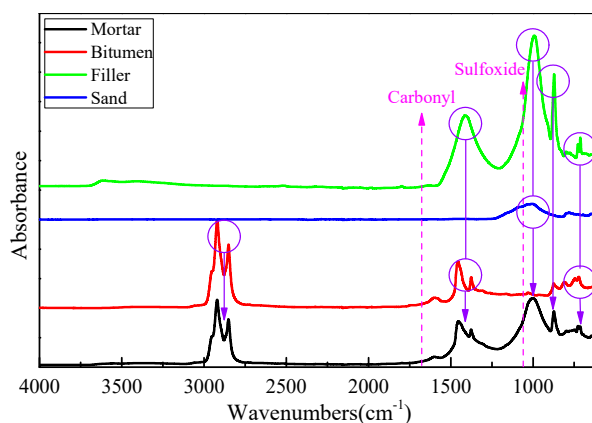


Figure 4. FTIR spectrum of mortar, bitumen, filler, and sand at fresh state.



### 3.1.2. Ageing Index

In this study, the effects of ageing were analyzed considering specific bands of wavenumber as defined by Lamontagne et al. [28–30] and the corresponding area under those bands. Then, the carbonyl and the sulfoxide indices were determined by dividing the area under a specific location of the spectrum by the sum of specific areas, Equations (1) and (2).

$$\text{Carbonyl index} = \frac{A_{1700}}{\sum A} \quad (1)$$

$$\text{Sulfoxide index} = \frac{A_{1030}}{\sum A} \quad (2)$$

where  $\sum A = A_{(2953,2862)} + A_{1700} + A_{1600} + A_{1460} + A_{1376} + A_{1030} + A_{864} + A_{814} + A_{743} + A_{724}$ .

Using the obtained spectra, the ageing indices (carbonyl and sulfoxide index) of each sample were calculated. Figure 5 shows the carbonyl and sulfoxide indices (average value of three measurements) of bitumen, mortar\_AM, and mortar\_MA. The error bar in Figure 5 is the standard deviation of the three measurements. It can be observed that under the same ageing conditions, the value of the carbonyl index for mortar\_AM was similar to that of bitumen. This can be attributed to the fact that carbonyls in the mortar only came from bitumen as illustrated in Figure 4. Previous studies have shown that carbonyls are formed later than sulfoxides because sulfur is more reactive than carbon in bitumen. Later, carbonyls increases due to the full consumption of sulfur [31]. Similar trends and values were found for the mortar in our study as well.

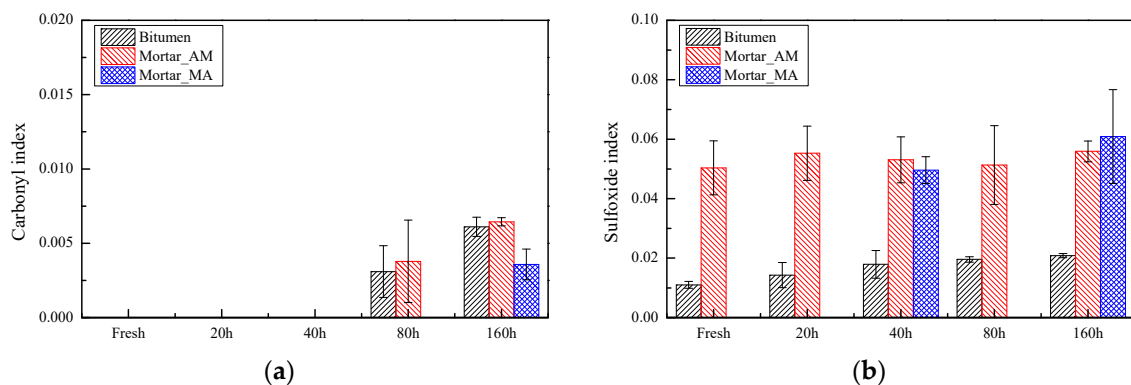


**Figure 5.** Function group index of mortar at different ageing conditions: (a) carbonyl index; (b) sulfoxide index.

Moreover, it can be observed that the carbonyl index of mortar\_MA was significantly smaller than that of mortar\_AM (Figure 5a), indicating that mortar\_MA had a lower ageing rate. This finding confirms the theory that the sand and filler particles present in the mortar can slow down the diffusion rate of oxygen due to an increased length of diffusion paths and consequently slow down the ageing process as well [32]. In addition, the diffusivity of mortar will decrease as the bitumen volume fraction decreases [33]. This happens because mortar is the mixtures of bitumen, filler, and sand, and its diffusivity should always be between that of the bitumen and the filler/sand. Moreover, the diffusivity of bitumen is much higher than that of filler/sand [34,35].

The sulfoxide index of mortar\_AM differed significantly with that of bitumen (Figure 4b). This was because sulfoxides in the mortar came not only from the bitumen component but also from the filler and sand particles as illustrated in Figure 3. The sulfoxides content in filler and sand was much higher than that in bitumen, and this led to obvious change in the sulfoxide index of the mortar. Moreover, as another result, the deviation of the mortar results was obviously higher than that of bitumen. The reason for this might be because the measuring area of the FTIR test was limited, meaning the

infrared radiation hit only one or few of the components of mortar. Another reason might be that the mix of mortar samples was not homogenous.

### 3.2. Dynamic Shear Rheometer

#### 3.2.1. Frequency Sweep Tests

At least three replicate samples were tested in DSR at each condition. Based on the time–temperature superposition (TTS) principle, master curves of complex shear modulus and phase angle were generated at reference temperature of 20 °C. Figure 6 shows the evolution of the rheological characteristics of bitumen with increased ageing time. The master curves of mortar\_AM and mortar\_MA at various ageing times are shown in Figure 7.

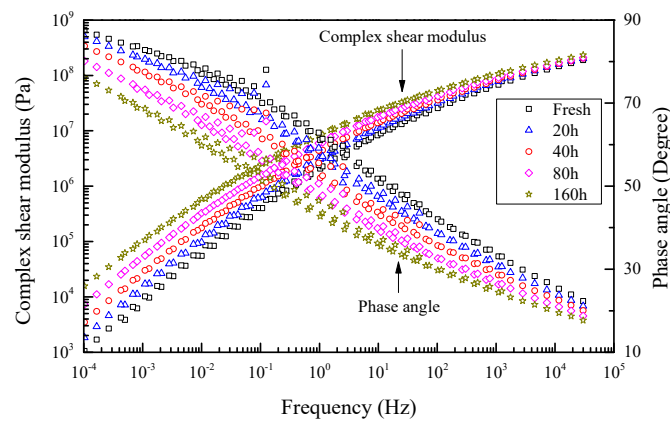


Figure 6. Master curves of PEN 70/100 at different ageing times.

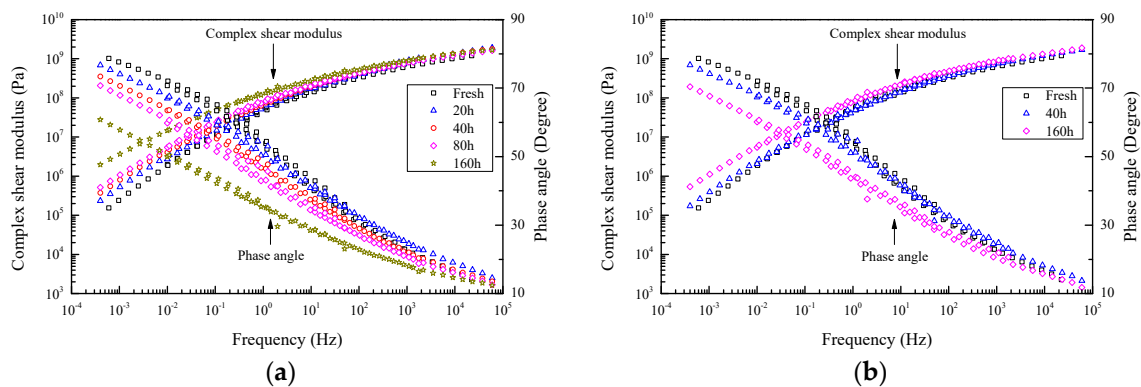
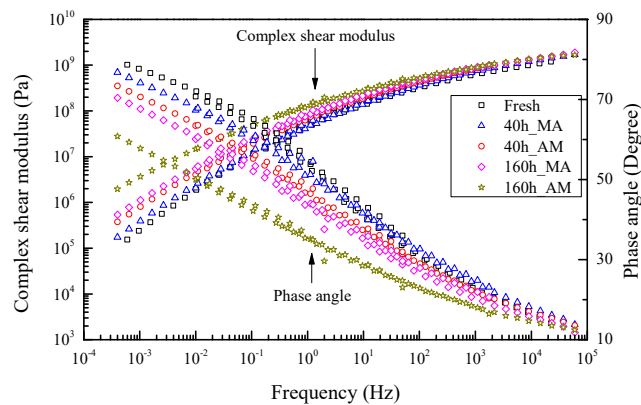


Figure 7. Master curve of mortar samples at different ageing times: (a) mortar\_AM; (b) mortar\_MA.

As shown in Figure 6, the observed differences were more pronounced at low frequencies, while they were diluted at higher frequencies. Specifically, the variation of complex modulus between fresh and aged materials was about one order of magnitude at low frequencies. Moreover, at the highest frequency, all samples tended to reach an asymptote at a value of  $10^8$  Pa. On the contrary, the phase angle differed substantially for the whole frequency range. The greater the value of complex shear modulus, the harder was the bitumen; the smaller the phase angle, the more elastic was the bitumen.

In Figure 7, it can be seen that the complex shear modulus of mortar sample increased as expected with increasing ageing, while the opposite was observed for the phase angle. Specifically, the variation of complex modulus between fresh and aged materials was one order of magnitude at low frequencies. Moreover, at the highest frequency, all samples tended to reach an asymptote at a value of  $10^9$  Pa. The threshold value at high frequency was one order of magnitude larger than that of bitumen due to the addition of filler and sand. On the other hand, the phase angle of the mortar samples differed

substantially for the whole frequency range. These results show that the material became stiffer and more brittle with ageing. The comparison between mortar\_AM and mortar\_MA is shown in Figure 8.



**Figure 8.** Master curve of mortar\_AM and mortar\_MA at different ageing times.

Figure 8 shows that compared to mortar\_AM, mortar\_MA had lower values of complex shear modulus and higher values of phase angle. In other words, mortar\_MA was softer under the same ageing conditions, thus the effect of ageing was less. This finding was in agreement with the FTIR results presented in Figure 5. Figure 9 shows the differences in the complex shear modulus and phase angle at 20 °C and at 10 Hz frequency for the bitumen, mortar\_MA, and mortar\_AM samples. The reason for choosing shear moduli at 10 Hz and 20 °C was that 10 Hz is the commonly used frequency in a dynamic test and 20 °C is considered to be room temperature [36–38].

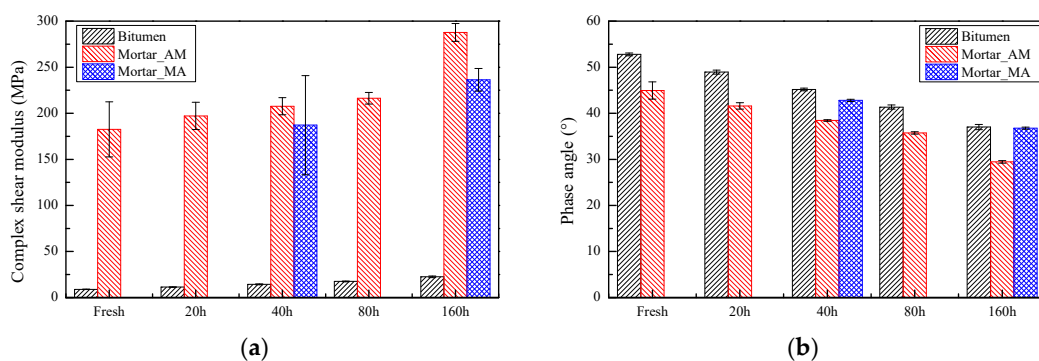


**Figure 9.** Complex shear modulus and phase angle at 20 °C, 10 Hz of bitumen, mortar\_AM, and mortar\_MA.: (a) complex shear modulus; (b) phase angle.

It can be observed that the complex shear modulus of mortar was significantly higher than that of bitumen, with the variation being about 200 times higher, while the phase angle of mortar was slightly smaller than that of bitumen. This high difference in stiffness occurred due to the presence of filler and sand particles, while the phase angle of mortar was mainly determined by the bitumen component.

### 3.2.2. Uniaxial Tension Tests

Uniaxial tension tests were performed using DSR. To obtain the effect of ageing on the tensile behavior of asphalt mortar, at least three samples were tested for each ageing condition. Tensile strength and failure strain are influenced by varying the temperature and strain rate due to the time–temperature dependency of bituminous materials. The tensile strength is higher for lower temperatures and higher strain rates. Therefore, uniaxial tensile tests in this study were performed at 0 °C with 0.2% (0.024 mm/s) tensile rate to make sure all tests can be conducted in a suitable testing range of the device. The normal force in relation to the displacement of the machine for mortar\_AM at different ageing times was recorded and is plotted in Figure 10.

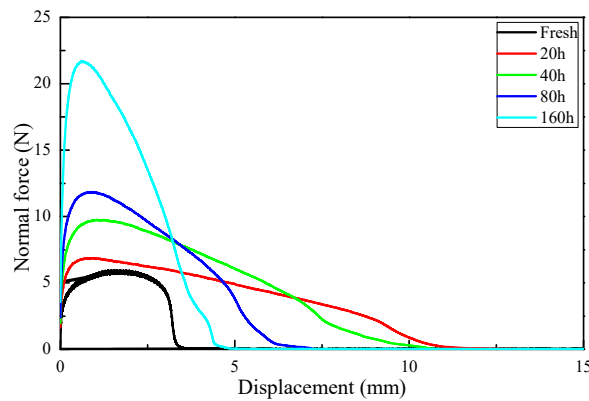


Figure 10. Normal force vs. displacement of mortar\_AM with different ageing times.

Figure 10 shows that higher peak normal forces and smaller displacement at failure were obtained for longer ageing times. In other words, aged samples tended to become more brittle. Meanwhile, the steeper initial slopes of the curves can be seen at the longer ageing times, which mean higher moduli for the aged sample. Tensile strength is the maximum normal force divided by the crossing area of the cylinder sample. It denotes the maximum stress that a material can withstand while being pulled before breaking. Figure 11 shows the tensile strength of asphalt mortar at different ageing times. It can be observed that the strength of mortar increased with ageing time. Another observation was that under the same ageing conditions, the strength of mortar\_AM was higher than that of mortar\_MA.

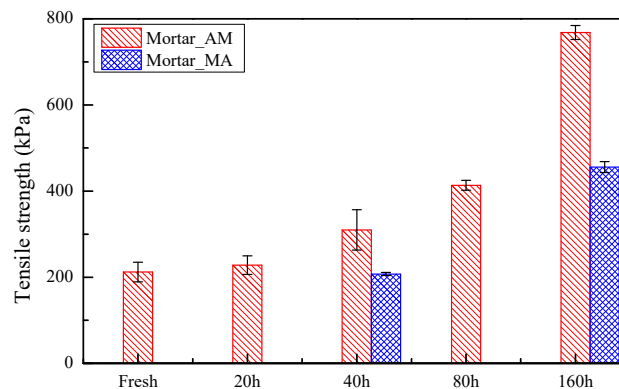


Figure 11. Tensile strength of mortar\_AM and mortar\_MA with different ageing times.

#### 4. Conclusions

Based on the findings and analysis presented in this paper, the following conclusions can be drawn: (1) Asphalt mortar—a mixture of bitumen, filler, and sand—has all functional groups as its three component materials. Carbonyl group that is present in the mortar originates only from the presence of bitumen, whereas sulfoxides can be present in all three components. (2) Ageing increases the complex shear modulus and decreases the phase angle of bitumen and asphalt mortar. The high difference in stiffness observed between bitumen and asphalt mortar is due to the presence of filler and sand particles. The less difference observed between the phase angle values of bitumen and mortar is due to the fact that the phase angle is mainly governed by the bitumen component. (3) Ageing leads to higher strength and smaller displacement at failure compared to unaged sample. In other words, aged samples tend to become more brittle. (4) Both chemical and mechanical test results have shown that the sand and filler particles present in the mortar may slow down the diffusion rate of oxygen. The hypothesis is that the presence of particles increases the length of the diffusion path and therefore slows down the ageing process. This will help to understand the interaction between components during ageing and develop a more suitable protocol to simulate ageing procedure of bituminous materials in the field.

The results of this study will help to understand the ageing process of asphalt mortar and more accurately predict evolution of its properties due to ageing. Based on the results, the relationship between the chemical and mechanical properties of asphalt mortar can be determined, and a chemo-mechanical model of asphalt mortar can be developed and implemented using the finite element method.

**Author Contributions:** R.J., X.L., and A.V. conceived the experimental plan and contributed to the interpretation of the results. R.J. carried out the experiments. A.S. and S.E. supervised all project activities.

**Funding:** This research received no external funding.

**Acknowledgments:** The authors gratefully acknowledge the Dutch Ministry of Transport, Public Works, and Water Management for funding this project.

**Conflicts of Interest:** The authors declare no conflicts of interest.

## References

1. Molenaar, A.A.; Meerkerk, A.J.; Miradi, M.; Van der Steen, T. Performance of porous asphalt concrete. *J. Assoc. Asphalt Paving Technol.* **2006**, *75*, 1053–1094.
2. Hagos, E.T. The Effect of Aging on Binder Properties of Porous Asphalt Concrete. Ph.D. Thesis, Delft University of Technology, Delft, The Netherlands, 2008.
3. Huber, G. *Performance Survey on Open-Graded Friction Course Mixes*; Transportation Research Board: Washington, DC, USA, 2000; Volume 284.
4. Yildirim, Y.; Dossey, T.; Fults, K.W.; Trevino, M. *Winter Maintenance Issues Associated with New Generation Open-Graded Friction Courses*; Center for Transportation Research, The University of Texas at Austin: Austin, TX, USA, 2006.
5. Huurman, M.; Mo, L.-T.; Woldekidan, M.F. Porous asphalt ravelling in cold weather conditions. *Int. J. Pavement Res. Technol.* **2010**, *3*, 110–118.
6. Airey, G.D.; Choi, Y.K. State of the Art Report on Moisture Sensitivity Test Methods for Bituminous *Pavement Mater. Road Mater. Pavement Des.* **2002**, *3*, 355–372. [CrossRef]
7. Saoula, S.; Soudani, K.; Haddadi, S.; Munoz, M.E.; Santamaria, A. Analysis of the rheological behavior of aging bitumen and predicting the risk of permanent deformation of asphalt. *Mater. Sci. Appl.* **2013**, *4*, 312–318. [CrossRef]
8. Siddiqui, M.N.; Ali, M.F. Investigation of chemical transformations by NMR and GPC during the laboratory aging of Arabian asphalt. *Fuel* **1999**, *78*, 1407–1416. [CrossRef]
9. Lv, S.; Wang, S.; Guo, T.; Xia, C.; Li, J.; Hou, H. Laboratory evaluation on performance of compound-modified asphalt for rock asphalt/styrene-butadiene rubber (SBR) and rock asphalt/nano-caco<sub>3</sub>. *Appl. Sci.* **2018**, *8*, 1009. [CrossRef]
10. Hardesty, J.H.; Attili, B. *Spectrophotometry and the Beer-Lambert Law: An Important Analytical Technique in Chemistry*; Collin College: Collin, TX, USA, 2010.
11. Huurman, M.; Mo, L.; Woldekidan, M.F. Unravelling porous asphalt concrete towards a mechanistic materials design tool. *Road Mater. Pavement Des.* **2010**, *11*, 583–612. [CrossRef]
12. He, Y.; Mohammad, Z.A.; Jones, D.; Harvey, J. Proposing a solvent-free approach to evaluate the properties of blended in asphalt mixes containing high quantities of reclaimed asphalt pavement and recycled asphalt shingles. *Construct. Build. Mater.* **2016**, *114*, 172–180. [CrossRef]
13. Kliewer, J.E.; Bell, C.A.; Sosnovske, D.A. *Investigation of the Relationship between Field Performance and Laboratory Aging Properties of Asphalt Mixtures, in Engineering Properties of Asphalt Mixtures and the Relationship to Their Performance*; ASTM International: West Conshohocken PA, USA, 1995.
14. Cui, S.; Deng, H.; Mo, L. Effect of laboratory long-term ageing simulation testing on response properties of bitumen and bituminous mortar. *World Build. Mater.* **2012**, *33*, 35–38.
15. Molenaar, A.A.A.; Hagos, E.T.; Van de Ven, M.F.C. Effects of aging on the mechanical characteristics of bituminous binders in PAC. *J. Mater. Civ. Eng.* **2010**, *22*, 779–787. [CrossRef]
16. Mo, L.; Huurman, M.; Wu, S.; Molenaar, A.A.A. Ravelling investigation of porous asphalt concrete based on fatigue characteristics of bitumen–stone adhesion and mortar. *Mater. Des.* **2009**, *30*, 170–179. [CrossRef]

17. Tong, Y.; Luo, R.; Lytton, R.L. Moisture and ageing damage evaluation of asphalt mixtures using the repeated direct tensional test method. *Int. J. Pavement Eng.* **2015**, *16*, 397–410. [CrossRef]
18. Zhang, Y.; Leng, Z. Quantification of bituminous mortar ageing and its application in raveling evaluation of porous asphalt wearing courses. *Mater. Des.* **2017**, *119*, 1–11. [CrossRef]
19. Huurman, M. *Lifetime Optimisation Tool–Main Report*; Report 7-07-170-1; Delft University of Technology: Delft, The Netherlands, 2007.
20. Mo, L. Damage Development in the Adhesive Zone and Mortar of Porous Asphalt Concrete. Ph.D. Thesis, Delft University of Technology, Delft, The Netherlands, 2010.
21. Van den Bergh, W. The Effect of Ageing on the Fatigue and Healing Properties of Bituminous Mortars. Ph.D. Thesis, Delft University of Technology, Delft, The Netherlands, 2011.
22. Mohammad, J.K.; Kyatham, V. Viscoelastic behavior of hydrated lime-modified asphalt matrix and hot-mix asphalt under moisture damage conditions. *J. Transp. Res. Board* **2008**, *2370*, 64–74.
23. Kuang, D.; Yu, J.; Feng, Z.; Li, R.; Chen, H.; Guan, Y.; Zhang, Z. Performance evaluation and preventive measures for aging of different bitumen. *Construct. Build. Mater.* **2014**, *66*, 209–213. [CrossRef]
24. Ahmed, F. *Diffusion of the Rejuvenators into Bitumen Studied by FTIR-ATR as a Function of Temperature and Bitumen Properties*; Aalto University: Helsinki, Finland, 2016.
25. Kandhal, P.; Chakraborty, S. Effect of asphalt film thickness on short-and long-term aging of asphalt paving mixtures. *Transp. Res. Record* **1996**, *1535*, 83–90. [CrossRef]
26. Ruan, Y.; Davison, R.R.; Glover, C.J. An Investigation of Asphalt Durability: Relationships Between Ductility and Rheological Properties for Unmodified Asphalts. *Petrol. Sci. Technol.* **2003**, *21*, 231–254. [CrossRef]
27. Lesueur, D. The colloidal structure of bitumen: Consequences on the rheology and on the mechanisms of bitumen modification. *Adv. Colloid Interface Sci.* **2009**, *145*, 42–82. [CrossRef] [PubMed]
28. Lamontagne, J.; Dumas, P.; Mouillet, V.; Kister, J. Comparison by Fourier Transform Infrared (FTIR) Spectroscopy of Different Ageing Techniques: Application to Road Bitumen. *Fuel* **2001**, *80*, 483–488. [CrossRef]
29. Hofko, B.; Alavi, M.Z.; Grothe, H.; Jones, D.; Harvey, J. Repeatability and sensitivity of FTIR-ATR spectral analysis method for bituminous binders. *Mater. Struct.* **2017**, *50*, 187. [CrossRef]
30. Hofko, B.; Porot, L.; Cannone, A.F.; Poulikakos, L.; Huber, L.; Lu, X.; Mollenhauer, K.; Grothe, H. FTIR spectral analysis of bituminous binders: Reproducibility and impact of ageing temperature. *Mater. Struct.* **2018**, *51*, 45. [CrossRef]
31. Jing, R.; Varveri, A.; Liu, X.; Scarpas, A.; Erkens, S. Chemo-mechanics of ageing on bitumen materials. In Proceedings of the Transportation Research Board 97th Annual Meeting Transportation Research Board, Washington, DC, USA, 7–11 January 2018.
32. Weller, K.R.; Stenhouse, N.S.; Watts, H. Diffusion of Gases in Porous Solids. I. Theoretical Background and Experimental Method. *Can. J. Chem.* **1974**, *52*, 2684–2691. [CrossRef]
33. Das, P.K.; Balieu, R.; Kringos, N.; Birgisson, B. On the oxidative ageing mechanism and its effect on asphalt mixtures morphology. *Mater. Struct.* **2015**, *48*, 3113–3127. [CrossRef]
34. Jing, R.; van Lent, D.; Kasbergen, C.; Scarpas, A.; Liu, X.; Erkens, S. Experimental and computational investigation of gas diffusion in bitumen. In Proceedings of the Transportation Research Board 96th Annual Meeting Transportation Research Board, Washington, DC, USA, 8–12 January 2017.
35. Peng, S.; Hu, Q.; Hamamoto, S. Diffusivity of rocks: Gas diffusion Measurements and correlation to porosity and pore size distribution. *Water Resour. Res.* **2012**, *48*, W02507. [CrossRef]
36. Rossi, C.O.; Caputo, P.; Loise, V.; Miriello, D.; Teltayev, B.; Angelico, R. Role of a food grade additive in the high temperature performance of modified bitumens. *Colloids Surf. A Physicochem. Eng. Aspects* **2017**, *532*, 618–624. [CrossRef]
37. Filonzi, A.; Delgadillo, R. Sample size correction factors for indentation on asphalt bitumens. *Constr. Build. Mater.* **2017**, *154*, 877–883. [CrossRef]
38. Schlosser, F.; Mikolaj, J.; Zatkalikova, V.; Sramek, J.; Durekova, D.; Remek, L. Deformation properties and fatigue of bituminous mixtures. *Adv. Mater. Sci. Eng.* **2013**, *2013*, 701764. [CrossRef]







Article

# Influence of Surface Texture Characteristics on the Noise in Grooving Concrete Pavement

Dingbang Wei <sup>1,2</sup>, Bo Li <sup>1,\*</sup>, Zhengwei Zhang <sup>1</sup>, Feng Han <sup>1</sup>, Xingjun Zhang <sup>1</sup>, Man Zhang <sup>2</sup>, Liangying Li <sup>1</sup> and Qicai Wang <sup>1</sup>

<sup>1</sup> Key Laboratory of Road & Bridge and Underground Engineering of Gansu Province, Lanzhou Jiaotong University, Lanzhou 730070, China; weidingbang@163.com (D.W.); zhangzhengwei@163.com (Z.Z.); hanfeng@126.com (F.H.); zhangxj@163.com (X.Z.); liliangying123@163.com (L.L.); 13909486262@139.com (Q.W.)

<sup>2</sup> State Key Laboratory of Silicate Materials for Architectures, Wuhan University of Technology, Wuhan 430070, China; zhangman@163.com

\* Correspondence: libolzjtu@hotmail.com; Tel.: +86-139-1998-0582

Received: 4 September 2018; Accepted: 30 October 2018; Published: 2 November 2018

**Abstract:** To thoroughly explore the relationship between concrete pavement texture characteristics and tire/pavement noise of grooving concrete pavement, the surface texture, i.e., roughness, macrotexture, and microtexture, was investigated in numerous highway pavements. The On-Board Sound Intensity (OBSI) method was used to test the pavement/tire noise. The statistical correlation between concrete pavement texture characteristics and tire/pavement noise was quantitatively described by two correlation analysis methods for highway concrete pavement: origin of linear regression and the Pearson two-sided test method. The results indicate that the effect of pavement roughness on tire/pavement noise is significant, while the noise level is minor for the flat pavement. The macro texture depth also has a marked impact on the tire/pavement noise. In addition, a large grooving depth of concrete pavement could cause a high tire/pavement noise level; however, there is no clear correlation between side-way force coefficient (SFC) and tire/pavement noise.

**Keywords:** road engineering; concrete pavement; textural characteristics; noise; correlation analysis

## 1. Introduction

With the rapid development of the economy, concrete pavement design should not only meet the basic requirements of vehicular traffic, but also improve its surface functions, such as skidding resistance, durability, and low noise. A serious concern in engineering to reduce the noise of concrete pavement, especially in heavily populated areas, highways near the city, and tunnels [1,2]. In recent years, noise barriers, green forest, and other ways were often used to reduce the tire/pavement noise level. However, the infrastructure is expensive and difficult to repair after damage [3]. Recently, some results have shown that concrete pavement surface textural features are closely correlated to the tire/pavement noise. Utilizing a “quiet” concrete pavement texture has a significant advantage in noise reduction on pavements [4–6].

Han et al. indicated an exposed aggregate cement concrete pavement (EACCP), a new style of cement concrete pavement with a superior performance, i.e., excellent skidding resistance and noise reduction, for a pavement texture depth of 0.7–1.8 mm and a pavement noise reduction amplitude of 3–4 dB(A) [7,8]. Liu et al. found that the porous cement concrete pavement, EACCP, and the longitudinal groove pavement have a similar noise level to that of the asphalt pavement, and each of them has a good skidding resistance performance [9]. Tian et al. tested the concrete pavement noise value of 10 different texture types using the control pass method. The results showed that



porous concrete pavement with a void ratio of 17% can reduce the tire/pavement noise value by about 4~8 dB(A) compared with the groove concrete pavement [10]. Ling Tianqing et al. found that, with the aim of ensuring the mechanical properties and wear resistance of pavement, adding ceramsite to concrete can reduce traffic noise by reducing the road slab stiffness [11]. The use of new cement concrete pavement, i.e., EACCP, porous concrete pavement, or ceramic, creates superior skidding resistance and has a great effect on the noise reduction of pavement; however, due to the relatively high construction costs and the difficulty of technology promotion and application, many countries still use the groove method in the concrete pavement surface texture. Jaecke et al. found that a uniform and random transverse tin plating produces a higher effect on internal and external noise than either skewed or longitudinal tin planting. Transversal tin plating, even in some randomly spaced textures, causes discrete frequencies or whine [12]. Burge provides a contrast between the longitudinal diamond road and the transverse diamond road for the newly built Portland cement concrete pavement. The results show that the noise of the longitudinal rhombic ground shows a low range from 2 to 5 dB and mainly depends on the composition of the traffic vehicles [13]. Kohler et al. also measured and compared the pavement noise level of existing concrete pavement by the onboard sound intensity method. The surfaces encountered were classified into five texture categories: burlap drag, diamond ground, diamond grooved, longitudinally broomed, and longitudinally tined [14]. The results show that the quietest section is measured on the surface of diamond abrasive particles. However, the longitudinal viewing surface as a group is the quietest, based on the average noise level of the assessed slices for each texture type. Liu et al. revealed that the noise level of the transverse groove concrete pavement is the highest, followed by smooth concrete pavement and longitudinal groove concrete pavement, and the noise level of porous concrete pavement is the lowest [15]. Li compared the noise characteristics of newly-built Portland cement concrete pavement with longitudinal and transverse diamond grooved pavement by the tire acceleration method [16,17]. The results show that, compared with the transverse grooving road surface, the longitudinal grooving has good performance at preventing vehicle sideslip and reducing noise.

Generally, the noise is a focus of concrete pavement. However, there is limited research on the correlation between texture features and noise of concrete pavement. In this paper, concrete pavement noises are collected by an on-board sound intensity system (OBSI). Statistical analysis is used to discuss the correlation between common concrete pavement surface texture and noise value.

## 2. Materials and Methods

The characteristics of concrete pavement surface texture in highway tunnels were collected in Gansu province. The test site information and textural characteristics of the samples are shown in Table 1.

**Table 1.** Test section information of concrete pavement.

Texture Type	Test Sites	Groove Spacing/Groove Width/Groove Depth (mm)	Number of Sample Group
Transverse groove	Wang Jiaba Tunnel	20, 5, 5	20
		25, 5, 5	20
	Guo Jiashan Tunnel	20, 5, 5	20
	Mai Jishan Tunnel	24–25, 5, 3–4	/
	Wu Shaoling 2# Tunnel	20, 4, 2–3	/
	Wu Shaoling 4# Tunnel	22–24, 4, 2–3	/
Longitudinal groove	Wang Jiaba Tunnel	25, 5, 5	20
	Guo Jiashan Tunnel	25, 5, 5	20
	Mai Jishan Tunnel	22–24, 5, 3–4	16
Transverse random spacing groove	Wang Jiaba Tunnel	25/50, 5, 5	25
		15/25, 5, 5	22
	Guo Jiashan Tunnel	20/40, 5, 5	22
Longitudinal random spacing groove	Wang Jiaba Tunnel	25, 5, 5	24
	Guo Jiashan Tunnel	25, 5, 5	24
	Mai Jishan Tunnel	24–25, 5, 3–4	22

### 2.1. Measurement of Concrete Pavement Texture

In this study, test methods of concrete pavement texture are shown in Figure 1. During the testing, the pavement roughness is measured by a continuous roughness tester (LXBP-3, Changsha Instruments Company, Changsha, China). Meanwhile, the macrotexture and microtexture are tested by the sanding method and friction coefficient test equipment (JGMC-2, Beijing JinGuShenJian Measuring and Control Technology Institute, Beijing, China), respectively.

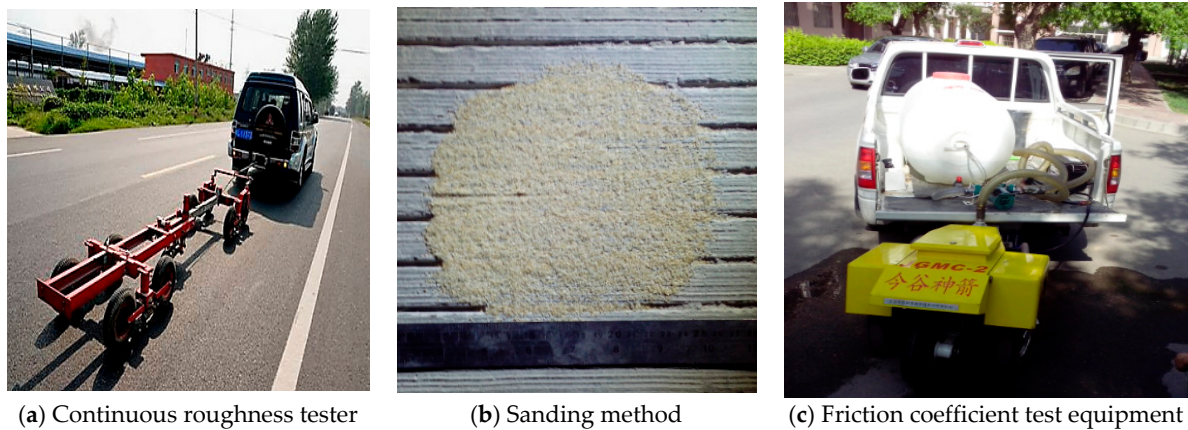


Figure 1. Test methods of concrete pavement texture.

### 2.2. Tire/Road Noise Test

The on-board sound intensity system (Figure 2) is a useful method in tire/road noise testing for measuring the noise level of each test section. The test vehicle ran at a constant speed of 60 km/h. Dewesoft 7.0 (DEWEsoft, Trbovlje, Slovenia) and Coinv DASP ET software (v2005, China Orient institute of Noise and Vibration, Beijing, China) were used to collect and analyze the noise characterization, respectively, and the frequency of collection was 10,000 Hz.

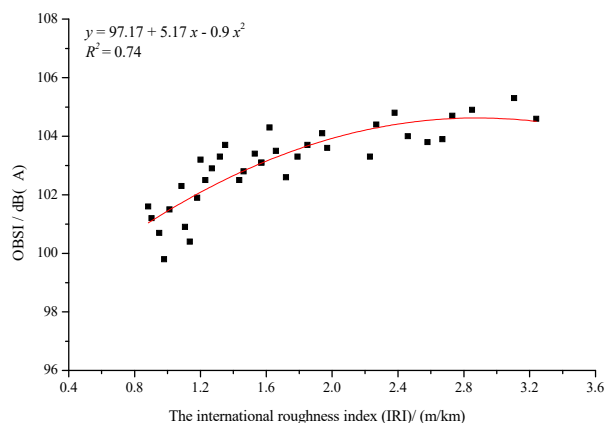


Figure 2. The on-board sound intensity system (OBSI).

## 3. Results

### 3.1. Pavement Roughness and Noise

Before the statistical analysis, the measurement data of pavement roughness must be revised to eliminate the obvious systematic errors such as the effect of concrete pavement joints. Then Origin Pro 8.5 was used to perform a regression analysis between the international roughness index (IRI) and the tire pavement noise level. The statistical results are shown in Figure 3.



**Figure 3.** Regression analyses between groove concrete pavement roughness and tire/road noise.

Figure 3 shows that there is a quadratic relation between the concrete pavement roughness and the noise level, and the correlation coefficient ( $R^2$ ) is 0.74. It is indicated that there exists a certain correlation between the pavement roughness and tire/pavement noise of concrete pavement. To further investigate this relationship, Statistical Program for Social Sciences (SPSS) 19.0 statistical analysis software was used for the correlation analysis of test samples. Table 2 presents the results of SPSS correlation analysis of descriptive statistics.

As can be seen from Table 2, the average IRI and OBSI values of the samples are 1.73 m/km and 103.1 dB(A), respectively, and the standard deviations of the two variables are relatively small. This indicates a small discrete degree among various samples, which to some extent reflects the accuracy of the test data.

Pearson correlation coefficient and  $p$ -value from the T statistics test were calculated through the SPSS correlation matrix analysis process. The results are shown in Table 3.

**Table 2.** Statistical description of international roughness index (IRI) and On-Board Sound Intensity System (OBSI).

	Sample Mean	Standard Deviation	N
IRI (m/km)	1.73	0.675	35
OBSI (dB(A))	103.1	1.366	35

**Table 3.** Correlation analysis between pavement roughness and tire/pavement noise.

	Statistical Test Parameters	IRI (m/km)	OBSI (dB(A))
IRI (m/km)	Pearson correlation coefficient	1.0	0.82 **
	Significant (bilateral)		0.0
	Sum of squared	16	26
	Covariance	0.46	0.76
	N	35	35
OBSI (dB(A))	Pearson correlation coefficient	0.82 **	1
	Significant (bilateral)	0.00	
	Sum of squared	26	63
	Covariance	0.76	1.9
	N	35	35

\*\* means the correlation was significant at the level of 0.01 (both sides).

Table 3 shows that the Pearson correlation coefficients of two variables are 1.0 and 0.82, respectively. This indicates that there is a strong correlation between the roughness and noise of concrete pavement. Indeed, a positive correlation between the concrete pavement roughness and tire/pavement noise can be observed. In other words, using the same test section the corresponding tire/pavement noise level

also increases when increasing the international roughness index (IRI). What needs to be noticed is that when the IRI increases over 2.4 m/km, the noise level does not increase any more. The reason is that the fast scroll wheels make contact with the uneven concrete pavement surface, which can generate vibrational noise during the high-speed driving. The worse the roughness of concrete pavement, the higher the corresponding vibration noise will be [18].

### 3.2. Macrotexture and Noise

#### 3.2.1. Transverse Groove Concrete Pavement

The statistical results of a correlation analysis between the macrotexture and the noise of a transverse groove concrete pavement are shown in Figure 4.

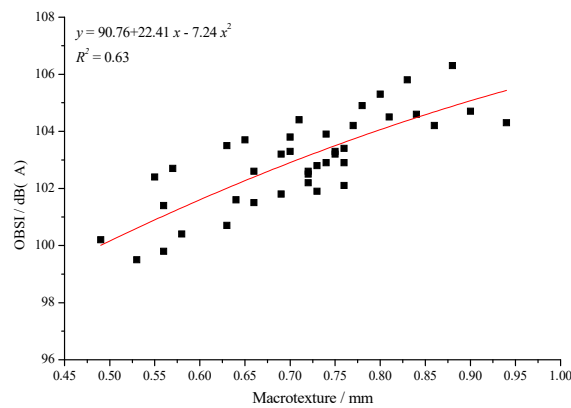


**Figure 4.** Regression analysis between macrotexture of transverse groove pavement and tire/road noise.

Figure 4 shows that there is a quadratic relationship between the macrotexture and tire/pavement noise of transverse groove pavement, and the correlation coefficient ( $R^2$ ) is 0.63. This implies that there is a certain correlation between macrotexture and tire/pavement noise of transverse groove concrete pavement. Likewise, SPSS 19.0 statistical analysis software was used for testing samples of two variables' correlation analysis. Table 4 presents the calculation results of an SPSS correlation analysis of descriptive statistics.

**Table 4.** Statistical description of macrotexture and OBSI of transverse groove concrete pavement.

	Sample Mean	Standard Deviation	N
Macrotexture (mm)	0.720	0.105	40
OBSI (dB(A))	103	1.59	40

As can be seen from Table 4, the sample mean of macrotexture is 0.720 mm, and the OBSI is 103 dB(A). In addition, the variable dispersions are small, reflecting well the accuracy of the experimental data.

Pearson correlation coefficient and  $p$ -value from the T statistics test are shown in Table 5.

Table 5 shows the Pearson correlation coefficient of the two variables is 0.79. This indicates that there is a strong, positive correlation between the macrotexture and the tire/pavement noise. In other words, under the same test conditions, the corresponding tire/pavement noise level will also increase with the increase of macrotexture. The main reason may be the direct contact of fast scroll wheels with road trench when the vehicle is driving at high speeds. Thus, a certain degree of deformation in rubber tires occurs because of the tire contact impact force. The vibration noise will be generated during the repeated tire deformation and recovery. The higher the macrotexture, the higher the corresponding vibration noise will be [19]. Meanwhile, it is noticed that the noise level does not increase obviously when further increasing the value of macrotexture.

**Table 5.** Correlation analysis between macrotexture and noise of transverse groove concrete pavement.

	Statistical Test Parameters	Macrotexture/mm	OBSI/dB(A)
Macrotexture/mm	Pearson correlation coefficient	1	0.79 **
	Significant (bilateral)		0.001
	sum of squared	0.427	5.19
	Covariance	0.011	0.133
	N	40	40
OBSI/dB(A)	Pearson correlation coefficient	0.790 **	1
	Significant (bilateral)	0.001	
	sum of squared	5.19	98.8
	Covariance	0.133	2.53
	N	40	40

\*\* means the correlation was significant at the level of 0.01 (both sides).

### 3.2.2. Longitudinal Groove Concrete Pavement

The statistical results of correlation analysis between macrotexture and noise of longitudinal groove concrete pavement are shown in Figure 5.

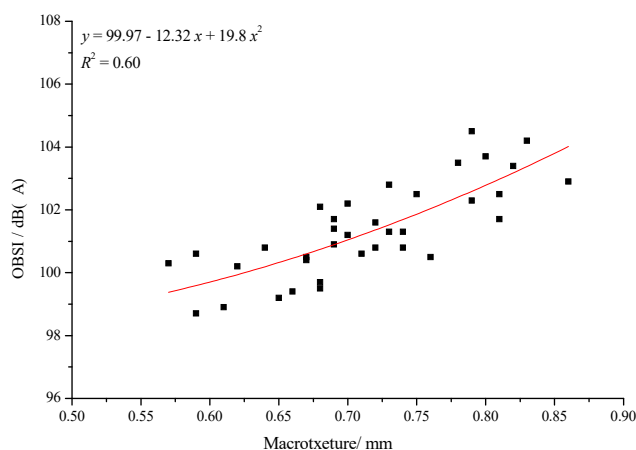


**Figure 5.** Regression analysis between macrotexture of longitudinal groove pavement and tire/road noise.

Figure 5 shows that there is a quadratic relationship between the macrotexture and tire/pavement noise of longitudinal groove pavement, and the correlation coefficient ( $R^2$ ) is  $\sim 0.60$ . This indicates that there is a certain correlation between macrotexture and tire/road noise of longitudinal groove concrete pavement. Likewise, SPSS 19.0 statistical analysis software was used to test samples for the two variables correlation analysis. Table 6 presents the calculation results of SPSS correlation analysis of descriptive statistics.

**Table 6.** Statistical description of macrotexture and OBSI of longitudinal groove pavement.

	Sample Mean	Standard Deviation	N
Macrotexture (mm)	0.71	0.729	36
OBSI (dB(A))	101	1.48	36

As can be seen from Table 6, the sample mean of macrotexture is 0.71, which meets the relevant requirement of the current industry standard. The standard deviations of the two variables are relatively small, which implies that the individual sample is closer to the sample mean with a less variation degree. Macrotexture of samples are consistent with the new concrete pavement construction, furthermore, validate the accuracy of the test data.

The Pearson correlation coefficient and *p*-value from the T statistics test are shown in Table 7. The Pearson correlation coefficients of the two variables are ~0.78, indicating that there is a high, positive correlation between the macrotexture and the tire/road noise of longitudinal groove concrete pavement. In addition, the corresponding pavement noise level will also increase when increasing the macrotexture under the same test conditions. Meanwhile, it is worthwhile noting that there is no saturation of noise level when varying the macrotexture.

**Table 7.** Correlation analysis between macrotexture and noise of longitudinal groove pavement.

	Statistical Test Parameters	Macrotexture/mm	OBSI/dB(A)
Macrotexture/mm	Pearson correlation coefficient	1	0.78 **
	Significant (bilateral)		0.001
	Sum of squared	0.186	2.97
	Covariance	0.005	0.085
	N	36	36
OBSI/dB(A)	Pearson correlation coefficient	0.78 **	1
	Significant (bilateral)	0.001	
	Sum of squared	2.97	76.7
	Covariance	0.085	2.19
	N	36	36

\*\* means the correlation was significant at the level of 0.01 (both sides).

### 3.3. Microtexture and Noise

Figure 6 shows the statistical results of the regression analysis between side-way force coefficient (SFC) and the corresponding tire/road noise.

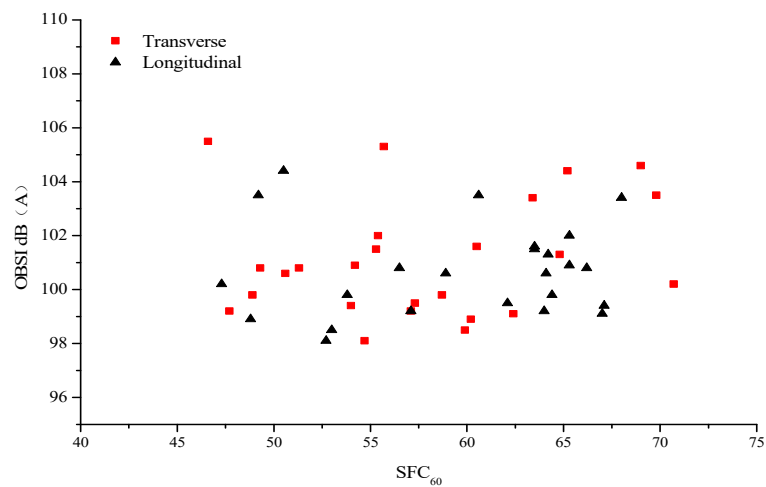


**Figure 6.** Regression analysis between side-way force coefficient (SFC) and tire/road noise.

As can be seen from Figure 6, there is no noticeable correlation between SFC and noise of concrete pavement. The pavement noise level of some test sections remains nearly unchanged for the same type of concrete pavement texture despite the varying of SFC. The tire/pavement noise level, however, varies greatly with SFC. Table 8 presents the results of an SPSS correlation analysis of descriptive statistics. As can be seen from Table 8, the sample mean of SFC is 57.8, which meets the requirements of the current industry standard. Nonetheless, the standard deviation of SFC is 7.299, indicating a high degree of dispersion.

**Table 8.** Statistical description of side-way force coefficient (SFC) and OBSI.

	Sample Mean	Standard Deviation	N
SFC	57.8	7.30	92
OBSI/dB(A)	100	2.27	92

The Pearson correlation coefficient and *p*-value from the T statistics test are shown in Table 9. Table 9 shows that the Pearson correlation coefficients of two variables is 0.136, which shows that the two variables may have a weak correlation. In another word, the SFC of concrete pavement has no obvious correlation with the noise. The main reason may be that SFC is mainly related to the material properties of pavement, water film thickness, speed, wear, and pollution of pavement surface [20].

**Table 9.** Correlation analysis between SFC and noise.

	Statistical Test Parameters	SFC	OBSI/dB(A)
SFC	Pearson correlation coefficient	1	0.136
	Significant (bilateral)		0.196
	Sum of squared	4847.652	204.803
	Covariance	53.271	2.251
	N	92	92
OBSI/dB(A)	Pearson correlation coefficient	0.136	1
	Significant (bilateral)	0.196	
	Sum of squared	204.803	466.972
	Covariance	2.251	5.132
	N	92	92

#### 4. Discussion

Based on current research, tire/road noise mainly comes from the air pumping effect and vibration effect, which depend on the surface texture characteristics of grooving concrete pavement [21].

From the test results, it was found that there is a significant correlation between tire/pavement noise and pavement surface texture index, such as IRI and macrotexture, besides the microtexture. The pavement noise increases with the groove depth, because of the increased volume embraced by the tire grooves in contact with the concrete pavement. With the tire rolling on the road, air pumped volume increases, leading to high noise. At the same time, as the groove depth increases, the volume of the gas pipeline cavity formed between groove and tire tread increases, which enhances the tire cavity resonance effect during the tire rolling. Additionally, when the tires leave the road, the air volume in the contact surface will increase, which causes an increased Helmholtz resonance effect and thus noise amplification. For microtexture that does not induce vibration and air pumping effect, there is no correlation with noise.

#### 5. Conclusions

Concrete pavement noises are collected by an on-board sound intensity system (OBSI) and statistical analysis results show that there are different correlations between pavement surface texture characteristics and the noise value.

The roughness of concrete pavement has a significant influence on the noise level. The corresponding noise level increases with the increase in the international roughness index (IRI).

The macrotexture of concrete pavement is closely related to the noise level. The noise level of transverse groove concrete pavement is lower than that of longitudinal groove concrete pavement.

The microtexture of concrete pavement has no significant influence on the tire/pavement noise level. In other words, pavement noise can be reduced by choosing superior pavement texture while ensuring vehicle safety.

**Author Contributions:** Conceptualization, D.W. and B.L.; Methodology, Z.Z.; Validation, F.H.; Formal analysis and investigation, X.Z. and M.Z.; Resources and Data Curation, L.L.; Writing—Original Draft Preparation and Writing—Review and Editing, D.W. and B.L.; Supervision, Q.W.

**Funding:** The research work reported in this paper was supported by the National Natural Science Foundation of China (Grant No. 51408287), Gansu DOT Research Project (2011-08), the Program for Changjiang Scholars and Innovative Research Team in University (IRT1139), the Young Scholars Science Foundation of Lanzhou Jiaotong University (2011031), and the Science and Technology Support Foundation of Lanzhou Jiaotong University (ZC2012004).

**Conflicts of Interest:** The authors declare no conflict of interest. The funders had no role in the design of the study; in the collection, analyses, or interpretation of data; in the writing of the manuscript, or in the decision to publish the results.

## References

1. Babisch, W. Road Traffic Noise and Cardiovascular Risk. *Noise Health* **2008**, *10*, 27–33. [CrossRef] [PubMed]
2. Hajek, J.J.; Blaney, C.T.; Hein, D.K. Framework for environmental assessment of tire-pavement noise. *Transp. Res. Rec. J. Transp. Res. Board* **2008**, *2058*, 140–146. [CrossRef]
3. Bo, T.; Liu, Y.; Niu, N.; Li, S.; Xie, J.; Li, X. Reduction of Tire-Pavement Noise by Porous Concrete Pavement. *J. Mater. Civ. Eng.* **2014**, *26*, 233–239.
4. Ongel, A.; Harvey, J. Pavement characteristics affecting the frequency content of tire/pavement noise. *Noise Control Eng. J.* **2010**, *58*, 563–571. [CrossRef]
5. Biligiri, K.P.; Way, G.B. Noise-damping characteristics of different pavement surface wearing courses. *Road Mater. Pavement Des.* **2014**, *15*, 925–941. [CrossRef]
6. Donovan, P.R. Noise evaluation of various pavement textures on new Portland cement concrete. *Noise Control Eng. J.* **2009**, *57*, 63–76. [CrossRef]
7. Han, S.; Dong, Y.M.; Chen, H.F.; Zhang, D.S.; Lu, X.M.; Shi, Y.Q. Noise reduction performance of exposed-aggregated cement concrete pavement. *J. Traffic Transp. Eng.* **2005**, *5*, 32–34.
8. Jia, J.; Han, S. Research on tunnel cement concrete pavement based on skid resistance and noise reduction. *J. Highw. Transp. Res. Dev.* **2008**, *4*, 42–45.
9. Liu, Y.; Tian, B.; Niu, K. Skid-resistance and Denoising Properties of Cement Concrete Pavement with Different Surface Texture. *J. Highw. Transp. Res. Dev.* **2012**, *29*, 28–33.
10. Tian, B.; Niu, K. Study on Cement Concrete Pavement Tire Noise and Noise Reduction Method. *J. Highw. Transp. Res. Dev.* **2008**, *25*, 172–176.
11. Ling, T.; Wang, R.; Zhang, J.; Liu, J.; Dong, Q. Influence of Ceramsite Mortar and Ceramic Concrete on Reducing Traffic Noise in Tunnel. *China J. Highw. Transp.* **2011**, *24*, 21–24.
12. Jaekel, J.R.; Kuemmel, D.A.; Becker, Y.Z.; Satanovsky, A.; Sonntag, R.C. Noise issues of concrete-pavement texturing. *Transp. Res. Rec.* **2000**, *1702*, 69–79. [CrossRef]
13. Burgé, P.L.; Travis, K.; Rado, Z. Transverse-Tined and Longitudinal Diamond-Ground Texturing for Newly Constructed Concrete Pavement: A Comparison. *Transp. Res. Rec.* **2002**, *1792*, 75–82. [CrossRef]
14. Kohler, E.; Harvey, J.; Motumah, L. Assessment of tire noise on concrete Pavement in California Highways. *Transp. Res. Rec.* **2013**, *2036*, 113–121. [CrossRef]
15. Liu, Y.-M.; Han, S.; Tao, Z.-J.; Guo, Z.-T. Noise evaluation of concrete pavements with different texture. *Nat. Sci. Ed.* **2012**, *36*, 16–20.
16. Li, B.; Kang, H.-W.; Han, S.; Tao, Z.J. Noise Characteristics of Concrete Pavement Based on the Method of Accelerating-falling Tire. *J. Wuhan Univ. Technol.* **2013**, *35*, 59–62.
17. Li, B.; Kang, H.-W.; Zhang, Z.-W. Comparison of skid resistance and noise between transverse and longitudinal grooving pavements in newly constructed concrete pavement. *Adv. Mater. Res.* **2012**, *446–449*, 2637–2640. [CrossRef]
18. Sun, L.-J.; Geng, Y.-J.; Zhou, X.-Q. Experimental Research on the Relation between Motor Vehicle Noise and Pavement Roughness of Urban Road. *J. Highw. Transp. Res. Dev.* **2007**, *24*, 24–28.
19. Bueno, M.; Luong, J.; Terán, F.; Viñuela, U.; Paje, S.E. Macrotecture influence on vibrational mechanisms of the tyre-road noise of an asphalt rubber pavement. *Int. J. Pavement Eng.* **2014**, *15*, 606–613. [CrossRef]



20. Gothie, M. The contribution to road safety of pavement surface characteristics. *Bulletin des Laboratoires des Ponts et Chaussées* **2000**, *244*, 5–12.
21. Ahammed, M.A. Safe, Quiet and Durable Pavement Surfaces. Ph.D. Thesis, University of Waterloo, Waterloo, ON, Canada, 2009.



© 2018 by the authors. Licensee MDPI, Basel, Switzerland. This article is an open access article distributed under the terms and conditions of the Creative Commons Attribution (CC BY) license (<http://creativecommons.org/licenses/by/4.0/>).

Article

# Analysis of the Fatigue Crack Propagation Process of the Stress-Absorption Layer of Composite Pavement Based on Reliability

Yazhen Sun <sup>1,\*</sup>, Ting Yan <sup>1</sup>, Changyu Wu <sup>1</sup>, Xiaofang Sun <sup>2</sup>, Jinchang Wang <sup>3</sup>  
and Xuezhong Yuan <sup>4,\*</sup>

<sup>1</sup> School of Transportation Engineering, Shenyang Jianzhu University, Shenyang 110168, China; yanting1996@stu.syzj.edu.cn (T.Y.); wcy1164521021@stu.syzj.edu.cn (C.W.)

<sup>2</sup> Cscec Science & Technology Changchun Co., Ltd., Changchun 130000, China; sxf19921220@163.com

<sup>3</sup> Institute of Transportation Engineering, Zhejiang University, Hangzhou 310058, China; wjc501@zju.edu.cn

<sup>4</sup> School of Science, Shenyang Jianzhu University, Shenyang 110168, China

\* Correspondence: syz16888@126.com (Y.S.); yuanxuezhong1@163.com (X.Y.); Tel.: +86-13940021867 (Y.S.); +86-13614040298 (X.Y.)

Received: 25 August 2018; Accepted: 25 October 2018; Published: 30 October 2018

**Abstract:** The stress-absorption layer in cement concrete pavement delays the development of reflection cracks and is good at fatigue resistance. Laboratory investigations of the anti-crack performance of the high viscous asphalt sand stress-absorption layer (HVASAL) and rubber asphalt stress-absorption layer (RASAL) were carried out by force-controlled fatigue crack propagation tests, for which three types of overlay structures with three types of pre-crack (i.e., the middle crack, the side crack, and the 45° inclined crack) were designed. A probability model was established to describe the propagation of the fatigue cracks. The fatigue crack propagation, the fatigue life, the crack propagation rate, and the crack propagation mechanism of the three types of overlay structure were compared and analyzed. The results show that the stress-absorption layers have good anti-crack fatigue performance, and that the RASAL is better than the HVASAL. The crack propagation patterns of the three types of overlay structure were found. In the double logarithmic coordinate, the curves of the three types of cracks are straight lines with different intercepts and slopes. The probability model quantifies the relationship between the crack propagation rate and  $\Delta K$ . The influences of the three types of crack on the fatigue properties of the asphalt overlays are different.

**Keywords:** road engineering; crack resistance; fatigue crack propagation test; reliability; rubber asphalt stress absorption layer (RASAL); high viscous asphalt sand stress absorption layer (HVASAL); asphalt overlay

## 1. Introduction

Nowadays, adding a paving asphalt layer on cracked cement concrete pavement is a widespread construction measure. Due to defects in the cement concrete layer, the bearing capacity of the structure decreases over time. As the pavement temperature increases, the effects of the interface bonding on the overlay response amplify [1], and reflection cracks are more prone to occur in the overlay subjected to temperature change and loading; however, study has shown that glass fiber reinforced modified asphalt could strengthen the bonding and mitigate cracking of the overlay [2]. In order to delay the development of reflection cracks, the stress-absorption layer has been adopted domestically, and some experiments have been carried out to validate the effects of anti-crack performance. The stress-absorption layer, set between the cement concrete layer and the asphalt layer, can delay the occurrence of a reflection crack, because the deformation and the ability of elastic recovery of the layer reduces the stress concentration [3]. The stress-absorption layer is good at fatigue resistance,

because the layer dissipates the concentrated stress and prevents the emergence of fatigue cracks in it, and consequently, it slows down the speed of propagation of the reflection crack, and thus attains the objectives of preventing and controlling the cracks. Nowadays, the theories and methods of fatigue fracture mechanics have been used to study the cracks of asphalt pavement. The nonlinear X-SBFEM (which is the extended proportional boundary finite element method) is capable of modeling the nonlinear fracture propagation process while taking into account the effects of cohesive interactions [4], because the main reason for the failure of the asphalt pavement is fatigue failure under the persistent actions of traffic load and temperature load. Therefore, research of the fatigue crack propagation law of the asphalt pavement is important. The fatigue failure of asphalt pavement can be divided into two stages: The fatigue-initiation stage and the fatigue fracture stage. Some experience has been accumulated in the study of the fatigue initiation stage, and the results have been used so far. The study of the fatigue fracture stage showed that the fractured area increased significantly as the interface bonding strength decreased. On the contrary, the fractured area decreased slightly as the interface stiffness decreased [5].

In the past, model I cracks were researched mainly through fatigue fracture tests for asphalt-overlay composite pavement. In fact, I-II composite cracks have existed extensively in pavement structures, but few experiments have been conducted [6–11]. The propagation behavior of composite cracks was previously simulated through the uniaxial compression experiment using a notched beam, but the cyclic loading was not applied, and the type of crack and the trend of the crack propagation were also lacking [12]. Test simulations of the propagation process of load reflective cracking and temperature reflective cracking have been carried out to evaluate the cracking resistance of the stress-absorption layer, and it has been proven that paving of the stress-absorption layer is a good method to delay reflection cracks; however, only the influence of loading and temperature on the stress-absorption layer was tested, the material of the stress-absorption layer and the crack were not included [13]. The effects of the thickness of the stress-absorption layer on the speed of the propagation of the reflection crack have also been investigated, but the mechanism of the stress-absorption layer was not quite clear [14–17]. With the increase of the thickness of the stress-absorption layer, the speed of the propagation of the reflection crack would decrease, but the flexural and tensile effects of the overlay would increase, and also the cost [18–20]. It has been verified by engineering that the optimal thickness of the interlayer is 20–40 mm [9,10,21]. Laboratory investigations of three types of stress-absorption layer have been carried out by fatigue experiments. The results showed that the fatigue property of the rubber asphalt stress absorption layer (RASAL) was the best, and the service life of the pavement could be improved significantly by the material; however, the crack resistance of the stress-absorption layer is not very clear [22]. The abovementioned research shows that the stress absorption-layer is good at crack resistance. However, the analyses of the effects of the stress-absorption layer on the crack propagation process and the propagation trend of different crack types were not enough. It is important to study the influence of anti-crack additives, different crack modes, and test configurations on the crack propagation process and the propagation trend. Much research has been done on this. The mixed mode I/III fracture toughness of asphalt concrete materials was determined using the Edge Notched Disc Bend specimen [23]. Mixed mode I/II fracture toughness of five modified asphalt mixtures containing poly phosphoric acid (PPA), Styrene Butadiene Styrene (SBS), anti-stripping agent, crumb rubber (CR), and F-T paraffin wax (Sasobit), and an unmodified one (with no additive), were investigated experimentally using a large number of cracked semi-circular bend (SCB) specimens [24]. Two circular shape test specimens were designed and examined for the experimental determination of mode I fracture toughness in different modified hot mix asphalt materials [25]. The effects of carbon nanotubes as a binder modifier on the fatigue and fracture performance of asphalt mixtures were investigated [26]. Asphalt characteristic effects on its mixed mode I/II low temperature fracture toughness have also been investigated experimentally [27].

One study showed that for top-down cracking when the pavement was under repeated loading, shear damage occurred first in the asphalt layer, and then the damage extended horizontally, resulting in a shear-damaged layer. The damaged layer then led to a higher tensile strain in the upper

mixture, which caused tension cracks, that finally propagated upwards to the pavement surface [28]. In this study, laboratory investigations of the anti-crack performance of the high viscous asphalt sand stress absorption layer (HVASAL) and the RASAL, and the propagation mechanism of different types of cracks, were carried out by force-controlled fatigue crack propagation tests, for which three types of overlay structure with three types of pre-crack were designed. The tests were conducted at room temperature and at the same loading rate, with the cyclic loading applied at the middle of the specimen. The three types of pre-crack were the middle crack, the side crack, and the 45° inclined crack. The fatigue crack propagation, fatigue life, crack propagation rate, and crack propagation mechanism of the three types of overlay structure were compared and analyzed. The crack propagation process of the three types of overlay with the same type of crack, and the three types of crack with the same type of overlay, were compared and analyzed as well. Considering the dispersion of the data of the crack propagations, a random probability model ( $p - \frac{da}{dN} - \Delta K$  model) based on the reliability theory was established to describe the propagation of the fatigue cracks. Using the least-square method, the relationships between the crack length  $a$  and the fatigue number  $N$  of the three types of crack were obtained by fitting the polynomials. The crack growth rates during the stable growth period of the three structures, and then the anti-crack performance of the structures, were compared. The curves of the three types of crack were analyzed. The variations of the intercept  $\lg C$  and the slope  $n$  with the reliability  $p$  were discussed.

## 2. Materials and Methods

The size of the composite structure specimen was  $300 \times 90 \times 100 \text{ mm}^3$ . The concrete composite had two or three layers: The No SAL type had a 50 mm AC-13 (a type of asphalt concrete) surface (layer I), and a 50 mm cement concrete layer (layer II); the HVASAL type had a 30 mm AC-13 surface (layer I), a 20 mm HVASAL (layer II), and a 50 mm cement concrete layer (layer III); the RASAL type had a 30 mm AC-13 surface (layer I), a 20 mm RASAL (layer II), and a 50 mm cement concrete layer (layer III). Three types of penetrating crack were designed (i.e., the middle crack, the side crack, and the 45° inclined crack), and the width of the cracks was 5 mm [29], as shown in Figures 1 and 2.

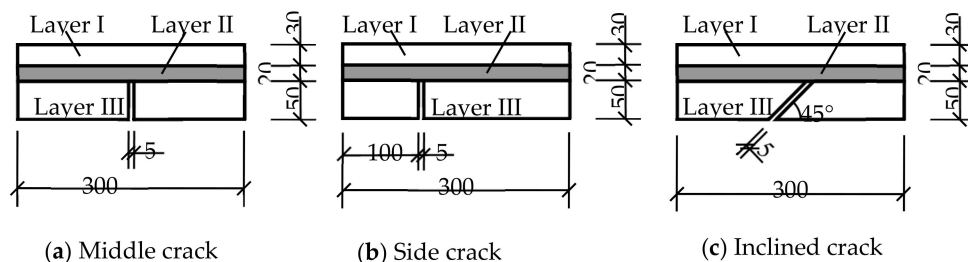


Figure 1. Specimens of three types of crack with a stress-absorption layer (in mm).

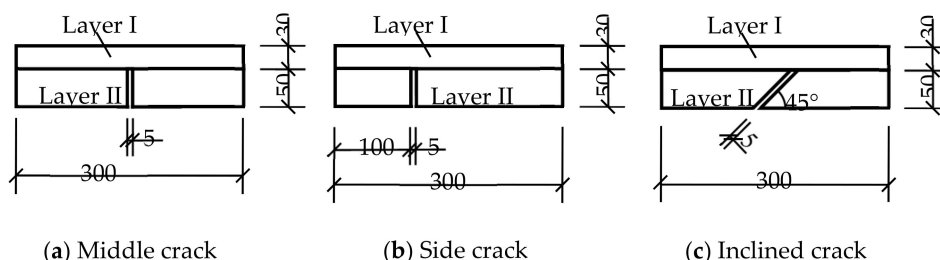


Figure 2. Specimens of three types of crack without a stress-absorption layer (in mm).

A 70# asphalt (marking in accordance with the Chinese standard of the Technical Specifications for Construction of Highway Asphalt Pavements (JTG F40—2017) with a penetration of 70 was used as the asphalt binder for preparation of the specimens, and its specifications provided by the manufacturer are listed in Table 1. Limestone was used as the aggregate. The ratio of binder to aggregate was 8.1%

by weight. The continuous aggregate gradation, having the nominal maximum size of 9.5 mm, is listed in Table 2. An additional 1% activated rubber crumb and 0.7% TCA additive (percentage of the mass of asphalt mixture) was added during the blending process.

**Table 1.** Properties of asphalt.

Properties	Standard	Value
Penetration (25 °C, 100 g, 5 s)	T0604—2011	70 (0.1 mm)
Softening point	T0606—2011	47 (°C)
Viscosity (177 °C)	T0625—2011	3.8 (Pa·s)
Elastic recovery (25 °C)	T0662—2011	72 (%)

**Table 2.** Aggregate gradation.

Sieve size (mm)	9.5	4.75	2.36	1.18	0.6	0.3	0.15	0.075
Passing percentage	100	80.4	45.	35.3	22.2	17.3	12.4	7.6

- (1) To set the pre-crack, a board was placed in the test mold, and then the cement concrete was poured into the mold and flattened.
- (2) The mixed asphalt mixture was poured into the cement concrete rutting boards and compaction was performed.
- (3) The composite board was cut into specimens.

The prepared specimens with the middle crack are shown in Figure 3.



**Figure 3.** Molded piece and finished specimen.

To accurately evaluate the crack resistance of HVASAL and RASAL, and investigate the propagation mechanism of the three types of crack, three-point bending failure tests and three-point bending fatigue performance tests were designed. Three-point bending failure tests were conducted to obtain the needed parameters for the three-point bending fatigue tests. Because of the thinness of the structure layer and the stress-absorption layer studied, the force control mode is closer to the actual stress state of the asphalt mixture in the pavement, so it can better explain the fatigue characteristics of the high viscosity asphalt [11]. Hence, the force-controlled loading mode was adopted for the three-point bending fatigue tests. For both the failure and the fatigue tests, the test temperature was set at 15 °C, the loading mode was the intermediate loading, the distance between the two ends was 250 mm, and the pressure head rate of the test machine was 2 mm/min, as shown in Figure 4. The ultimate load of the specimen was obtained by the three-point bending failure test. Forty percent of the ultimate load was used as the load for the three-point bending fatigue test.



Figure 4. Test machine with formed specimen.

### 3. Results

#### 3.1. Test Results and Data Processing

To obtain the ultimate failure load and the load for the fatigue tests of the three types of crack, the failure experiments on the composite specimens without a stress-absorption layer were carried out at 15 °C. In order to reduce the test error, three identical specimens were used in each experiment configuration, and the average of the failure loads for the three specimens was taken as the final value, as listed in Table 3.

Table 3. Ultimate failure loads and fatigue test loads for three types of crack.

Crack Type	Ultimate Failure Load				Fatigue Test Load (kN)
	Test Results (kN)	Average Value (kN)	Coefficient of Variation	Standard Deviation	
Middle Crack	1.721 1.723 1.731	1.725	0.2505%	0.004320	0.690
Side Crack	1.538 1.558 1.554	1.550	0.5818%	0.009019	0.620
Inclined Crack	1.765 1.759 1.771	1.765	0.4033%	0.007118	0.706

The test data was collected using a magnifying glass, the scale was marked across the overlay for easy observation, and the number of cycle loads corresponding to a crack propagation of 5 mm was used as the observation index [30]. The propagation of crack length corresponding to the load cycles was observed and recorded, as listed in Table 4.

Table 4. Fatigue loading times for three types of crack.

Overlay Structure Type	Crack Type					
	Middle Crack		Side Crack		Inclined Crack	
	Initial Crack (mm)	Final Crack (mm)	Initial Crack (mm)	Final Crack (mm)	Initial Crack (mm)	Final Crack (mm)
No SAL	87	365	63	308	102	469
HVASAL	204	653	199	496	290	728
RASAL	283	734	255	579	334	809

### 3.2. Comparative Analysis of Anti-Crack Performance

To further investigate the anti-crack performance of the stress-absorption layers in the HVASAL and RASAL types, the crack propagation process of the three types of overlay with the same type of crack, and three types of crack with the same type of the overlay, were compared and analyzed.

#### 3.2.1. Comparison and Analysis of the Crack Propagation Trends of the Three Types of Overlay with the Same Type of Crack

Two types of crack in the overlay of the specimen with the stress-absorption layer, propagated upwards across layers I and II. The data of the  $a-N$  curves with the stress-absorption overlay was graphed per each layer ( $a$  is the scale value of cracks in the overlay, and  $N$  is the corresponding number of load cycles). The  $a-N$  test curves of layer I and layer II for the three types of overlay with the middle crack are shown in Figure 5.

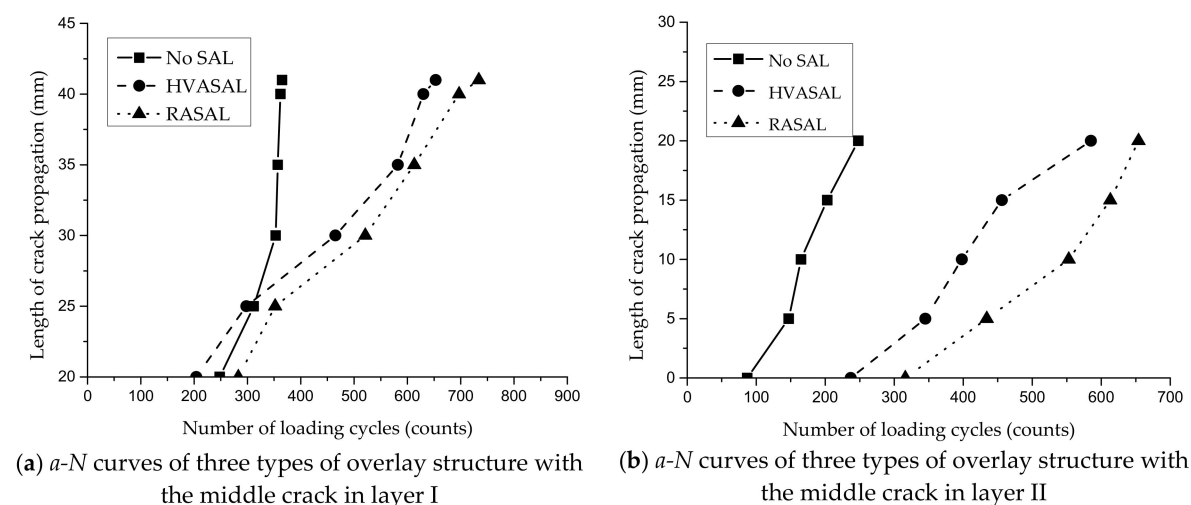
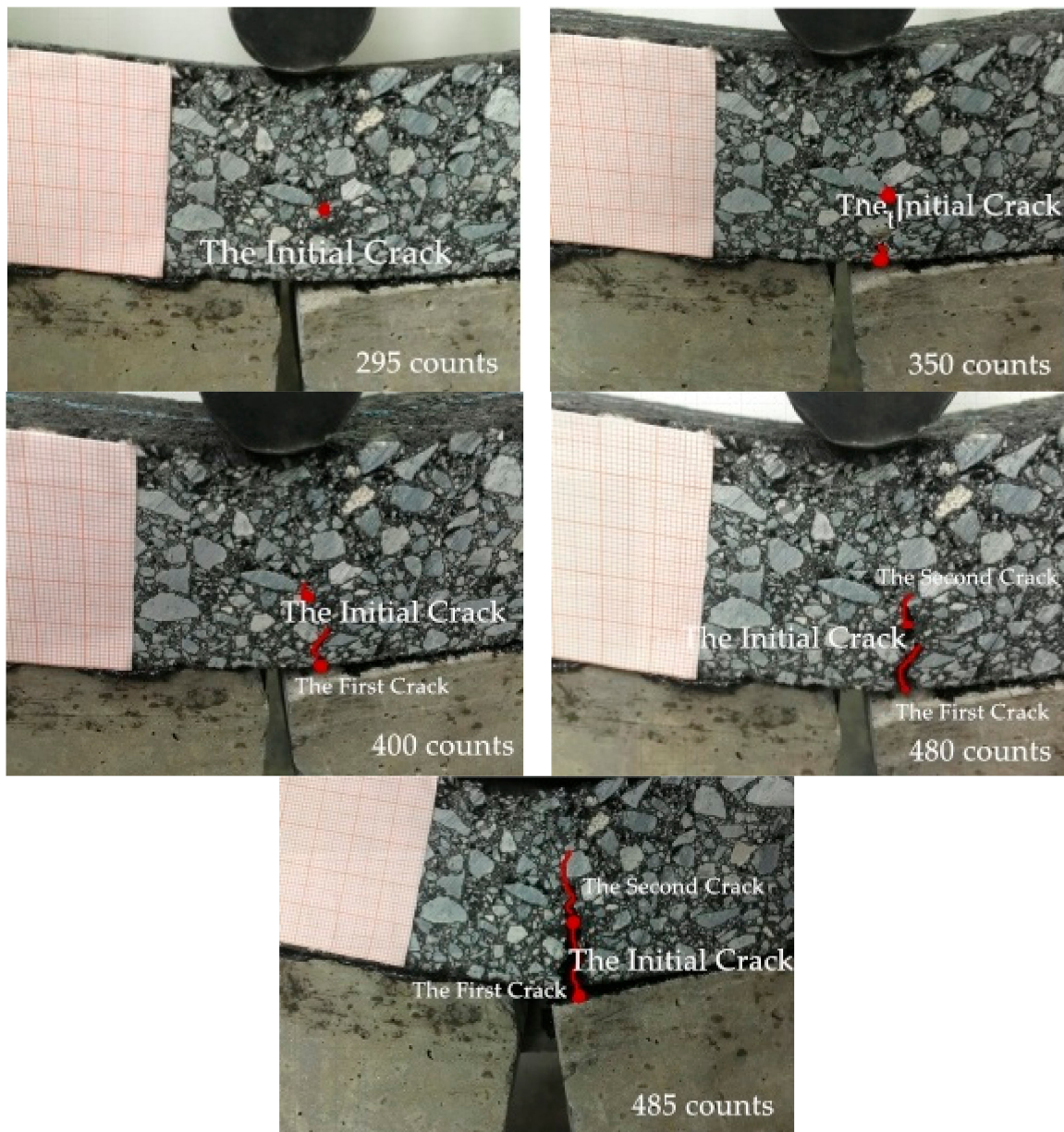


Figure 5.  $a-N$  curves of three types of overlay structure with the middle crack in two layers.

It was observed through the experiment that the initial cracking points for the middle cracks of the HVASAL and RASAL type structures were located at the interface between the stress-absorption layer and the surface layer. The cracks slowly propagated upwards, then some new cracks began to appear at the bottom of the stress-absorption layer, and the two cracks propagated upwards at the same time. The cracks in the two layers met as the length of crack in the stress-absorption layer reached 20 mm. It could be clearly observed that the cracks bypass the aggregate. As an example, the fatigue crack propagation process of the RASAL overlay structure is shown in Figure 6.





**Figure 6.** Fatigue crack propagation of the middle crack of the rubber asphalt stress absorption layer (RASAL) type.

It was observed in the experiment with the No SAL type specimen with the middle crack, that the reflection cracks occurred along the interface of the cement concrete layer, as shown in Figure 7. The test results show that the number of load cycles for the initial-crack of the HVASAL and RASAL types is 2.34 and 3.25 times that of the No SAL type, respectively; and the fatigue life of the HVASAL and RASAL types is 1.79 and 2.01 times that of the No SAL type, respectively. The results show that the stress-absorption layer has the ability to retard the crack propagation, and the anti-crack performance of the RASAL type is better than that of the HVASAL type.



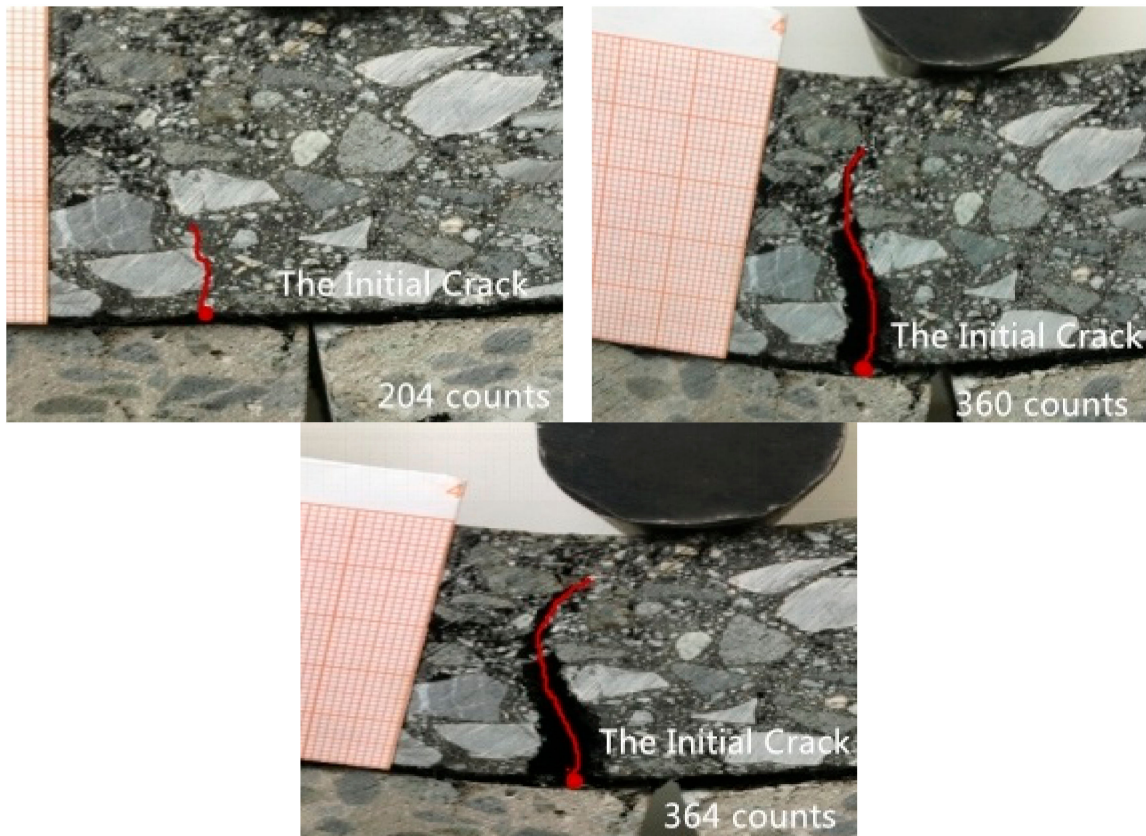


Figure 7. Fatigue crack propagation of the middle crack of the No SAL type.

The  $a-N$  test curves of the three types of overlay structure in layers I and II with side cracks are shown in Figure 8.

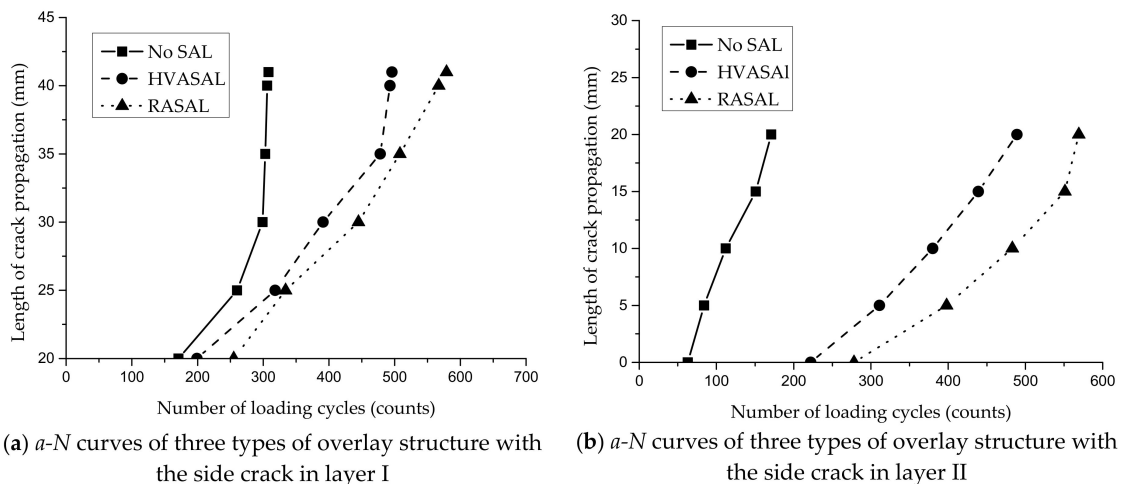
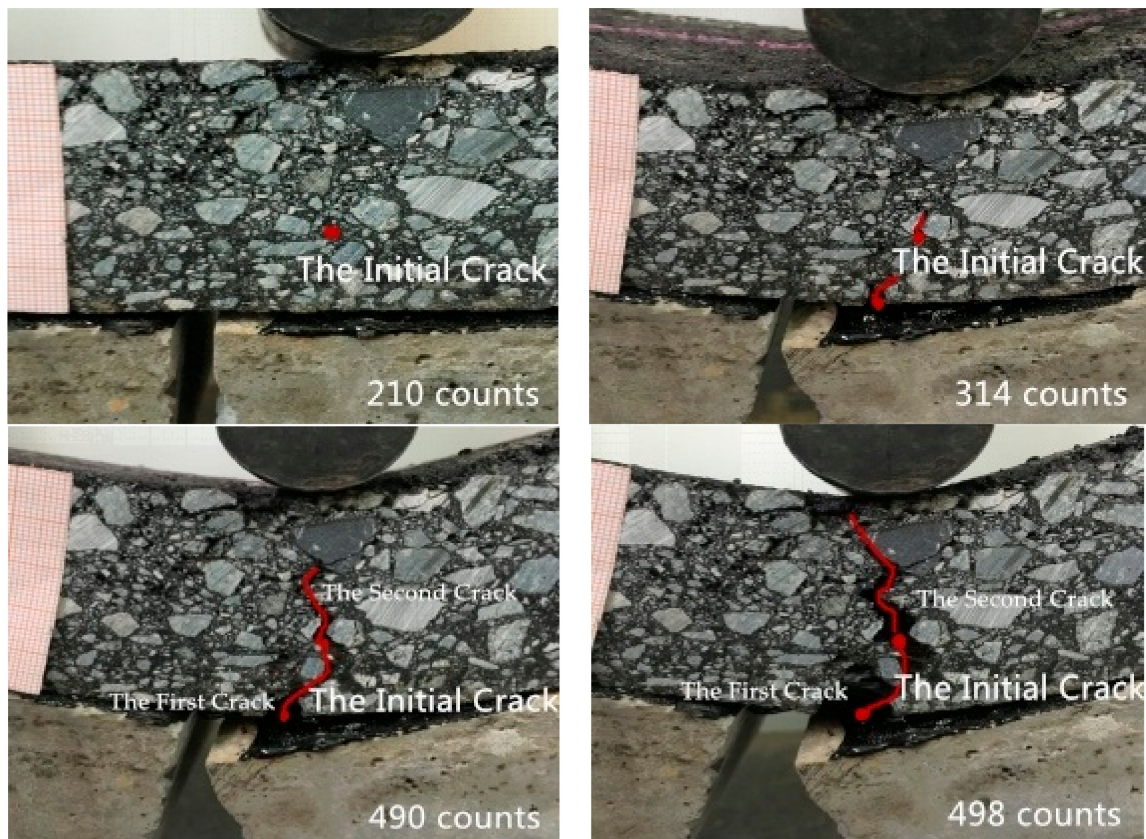


Figure 8.  $a-N$  curves of three types of overlay structure with the side crack in two layers.

It was observed that the experimental phenomena of the HVASAL and RASAL type overlay structures with side cracks were the same as those of the middle crack tests. However, the crack propagation direction was obviously deviated from the pressure head, and the propagation mode was open and shear composite. Furthermore, both mode cracks propagated at the same time, until the whole specimen was penetrated and broken. As an example, the fatigue crack propagation process of the HVASAL type overlay structure is shown in Figure 9.



**Figure 9.** Fatigue crack propagation of the side crack of the high viscous asphalt sand stress absorption layer (HVASAL) type.

It was observed that the initial cracking point of the side cracks of the No SAL type were located at the interface between the concrete layer and the surface layer, the crack propagation direction deviated from the pressure head, and the propagation mode was open and shear composite. Then the specimen produced small cracks at the bottom of the middle span which developed vertically, showing an open mode of crack propagation. The cracks of both modes began propagating at the same time, and the speed of the crack propagation of the former was faster than the latter in the initial stage. The latter propagated rapidly towards the top when the latter was longer than the former, and then the former no longer propagated, until the whole specimen was penetrated by the mid-span crack and broken. The crack propagation processes are shown in Figure 10. The test results show that the number of load cycles for initial-cracking of the HVASAL and RASAL types is 3.15 times and 4.05 times that of the No SAL type, respectively; and the fatigue life of the HVASAL and RASAL types is 1.61 times and 1.87 times that of the No SAL type, respectively. The results show that the stress-absorption layer has the ability to retard the crack propagation, and the anti-crack performance of the RASAL type is better than that of the HVASAL type.



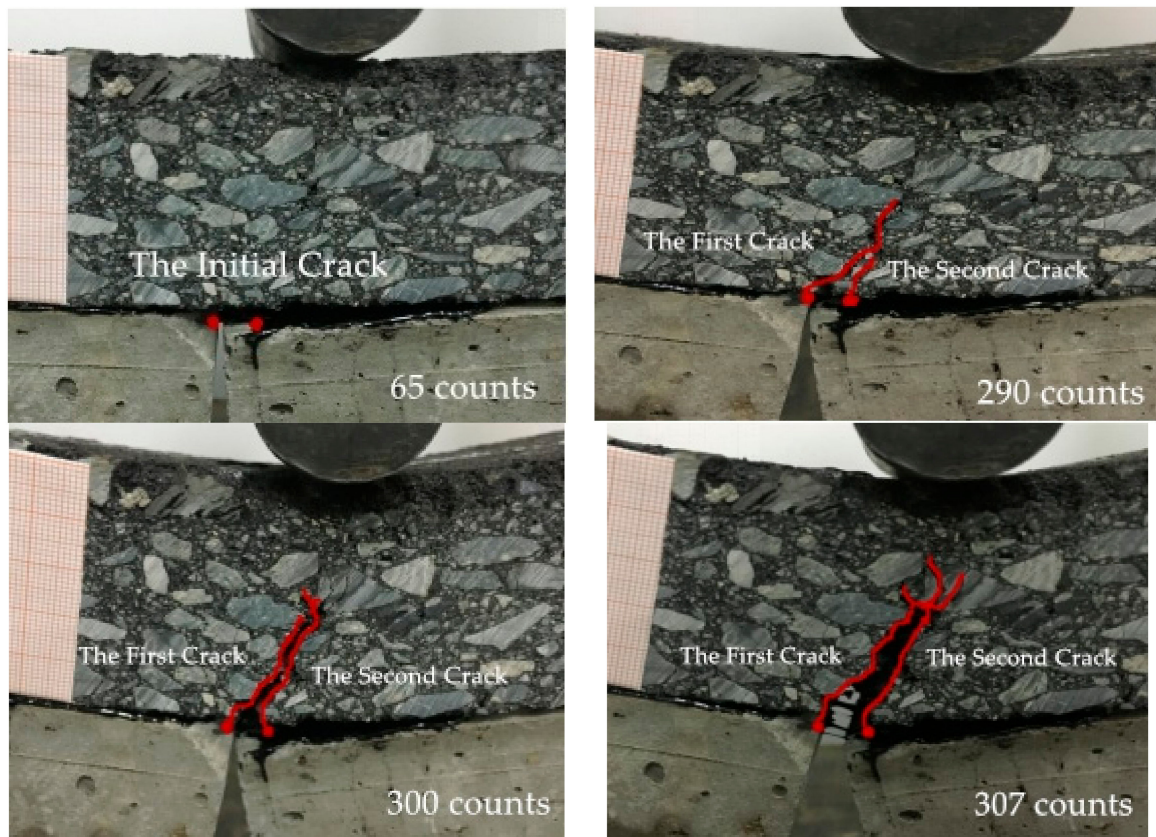


Figure 10. Fatigue crack propagation of the side crack of the No SAL type.

The  $a-N$  test curves of the three types of overlay structure with the inclined crack were compared with that of layers I and II, as shown in Figure 11.

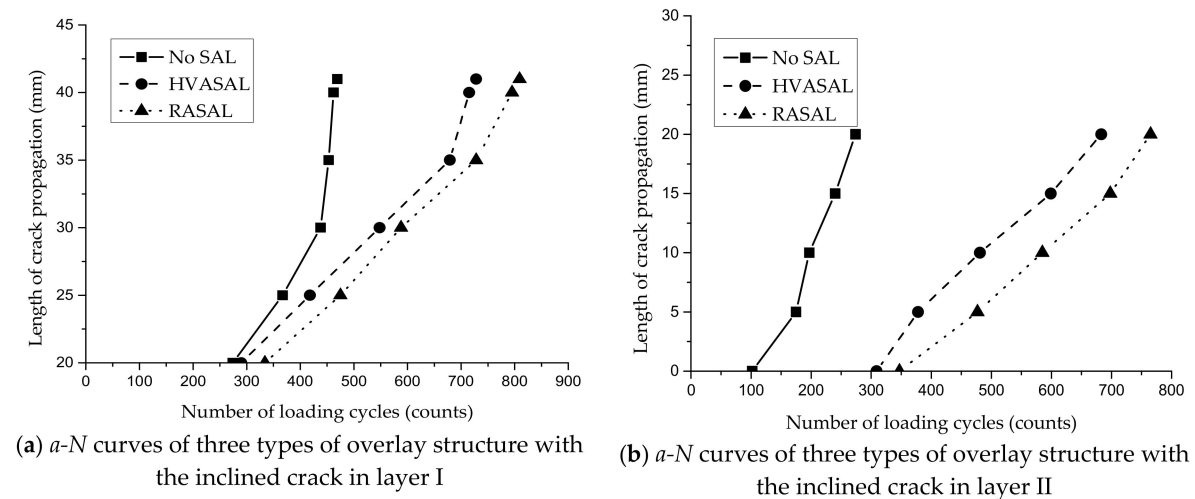


Figure 11.  $a-N$  curves of three types of overlay structure with the inclined crack in two layers.

It was observed in the experiment that the pre-crack point of the inclined cracks of the No SAL type appeared directly under the pressure head. Then, on the upper right of the crack, and in the middle of the specimen, another crack appeared. The two cracks propagated upwards at the same time, they met, and became one crack propagating upwards until the cycles stopped. The pre-crack points of the inclined cracks of the HVASAL and RASAL types were located at the bottom of the surface layer, and there were soon many small cracks at the interface. The small cracks in the stress-absorption

layer grew slowly, and when the cracks of the two layers were connected, the specimen was crushed and the cycles were stopped. The test results show that the number of load cycles for pre-crack of the HVASAL and RASAL types is 2.84 times and 3.27 times that of the No SAL type, respectively; and the fatigue life of the HVASAL and RASAL types is 1.55 times and 1.72 times that of the No SAL type, respectively. This shows that the stress-absorption layer has the ability to retard the crack propagation, and the anti-crack performance of the RASAL type is better than that of the HVASAL type.

The phenomenon of the pre-crack points always being located at the junction of two layers may be due to the difference of the elastic moduli and the poor bonding of the two layers. Therefore, we think that this is of great significance in road engineering. The bonding of the layers should be improved to decrease the rate of crack propagation and enhance the fatigue life of the pavement.

### 3.2.2. Analysis of the Crack Propagation Mechanism of Three Types of Crack with the Same Type of Overlay

The  $a-N$  curves of the crack propagation of the No SAL type structure with the three types of crack in layers I and II are shown in Figure 12.

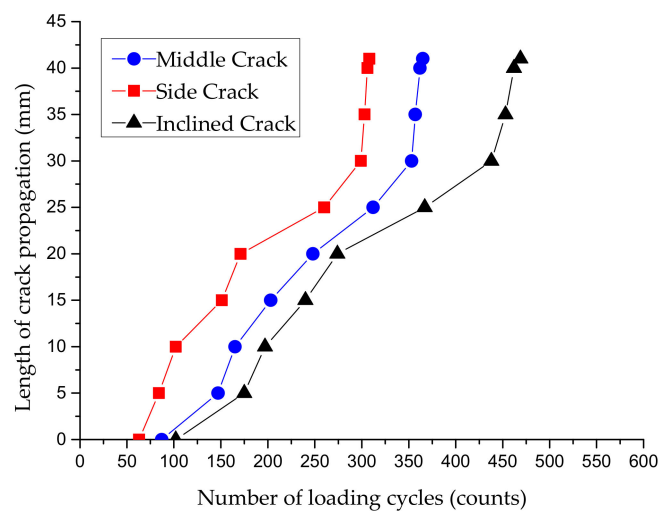


Figure 12.  $a-N$  curves of three types of crack with the No SAL type.

For the No SAL type, the average fatigue numbers of the crack initiation of the middle crack, side crack, and inclined crack are 87 times, 63 times, and 102 times, respectively; and the average fatigue lives are 365 times, 308 times, and 469 times, respectively. The fatigue life of the side crack is shorter than the other two cracks, so the mode of open and shear composite crack caused by the side crack is more prone to fracture than the mode of a single open crack. Although the inclined crack is also the mode of open and shear composite, it has the longest fatigue life, and this can be attributed to the effect of partial healing of the cracks, and the propagation of the crack in the loading process is prevented.

The  $a-N$  curves of the crack propagation of the HVASAL type with the three types of crack in layers I and II are shown in Figure 13.

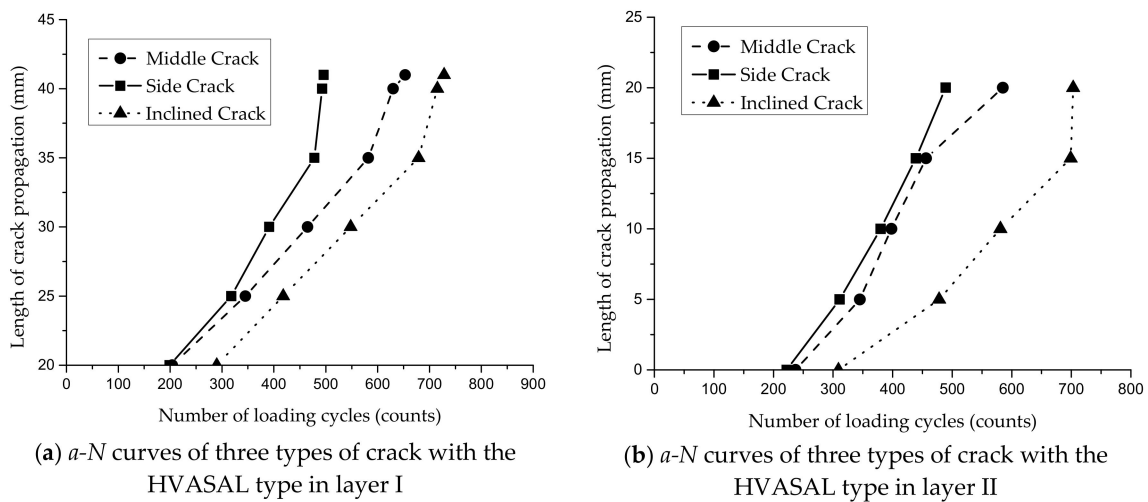


Figure 13. *a-N* curves of three types of crack with the HVASAL type in two layers.

For the HVASAL type, in layer I, the average fatigue numbers of the crack initiation of the middle crack, side crack, and inclined crack are 204 times, 199 times, and 290 times, respectively; in layer II, the average fatigue numbers of crack initiation of the three types of crack are 237 times, 222 times, and 309 times, respectively; and the average fatigue lives are 653 times, 496 times, and 728 times, respectively. Compared with the No SAL type, the stress-absorption layer can absorb and disperse the stress, and increase the stress distribution area, so it greatly improves the anti-crack ability of the asphalt pavement surface under the fatigue load cycles.

The *a-N* curves of the crack propagation of three types of crack in layers I and II of the RASAL type are shown in Figure 14.

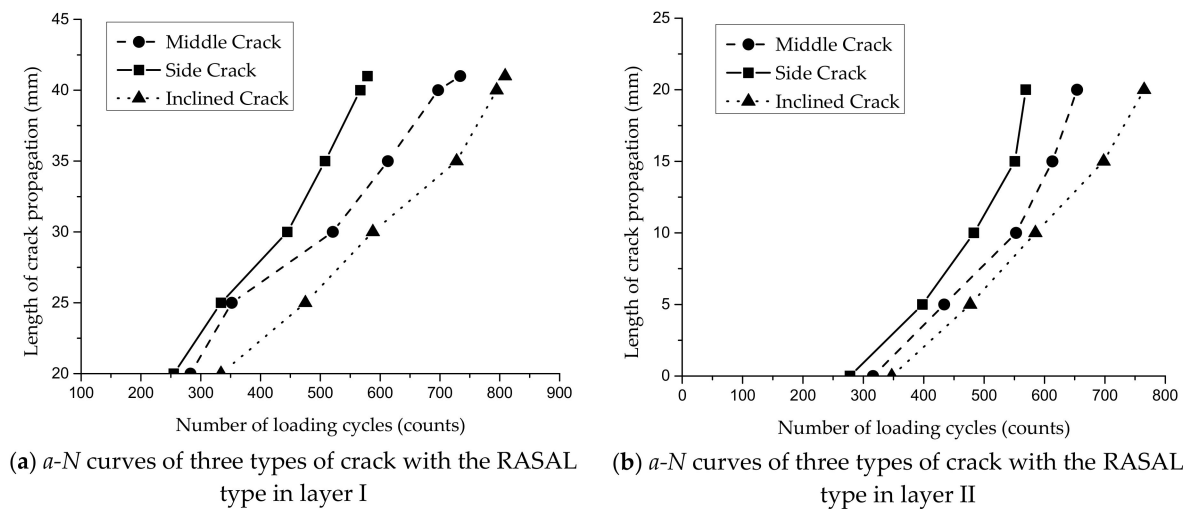


Figure 14. *a-N* curves of three types of crack with the RASAL type in two layers.

For the RASAL type, in layer I, the average fatigue numbers of the crack initiation of the middle crack, side crack, and inclined crack are 283 times, 255 times, and 334 times, respectively; in layer II, the average fatigue numbers are 316 times, 278 times, and 347 times, respectively; and the average fatigue life is 734 times, 509 times, and 809 times, respectively. What the three types of crack have in common is that the pre-crack points appear in layer I, and then cracks appear in layer II. The effect of cracks on the fatigue life of the RASAL type has the same trend as the No SAL and HVASAL types, but the RASAL type has a better anti-crack performance. It can be seen from the *a-N* curves of the three materials in Figures 12–14 that different types of cracks (the middle crack, side crack,

and inclined crack) in the cement concrete base have different effects on the fatigue properties of the overlay. As shown in Figures 12–14, the inclined crack has the maximum fatigue life, the side crack has the minimum life, and the middle crack has an in-between life.

### 3.3. Analysis of Fatigue Fracture of Different Cracks Based on Reliability

Due to the effects of material properties, loading process, environmental factors, and crack propagation behaviors, the lives of the same specimens are uncertain. Take into account the effects and the dispersion of the fatigue crack propagation of different types of cracks; the  $p - \frac{da}{dN} - \Delta K$  probability model to describe the fatigue crack propagation was established based on the original Paris formula [31,32] in this paper. The probability model can quantitatively relate the fatigue crack propagation rate and the impact of the types of crack to  $\Delta K$ , and the change rules of parameters  $C$  and  $n$ .

Taking the logarithm on both sides of the Paris formula, we have

$$\lg\left(\frac{da}{dN}\right) = \lg C + n \lg(\Delta K) \tag{1}$$

The relation based on reliability  $p$  can be expressed as

$$\lg\left(\frac{da}{dN}\right)_p = \lg C_p + n_p \lg(\Delta K) \tag{2}$$

The distribution of fatigue crack propagation rate under the same stress intensity factor  $\Delta K$  is logarithmic normal; that is,  $\lg\left(\frac{da}{dN}\right) \sim N(\mu, \sigma^2)$ , and is defined as

$$\lg\left(\frac{da}{dN}\right)_p = \mu + \mu_p \sigma \tag{3}$$

$$p = \Phi(\mu_p) = \int_{-\infty}^{\mu_p} \frac{1}{\sqrt{2\pi}} e^{-\frac{\mu^2}{2}} d\mu \tag{4}$$

where  $\mu_p$  is the standard normal deviation and can be found in the standard normal distribution table. In this paper, five reliability values were used as examples to study the variation of the parameters of the probability model for different fracture types. The test results are listed in Tables 5–7.

$da/dN$  is determined by the method of increasing polynomial data from the  $a-N$  data measured in the experiment, and the approximate formula for calculating the range of the stress intensity factor  $\Delta K$  is as follows:

$$\Delta K = \frac{\Delta P}{B\sqrt{W}} \cdot \frac{2 + \frac{a}{W}}{\left(1 - \frac{a}{W}\right)^{\frac{3}{2}}} \left[ 0.886 + 4.64 \frac{a}{W} - 13.32 \left(\frac{a}{W}\right)^2 + 14.72 \left(\frac{a}{W}\right)^3 - 5.6 \left(\frac{a}{W}\right)^4 \right] \dots \tag{5}$$

where  $a$  is the length of the crack,  $B$  is the width of the specimen, and  $W$  is the width of the crack.

**Table 5.**  $\lg\left(\frac{da}{dN}\right)_p$  in No SAL type with different crack types.

Crack Type	$\Delta K$	$\lg\left(\frac{da}{dN}\right)_{50}$	$\lg\left(\frac{da}{dN}\right)_{90}$	$\lg\left(\frac{da}{dN}\right)_{95}$	$\lg\left(\frac{da}{dN}\right)_{99}$	$\lg\left(\frac{da}{dN}\right)_{99.9}$
Middle crack	1.218	0.0646	0.0706	0.0812	0.0902	0.1009
	1.345	0.0854	0.0996	0.1094	0.3029	0.514
	1.499	0.1327	0.2969	0.363	0.5183	0.8412
	1.588	0.1951	0.4167	0.515	0.7683	1.2085
Side crack	1.172	0.0571	0.0697	0.0738	0.082	0.0924
	1.299	0.0758	0.088	0.0918	0.0993	0.1086
	1.454	0.1419	0.1584	0.1639	0.1747	0.1823
	1.651	0.2502	0.2674	0.2724	0.2822	0.2936
Inclined crack	1.228	0.0535	0.0633	0.0664	0.0725	0.0802
	1.355	0.0716	0.0914	0.0978	0.1113	0.1287
	1.509	0.1092	0.1261	0.1337	0.1459	0.1547
	1.706	0.1519	0.1712	0.177	0.1884	0.2023

**Table 6.**  $\lg\left(\frac{da}{dN}\right)_p$  in HVSAL type with different fracture types.

Crack Type	$\Delta K$	$\lg\left(\frac{da}{dN}\right)_{50}$	$\lg\left(\frac{da}{dN}\right)_{90}$	$\lg\left(\frac{da}{dN}\right)_{95}$	$\lg\left(\frac{da}{dN}\right)_{99}$	$\lg\left(\frac{da}{dN}\right)_{99.9}$
Middle crack	0.046	0.0613	0.0765	0.0852	0.1042	0.0468
	0.053	0.0743	0.0835	0.1024	0.1165	0.0531
	0.077	0.0956	0.0993	0.113	0.1279	0.0776
	0.105	0.1227	0.1247	0.1287	0.1334	0.1056
Side crack	1.172	0.0267	0.0298	0.0307	0.0326	0.0348
	1.299	0.0375	0.0462	0.049	0.0548	0.0621
	1.454	0.0666	0.0821	0.0978	0.1247	0.146
	1.651	0.0919	0.1224	0.1317	0.1542	0.1829
Inclined crack	1.228	0.0231	0.0288	0.0306	0.0344	0.0393
	1.355	0.0494	0.058	0.0607	0.0661	0.0729
	1.509	0.0616	0.0806	0.0869	0.1001	0.1175
	1.706	0.1019	0.1112	0.1277	0.1384	0.1623

**Table 7.**  $\lg\left(\frac{da}{dN}\right)_p$  in RASAL type with different fracture types.

Crack Type	$\Delta K$	$\lg\left(\frac{da}{dN}\right)_{50}$	$\lg\left(\frac{da}{dN}\right)_{90}$	$\lg\left(\frac{da}{dN}\right)_{95}$	$\lg\left(\frac{da}{dN}\right)_{99}$	$\lg\left(\frac{da}{dN}\right)_{99.9}$
Middle crack	1.218	0.0296	0.0326	0.0335	0.0352	0.0373
	1.345	0.0329	0.0374	0.0388	0.0416	0.045
	1.499	0.0545	0.06	0.0617	0.065	0.0689
	1.588	0.0719	0.0912	0.0977	0.104	0.1123
Side crack	1.172	0.0283	0.0318	0.0329	0.0349	0.0375
	1.299	0.0396	0.0433	0.0544	0.0565	0.0591
	1.454	0.0531	0.0568	0.0578	0.0599	0.0624
	1.651	0.0722	0.0752	0.0784	0.0822	0.0864
Inclined crack	1.228	0.0274	0.0333	0.0352	0.039	0.0439
	1.355	0.0517	0.0574	0.0591	0.0625	0.0666
	1.509	0.0676	0.0785	0.0819	0.0886	0.0969
	1.706	0.0949	0.1099	0.1144	0.1225	0.1289

### 3.3.1. Analysis of the Reliability of Fracture Propagation Rate under the Same Fracture

The relationships between  $\lg\left(\frac{da}{dN}\right)$  and  $\lg\Delta K$  for the three types of structures of different cracks on the basis of different reliability values were obtained by linear regressions using Origin software. The fitting results are shown in Figures 15–17.

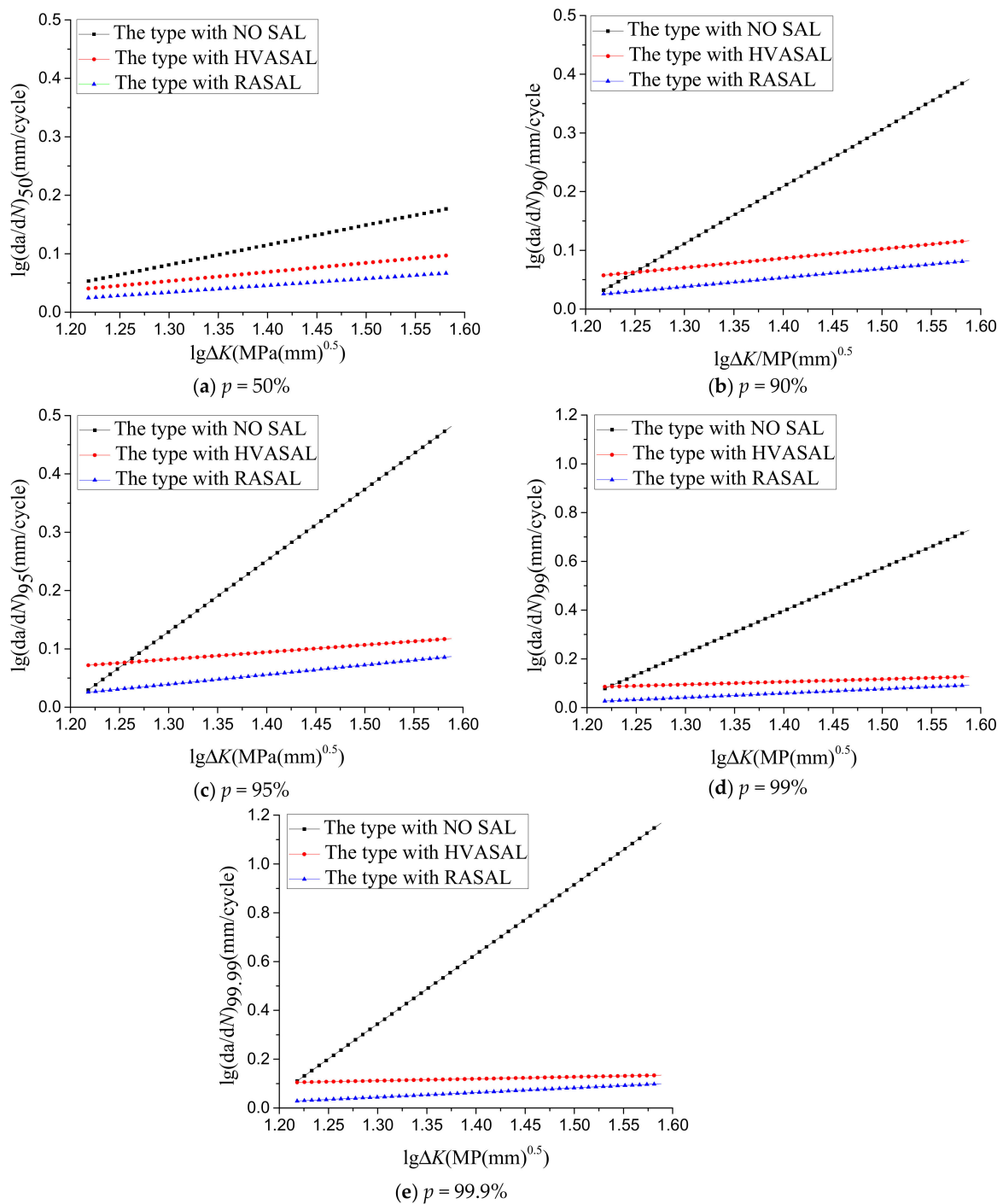


**Figure 15.** Fitting results of three types of structure with different reliability values of the middle crack.



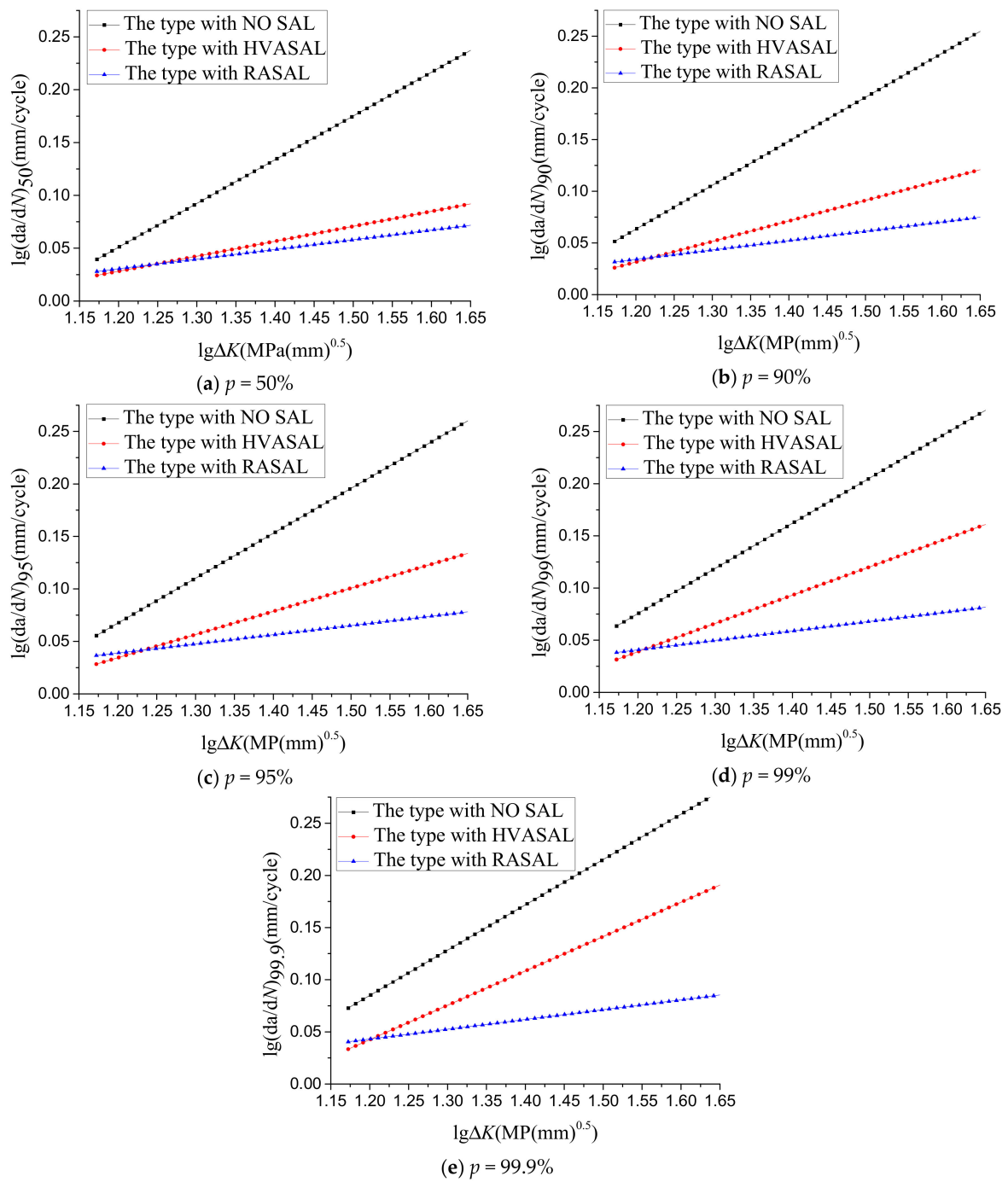
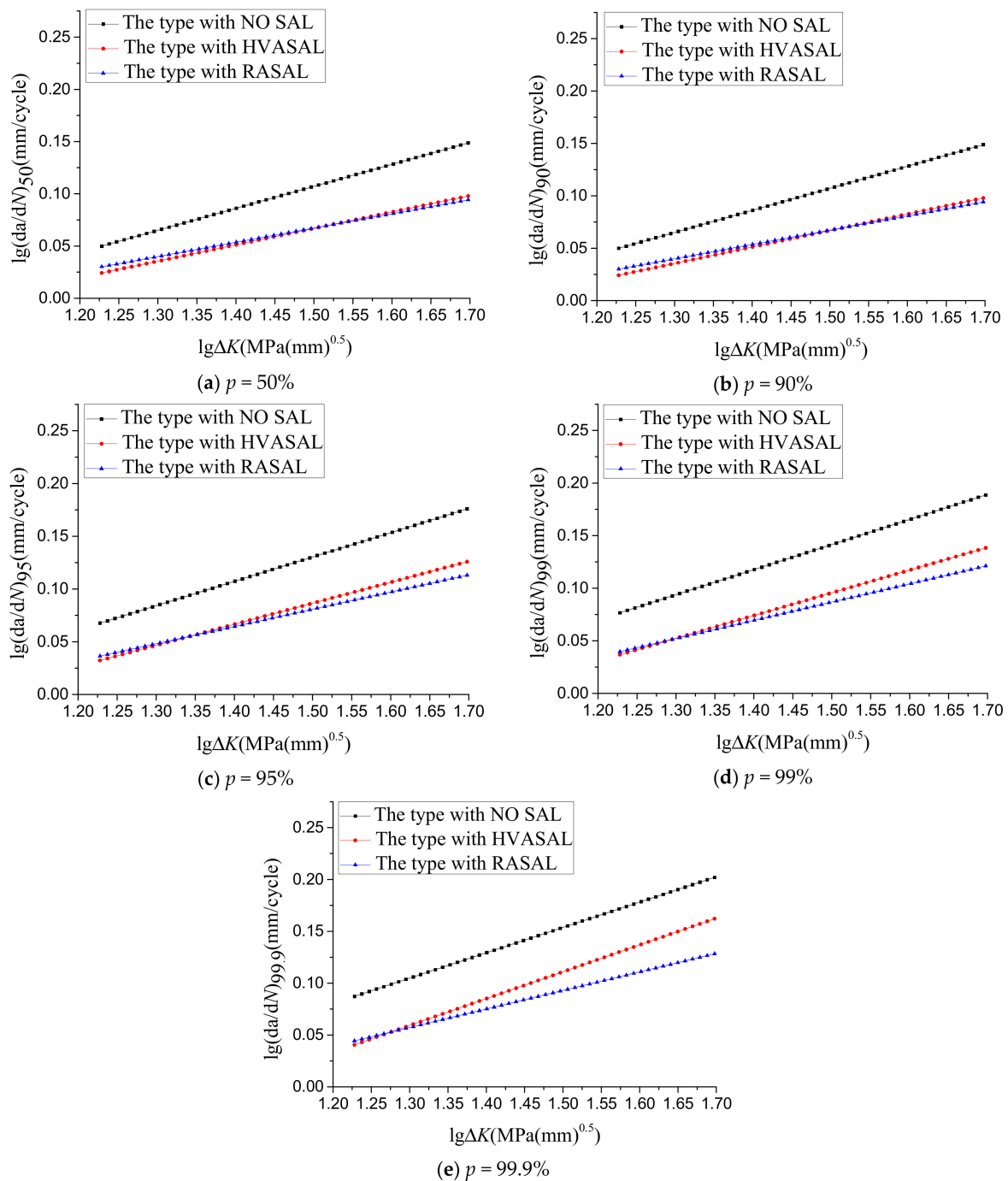


Figure 16. Fitting results of three types of structure with different reliability values of the side crack.



**Figure 17.** Fitting results of three types of structure with different reliability values of the inclined crack.

As shown in the figures, the parameter  $n$  always has the biggest value in the No SAL type with different reliability values. The greater the slope is, the faster the crack propagation, the poorer the crack resistance performance, and the shorter the fatigue life. Therefore, the rate of crack propagation can be effectively reduced with a stress-absorption layer, and the life of pavement can be effectively extended.

### 3.3.2. Analysis of the Reliability of Different Crack Growth Rates under the Same Structure

The results that the  $da/dN$ - $\Delta K$  functions are linear on a double-logarithmic plot were obtained by fitting the data in Tables 5–7. The fitted model and the test data were compared, and the correlation coefficient ( $R^2$ ) was greater than 0.8, which indicates that  $da/dN$ - $\Delta K$  functions are linear on a double-logarithmic plot, as shown in Figures 18–20.

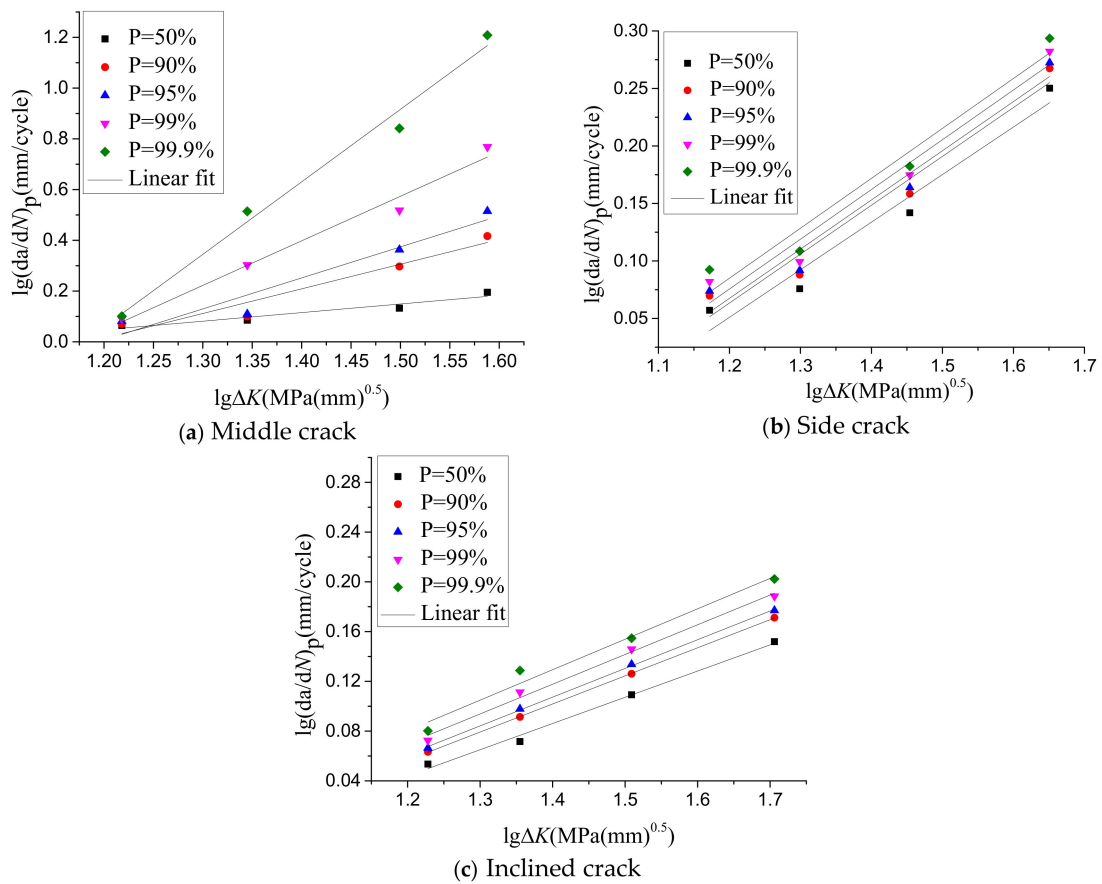


**Figure 18.** Comparison of the fitting results and test results of three types of fracture of the No SAL type structure with different reliability values.

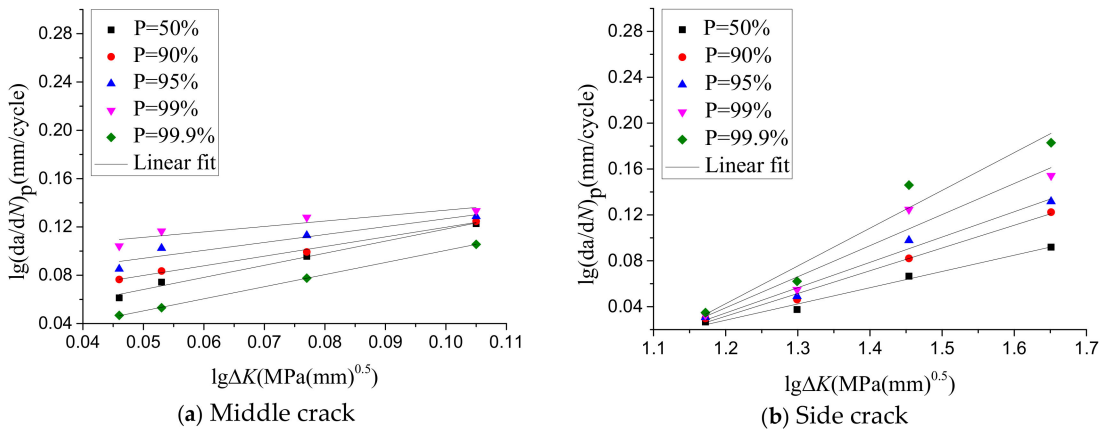


**Figure 19.** Cont.

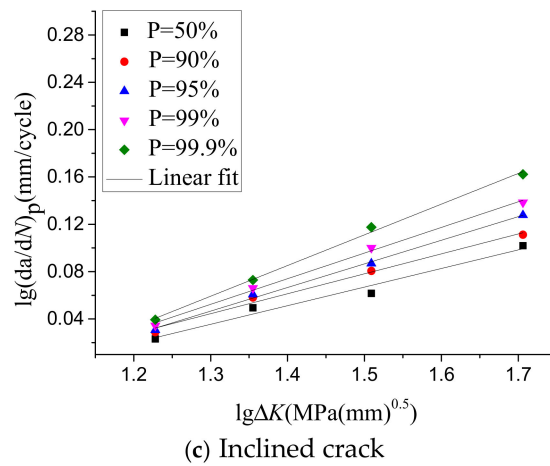


**Figure 19.** Comparison of the fitting results and test results of three types of fracture of the HVASAL type structure with different reliability values.

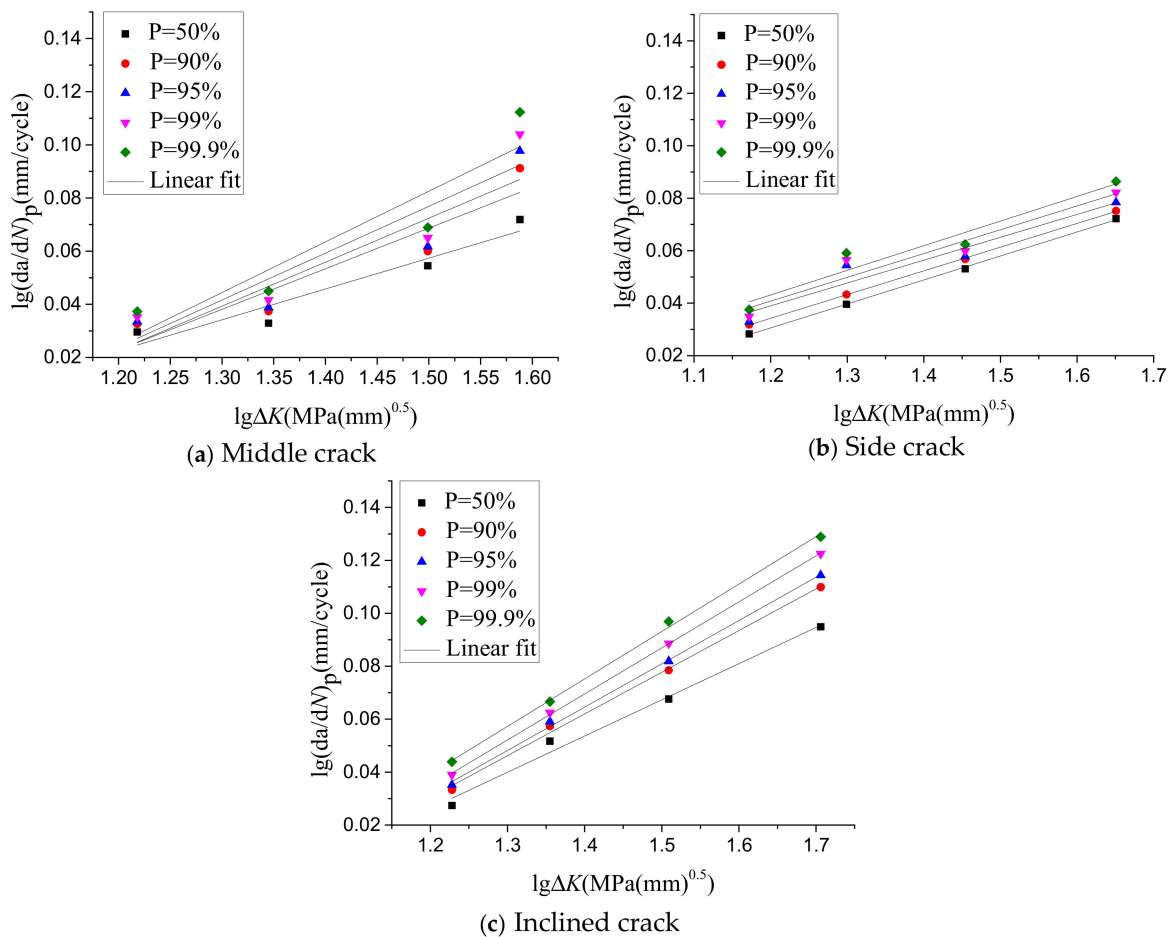


**Figure 20.** Comparison of the fitting results and test results of three types of fracture of the RASAL type structure with different reliability values.

#### 4. Discussion and Conclusions

(1) Fatigue crack propagation experiments with the cyclic loadings acting in the middle of the specimens were carried out for three types of the old cement concrete asphalt overlay. The results show that for the fatigue numbers of the pre-crack of the three types of crack, the HVASAL type is 2.34 times, 3.15 times, and 2.84 times than that of the No SAL type; and the RASAL type is 3.25 times, 4.05 times,

and 3.27 times that of the No SAL type. The results show that for the final fatigue lives of the three types of crack, the HVASAL type is 1.79 times, 1.61 times, and 1.55 times that of the No SAL type; and the RASAL type is 2.01 times, 1.87 times, and 1.72 times that of the No SAL type. After the stress-absorption layers were added, the fatigue lives of the structures increased significantly. The anti-crack performance of the RASAL is better than that of the HVASAL.

(2) The propagation processes, and the directions of the overlay cracks of the composite specimens, were analyzed and recorded. It was found that the cracks in the stress-absorption layer always initiated from the interface of layers I and II, then once there was a crack in the stress-absorption layer, the two cracks expanded at the same time. The crack propagation direction of the No SAL type structure was the same as the structure with a stress-absorption layer, but the crack expansion area was relatively concentrated. This demonstrated that the stress absorption layer could disperse the concentrated stress and reduce the peak stress caused by cracks in cement concrete, hence the reflection cracks were delayed.

(3) The three types of structure and three types of crack (the middle crack, the side crack, and the inclined crack) have different effects on the fatigue properties of the asphalt overlay on the cement concrete basement. The inclined crack has the maximum fatigue life, the side crack has the minimum life, and the middle crack has an in-between life.

(4) These three test configurations provide three different mixed mode behaviors of cracks. As middle cracks occurred, there were two initial cracking points in the structure with the stress-absorption layer, with one located at the interface between the stress-absorption layer and the surface layer, and the other located at the bottom of the stress-absorption layer; subsequently, the stress-absorption layer and asphalt overlay would fracture. When there is no stress-absorption layer, the crack occurred along the interface of the cement concrete layer, passing through the overlay to all the specimens; the crack propagated in the direction of a certain lateral deviation and then had a straight upward expansion. For the side crack, the mechanism of the initial cracking points in the structure with stress-absorption layer were the same as that of the middle crack; one propagated vertically upward in mode I, the other propagated to the span center at a 45° angle in a mixed mode I and II. When there is no stress-absorption layer, the initiation of the crack was the same as that of the middle crack; that is, it propagated to the span center in a mixed mode I and II, extended directly below the pressure head, and then the specimen was destroyed. For the inclined crack, the mechanism of the crack propagation with the stress-absorption layer is the same as the former two types. When there is no stress-absorption layer, the crack occurred at the bottom of the asphalt overlay, and then some cracks appeared in the middle of the specimen due to the loading at the right of the crack, and propagated to the pressure head until the specimen failed. The mechanism of crack initiation is the same; however, the propagation direction and mode are different due to the relative loading position and the type of cracks.

(5) The probability model quantifies the relationship between the crack propagation rate and  $\Delta K$ . Two important parameters  $C$  and  $n$ , in Paris formula based on reliability, are consistent with the variation of the crack type in crack propagation. The effects of the three types of crack on the fatigue properties of the asphalt overlay are different. The reliability values of fatigue fracture by different crack types can be studied further to improve existing reliability theories, while solving practical problems.

(6) The  $p$ - $da/dN$  probabilistic model can be used to study the effects of different cracks on  $C$  and  $n$ . Two important parameters of the Paris formula and the variation of crack type in crack propagation were obtained. Under different reliability, the parameter  $n$  is the largest in the No SAL type. The larger the slope is, the faster the crack growth, the worse the crack resistance, and the shorter the fatigue life. Therefore, the structure with the stress-absorption layer can effectively reduce the crack propagation rate, and effectively extend the service life of pavement.

(7) Asphalt mixture has an obvious brittle or quasi-brittle behavior at low temperature, so the fatigue crack propagation can be analyzed based on fracture mechanics. The critical fatigue crack

propagation of the specimen with the middle crack occurs at the center of the bottom of the specimen, and the critical fatigue crack propagation of the specimens with the side crack and inclined crack occurs in the direction of maximum circumferential normal stress. There exist three stages of fatigue crack propagation (i.e., the crack initiation stage, the stable crack propagation stage, and the unstable fracture stage) in brittle or quasi-brittle materials, like the asphalt mixture at low temperature. After the cracking initiation, the toughness of the material increases with a stable crack growth until the unstable fracture happens. The increase of the toughness of material during the stable crack propagation is due to the cohesive force on the fictitious crack zone. The initial cracking point and the critical fracture point can be distinguished from a complete process of crack propagation, which can be described by the double-K criterion.

**Author Contributions:** Conceptualization, Y.S. and T.Y.; Methodology, Y.S.; Software, J.W.; Validation, T.Y., C.W., and X.S.; Formal analysis, C.W.; Investigation, T.Y.; Resources, Y.S.; Data curation, X.S.; Writing—review and editing, T.Y. and C.W.; Supervision, X.Y. and Y.S.

**Funding:** This research was funded by the National Natural Science Fund (51478276) and the Natural Science Foundation of Liaoning Province (20170540770).

**Acknowledgments:** This research was performed at the Shenyang Jianzhu University and the Institute of Transportation Engineering of Zhejiang University.

**Conflicts of Interest:** The authors declare no conflict of interest.

## References

1. Ozer, H.; Al-Qadi, I.L.; Wang, H.; Leng, Z. Characterisation of interface bonding between hot-mix asphalt overlay and concrete pavements: Modelling and in-situ response to accelerated loading. *Int. J. Pavement Eng.* **2012**, *13*, 181–196. [CrossRef]
2. Ge, Z.S.; Wang, H.; Zhang, Q.S.; Xiong, C.L. Glass fiber reinforced asphalt membrane for interlayer bonding between asphalt overlay and concrete pavement. *Constr. Build. Mater.* **2015**, *101*, 918–925. [CrossRef]
3. Zang, Z.-S.; Cai, Y.-X. Treatment Method and Evaluation of Interlayer Interface of Concrete Pavement Based on Rubber Asphalt Stress Absorption Layer. *Highway* **2017**, *4*, 9–11.
4. Li, J.-B.; Gao, X.; Fu, X.-A.; Wu, C.-L.; Lin, G. A Nonlinear Crack Model for Concrete Structure Based on Extended Scaled Boundary Finite Element Method. *Appl. Sci.* **2018**, *8*, 1067. [CrossRef]
5. Baek, J.; Ozer, H.; Wang, H.; Al-Qadi, I.L. Effects of interface conditions on reflective cracking development in hot-mix asphalt overlays. *Road Mater. Pavement Des.* **2010**, *11*, 307–334. [CrossRef]
6. Dempsey, B.J. Development and Performance of Interlayer Stress-Absorbing Composite in Asphalt Concrete Overlays. *Transp. Res. Rec.* **2002**, *1809*, 175–183. [CrossRef]
7. Wang, H.; Wu, Y.F.; Ye, S. Analysis of the Mode of Crushing and Stability in Old Cement Pavement during Asphalt Overlay Project. *Appl. Mech. Mater.* **2012**, *204–208*, 1941–1944. [CrossRef]
8. Robertson, D. Numerical Simulations of Crushable Aggregates. Ph.D. Thesis, University of Cambridge, Cambridge, UK, 2000.
9. Wang, H. A Comparative Study of Fatigue Performance to Resist Reflective Cracking among three Different Stress-Absorbing Materials. *Appl. Mech. Mater.* **2013**, *303–306*, 2625–2635. [CrossRef]
10. Ogundipe, O.M.; Thom, N.H.; Collop, A.C. Evaluation of performance of stress-absorbing membrane interlayer (SAMI) using accelerated pavement testing. *Int. J. Pavement Eng.* **2013**, *14*, 569–578. [CrossRef]
11. Moreno-Navarro, F.; Sol-Sánchez, M.; Rubio-Gámez, M.C. Reuse of deconstructed tires as anti-reflective cracking mat systems in asphalt pavements. *Constr. Build. Mater.* **2014**, *53*, 182–189. [CrossRef]
12. Mao, C. Study on Formation Mechanism and Expansion Behavior of Crack in Asphalt Pavement. Ph.D. Thesis, Xinan Jiaotong University, Chengdu, China, 2004.
13. Liao, W.-D. Study on Asphalt Overlay Structure and Material of Old Cement Concrete Pavement Based on Stress Absorption Layer. Ph.D. Thesis, Wuhan University of Technology, Wuhan, China, 2007.
14. Luo, H.; Zhu, H.-P.; Chen, C.-Y. Study on Fatigue Test of Pre Cut Asphalt Mixture Trabeculae. *J. Civ. Eng. Manag.* **2008**, *25*, 47–50.
15. Cai, Y.-X. Study on Structural Behavior and Road Performance of Stress Absorption Layer of Rubber Bitumen. Ph.D. Thesis, Chang'an University, Xi'an, China, 2016.

16. Yang, Y.; Zhang, K.; Ji, S.-P. Study on Anti Reflective Cracking Performance of Rubber Asphalt Stress Absorption Layer. *Chin. For. Highw.* **2013**, *33*, 323–326.
17. Zhao, Y.-T. Theoretical Analysis and Experimental Study of Stress Absorbing Layer in Semi—Rigid Pavement Reflective Crack Control. Mater's Thesis, Hebei University of Technology, Wuhan, China, 2014.
18. Tao, J. Study on Fatigue Behavior of Asphalt Overlay Structure of Old Cement Concrete Pavement under Traffic Load. Mater's Thesis, Wuhan University of Technology, Wuhan, China, 2008.
19. Cheng, Y. Study on Asphalt Overlay Structure of Cement Concrete Pavement with Stress Absorption Layer. Mater's Thesis, Chang'an University, Xi'an, China, 2006.
20. Zamora-Barraza, D.; Calzada-Pérez, M.A.; Castro-Fresno, D.; Vega-Zamanillo, A. Evaluation of anti-reflective cracking systems using geosynthetics in the interlayer zone. *Geotext. Geomembr.* **2011**, *29*, 130–136. [CrossRef]
21. Guo, J.; Zhang, R.-H. Study on the Properties of Stress Absorption Layer of Rubber Bitumen. *Guangdong Build. Mater.* **2012**, *28*, 31–35.
22. Hou, Y.-M. Experimental Study on Fatigue Performance of Stress Absorption Layer of Rubber Asphalt. *Highw. Eng.* **2009**, *4*. [CrossRef]
23. Aliha, M.R.M.; Bahmani, A.; Akhondi, S. A novel test specimen for investigating the mixed mode I+ III fracture toughness of hot mix asphalt composites—Experimental and theoretical study. *Int. J. Solids Struct.* **2016**, *90*, 167–177. [CrossRef]
24. Aliha, M.R.M.; Fazaeli, H.; Aghajani, S.; Nejad, F.M. Effect of temperature and air void on mixed mode fracture toughness of modified asphalt mixtures. *Constr. Build. Mater.* **2015**, *95*, 545–555. [CrossRef]
25. Aliha, M.R.M.; Sarbijan, M.J.; Bahmani, A. Fracture toughness determination of modified HMA mixtures with two novel disc shape configurations. *Constr. Build. Mater.* **2017**, *155*, 789–799. [CrossRef]
26. Ameri, M.; Nowbakht, S.; Molayem, M.; Aliha, M.R.M. Investigation of fatigue and fracture properties of asphalt mixtures modified with carbon nanotubes. *Fatigue Fract. Eng. Mater. Struct.* **2016**, *39*, 896–906. [CrossRef]
27. Aliha, M.R.M.; Behbahani, H.; Fazaeli, H.; Rezaifar, M.H. Study of characteristic specification on mixed mode fracture toughness of asphalt mixtures. *Constr. Build. Mater.* **2014**, *54*, 623–635. [CrossRef]
28. Sun, L.-J.; Wang, G.; Zhang, H.-C.; Liu, L.-P. Initiation and Propagation of Top-Down Cracking in Asphalt Pavement. *Appl. Sci.* **2018**, *8*, 774. [CrossRef]
29. Li, S.-Q.; Wang, X.-C. Study on fatigue Simulation of reflection crack Development in Asphalt overlay. *J. China For. Highw.* **2009**, *29*, 190–193.
30. Song, L.-X.; Wu, X.-H.; Song, L.-J. Research on Asphalt Overlay Material of Old Cement Concrete Pavement Based on Stress Absorption Layer. *Highw. Eng.* **2017**, *42*, 286–291.
31. Wu, H.-Z.; Guo, H.-D.; Gao, D.-P. A Review on the Probability and Statistics Method of Fatigue Failure Life. *Intensity Environ.* **2002**, *29*, 38–44.
32. Wang, K.-Q. Study on Reliability of Fatigue Crack Propagation under Different Stress Ratio. Ph.D. Thesis, Kunming University of Technology, Kunming, China, 2012.



© 2018 by the authors. Licensee MDPI, Basel, Switzerland. This article is an open access article distributed under the terms and conditions of the Creative Commons Attribution (CC BY) license (<http://creativecommons.org/licenses/by/4.0/>).

Article

# Preparation Technique and Properties of Nano-TiO<sub>2</sub> Photocatalytic Coatings for Asphalt Pavement

Hui Wang <sup>1,2,\*</sup>, Ke Jin <sup>1</sup>, Xinyu Dong <sup>1</sup>, Shihao Zhan <sup>1</sup> and Chenghu Liu <sup>1</sup>

<sup>1</sup> School of Transportation Engineering, Changsha University of Science and Technology, 960, 2nd Section, Wanjiali RD (S), Changsha 410004, China; ke15526449298@outlook.com (K.J.); dxy620@hotmail.com (X.D.); micro528706637@outlook.com (S.Z.); tonyxiaohu@163.com (C.L.)

<sup>2</sup> National Engineering Laboratory of Highway Maintenance Technology, Changsha University of Science and Technology, Changsha 410004, China

\* Correspondence: whui@csust.edu.cn; Tel.: +86-139-7318-8915

Received: 17 September 2018; Accepted: 22 October 2018; Published: 25 October 2018

**Featured Application:** Due to having the same color with the asphalt, the prepared nano-TiO<sub>2</sub> photocatalytic coating could be applied directly onto the pavement surfaces, located in densely-populated areas, environmentally-sensitive areas, service areas and parking lots etc., to further play a better role in the degradation of exhaust gas.

**Abstract:** According to the characteristics of asphalt pavement, a kind of nano-TiO<sub>2</sub> photocatalytic coating was prepared by using the emulsified asphalt as the carrier. All of its properties met the technical requirements. An exhaust gas degradation test device and its test steps were developed. The evaluation indexes, cumulative degradation rate, and degradation efficiency, were put forward. From the two aspects of the nano-TiO<sub>2</sub> content in photocatalytic coatings and the spraying amount of photocatalytic coatings in the surface of slabs (300 mm × 300 mm), the exhaust gas degradation effects, the performances of skid resistance, and the water permeability of asphalt mixture were analyzed. The test results showed that the cumulative degradation rate of exhaust gas was better when nano-TiO<sub>2</sub> content was increased in the range of 0–8% and the spraying amount was changed in the range of 0–333.3 g/m<sup>2</sup>. In practical engineering applications, the anti-skid performance of asphalt pavement can be satisfied when the spraying amount of photocatalytic coating was limited to under 550 g/m<sup>2</sup>. The spraying amount of nano-TiO<sub>2</sub> photocatalytic coating had little effect on the water permeability of the asphalt mixture. Therefore, 8% nano-TiO<sub>2</sub> content in the coating and a 400 g/m<sup>2</sup> spraying amount were finally recommended based on the photocatalytic properties, as well as for economic reasons.

**Keywords:** preparation technique; emulsified asphalt; nano-TiO<sub>2</sub>; photocatalytic coating; degradation of exhaust gas

## 1. Introduction

Vehicles have brought convenience to people but also more and more serious air pollution. A lot of studies on the purification technology of automobile exhaust have been conducted in many countries around the world [1–4]. TiO<sub>2</sub> is generally considered as one of the most effective photoinduced catalysts and is frequently used to oxidize organic and inorganic compounds in the air and water due to its strong oxidative ability and long-term photostability, as well as being a non-expensive and non-toxic material. Therefore, titania-mediated photocatalysis is a very promising approach to the increasing crucial issues associated with environmental pollution [5,6]. Indeed, among the possible solutions, TiO<sub>2</sub>-coated materials can significantly decompose a variety of organic (e.g., volatile



organic compounds) and inorganic (e.g., NO<sub>x</sub> and SO<sub>2</sub>) pollutants due to its unique photocatalytic property, which contributes to its ability toward air-purifying and self-cleaning. Nano-TiO<sub>2</sub> has been proved to be a good photocatalytic material, which can degrade harmful substances in waste gas [7,8]. A series of new photocatalytic materials related to TiO<sub>2</sub> have been developed and applied in different situations [6,9–11]. The emissions of harmful air pollutants associated with highway operations often surpass the concentrations from industrial sources, rendering traffic emissions the primary source of urban air pollution [12,13]. Therefore, TiO<sub>2</sub> is widely used in road engineering due to its excellent photocatalytic properties in many countries such as China, Italy, and so on. The air purification effect on both sides of the road area has been improved to a greater extent [14–16].

Currently, there are two ways to apply nano-TiO<sub>2</sub> on the road, which are a blending method (i.e., nano-TiO<sub>2</sub> was directly added to the aggregate and mixed with the asphalt to form a nano-TiO<sub>2</sub> asphalt mixture) and a spraying method (i.e., coatings containing nano-TiO<sub>2</sub> were sprayed on the surface of the pavement or other road-affiliated facilities) [17]. Tan et al. [18] applied nano-TiO<sub>2</sub> to an asphalt pavement using both methods to analyze the photocatalytic degradation of automobile exhaust gas. Test results showed that nano-TiO<sub>2</sub> under the two kinds of applications had a good photocatalytic degradation effect. However, for the blending method, the amount of nano-TiO<sub>2</sub> used was large and the cost was high. Marwa, Hassan, and co-workers [19–21] studied a sustainable photocatalytic asphalt pavement by using TiO<sub>2</sub> as a photocatalytic material to reduce nitrogen oxides and sulfur dioxide. The development of this new sustainable road has the potential to reduce the high pollution level caused by traffic vehicles. The environmental effectiveness of a TiO<sub>2</sub> coating in photodegrading mixed NO<sub>2</sub> and NO gases from the atmosphere was evaluated. David et al. [22] studied the performance of asphalt pavement with a TiO<sub>2</sub> photocatalyst. They developed and tested a new photocatalytic method to quantify the short-term durability of TiO<sub>2</sub> spraying on two kinds of pavements: concrete and asphalt. Clement et al. [23] applied three commercially-available photocatalytic coatings to roadside concrete to elucidate how environmental parameters, exposure, and real roadside conditions impact the degradation of NO<sub>x</sub>. The test results for a 20-month period indicated that the efficacy diminished over time. This research shows that the application of photocatalysis technology has a good effect in dealing with automobile exhaust and is rather promising. Under the effect of light, the photocatalyst can react with the automobile exhaust to form water, carbon dioxide, and salt, which prevents secondary pollution to the environment. In spite of these promising findings, the application of this technology to pavements is still in its infancy. Usually photocatalytic compounds used only as a coating are painted on the roadside or crash barrier. Therefore, based on the characteristics of the sprayed asphalt pavement, a photocatalytic coating of nano-TiO<sub>2</sub> and emulsified asphalt as a carrier was prepared in this paper. The effect of the degradation performance of a photocatalytic coating on the exhaust gas was evaluated, and the pavement performance of the asphalt pavement with a photocatalytic coating was analyzed.

## **2. Materials and Experimental Preparation**

### *2.1. Selection of Nano-TiO<sub>2</sub> Crystals*

TiO<sub>2</sub> was divided into three different crystal structures, namely anatase, rutile, and brookite. Table 1 shows the basic properties of the three types of crystal structures. The common ones are anatase and rutile. The internal structures of these crystals composed of TiO<sub>2</sub> are all octahedral and connect with each other. However, they have different material properties and internal electronic structures due to the differences of the degree of deformation of the octahedral and the connection forms. Despite the valence band of the phase, the electron transition produces the same cavitation oxidation performance. However, the band width of anatase is 3.2 eV, while rutile is only 3.0 eV. Therefore, the rutile is more negative, and the reducibility of transitional electrons is stronger. In addition, the electron (e<sup>-</sup>)-hole (h<sup>+</sup>) pairs produced by the lower-bandwidth rutile electron transition are easier to recover, reducing the redox activity. Therefore, the anatase TiO<sub>2</sub> has better photocatalytic performance than the rutile

one. In this study, the anatase TiO<sub>2</sub> was selected. The technical indicators of anatase nano-TiO<sub>2</sub>, which were provided by the manufacturer Xuancheng Jingrui New Material Co., Ltd. (Xuancheng, China), are shown in Table 2.

**Table 1.** The physical properties of nano-TiO<sub>2</sub> crystals.

Crystal Type	Relative Density	Crystal System	The Lattice Constant (nm)		Ti–O Distance (nm)	The Forbidden Band Width (eV)
			a	c		
anatase	3.84	tetragona	5.27	9.37	0.195	3.2
rutile	4.26	tetragona	9.05	5.80	0.199	3.0
brookite	4.17	lorthorhombic	–	–	–	–

**Table 2.** Technical indicators of anatase nano-TiO<sub>2</sub>.

Appearance	Specific Surface Area (m <sup>2</sup> /g)	pH	Particle Size (nm)	Loss on Drying (%)	Loss on Ignition (%)	Purity (%)
white powder	80	5	20	0.2	0.25	>99.8

### 2.2. Materials for TiO<sub>2</sub> Photocatalytic Coating

Besides nano-TiO<sub>2</sub>, the materials for the preparation of nano-TiO<sub>2</sub> photocatalytic coatings include:

- Dispersants: Two kinds of dispersants, S-5040 and sodium hexametaphosphate (SHP), were used. The detailed technical indicators, which were provided by the manufacturer Shandong Huali Bio-tech Co., Ltd. (Zibo, China), are shown in Table 3.
- Emulsifiers: Three kinds of representative emulsifiers—rapid-setting cationic emulsifier SY-QCE, medium-setting cationic emulsifier KZW-802, and slow-setting cationic emulsifier SY-CME—were chosen. The technical indicators, which were provided by the manufacturer Jiangsu Xinyue Asphalt Co., Ltd. (Zhenjiang, China), are shown in Table 4.
- Asphalt: A kind of 70# penetration “A” grade asphalt binder was selected (Shell (China) Limited). The main physical properties of the asphalt binder were tested following the Chinese Standard Test Methods of Bitumen and Bituminous Mixtures for Highway Engineering (JTG E20-2011) [24] and met the requirements in the Chinese Specifications for Construction of Highway Asphalt Pavements (JTG F40-2004) [25], as shown in Table 5.
- In addition, CaCl<sub>2</sub> (Wuhan Fude Chemical Co., Ltd., Wuhan, China) and hydrochloric acid (Wuhan Fude Chemical Co., Ltd., Wuhan, China) were selected as additives.

**Table 3.** Technical indicators of dispersants.

Dispersants	Appearance	Solid Content (%)	Viscosity (Pa·s)	Boiling Point (°C)	Solubility
S-5040	Colorless, viscous, and transparent liquid	40	400	110	Extremely easy to dissolve in water
SHP	Transparent glass flake or white powder	—	—	1500	Extremely easy to dissolve in water

**Table 4.** Technical indicators of emulsifiers.

Emulsifiers	SY-QCE	KZW-802	SY-CME
Appearance (25 °C)	Light yellow liquid	Creamy white paste	Light yellow liquid
Purity of emulsifiers (%)	≥60	≥50	≥75
pH value	9–10	2–4	3–4
Solubility	Easy to dissolve in water	Easy to dissolve in water	Easy to dissolve in water
Type of Emulsifiers	Rapid-setting	Medium-setting	Slow-setting
Adding content of emulsifiers (%)	0.5	0.8	2

**Table 5.** Basic physical properties of asphalt.

Index	Test Results	Requirements [25]	Methods [24]
25 °C Penetration (0.1 mm)	72	≈60–80	T0604
Penetration index (PI)	0.11	−1.5 to +1.0	T0604
Softening point (°C)	48	≥46	T0606
15 °C Ductility (cm)	>100	>100	T0605
60 °C Viscosity (Pa·s)	213	>180	T0625
Flash point (°C)	288	≥260	T0611
Wax content (%)	1.2	≤2.2	T0615

### 2.3. Asphalt Mixture for Base Sample

A kind of styrene-butadiene-styrene block copolymer (SBS) modified asphalt binder with 8% high viscosity modified additive by the weight of asphalt was used in this paper. The main technical indexes were tested according to the test methods in the Chinese Standard Test Methods of Bitumen and Bitumen Mixtures for Highway Engineering (JTG E20-2011) [24]. Its basic properties met the Chinese Specifications for Construction of Highway Asphalt Pavements (JTG F40-2004) [25], as shown in Table 6. The aggregate used was taken from a basalt quarry (Qiangyuan Basalt Development Co., Ltd., Zhuzhou, China). It was completely crushed to give larger particles with an angular shape and rough surface texture. The test methods were based on the Chinese Test Methods of Aggregate for Highway Engineering (JTG E42-2005) [26]. Its basic properties met the Chinese Specifications for Construction of Highway Asphalt Pavements (JTG F40-2004) [24], which are listed in Table 7. In order to make nano-TiO<sub>2</sub> play a better photocatalytic role, open-graded friction course (OGFC) gradation was selected owing to its large air voids and deep structural texture. The design gradation of the aggregate met the requirements of OGFC-10 according to the Chinese Technical Specifications for Construction of Highway Asphalt Pavements (JTG F40-2004) [25], as shown in Figure 1. The designed asphalt aggregate ratio was 4.5%. The results of OGFC design are shown in Table 8.

**Table 6.** The main technical indexes of high-viscosity modified asphalt.

Index	Test Results	Requirements [25]	Methods [24]
25 °C Penetration (0.1 mm)	42.6	≥40	T0604
Penetration index (PI)	1.21	≥0	T0604
Softening point (°C)	91.0	≥80	T0606
15 °C Ductility (cm)	77.3	≥50	T0605
Toughness (N·m)	38	≥20	T0624
60 °C Viscosity (Pa·s)	73,550	≥20,000	T0625
Flash point (°C)	275.0	≥260	T0611
25 °C Elastic recovery (%)	94.3	≥75	T0662

**Table 7.** Basic physical properties of the aggregate.

Index	Test Results	Requirements [25]	Methods [26]
Los Angeles abrasion loss (%)	15.6	≤28	T0317
Soundness (%)	0.88	≤12	T0314
Elongated or flat particles (%)	13.3	≤15	T0312
Water absorption (%)	0.52	≤2.0	T0304
Apparent specific gravity	2.774	≥2.6	T0304

Table 8. Results of OCFG-10 design.

Index	Test Results	Requirements [25]	Methods [24]
Volumes of air voids (%)	20.1	18–25	T0705
Draindown (%)	0.25	<0.3	T0732
Cantabro loss (%)	5.9	<20	T0733
Marshall stability (kN)	8.33	≥3.5	T0709

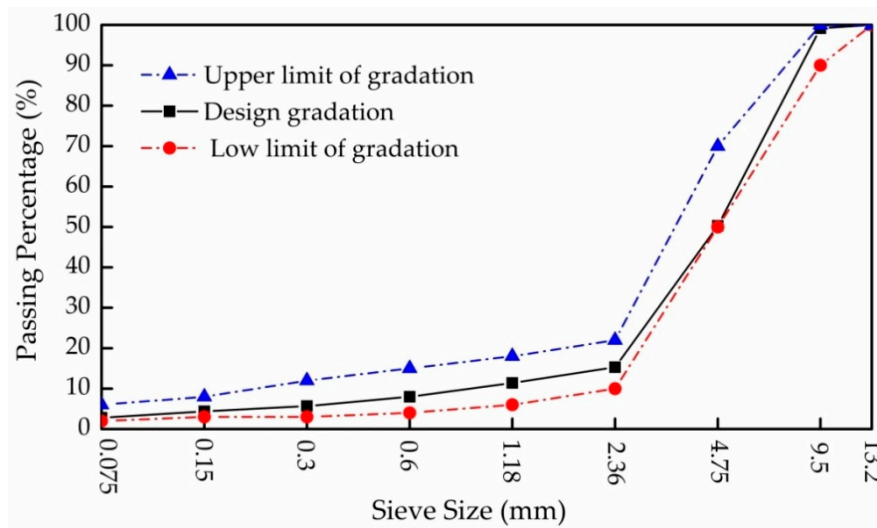


Figure 1. OGFC-10 aggregate gradation curve.

#### 2.4. Exhaust Gas Degradation Test Device and Evaluation Indexes

##### 2.4.1. Exhaust Gas Test Devices and Test Steps

The test devices for measuring the degradation efficiency of exhaust gas were developed, including the exhaust gas analyzer, degradation reaction chamber with build-in two parallel UVA-340 ultraviolet lamps and a small fan, voltage regulator, and a gas cylinder filled with CO, HC, and NO<sub>x</sub>. The composition and concentration of the gas mix in the cylinder were similar to automobile exhaust. The test devices are illustrated in Figure 2.

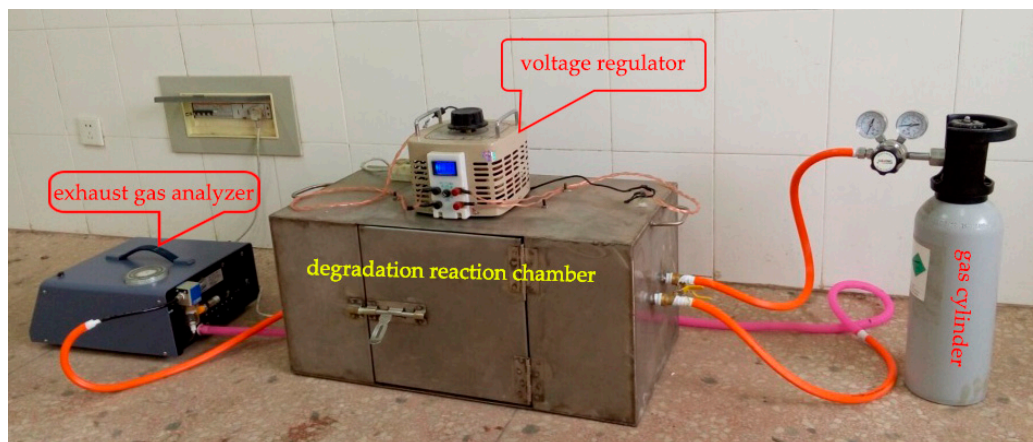


Figure 2. Exhaust gas degradation test device.

Test steps:

- The nano-TiO<sub>2</sub> photocatalytic coating was prepared (the detailed procedures are shown in Section 3.2).
- The coating was then sprayed on the surface of the slab specimen according to the designated amount. The emulsified asphalt coating containing a certain amount of nano-TiO<sub>2</sub> was uniformly painted onto the slab sample with a brush, as shown in Figure 3.
- The coating was put in a dry and ventilated place for more than 24 h to ensure that the coating was completely dry. After that, the slab was put into the degradation reaction chamber. The exhaust gas analyzer was turned on and a certain concentration of exhaust gas was injected into the degradation reaction chamber.
- The UV lamps were turned on, along with a small fan, and the voltage of the UV lamps was adjusted such that the UV irradiance could reach the average outdoor UV irradiance of 26.7 W/m<sup>2</sup>.
- The gas concentration in the degradation reaction chamber was recorded every 10 min. The test time was set to 90 min for every specimen. At least three specimens were prepared for each nano-TiO<sub>2</sub> content or spraying amount of photocatalytic coating.



Figure 3. Painting the emulsified asphalt coating on the slab sample.

#### 2.4.2. Evaluation Indexes

##### 1. Cumulative degradation rate

Under a certain initial concentration of the exhaust gas and light intensity, the cumulative degradation rate is defined as a ratio of the decreasing value of the exhaust gas concentration at the time  $t$  caused by the nano-TiO<sub>2</sub> photocatalytic coating to the initial concentration of the exhaust gas:

$$e = \frac{C_0 - C_t}{C_0} \times 100\%, \quad (1)$$

where  $e$  is the cumulative degradation rate, %;  $C_0$  is the initial concentration of exhaust gas, ppm; and  $C_t$  is the exhaust gas concentration at the time  $t$ , ppm.

##### 2. Degradation efficiency

Degradation efficiency is defined as a ratio of the photocatalytic degradation mass of the exhaust gas caused by the photocatalytic coating with a certain nano-TiO<sub>2</sub> content in the test sample to the maximum photocatalytic degradation mass of the exhaust gas caused by the same mass of no carrier nano-TiO<sub>2</sub> powder that was evenly distributed on the slab within time 0– $t$ :

$$r = \frac{m_t}{m_{\max}} \times 100\%, \quad (2)$$

where  $r$  is the degradation efficiency, %;  $m_t$  is the degraded mass of exhaust gas under nano-TiO<sub>2</sub> with emulsified asphalt as the carrier during the time  $t$ , mg; and  $m_{max}$  is the maximum photocatalytic degradation of the exhaust gases under nano-TiO<sub>2</sub> without the carrier during the time  $t$ , mg.

### 3. Preparation of the Nano-TiO<sub>2</sub> Photocatalytic Coating

#### 3.1. Materials Selection

##### 3.1.1. Dispersant

Two dispersants were mixed with nano-TiO<sub>2</sub> in the ratios (dispersant versus nano-TiO<sub>2</sub>) of 0, 1:5, 1:10, 1:15, and 1:20. Then, the high purity water was added into the mixture to ensure that the content of nano-TiO<sub>2</sub> in the slurry was 20%. Taking the preparation of the 300 g slurry as an example, the amount of each material in the slurry is shown in Table 9. After that, the conventional mechanical stirring device of DF-101 was used to stir the slurry for 10 min. Then, 50 mL of slurry was poured into the cylinder immediately to observe the stratification states of the slurry at different times. The stratification states of nano-TiO<sub>2</sub> after 72 h are shown in Figure 4.

**Table 9.** The amount of each material in 300 g slurry.

Ratios	Nano-TiO <sub>2</sub> (g)	Dispersant (g)	High Purity Water (g)
0	60	0	240
1:5	60	12	228
1:10	60	6	234
1:15	60	4	236
1:20	60	3	237

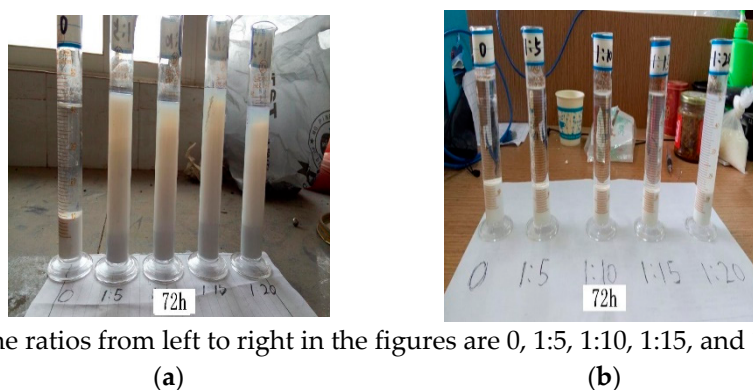


**Figure 4.** The stratification states of nano-TiO<sub>2</sub> after 72 h with (a) S-5040, and (b) SHP.

As shown in Figure 4, the dispersion effect of S-5040 to nano-TiO<sub>2</sub> is better than that of SHP. When the proportion of S-5040 to nano-TiO<sub>2</sub> was 1:5, the mixed slurry had no obvious stratification and kept better dispersibility and stability after 72 h. All mixtures of SHP and nano-TiO<sub>2</sub> were stratified and separated after 72 h. As a result, S-5040 was chosen to disperse nano-TiO<sub>2</sub>, and the ratio was chosen to be 1:5, that is, the amount of dispersant was 20% of the amount of nano-TiO<sub>2</sub>.

##### 3.1.2. Emulsifier

Nano-TiO<sub>2</sub> photocatalytic coatings were prepared with three types of emulsifiers for performance comparison. Test conditions: the content of nano-TiO<sub>2</sub> was 8%; the content of dispersant S-5040 was 20% of that of nano-TiO<sub>2</sub>; the content of 70# penetration grade asphalt was 50%; the contents of three kinds of emulsifiers (SY-QCE, KZW-802, SY-CME) were 0.5%, 0.8%, and 2%; the temperature of soap solution was 70 °C; the temperature of hot asphalt was 140 °C; the content of the stabilizer (CaCl<sub>2</sub>) was 0.2%; and a colloid mill (Denimo TECH A/S, Aarslev, Denmark) was adopted as an emulsifying

device. The pH value of the SY-QCE solution was adjusted to a range of 3–4 using hydrochloric acid, and the others did not require acid value adjustment. The basic performances are shown in Table 10.

**Table 10.** Basic performances of nano-TiO<sub>2</sub> photocatalytic emulsion coatings.

Emulsifiers	SY-QCE	KZW-802	SY-CME	Requirements [25]	Methods [24]
Color of emulsion	Brown	Brown	Brown	—	—
Standard viscosity C25,3 (s)	8.32	15.55	15.98	8–20 for SY-QCE and KZW-80210–25 for SY-CME	T0621
1-day storage stability	0.4	1.8	0.5	≤1	T0655

The color of emulsified asphalt was brown, which indicated that asphalt emulsification was in good condition. However, the standard viscosity of SY-QCE emulsified asphalt was only 8 s, approaching the lower limit of the technical requirement of PC-1 (sprinkling cationic rapid-setting emulsified asphalt) in the Chinese Technical Specifications for Construction of Highway Asphalt Pavements (JTG F40-2004) [25]. Therefore, it is improper to spray SY-QCE emulsified asphalt in a practical project.

The standard viscosities of KZW-802 and SY-CME emulsified asphalt met the technical requirements, but the storage stability of KZW-802 was poor. As a result, SY-CME was selected as the carrier of the nano-TiO<sub>2</sub> photocatalytic coating.

### 3.2. Preparation Process

Taking 1 kg of photocatalytic coating with 8% nano-TiO<sub>2</sub> as an example, the preparation process is given below with the content of each material (by weight) in the coating shown in Table 11. The temperature of the soap solution was 70 °C, the temperature of the hot asphalt was 140 °C, and the colloid mill was adopted as an emulsifying device.

**Table 11.** The content of each material (by weight) in the photocatalytic coating.

Asphalt	Soap Solution				
	Nano-TiO <sub>2</sub>	S-5040	SY-CME	CaCl <sub>2</sub>	High Purity Water
50%	8%	1.6%	2%	0.2%	38.2%

#### 1. Soap solution

- A total of 2 g CaCl<sub>2</sub> was added into 382 g of high purity water. Then, the water was heated and stirred to fully dissolve the CaCl<sub>2</sub>.
- A total of 20 g of SY-CME was added into the solution and dissolved thoroughly.
- A total of 16 g of dispersant S-5040 was added into the solution and stirred thoroughly, then 80 g of nano-TiO<sub>2</sub> was added and stirred for 15 min. After that, the soap solution was kept at a temperature of 70 °C for later use.

#### 2. Asphalt

The asphalt was heated to the flowing state. Then, 500 g of heated asphalt was weighed and the temperature of the asphalt was kept on standby at 140 °C.

#### 3. Emulsification

The prepared soap solution and heated asphalt were added into the colloid mill successively. After 3 min of emulsification, the emulsified asphalt was cooled. Finally, the emulsified asphalt was placed in a plastic bucket as a reserve.

For the preparation of photocatalytic coatings with different nano-TiO<sub>2</sub> contents, only the amounts of nano-TiO<sub>2</sub> and dispersant needed to be adjusted.

### 3.3. Performance of the Nano-TiO<sub>2</sub> Photocatalytic Coating

The photocatalytic coatings with different nano-TiO<sub>2</sub> contents were prepared and their basic properties met the Chinese Technical Specifications for Construction of Highway Asphalt Pavements (JTG F40-2004) [25], as shown in Table 12.

1. The color of the photocatalytic coating emulsion with different nano-TiO<sub>2</sub> contents was brown, which indicated that the emulsification effect was better.
2. With the increase of the amount of nano-TiO<sub>2</sub>, the standard viscosity of photocatalytic coatings decreased, indicating that the photocatalytic coatings gradually became viscous. The main reason was that nano-TiO<sub>2</sub> had a good adsorption capacity to asphalt because of its small particle size and large specific surface area. Although the coatings became viscous with increasing nano-TiO<sub>2</sub> content, all of the photocatalytic coatings met the technical requirements of the standard viscosity of PC-2 (sprinkling cationic slow-setting emulsified asphalt) in the Chinese Technical Specifications for Construction of Highway Asphalt Pavements (JTG F40-2004) [25].
3. With the increase of the nano-TiO<sub>2</sub> content, the storage stability of the photocatalytic coating became worse. This is mainly due to the increase of the content of nano-TiO<sub>2</sub>, which made the nano-TiO<sub>2</sub> particles prone to agglomerate, finally resulting in the reduction of storage stability of the photocatalytic coatings.
4. The abrasion resistance of nano-TiO<sub>2</sub> photocatalytic coating was evaluated using the wet track abrasion loss test. The test results showed that the wet track abrasion loss value of all the asphalt mixture with nano-TiO<sub>2</sub> photocatalytic coating after the specimen being immersed into water for 1 h met the technical requirements of the Chinese Technical Specifications for Construction of Highway Asphalt Pavements (JTG F40-2004) [25] (no more than 540 g/m<sup>2</sup>). It showed that the nano-TiO<sub>2</sub> photocatalytic coating had good abrasion resistance.

**Table 12.** Basic properties of photocatalytic coatings with different nano-TiO<sub>2</sub> content.

Nano-TiO <sub>2</sub> Content	3%	5%	8%	10%	15%	Requirements [25]	Methods [24]
Color of emulsion	Brown	Brown	Brown	Brown	Brown	—	—
Standard viscosity C25,3 (s)	16.56	16.12	15.98	15.54	14.65	12–60	T0621
5-day storage stability (%)	3.45	3.76	3.63	3.88	4.13	≤5	T0655
Adhesion, covering area	>2/3	>2/3	>2/3	>2/3	>2/3	>2/3	T0654
1 h wet track abrasion loss (g/m <sup>2</sup> )	321	356	380	423	463	<540	T0752

## 4. Evaluation of Exhaust Gas Degradation Effect

### 4.1. Effects of the Nano-TiO<sub>2</sub> Content on Exhaust Gas Degradation

A total of 30 g of photocatalytic coatings with nano-TiO<sub>2</sub> content of 3%, 5%, 8%, 10%, and 15% were uniformly applied to the surface of the 300 × 300 mm OGFC-10 slab samples to perform photocatalytic degradation of the exhaust gas test. The test specimens are shown in Figure 5. The effect of degradation of exhaust gas by photocatalytic coating with different nano-TiO<sub>2</sub> contents was studied. The test results are shown in Figures 6 and 7.



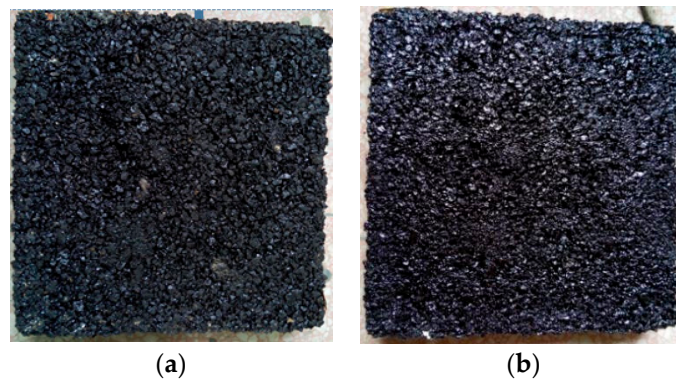


Figure 5. Test specimens: (a) without photocatalytic coating, and (b) with sprayed photocatalytic coating.

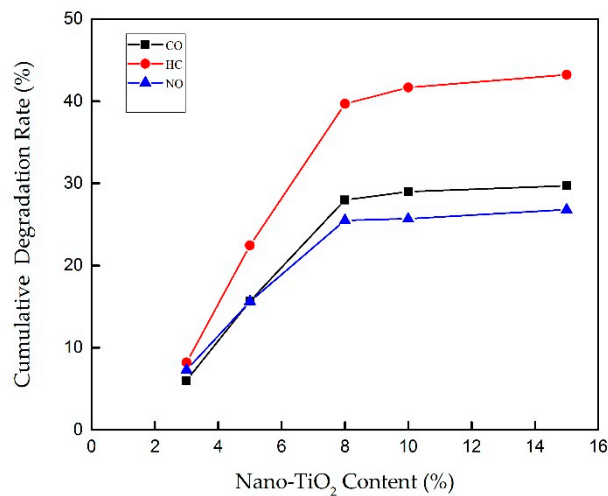


Figure 6. Changes of the cumulative degradation rate of the exhaust gas at different nano-TiO<sub>2</sub> contents.

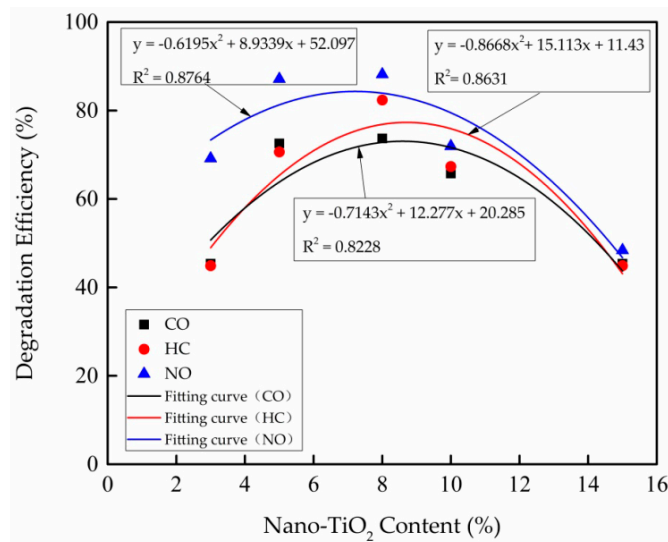


Figure 7. Changes of the degradation efficiency of the exhaust gas at different nano-TiO<sub>2</sub> contents.

As can be seen from Figure 6, with the increase of nano-TiO<sub>2</sub> content, the performance of photocatalytic coatings for degradation of exhaust gas was better. When the content of nano-TiO<sub>2</sub> increased from 0 to 8%, the cumulative degradation rate of CO, HC, and NO increased rapidly. However, the cumulative degradation rate of the CO, HC, and NO grew slowly when the content of nano-TiO<sub>2</sub> was above 8%. Figure 7 illustrates that the nano-TiO<sub>2</sub> content had a good quadratic nonlinear

correlation with the degradation efficiency of CO, HC, and NO. With the increase of nano-TiO<sub>2</sub> content, the degradation efficiency of three kinds of exhaust gas increased gradually. However, the degradation efficiency of nano-TiO<sub>2</sub> to three kinds of exhaust gas tended to decrease when the content of nano-TiO<sub>2</sub> was above 8%.

The exhaust gas degradation performance of the coating was related to the size of the effective contact area between the nano-TiO<sub>2</sub> and exhaust gas, and ultraviolet intensity. When the nano-TiO<sub>2</sub> content exceeded 8%, the entire surface of the slab sample was covered by a saturated nano-TiO<sub>2</sub> thin layer. Therefore, there was no substantial increase in the effective number of nano-TiO<sub>2</sub> particles touching with the exhaust gas per unit area with the continuous increase of the content of nano-TiO<sub>2</sub>. The degradation performance of the photocatalytic coating was not significantly improved. Furthermore, the degradation efficiency of nano-TiO<sub>2</sub> gradually decreased.

#### 4.2. Effects of the Spraying Amount on Exhaust Gas Degradation

Separately, 10 g, 20 g, 30 g, 40 g, and 55 g of photocatalytic coatings with 8% nano-TiO<sub>2</sub> were uniformly sprayed on the slab samples of OGFC-10 to perform the photocatalytic degradation of exhaust gas test. The performances of nano-TiO<sub>2</sub> photocatalytic coatings with different spraying amounts on the degradation of exhaust gas were studied. The test results are shown at Figures 8 and 9.

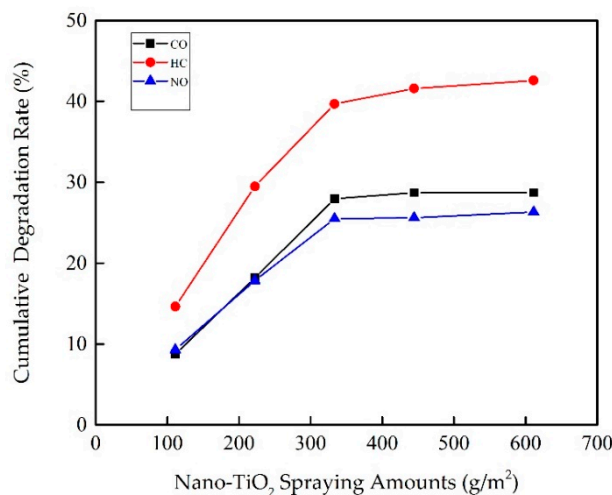


**Figure 8.** Changes of the cumulative degradation rate of the exhaust gas at different nano-TiO<sub>2</sub> spraying amounts.

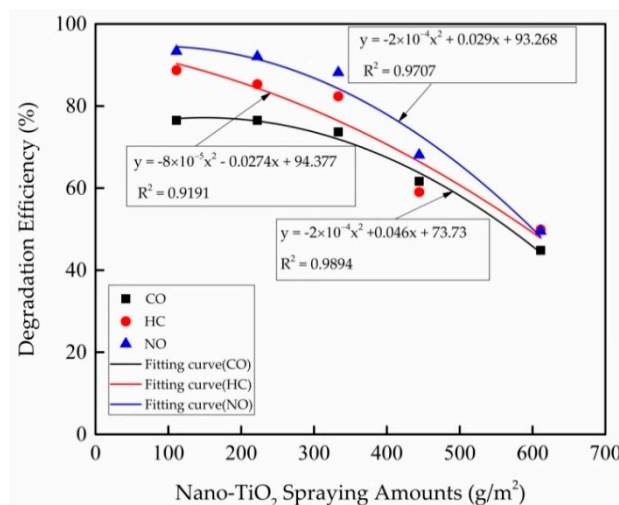


**Figure 9.** Changes of the degradation efficiency of the exhaust gas at different nano-TiO<sub>2</sub> spraying amounts.

As can be seen from Figure 8. The cumulative degradation rate of CO, HC, and NO increased gradually with the increase of the amount of photocatalytic coating. However, when the spraying amount was over 333.3 g/m<sup>2</sup>, the cumulative degradation rate of CO, HC, and NO gas remained unchanged with the continuous increasing of spraying amount. When the spraying amount of nano-TiO<sub>2</sub> photocatalytic coating was less than 333.3 g/m<sup>2</sup>, with the increase of spraying amount, the number of nano-TiO<sub>2</sub> particles on the surface of the slab sample and the effective contact area with the exhaust gas and the ultraviolet light gradually increased and the effect of degradation improved. When the nano-TiO<sub>2</sub> photocatalytic coating spraying amount reached 333.3 g/m<sup>2</sup>, the effective contact area and quantities of nano-TiO<sub>2</sub> with the car exhaust and ultraviolet also achieved a peak value. After that, the increase of the spray volume only resulted in an even thicker coating that had little effect on improving the effect of degradation on vehicle exhaust gas.

As can be seen from Figure 9, with the continuous increase in the spraying amount of photocatalytic nano-TiO<sub>2</sub>, the degradation efficiency of CO, HC, and NO decreased gradually. This was mainly because a small amount of coating being sprayed on the surface of the slab samples can form a very thin film layer. At this time, most of the nano-TiO<sub>2</sub> could act in its photocatalytic role. However, with the increase of the spraying amount, the thickness of the coating film also increased. Those nano-TiO<sub>2</sub> particles at the bottom of film could not effectively contribute to photocatalytic reactions, resulting in the decrease of degradation efficiency.

After comprehensive consideration, when the added content of nano-TiO<sub>2</sub> in the coating reached 8%, the photocatalytic coating had the best performance of degradation of the automobile exhaust gas. When the dosage of nano-TiO<sub>2</sub> increased to more than 8%, the ability of photocatalytic degradation exhaust was no longer a definite improvement with the increase of nano-TiO<sub>2</sub>. In addition, the photocatalytic coating containing 8% of nano-TiO<sub>2</sub> was evenly sprayed on the slabs for the photocatalytic degradation of the exhaust gas test. It indicated that with the continuous increase of the spraying amount of coating, the photocatalytic degradation property of exhaust gas was gradually improved. However, the performance of the photocatalytic degradation property of exhaust gas basically kept at the same level after the spraying amount was over 333.3 g/m<sup>2</sup>.

## **5. Pavement Performance Evaluation**

### *5.1. Skid Resistance*

The friction coefficient and texture depth were used to evaluate the skid resistance of asphalt pavement at the different spraying amounts of nano-TiO<sub>2</sub> photocatalytic coatings. The friction coefficient of the sprayed nano-TiO<sub>2</sub> asphalt mixture was measured using the pendulum friction meter (Shuyang highway equipment plant, Suqian, China) according to the test method of T0964 in the Chinese Field Test Methods of Subgrade and Pavement for Highway Engineering (JTG E60-2008) [27] and the surface texture depth was determined using the test method of T0731 in the Chinese Standard Test Methods of Bitumen and Bituminous Mixtures for Highway Engineering (JTG E20-2011) [24]. The test results are shown in Figure 10.

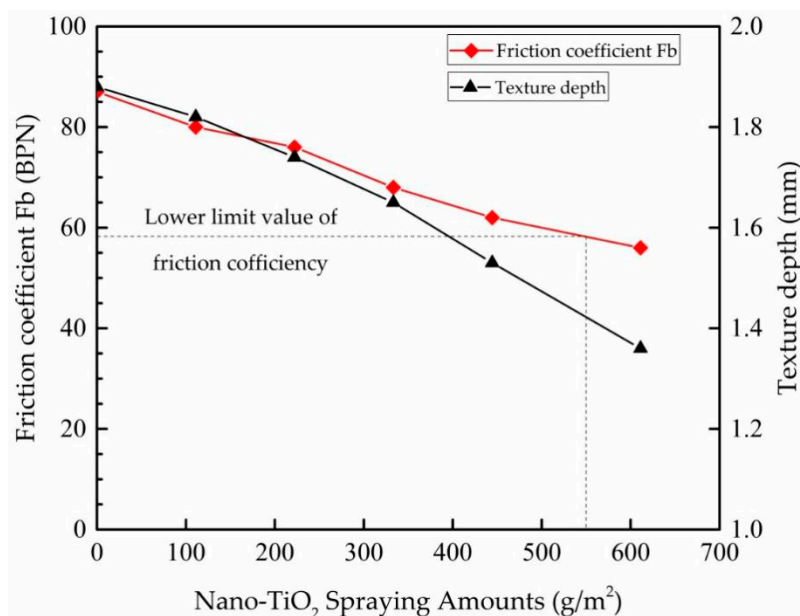


Figure 10. Effect of spraying amount on the skid resistance of asphalt pavement.

It can be seen from Figure 10, both the friction coefficient and the texture depth of the asphalt mixture were reduced with the increase of the spraying amount of photocatalytic coating. It indicated that the skid resistance of the asphalt mixture was decreased due to spraying the nano-TiO<sub>2</sub> photocatalytic coating on the sample surface. When the nano-TiO<sub>2</sub> photocatalytic coating spraying amount was greater than 550 g/m<sup>2</sup>, the friction coefficient was close to the critical lower limit value (58BPN) of the technical requirement in the Chinese Specifications for Design of Highway Asphalt Pavement (JTG D50-2006) [28]. Therefore, it is recommended that the spraying amount of nano-TiO<sub>2</sub> photocatalytic coating should not exceed 550 g/m<sup>2</sup> in practical projects.

### 5.2. Water Permeability

The water permeability of asphalt pavement with different nano-TiO<sub>2</sub> photocatalytic coatings was investigated. The corresponding technical indicator met the requirements of Chinese Technical Specifications for Construction of Highway Asphalt Pavements (JTG F40-2004) [25]. The test results are summarized in Table 13.

Table 13. Effect of spraying amount on permeability of asphalt mixture.

Spraying Amount (g/m <sup>2</sup> )	0	111.1	222.2	333.3	444.4	611.1	Method [24]
Permeability coefficient C <sub>w</sub> (mL/15 s)	>400	>400	>400	>400	>400	>400	T0730

It can be seen from the Table 13 that the water permeability performance of the asphalt mixture was basically not affected by the spraying amount of nano-TiO<sub>2</sub> photocatalytic coating. This was because the amount of photocatalytic coating that was sprayed was so little that it cannot effectively fill the void in the surface of the asphalt mixture. Therefore, the influence of the spraying amount of nano-TiO<sub>2</sub> photocatalytic coating on the water permeability performance of the asphalt pavement can be ignored in practical projects.

## 6. Conclusions

According to the application characteristics of the spraying method, the emulsified asphalt was selected to act as the carrier, and the materials for preparing nano-TiO<sub>2</sub> photocatalytic coating were determined by comprehensive comparison and selection. The test results indicated that the properties

of prepared nano-TiO<sub>2</sub> photocatalytic coating met the Chinese specifications technical requirements. Meanwhile, the color of the coating (seen in Figure 5) was the same as that of the asphalt after setting, having offset the deficiency of different colors between traditional photocatalytic coating and the pavement. Therefore, the coating could be applied directly onto the surface of the pavement using an asphalt distributor, just like fog seal, to play a better role in the degradation of exhaust gas. The coating could be applied to pavement surfaces that are located in densely-populated areas, environmentally-sensitive areas, service areas and parking lots, and so on.

An exhaust gas degradation test device was developed, and its test steps were described in detail. The evaluation indexes, cumulative degradation rate, and degradation efficiency were put forward.

The test results of the performance of exhaust gas degradation of nano-TiO<sub>2</sub> photocatalytic coating showed that, when nano-TiO<sub>2</sub> content was changed in the range from 0–8% and the spraying amount was changed in range from 0–333.3 g/m<sup>2</sup>, the performance of the photocatalytic coating on the degrading exhaust gas was significantly improved with the increase of nano-TiO<sub>2</sub> content and photocatalytic coating spraying amount. When over those dosages, the efficacy of photocatalytic coating was not significantly improved regarding exhaust gas degradation.

In practical projects, the amount of spraying should be controlled strictly because the nano-TiO<sub>2</sub> photocatalytic coating can influence the skid resistance of the asphalt pavement to a certain extent. It is recommended that the spraying amount of nano-TiO<sub>2</sub> photocatalytic coating should not exceed 550 g/m<sup>2</sup>. The nano-TiO<sub>2</sub> photocatalytic coating had little effect on the water permeability performance of asphalt pavement. As such, excessive dosage cannot effectively degrade exhaust gas but thickens the oil membrane, which leads to an inadequate skid resistance of the pavement, which is unsafe and uneconomical. Therefore, 8% nano-TiO<sub>2</sub> in coating and a 400 g/m<sup>2</sup> spraying amount (considering the loss of construction, etc.) were finally chosen to be the optimum parameters based on the photocatalytic properties as well as economic reasons.

**Author Contributions:** H.W. designed the experiment and wrote the manuscript; K.J. and X.D. conducted experiments, analyzed experimental data and wrote the manuscript; S.Z. and C.L. helped conducting tests.

**Funding:** This research was funded by “the National Natural Science Foundation of China, grant number 51478052”, and “Guangdong Transportation Department, grant number 2013-01-002”.

**Conflicts of Interest:** The authors declare no conflict of interest.

## References

1. Zhang, W.G.; Zou, Y.X.; Sun, G.Q. Research on photocatalytic performance influencing factors of asphalt mixture adulterated with TiO<sub>2</sub>. *J. Wuhan Univ. Technol.* **2012**, *34*, 38–41.
2. Li, L.P.; Li, W.B.; Hu, B.Y.; Yu, J.; Ye, F. Photocatalytic Degradation of Tail Gas Pavement Material by Nano-TiO<sub>2</sub> Epoxy Resin. *Sci. Technol. Eng.* **2017**, *17*, 328–333.
3. Poon, C.S.; Cheung, E. No Removal Efficiency of Photocatalytic Paving Blocks Prepared with Recycled Materials. *Constr. Build. Mater.* **2007**, *21*, 1746–1753. [CrossRef]
4. Hassan, M.; Mohammad, L.N.; Dylla, H.; Asadi, S.; Cooper, S., III. Laboratory and Field Evaluation of Sustainable Photocatalytic Asphalt Pavements. *J. Assoc. Asphalt Paving Technol.* **2012**, *81*, 1–20.
5. Binas, V.; Venieri, D.; Kotzias, D.; Kiriakidis, G. Modified TiO<sub>2</sub> based photocatalysts for improved air and health quality. *J. Mater.* **2017**, *13*, 3–16.
6. Mikaeili, F.; Topcu, S.; Jodhani, G.; Gouma, P.I. Flame-Sprayed Pure and Ce-Doped TiO<sub>2</sub> Photocatalysts. *Catalysts* **2018**, *8*, 342. [CrossRef]
7. Petronella, F.; Truppi, A.; Ingrosso, C.; Placido, T.; Striccoli, M.; Curri, M.L.; Agostiano, A.; Comparelli, R. Nanocomposite materials for photocatalytic degradation of pollutants. *Catal. Today* **2017**, *281*, 85–100. [CrossRef]
8. Truppi, A.; Petronella, F.; Placido, T.; Striccoli, M.; Agostiano, A.; Curri, M.; Comparelli, R. Visible-Light-Active TiO<sub>2</sub>-Based Hybrid Nanocatalysts for Environmental Applications. *Catalysts* **2017**, *7*, 100. [CrossRef]

9. Zhao, Y.; Ma, L.; Chang, W.K.; Huang, Z.H.D.; Feng, X.G.; Qi, X.X.; Li, Z.H. Efficient photocatalytic degradation of gaseous N, N-dimethylformamide in tannery waste gas using doubly open-ended Ag/TiO<sub>2</sub> nanotube array membranes. *Appl. Surface Sci.* **2018**, *444*, 610–620. [CrossRef]
10. Deng, A.Q.; Zhu, Y.F.; Gou, X.; Zhou, L.; Jiang, Q.S. Synthesis of Various TiO<sub>2</sub> Micro-/Nano-Structures and Their Photocatalytic Performance. *Materials* **2018**, *11*, 995. [CrossRef] [PubMed]
11. Ali, H.M.; Babar, H.; Shah, T.R.; Sajid, M.U.; Qasim, M.A.; Javed, S. Preparation Techniques of TiO<sub>2</sub> Nanofluids and Challenges: A Review. *Appl. Sci.* **2018**, *8*, 587.
12. Baldauf, R.; Thoma, E.; Hays, M.; Shores, R.; Kinsey, J.; Gullett, B.; Kimbrough, S.; Isakov, V.; Long, T.; Snow, R.; et al. Traffic and meteorological impacts on near-road air quality: Summary of methods and trends from the Raleigh near-road study. *J. Air Waste Manag. Assoc.* **2008**, *58*, 865–878. [CrossRef] [PubMed]
13. Thomas, E.D.; Shores, R.C.; Isakov, V.; Baldauf, R.W. Characterization of near-road pollutant gradients using path-integrated optical remote sensing. *J. Air Waste Manag. Assoc.* **2008**, *58*, 879–890. [CrossRef]
14. Venturini, L.; Bacchi, M. Research, design, and development of a photocatalytic asphalt pavement. In Proceedings of the 2nd International Conference on Environmentally Friendly Roads, Warsaw, Poland, 15–16 October 2009; pp. 1–16.
15. Chen, M.; Liu, Y.H. NO<sub>x</sub> removal from vehicle emissions by functionality surface of asphalt road. *J. Hazard. Mater.* **2010**, *174*, 375–379. [CrossRef] [PubMed]
16. Xu, H.M.; Liu, L.P.; Sun, L.J.; Li, J.F. The application of Nanometer Titanium dioxide in road engineering. *Highw. Eng.* **2011**, *36*, 189–191.
17. Wang, X.X. Degrading Performance Research of OGFC Pavement on Vehicle Exhaust. Master's Thesis, Beijing University of Civil Engineering and Architecture, Beijing, China, 2015.
18. Tan, Y.Q.; Li, L.K.; Wei, P.; Sun, Z.H. Application performance evaluation on material of automobile exhaust degradation in asphalt pavement. *China J. Highw. Transp.* **2010**, *23*, 21–27.
19. Hassan, M.; Mohammad, L.N.; Asadi, S.; Dylla, H.; Cooper, S., III. Sustainable Photocatalytic Asphalt Pavements for Mitigation of Nitrogen Oxide and Sulfur Dioxide Vehicle Emissions. *J. Mater. Civ. Eng.* **2013**, *25*, 365–371. [CrossRef]
20. Hassan, M.M.; Dylla, H.; Asadi, S.; Mohammad, L.N.; Cooper, S. Mohammad; Samuel Cooper. Laboratory. Evaluation of Environmental Performance of Photocatalytic Titanium Dioxide Warm-Mix Asphalt Pavements. *J. Mater. Civ. Eng.* **2012**, *24*, 599–605. [CrossRef]
21. Dylla, H.; Hassan, M.M.; Schmitt, M.; Rupnow, T.; Mohammad, L.N.; Wright, E. Effects of roadway contaminants on titanium dioxide photodegradation of nitrogen oxides. *Transp. Res. Rec.* **2011**, *2240*, 22–29. [CrossRef]
22. Osborn, D.; Hassan, M.; Asadi, S.; White, J.R. Durability Quantification of TiO<sub>2</sub> Surface Coating on Concrete and Asphalt Pavements. *J. Mater. Civ. Eng.* **2014**, *26*, 331–337. [CrossRef]
23. Cros, C.J.; Terpeluk, A.L.; Burris, L.E.; Crain, N.E.; Corsi, R.L.; Juenger, M.C. Effect of weathering and traffic exposure on removal of nitrogen oxides by photocatalytic coatings on roadside concrete structures. *Mater. Struct.* **2014**, *48*, 3159–3171. [CrossRef]
24. *The Chinese Standard Test Methods of Bitumen and Bituminous Mixtures for Highway Engineering*; JTG E20-2011; Renmin Communication Press: Beijing, China, 2011.
25. *The Chinese Technical Specifications for Construction of Highway Asphalt Pavements*; JTG F40-2004; Renmin Communication Press: Beijing, China, 2004.
26. *The Chinese Test Methods of Aggregate for Highway Engineering*; JTG E42-2005; Renmin Communication Press: Beijing, China, 2005.
27. *The Chinese Field Test Methods of Subgrade and Pavement for Highway Engineering*; JTG E60-2008; Renmin Communication Press: Beijing, China, 2008.
28. *The Chinese Specifications for Design of Highway Asphalt Pavement*; JTG D50-2006; Renmin Communication Press: Beijing, China, 2006.







Article

# The Effect of Intermediate Principal Stress on Compressive Strength of Different Cement Content of Cement-Stabilized Macadam and Different Gradation of AC-13 Mixture

Hong-xin Guan <sup>1,2,\*</sup>, Hao-qing Wang <sup>3</sup>, Hao Liu <sup>1,3</sup>, Jia-jun Yan <sup>1,4</sup> and Miao Lin <sup>1,5</sup>

<sup>1</sup> School of Traffic & Transportation Engineering, Changsha University of Science & Technology, Changsha 410114, Hunan, China; crbcluh1@gmail.com (H.L.); yanjiajun229@hotmail.com (J.-j.Y.); m170510015@fzu.edu.cn (M.L.)

<sup>2</sup> State Engineering Laboratory of Highway Maintenance Technology, Changsha University of Science & Technology, Changsha 410114, Hunan, China

<sup>3</sup> China Road & Bridge Corporation, Beijing 100011, China; whqcrb@hotmail.com

<sup>4</sup> Hubei Expressway Business Development Co. Ltd., Wuhan 430050, Hubei, China

<sup>5</sup> School of Civil Engineering, Fuzhou University, Fuzhou 350116, Fujian, China

\* Correspondence: ghx\_cs@csust.edu.cn; Tel.: +86-0731-8525-8249

Received: 17 September 2018; Accepted: 17 October 2018; Published: 22 October 2018

**Abstract:** Since the effect of intermediate principal stress on the strength of pavement materials is not entirely clear so far, a proprietary true triaxial apparatus was developed to simulate the spatial status of principal stresses to conduct compressive strength tests on different gradations of AC-13, different cement contents of cement-stabilized macadam. With the same minimum principal stress, the triaxial compressive strengths of cube specimens under different intermediate principal stresses were compared. The results indicate that, as the intermediate principal stress increases, the compressive strength of the specimen increases and then decreases; different gradations of AC-13 do not show much difference in triaxial compressive strength while different cement contents of cement-stabilized macadam indicate considerable difference. Analysis results suggest significant effect of intermediate principal stress on the compressive strength of pavement materials: for AC-13, the coarser the gradation, the greater the effect of intermediate principal strength on its strength; for cement-stabilized Macadam, the higher the cement content, the greater the effect of intermediate principal stress. Strength model analysis results suggest that Double-Shear-Corner Model is more suitable to characterize cement-stabilized macadam's strength performance compared to the Mohr–Coulomb model and Double-Shear Model.

**Keywords:** intermediate principle stress; compressive strength; true-triaxial; asphalt mixtures; cement stabilized macadam; gradation; cement content

## 1. Introduction

Strength is one of the main indicators for evaluating the mechanical properties of pavement materials. The normal laboratory test methods to evaluate the strength of pavement materials include uniaxial compression test, uniaxial tensile test, Brazilian splitting test, bending test and the conventional triaxial test. However, any point inside a pavement is in a three-dimensional stress state. The conventional triaxial test is very popular because of its complex stress state. However, the intermediate principal stress is always equal to the minimum stress for the conventional triaxial test. It means that the intermediate principal stress effect can't be considered. Therefore, it is necessary to study how the pavement materials' strength can be influenced by intermediate principal stress.



Many researchers have carried out true triaxial tests for materials such as rock, soil, and concrete, which obtained highly significant achievements. For example, Shao-kun carried out the constant water content triaxial tests on Yunnan red clay to study soil-water characteristics and shear strength [1]. The true triaxial test performed by Hang-zhou for joint rock mass shows that the established strength criteria can precisely reflect the strength of the rock mass [2]. Wang carried out biaxial and triaxial tests for mass concrete and put forward the failure criteria of mass concrete in principal stress space and octahedral stress space [3]. Saurav carried out a true triaxial test on cubical sample of plain cement concrete. The results show that the ratio of intermediate and minor principal stress had an incremental effect on the strength of the concrete [4]. Huai-shuai studied the triaxial compressive strength and deformation of air-entrained concrete under freeze-thaw cycles [5]. Rukhaiyar carried out polyaxial tests on cubical specimens of sandstone. The results show that the intermediate principle stress effect can not be ignored, and modified Mohr–Coulomb criterion is suitable for sandstone [6]. Jian-hua conducted a true triaxial test on different materials in the context of new mixed-boundary conditions to identify their stress-strain and strength under triaxial stress [7]. Wei-cheng conducted a true triaxial test on gravel and coarse-grained soil materials and discovered that the rules reflected by the Lade-Duncan criterion is the closest to test results [8,9]. Undrained triaxial and simple shear tests were carried out by Eghbali under the condition of different cement dosages and different stress paths [10]. Triaxial compression tests were carried out by Jia-jia on the high-performance concrete specimens with different mixing proportions [11]. Under conditions of different stress ratios, the triaxial tests on recycled aggregate concrete were carried out by Zhen-jun [12]. By comparing the true triaxial test and the discrete element analysis method, Daraporn studied the effect of different intermediate principal stress ratio on the mechanical properties of granular materials [13]. Triaxial compression tests were carried out by Yang to study the influence of intermediate principal stress ratio  $b$  on the stress-dilatancy relational of coarse granular soil [14]. However, little has been reported regarding true triaxial test on asphalt mixture or cement-stabilized materials. Hong-xin conducted a triaxial compressive strength test on modified asphalt AC-13 mixture with an apparatus allowing triaxial independent loading [15]. Li-jun qualitatively validated the applicability of twin-shear strength for asphalt mixture using a proprietary plane strain apparatus [16]. Lin-bing verified the anisotropy of asphalt mixture through modulus variation during true-triaxial independent loading test [17]. Xin-jiang compared the respective stress–strain curves of maximum, intermediate and minor principal stresses for the true triaxial test on cemented soil [18]. Tuo carried out triaxial tests on hollow cylinder asphalt mixture specimen at tensile-compress and compress–compress state. An octahedral failure criterion was developed for asphalt mixture [19,20]. Qun compared the strength analysis theory with the traditional theory [21].

Compared with the research in the geotechnical field [1–14], despite some research on some pavement materials strength under complex stresses being reported [15–21], it is necessary to study the true triaxial strength of the two most important pavement materials in China more deeply: asphalt mixture and cement-stabilized macadam with respect to, for example, the impact of intermediate principal stress on different gradations of the same type of mixtures. These studies will help to more accurately guide the pavement materials' composition design and even to provide a solution for early cracking of pavements.

In this paper, a true triaxial test will be conducted on different gradations of asphalt mixture and cement-stabilized macadam, using a simple proprietary true triaxial apparatus, to examine the effect of intermediate principal stress on their strengths.

## **2. Test Method**

### *2.1. Test Apparatus*

A simple true triaxial apparatus designed by the project team, consisting of a reactive frame and a hydraulic system, as shown in Figures 1 and 2, was used for the test. The reaction frame serves as

the support while the hydraulic system supplies the power needed. Different from other common triaxial apparatuses, this apparatus can provide triaxial independent loading forces, which allows any compressive stress combination of the three principal stresses.



Figure 1. Self-developed true triaxial test machine.

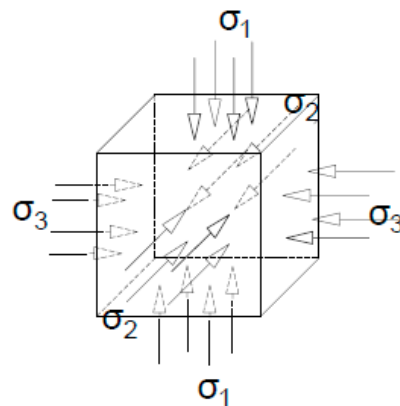


Figure 2. Schematic diagram for loading on specimen.

## 2.2. Test Conditions

### 2.2.1. Test Temperature

For ease of analysis, the compressive stress is assumed as positive while the tensile stress is negative. All sides of the specimen in this paper are pressed, so the stresses on it are all recorded as positive. Under principal stress space state, there are only three mutually perpendicular normal stresses which are also called principal stresses. When the three-way principal stress is sorted from large to small, they are called maximum principal stress, intermediate principal stress and minimum principal stress, respectively, which are represented by  $\sigma_1$ ,  $\sigma_2$  and  $\sigma_3$ , respectively.

Asphalt mixture is closer to brittle solids at low temperature. Compared with the relatively high temperature condition, asphalt mixture's creep effect at low temperature has less influence on its strength. According to the test temperature of Low Temperature Bending Test for asphalt mixture being set at  $-10\text{ }^\circ\text{C}$  in Chinese Specifications, test temperature in this paper was set at  $-10\text{ }^\circ\text{C}$ .

As for cement-stabilized macadam, it is less sensitive to temperature and the recommended test temperature for cement-stabilized materials in relevant test specifications is  $20\text{ }^\circ\text{C}$ , regardless of it being a curing test or an unconfined compressive strength or indirect tensile test. The test temperature was set at  $20\text{ }^\circ\text{C}$  in this paper triaxial compressive strength tests on cement-stabilized macadam.

### 2.2.2. Loading Rate

It is generally known that the strength of the asphalt mixture will increase with the increase of loading rate when all the other conditions are the same. In view of the test specifications for asphalt mixtures in China, abroad and particularly in these tests, the subsequent triaxial strength tests on AC-13 asphalt mixture were conducted at the loading rate of 18 mm/min.

Since Chinese test specifications recommend a loading rate of 1 mm/min for unconfined compressive strength and splitting strength of cement-stabilized macadam, the loading rate of a true-triaxial compressive test on cement-stabilized material was set at 1 mm/min.

### 2.2.3. Loading Path

The proprietary test apparatus features a simple loading path. First, the  $\sigma_3$  and  $\sigma_2$  control values are set. Then, the three principal stresses are loaded synchronously at the same loading rate. When  $\sigma_3$  reaches its predetermined value, it is held while continuing to increase  $\sigma_2$  and  $\sigma_1$ . When  $\sigma_2$  reaches its predetermined value,  $\sigma_3$  and  $\sigma_2$  are held while continuing to increase  $\sigma_1$  until the specimen eventually fails. The failure stress then is  $\sigma_1$ .

### 2.3. Specimen Preparation

Cubic specimens were used in the tests. The asphalt mixture specimen was first rotationally compacted into a  $\Phi 150$  mm, 100 mm-tall cylinder before it was cut by an infrared-ray cutter into an 88 mm  $\times$  88 mm  $\times$  88 mm specimen.

Since there is an optimal content of bituminous in asphalt mixture, only the effects of aggregate gradation will be discussed here. Gradations of asphalt mixture AC-13 used for this test are listed in Table 1. The bituminous type was 70#A class made in China. In Table 1, AC-13F\*, AC-13M and AC-13C means separately fine gradation, median gradation and course gradation within the range of AC-13 gradation [22]. The bitumen aggregate ratio of AC-13F\*, AC-13M and AC-13C is 5.05%, 4.85% and 4.8%, respectively.

**Table 1.** The aggregate passing rate (%) from sieve pore for Asphalt Mixture.

Mixture Type \ Sieve Pore (mm)	16	13.2	9.5	4.75	2.36	1.18	0.6	0.3	0.15	0.075
AC-13F*	100.0	97.3	75.8	61	38.5	23.6	17.3	9.6	5.8	3.7
AC-13M	100	95	76.5	53	37	26.5	19	13.5	10	6
AC-13C	100	97.7	80	53.3	30.4	19.3	14.4	8.5	5.4	4

The cement-stabilized macadam specimens were molded into 15 mm  $\times$  15 mm  $\times$  15 mm specimen with static pressure. After it was prepared, the cube was delivered into a standard curing room and cured for 90 d under the temperature of 20 °C and humidity of 95% as specified by Chinese standard [23].

Since there is not an optimal content of cement for cement-stabilized macadam, and cement usage is often paid more attention, only the effects of cement content will be discussed here. The gradation of cement-stabilized macadam used for this test is listed in Table 2. The cement content for this paper includes 3.5%, 4.5% and 5.5% with the same aggregate gradation.

**Table 2.** The aggregate gradation of cement-stabilized macadam.

Sieve pore (mm)	31.5	19	9.5	4.75	2.36	0.6	0.075
Aggregate passing rate (%)	100	94.9	74.19	28.2	19.2	11.2	1.3

### 3. Effect of Intermediate Principal Stress on the Compressive Strength of Asphalt Mixture

In order to prove the suitability of the test apparatus as shown in Figure 1, compressive strength tests on AC-13C were carried out with the self-developed true triaxial test machine at the condition of  $\sigma_2 = \sigma_3$ , as this stress state is similar to that of conventional triaxial test. The test result is shown in Figure 3. In Figure 3, the Mohr stress circle curve 1–9 was obtained under the condition of  $\sigma_2 = \sigma_3 = 0, 1, 2, 3, 4, 5, 6, 7, 8, 9$  MPa, respectively. The vertical axis is the maximum shear stress and the horizontal axis is the normal stress at the plane of the maximum shear stress.

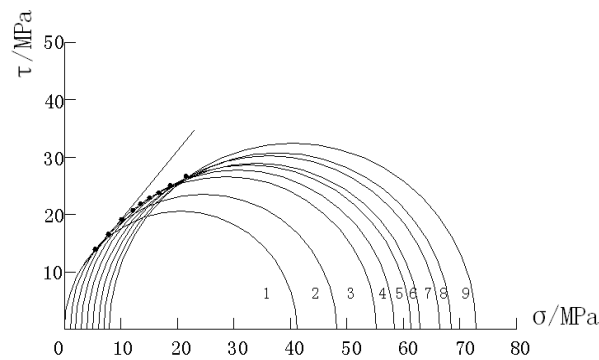


Figure 3. The Mohr stress circles and shear strength envelope of AC-13C.

Figure 3 shows that the shear strength envelope of AC-13C gradually bends as the stress  $\sigma_3$  increases. This changing rule is consistent with the study results of reference [24].

Under the condition that the minimum principal stress  $\sigma_3 = 2$ MPa and  $\sigma_2$  varied between the minimum and the maximum principal stresses, triaxial compressive strength tests were carried out on AC-13 mixture specimens as shown in Table 1. The results are shown in Figures 4 and 5.

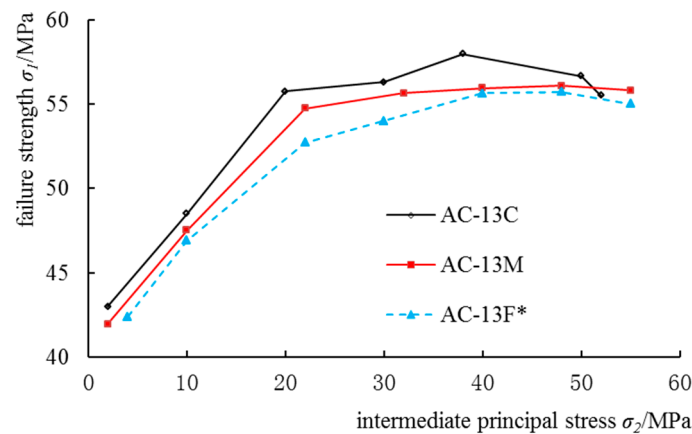


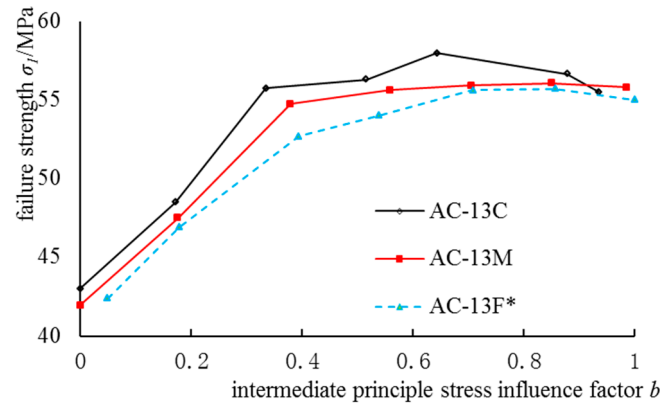
Figure 4. AC-13 triaxial compressive strength changing with intermediate principal stress.

Figure 4 shows that, in case there are compressive stresses in three directions and  $\sigma_3$  is a constant, the strength of the asphalt mixture changes parabolically as the intermediate principal stress increases. This indicates that the intermediate principal stress has an effect on the failure strength of the asphalt mixture, and there is an interval effect involved. In addition, when the asphalt mixture specimen is under the true triaxial conditions, the stresses at all the failure points are higher than the ordinary uniaxial compressive strength, indicating that the existence of the intermediate principal stress can increase the compressive strength of the asphalt mixture dramatically.

To reflect the effect of intermediate principal stress on the failure strength of the materials, an intermediate principal stress influence factor  $b$  was defined as  $b = \frac{\sigma_2 - \sigma_3}{\sigma_1 - \sigma_3}$ . When  $\sigma_2 = \sigma_3$ ,  $b = 0$ ; when  $\sigma_1 = \sigma_2$ ,  $b = 1$ . Under the test condition of  $\sigma_3$  be a constant, if the setting value of  $\sigma_2$  gradually increases

from the value of  $\sigma_3$ , the factor  $b$  can intuitively reflect the level of intermediate principal stress in the three principal stresses.

Based on the test results, a figure was developed to show the impact of the intermediate principal stress factor on the failure strength of AC13 mixture, as shown in Figure 5.



**Figure 5.** Intermediate principle stress influence factor  $b$  vs. strength of different gradation AC-13 mixture.

Figure 5 shows that the effect of intermediate principal stress factor  $b$  on the failure strength of AC-13 mixture also exists, and the failure strength tends to be rising followed by a fall. The three curves are quite similar to each other, which suggest that, for the same type of asphalt mixture, gradation differences do not make much difference to its triaxial strength.

To further reflect how intermediate principal stress affects the strength of different gradations of AC mixture, the intermediate principal stress influence factor at the peak point,  $b_m$ , and the failure stress will be used. If  $b_m$  is small while the failure stress is large, the curve of  $\sigma_2$  arriving at the peak point from  $\sigma_3$  is steep. That is, the steeper the curve, the greater the effect of intermediate principal stress on the failure strength of this gradation of AC mixture.

Table 3 shows the intermediate principal stresses and failure stresses at the peak points of different gradations, and the peak intermediate principal stress influence factor,  $b_m$ , when the minimum principal stress  $\sigma_3 = 2$  MPa.

**Table 3.** Principal stress combination of AC-13 mixtures with different gradation.

Gradation Types	Intermediate Principal Stress Corresponding to Peak Point/MPa	Failure Stress Corresponding to Peak Point/MPa	$b_m$
AC-13F*	40	55.64	0.708
AC-13M	40	55.93	0.705
AC-13C	38	57.96	0.643

From this table, AC-13C mixture’s failure stress is the largest and its intermediate principal stress factor at the peak point is the smallest, suggesting that the curve for the intermediate principal stress  $\sigma_2$  of AC-13C mixture from  $\sigma_2$  to arrive at the peak point is the steepest, i.e., the curve has the largest slope. Hence, a coarser gradation will mean a greater effect of intermediate principal stress on its failure strength.

#### 4. Effect of Intermediate Principal Stress on the Compressive Strength of Cement-Stabilized Macadam

Triaxial tests were carried out with a self-developed true triaxial test machine for cement-stabilized macadam specimens with cement content of 3.5%, 4.5% and 5.5%. In the test, the minimum principal stress was set at  $\sigma_3 = 2$  MPa, 5 MPa and 8 MPa, and  $\sigma_2$  was set between the minimum principal stress and the maximum principal stress.

Based on the test results, a figure was developed to show the failure stresses under different cement contents as shown in Figure 6.

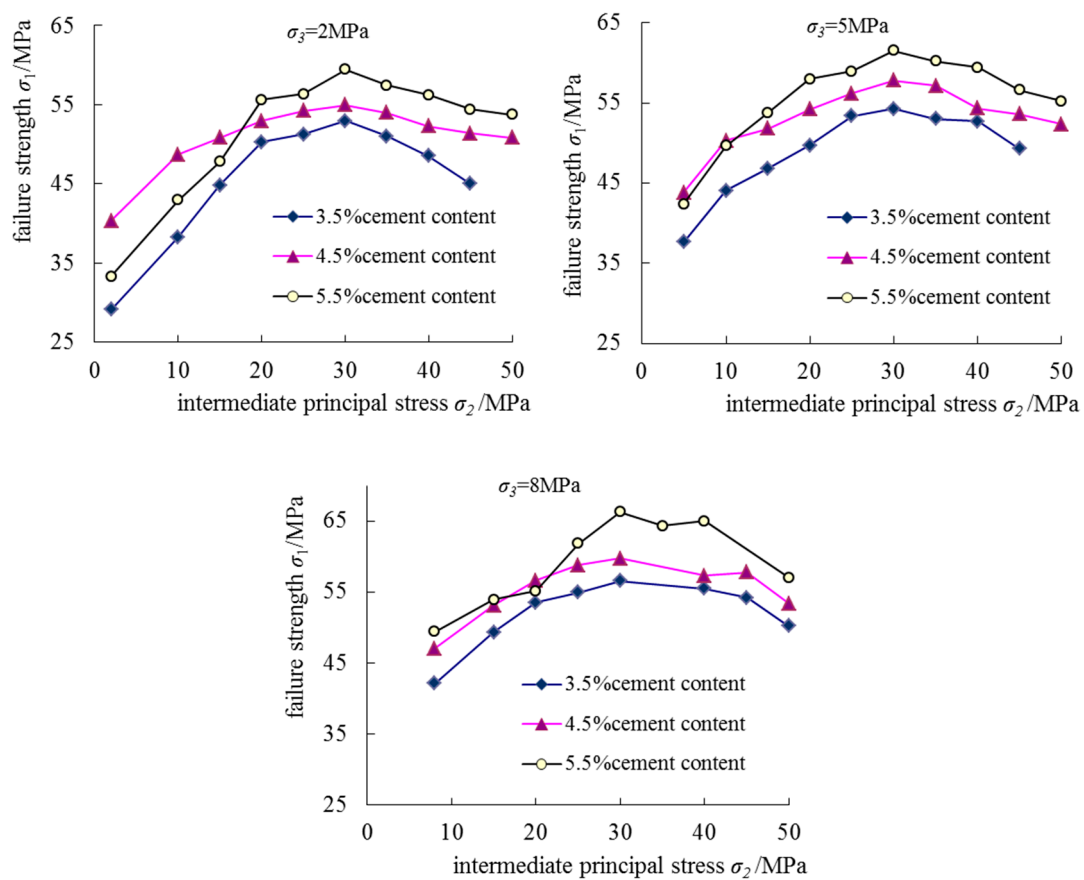


**Figure 6.** The principal stress effect on the cement stabilized macadam strength of different cement dosage.

Figure 6 demonstrates a distinct effect of the intermediate principal stress on the compressive strength of cement-stabilized macadam: as the intermediate principal stress increases, so does the strength of cement-stabilized macadam; after the intermediate principal stress reaches a given level, the strength of the material starts to decrease, suggesting an interval feature of the effect of intermediate principal stress on the strength of cement-stabilized macadam.

Based on the test results above, the impact of the intermediate principal factor,  $b$ , on the failure strength of cement-stabilized macadam was analyzed. The definition of  $b$  is the same as before.

The same as the previous section, the intermediate principal stress influence factor at the peak point,  $b_m$ , was introduced to explain the degree of effect of intermediate principal stress on the failure strength of different content cement-stabilized macadam. Table 4 gives the failure stresses and intermediate principal stresses at peak points and the factor  $b_m$ .

From Figure 6 and Table 4:

- For the same cement-stabilized macadam, the larger the minimum principal stress, the larger the failure strength;
- For the same gradation of cement-stabilized macadam, as a general rule, as the cement content increases, the failure stress at the peak point increases while the intermediate principal stress influence factor at the peak point,  $b_m$ , reduces. This suggests that larger cement content means a greater effect of intermediate principal stress on the strength of cement-stabilized macadam.

**Table 4.** Intermediate principal stress on the compressive strength of cement stabilized macadam.

Cement Content	Minimum Principal Stress/MPa	Peak Intermediate Principle Stress Influence Factor $b_m$	Failure Stress Corresponding to the Peak Point/MPa
5.5%	2	0.49	58.75
	5	0.44	61.38
	8	0.38	65.26
4.5%	2	0.53	54.97
	5	0.47	57.89
	8	0.43	60.58
3.5%	2	0.55	52.79
	5	0.51	54.32
	8	0.45	56.95

### 5. Discussion

All the curves in Figures 3–5 show that the compressive strength of AC-13 and cement-stabilized macadam in a complex stress state is very different to that from the uniaxial compression test. However, uniaxial strength theory is still the mainstream methods to design pavements structure and materials. For example, the stress at one direction of a point in pavements is always calculated to compare with its material’s uniaxial strength, which is used as the failure criteria for pavement design. In fact, any point inside pavements is in a three-dimensional stress state. The stress state is different between the calculating point and uniaxial strength test, which will result in design error. Therefore, more complex strength theory should be introduced to evaluate pavement materials’ performance, such as the strength theory considering all of the three-principal stress.

It has been proved that intermediate principal stress has a great influence on the strength of AC-13 and cement-stabilized macadam. In this section, how to use the results will be discussed. Since the strength model had been developed for AC-13 in Reference [15], only the cement-stabilized macadam’s strength model will be discussed here.

Many scholars have proposed various strength models for engineering materials. Several strength models considering the effect of intermediate principal stress will be discussed on its applicability for cement stabilized macadam at following, which include a Mohr–Coulomb model, Double-Shear-Corner Model and Double-Shear Model.

The coordinate system  $(\sigma_1, \sigma_2, \sigma_3)$  in principal stress space will be converted to a cylindrical coordinate system  $(\xi, r, \theta)$  which includes hydrostatic stress axis  $\xi$  and  $\pi$  plane. A  $\pi$  plane can be determined by  $\xi, \theta$  and  $r$  represents the stress angle and radius vector on a  $\pi$  plane respectively. There is a corresponding limit curve on a  $\pi$  plane, which represents the strength boundary on that  $\pi$  plane. When the value of  $r$  calculating with test data  $(\sigma_1, \sigma_2, \sigma_3)$  is greater than the value  $r(\theta)$  on failure  $(\xi, \theta)$ , it means the structure or material will be in a state of failure.

For comparison purposes,  $r(\theta)$  will be nondimensionalized as follows:

$$g(\theta) = r(\theta)/r(60^\circ), \tag{1}$$

where  $r(\theta)$  is the radius vector on a  $\pi$  plane when stress angle is  $\theta$ , and

$$\text{tg}\theta = \sqrt{3}(\sigma_1 - \sigma_2)/(\sigma_1 + \sigma_2 - 2\sigma_3). \tag{2}$$

Based on the strength data of different cement content cement-stabilized macadam, its  $\theta, r(\theta)$  and  $r(60^\circ)$  can be directly calculated. Then, the limit curve  $g(\theta)$  based on measured data can be obtained. This limit curve  $g(\theta)$  will be compared with strength models. The  $g(\theta)$  of the Mohr–Coulomb model, Double-Shear-Corner Model and the Double-Shear Model will be calculated with test data  $\theta$  according to relevant equations in Reference [25]. The calculating results are shown in Tables 5–7.

**Table 5.** The  $g(\theta)$  on  $\pi$  plane which hydrostatic stress is 34 MPa for 5.5% cement content cement-stabilized macadam.

$g(\theta)$	9.7°	16.9°	19°	27.1°	38.1°	60°
Calculating directly with test data	0.868	0.865	0.830	0.860	0.915	1
Calculation value with Mohr–Coulomb model	0.787	0.775	0.773	0.778	0.810	1
Calculation value with Double Shear Corner Model	0.834	0.850	0.856	0.885	0.933	1
Calculation value with Double Shear Model	0.838	0.863	0.874	0.928	1.048	1

**Table 6.** The  $g(\theta)$  on  $\pi$  plane whose hydrostatic stress is 32.8 MPa for 4.5% cement content cement-stabilized macadam.

$g(\theta)$	6.8°	16.4°	25°	42.8°	60°
Calculating directly with test data	0.918	0.867	0.894	0.981	1
Calculation value with Mohr–Coulomb model	0.803	0.781	0.780	0.837	1
Calculation value with Double Shear Corner Model	0.838	0.856	0.883	0.958	1
Calculation value with Double Shear Model	0.840	0.870	0.921	1.047	1

**Table 7.** The  $g(\theta)$  on  $\pi$  plane whose hydrostatic stress is 30.9 MPa for 3.5% cement content cement-stabilized macadam.

$g(\theta)$	9.9°	14.9°	21.8°	33.1°	60°
Calculating directly with test data	0.959	0.957	0.940	0.942	1
Calculation value with Mohr–Coulomb model	0.893	0.872	0.854	0.852	1
Calculation value with Double Shear Corner Model	0.965	0.968	0.973	0.984	1
Calculation value with Double Shear Model	0.976	0.995	1.036	1.000	1

From Tables 5–7, it can not be found intuitively which model is more suitable to characterize the strength performance of cement-stabilized macadam. Mathematical analysis methods were applied to compare the group data in Tables 5–7. The Residual Sum of Squares Q between  $g(\theta)$  from test data and from three known models was calculated, respectively. Q represents the dispersion degree of the  $g(\theta)$  based on test data from the model curve  $g(\theta)$ . The larger the Q value, the greater the dispersion degree.

It can be observed from Table 8 that the Double-Shear-Corner Model is the most suitable model in the three models to characterize the strength performance of cement-stabilized macadam. Even for a relatively advanced model, the Mohr–Coulomb model, being applied in pavement fields, its application to characterize cement-stabilized macadam’s strength performance will also result in a large error.

**Table 8.** The residual sum of squares between  $g(\theta)$  from test data and from three known models.

Cement-Stabilized Macadam	Known Models	Mohr–Coulomb Model	Double-Shear-Corner Model	Double-Shear-Model
5.5% cement content		0.036	0.003	0.025
4.5% cement content		0.054	0.007	0.011
3.5% cement content		0.027	0.003	0.014

## 6. Conclusions

- (1) True triaxial compression test on different gradations of AC-13 mixture and cement-stabilized macadam indicates that intermediate principal stress has a role to play in the failure strength of pavement materials, and this effect has an interval. That is, as the intermediate principal stress increases, the compressive strength increases first and then reduces.
- (2) Under triaxial compression, the minimum principal stress has influence on the compressive strength of cement-stabilized materials: a larger minimum principal stress will result in a greater compressive strength.



- (3) For AC-13 mixture, gradation differences do not make much difference to its triaxial compressive strength except that a coarser gradation means greater impact of intermediate principal stress on its compressive strength.
- (4) For cement-stabilized macadam, as the cement content increases, the strength at the peak point increases while the intermediate principal stress influence factor,  $b_m$ , reduces, suggesting that intermediate principal stress is more effective on the strength of cement-stabilized macadam with higher cement content.
- (5) Compared with the Mohr–Coulomb model and Double-Shear Model, the Double-Shear-Corner Model is more suitable to characterize a cement-stabilized macadam's strength performance.

This paper only addresses triaxial compressive strength, yet tensile-compressive stresses' combination condition also exists in the pavement structures, and strength tests under more complex stress combinations will be one of the targets for subsequent studies.

**Author Contributions:** H.-x.G. conceived and designed the experiments, H.L. and J.-j.Y. performed the experiments, H.-x.G. and H.-q.W. analyzed the data, and H.-X.G. and M.L. wrote the paper.

**Funding:** This research was funded by the National Natural Science Foundation of China under Grant No. 51408064 and No. 51478052. These supports are gratefully acknowledged.

**Conflicts of Interest:** The authors declare no conflict of interest.

## References

1. Ma, S.K.; Huang, M.S.; Hu, P.; Yang, C. Soil-water characteristics and shear strength in constant water content triaxial tests on Yunnan red clay. *J. Cent. South Univ.* **2013**, *20*, 1412–1419. [CrossRef]
2. Li, H.Z.; Liao, H.J. Anisotropy of Strength of Rock Mass under Complicated Stress State. *Chin. J. Rock Mech. Eng.* **2010**, *29*, 1397–1403.
3. Wang, H.L.; Song, Y.P. Behavior of Mass Concrete under Biaxial Compression-tension and Triaxial Compression-tension. *Mater. Struct.* **2009**, *42*, 241–249. [CrossRef]
4. Rukhaiyar, S.; Sajwan, G.; Samadhiya, N.K. Strength behavior of plain cement concrete subjected to true triaxial compression. *Can. J. Civ. Eng.* **2018**, *45*, 179–196. [CrossRef]
5. Shang, H.S.; Ji, G.J. Mechanical behavior of different types of concrete under multiaxial compression. *Mag. Concr. Res.* **2014**, *66*, 870–876. [CrossRef]
6. Rukhaiyar, S.; Samadhiya, N.K. Strength behaviour of sandstone subjected to polyaxial state of stress. *Int. J. Min. Sci. Technol.* **2017**, *27*, 889–897. [CrossRef]
7. Yin, J.H.; Cheng, C.M.; Kumruzzaman, M.; Zhou, W.H. New Mixed Boundary, True Triaxial Loading Device for Testing Three-dimensional stress-strain- strength Behavior of Geomaterials. *Can. Geotechnol. J.* **2010**, *47*, 1–15. [CrossRef]
8. Shi, W.C.; Zhu, J.G.; Liu, H.L. Influence of Intermediate Principal Stress on Deformation and Strength of Gravel. *Chin. J. Geotech. Eng.*; **2008**, *30*, 1449–1453.
9. Shi, W.C.; Zhu, J.G.; Chiu, C.F.; Liu, H.L. Strength and deformation behavior of coarse-grained soil by true triaxial tests. *J. Cent. South Univ. Technol.* **2010**, *5*, 1095–1102. [CrossRef]
10. Eghbali, A.H.; Fakharian, K. Effect of principal stress rotation in cement-treated sands using triaxial and simple shear tests. *Int. J. Civ. Eng.* **2014**, *12*, 1–14.
11. Jia, Z.J.; Long, P.J.; Ying, L.C.K.; Jin, L.Z. Experimental study on mechanical behavior of high performance concrete under multi-axial compressive stress. *Sci. China Technol. Sci.* **2014**, *57*, 2514–2522.
12. He, Z.J.; Cao, W.L.; Zhang, J.X.; Wang, L. Multiaxial mechanical properties of plain recycled aggregate concrete. *Mag. Concr. Res.* **2015**, *67*, 401–413. [CrossRef]
13. Phusing, D.; Suzuki, K.; Zaman, M. Mechanical Behavior of Granular Materials under Continuously Varying  $b$  Values Using DEM. *Int. J. Geomech.* **2015**, *16*, 1–12. [CrossRef]
14. Xiao, Y.; Liu, H.; Sun, Y.; Liu, H.; Chen, Y. Stress–dilatancy behaviors of coarse granular soils in three-dimensional stress space. *Eng. Geol.* **2015**, *195*, 104–110. [CrossRef]
15. Guan, H.X.; Li, L.Y.; Yang, H.Y. The Intermediate Principal Stress Effect on Asphalt Mixture. *China J. Highway Transp.* **2014**, *27*, 11–16.

16. Suo, L.; Tong, H.; Wang, B. Influence of Intermediate Principal Stress on Asphalt Mixture Strength in Positive Temperature. *J. Chang'an Univ.* **2011**, *31*, 12–16.
17. Wang, L.; Hoyos, L.R.; Wang, J.; Voyiadjis, G.; Abadie, C. Anisotropic Properties of Asphalt Concrete: Characterization and Implications for Pavement Design and Analysis. *J. Mater. Civ. Eng.* **2005**, *17*, 535–543. [CrossRef]
18. Song, X.J.; Xu, H.B.; Wang, Y.L.; Wang, W.; Zhou, A.Z. Study of the Characteristics of Cement-soil Anisotropic Deformation. *Rock Soil Mech.* **2012**, *33*, 1619–1624.
19. Huang, T.; Li, Y.P.; Zheng, J.L. Intermediate principal stress effect and failure criterion of asphalt mixture under triaxial compression state. *J. Cent. South Univ.* **2016**, *47*, 3225–3230.
20. Huang, T.; Chang, Z.D.; Yang, Y. Failure criterion of asphalt mixture in triaxial tension and compression state. *J. Cent. South Univ.* **2017**, *48*, 1908–1914.
21. Yang, Q.; Chen, L.; Wang, P.; Dai, J. New Asphalt Pavement Failure Criterion Based on Unified Strength Theory. *J. Wuhan Univ. Technol.* **2015**, *30*, 528–532. [CrossRef]
22. *Technical Specifications for Construction of Highway Asphalt Pavements*; China Communications Press: Beijing, China, 2004; JTG F40-2004; p. 26.
23. *Test Methods of Materials Stabilized with Inorganic Binders of Highway Engineering*; China Communications Press: Beijing, China, 2009; JTG E51-2009; p. 93.
24. Li, Z.; Zhang, H.; Hou, Y.; Tian, X. Triaxial Test Study on Mechanical Characteristics of Asphalt Concrete in the Core Wall of Earth-rock Fill Dam. *Chin. J. Rock Mech. Eng.* **2006**, *25*, 997–1002.
25. Yu, M.H. *Strength Theories New System: Theories Development and Applying*; Xi'an Jiaotong University Press: Xi'an, China, 2011.



© 2018 by the authors. Licensee MDPI, Basel, Switzerland. This article is an open access article distributed under the terms and conditions of the Creative Commons Attribution (CC BY) license (<http://creativecommons.org/licenses/by/4.0/>).



Article

# Fatigue Performance and Model of Polyacrylonitrile Fiber Reinforced Asphalt Mixture

Hui Wang \*, Zhen Yang, Shihao Zhan, Lei Ding and Ke Jin

School of Transportation Engineering, Changsha University of Science and Technology, Changsha 410004, Hunan, China; yz15084723520@outlook.com (Z.Y.); micro528706637@outlook.com (S.Z.); DL729995231@outlook.com (L.D.); ke15526449298@outlook.com (K.J.)

\* Correspondence: whui@csust.edu.cn; Tel.: +86-139-7318-8915

Received: 1 September 2018; Accepted: 29 September 2018; Published: 3 October 2018

**Abstract:** Fatigue is considered a major pavement structural distress and an important part of a performance-based mix design. Currently, the fatigue model of asphalt mixture, especially the mixture incorporated with fibers, is not perfect. In this paper, the central-point bending fatigue test was conducted by constant strain mode with MTS apparatus. The fatigue performance and model of polyacrylonitrile (PAN) fiber-reinforced asphalt mixture produced with different fiber contents and asphalt contents were reported. The results indicated that the fatigue life of fiber reinforced mixture was higher than the reference one. The effects of fiber contents and asphalt contents on fatigue life were discussed. The mechanism of an optimum fiber content for the fatigue life in the fiber reinforced asphalt mixture was explained. The statistical analysis of variance (ANOVA) method and regression method were used to evaluate the effects of fiber content, strain level, and volumetric parameters, etc. on the fatigue life of an asphalt mixture. This paper presents a new fatigue performance model of a PAN fiber-reinforced asphalt mixture, including the fiber content, tensile strain, mixture initial flexural stiffness, and voids filled with asphalt (VFA). Compared to the earlier fatigue equations, the accuracy of the new fatigue model with the fiber content is improved significantly according to the statistical analysis results. Meanwhile, the model can preferably reveal the effect of fiber content, strain level, initial stiffness, and VFA on fatigue life.

**Keywords:** asphalt mixture; PAN fiber; fatigue performance; fatigue model; loading condition

---

## 1. Introduction

The fatigue resistance of an asphalt mixture refers to its ability to withstand repeated bending without fracture. The fatigue in asphalt pavements mainly appears as cracking on the surface of the pavement. These fatigue cracks are usually a series of interconnecting cracks caused by fatigue failure of the asphalt surface under repeated traffic loading. These tensile cracks caused by repeated flexural stresses propagate and grow continuously. Finally, these cracks are interconnected, forming multi-sided, sharp-angled pieces, which develop a pattern resembling alligator skin. Fatigue cracking is considered one of the main structural distress modes in asphalt pavement. It is also essential to consider the loss of asphalt pavement serviceability in the performance-based design of asphalt mixtures and the structural design of flexible pavements [1,2].

Some reports have revealed that the incorporation of fibers into asphalt mixture can improve the properties of the mixture to some extent [3–6]. Kim et al. [7] concluded that the reinforcing efficiencies of polyester and nylon fibers on the mechanical performance of asphalt concrete increased as the fiber content increased from 0.5% to 1.0%. Xiang et al. [8] found that basalt fiber, whose surface was modified by a silane coupling agent, had good interfacial compatibility with asphalt by the reaction with free silane groups. Morea and Zerbino [9] found that fracture behavior at low to medium temperatures

and rutting behavior was significantly improved by the addition of glass macro fibers and could reduce permanent deformation by up to 50% compared to a mixture without fibers. Klinsky et al. [10] found that pavement overlays with a compound of polypropylene and aramid fiber modified hot mix asphalt can better resist reflective cracking and reduce rutting rate evolution. Yanping et al. [11] investigated the effect of phosphorus slag powder (PSP) and polyester fiber (PF) on the rheological properties of asphalt binder and the mechanical properties of the resultant mixture, and concluded that PSP in combination with PF can provide satisfactory rutting, moisture susceptibility, and low temperature cracking of the resultant mixture. Davar et al. [12] found that the use of basalt fiber in a reinforced mixture with diatomite (which were of a higher stiffness) ended up doubling the fatigue life of the asphalt mixture. In this study, the composite of basalt fiber and diatomite was used to enhance the fatigue life and tensile strength of hot mix asphalt. Dehghanan and Modarres [13] evaluated the fatigue response of polyethylene terephthalate (PET) fiber modified asphalt specimens by a four-point bending test and found that PET fiber increased the fatigue life of hot mix asphalt (HMA) by up to 70%. Badeli et al. [14] found that aramid pulp fiber asphalt mixture had a lower fatigue life at high strain amplitudes (heavy truckloads). Brovelli et al. [15] concluded that the use of 6% and 9% of amorphous polyolefin and a compound of low density polyethylene (LDPE) and ethylene/vinyl acetate (EVA), as well as cellulose and synthetic fibers, could improve the fatigue resistance of asphalt mixture and energetic methods can be effectively applied to data from indirect tensile fatigue tests. Guo et al. [16] evaluated the effects of diatomite and glass fiber on the properties of asphalt mixture using the statistical analysis of variance (ANOVA) method and statistical regression method. They found that diatomite and glass fiber can improve the rutting resistance and fatigue properties of asphalt mixture.

Traditionally, fatigue models are proposed as a result of fitting laboratory test data. The fatigue characteristics are usually represented as relationships between the initial longitudinal stress and strain versus the number of load repetitions to failure. However, accurate description of the fatigue behavior of asphalt mixture is a difficult task due to the complexity of fatigue phenomenon under varying material, loading, and environmental conditions. For the past several decades, significant research efforts have been devoted to the selection of an appropriate laboratory test procedure and developing reliable fatigue models that could be used to predict the fatigue life of HMA pavements. Monismith and Deacon [17] suggested that the controlled-strain mode of loading be approached by asphalt pavements when the thickness of the HMA layer is less than 50 mm (except when the HMA layer is extremely stiff or the base is very weak). The researchers of the University of California Berkeley recommended that the repeated flexural beam (three point loading) fatigue test method under the controlled-strain mode of loading be a relatively simple test, which can best simulate field conditions, compared with various laboratory fatigue tests under the Strategic Highway Research Program (SHRP) Project [18]. Hajj et al. [19] conducted tests to evaluate the fatigue characteristics of HMA, designed using the Superpave volumetric method and Nevada’s Hveem method. Their tests used the flexural beam fatigue test under the strain-controlled mode of loading. The influence of long-term oven aging on the fatigue performance was also evaluated. Shen et al. [20] developed a new fatigue response model based on the dissipated energy equation and the equation correlating the cumulative energy and fatigue life under the same strain level. Zhesheng and Xiaoming [21] conducted five kinds of asphalt mixtures’ fatigue tests on the control strain mode. They concluded that asphalt mixtures’ logarithm fatigue life follows a normal distribution at the same strain level. Meanwhile, the strain level has a linear relationship with the logarithm fatigue life. In the fatigue testing of the control strain mode, when asphalt mixtures modulus is much lower, its fatigue life is much longer.

Based on the phenomenological approach, many fatigue response models have been generalized. For many years, the most commonly accepted model of the fatigue life for a given asphalt mixture can be characterized by the following relationships:

$$N_f = k_1 \left( \frac{1}{\varepsilon_t} \right)^{k_2}, \quad (1)$$

$$\text{or } N_f = k_1 \left( \frac{1}{\sigma_t} \right)^{k_2}, \quad (2)$$

where,  $N_f$  is the fatigue life;  $\varepsilon_t$  or  $\sigma_t$  is the applied tensile strain or stress, respectively; and  $k_1$  and  $k_2$  are experimental coefficients. These relationships were consistently confirmed in the SHRP project for the ranges of stresses and strains to which laboratory specimens were subjected [18].

Monismith et al. [22] suggested introducing the mixture stiffness term to the original form so that the original effects of asphalt mixture could be taken into consideration:

$$N_f = k_1 \left( \frac{1}{\varepsilon_t} \right)^{k_2} \left( \frac{1}{S_0} \right)^{k_3}, \quad (3)$$

where,  $N_f$  is the fatigue life;  $\varepsilon_t$  is the applied tensile strain;  $S_0$  is the mixture initial flexural stiffness; and  $k_1$ ,  $k_2$ , and  $k_3$  are experimental coefficients.

Prior to Monismith's contribution, Pell and Cooper [23] suggested introducing the effect of the volumetric asphalt content ( $V_a$ ) and the air void ( $AV$ ) content to the fatigue performance model of HMA mixtures:

$$N_f = k_1 \left( \frac{1}{\varepsilon_t} \right)^{k_2} \left( \frac{1}{S_0} \right)^{k_3} \left( \frac{V_a}{V_a + AV} \right)^{k_4}, \quad (4)$$

where,  $N_f$  is the fatigue life;  $\varepsilon_t$  is the applied tensile strain;  $S_0$  is the mixture initial flexural stiffness;  $V_a$  is the asphalt content;  $AV$  is the air void content; and  $k_1$ ,  $k_2$ ,  $k_3$ , and  $k_4$  are experimental coefficients. For asphalt mixture, the concept of an improved performance with a reduced air void content and/or increased asphalt content has often been expressed in terms of voids filled with asphalt ( $VFA$ ). Therefore, Equation (4) can also be characterized by:

$$N_f = k_1 \left( \frac{1}{\varepsilon_t} \right)^{k_2} \left( \frac{1}{S_0} \right)^{k_3} VFA^{k_4} \quad (5)$$

Hajj et al. [19] investigated the fatigue characteristics of Superpave and Hveem mixtures. In comparison with Equation (3), they concluded that the accuracy of Equation (4), in which the volumetric term is included, increases significantly.

However, little information is available on the fatigue model of polymer fiber-reinforced asphalt mixtures. None of these studies researched the flexural fatigue behavior of the composite. In this paper, the fatigue property of PAN fiber-reinforced asphalt mixtures is analyzed and a new fatigue equation for PAN fiber-reinforced asphalt mixtures has been generated.

## 2. Materials

The aggregate used in this study was taken from a basalt quarry. It was completely crushed, with the larger particles having an angular shape and rough surface texture. Its basic properties are listed in Table 1. The design gradation of aggregate met the gradations requirements of the AC-16 dense-graded asphalt mixture according to the Chinese Technical Specifications for Construction of Highway Asphalt Pavements (JTG F40-2004) [24]. As shown in Figure 1, a 70# penetration "A" grade asphalt binder was selected. The main physical properties of the asphalt binder were tested following the Chinese Standard Test Methods of Bitumen and Bituminous Mixtures for Highway Engineering (JTG E20-2011) [25]. The results are listed in Table 2. All properties of the aggregate and asphalt comply with the requirements of the Chinese Technical Specifications for Construction of Highway Asphalt Pavements (JTG F40-2004) [24]. A commercially available PAN fiber was used to reinforce the asphalt mixture. The properties of the PAN fiber are presented in Table 3. Moreover, the PAN fibers are shown in Figure 2. In this study, four kinds of PAN fiber contents (0, 0.15%, 0.30%, and 0.45% by weight of the mixture) are used.

Table 1. Basic physical properties of the aggregate.

Test Items	Los Angeles Abrasion (%)	Soundness (%)	Elongated and Flat Particles (%)	Water Absorption (%)	Apparent Specific Gravity
results	17	1.4	8.2	1.27	2.741

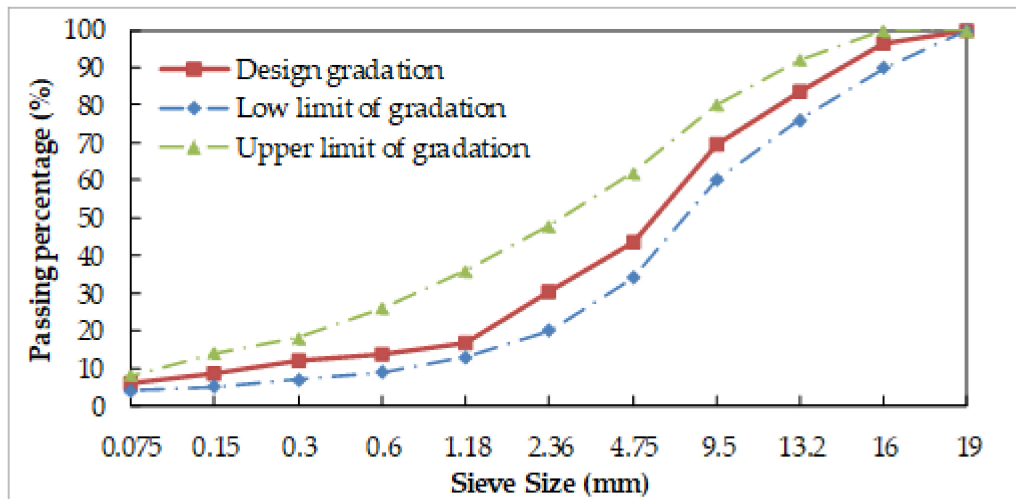


Figure 1. AC-16 aggregate gradation curve.

Table 2. Basic physical properties of the asphalt.

Test Items	Penetration (25 °C, 0.1 mm)	Ductility (15 °C, cm)	Softening Point (°C)	Penetration Index	Viscosity at 60 °C (Pa.s)	Flash Point (°C)
results	65	>100	48	-0.24	271	269

Table 3. The properties of PAN fiber.

Test Items	Diameter (μm)	Length (mm)	Tensile Strength (MPa)	Percentage of Max. Extend (%)	Initial Modulus (MPa)	Density (g/cm <sup>3</sup> )	Section Shape
results	13	6	>910	8-12	17100	1.18	peanut

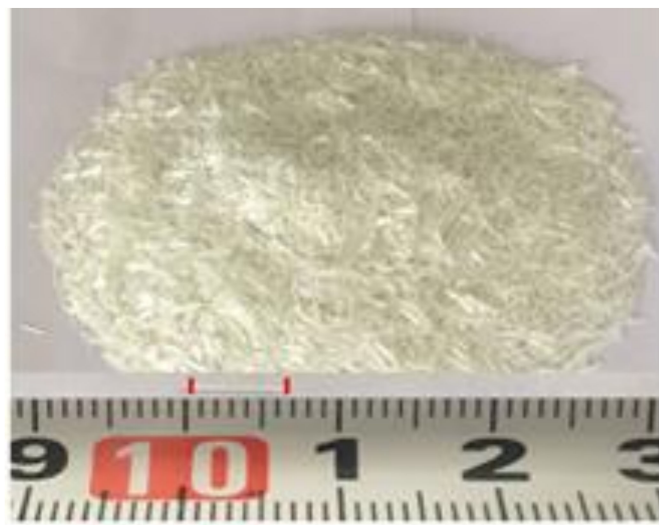


Figure 2. View of PAN fiber.

The Marshall method of mix design was used to determine the optimum asphalt content (OAC) for all kinds of asphalt mixture. The Marshall test results of all mixtures at the OAC are shown in Table 4.

**Table 4.** Results of all of AC-16 mixtures at the optimum asphalt content (OAC) based on the Marshall method.

PAN Fiber Content by Weight (%)	OAC (%)	Air Voids (%)	VMA (%)	VFA (%)	Stability (kN)	Flow (0.1 mm)
0	4.9	4.1	14.2	71.1	10.4	28.7
0.15	5.0	3.9	13.9	71.9	12.7	32.1
0.30	5.1	4.0	14.1	71.6	13.6	30.5
0.45	5.3	4.2	14.1	70.2	14.2	35.9

### 3. Specimen Preparation and Test Procedure

Three asphalt contents (OAC, OAC+0.5%, and OAC−0.5%) and four PAN fiber contents (0, 0.15%, 0.3%, and 0.45% by weight) were used in the experimental design. The mixture was compacted using a roller compactor following the Chinese Standard Test Methods of Bitumen and Bituminous Mixtures for Highway Engineering (JTG E20-2011) [25]. After compaction, the slabs were cut into flexural fatigue beam specimens with dimensions of 50 mm width, 50 mm height, and 250 mm length, as shown in Figure 3. At least three beams were prepared for every strain level. Air voids of flexural beams ranged between  $7 \pm 1\%$ .

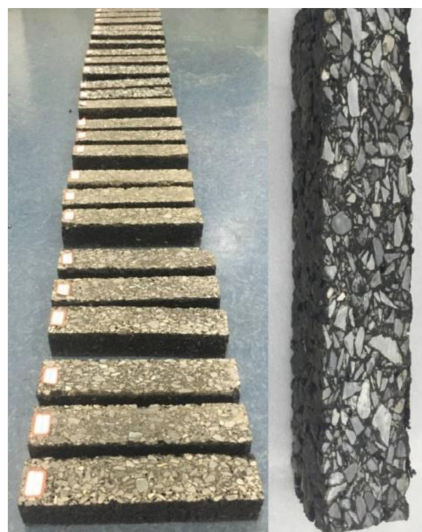


**Figure 3.** Beam-shaped specimens prepared for the fatigue test.

The fatigue tests shown in Figure 4 were performed by using a Mechanical Testing & Simulation (MTS) testing apparatus according to the Chinese Standard Test Methods of Bitumen and Bituminous Mixtures for Highway Engineering (JTG E20-2011) [25]. All fatigue tests were based on the strain-controlled mode of loading. A central-point load and a haversine-shaped wave at a frequency of 10 Hz were used in this study. The span of beam was 200 mm. All specimens were tested at 20 °C. Based on the ultimate flexural tensile-strain, five strain levels (600, 1000, 1500, 2000, and 2500 microstrain) were chosen for the mixture with fibers and four strain levels (600, 1000, 1200, and 1500 microstrain) were chosen for that without fibers.

During the fatigue tests on the strain-controlled mode, the fracture of the flexural beam is not often observed obviously. Therefore, the fatigue life is defined as the number of repetition cycles when the stiffness of the mixture reaches half of its initial stiffness value, taken at the 50th cycle. To minimize



the effect of the variability in the stiffness caused by sample preparation and testing, the average initial stiffness of each mixture was defined as the geometric mean, calculated as follows:

$$S = \sqrt[n]{\prod_{i=1}^n S_i} \tag{6}$$

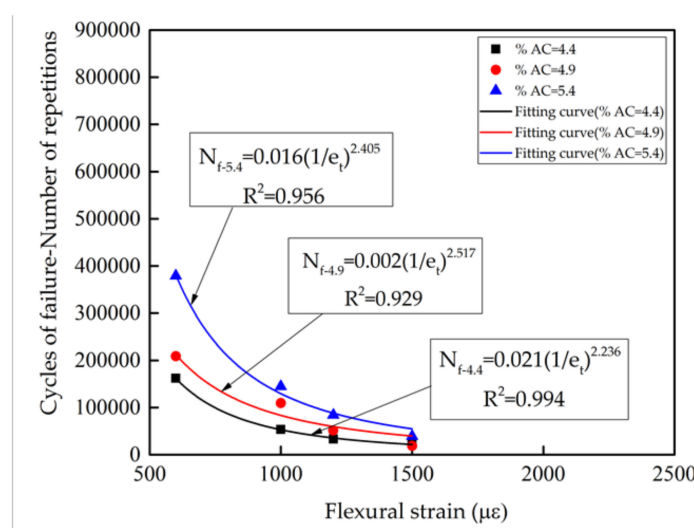
where,  $S$  is the average initial stiffness;  $S_i$  is the specimens' initial stiffness; and  $n$  is number of specimens.



Figure 4. Fatigue test.

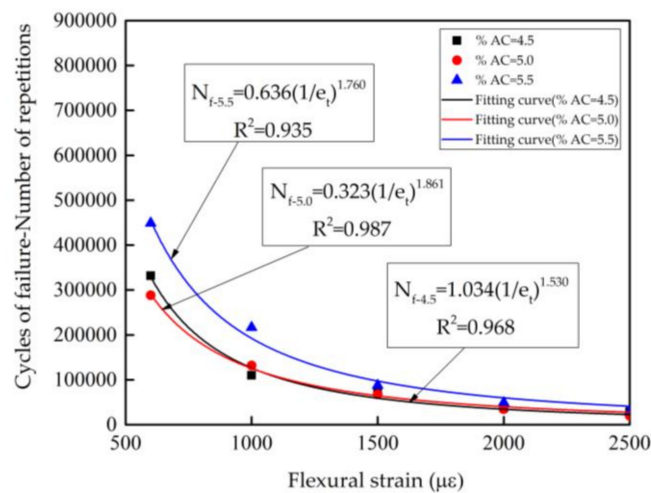
#### 4. Test Results and Discussion

The fatigue test results of the fiber reinforced asphalt mixture with different fiber contents and asphalt contents are shown in Table 5 and Figure 5.

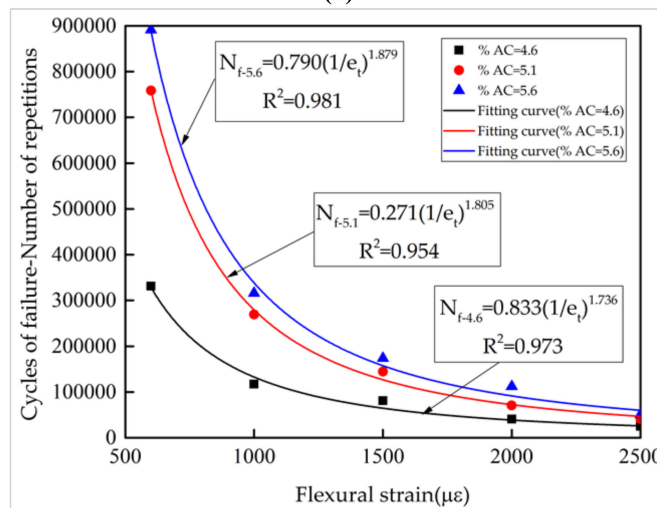


(a)

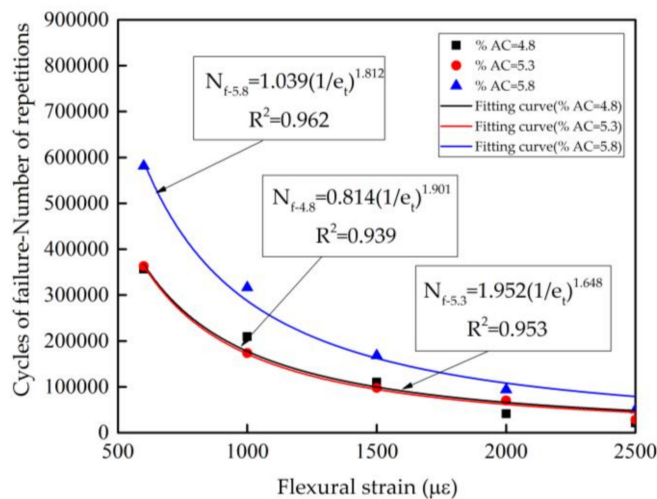
Figure 5. Cont.



(b)



(c)



(d)

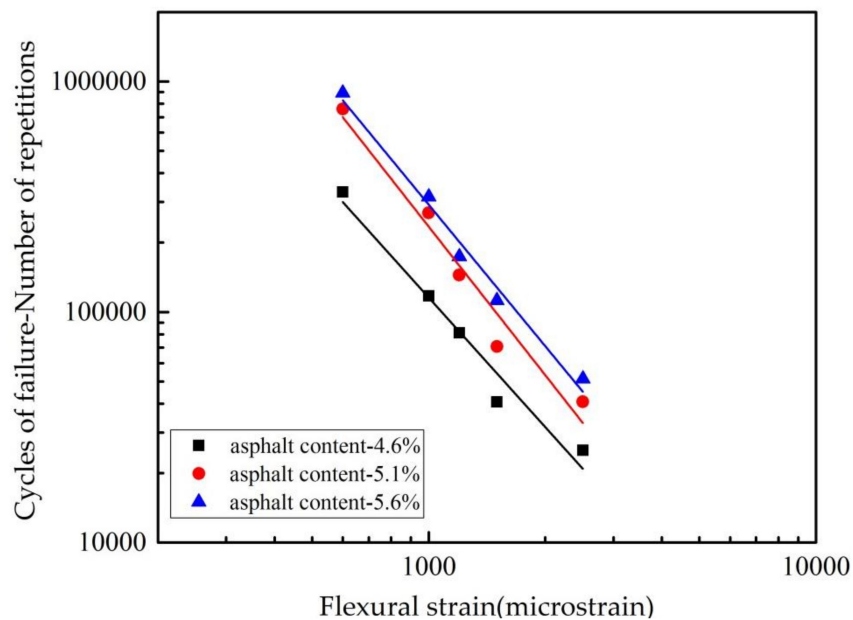
**Figure 5.** Relationship between flexural strain and fatigue life (%AC is asphalt content in figure). (a) Without fiber; (b) 0.15% fiber content; (c) 0.30% fiber content; and (d) 0.45% fiber content.

Table 5. Test results of volumetric parameters and fatigue coefficients.

Fiber Content (%)	Asphalt Content (%)	Volumetric Parameters			Strain Range ( $\mu\epsilon$ )	Fatigue Coefficients <sup>1</sup>		$R^2$ (%)
		Air Void (%)	VMA (%)	VFA (%)		$k_1$	$k_2$	
0	4.4	7.2	16.5	56.4	600–1500	0.021	2.236	99.4
	4.9	6.9	17.9	61.5	600–1500	0.002	2.517	92.9
	5.4	7.5	16.6	54.9	600–1500	0.016	2.405	95.6
0.15	4.5	6.8	17.9	62.1	600–2500	1.034	1.530	96.8
	5	7.1	18.0	60.6	600–2500	0.323	1.861	98.7
	5.5	6.5	18.7	65.3	600–2500	0.636	1.760	93.5
0.3	4.6	6.9	18.4	62.5	600–2500	0.833	1.736	97.3
	5.1	6.7	18.8	64.3	600–2500	0.271	1.805	95.4
	5.6	7.4	18.0	59	600–2500	0.790	1.879	98.1
0.45	4.8	7.2	17.0	57.7	600–2500	0.814	1.901	93.9
	5.3	6.9	17.5	60.5	600–2500	1.952	1.648	95.3
	5.8	6.4	18.5	65.4	600–2500	1.039	1.812	96.2

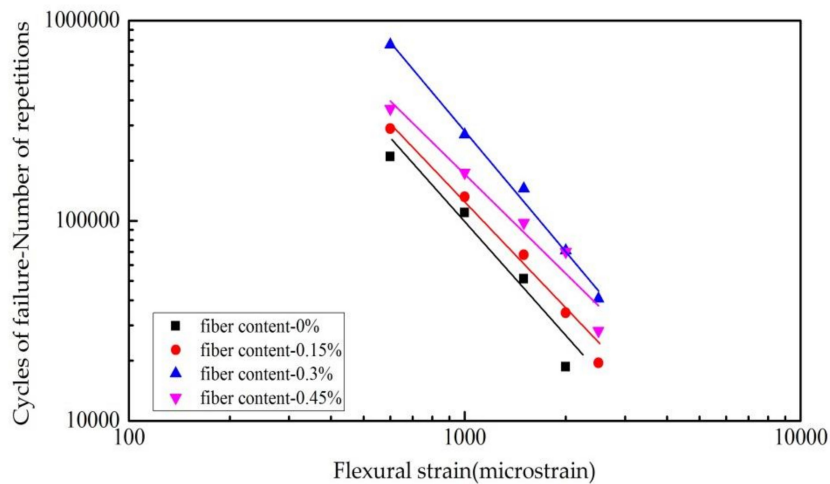
<sup>1</sup> Fatigue coefficients,  $k_1$  and  $k_2$ , are determined by Equation (1).

From Table 5 and Figures 5 and 6, it can be seen that the regression results have shown that the correlation coefficient,  $R^2$ , of each regression equation determined by Equation (1) is quite high. This means that the regression equation fits well. Compared with the mixture with fiber or without, the average value of the fatigue parameter,  $k_2$ , declined by about 25%. It is shown that the fatigue sensitivity to the strain decreased significantly after adding fiber into the mixture. The anti-fatigue ability improved significantly. As seen in Figure 6a, the fatigue performance of the mixture was also improved with the asphalt content increasing at the same fiber content. It also can be seen from Figure 7, in the condition of low strain, that the effect of the fiber content on the fatigue life is more obvious than that in the condition of high strain.



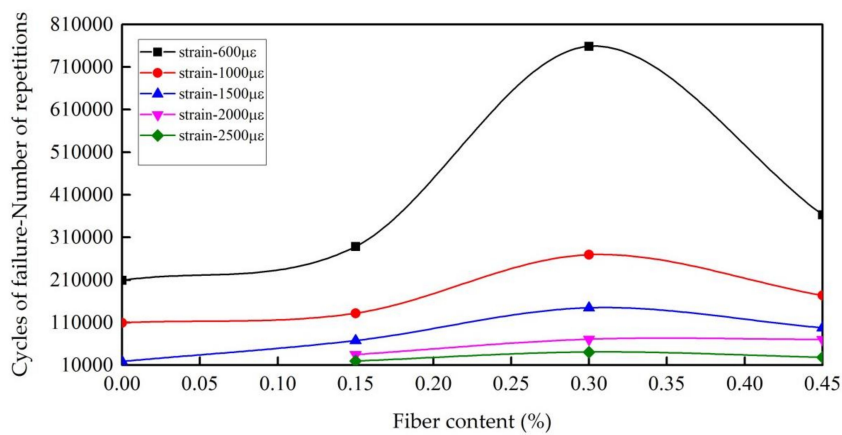
(a)

Figure 6. Cont.



(b)

**Figure 6.** Fatigue properties. (a) Different asphalt contents at 0.3% fiber content; (b) different fiber contents at the optimum asphalt content.



**Figure 7.** Effect of fiber content on fatigue life at the same strain level.

In Figures 6b and 7, the reinforced asphalt mixture obviously has an optimum fiber content for the fatigue life. When the fiber content is less than the optimum level, the fatigue life increases monotonically as the fiber content increases. Once above the optimum level, the fatigue life actually falls as fiber content increases. The potential reasons are:

- As seen from Table 4, the optimum asphalt content of 0.3% fiber content in the asphalt mixture increased by nearly 8% compared to that without fiber. The total surface area of aggregates is basically equal for the same gradation aggregates. This means that the thickness of the asphalt film around aggregates increases by nearly 8%, which is beneficial to the fatigue life of the asphalt mixture;
- On the one hand, the physical and chemical reactions occur on the interface between the asphalt and fiber; on the other hand, the asphalt mortar with a higher viscosity is formed after the addition of fibers. Therefore, the thickness of the structural asphalt film on the aggregate surface and the toughness of the asphalt, as well as the adhesive force to the aggregate, has been increased, which will help to improve the adhesive capacity between the aggregate and asphalt;
- A large number of fibers distributed randomly in three dimensions and evenly formed net-like structures in the mixture, which inhibited the appearance and propagation of cracks, as shown in Figure 8. The healing of cracks of asphalt pavement by themselves is enhanced and the

occurrence of cracks is postponed. The reinforced role is similar to the traditional mortar mixed with short straws;

- With the mixture fiber content increasing, the aforesaid reinforced action will be more frequent and the fatigue life will be improved; and
- It also can be seen from Figure 8c, when the amount of fiber is excessive (above the optimum content), the redundant “free fibers” will appear in the mixture. Those “free fibers” even agglomerate somewhere. These “free fibers” and agglomerated fibers will weaken the cohesion between the asphalt and aggregate. It leads to a decrease of the fatigue life of the mixture.

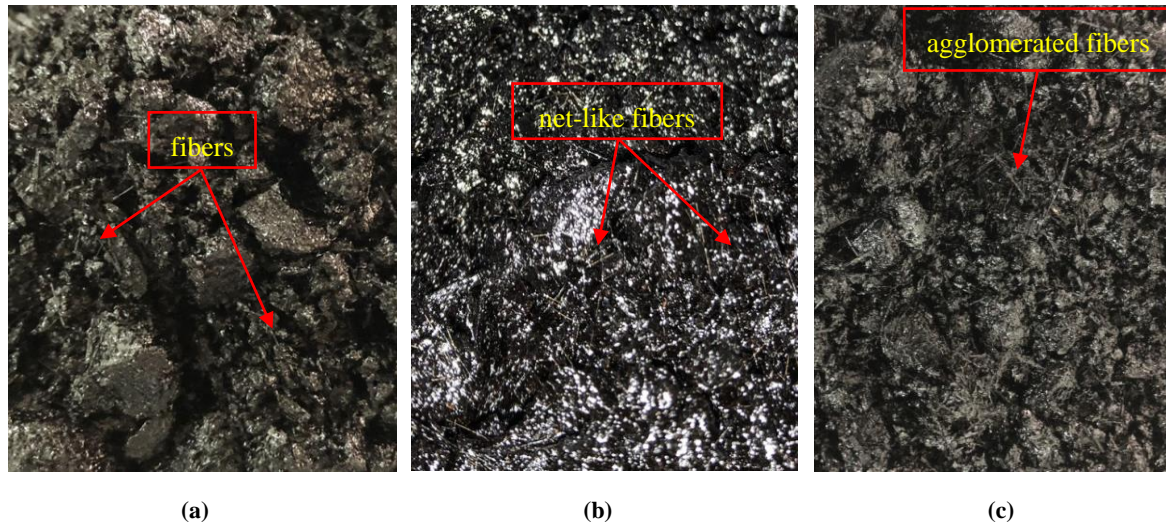


**Figure 8.** Distribution pattern of the fiber in the asphalt mixture. (a) 0.15% fiber content; (b) 0.3% fiber content; and (c) 0.45% fiber content.

## 5. The Fatigue Model of Fiber Reinforced Asphalt Mixture

According to the trial results, it was found that the strain and fiber content have a significant impact on the fatigue properties of the asphalt mixture by using statistical analysis of variance (ANOVA). Besides, the volume parameter, *VFA*, can also influence the fatigue properties of the asphalt mixture. However, the common fatigue models of asphalt mixture do not reflect the influence of fibers on the fatigue life. There exists an optimum fiber content (*OFC*) in the asphalt mixture from the above analysis. Therefore, a variable,  $(1 + 2OFC \cdot FC - FC^2)$ , which can reflect the influence of the fiber on the fatigue life, is introduced. Based on Equation (5), a new fiber reinforced asphalt mixture fatigue equation is developed and characterized by Equation (7). The new model reflected the impact of the strain of loading, initial flexural stiffness of mixture, volumetric parameters, *VFA*, and the fiber content on the fatigue life. By fitting all the test data in this study by multiple nonlinear regressions, the regression coefficients,  $R^2$ , are showed in Table 6. According to the test data, the results of Equations (3) and (5) after fitting are shown in Table 6.

$$N_f = k_1 \left( \frac{1}{\varepsilon_t} \right)^{k_2} \left( \frac{1}{S_0} \right)^{k_3} VFA^{k_4} (1 + 2OFC \cdot FC - FC^2)^{k_5}, \quad (7)$$

where,  $N_f$  is the fatigue life;  $\varepsilon_t$  is the applied tensile strain;  $S_0$  is the mixture initial flexural stiffness; *VFA* is voids filled with asphalt; *FC* is the fiber content; *OFC* is the optimum fiber content; and  $k_1$ ,  $k_2$ ,  $k_3$ ,  $k_4$ , and  $k_5$  are experimental coefficients.

By comparing the correlation coefficient,  $R^2$ , of each regression fatigue equation, it can be concluded that after introducing fiber content into the fatigue equation, the correlation coefficient,  $R^2$ ,

increases from about 81.6% to 95.4%. Therefore, the accuracy of the model (Equation (7)) is significantly improved, which can also be seen from the F statistics in Table 6.

**Table 6.** Regression coefficients and statistical parameters of fatigue equations.

Fatigue Equations	$k_1$	$k_2$	$k_3$	$k_4$	$k_5$	$R^2$ (%)	F Statistic
$N_f = k_1 \left(\frac{1}{\epsilon_t}\right)^{k_2} \left(\frac{1}{S_0}\right)^{k_3} VFA^{k_4} (1 + 2OFC \cdot FC - FC^2)^{k_5}$	$5.437 \times 10^{-4}$	1.746	1.032	2.968	9.931	95.4	254.92
$N_f = k_1 \left(\frac{1}{\epsilon_t}\right)^{k_2} \left(\frac{1}{S_0}\right)^{k_3} VFA^{k_4}$	0.6355	1.369	1.216	3.200	-	81.6	113.73
$N_f = k_1 \left(\frac{1}{\epsilon_t}\right)^{k_2} \left(\frac{1}{S_0}\right)^{k_3}$	$8.563 \times 10^6$	1.598	2.164	-	-	76.5	76.49

From the fatigue models above, it is shown that fatigue life decreases as the strain level and the initial stiffness increase. The fatigue life increases with VFA increasing. It means that increasing the asphalt content and/or reducing air voids would increase the fatigue life. For the fiber content, when the content is less than the optimum fiber content, increasing the fiber content will also lead to an increase of the fatigue life. However, when the fiber content is above the optimum content level, the fatigue life will decline as the fiber content increases.

### 6. Conclusions

By comparing the fatigue test results of the mixture with and without PAN fibers, it was shown that the sensitivity of the fatigue life of the mixture to the strain was decreased significantly after adding fiber. Therefore, adding a proper content PAN fiber in asphalt mixture can significantly improve the anti-fatigue properties. At the same fiber content, the fatigue performance of the mixture was been improved and the fatigue sensitivity declined with an increasing asphalt content. The effect of the fiber content on the fatigue life at a low strain level was more obvious than that in the high strain level.

From a comparison of the asphalt mixture fatigue life with different fiber contents, it was obvious that reinforced asphalt mixture has an optimum fiber content. When the fiber content was less than the optimum fiber content, the fatigue life increased with the fiber content increasing. Once the fiber content exceeded its optimum level, the fatigue life decreased with the fiber content increasing.

By introducing a new variable that can reflect the effects of fiber on the fatigue life, a new fatigue model of fiber reinforced asphalt mixture was generated. Its accuracy has been improved significantly compared to other earlier models. Meanwhile, the model can preferably reveal the effect of the fiber content, strain level, initial stiffness, and VFA on the fatigue life. Fatigue life decreased as the strain level and the stiffness increased, while it increased as VFA increased. For the fiber content, when the content is less than the optimum fiber content, increasing the fiber content will improve the fatigue life; and while over the optimum content, increasing the fiber content will compromise the fatigue life.

**Author Contributions:** H.W. designed the experiment and wrote manuscript; Z.Y. and S.Z. conducted experiments and wrote manuscript; L.D. and K.J. helped analyzing experimental data.

**Funding:** This research was funded by “the National Natural Science Foundation of China, grant number 51478052”, and “Hunan Transportation Department, grant number 201302”, and “Guangdong Transportation Department, grant number 2013-01-002”.

**Conflicts of Interest:** The authors declare no conflict of interest.

### References

1. Pronk, A.C. Comparison of 2 and 4 point fatigue tests and healing in a 4 point dynamic bending test based on the dissipated energy concept. In Proceedings of the 8th International Conference on Asphalt Pavements, Seattle, DC, USA, 10–14 August 1997; pp. 986–994.
2. Zheng, J.; Zhou, Z.; Zhang, Q. *Design Theory and Methodology for Reducing Asphalt Pavement Cracks*; People Communications Press: Beijing, China, 2003; ISBN 7-114-045913.



3. Chen, X.; Li, N.; Hu, C.; Zhang, Z. Mechanical performance of fibers-reinforced asphalt mixture. *J. Chang. Univ. (Nat. Sci. Ed.)* **2004**, *24*, 1–6.
4. Reed, B.F.; James, L.B. Polyester fibers in asphalt paving mixtures. *AAPT* **1996**, *65*, 387–409.
5. Chen, H.; Xu, Q. Experimental study of fibers in stabilizing and reinforcing asphalt binder. *Fuel* **2010**, *89*, 1616–1622. [CrossRef]
6. Ge, Z.; Wang, H.; Zhang, Q.; Xiong, C. Glass fiber reinforced asphalt membrane for interlayer bonding between asphalt overlay and concrete pavement. *Constr. Build. Mater.* **2015**, *101*, 918–925. [CrossRef]
7. Kim, M.-J.; Kim, S.; Yoo, D.-Y.; Shin, H.-O. Enhancing mechanical properties of asphalt concrete using synthetic fibers. *Constr. Build. Mater.* **2018**, *178*, 233–243. [CrossRef]
8. Xiang, Y.; Xie, Y.; Long, G. Effect of basalt fiber surface silane coupling agent coating on fiber-reinforced asphalt From macro-mechanical performance to micro-interfacial mechanism. *Constr. Build. Mater.* **2018**, *179*, 107–116. [CrossRef]
9. Morea, F.; Zerbino, R. Improvement of asphalt mixture performance with glass macro-fibers. *Constr. Build. Mater.* **2018**, *164*, 113–120. [CrossRef]
10. Klinsky, L.M.G.; Kaloush, K.E.; Faria, V.C.; Bardini, V.S.S. Performance characteristics of fiber modified hot mix asphalt. *Constr. Build. Mater.* **2018**, *176*, 747–752. [CrossRef]
11. Sheng, Y.; Zhang, B.; Yan, Y.; Chen, H.; Xiong, R.; Geng, J. Effects of phosphorus slag powder and polyester fiber on performance characteristics of asphalt binders and resultant mixtures. *Constr. Build. Mater.* **2017**, *141*, 289–295. [CrossRef]
12. Davar, A.; Tanzadeh, J.; Fadaee, O. Experimental evaluation of the basalt fibers and diatomite powder compound on enhanced fatigue life and tensile strength of hot mix asphalt at low temperatures. *Constr. Build. Mater.* **2017**, *153*, 238–246. [CrossRef]
13. Dehghan, Z.; Modarres, A. Evaluating the fatigue properties of hot mix asphalt reinforced by recycled PET fibers using 4-point bending test. *Constr. Build. Mater.* **2017**, *139*, 384–393. [CrossRef]
14. Badeli, S.; Carter, A.; Doré, G.; Saliani, S. Evaluation of the durability and the performance of an asphalt mix involving Aramid Pulp Fiber (APF) Complex modulus before and after freeze-thaw cycles, fatigue, and TSRST tests. *Constr. Build. Mater.* **2018**, *174*, 60–71. [CrossRef]
15. Brovelli, C.; Crispino, M.; Pais, J.C.; Pereira, P.A.A. Assessment of Fatigue Resistance of Additivated Asphalt Concrete Incorporating Fibers and Polymers. *J. Mater. Civ. Eng.* **2014**, *26*, 554–558. [CrossRef]
16. Guo, Q.; Li, L.; Cheng, Y.; Jiao, Y.; Xu, C. Laboratory evaluation on performance of diatomite and glass fiber compound modified asphalt mixture. *Mater. Des.* **2015**, *66*, 51–59. [CrossRef]
17. Monismith, C.L.; Deacon, J.A. Fatigue of asphalt paving mixtures. *Transp. Eng. J.* **1969**, *95*, 317–346.
18. Strategic Highway Research Program (SHRP). *Fatigue Response of Asphalt-Aggregate Mixes*; SHRP-A-404; National Research Council: Washington, DC, USA, 1994.
19. Hajj, E.Y.; Sebaaly, P.E.; Weitzel, D. Fatigue characteristics of Superpave and Hveem mixtures. *J. Transp. Eng.* **2005**, *131*, 302–310. [CrossRef]
20. Shen, S.; Carpenter, S.H. Application of the dissipated energy concept in fatigue endurance limit testing. *J. Transp. Res. Board* **2005**, *1929*, 165–173. [CrossRef]
21. Ge, Z.; Huang, X. Study on asphalt mixtures fatigue properties by testing. *J. Traffic Transp. Eng.* **2002**, *2*, 34–37.
22. Monismith, C.L.; Epps, J.A.; Finn, F.N. Improved asphalt mix design. *J. Assoc. Asphalt Paving Technol.* **1985**, *54*, 347–391.
23. Pell, P.S.; Cooper, K.E. The effect of testing and mix variables on the fatigue performance of bituminous materials. *J. Assoc. Asphalt Paving Technol.* **1975**, *44*, 1–37.
24. JTG F40-2004. In *The Chinese Technical Specifications for Construction of Highway Asphalt Pavements*; Renmin Communication Press: Beijing, China, 2004.
25. JTG E20-2011. In *The Chinese Standard Test Methods of Bitumen and Bituminous Mixtures for Highway Engineering*; Renmin Communication Press: Beijing, China, 2011.



Article

# Non-Newtonian Behaviors of Crumb Rubber-Modified Bituminous Binders

Haopeng Wang <sup>1,\*</sup>, Xueyan Liu <sup>1</sup>, Panos Apostolidis <sup>1</sup> and Tom Scarpas <sup>1,2</sup>

<sup>1</sup> Section of Pavement Engineering, Faculty of Civil Engineering and Geosciences, Delft University of Technology, Stevinweg 1, 2628 CN Delft, The Netherlands; x.liu@tudelft.nl (X.L.); p.apostolidis@tudelft.nl (P.A.); a.scarpas@tudelft.nl (T.S.)

<sup>2</sup> Department of Civil Infrastructure and Environmental Engineering, Khalifa University of Science and Technology, Abu Dhabi 127788, UAE

\* Correspondence: haopeng.wang@tudelft.nl; Tel.: +31-(0)625361801

Received: 27 August 2018; Accepted: 26 September 2018; Published: 29 September 2018

**Featured Application:** The evaluation procedure developed in this study can be generalized for characterizing the non-Newtonian behaviors of most modified bituminous binders.

**Abstract:** Crumb rubber-modified bitumen (CRMB) has been utilized in the asphalt paving industry for decades due to its various benefits. The complex interaction between bitumen and crumb rubber as well as the addition of warm-mix additives makes the typical laws of Newtonian fluids insufficient to describe the behaviors of highly modified bituminous binders. To systematically explore the non-Newtonian behaviors of CRMB, a dynamic shear rheometer was utilized to apply shear loading on the samples at various temperatures and shear rates. Results show that the viscosity of different binders are highly temperature- and shear rate-dependent, while highly modified binders exhibit more obvious shear-thinning behaviors at certain temperatures. With the help of zero shear viscosity and yield stress, the shear-thinning behaviors of non-Newtonian binders can be sufficiently characterized. The Arrhenius equation is invalid to describe viscosity-temperature characteristics of bitumen in the non-Newtonian region. A second-order polynomial function was proposed to characterize the viscosity-temperature dependence with a high correlation degree.

**Keywords:** non-Newtonian behavior; viscosity; bitumen; crumb rubber modifier (CRM); warm mix asphalt

---

## 1. Introduction

Bitumen is a complex mix of various hydrocarbons that is produced from the natural deposits or the residue of the crude oil distillation process [1,2]. The complex chemical composition of bitumen determines its various physical and mechanical properties. Bitumen is usually categorized as a viscoelastic material, which means its mechanical behavior is time of loading and temperature dependent. The primary application of bituminous binders is in road construction and other uses include roofing products, sealing and insulating materials. Viscosity, defined as a measure of resistance to deformation or flow, is one of the most important properties of bituminous binders used as paving materials. Profound knowledge of the viscosity of these binders at manufacturing and construction temperatures (generally above 135 °C) provides vital information about their pumpability, mixability and workability [3,4]. Workability can be defined as a property that describes the ease with which hot mix asphalt can be placed, worked by hand, and compacted. The viscosity of bitumen should be controlled within a certain range to facilitate its application in production and construction as well as to guarantee the bitumen grade [5].



Generally, bituminous binders can exhibit Newtonian or non-Newtonian behaviors under different conditions. The dominant characteristic of a Newtonian behavior in simple shear experiments conducted at constant temperature and pressure is the exerted shear stress that is constantly proportional to the applied shear rate. In contrast, any deviation from the Newtonian behavior (i.e., viscosity is dependent on applied shear rate and shear stress) is called non-Newtonian. Non-Newtonian fluids have two main categories: shear-thinning (pseudoplastic) fluids and shear-thickening (dilatant) fluids. Shear thinning is the behavior of fluids whose viscosity decreases with the rate of shear strain while the viscosity increases with the rate of shear strain for shear-thickening fluids. Apart from the applied shear rate, shearing time and temperature also have effects on the non-Newtonian behaviors [6]. Different mathematical equations were developed to describe the flow curves (viscosity measured over a range of shear rates or shear stresses under isothermal conditions) of various products, among them the Cross model, the Carreau model and the Sisko mode which are the modified versions of the Cross model [7]. The temperature dependence of viscosity can be characterized by the William–Landel–Ferry (WLF) function and the Arrhenius-type equation or some empirical equations [8]. However, these equations developed based on different theories have different applicable conditions. Misuse of these equations may result in biased predictions and explanations [9]. This issue will be addressed in the results section.

Practically, two measures of viscosity in asphalt paving industry have been used: absolute viscosity and apparent viscosity [10]. Performing absolute viscosity assumes the material as a Newtonian fluid whose properties are independent of applied shear rate or stress level. Unmodified bituminous binders usually exhibit Newtonian behavior at relatively elevated temperatures (generally above the softening point) or at very low shear rates. However, considering the large service temperature range of these binders or short loading times, their viscosity is not always an absolute value at intermediate and low temperatures. Rather, it varies with the applied shear rate and shear stress. That is why it is an apparent value which needs a well-defined temperature, shear rate and shear stress. For the majority of highly modified bituminous binders, they exhibit obvious non-Newtonian behaviors due to the interaction between the bitumen and the modifier [11]. Apart from the difference among the viscometers and rheometers, the non-Newtonian behavior of some binders (e.g., polymer modified bitumen) is a main reason for the observed measurement difficulties and this subsequently leads to issues in the interpretation and comparison of interlaboratory test results [12]. Therefore, it is necessary to investigate the non-Newtonian behaviors of highly modified bituminous binders and propose universal parameters (e.g., zero shear viscosity) [13] that are independent of applied shear loading instead of merely comparing the apparent viscosity values.

Crumb rubber modified bitumen (CRMB) has been utilized in the asphalt paving industry for decades due to its various benefits. It not only provides an environmental friendly disposal solution to scrap tires, but also improves the overall pavement performance, e.g., higher resistance to rutting, ageing, fatigue and thermal cracking [14]. The increasing use of crumb rubber modifiers (CRMs) in bituminous pavements requires a better understanding of their effects on the chemical, physical and rheological properties of CRM binders so that their processing at the plant can be optimized, their production at the site can be controlled, and their performance in the field can be more accurately predicted [15,16]. It was shown that the interactions of bitumen and rubber and their effects on the final properties of CRMB depend on the raw material parameters (e.g., bitumen composition, CRM type, morphology, particle size and dosage) and interaction conditions (e.g., mixing temperature, time and rate, energy type of the mechanical mixing exerted) [17,18]. Many studies have demonstrated that CRMs improve the rheological properties of base bitumen with evident non-Newtonian behaviors [19,20]. The addition of CRMs into base bitumen dramatically increases the viscosity of the binder, which on the one hand improves the rutting resistance, but on the other hand creates workability issues through pumping, mixing and compaction [21]. The technology of warm mix additives offers promising solutions to the above drawback which can significantly lower the viscosity of binders at mixing and construction temperatures [14,22]. As mentioned before, the neat

bitumen’s viscosity can be measured at 60 °C or higher in the Newtonian region. This statement is of no validity for the CRMB binders. The addition of warm-mix additives further complicates the non-Newtonian behaviors of CRMB.

Based on the above considerations, this study aims to investigate the fundamental non-Newtonian behaviors of CRMB with/without warm-mix additives from the prime parameter in rheology-viscosity. The shear rate dependency of viscosity and temperature effects were investigated with different rheological models.

## 2. Materials and Methods

### 2.1. Materials

Base bitumen of 70/100 penetration grade commonly used in the Netherlands was provided by Nynas (Stockholm, Sweden). The specification of the base bitumen is shown in Table 1 according to EN 12591. The SARA (saturated hydrocarbons, aromatic hydrocarbons, resins, asphaltenes) analysis of base bitumen was done by Iatroscan TLC-FID (Bechenheim, Germany). The four-component proportions are 7% for saturates, 51% for aromatics, 22% for resins, and 20% for asphaltenes, respectively. The ambient grinding CRM from waste truck tires has particle sizes ranging from 0 to 0.5 mm. The gradation of CRM particles is shown in Table 2. The basic properties and composition of CRM are shown in Table 3. The morphology of CRM and base bitumen was obtained through environment scanning electron microscopy (ESEM) in Figure 1. The ESEM images confirmed that rubber particles from ambient grinding have an irregular shape and porous appearance. The surface of bitumen is very smooth and homogenous except for some impurities. This study included two types of non-foaming warm mix additives, the wax-based product W and the chemical-based product C. Additive W is a synthetic microcrystalline wax that is free of sulfur and other impurities. Additive C is a liquid blend of chemicals, such as surfactants and polymers.

**Table 1.** Specifications of Nynas 70/100.

	Test Description	Unit	Value
Consistency at intermediate service temperature	Penetration at 25 °C	mm/10	80
Consistency at elevated service temperature	Softening Point	°C	46
Resistance to hardening at 163°C	Change in mass	%	0.72
	Retained penetration	%	52
	Softening point after hardening	°C	51
Technical characteristic	Density at 25 °C	g/cm <sup>3</sup>	1.027
	Kinematic viscosity at 135 °C	mm <sup>2</sup> /s	265
	Solubility	%	>99.0

**Table 2.** Particle size distribution of crumb rubber modifier (CRM).

Sieves (mm)	Passing (%)
0.710	100
0.500	93
0.355	63
0.180	21
0.125	9
0.063	2

Table 3. Basic properties of CRM.

Properties	Description or Value
Source	Scrap truck tyres
Colour	Black
Morphology	Porous
Specific gravity (kg/L)	1.15
Decomposition temperature (°C)	~200
Total rubber (natural and synthetic)	55
Carbon Black (%)	30
Zinc oxide (%)	1.5
Sulphur (%)	1
Benzene extraction (%)	5.5
Ash content (%)	7

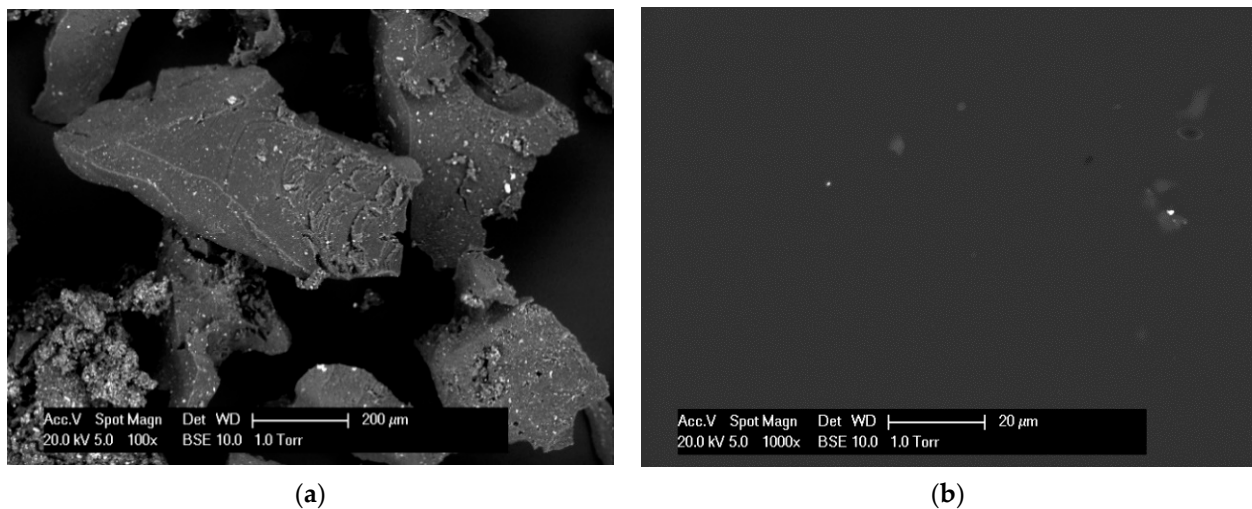
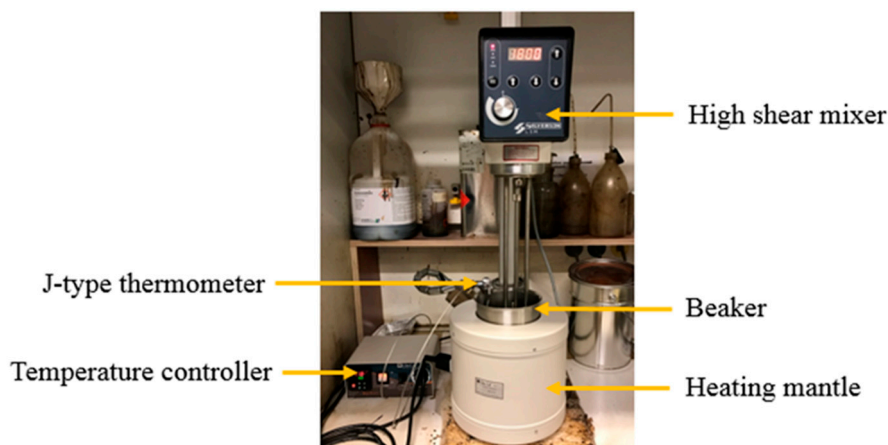


Figure 1. Environment scanning electron microscopy (ESEM) images of (a) CRM and (b) base bitumen.

## 2.2. Binder Preparation

The CRMB was produced in the laboratory by blending 18% CRMs by the weight of the total blend based on the previous studies [23] and trial mixing. Adding more than 18% CRMs will cause mixing problems and undesired binder properties (e.g., extremely high viscosity). Manual stirring for 5 min was applied to pre-distribute CRMs into the base bitumen, then the blend was mixed using a Silverson high shear mixer with a square hole screen (Figure 2) at 180 °C with the shearing speed of 6000 rpm for 30 min. This mixing condition was optimized based on the criteria to obtain better mechanical properties of CRMB. During the bitumen–rubber interaction, there are generally two processes happens: rubber swelling and chemical degradation [24]. Mixing at relatively low temperatures causes inefficient swelling of rubber, while mixing at relatively high temperatures results in severe degradation of rubber particles. Both scenarios are detrimental to the property development of CRMB. During the laboratory mixing process, the mixing head was immersed into the hot bitumen to avoid vortex which may involve the potential oxygen. Each warm mix additive was incorporated into both base bitumen and CRMB with the same dosage at 140 °C. The percentages of additives W and C were 2.0% and 0.6% based on manufacturers’ recommended dosage and preliminary tests. Therefore, a total of six types bituminous binders were prepared in this study, namely 70/100, 70/100-W, 70/100-C, CRMB, CRMB-W, and CRMB-C. To solely investigate the influence of warm mix additives on the rheological properties of binders, all binder samples were tested in fresh states without artificial ageing.



**Figure 2.** Laboratory equipment used to prepare crumb rubber-modified bitumen (CRMB).

### 2.3. Testing Methods

A dynamic shear rheometer (Anton Paar) was utilized to obtain the rheological parameters (complex shear modulus, phase angle and complex viscosity) of different binders following the standard test method. Frequency sweep tests were carried out from 0.01 to 100 rad/s over a temperature range of 10 °C~50 °C with an increment of 10 °C. Before the frequency sweep tests, strain amplitude sweep tests were conducted to identify the linear viscoelastic (LVE) range of different binders and thus to ensure the frequency sweep tests were undertaken within the binder’s LVE region of response. The LVE limit was defined as the point where complex modulus has decreased to 95% of its initial value [25]. Based on the LVE limits, all the measurements were carried out at a strain level of 0.1% under strain-controlled mode. Complex viscosity is defined as complex modulus divided by angular frequency under dynamic conditions. It can be plotted as a function of angular frequency which can be further correlated to shear viscosity as a function of shear rate under steady-state conditions based on the Cox–Merz rule [26].

## 3. Results and Discussion

### 3.1. Influence of Temperature and Shear Rate on Complex Viscosity

Figure 3 plotted the complex viscosity of different bituminous binders as a function of shear rate (angular frequency) at 10 °C and 50 °C respectively. Viscosities at other temperatures showed similar trends between these two cases therefore omitted here. In Figure 3a, the behaviour of binders is non-Newtonian and dependent on frequency and temperature. Figure 3b shows that at 50 °C, base bitumen 70/100 and chemical additive modified bitumen 70/100-C both behave like Newtonian fluids, whose viscosities are almost independent of shear rates. In contrast, 70/100-W and all CRMB based binders exhibit non-Newtonian behaviors as the viscosities increase significantly with the shear rate decreases, which is categorized as the shear-thinning behavior. However, the above statements are of no validity when the testing temperature shifted to 10 °C while all binders exhibit obvious non-Newtonian behaviors as shown in Figure 3a. In addition, it is notable from Figure 3a that although the viscosity of CRMB is higher than that of base bitumen at lower shear rates, it becomes lower when the shear rate reaches 100 rad/s. This is due to the more evident shear-thinning behavior of CRMB, whose mechanism will be explored in the following subsections.

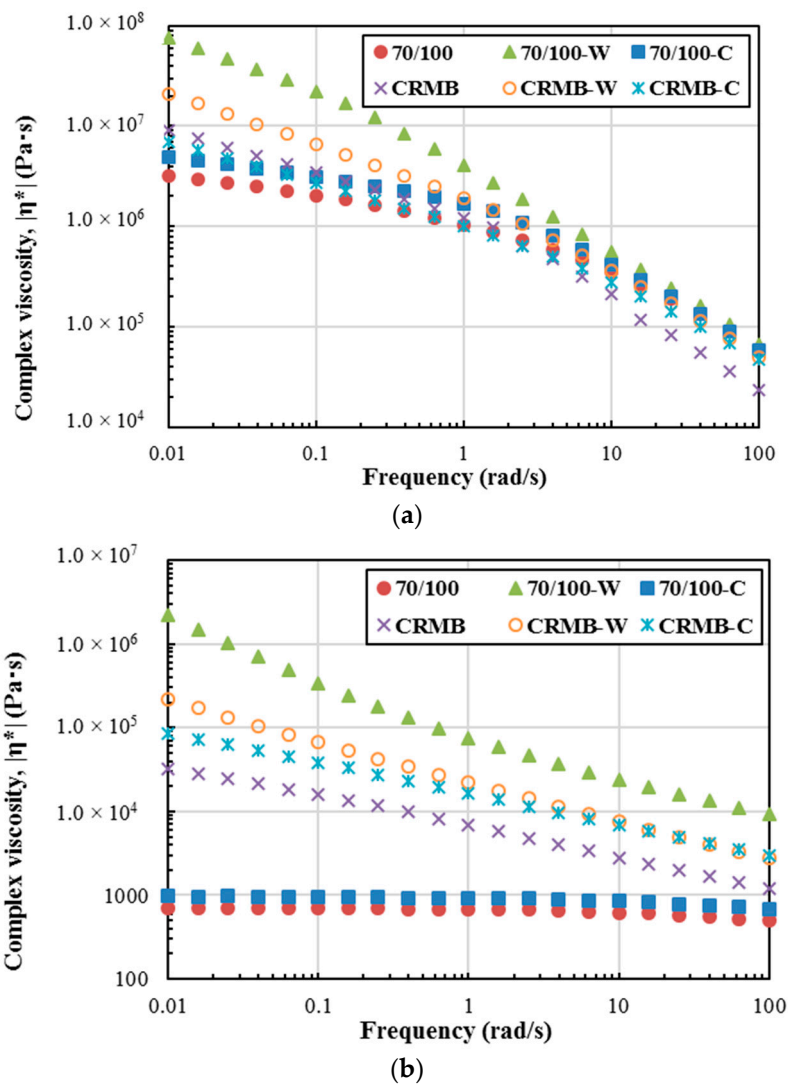


Figure 3. Complex viscosity as a function of shear rate (a) at 10 °C; (b) at 50 °C.

In terms of the warm additives, the addition of chemical additive slightly increases the viscosity of both base and CRMB binders at a certain shear rate. However, organic additive dramatically increases the viscosities of base and CRMB binders, which seems contradictory to the reported viscosity-reduction effect of wax-based additive at high construction temperatures [27]. It should be noted that additive W is a synthetic wax with high molecular hydrocarbon chains ( $C_{40}\sim C_{120}$ ), and its melting point is around 100 °C [28]. Therefore, when tested at 50 °C, additive W exists in bituminous binders as the form of microcrystalline and hence make the binders stiffer. Beyond its melting point, the wax liquefies and can be fully miscible in the binder, which significantly reduces the binder viscosity [29]. Rheological tests at temperatures around 100 °C are recommended to be carried out in the future to verify this conclusion.

### 3.2. Shear-Thinning Behaviors

The previous subsection has shown the shear-thinning behaviors of different bituminous binders at certain temperatures. The occurrence of shear-thinning in non-Newtonian fluids can be attributed to the changes in particle/molecular orientations and/or alignment in the direction of flow. Specifically, there are three types of mechanisms as shown in Figure 4 can explain the complex shear-thinning behaviors of the unmodified and modified binders [6]. For polymer solutions or melts, polymer entanglements or coils are formed in the polymer network at rest. When the polymer solution/melts are

subjected to shear loading, the entanglements or coils will unfold and align with the applied shear force, which in turn makes the polymer network easy to deform as shown in Figure 4a. For suspensions, solid particles in the liquid are prone to agglomerate at rest. With the applied shear loading, agglomerates tend to break up and disseminate into the matrix as shown in Figure 4b. For colloidal dispersions, when particles are introduced into a liquid at rest, they are randomly oriented to reach a thermodynamic equilibrium state (disordered state). With the applied shear force, particles will try to align themselves to the shear direction as shown in Figure 4c. In all cases, materials in a disordered state at rest will shift to an orientational ordered state with applied shear, which corresponds to a shift from high viscosity to low viscosity. This means shear-thinning behavior is an entropy-decreasing process [30,31]. Bitumen is commonly recognized as a multi-disperse colloidal system, where high molecular weight asphaltene micelles are peptized by resins in low molecular weight maltenes. For base bitumen, the asphaltene can be regarded as particles which are randomly oriented in the maltenes and have the tendency to aggregate at rest. When the bitumen is subjected to shear loading at certain temperatures, the asphaltenes which contribute mainly to the viscosity will tend to an orientational ordered state in the maltenes. Therefore, shear-thinning happens. A similar explanation which regards wax as solid particles can be applied for the shear-thinning behavior of wax-modified bitumen. In terms of rubber modified bitumen, the potential polymer entangled network formed in the bitumen microstructure due to the rubber-bitumen interaction will unfold and stretch itself to adjust with the applied shear forces. The other two types of shear-thinning mechanism may also exist in CRMB. For the rest bituminous binders, a combination of these three types of mechanism will be capable to explain the shear-thinning behavior.

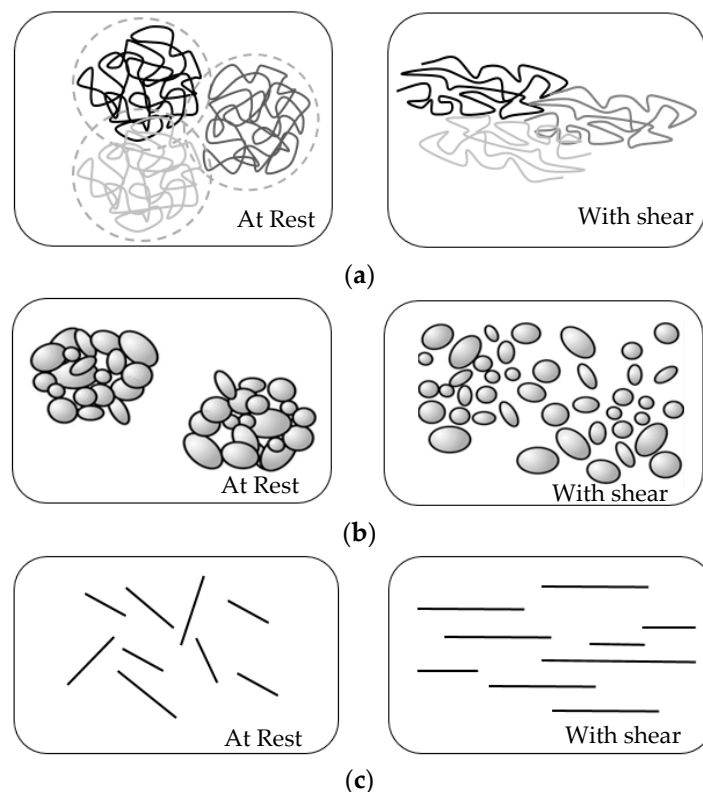


**Figure 4.** Schematic representation of shear-thinning mechanisms (a) polymer solutions/melts; (b) suspensions; (c) dispersions, adapted from [6].

### 3.3. Zero Shear Viscosity

Since bitumen viscosity at relatively low temperatures is highly shear rate dependent, directly comparing the viscosity value at a certain shear rate seems quite tedious. A parameter describing

the viscosity that independent of shear rate is plausible. At very low shear rates, Brownian motion dominates and causes all molecules or particles to be oriented randomly despite the initial effects of any applied shear stress. Under this circumstance, structured liquids behave similarly to Newtonian liquids, with a defined viscosity independent of shear rate or angular frequency. This viscosity, measured in the shear deformation when the shear rate approaches zero, is called zero shear viscosity (ZSV). ZSV is reported to be a good indicator of rutting resistance of bituminous binders [32]. Various methods were proposed to estimate the theoretical ZSV value [13]. In this study, data obtained from the frequency sweep tests were applied to the Cross model to determine the ZSV. The Cross model defined in the form of a four-parameter equation (Equation (1)) was able to fit the flow behavior of binders over a wide range of shear rates.

$$|\eta^*| = \frac{\eta_0 - \eta_\infty}{1 + (K\omega)^m} + \eta_\infty \tag{1}$$

in which  $\eta^*$  is the complex viscosity;  $\eta_0$  is ZSV or the first Newtonian region viscosity;  $\eta_\infty$  is infinite shear viscosity in the second Newtonian region;  $\omega$  is angular frequency (rad/s);  $K$  is a material parameter with the dimension of time; and  $m$  is a dimensionless material parameter. In the frequency range tested in this study, it is reasonable to assume that  $\eta^* \gg \eta_\infty$ . Therefore, the Cross model reduces to a three-parameter equation as shown in Equation (2).

$$|\eta^*| = \frac{\eta_0}{1 + (K\omega)^m} \tag{2}$$

Non-linear regression analysis was used to estimate ZSV at 50 °C with the available data. The measured viscosity and the model predicted results are plotted in Figure 5. The complex viscosities of two binders containing wax additives did not approach a plateau when the shear rate approaches zero. This was observed through the model fitting results that the solver to the solution of binder 70/100-W and CRMB-W cannot converge with defined constraints and convergence. Therefore, there are no practical ZSV values for these two binders. ZSV values and corresponding model parameters for the other four binders are summarized in Table 4. ZSV of CRMB is much higher than the base bitumen 70/100, which indicates superior high-temperature rutting resistance. Besides, ZSV also reveals the molecular weight of binders [6]. CRMB with higher ZSV possesses higher molecular weight than base bitumen due to the rubber-bitumen interaction. Both natural rubber and synthetic rubber in CRMs are macromolecules with much higher molecular weight than bitumen [33]. The formed polymer network within the bitumen matrix after rubber-bitumen interaction increases the viscosity and molecular weight of binder [34]. The addition of chemical additives increases the ZSV of both binders. From the definition of the Cross model, it can be noted that parameter  $m$  is related to shear susceptibility. Based on the data in Table 4, it is inferred that the rheological behavior of a binder with smaller  $m$  is closer to Newtonian behavior. Furthermore, the level of non-Newtonian behavior is reflected in parameter  $K$ . The higher value  $K$  is, the higher level of non-Newtonian behavior the binder has.

**Table 4.** Zero shear viscosity (ZSV) fitting results using the Cross model.

Binder Type	70/100	70/100-C	CRMB	CRMB-C
$\eta_0$ (Pa·s)	1377	1848	$1.2 \times 10^5$	$3.55 \times 10^5$
$K$ (s)	4.31	3.10	1191.18	2144.81
$m$	0.0644	0.0639	0.3951	0.3924

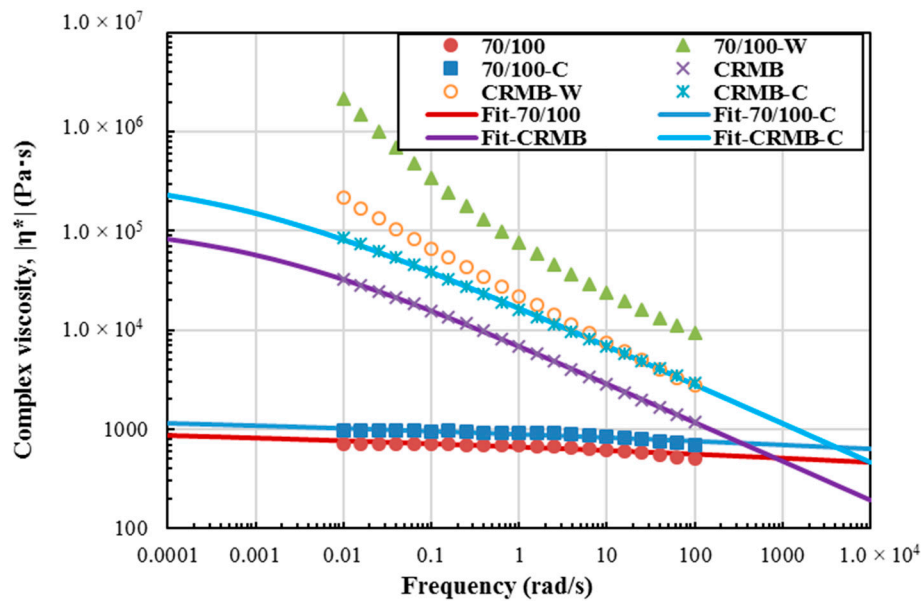


Figure 5. Measured and model predicted viscosity values for different binders at 50 °C.

### 3.4. Yield Stress

As observed in previous subsection, bituminous binders modified by wax additives do not show a practical or show an infinite viscosity approaching zero shear rate. The reason for this special non-Newtonian behavior can be attributed to the yield stress characteristic which is a property associated with numerous types of complex fluids. For example, paint can only flow with the help of brush, but remains fixed on a vertical wall despite the force of its own gravity. The yield stress is defined as a critical stress that must be applied to the material before flow or continuous deformation is observed [7]. Below the yield stress, the solid-like bituminous binder will deform elastically which results from elastic elements being stretched in the shear field. Above the yield stress, such elastic elements begin to break down causing shear-thinning behaviors and consequent flow. Although many researchers have doubt about whether the true yield stress exists [35], the concept of yield stress, if defined properly, is very useful in a whole range of applications, such as stirring, mixing and pumping.

To determinate the yield stress of the wax-modified bituminous binders, the Herschel–Bulkley model was applied to fit the measured data (shear stress versus shear rate) and extrapolate to a zero-shear rate. The Herschel–Bulkley model [7] describes non-Newtonian behavior after yielding and is basically composed of a power law model with a yield stress term as shown in Equation (3):

$$\sigma = \sigma_y + K\omega^n \quad (3)$$

In Equation (3) above  $\sigma$  is the shear stress;  $\sigma_y$  is the yield stress;  $K$  is the consistency; and  $n$  is the flow behavior index. The parameter  $n$  describes the material as shear thinning when  $n < 1$ , or shear thickening when  $n > 1$ , or Newtonian when  $n = 1$ .

The yield stress determined through the Herschel–Bulkley model was shown in Figure 6. As analyzed before, for bituminous binders having practical ZSV do not have a yield stress. This is also verified in Figure 6a as the fitted equations do not have the yield stress term. The yield stresses of wax modified binder 70/100-W and CRMB-W are clearly plotted in Figure 6b with the values of 190.60 Pa and 4.22 Pa, respectively. The significant difference between the yield stresses shows additive W has different extents of effect on the base bitumen and CRMB. This is possibly due to the different microstructures of these two binders which stem from the potentially complex interaction between bitumen, rubber and warm mix additives. Generally, larger yield stress indicates more stable internal structure of the material [35]. The yield stress brings both positive and negative effects to the material



depending on the application conditions. For instance, higher yield stress can be a hindrance if the binder is being pumped or mixed while it will benefit the binder making it more stable during the service stage on the pavement. One also should note that the predicted yield stress is highly dependent on the instrument resolution, measuring conditions and analysis method.

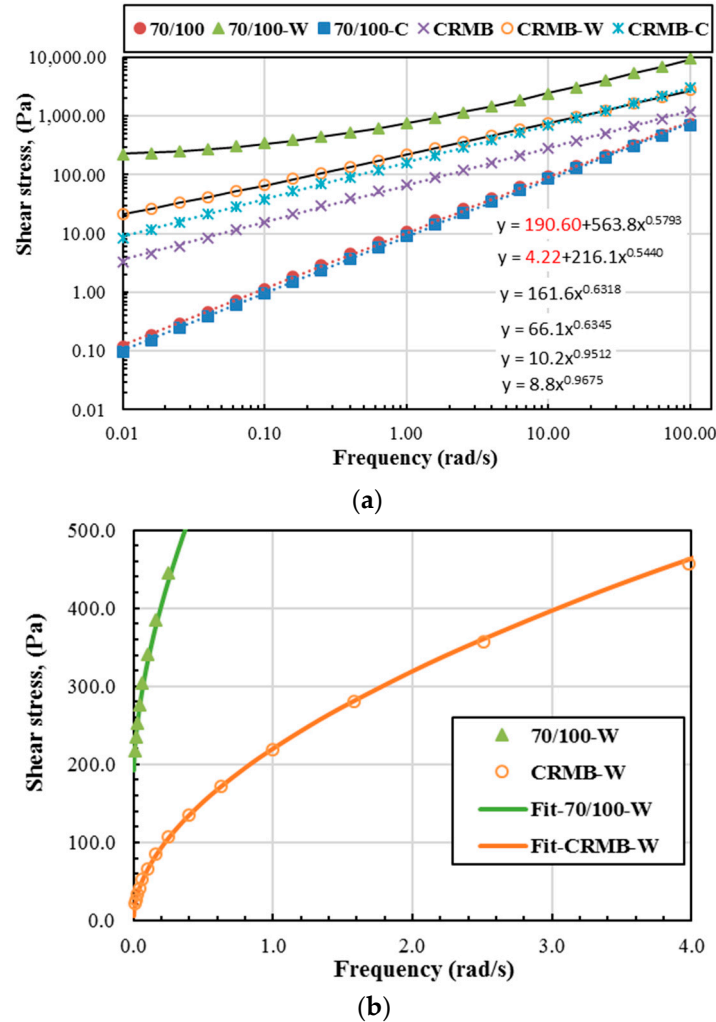


Figure 6. Yield stress calculation of different binders at 50 °C (a) entire curve; (b) partial curve.

### 3.5. Complex Viscosity as a Function of Temperature

The viscosity of bituminous binders is highly temperature-dependent. Generally, there are two common equations to evaluate the viscosity-temperature characteristics of binders, namely the William–Landel–Ferry (WLF) function based on the free volume theory and the Arrhenius-type equation based on the absolute theory of reaction rate [36]. These two equations correspond to two temperature regions. At temperatures well above the glass transition temperature  $T_g$ , i.e.,  $T_g + 100$  °C or  $\sim 1.3T_g$ , the viscosity follows the Arrhenius equation:

$$\eta^* = Ae^{\frac{E_a}{RT}} \quad (4)$$

where  $A$  is a pre-exponential parameter;  $R$  is the universal gas constant (8.314 J/(mol.K)); and  $E_a$  is the flow activation energy (J/mol).  $T$  is temperature (K). At lower temperatures ranging from  $T_g$  to

$T_g + 100$  °C, the WLF function should be used instead. A strictly equivalent form to the WLF function is described by the Vogel-Fulcher-Tammann (VFT) expression:

$$\eta^* = A_0 e^{\frac{E_0}{R(T-T_0)}} \tag{5}$$

where  $A_0$ ,  $E_0$ , and  $T_0$  are material constants. Apart from these two common equations, a number of empirical expressions have been proposed to represent the viscosity-temperature dependence based on available experimental data. The proposed equations of viscosity-temperature characteristics have the following general form [8,37]:

$$\ln \eta^* = A + \frac{B}{T+C} + a \ln T + bT + cT^2 + \frac{D}{T^2} \tag{6}$$

where  $A$ ,  $B$ ,  $C$ ,  $D$ ,  $a$ ,  $b$ ,  $c$  are fitting constants. It is possible to add more power-law terms of  $T$  into the above empirical equation.

Figure 7 presents the plot of logarithmic viscosity as a function of the reciprocal of temperature ranging from 283.15 K to 323.15 K at two extreme shear rates. At a low shear rate of 0.01 rad/s, the viscosity-temperature curve can be fitted by a linear line, which is an Arrhenius-type equation. The reason that Arrhenius equation requires elevated-temperature condition is to guarantee the material is in the Newtonian state. Based on the time-temperature superposition principle as well as the test results in this study, bituminous binders can be regarded as Newtonian-like fluids at a low shear rate of 0.01 rad/s, so that Arrhenius equation is applicable. However, this observation is invalid at a high shear rate of 100 rad/s, under which bituminous binders exhibit apparent non-Newtonian behaviors. The viscosity-temperature curve at the higher shear rate of 100 rad/s can be fitted by a second-order polynomial equation with enough high correlation degree instead of a linear one. Based on the above findings, it is not reasonable to fit the viscosity-temperature curve with only an Arrhenius equation over a wide range of temperatures or shear rates.

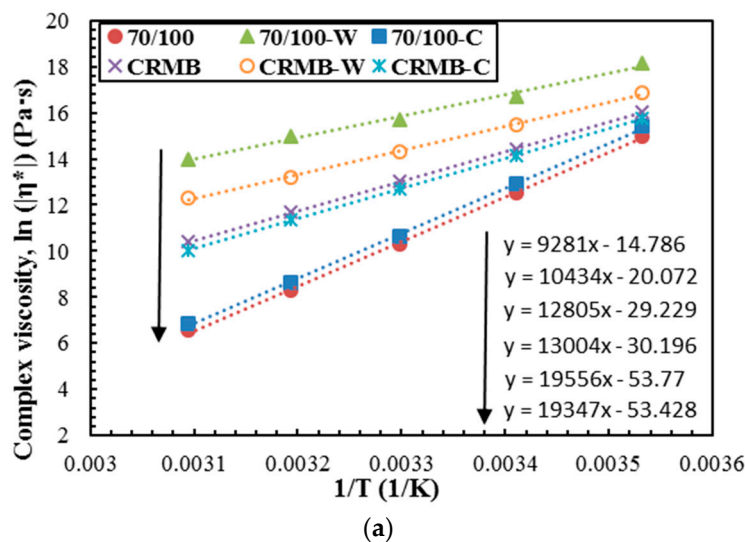
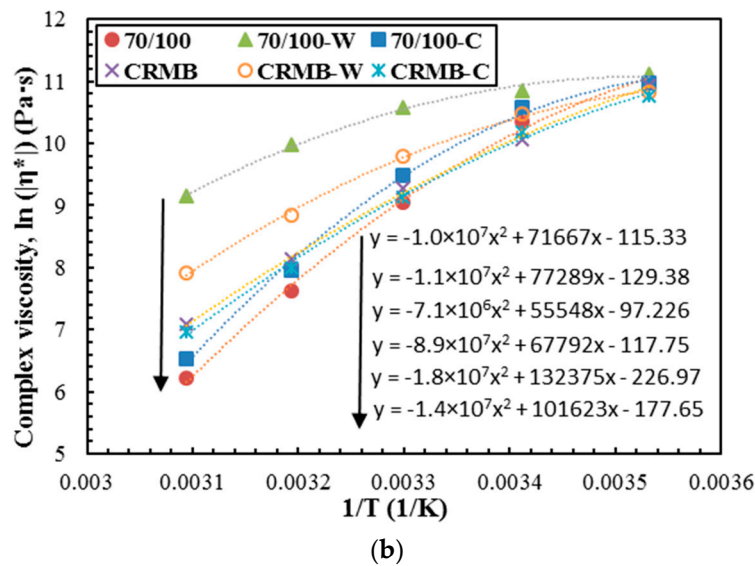


Figure 7. Cont.



**Figure 7.** Logarithmic complex viscosity as a function of the reciprocal of temperature (a) at shear rate of 0.01 rad/s; (b) at shear rate of 100 rad/s.

#### 4. Conclusions

Non-Newtonian behaviors of highly modified bituminous binders challenge the traditional interpretation of viscosity measurements of blends. Crumb rubber modified bitumen and binders with wax additives show apparent shear-thinning behaviors at certain temperatures. The shear-thinning mechanisms of different binders can be attributed to three types: polymer solutions/melts, suspensions and dispersions. Zero shear viscosity of different binders calculated using the Cross model and yield stresses derived based on the Herschel–Bulkley model are two important parameters to characterize the non-Newtonian behaviors of bitumen. It is emphasized that characteristics of zero shear viscosity and yield stress are highly temperature-dependent. The Arrhenius equation is only valid to model the temperature dependence of viscosity in the Newtonian region. The viscosity-temperature dependence of bitumen should be described with distinct equations in different temperature regions, namely Newtonian and non-Newtonian regions.

The testing temperature range in this study covers the average pavement temperature and high pavement temperature. For further research, viscosities of different bituminous binders tested at a wider temperature range (including mixing temperatures around 135 °C) and using different measuring systems (e.g., concentric cylinder, cone-plate) in DSR (Dynamic Shear Rheometer) are needed to examine the repeatability and accuracy of the model predictions. Systematic approaches to measure the yield stress of bituminous binders can be developed to compare with that predicted by the model.

**Author Contributions:** Conceptualization, X.L.; Formal analysis, H.W.; Methodology, P.A. and T.S.; Project administration, T.S.; Supervision, X.L. and T.S.; Writing—original draft, H.W.; Writing—review and editing, H.W. and X.L.

**Funding:** This research received no external funding.

**Acknowledgments:** The authors acknowledge RUMAL for providing testing materials. The first author would like to thank the China Scholarship Council for financial support.

**Conflicts of Interest:** The authors declare no conflict of interest.

## References

1. Lesueur, D. The colloidal structure of bitumen: Consequences on the rheology and on the mechanisms of bitumen modification. *Adv. Colloid Interface Sci.* **2009**, *145*, 42–82. [CrossRef] [PubMed]
2. Polacco, G.; Filippi, S.; Merusi, F.; Stastna, G. A review of the fundamentals of polymer-modified asphalts: Asphalt/polymer interactions and principles of compatibility. *Adv. Colloid Interface Sci.* **2015**, *224*, 72–112. [CrossRef] [PubMed]
3. Wang, H.; Yang, J.; Gong, M. *Rheological Characterization of Asphalt Binders and Mixtures Modified with Carbon Nanotubes*; Rilem Bookser; Springer: Berlin, Germany, 2016; pp. 141–150.
4. Wang, H.; You, Z.; Mills-Beale, J.; Hao, P. Laboratory evaluation on high temperature viscosity and low temperature stiffness of asphalt binder with high percent scrap tire rubber. *Constr. Build. Mater.* **2012**, *26*, 583–590. [CrossRef]
5. Sybilski, D. Non-newtonian viscosity of polymer-modified bitumens. *Mater. Struct.* **1993**, *26*, 15–23. [CrossRef]
6. Barnes, H.A.; Hutton, J.F.; Walters, K. *An Introduction to Rheology*; Elsevier: New York, NY, USA, 1989; Volume 3.
7. Larson, R.G. *The Structure and Rheology of Complex Fluids*; Oxford University Press: New York, NY, USA, 1999; Volume 150.
8. Haj-Kacem, R.B.; Ouerfelli, N.; Herráez, J.V.; Guettari, M.; Hamda, H.; Dallel, M. Contribution to modeling the viscosity arrhenius-type equation for some solvents by statistical correlations analysis. *Fluid Phase Equilib.* **2014**, *383*, 11–20. [CrossRef]
9. Jamshidi, A.; Hamzah, M.O.; Shahadan, Z.; Yahaya, A.S. Evaluation of the rheological properties and activation energy of virgin and recovered asphalt binder blends. *J. Mater. Civ. Eng.* **2015**, *27*, 04014135. [CrossRef]
10. Bahia, H.; Anderson, D. The new proposed rheological properties of asphalt binders: Why are they required and how do they compare to conventional properties. In *Physical Properties of Asphalt Cement Binders*; ASTM International: West Conshohocken, PA, USA, 1995.
11. Zoorob, S.E.; Castro-Gomes, J.P.; Pereira Oliveira, L.A. Assessing low shear viscosity as the new bitumen softening point test. *Constr. Build. Mater.* **2012**, *27*, 357–367. [CrossRef]
12. Sybilski, D. Zero-shear viscosity of bituminous binder and its relation to bituminous mixture's rutting resistance. *Transp. Res. Rec. J. Transp. Res. Board* **1996**, *1535*, 15–21. [CrossRef]
13. Anderson, D.; Le Hir, Y.; Planche, J.-P.; Martin, D.; Shenoy, A. Zero shear viscosity of asphalt binders. *Transp. Res. Rec. J. Transp. Res. Board* **2002**, *1810*, 54–62. [CrossRef]
14. Wang, H.; Liu, X.; Apostolidis, P.; Scarpas, T. Review of warm mix rubberized asphalt concrete: Towards a sustainable paving technology. *J. Clean. Prod.* **2018**, *177*, 302–314. [CrossRef]
15. Lo Presti, D. Recycled tyre rubber modified bitumens for road asphalt mixtures: A literature review. *Constr. Build. Mater.* **2013**, *49*, 863–881. [CrossRef]
16. Heitzman, M. Design and construction of asphalt paving materials with crumb rubber modifier. *Transp. Res. Rec.* **1992**, *1339*, 1–44.
17. Abdelrahman, M. Controlling performance of crumb rubber-modified binders through addition of polymer modifiers. *Transp. Res. Rec. J. Transp. Res. Board* **2006**, *1962*, 64–70.
18. Shen, J.; Amirkhanian, S.; Xiao, F.; Tang, B. Influence of surface area and size of crumb rubber on high temperature properties of crumb rubber modified binders. *Constr. Build. Mater.* **2009**, *23*, 304–310. [CrossRef]
19. Tang, N.; Huang, W.; Xiao, F. Chemical and rheological investigation of high-cured crumb rubber-modified asphalt. *Constr. Build. Mater.* **2016**, *123*, 847–854. [CrossRef]
20. Ragab, M.; Abdelrahman, M.; Ghavibazoo, A. Performance enhancement of crumb rubber-modified asphalts through control of the developed internal network structure. *Transp. Res. Rec. J. Transp. Res. Board* **2013**, *2371*, 96–104. [CrossRef]
21. Hajj, E.Y.; Sebaaly, P.E.; Hitti, E.; Borroel, C. Performance evaluation of terminal blend tire rubber hma and wma mixtures—Case studies. *J. Assoc. Asph. Paving Technol.* **2011**, *80*, 665–696.
22. Zhang, W.; Shen, S.; Wu, S.; Mohammad, L.N. Long-term field aging of warm-mix and hot-mix asphalt binders. *Transp. Res. Rec. J. Transp. Res. Board* **2017**, *2632*, 140–149. [CrossRef]


23. Huang, S.C. Rubber concentrations on rheology of aged asphalt binders. *J. Mater. Civ. Eng.* **2008**, *20*, 221–229. [CrossRef]
24. Abdelrahman, M.A.; Carpenter, S.H. Mechanism of the interaction of asphalt cement with crumb rubber modifier. *Transp. Res. Rec. J. Transp. Res. Board* **1999**, *1661*, 106–113. [CrossRef]
25. Airey, G.D.; Rahimzadeh, B.; Collop, A.C. Linear viscoelastic limits of bituminous binders. *J. Assoc. Asph. Paving Technol.* **2002**, *71*, 89–115.
26. Shan, L.; Tan, Y.; Richard Kim, Y. Applicability of the cox–merz relationship for asphalt binder. *Constr. Build. Mater.* **2012**, *37*, 716–722. [CrossRef]
27. Baumgardner, G.L.; Reinke, G.R. Binder additives for warm mix asphalt technology. *J. Assoc. Asph. Paving Technol.* **2013**, 685–709.
28. Wang, H.; Liu, X.; Apostolidis, P.; Scarpas, T. Rheological behavior and its chemical interpretation of crumb rubber modified asphalt containing warm-mix additives. *Transp. Res. Rec. J. Transp. Res. Board* **2018**. [CrossRef]
29. Jamshidi, A.; Hamzah, M.O.; You, Z. Performance of warm mix asphalt containing sasobit®: State-of-the-art. *Constr. Build. Mater.* **2013**, *38*, 530–553. [CrossRef]
30. Angelico, R.; Burgemeister, D.; Ceglie, A.; Olsson, U.; Palazzo, G.; Schmidt, C. Deuterium nmr study of slow relaxation dynamics in a polymer-like micelles system after flow-induced orientation. *J. Phys. Chem. B* **2003**, *107*, 10325–10328. [CrossRef]
31. Angelico, R.; Rossi, C.O.; Ambrosone, L.; Palazzo, G.; Mortensen, K.; Olsson, U. Ordering fluctuations in a shear-banding wormlike micellar system. *Phys. Chem. Chem. Phys.* **2010**, *12*, 8856–8862. [CrossRef] [PubMed]
32. Morea, F.; Agnusdei, J.O.; Zerbino, R. Comparison of methods for measuring zero shear viscosity in asphalts. *Mater. Struct.* **2009**, *43*, 499–507. [CrossRef]
33. Mark, J.E.; Erman, B.; Roland, M. *The Science and Technology of Rubber*; Academic Press: Cambridge, MA, USA, 2013.
34. Ragab, M.; Abdelrahman, M. Effects of interaction conditions on internal network structure of crumb rubber-modified asphalts. *Transp. Res. Rec. J. Transp. Res. Board* **2014**, *2444*, 130–141. [CrossRef]
35. Barnes, H.A. The yield stress—A review or ‘ $\pi\alpha\nu\tau\alpha\ \rho\epsilon\iota$ ’—Everything flows? *J. Non-Newton. Fluid Mech.* **1999**, *81*, 133–178. [CrossRef]
36. Saini, D.; Shenoy, A. A new method for the determination of flow activation energy of polymer melt. *J. Macromol. Sci. Part B Phys.* **1983**, *22*, 437–449. [CrossRef]
37. Messaâdi, A.; Dhouibi, N.; Hamda, H.; Belgacem, F.B.M.; Adbelkader, Y.H.; Ouerfelli, N.; Hamzaoui, A.H. A new equation relating the viscosity arrhenius temperature and the activation energy for some newtonian classical solvents. *J. Chem.* **2015**, *2015*. [CrossRef]



© 2018 by the authors. Licensee MDPI, Basel, Switzerland. This article is an open access article distributed under the terms and conditions of the Creative Commons Attribution (CC BY) license (<http://creativecommons.org/licenses/by/4.0/>).

Article

# Rheological Performance of Bio-Char Modified Asphalt with Different Particle Sizes

Ran Zhang <sup>1,2</sup>, Qingli Dai <sup>2,\*</sup>, Zhanping You <sup>2,\*</sup> , Hainian Wang <sup>1,\*</sup> and Chao Peng <sup>2,3</sup>

<sup>1</sup> School of Highway, Chang'an University, South Erhuan Middle Section, Xi'an 710064, China; ranzhang@mtu.edu

<sup>2</sup> Department of Civil and Environmental Engineering, Michigan Technological University, 1400 Townsend Drive, Houghton, MI 49931, USA; pengchao@cug.edu.cn

<sup>3</sup> Faculty of Engineering, China University of Geosciences, Wuhan 430074, China

\* Correspondence: qingdai@mtu.edu (Q.D.); zyou@mtu.edu (Z.Y.); wanghncd@gmail.com (H.W.); Tel.: +1-(906)-487-2620 (Q.D.); +1-(906)-370-0826 (Z.Y.); +86-(029)-8233-4432 (H.W.)

Received: 25 August 2018; Accepted: 13 September 2018; Published: 15 September 2018

**Abstract:** To improve the performance of petroleum asphalt, bio-char was used as a modifier for a petroleum asphalt binder, in this study. The rheological properties of bio-char modified asphalt binders were compared with different particle sizes and contents, with one control and one flake graphite modified asphalt binder. Specifically, the bio-char modifiers with two particle sizes (ranging from 75  $\mu\text{m}$ –150  $\mu\text{m}$  and less than 75  $\mu\text{m}$ ) and three contents of 2%, 4%, and 8% were added into the asphalt binder. A flake graphite powder with particle sizes less than 75  $\mu\text{m}$  was used as a comparison modifier. The Scanning Electron Microscopy (SEM) image showed the porous structure and rough surface of bio-char as well as dense structure and smooth surface of flake graphite. A Rotational Viscosity (RV) test, Dynamic Shear Rheometer (DSR) test, aging test, and Bending Beam Rheometer (BBR) test were performed to evaluate the properties of bio-char modified asphalt in this study. Both modifiers could improve the rotational viscosities of the asphalt binders. The porous structure and rough surface of bio-char lead to larger adhesion interaction in asphalt binder than the smooth flake graphite. As a result, the bio-char modified asphalts had better high-temperature rutting resistance and anti-aging properties than the graphite modified asphalt, especially for the binders with the smaller-sized and higher content of bio-char particles. Furthermore, the asphalt binder modified by the bio-char with sizes less than 75  $\mu\text{m}$  and about 4% content could also achieve a better low-temperature crack resistance, in comparison to other modified asphalt binders. Thus, this type of bio-char particles is recommended as a favorable modifier for asphalt binder.

**Keywords:** bio-char; asphalt; modified asphalt; microscopic morphology; rheological properties; anti-aging properties

## 1. Introduction

Bio-char has been studied since the 20th century [1]. It is a product rich in carbon consisting of organic compounds, generally produced by pyrolysis technology [2,3]. The pyrolysis process is the biomass decomposition under free oxygen, with the products of gas, liquid (bio-oil) and solid (bio-char) [4,5]. There are various processes for pyrolysis: fast pyrolysis, slow pyrolysis, carbonization, and gasification according to the heating temperature and residence time [6–9]. The yield of by-products depends on the conditions of pyrolysis process, including heating temperature, heating rate, residence time, condensate rate and so on [10–13]. More bio-char can be produced within 400–500 °C, while the pyrolysis temperatures above 700 °C benefit the production of bio-based liquid and gas. The pyrolysis process occurs faster at high temperatures, usually taking a few seconds instead

of a few hours. Typical yields at high-temperature conditions include 60% bio-oil, 20% bio-char and 20% gases. In contrast, a higher yield of bio-char can be produced through slow pyrolysis, nearly a 50% yield [14].

The majority of studies on bio-char have been focused on its ability to act as an amendment for soil, to increase the soil productivity and to enhance the nutrient cycling and plant growth [15–18]. However, according to studies in recent years, it has been found that in some cases, the crop productivity cannot be increased and could even decrease because of the sorption of pesticides and water [19]. The use of bio-char in soil has a negative impact on the environment. It can lead to a detrimental impact on Greenhouse Gas (GHG) levels and the environment [20]. Bio-char can act as a sink of soil pollutants. Various toxic substances can be retained by bio-char through sorption or physicochemical reactions. Moreover, bio-char is difficult to be separated again from the soil, after its inactivation [19,21]. Currently, as one of the biomass pyrolysis waste by-products, bio-oil can get efficient use as a biofuel [11,22–24]. Along with bio-oil, bio-char is also produced as another byproduct, and if it cannot be used appropriately, and is instead randomly stacked, the bio-char in the air will also be a health risk for humans [25].

It is likely that bio-char can be used as a modifier for asphalt modification, to reduce environmental impacts and human health concerns. Meanwhile, carbon-based materials, such as carbon fiber, graphite, and carbon black, have been successfully applied in asphalt modification. With the addition of carbon fiber, the high-temperature properties and rutting resistance of asphalt binder, as well as the alleviation of the aging and oxidation processes, were improved [26,27]. Moreover, the fatigue life could be increased with the action of carbon nano-fiber [28]. The combination filler of graphite and carbon fiber improved the electrical property and the mechanical performance of asphalt concrete [29]. Carbon black could also be used to increase the anti-aging property, high-temperature performance and thermal conductivity of asphalt binder [30]. In addition, there has been a limited number of studies, over the past few years, about the application of bio-char as a construction and building material. A 1 wt% bio-char generated from food waste was found to increase the impermeability of mortar [31]. A pulp and paper mill sludge bio-char, with a content of 0.1% of total volume, was found to improve the mechanical strength of conventional concrete [32]. A 10 wt% swine manure bio-char decreases the temperature susceptibility and shear susceptibility of asphalt binder [33]. A 10 wt% switchgrass bio-char also significantly reduces the temperature susceptibility of asphalt binder and increases the moisture, cracking and rutting resistance of asphalt mixture [34,35].

Overall, a limited number of studies have focused on the performance evaluation of modified asphalt by using bio-char from waste wood as a modifier. Moreover, the application of bio-char as a pavement material can not only reduce the environmental pollution caused by bio-char but can also achieve the reuse of waste biomass sources. Motivated by these, the rheological properties of asphalt binder modified by bio-char, with different particle sizes, were evaluated in this study.

## **2. Motivation and Objectives**

In order to seek a performance-favorable modifier, this study made a comprehensive investigation of the properties of asphalt binder modified by bio-char (different size ranges and contents) and flake graphite. The rheological properties were evaluated in the laboratory, and the effect of microscopic morphology, the particle size and the content of bio-char in the properties of bio-char modified asphalt binder, were researched in this study. Performance grade petroleum asphalt PG 58-28 and asphalt modified by commercial flake graphite were selected for comparison, in this study.

### 3. Materials and Preparation

#### 3.1. Control Asphalt PG 58-28

The performance grade asphalt, PG 58-28, was one of the control binders in this study. It was obtained from Detroit, Michigan in the United States. The detailed properties of PG 58-28 are shown in Table 1. The test results all met the requirement of the specification [36].

**Table 1.** The properties of performance grade asphalt PG 58-28.

Test Properties	Test Results	Requirement of Specification
Specific gravity	1.03	–
Rotational viscosity @135 °C (Pa·s)	0.350	<3.0
G*/sinδ @ 58 °C for original binder (kPa)	1.995	>1.0
G*/sinδ @ 58 °C for RTFO binder (kPa)	5.018	>2.2

#### 3.2. Graphite and Preparation of Graphite Modified Asphalt

Graphite was used in this study for comparison. The particle size of graphite was less than 75 μm and its density was 2.25 g/cm<sup>3</sup>. The minimum thickness of the flake graphite layer was 0.11 mm [37]. The graphite was added to the base asphalt PG 58-28, based on the selected weight percentage of 4%, and was mixed by a high-speed shearing mixer, at 120 °C for approximately 1 h.

#### 3.3. Bio-Char and Preparation of Bio-Char Modified Asphalt

The bio-char was supplied by an energy company. It was generated from waste wood resources, at temperatures ranging from 500–650 °C, through the pyrolysis technology, with a high heating rate of 104–105 °C/s. The bio-char particles were sieved to separate the different size ranges of particles. Only smaller particle sizes of bio-char were used in this study to achieve homogeneous and uniform mixing. The specific particle sizes of bio-char ranging from 75 μm–150 μm and less than 75 μm, were chosen in this study. The bio-char contents were 2%, 4% and 8% by weight of the total asphalt and its density was about 0.4 g/cm<sup>3</sup>, in this study. The bio-char was added into the base asphalt PG 58-28, based on the selected weight percentages, by a high-speed shearing mixer, at 120 °C for approximately 1 h.

Petroleum asphalt PG 58-28 sample and graphite modified asphalt sample were used in this study, for comparison purposes. As can be seen in Table 2, a total of seven bitumen blended with additives and one original binder of PG 58-28 were produced. In this research, ‘B’ stands for bio-char, ‘G’ stands for graphite, ‘L’ for larger particle size, and ‘S’ for smaller particle size.

**Table 2.** Sample range matrix.

Binder Types	Modifier Type	Modifier Content (wt %)	Particle Size
PG58-28	N/A	N/A	N/A
2% BL	Bio-char	2	75 μm < d < 150 μm
4% BL	Bio-char	4	75 μm < d < 150 μm
8% BL	Bio-char	8	75 μm < d < 150 μm
2% BS	Bio-char	2	d < 75 μm
4% BS	Bio-char	4	d < 75 μm
8% BS	Bio-char	8	d < 75 μm
4% GS	Graphite	4	d < 75 μm

### 4. Experimental Program

#### 4.1. Scanning Electron Microscopy (SEM) Test

SEM test was applied to obtain the microscopic morphology of materials [38]. In this study, the SEM test was conducted by a Hitachi (Schaumburg, IL, USA) S-4700 and JEOL (Peabody, M, USA)-6400. The bio-char or graphite particles were dispersed onto double-sided adhesive carbon



tape, which was applied to the aluminum sample mounts. For the operation of Hitachi S-4700, the accelerating voltage was 1–5 kV, the emission current was 9 A, and the working distance was 2.8–8 mm. For the operation of JEOL-6400, the accelerating voltage was 20 kV and the working distance was 39 mm. The bio-char and graphite samples were coated with a carbon thin film.

#### 4.2. Rotational Viscosity (RV) Test

The rotational viscosity test was applied to measure the asphalt's resistance to flow and the workability of asphalt binders. The viscosity measurements were conducted on asphalt by a Brookfield Rotational Viscometer following the American Association of State Highway and Transportation Officials (AASHTO) Designation: T 316-13 [39]. The test temperatures were: 90 °C, 110 °C, 135 °C, 150 °C, and 165 °C, respectively, and the shear rate was set at 20 r/min. Three replicates were used for each type of asphalt sample.

#### 4.3. Dynamic Shear Rheometer (DSR) Test

The Dynamic Shear Rheometer (DSR) test can be conducted to determine the rheological behavior of asphalt binders in varying temperature and frequency conditions [40,41]. The asphalt PG 58-28, graphite modified asphalt and bio-char modified asphalts were tested by the DSR in the original RTFO (Rolling Thin-Film Oven)-aged and PAV (Pressurized Aging Vessel)-aged states. The test temperatures chosen for the original and the RTFO-aged asphalt were, 52 °C, 58 °C, 64 °C, 70 °C, and 76 °C, to characterize the rutting resistance. The test temperatures were 13 °C, 19 °C, 25 °C, 31 °C, and 37 °C, for PAV-aged asphalt binders. A water bath was used to control the temperature. The AASHTO T315 [42] test procedure was followed for the DSR test. Three replicates were used for each type of asphalt sample.

#### 4.4. Aging Test

The RTFO test and PAV test were conducted for asphalt binders. The RTFO test and the PAV test were applied to simulate the aging of asphalt binder, during the process of construction and its service life, respectively [7,43]. In the standard RTFO test, the binders were conditioned at 163 °C, for 85 min, with sufficient air. The procedures of the standard RTFO test followed the AASHTO T240 [44]. Then, the RTFO-aged samples were used for the PAV test, under an air pressure of 2.1 MPa, for 20 h, based on the AASHTO R28 [45].

#### 4.5. Bending Beam Rheometer (BBR) Test

The Bending Beam Rheometer (BBR) test was used for the evaluation of the rheological and thermal cracking properties of asphalt binders. The specific operation process of this test was based on AASHTO standard T 313-12 [46]. The results of the BBR test could be applied to indicate the resistance to cracking in asphalt binders, at low temperatures. The asphalt samples were aged by the PAV test before the BBR test. The test temperature was controlled to be kept at the low temperature of –18 °C, by using an ethanol fluid. Moreover, stiffness was calculated based on Equation (1) [47].

$$S_t = (PL^3)/(4bh^3\delta_t) \quad (1)$$

where

- P—Applied constant load (100 g or 0.98 N);
- L—Distance between beam supports (102 mm);
- b—Beam width (12.5 mm);
- h—Beam thickness (6.25 mm);
- $S_t$ —Asphalt binder stiffness at a specific time;
- $\delta_t$ —Deflection at a specific time.

## 5. Results and Discussions

### 5.1. Microscopic Morphology Analysis

The microscopic morphologies of graphite and bio-char were observed by using the SEM test. The images of graphite and bio-char, magnified by the SEM, are shown in Figure 1.

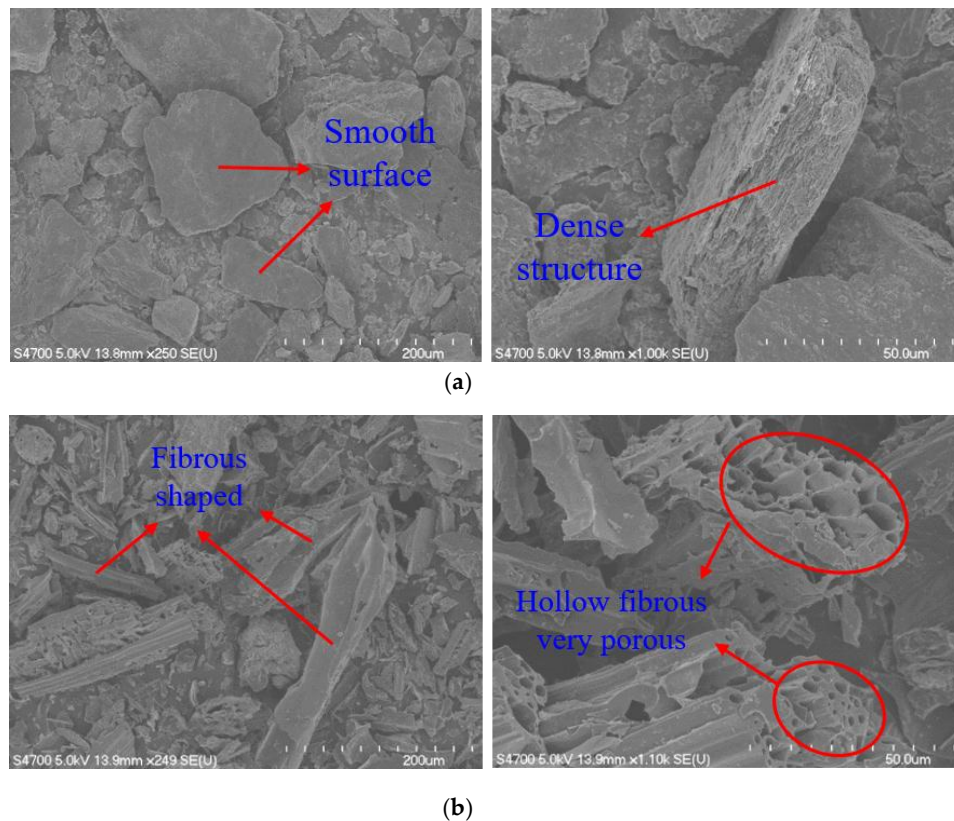


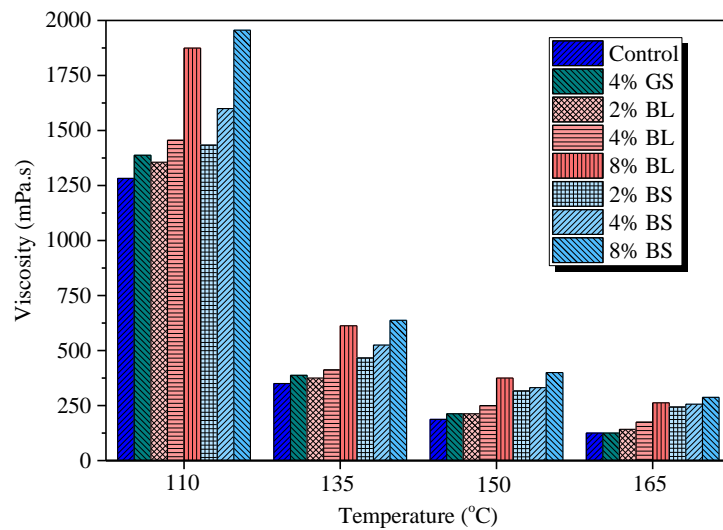
**Figure 1.** (a) Images of graphite magnified by SEM; (b) images of bio-char magnified by SEM.

It could be seen that the flake graphite and the bio-char had different structures and surface textures. The flake graphite had a smooth surface texture. Meanwhile, graphite had a dense microscopic morphology, that could be determined on the basis of Figure 1, and had a higher density of  $2.25 \text{ g/cm}^3$ . The bio-char was irregular hollow fibrous particles and had a very porous structure. The bio-char had a more complex and rough surface texture than the graphite. The hollow, fibrous, porous structure, and rough surface texture led the bio-char to have a higher surface area, which then led to a larger adhesion interaction, in the asphalt. Therefore, the special microscopic morphology of bio-char, the hollow, fibrous, porous structure and rough surface texture, might have contributed to the form of a strong biochar-binder matrix structure [34]. This might have led the bio-char modified asphalts to have a better resistance to deformation, at high temperatures. Meanwhile, the solid particles of bio-char and graphite were stiff particles. The addition of bio-char and graphite particles might have stiffened the asphalt binder to some degree.

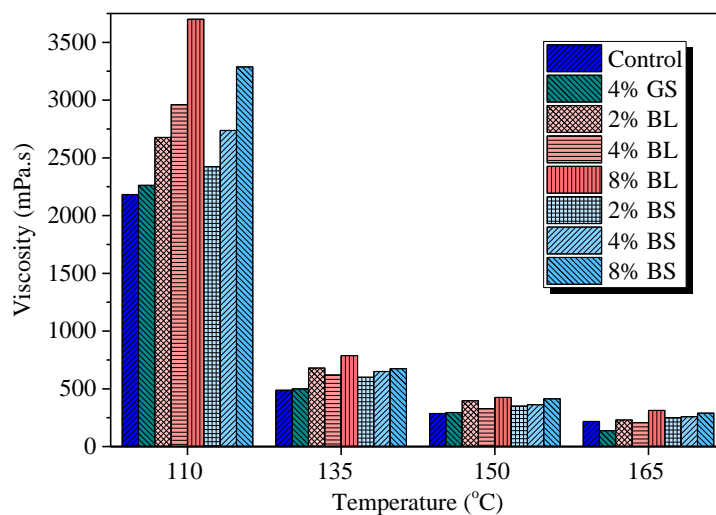
### 5.2. Rotational Viscosity Test

#### 5.2.1. Rotational Viscosity Analysis

The rotational viscosities of asphalt binders before and after RTFO aging, are shown in Figure 2a,b, respectively.



(a)



(b)

**Figure 2.** (a) Rotational viscosities of original control, graphite modified and bio-char modified asphalts; (b) rotational viscosities of control, graphite modified and bio-char modified asphalts after RTFO aging.

From Figure 2a, it is noteworthy that all the asphalt binders could satisfy the specification requirement for the rotational viscosity of no more than 3000 mPa·s, at 135 °C. The addition of the graphite or the bio-char contributed to the increase of rotational viscosities of the asphalt binders. As the bio-char content increased, the rotational viscosities of the bio-char modified asphalts had an increasing trend. For example, the rotational viscosities of 4% GS, 2% BL, 4% BL and 8% BL increased by an average of 8.06%, 9.90%, 26.19%, and 82.81%, respectively, as compared with the control asphalt binder at 110–165 °C. However, the increased value was smaller when the bio-char content was lower. For example, the rotational viscosities of 2% BL and 2% BS were only higher than that of the control asphalt binder by 25 mPa·s and 116.6 mPa·s, respectively. These could be explained by the stiffening influence from the increasing concentration of stiff particles. The addition of bio-char or graphite increased the concentration of stiff particles in asphalt and contributed to the increase of elastic components, which accordingly increased the viscosity of the asphalt binder. The bio-char size

had an effect on the rotational viscosities of bio-char modified asphalt. At 135 °C, the viscosities of 2% BS, 4% BS, and 8% BS were higher than 2% BL, 4% BL, and 8% BL by 91.7 mPa·s, 112.5 mPa·s, and 25.0 mPa·s, respectively (Figure 2a). This illustrated that bio-char modified asphalt binders with smaller-sized particles had higher viscosities than those with larger-sized particles. Furthermore, the bio-char modified asphalts had higher viscosities compared to the graphite modified asphalt binder. The rotational viscosities of 4% BL and 4% BS were higher than that of 4% GS, by 17.26% and 52.93%, on average, respectively. Under the same dosage, the bio-char had a higher volume and surface area than the graphite because of its lower density and porous structure. Moreover, the smaller-sized bio-char particles had a higher number of particles than the larger-sized ones, thereby, this also led to a higher surface area. The higher surface area and porous structure of bio-char led to a larger adhesion interaction in the base asphalt binder, which lowered the fluidity of asphalt binder and increased the viscosity.

After RTFO aging (Figure 2b), all the asphalt binders had higher viscosities than the original asphalt binders, because of the oxidation of the asphalt binders [48,49]. However, all the rotational viscosities of asphalt binders were still far less than 3 Pa·s. The obvious change was that the viscosity differences of the bio-char modified asphalts, with different bio-char contents, were lower than those before the RTFO aging had. When unaged, the viscosities of 4% BS and 8% BS were higher than 2% BS by 8.44% and 29.31%, on average, respectively. But after the RTFO aging, the viscosities of 4% BS and 8% BS were higher than 2% BS by 7.03% and 20.58%, on average, respectively. This indicated that the bio-char modified asphalts had different age degrees.

### 5.2.2. Anti-Aging Property Analysis

To further compare the anti-aging properties of different asphalt binders, the aging index was applied, in this study. The aging index was obtained from Equation (2).

$$I_{ag}^r = V_{RTFO}/V_{origin} \quad (2)$$

where

$I_{ag}^r$ —Aging index of the asphalt binder;

$V_{RTFO}$ —Rotational viscosity of RTFO aged asphalt binder;

$V_{origin}$ —Rotational viscosity of the original asphalt binder.

The aging indexes of all asphalt binders, at 135 °C, were calculated and are displayed in Figure 3. The higher the aging index, the worse the anti-aging property of asphalt binder was found to be. The aging indexes of 2% BS, 4% BS, and 8% BS decreased by 29.13%, 17.58, and 17.65% more than those of 2% BL, 4% BL, and 8% BL, respectively. This illustrated that as the bio-char content increased, the anti-aging properties of bio-char modified asphalts increased. This could be explained by the stiffening effect caused by the high content of bio-char, which reduced the aging effects. Meanwhile, the bio-char modified asphalts with smaller-sized particles had better anti-aging properties than those with larger-sized particles. At the same content, the smaller-sized bio-char led to higher numbers of stiff particles, as a result, the aging effects were more likely to be suppressed with this stronger stiffening effect. Moreover, 2% BS, 4% BS, and 8% BS had higher anti-aging property compared to the control asphalt binder. In addition, the 4% BS had a better anti-aging property than 4% GS. The bio-char had lower density and higher volume than graphite, at the same dosage. On one hand, this could be explained by the higher volume filling, which decreased the oxidation. On the other hand, the complex fibrous and porous structure of bio-char might have led to larger adhesion interaction between the bio-char and the base asphalt binder molecules, and thus decreased the oxidation.

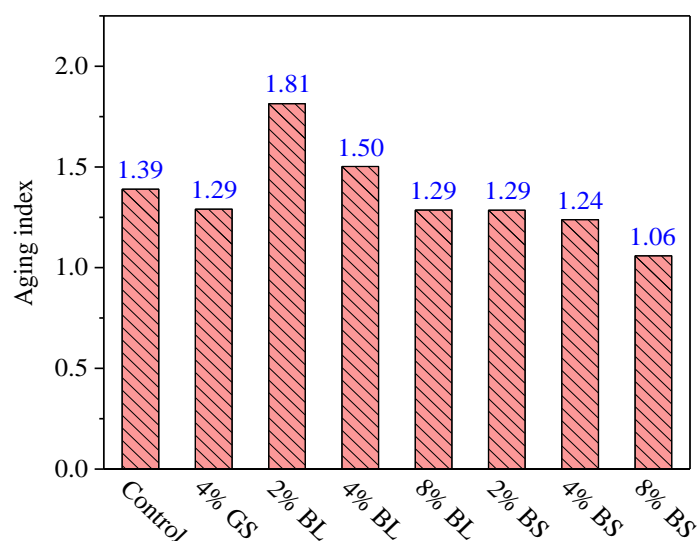


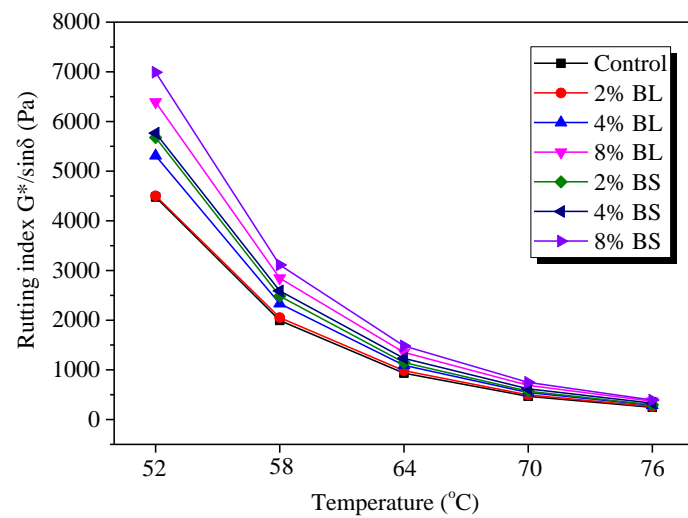
**Figure 3.** Aging indexes of control, graphite modified and bio-char modified asphalts.

### 5.3. Dynamic Shear Rheometer Test

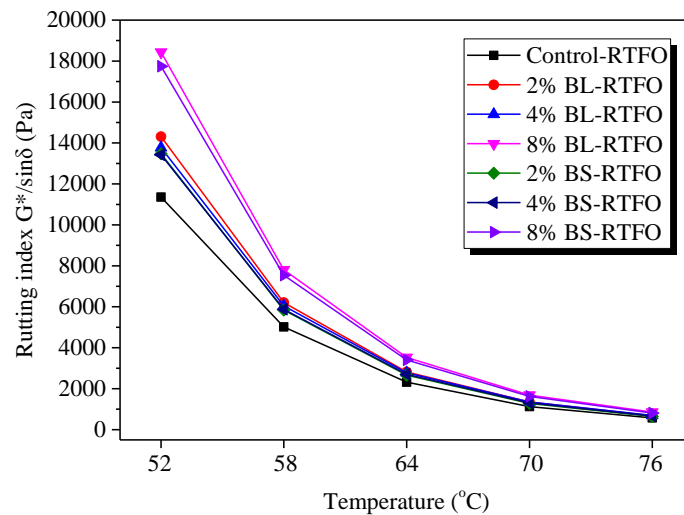
#### 5.3.1. Rutting Resistance Analysis

From Figure 4a, the rutting indexes of 2% BL, 4% BL, 8% BL, 2% BS, 4% BS, and 8% BS increased by 4.55%, 17.49%, 45.72%, 23.61%, 31.70%, and 58.40%, on average, as compared to that of the control asphalt binder within a 52 °C to 76 °C temperature range. This meant that bio-char modified asphalts had better resistance to rutting at higher temperatures than the control asphalt binder. This was partially attributed to the stiff volume-filling particles, such as the bio-char particles. The other reason might be that the porous structure of bio-char led to a higher surface area which, accordingly, led to the higher adhesion between the bio-char and the base asphalt binder. With the increasing of bio-char content, the rutting resistance became stronger. The enforcement of interaction among the bio-char particles might be a contributor to the higher rutting resistance. With the increase of bio-char content, stiff porous particles came into contact with each other, and a skeleton framework could be formed when the bio-char content increased to a higher amount. The higher rutting resistance also could be explained by the higher viscosity. The conclusions were consistent with the above conclusions about the viscosities.

From Figure 4b, after the RTFO aging, the rutting indexes of bio-char modified asphalts were higher than those before RTFO aging, because of the aging. Additionally, the bio-char modified asphalts still had higher aging resistance than the control asphalt binder. It was evident that bio-char modified asphalts, with larger-sized particles, had a more obvious change than those with smaller-sized particles. The rotational viscosities of 2% BL, 4% BL, and 8% BL were 5.80%, 3.09%, and 4.16% higher than those of 2% BS, 4% BS, and 8% BS, respectively, after the RTFO aging, while they were 15.36%, 10.76%, and 8.01% lower, respectively, before the RTFO aging. This could be attributed to the relatively weak aging resistance of bio-char modified asphalts with larger particle sizes. These conclusions were consistent with the above conclusions about the anti-aging properties.



(a)



(b)

**Figure 4.** (a) Rutting indexes ( $G^*/\sin\delta$ ) of original control and bio-char modified asphalts; (b) rutting indexes ( $G^*/\sin\delta$ ) of control and bio-char modified asphalts after RTFO aging.

The rutting indexes of the control asphalt binder, 4% GS, 4% BL, and 4% BS, before and after RTFO aging, are displayed in Figure 5. Before the RTFO aging, the rutting indexes of 4% GS, 4% BL, and 4% BS increased by 2.32%, 17.49%, and 31.70%, on average, compared to that of the control asphalt. Therefore, the graphite modified asphalt had a similar rutting index to that of the control asphalt, and bio-char modified asphalt has better rutting index than that of the graphite modified asphalt. After the RTFO aging, the rutting indexes of 4% GS, 4% BL, and 4% BS increased by 7.07%, 20.59%, and 16.98%, on average, compared to that of the control asphalt binder. This indicated, to a large extent, that the bio-char modified asphalts had better aging resistance than the graphite modified asphalt, especially, for the bio-char modified asphalt with smaller-sized particles. The higher number of stiff particles and the fibrous and porous structure of the bio-char contributed to the form of a biochar-binder matrix.

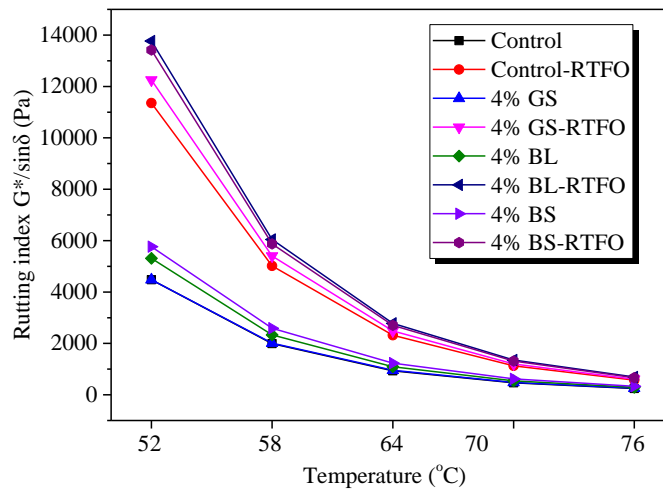


Figure 5. Rutting indexes ( $G^*/\sin\delta$ ) of different types of asphalt binders.

### 5.3.2. High Critical Temperature Analysis

According to the Superpave TM specification, the high critical temperature of asphalt is the temperature at which the rutting index at 1.59 Hz (10 rad/s) is 1.0 KPa for the unaged asphalt, and is 2.2 KPa for the RTFO aged asphalt. The high critical temperatures of asphalt binders were determined based on Equation 3, and the results are shown in Table 3. It is obvious that bio-char modified asphalts had better high-temperature properties than the control and graphite modified asphalts. The high critical temperatures of 4% GS, 4% BL, and 4% BS were higher than the control asphalt binder by 0.31 °C, 1.57 °C, and 2.92 °C, respectively. Moreover, the bio-char modified asphalts with smaller-sized particles had the best high-temperature properties. The bio-char has a lower density than graphite, therefore, the amount of stiff bio-char particles were higher as compared to that of graphite, at the same dosage. Furthermore, the smaller-sized bio-char particles had the highest number of stiff particles and the highest surface area. The porous structure and higher surface area might have played a significant role, which led to larger adhesion interaction in the asphalt binder, promoted the formation of a biochar-binder matrix and, thus, decreased the thermal influence [34].

$$T^{(G^*/\sin\delta)} = \text{Minimum} (T_o^{(G^*/\sin\delta)}, T_R^{(G^*/\sin\delta)}) \tag{3}$$

where

$T^{(G^*/\sin\delta)}$  = The high critical temperatures of asphalts;

$T_o^{(G^*/\sin\delta)}$  = The high critical temperatures of original asphalts;

$T_R^{(G^*/\sin\delta)}$  = The high critical temperatures of RTFO aged asphalts.

Table 3. The high critical temperatures of control, graphite modified, and bio-char modified asphalts.

	Control Asphalt	4% GS	2% BL	4% BL	8% BL	2% BS	4% BS	8% BS
$T_o(G^*/\sin\delta)$	63.56	63.87	63.90	65.13	67.07	65.76	66.48	68.03
$T_R(G^*/\sin\delta)$	64.61	65.18	66.62	66.34	68.21	65.91	66.22	68.09
$T(G^*/\sin\delta)$	63.56	63.87	63.90	65.13	67.07	65.76	66.48	68.03

### 5.4. Bending Beam Rheometer Test

#### 5.4.1. Low-Temperature Cracking Resistance Analysis

The BBR test was conducted for all the asphalt binders, to evaluate their low temperature cracking resistance. Based on the Superpave TM specification,  $-18\text{ }^\circ\text{C}$  is recommended for the test temperature.

And the specification requirement for the PAV-aged sample is the creep stiffness of less than 300 MPa and an m-value of higher than 0.3. The test results of creep stiffness and m-value for control, graphite modified, and bio-char modified asphalts are shown in Table 4.

The stiffness of 2% BL, 4% BL, 8% BL, 2% BS, 4% BS, and 8% BS was higher by −2 MPa, 64 MPa, 66 MPa, 34 MPa, 83 MPa, and 105 MPa, respectively, compared to the control asphalt. Though bio-char modified asphalts had higher creep stiffness than the control asphalt binder, they all satisfied the specification requirement of less than 300 MPa. The m-values of 4% BL, 8% BL, and 8% BS were 0.29, 0.28, and 0.28, respectively, which could not satisfy the requirements of the specification. As the bio-char content increased, the low-temperature properties of bio-char modified asphalts decreased. Therefore, there should have been a limit on the bio-char content of less than 4%. The reason is that stiff particles made the asphalt binder stiffer and more brittle, at low temperatures. This led to the smaller deformation capacity or compliance, according to the weak low-temperature properties. It could also be found that the bio-char particle size had an effect on the low-temperature performances, and the bio-char modified asphalts, with smaller-sized particles, had better low temperature cracking resistance than those with larger-sized particles. The m-values of 2% BS and 4% BS were 0.33% and 2.4% higher than those of 2% BL and 4% BL, respectively. The PAV-aged samples were used in the BBR test. This might have been caused by the more uniform distribution and interaction with the smaller stiff particles. Alternatively, the better anti-aging properties of bio-char modified asphalts, with smaller-sized particles, might have made the asphalt binder softer, and, thus, led to better cracking resistance at low temperatures. The m-values of 4% BS and 4% GS were both 0.30. This illustrated that bio-char modified asphalts had very similar low-temperature properties as that of the graphite asphalt binder, for the same particle sizes.

**Table 4.** The Bending Beam Rheometer (BBR) results of control, graphite modified and bio-char modified asphalts at −18°C.

Asphalt Binder	Time (s)	Deflection (mm)	Stiffness (mPa)	m-Value	Remarks (for Stiffness and m-Value)
Control	60.0	0.446	179	0.31	Pass the specification
4% GS	60.0	0.422	187	0.30	Pass the specification
2% BL	60.0	0.447	177	0.30	Pass the specification
4% BL	60.0	0.329	243	0.29	Fail the specification
8% BL	60.0	0.328	245	0.28	Fail the specification
2% BS	60.0	0.378	213	0.30	Pass the specification
4% BS	60.0	0.308	262	0.30	Pass the specification
8% BS	60.0	0.284	284	0.28	Fail the specification

#### 5.4.2. Low Critical Temperature Analysis

The low critical temperature of asphalt was determined on the basis of the Superpave TM specification, in which the creep stiffness is 300 MPa and the m-value is 0.3 [36]. The low critical temperatures of all asphalts are shown in Figure 6.

From Figure 6, it could be seen that 4% BS had better low critical temperature than 4% GS. The 2% BL, 2% BS, and 4% BS had better low critical temperatures which were no higher than −18 °C. The bio-char content should have been less than 4% because the low critical temperatures of bio-char modified asphalts increased with the added bio-char, and the low critical temperatures of 8% BL and 8% BS were much higher than −18 °C. Furthermore, the low critical temperatures of 2% BS and 4% BS were lower than those of 2% BL and 4% BL. Therefore, the smaller bio-char particles size of less than 75 μm were recommended to be used as the modifier.



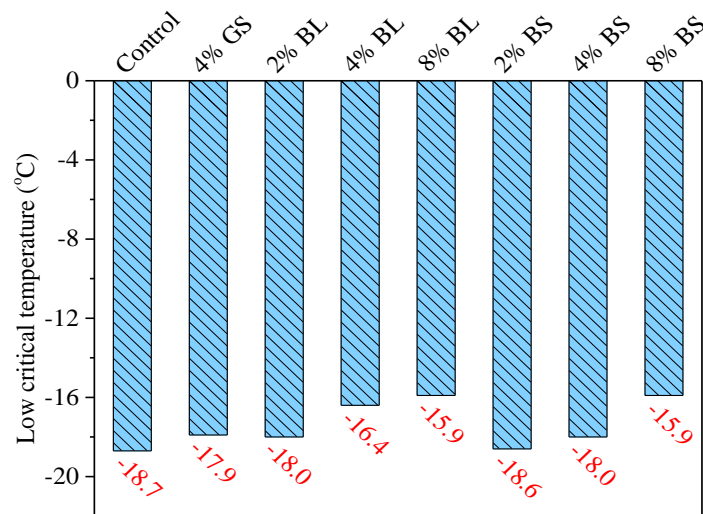


Figure 6. Low critical temperatures of control, graphite modified and bio-char modified asphalts.

## 6. Summaries and Conclusions

The bio-char was investigated as a favorable modifier to improve the rheological performance of asphalt binders. Bio-char with two particle size ranges of 75  $\mu\text{m}$ –150  $\mu\text{m}$  and less than 75  $\mu\text{m}$  were used as the modifiers. The content of bio-char was 2%, 4%, and 8% respectively. The flake graphite with a size range of less than 75  $\mu\text{m}$  and a content of 4% was utilized as a modifier of asphalt, for comparison. The Scanning Electron Microscopy characterization, Rotational Viscosity test, Dynamic Shear Rheometer test, and the Bending Beam Rheometer test were conducted to evaluate the modified binder performance. The conclusions obtained are as follows:

- (1) Compared with dense and smooth flake graphite, the bio-char particle had a more porous microstructure and rough surface texture.
- (2) Both bio-char and graphite could increase the rotational viscosity of the asphalt, with the added contents. The bio-char modified asphalt binders with smaller-sized particles had higher viscosities than those with larger-sized particles. They all satisfied the requirement for the specifications of rotational viscosity—less than or equal to 3000 mPa·s at 135 °C.
- (3) The porous structure and rough surface of bio-char could lead to a larger adhesion interaction in asphalt binder than those of the smooth flake graphite. As a result, the bio-char modified asphalts had a better high-temperature rutting resistance and better anti-aging properties than that of the graphite modified asphalt. A more noticeable improvement was found for the bio-char modified asphalt with the smaller-sized and higher number of particles. Moreover, the bio-char modified asphalts with the smaller-sized particles had the highest critical temperatures among all other binder types.
- (4) Though the crack resistance, at low temperatures, of the bio-char modified asphalts decreased with the added bio-char, as seen in the BBR test results, the low critical temperatures were still lower than  $-18$  °C, with the smaller-sized bio-char particles. The bio-char modified asphalts had similar low-temperature properties as that of the graphite modified asphalt binder.

In summary, it is possible to use bio-char as a modifier for the petroleum asphalt binder. This study showed that the bio-char with a size range of less than 75  $\mu\text{m}$  and a content of less than 4% could increase the anti-aging property and rutting resistance of the asphalt binder, as well as keep a good low-temperature crack resistance in the asphalt binder. Thus, this type of bio-char particles could be used as an environment-friendly and favorable modifier for the asphalt binder. In future studies, the porous structure of bio-char and the interface bonding between the bio-char and the asphalt will be investigated to facilitate this application.

**Author Contributions:** Conceptualization and methodology, R.Z., Q.D., Z.Y., H.W.; Writing-Original Draft Preparation, R.Z.; Writing-Review & Editing, Q.D., Z.Y., H.W. and C.P.; Funding Acquisition, R.Z. and Z.Y.

**Funding:** This research was funded by the Fundamental Research Foundation of the Central Universities of China under Grant No. 300102218701 and the U.S. National Science Foundation (NSF) under Grant CMMI 1300286.

**Acknowledgments:** This work was completed with the assistance of Huaguang Wang from the Department of Materials Science and Engineering at Michigan Technological University. Ran Zhang is supported by China Scholarship Council under Grant No. 201606560020. Any opinion, finding, and conclusions expressed in this paper are those of the authors and do not necessarily represent the view of any organization.

**Conflicts of Interest:** The authors declare no conflict of interest.

## References

1. Demirbas, A.; Pehlivan, E.; Altun, T. Potential evolution of Turkish agricultural residues as bio-gas, bio-char and bio-oil sources. *Int. J. Hydrogen Energy* **2006**, *31*, 613–620. [CrossRef]
2. Jaiswal, A.K.; Elad, Y.; Graber, E.R.; Frenkel, O. Rhizoctonia solani suppression and plant growth promotion in cucumber as affected by biochar pyrolysis temperature, feedstock and concentration. *Soil Biol. Biochem.* **2014**, *69*, 110–118. [CrossRef]
3. Muñoz, E.; Curaqueo, G.; Cea, M.; Vera, L.; Navia, R. Environmental hotspots in the life cycle of a biochar-soil system. *J. Clean. Prod.* **2017**, *158*, 1–7. [CrossRef]
4. Mohan, D.; Pittman, C.U.; Steele, P.H. Pyrolysis of wood/biomass for bio-oil: A critical review. *Energy Fuels* **2006**, *20*, 848–889. [CrossRef]
5. Zhong, Z.; Song, B.; Zaki, M. Life-cycle assessment of flash pyrolysis of wood waste. *J. Clean. Prod.* **2010**, *18*, 1177–1183. [CrossRef]
6. Zhang, R.; Wang, H.; You, Z.; Jiang, X.; Yang, X. Optimization of bio-asphalt using bio-oil and distilled water. *J. Clean. Prod.* **2017**, *165*, 281–289. [CrossRef]
7. Yang, X.; You, Z.-P.; Dai, Q.-L. Performance evaluation of asphalt binder modified by bio-oil generated from waste wood resources. *Int. J. Pavement Res. Technol.* **2013**, *6*, 431–439.
8. Imam, T.; Capareda, S. Characterization of bio-oil, syn-gas and bio-char from switchgrass pyrolysis at various temperatures. *J. Anal. Appl. Pyrolysis* **2012**, *93*, 170–177. [CrossRef]
9. Zhang, R.; Wang, H.; Jiang, X.; You, Z.; Yang, X.; Ye, M. Thermal storage stability of bio-oil modified asphalt. *J. Mater. Civ. Eng.* **2018**, *30*, 04018054. [CrossRef]
10. Gaunt, J.L.; Lehmann, J. Energy balance and emissions associated with biochar sequestration and pyrolysis bioenergy production. *Environ. Sci. Technol.* **2008**, *42*, 4152–4158. [CrossRef] [PubMed]
11. Zhang, R.; Wang, H.; Gao, J.; You, Z.; Yang, X. High temperature performance of sbs modified bio-asphalt. *Constr. Build. Mater.* **2017**, *144*, 99–105. [CrossRef]
12. Zhang, R.; Wang, H.; Gao, J.; Yang, X.; You, Z. Comprehensive performance evaluation and cost analysis of sbs-modified bioasphalt binders and mixtures. *J. Mater. Civ. Eng.* **2017**, *29*, 04017232. [CrossRef]
13. Zhao, B.; O'Connor, D.; Zhang, J.; Peng, T.; Shen, Z.; Tsang, D.C.; Hou, D. Effect of pyrolysis temperature, heating rate, and residence time on rapeseed stem derived biochar. *J. Clean. Prod.* **2018**, *174*, 977–987. [CrossRef]
14. Smith, J.L.; Collins, H.P.; Bailey, V.L. The effect of young biochar on soil respiration. *Soil Biol. Biochem.* **2010**, *42*, 2345–2347. [CrossRef]
15. Mukherjee, A.; Zimmerman, A.R. Organic carbon and nutrient release from a range of laboratory-produced biochars and biochar-soil mixtures. *Geoderma* **2013**, *193*, 122–130. [CrossRef]
16. Masiello, C.; Dugan, B.; Brewer, C.; Spokas, K.; Novak, J.; Liu, Z.; Sorrenti, G. Biochar effects on soil hydrology. In *Biochar for Environmental Management*, 2nd ed.; Routledge: Earthscan, UK, 2015.
17. Suliman, W.; Harsh, J.B.; Abu-Lail, N.I.; Fortuna, A.-M.; Dallmeyer, I.; Garcia-Pérez, M. The role of biochar porosity and surface functionality in augmenting hydrologic properties of a sandy soil. *Sci. Total Environ.* **2017**, *574*, 139–147. [CrossRef] [PubMed]
18. Ali, S.; Rizwan, M.; Qayyum, M.F.; Ok, Y.S.; Ibrahim, M.; Riaz, M.; Arif, M.S.; Hafeez, F.; Al-Wabel, M.I.; Shahzad, A.N. Biochar soil amendment on alleviation of drought and salt stress in plants: A critical review. *Environ. Sci. Pollut. Res.* **2017**, *24*, 12700–12712. [CrossRef] [PubMed]

19. Six, J. Biochar: Is There a Dark Side? 2014. Available online: <https://www.ethz.ch/en/news-and-events/eth-news/news/2014/04/biochar-is-there-a-dark-side.html> (accessed on 1 April 2014).
20. Downie, A. *Biochar Production and Use: Environmental Risks and Rewards*; University South Wales: Treforest, UK, 2011.
21. An, C.; Huang, G. Environmental concern on biochar: Capture, then what? *Environ. Earth Sci.* **2015**, *74*, 7861–7863. [CrossRef]
22. Yang, X.; You, Z.; Dai, Q.; Mills-Beale, J. Mechanical performance of asphalt mixtures modified by bio-oils derived from waste wood resources. *Constr. Build. Mater.* **2014**, *51*, 424–431. [CrossRef]
23. Fini, E.H.; Al-Qadi, I.L.; You, Z.; Zada, B.; Mills-Beale, J. Partial replacement of asphalt binder with bio-binder: Characterisation and modification. *Int. J. Pavement Eng.* **2012**, *13*, 515–522. [CrossRef]
24. Yang, X.; Mills-Beale, J.; You, Z. Chemical characterization and oxidative aging of bio-asphalt and its compatibility with petroleum asphalt. *J. Clean. Prod.* **2017**, *142*, 1837–1847. [CrossRef]
25. Brick, S.; Lyutse, S. *Biochar: Assessing the Promise and Risks to Guide US Policy*; NRDC Issue Paper; Natural Resources Defense Council: New York, NY, USA, 2010.
26. Cleven, M.A. *Investigation of the Properties of Carbon Fiber Modified Asphalt Mixtures*; Michigan Technological University: Houghton, MI, USA, 2000.
27. Yao, H.; You, Z.; Li, L.; Goh, S.W.; Lee, C.H.; Yap, Y.K.; Shi, X. Rheological properties and chemical analysis of nanoclay and carbon microfiber modified asphalt with fourier transform infrared spectroscopy. *Constr. Build. Mater.* **2013**, *38*, 327–337. [CrossRef]
28. Khattak, M.J.; Khattab, A.; Rizvi, H.R.; Zhang, P. The impact of carbon nano-fiber modification on asphalt binder rheology. *Constr. Build. Mater.* **2012**, *30*, 257–264. [CrossRef]
29. Liu, X.; Wu, S. Study on the graphite and carbon fiber modified asphalt concrete. *Constr. Build. Mater.* **2011**, *25*, 1807–1811. [CrossRef]
30. Cong, P.; Xu, P.; Chen, S. Effects of carbon black on the anti aging, rheological and conductive properties of sbs/asphalt/carbon black composites. *Constr. Build. Mater.* **2014**, *52*, 306–313. [CrossRef]
31. Gupta, S.; Kua, H.W.; Koh, H.J. Application of biochar from food and wood waste as green admixture for cement mortar. *Sci. Total Environ.* **2018**, *619*, 419–435. [CrossRef] [PubMed]
32. Akhtar, A.; Sarmah, A.K. Novel biochar-concrete composites: Manufacturing, characterization and evaluation of the mechanical properties. *Sci. Total Environ.* **2018**, *616*, 408–416. [CrossRef] [PubMed]
33. Walters, R.C.; Fini, E.H.; Abu-Lebdeh, T. Enhancing asphalt rheological behavior and aging susceptibility using bio-char and nano-clay. *Am. J. Eng. Appl. Sci.* **2014**, *7*, 66–76. [CrossRef]
34. Zhao, S.; Huang, B.; Ye, X.P.; Shu, X.; Jia, X. Utilizing bio-char as a bio-modifier for asphalt cement: A sustainable application of bio-fuel by-product. *Fuel* **2014**, *133*, 52–62. [CrossRef]
35. Zhao, S.; Huang, B.; Shu, X.; Ye, P. Laboratory investigation of biochar-modified asphalt mixture. *Transp. Res. Rec. J. Transp. Res. Board* **2014**, *2445*, 56–63. [CrossRef]
36. AASHTO. *Standard Specification for Performance-Graded Asphalt Binder (m320-10)*; American Association of State Highway and Transportation Officials: Washington, DC, USA, 2013.
37. Wang, Z.; Dai, Q.; Guo, S. Laboratory performance evaluation of both flake graphite and exfoliated graphite nanoplatelet modified asphalt composites. *Constr. Build. Mater.* **2017**, *149*, 515–524. [CrossRef]
38. You, L.; You, Z.; Dai, Q.; Zhang, L. Assessment of nanoparticles dispersion in asphalt during bubble escaping and bursting: Nano hydrated lime modified foamed asphalt. *Constr. Build. Mater.* **2018**, *184*, 391–399. [CrossRef]
39. AASHTO. *Standard Method of Test for Viscosity Determination of Asphalt Binder Using Rotational Viscometer (t 316-13)*; American Association of State Highway and Transportation Officials: Washington, DC, USA, 2013.
40. You, L.; You, Z.; Yang, X.; Ge, D.; Lv, S. Laboratory testing of rheological behavior of water-foamed bitumen. *J. Mater. Civ. Eng.* **2018**, *30*, 04018153. [CrossRef]
41. Lv, S.; Wang, S.; Guo, T.; Xia, C.; Li, J.; Hou, G. Laboratory evaluation on performance of compound-modified asphalt for rock asphalt/styrene-butadiene rubber (sbr) and rock asphalt/nano-CaCO<sub>3</sub>. *Appl. Sci.* **2018**, *8*, 1009. [CrossRef]
42. AASHTO. *Standard Method of Test for Determining the Rheological Properties of Asphalt Binder Using a Dynamic Shear Rheometer (dsr) (t 315-12)*; American Association of State Highway and Transportation Officials: Washington, DC, USA, 2013.

43. Ge, D.; Yan, K.; You, L.; Wang, Z. Modification mechanism of asphalt modified with sasobit and polyphosphoric acid (ppa). *Constr. Build. Mater.* **2017**, *143*, 419–428. [CrossRef]
44. AASHTO. *Effect of Heat and Air on a Moving Film of Asphalt Binder (Rolling Thin-film Oven Test)*; American Association of State Highway and Transportation Officials: Washington, DC, USA, 2013.
45. AASHTO. *Standard Practice for Accelerated Aging of Asphalt Binder Using a Pressurized Aging Vessel (pav)*; American Association of State Highway and Transportation Officials: Washington, DC, USA, 2013.
46. AASHTO. *Determining the flexural creep stiffness of asphalt binder using the bending beam rheometer (bbr) (t313-12)*; American Association of State Highway and Transportation Officials: Washington, DC, USA, 2013.
47. Yao, H.; You, Z.; Li, L.; Goh, S.W.; Mills-Beale, J.; Shi, X.; Wingard, D. Evaluation of asphalt blended with low percentage of carbon micro-fiber and nanoclay. *J. Test. Eval.* **2013**, *41*, 278–288. [CrossRef]
48. Peng, C.; Yu, J.; Dai, J.; Yin, J. Effect of zn/al layered double hydroxide containing 2-hydroxy-4-n-octoxy-benzophenone on uv aging resistance of asphalt. *Adv. Mater. Sci. Eng.* **2015**, *2015*. [CrossRef]
49. Peng, C.; Dai, J.; Yu, J.; Yin, J. Intercalation of p-methycinnamic acid anion into zn-al layered double hydroxide to improve uv aging resistance of asphalt. *AIP Adv.* **2015**, *5*, 027133. [CrossRef]



© 2018 by the authors. Licensee MDPI, Basel, Switzerland. This article is an open access article distributed under the terms and conditions of the Creative Commons Attribution (CC BY) license (<http://creativecommons.org/licenses/by/4.0/>).



Article

# Laboratory Evaluation on Performance of Compound-Modified Asphalt for Rock Asphalt/Styrene–Butadiene Rubber (SBR) and Rock Asphalt/Nano-CaCO<sub>3</sub>

Songtao Lv <sup>1,2</sup>, Shuangshuang Wang <sup>1</sup>, Tong Guo <sup>3</sup>, Chengdong Xia <sup>1,\*</sup>, Jianglong Li <sup>1</sup> and Gui Hou <sup>4</sup>

<sup>1</sup> National Engineering Laboratory of Highway Maintenance Technology, Changsha University of Science & Technology, Changsha 410004, China; lst@csust.edu.cn (S.L.); wsscust@126.com (S.W.); lj11530@126.com (J.L.)

<sup>2</sup> Department of Civil and Environmental Engineering, Michigan Technological University, Houghton, MI 49931, USA

<sup>3</sup> XIANDAI TOUZI Co., Ltd., Changsha 410004, China; 18569412272@163.com

<sup>4</sup> Inner Mongolia Communications Construction Engineering Quality Supervision Bureau, Hohhot 010051, China; hhhthougui@163.com

\* Correspondence: xiachengdong@stu.csust.edu.cn

Received: 11 May 2018; Accepted: 18 June 2018; Published: 20 June 2018

**Abstract:** As a natural modifier of asphalt, rock asphalt has been widely used to improve its thermal stability and aging resistance. However, the thermal cracking resistance of asphalt modified by rock asphalt is unsatisfactory. In order to improve the thermal cracking resistance in low temperature, two kinds of modifiers—styrene–butadiene rubber (SBR) and nano-CaCO<sub>3</sub>—were selected as the compound modifiers, and then implemented to improve the low-temperature performance of the binder. Then, compound asphalt modified by Buton rock asphalt (BRA) was chosen as the study subject. The thermal stability and aging resistance of asphalt modified by BRA, compound-modified asphalt by BRA/SBR, and compound-modified asphalt by BRA and nano-CaCO<sub>3</sub> were determined to identify whether the compound modifiers in the asphalt would have a negative effect on the thermal stability and aging resistance of the asphalt. The dynamic shear rheometer (DSR) test was employed to evaluate the thermal stability. The thin film oven test (TFOT) and pressure aging vessel (PAV) were adopted to determine the aging resistance. The viscoelastic characteristics of asphalt with and without modifiers were revealed to evaluate the low-temperature crack resistance of asphalt modified by compound modifiers. The bending beam rheometer (BBR) creep test was conducted in three test temperatures in order to determine the creep stiffness modulus of the BRA compound-modified asphalt. The viscoelastic model considering the damage caused by loading was established; then, the creep compliance and parameters of the viscoelastic damage model were implemented to evaluate the low-temperature performance of the compound-modified asphalt. The results show that the compound modifiers have little negative effects on the thermal stability and aging resistance of asphalt. The thermal crack resistance of the compound-modified asphalt by BRA/SBR was the best, followed by the compound-modified asphalt by BRA and nano-CaCO<sub>3</sub> within the three materials. The accuracy of forecasting the characteristics of compound-modified asphalt was improved by using the viscoelastic model and considering the damage effect.

**Keywords:** modified asphalt; rock asphalt; creep test; thermal crack; viscoelastic model

## 1. Introduction

The asphalt pavement structure is widely employed in most high-grade road projects. However, due to the characteristics of the axle load, heavy traffic flow, and traffic channelization of modern highway traffic, the requirements of road materials are constantly improved. The traditional asphalt materials and design methods [1–4] can no longer meet the requirements of the durability of asphalt pavement. Therefore, in order to develop a new type of compound-modified asphalt with excellent thermal stability, low-temperature crack resistance, and good durability, it is necessary to study the performance of modified asphalt.

Buton rock asphalt (BRA) produced from Buton island of South Pacific Indonesia is naturally formed by petroleum or oil continuously emerging from the Earth's crust and impregnating into rocks, followed by evaporation and solidification over millions of years [5,6]. In recent years, BRA has been successfully applied to Chinese road construction for its advantages such as good pavement performance, simple construction technology, et al. There are many studies on Buton rock asphalt. Studies by Wentong Huang have shown that BRA could effectively improve the water stability of the asphalt mixture [7]. Yingmei Yin et al. used dynamic shear rheometer (DSR) to study BRA-modified asphalt that was tested by strain sweep, frequency sweep, and temperature sweep. The results have shown that the rutting factor of the asphalt increased, and the rheological behavior of the asphalt at high temperature was dramatically varied with the increase of the mixing amount of BRA in the asphalt [8]. Ruixia Li et al. tested the chemical composition and structure of BRA-modified asphalt with X-Ray diffraction, infrared spectrum, and thermal analysis. These tests indicated that BRA could effectively improve the adhesion property between asphalt and aggregate [9]. Shaowen Du found that BRA could improve the fatigue resistance of asphalt mixtures [10]. In addition, asphalt mixtures modified by BRA can improve the rutting and skid resistance of asphalt pavement [11,12]. Although BRA has many advantages related to improving the performance of asphalt mixtures and pavement, it can reduce the low-temperature performance of asphalt and asphalt mixtures [13]. The low-temperature performance of BRA-modified asphalt is important, especially in cold regions, so this paper was aimed at finding a modifier to improve the low-temperature of BRA-modified asphalt.

The modification of asphalt binder with polymeric materials and crumb rubber is the most common method to improve the performance of the asphalt binder against most types of distresses [14–17]. Styrene-butadiene rubber (SBR) is widely used as the asphalt modifier for the preparation of polymer-modified asphalt (PMA). SBR is considered to be one of the most effective modifiers for asphalt pavements [18]. The Engineering Brief published [19] on the Federal Aviation Administration website in 1987 described the benefits of SBR-modified asphalt in improving the performance of asphalt concrete pavements and sealant coatings. The low-temperature ductility was improved, the viscosity was increased, the elastic recovery was improved, and the adhesive and cohesive properties were improved. The morphological features of nanomaterials have special features derived from their nanoscale dimensions [20]. Due to the very tiny size and large surface area, the properties of nanomaterials are very different from the normal-sized materials [21]. In recent years, nanomaterials have attracted much attention because of their ability to improve the properties of bituminous materials. Nanotechnology is widely employed in the development of a new generation of materials to improve the macroscopic properties of materials [22,23]. H Raufi et al. studied the performance of nano-CaCO<sub>3</sub> modified bitumen in hot mix asphalt; the results showed that an asphalt mixture prepared with 6% nano-CaCO<sub>3</sub> modified bitumen exhibited good performances against moisture susceptibility and high-temperature performance [24]. Unique mechanical and rheological properties of nanomaterials are conducive to the design and construction of durable pavement materials [25]. Adding these nanosized particles to another material may overcome the monolithic limitations, and asphalt binders are no exception. The addition of nanomaterials changes the rheological properties of asphalt binders, and may also lead to the changes in the intermolecular forces within the asphalt binder structure [26]. This is because the interaction at the phase interface is greatly increased when the size reaches the nanoscale.

As for evaluation indicators of the low-temperature performance of asphalt, penetration, ductility, equivalent brittle point et al. were adopted widely, but these indicators are empirical and have less relation to the mechanical properties of materials. Therefore, strategic highway research program (SHRP) proposed that the low-temperature performance of asphalt could be evaluated by stiffness modulus obtained by a bending beam rheometer (BBR) creep test, which could set relations between low-temperature performance and mechanical properties [27]. A low-temperature creep test, which tests the property of a material under a constant stress and low temperature, was employed in this paper. In the creep test, the flexibility of material was evaluated by creep compliance, which is the reciprocal of the stiffness modulus. Burgers’ model was widely adopted in the studies on the viscoelasticity of asphalt and asphalt mixtures, but it didn’t consider the influence of the damage and its distribution. To make Burgers’ model conform to the practical test conditions, the Burgers’ model coupling the damage was established.

The main objective of this paper is to improve the low-temperature performance of Buton rock asphalt (BRA)-modified asphalt and to establish a characterization method of the low-temperature performance. Two compound modifiers, SBR and nano-CaCO<sub>3</sub>, were added to the BRA-modified asphalt, respectively. The bending beam rheometer (BBR) creep test was employed under three test temperatures to determine the creep stiffness module of the two compound-modified asphalts. Meanwhile, the amounts of the two mixing modifiers were considered. The viscoelastic model of creep compliance considering the damage effects was proposed.

## 2. Materials

### 2.1. Materials

The properties of asphalt binders were measured according to the test methods of specification, the Standard Test Methods of Bitumen and Bituminous Mixtures for Highway Engineering (JTG E20-2011) [28]. AH-70 (penetration grade) base asphalt was used as the binder in this work, and its main technical indicators are summarized in Table 1. The Buton rock asphalt (BRA, Figure 1) that was used in this test had been sifted with an 0.15-mm sieve. The technical indicators of BRA are shown in Table 2. Two kinds of low-temperature modifiers, styrene–butadiene rubber (SBR, Figure 1) and nano-CaCO<sub>3</sub> (Figure 1), were adopted in this test. Their main technical properties are presented in Tables 3 and 4, respectively.

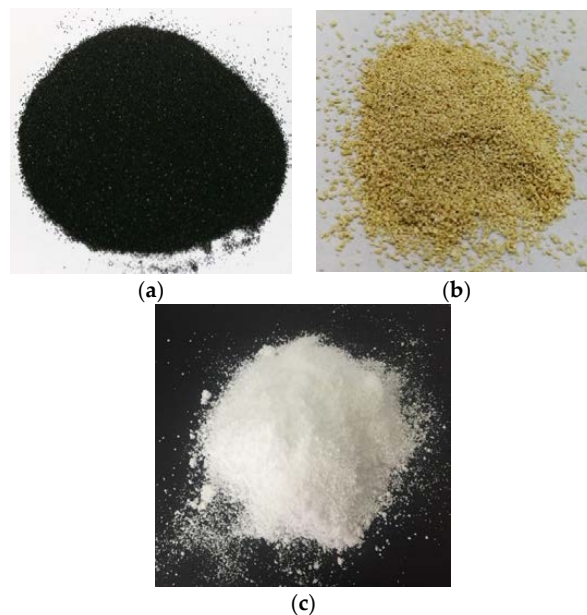


**Figure 1.** Materials: (a) Buton rock asphalt (BRA); (b) styrene–butadiene rubber (SBR); (c) Nano-CaCO<sub>3</sub>.



**Table 1.** Technical properties of base asphalt binder AH-70.

Test Items	Industry Standard	Test Results	Test Methods [28]
Penetration at 25 °C (0.1 mm)	60	75.2	T 0604-2000
Penetration Index	−2~2	0.968	T 0604-2000
Softening point (°C)	≥100	51.5	T 0606-2000
Ductility at 15 °C (cm)	≥46	>150	T 0605-1993
Rotation viscosity/135 °C (Pa·s)	\	0.451	T 0615-2000

**Table 2.** Technical properties of BRA.

Test Items	Industry Standard	Test Results	Test Methods [29]
Appearance	Brown powder	Brown powder	
Ash content (%)	<75	74.14	
Solubility (%)	>25	25.6	
Water content (%)	<2	0.97	JT/T860.5-2014
Percentage passing (%)	<4.75 mm	100	
	<2.36 mm	90~100	
	<0.6 mm	10~60	

**Table 3.** Technical properties of SBR.

Test Items	Industry Standard	Test Results	Test Methods
Volatile matter content (%)	≤0.60	0.30	GB/T 6737
Ash content (%)	≤0.50	0.10	GB/T 4498
Organic acids content (%)	4.50~6.75	6.15	GB/T 8657
Soap content (%)	≤0.50	0.01	
Bound styrene content (%)	22.5~24.5	23.7	GB/T 8658
Raw rubber Mooney viscosity [50 ML(1 + 4)100 °C]	45~55	52	GB/T1232.1
Compound rubber Mooney viscosity [50 ML(1 + 4)100 °C]	≤93	70	
Tensile strength (MPa)	≥25.5	25.8	
Tensile elongation (%)	≥340	412	GB/T 8656 A
300% fixed elongation stress at 145 °C (MPa)	25 min	17.7 ± 2.0	16.6
	35 min	20.6 ± 2.0	20.8
	50 min	21.5 ± 2.0	21.6

**Table 4.** Technical properties of nano-CaCO<sub>3</sub>.

Test Items	Test Results	Test Methods [30]
Appearance	White powder	
Nano-CaCO <sub>3</sub> content (%)	≥98	
PH value	8.0~10.5	
Whiteness (%)	≥95	
Activation rate (%)	≥98	
Volatile matter content at 105 °C (%)	≤0.5	GB/T19590-2011
Insoluble matter content in hydrochloric acid (%)	≤0.03	
Passing rate for 45-µm experimental sieve (%)	≤0.02	
Oil absorption value (%)	≤35	
Insoluble matter content in hydrochloric acid (%)	≤0.03	
Passing rate for 45-µm experimental sieve (%)	≤0.02	
Oil absorption value (%)	≤35	

## 2.2. Preparation of Modified Asphalt

Based on the Marshall test results, the determined optimum asphalt content of a base asphalt mixture and BRA-modified mixture of AC-16C were 4.2% and 4.4% by mass of the mixture, respectively. According to the test results and engineering experience, it was determined that the quality content of the BRA was 3% in the BRA-modified asphalt mixture. In the experiment, according to the composition of asphalt and mineral elements (ash) in the BRA, the amount of mineral powder and asphalt was adjusted to ensure that the asphalt content was constant in the BRA-modified asphalt mixture. Based on this, the calculated ratio between the BRA and the base asphalt was 0.83:1. To investigate the effect of the content of SBR and nano-CaCO<sub>3</sub> on BRA, BRA with different SBR contents (3%, 5%) and nano-CaCO<sub>3</sub> (5%, 10%) contents were prepared, respectively.

Firstly, base asphalt AH-70 was heated to 140 °C. Within the range of 140–145 °C, the asphalt was mixed by a glass rod when it was heated. When the base asphalt melted, the BRA was added into the base asphalt by using the external addition method. Then, the asphalt was kept at 140 °C for 10 min with high-speed shearing equipment running at 4000 rpm. After that, the low-temperature modifiers were respectively added into the asphalt, which having been mixed well, and then, the compounds continued to be mixed for 25–30 min. When all of the processes were finished, the two BRA compound-modified asphalts were prepared. The properties of the modified asphalts were tested, and the results are shown in Table 5.

**Table 5.** The basic technical properties of modified asphalts.

Test Items	BRA	BRA + 3% SBR	BRA + 5% SBR	BRA + 5% Nano-CaCO <sub>3</sub>	BRA + 10% Nano-CaCO <sub>3</sub>
Penetration (25 °C, 0.1 mm)	26.3	24.0	22.4	24.2	22.7
PI	1.862	1.703	1.961	1.870	1.912
T <sub>1,2</sub> (°C)	−18.8	−16.6	−17.1	−17.7	−17.0
T <sub>800</sub> (°C)	73.5	73.7	76.5	73.5	74.7
Softening Point (°C)	64.7	75.8	81.4	65.4	66.9
Ductility (5 cm/min, 15 °C, cm)	7.5	20.1	26.7	8.4	12.8

According to the analysis of the basic properties of the compound-modified asphalt in Table 5, it can be concluded that the addition of nano-CaCO<sub>3</sub> and SBR can improve the high-temperature stability of the BRA.

To further reveal the impact of the modifier on the performance of the asphalt material, the test of thermal (high and low) performance and aging resistance of BRA compound-modified asphalts was conducted. The thermal stability of the BRA compound-modified asphalt was determined by determining the rheological properties of the asphalt binder using a dynamic shear rheometer. The thermal cracking property characterized by the creep stiffness modulus was tested through using the bending beam rheometer (BBR) test. The creep compliance and parameters of the viscoelastic damage model were implemented to evaluate the low-temperature performance of the compound-modified asphalts. The thin film oven test (TFOT) test was employed to evaluate the short-term aging properties of the compound-modified asphalts and its long-term aging properties were tested by a pressure aging vessel (PAV) test.

## 3. Tests and Results

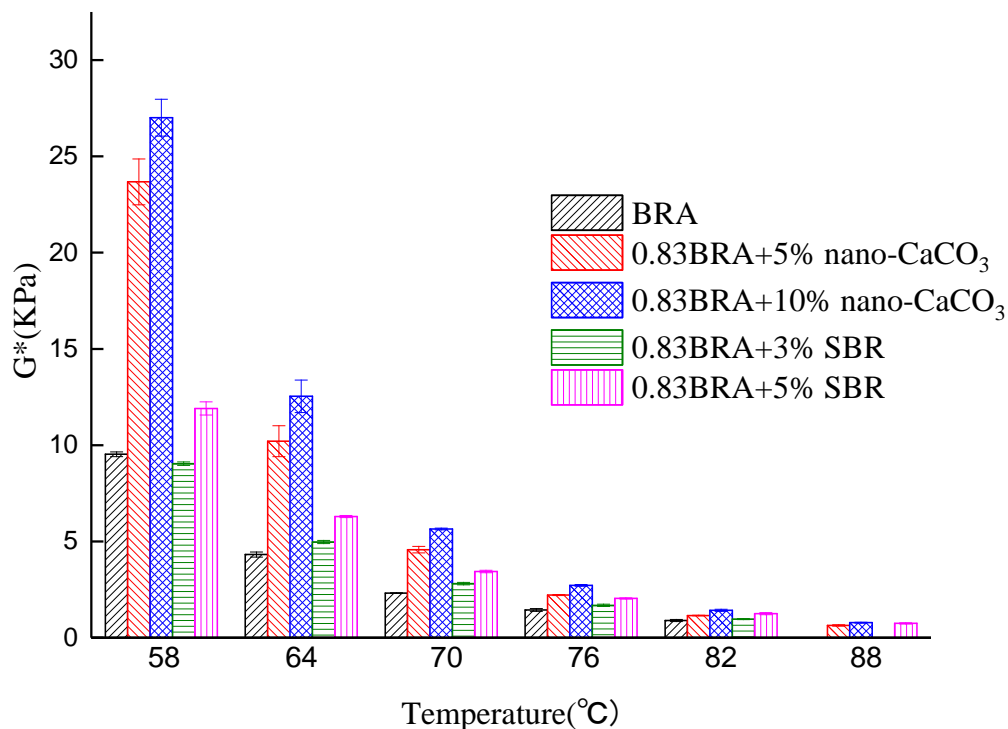
### 3.1. The Evaluation of the Thermal Stability and Aging Resistance for Modified Asphalt

#### 3.1.1. Thermal Stability

The dynamic shear rheometer (DSR) can be employed to measure the rheological properties of asphalt at high and medium temperatures to evaluate the thermal stability of asphalt. Within the viscoelastic range, it was implemented to detect the complex shear modulus  $G^*$ , phase angle  $\delta$ ,

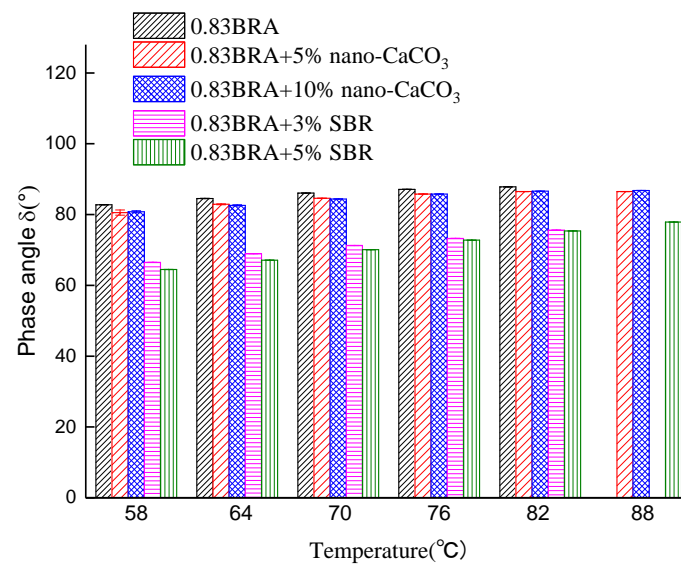
and anti-rutting factor  $G^*/\sin\delta$  of asphalt, and its rheological properties can be evaluated. The test temperature of a dynamic shear rheometer (DSR) starts from 58 °C. If the anti-rutting factor  $G^*/\sin\delta$  is qualified, the test was performed at 64 °C for one grade, and the requalification continues to increase to 70 °C for testing until a test temperature of  $G^*/\sin\delta < 1.0$  KPa then stopped the test. The complex shear modulus  $G^*$  indicates the ability of the material to resist the shear deformation. The greater the value of  $G^*$ , the harder the asphalt, which meant a better rutting resistance. The smaller the phase angle was, the more elastic the components in the asphalt.

The dynamic shear rheometer (DSR) test was implemented to qualify the high temperature performance of nano- $\text{CaCO}_3$ /BRA and SBR/BRA compound-modified asphalt. The results of dynamic shear rheometer (DSR) tests before the aging of nano- $\text{CaCO}_3$ /BRA and SBR/BRA compound-modified asphalts with different contents are shown in Figures 2–4, respectively.



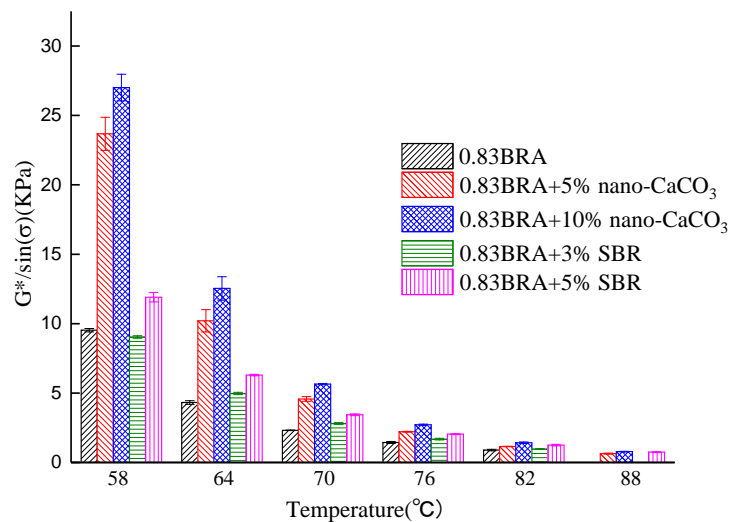
**Figure 2.** The relationship between complex shear modulus  $G^*$  and the temperature of nano- $\text{CaCO}_3$ /BRA and SBR/BRA compound-modified asphalt.

Figure 2 shows that the complex shear moduli  $G^*$  of the five modified asphalts decreasing with increasing temperature. Under the same temperature conditions, the complex shear modulus  $G^*$  of 10% nano- $\text{CaCO}_3$ /BRA compound-modified asphalt is the largest. The BRA has the smallest complex shear modulus  $G^*$ . The complex shear modulus of 5% SBR/BRA compound-modified asphalt is much larger than that of 3% SBR/BRA compound-modified asphalt. This shows that the addition of nano- $\text{CaCO}_3$  and SBR can significantly improve the resistance of BRA to deformation, and with the increase of the amount of addition, the deformation resistance is enhanced.



**Figure 3.** The relationship between phase angle  $\delta$  and temperature of nano-CaCO<sub>3</sub>/BRA and SBR/BRA compound-modified asphalt.

As can be observed from Figure 3, under the same temperature conditions, the phase angle  $\delta$  of the 5% SBR/BRA compound-modified asphalt is the smallest, and that of the BRA is the largest. This shows that the addition of nano-CaCO<sub>3</sub> and SBR can improve the elastic composition of the BRA, and the 5% SBR/BRA compound-modified asphalt is the most likely to restore deformation compared with the other four kinds of modified asphalt.



**Figure 4.** The relationship between anti-rutting factors  $G^*/\sin\delta$  and the temperature of nano-CaCO<sub>3</sub>/BRA and SBR/BRA compound-modified asphalt.

It can be observed from Figure 4 that at the same temperature, the anti-rutting factors  $G^*/\sin\delta$  of the four kinds of BRA compound-modified asphalt are larger than that of BRA at the same temperature, and the rutting resistance of 10% nano-CaCO<sub>3</sub>/BRA compound-modified asphalt is the best. The failure temperature of 10% nano-CaCO<sub>3</sub>/BRA and 5% SBR/BRA compound-modified asphalts reached 88 °C, which is a temperature grade higher than the failure temperature of 82 °C. It shows that the high temperature properties of nano-CaCO<sub>3</sub>/BRA, SBR/BRA compound-modified asphalt, and anti-rutting performance are more superior to those of BRA.

### 3.1.2. Aging Resistance

Asphalt will be aging during the process of storage, mixing, transportation, construction, and service. Due to the long-time contact with air, under the influence of natural conditions, a series of physical and chemical reactions will happen, which will adversely affect the performance of asphalt pavement. The short-term aging of asphalt is mainly caused by the mixing and paving process. There are two test methods for indoor tests to simulate short-term aging: the thin film oven test (TFOT), and the rolling thin film oven test (RTFOT).

#### (1) Thin Film Oven Test (TFOT) test

The short-term aging test using the thin film oven test (TFOT) was employed in this paper. The stainless steel discs (diameter 140 mm × deep 9.5 mm) were loaded into the ventilation oven. The temperature of the oven was kept at 163 °C and the speed was kept at 5.5 r/min. After 5 h, the weight loss, penetration ratio, and rutting factor [31] of the aged asphalt samples were determined. The changes of indicators for nano-CaCO<sub>3</sub>/BRA and SBR/BRA compound-modified asphalt after the thin film oven test (TFOT) aging are shown in Table 6.

**Table 6.** The changes of indicators for nano-CaCO<sub>3</sub>/BRA and SBR/BRA compound-modified asphalt after thin film oven test (TFOT) aging.

Test Items	BRA	BRA + 3% SBR	BRA + 5% SBR	BRA + 5% Nano-CaCO <sub>3</sub>	BRA + 10% Nano-CaCO <sub>3</sub>
Mass loss (%)	0.343	0.279	0.260	0.254	0.229
Penetration (25 °C, 0.1 mm)	26.3	24.0	22.4	24.2	22.7
Penetration of after TFOT aging (0.1 mm)	18.8	22.5	21.4	21.2	20.4
Penetration ratio (%)	70.7	93.8	95.5	87.6	89.9

From Table 6, it can be observed that the quality of the five modified asphalts has been lost, and the quality loss of the 10% nano-CaCO<sub>3</sub>/BRA compound-modified asphalt is the least compared to that of the BRA. It shows that, during the aging process, the nano-CaCO<sub>3</sub>/BRA compound-modified asphalt has relatively less volatilization. The penetration ratio of 5% SBR/BRA compound-modified asphalt is the largest compared to that of BRA, even reaching 95.5%. This indicates that the 5% SBR can significantly improve the anti-aging properties of BRA.

The rutting resistance of the five modified asphalt samples after the thin film oven aging test was compared with rutting resistance before aging. The test data are shown in Figure 5.

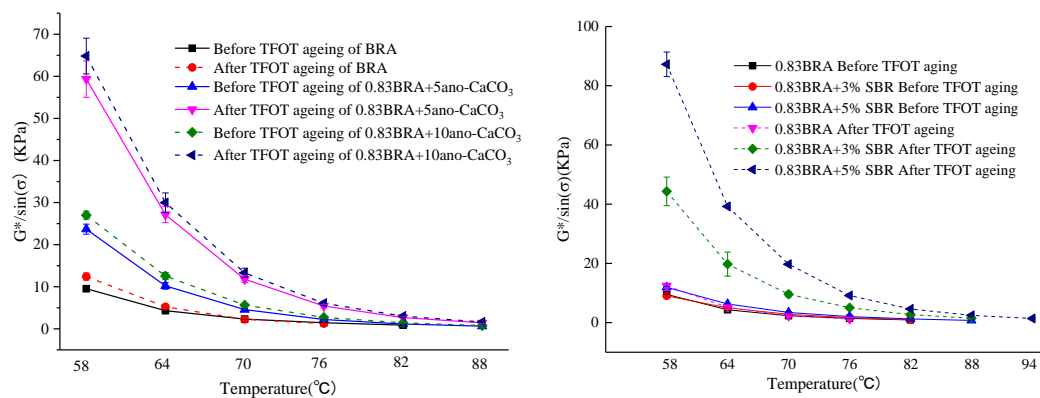


**Figure 5.** The relationship between Nano-CaCO<sub>3</sub>/BRA and SBR/BRA compound-modified asphalt before and after thin film oven test (TFOT) aging anti-rutting factors ( $G^*/\sin\delta$ ) and temperature.

The results can be observed from the curve change in Figure 5. It is known that both the original anti rutting factor and the anti-rutting factor after thin film oven test (TFOT) aging, the nano-CaCO<sub>3</sub>/BRA, and SBR/BRA compound-modified asphalt are all larger than the BRA. This shows that the addition of SBR and nano-CaCO<sub>3</sub> can improve the anti-rutting performance of BRA.

(2) Pressure Aging Vessel (PAV) test

The pressure aging vessel (PAV) aging test is a simulated oxidation aging of asphalt pavement over approximately five to eight years, which is employed to evaluate the antioxidant aging ability of different asphalts under the conditions of temperature and pressure. The test method of pressure aging vessel (PAV) aging is to put a thin film oven test (TFOT) sample into a pressure vessel with a pressure of 2.1 MPa ± 0.1 MPa and temperature of 90~110 °C for 20 h.

The samples of SBR/BRA and nano-CaCO<sub>3</sub>/BRA compound-modified asphalt with different content were tested with the bending beam rheometer (BBR), and test temperatures of -6 °C and -12 °C were adopted and compared with those before aging. The creep stiffness *S* and the creep slope *m* value of SBR/BRA and nano-CaCO<sub>3</sub>/BRA compound-modified asphalts were compared before and after pressure aging vessel (PAV) aging, as shown in Figures 6 and 7.

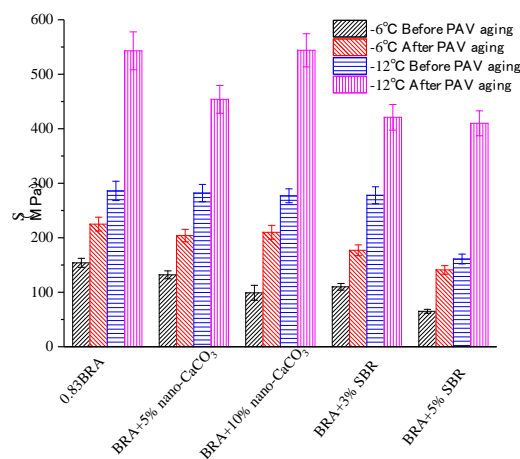


**Figure 6.** Creep stiffness *S* of nano-CaCO<sub>3</sub>/BRA and SBR/BRA compound-modified asphalt before and after pressure aging vessel (PAV) aging.

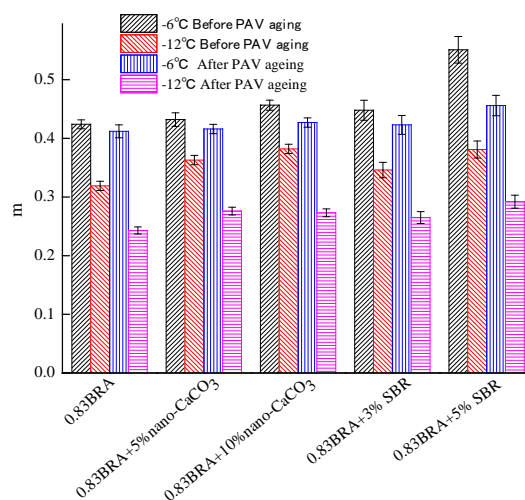


**Figure 7.** *m* value of nano-CaCO<sub>3</sub>/BRA and SBR/BRA compound-modified asphalt before and after pressure aging vessel (PAV) aging.

From Figures 6 and 7, it can be observed that at  $-6\text{ }^{\circ}\text{C}$ , the stiffness  $S$  and  $m$  value before and after pressure aging vessel (PAV) aging of nano- $\text{CaCO}_3$ /BRA and SBR/BRA compound-modified asphalt with different contents are satisfied with the requirements of  $S \leq 300\text{ MPa}$  and  $m \geq 0.3$ . Under the conditions of  $-6\text{ }^{\circ}\text{C}$  and  $-12\text{ }^{\circ}\text{C}$ , the  $S$  value of the 5% SBR compound-modified asphalt is the smallest relative to the other four kinds of modified asphalt before and after the pressure aging vessel (PAV) aging, but the  $m$  value is the largest, compared with the other four kinds of modified asphalt. This indicates that the 5% SBR/BRA compound-modified asphalt has the better low-temperature performance. The reason is that the SBR swells in the asphalt and forms a network structure, which is more resilient and more resistant to deformation.

From Figures 6 and 7, it can be observed that at the different content of nano- $\text{CaCO}_3$ , the low-temperature performance of BRA slightly improved. This is mainly because the BRA is a porous honeycombed structure, and nano- $\text{CaCO}_3$  is a nano-inorganic powder material that can be interspersed in the BRA to better integrate the BRA with the base asphalt. However, nano- $\text{CaCO}_3$  is prone to slight agglomeration, which affects the modification effect of base asphalt to some extent.

### 3.2. The Evaluation of Low-Temperature Performance for Modified Asphalt

#### 3.2.1. Test of Creep Compliance

Strategic highway research program (SHRP) proposed that the low-temperature performance of asphalt can be evaluated by the stiffness modulus obtained by the bending beam rheometer (BBR) creep test, which could build the relationship between the low-temperature performance and mechanical properties [27]. The creep compliance can be employed to characterize the flexibility of the material at low temperature.

The creep compliance is calculated as follows:

$$\sigma_0 = \frac{3PL}{2bh^2} \quad (1)$$

$$\varepsilon(t) = \frac{6h\delta(t)}{L^2} \quad (2)$$

where  $b$  is the width of a simply supported beam in mm;  $h$  is the height of a simply supported beam in mm;  $L$  is the span of a simply supported beam in mm;  $P$  is a constant load added on a simply supported beam,  $P$  is  $100\text{ g} \times 9.8\text{ N/kg} = 0.98\text{ N}$ ;  $\delta(t)$  is the mid-span deflection of the beam changing with time in mm.

Let Equation (2) divide by Equation (1); then, the creep compliance can be calculated:

$$J(t) = \frac{\varepsilon(t)}{\sigma_0} = \frac{48I}{PL^3}\delta(t) \quad (3)$$

where  $J(t)$  is the creep compliance in  $\text{MPa}^{-1}$ ;  $\varepsilon(t)$  is the strain of the creep test at different times in mm/mm;  $\sigma_0$  is the constant stress of creep test in MPa; and  $I$  is the moment of inertia for a cross-section of a beam specimen ( $=bh^3/12$ ) in  $\text{mm}^4$ .

#### 3.2.2. Bending Beam Rheometer Test

The bending beam rheometer (BBR) creep test, according to the controlled stress procedure of ASTM D6648, was conducted [27]. The creep tests of compound-modified asphalt are tested in different test temperatures ( $-6\text{ }^{\circ}\text{C}$ ,  $-12\text{ }^{\circ}\text{C}$ , and  $-18\text{ }^{\circ}\text{C}$ ) by Thermoelectric bending beam rheometer (TE-BBR) (Figure 8), respectively. The load and deformation in the testing process were automatically collected by a computer data acquisition system.

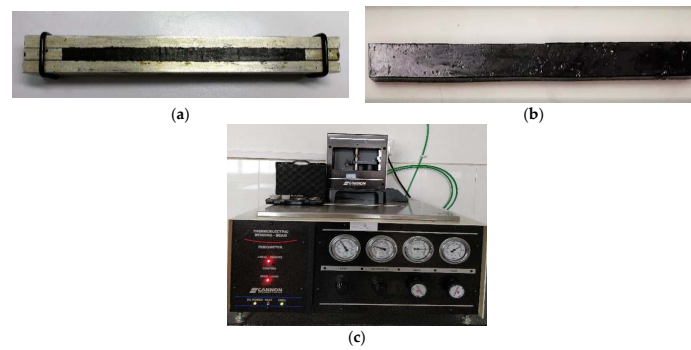


**Figure 8.** Thermoelectric bending beam rheometer (BBR) and specimen: (a) metal die of BBR; (b) asphalt beam of BBR; (c) thermoelectric bending beam rheometer.

### 3.2.3. Results of Creep Test

The curves of creep compliance of BRA compound-modified asphalt in  $-6\text{ }^{\circ}\text{C}$ ,  $-12\text{ }^{\circ}\text{C}$ , and  $-18\text{ }^{\circ}\text{C}$  are shown in Figure 9. From analyzing the creep compliance in Figure 9, conclusions can be drawn as below:

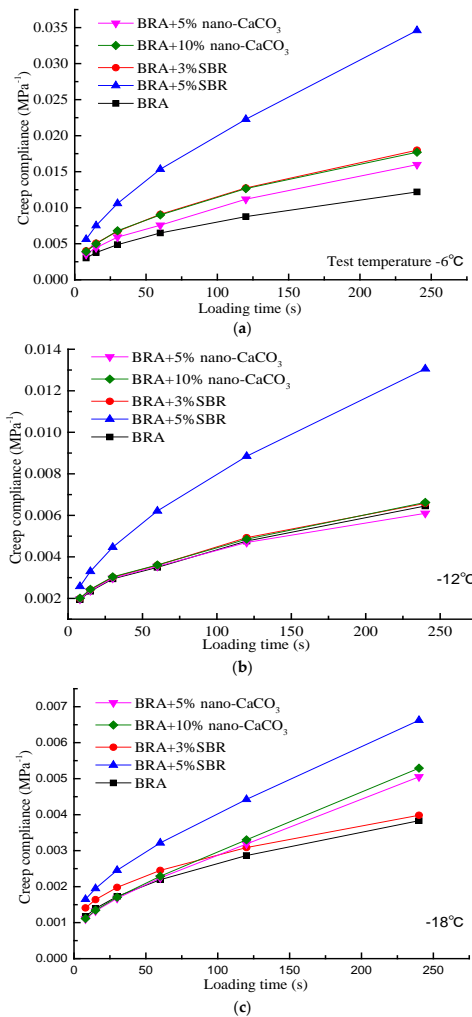


**Figure 9.** Creep compliance curve of different compound-modified asphalts: (a) the curves of creep compliance of BRA compound-modified asphalt in  $-6\text{ }^{\circ}\text{C}$ ; (b) the curves of creep compliance of BRA compound-modified asphalt in  $-12\text{ }^{\circ}\text{C}$ ; (c) the curves of creep compliance of BRA compound-modified asphalt in  $-18\text{ }^{\circ}\text{C}$ .



- (1) Comparison under the same temperature
  - (a) With the increase of the amounts of SBR, the creep compliance of BRA/SBR compound-modified asphalt will be increased, which means that SBR can improve the flexibility of BRA-modified asphalt. So, the low-temperature performance of BRA-modified asphalt can be improved.
  - (b) The creep compliance of BRA/nano-CaCO<sub>3</sub> compound-modified asphalt slightly increased with an increase of the mixing amount of nano-CaCO<sub>3</sub> at the same temperature, which means that the low-temperature performance of BRA/nano-CaCO<sub>3</sub> compound-modified asphalt slightly improved. Moreover, the improving effect of nano-CaCO<sub>3</sub> on the low-temperature performance of BRA-modified asphalt was less obvious when the temperature was lower.
- (2) Comparison under same time
  - (a) When the temperature was lowered, the compliance of two kinds of BRA compound-modified asphalt decreased, and the modified asphalt hardened.
  - (b) The creep compliance of BRA/SBR polymer compound-modified asphalt was larger than BRA-modified asphalt.
  - (c) As the temperature decreased, the creep compliance of BRA/nano-CaCO<sub>3</sub> compound-modified asphalt was close to that of BRA. It means that the improving effect of nano-CaCO<sub>3</sub> on the low-temperature performance of BRA-modified asphalt was not obvious.

In conclusion, BRA/SBR polymer compound-modified asphalt containing 5% SBR had the greatest creep compliance compared with the other asphalts in the same temperature and the same test time. So, SBR can improve the low-temperature performance of BRA-modified asphalt, and its suitable content is 5% in BRA-modified asphalt.

#### 4. Viscoelastic Damage Model Considering the Damage Effect

##### 4.1. The Establishment of Viscoelastic Damage Model Considering the Damage

To obtain the viscoelastic characteristics for asphalt, Burgers' model was used in many research studies. Lots of studies have demonstrated that asphalt is a viscoelastic fluid material, so asphalt's elasticity, viscoelasticity and flow limitation should be considered when the mechanical characteristics of asphalt are analyzed. Burgers' model is a viscoelastic model that is suitable for analyzing asphalt's rheological behavior. Burgers' model is made up of the Maxwell model and the Kelvin model, and is successfully applied to the viscoelastic analysis of asphalt and asphalt mixtures [32–35].

Burgers' model is shown in Figure 10.

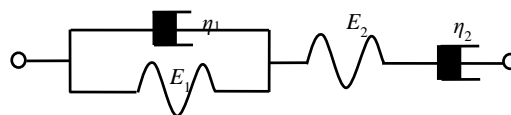


Figure 10. Burgers' model.

The expression for the creep compliance of Burgers' model is given by:

$$J(t) = \frac{1}{E_1} + \frac{t}{\eta_1} + \frac{1}{E_2} \left[ 1 - \exp\left(-\frac{t}{\tau}\right) \right] \quad (4)$$

where  $\tau = \eta_2/E_2$ ;  $E_1$ ,  $\eta_1$ ,  $E_2$  and  $\eta_2$  are the viscoelastic parameters of Burgers' model.

However, from the point of view of the mechanics of damage, if asphalt is under a constant load in the bending creep test, lots of microdefects in the materials will occur [36]. Therefore, if the prediction

of creep compliance is under the consideration of the damage factor in a special test temperature, the actual values and the fitted values have a very high fitting precision.

It is known from the formation and distribution of material defects that the defects are discrete in the material. However, in the need of research, continuum damage mechanics make material defects continuous, and use damage variables to characterize the effect of defects on the material. Many studies suggest that the Weibull distribution is suitable for the characterization of the defects distribution within a material, and has been widely used to analyze the fatigue damage characterization of asphalt and asphalt mixtures [37–41]. If microdefects in BRA compound-modified asphalt obey the Weibull distribution, the microdefects' density function changing with time is under:

$$f(t) = \frac{m}{n}(t - \gamma)^{m-1} \exp\left[-\frac{(t - \gamma)^m}{n}\right] \tag{5}$$

where  $m$  and  $n$  are the material parameters obtained by the regression of data of experiments.

$$\frac{dD(t)}{dt} = f(t) \tag{6}$$

The results of integrating Equations (2) and (3) are calculated as follows:

$$D(t) - D(\gamma) = \int_{\gamma}^t \frac{m}{n}(x - \gamma)^{m-1} \exp\left[-\frac{(x - \gamma)^m}{n}\right] dx \tag{7}$$

If the initial damage factor  $D(\gamma) = 0$ , Equation (7) is simplified as:

$$D(t) = 1 - \exp\left[-\frac{(t - \gamma)^m}{n}\right] \tag{8}$$

where  $\gamma$  = critical time of defects starting to form,  $\gamma$  is considered as 0 in the test, and then the continuous damage factor is simplified as:

$$D(t) = 1 - \exp\left(-\frac{t^m}{n}\right) \tag{9}$$

$$\begin{aligned} \varepsilon(t) &= [1 - D(t)]^{-1} \sigma_0 J(t) \\ &= \exp\left(\frac{t^m}{n}\right) \sigma_0 \left\{ \frac{1}{E_1} + \frac{t}{\eta_1} + \frac{1}{E_2} [1 - \exp(-\frac{t}{\tau})] \right\} \end{aligned} \tag{10}$$

From Equation (9), the existence of defects increases the creep strain's growth. Thus, if the damage is considered, the model for the variation of creep compliance of viscoelastic material will be accurate.

After putting  $\sigma_0$  to the left of Equation (10), Burgers' constitutive mode considering defects in material is given by:

$$\begin{aligned} J'(t) &= \frac{\varepsilon(t)}{\sigma_0} \\ &= \exp\left(\frac{t^m}{n}\right) \left\{ \frac{1}{E_1} + \frac{t}{\eta_1} + \frac{1}{E_2} [1 - \exp(-\frac{t}{\tau})] \right\} \end{aligned} \tag{11}$$

#### 4.2. Fitting Results of Viscoelastic Damage Model

The viscoelastic properties of two kinds of BRA compound-modified asphalt are analyzed by the viscoelastic damage model established in this paper. This Levenberg–Marquardt method was implemented to fit the creep compliance of BRA-modified asphalt in  $-6$  °C,  $-12$  °C, and  $-18$  °C. The parameters of creep compliance of the viscoelastic damage model are shown in Table 7. The columnar diagram viscoelastic parameters ( $E_1$ ,  $E_2$ ,  $\eta_1$  and  $\eta_2$ ) of the model changed with temperature are shown in Figure 11.

**Table 7.** Fitting results of viscoelastic damage model and Burgers’ model for different asphalts.

T (°C)	Asphalt Type	m	n	E <sub>1</sub> (MPa)	E <sub>2</sub> (MPa)	η <sub>1</sub> (MPa·s)	η <sub>2</sub> (MPa·s)	τ (s)	R <sup>2</sup>
-6	BRA	0.123	321.869	546.8	302.0	33,912.3	8225.6	27.24	0.9989
	+3% SBR	0.100	442.900	423.1	209.7	21,979.7	6223.6	29.68	0.9990
	+5% SBR	0.010	2634.839	357.9	127.0	9948.6	3930.3	30.95	0.9994
	+5% nano-CaCO <sub>3</sub>	0.093	452.713	446.0	277.2	23,538.8	8207.3	29.61	0.9985
	+10% nano-CaCO <sub>3</sub>	0.086	513.592	480.0	182.9	22,868.5	5118.1	27.98	0.9988
-12	BRA	0.159	321.821	717.6	680.1	66,678.5	16,874.3	24.81	0.9983
	+3% SBR	0.168	275.811	706.5	631.0	66,919.3	16,043.5	25.43	0.9979
	+5% SBR	0.066	854.2	684.2	326.3	27,941.3	9520.7	29.18	0.9993
	+5% nano-CaCO <sub>3</sub>	0.190	167.516	759.9	590.2	78,495.5	13,824.1	23.42	0.9976
	+10% nano-CaCO <sub>3</sub>	0.152	392.156	691.7	678.2	64,479.4	15,774.8	23.26	0.9985
-18	BRA	0.215	192.268	1220.6	998.7	121,513.3	27,984.9	28.02	0.9988
	+3% SBR	0.272	142.491	981.0	937.4	132,872.4	24,969.3	26.64	0.9985
	+5% SBR	0.148	1955.665	790.8	966.2	55,410.8	30,105.7	31.159	0.9999
	+5% nano-CaCO <sub>3</sub>	-20.539	0.005	1150.8	1848.8	65,875.3	55,528.0	30.03	0.9999
	+10% nano-CaCO <sub>3</sub>	-10.058	0.431	1128.3	1975.7	61,545.1	59,415.5	30.07	0.9999

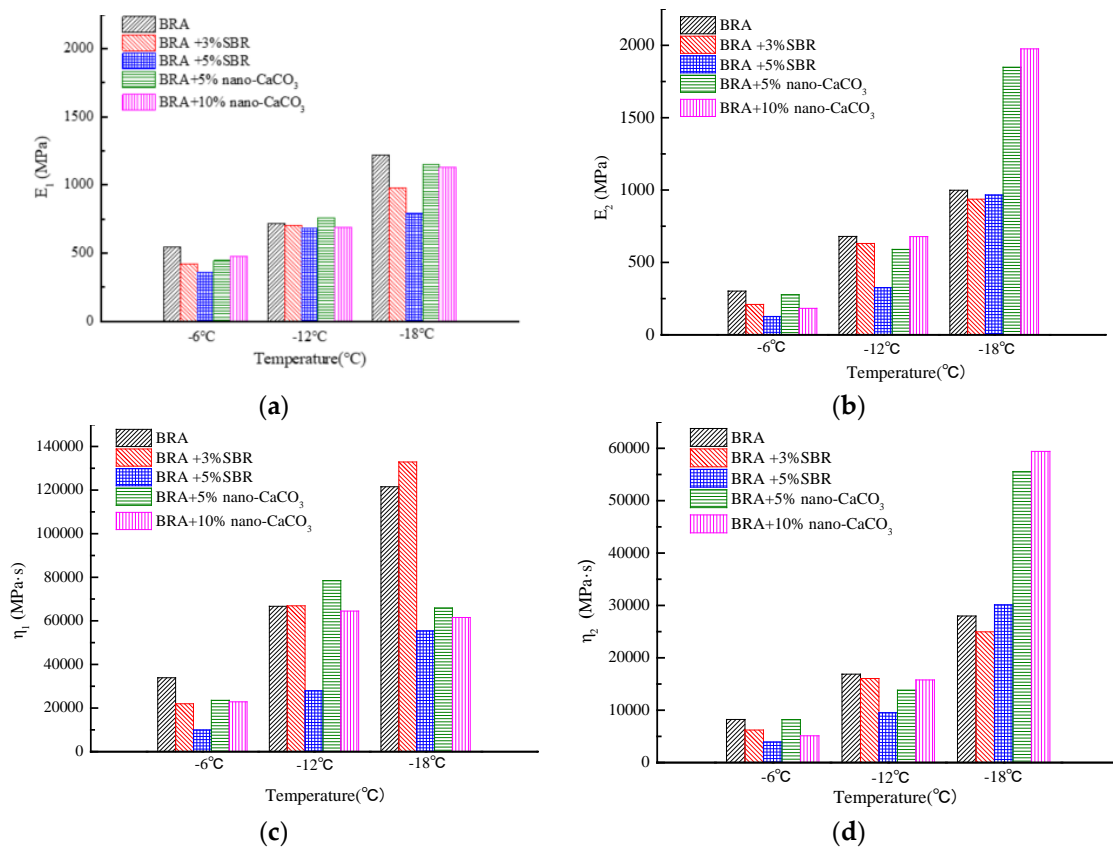


**Figure 11.** The comparison among viscoelastic damage model’s parameters of creep compliance: (a) the viscoelastic parameters ( $E_1$ ) of the model changed with temperature; (b) the viscoelastic parameters ( $E_2$ ) of the model changed with temperature; (c) the viscoelastic parameters ( $\eta_1$ ) of the model changed with temperature; (d) the viscoelastic parameters ( $\eta_2$ ) of the model changed with temperature.

(a) The coefficient of determination  $R^2$  between the model and test data shown in Table 7 indicated that the fitting degree of test data and creep compliance of viscoelastic damage model is very precise. So, considering the effect of microdefects during the loading process can improve the precision in the prediction of viscoelastic parameters of compound-modified asphalt.

- (b) As shown in Figure 11a,b,d, the viscoelastic parameters ( $E_1$ ,  $E_2$  and  $\eta_2$ ) of BRA compound-modified asphalt increased as the temperature decreased, which indicated that the low-temperature performance of the material decreased. Among the viscoelastic parameters,  $E_2$  and  $\eta_2$  had the same change trend as the temperature decreased, so both have good correlation with each other.
- (c) In three test temperatures, the viscoelastic parameters ( $E_1$ ,  $E_2$ , and  $\eta_1$ ) of BRA compound-modified asphalt, in which 5% SBR was the smallest among the test conditions, indicated that SBR could improve the flexibility and low-temperature performance of BRA-modified asphalt. The difference of viscoelastic parameters between BRA/nano-CaCO<sub>3</sub> compound-modified and BRA-modified asphalt is not obvious, which indicated that nano-CaCO<sub>3</sub> couldn't effectively improve the low-temperature performance of BRA-modified asphalt.

In conclusion, SBR can reduce the parameter values of BRA-modified asphalt and improve its flexibility effectively at low temperature. In order to improve the low-temperature performance, it is effective to add SBR into BRA-modified asphalt.

In this paper, the low-temperature performance of BRA compound-modified asphalt was evaluated only through asphalt, whereas the performance of an asphalt mixture is even closer to asphalt pavement than asphalt itself. So, subsequent research should focus on the performance of a SBR/BRA compound-modified asphalt mixture.

## 5. Conclusions

According to test and analysis results, the following conclusions were drawn:

1. The suitable addition of nano-CaCO<sub>3</sub> and SBR can improve the thermal stability and without negative effects to the aging resistance of BRA-modified asphalt to some extent. The anti-rutting performance of 10% BRA/nano-CaCO<sub>3</sub> compound-modified asphalt was the best. The thermal cracking performance of 5% BRA/SBR-modified asphalt has been effectively improved, and that of nano-CaCO<sub>3</sub> is not obvious.
2. The prediction accuracy of the viscoelasticity for compound-modified asphalt has been raised by the improved Burgers' model, and considered the effect of damage. The creep compliance shows a good agreement with the experimental results, so it can be applied to analyze the viscoelasticity of compound-modified asphalt.
3. The viscoelastic parameters ( $E_1$ ,  $E_2$  and  $\eta_1$ ) of BRA compound-modified asphalt increased with the decrease of temperature, which indicated that the flexibility of the material decreased.

**Author Contributions:** Data curation, S.L., S.W. and C.X.; Formal analysis, S.L., S.W. and C.X.; Funding acquisition, S.L., T.G. and G.H.; Investigaton, S.L.; Methodology, S.L.; Project administration, S.L.; Resources, S.L.; Supervision, S.L.; Visualization, S.L.; Writing—original draft, S.L., S.W., T.G., C.X. and J.L.; Writing—review & editing, S.L. and C.X.

**Funding:** This research was funded by National Natural Science Foundation of China (Grant number [51578081, 51608058]; The Ministry of Transport Construction Projects of Science and Technology [2015318825120]; The Guangxi Zhuang Autonomous Region Traffic and Transportation Department Transportation Projects of Science and Technology [2013-32], and The Inner Mongolia Autonomous Region Traffic and Transportation Department Transportation Projects of Science and Technology [NJ-2016-35].

**Acknowledgments:** This work is supported by Key Projects of Hunan Province-Technological Innovation Project in Industry [2016GK2096], National Engineering Laboratory Open Fund Project [kfh160102], Scientific and Technological Innovation Project of Hunan Province for University Graduate Students [CX2017B457]. The authors gratefully acknowledge their financial support.

**Conflicts of Interest:** The authors declare no conflict of interest.

## References

1. Lv, S.; Liu, C.; Yao, H.; Zheng, J. Comparisons of synchronous measurement methods on various moduli of asphalt mixtures. *Constr. Build. Mater.* **2018**, *158*, 1035–1045. [CrossRef]
2. Lv, S.; Liu, C.; Chen, D.; Zheng, J.; You, Z.; You, L. Normalization of fatigue characteristics for asphalt mixtures under different stress states. *Constr. Build. Mater.* **2018**, *177*, 33–42. [CrossRef]

3. Zhang, C.; Wang, H.; You, Z.; Liu, Y.; Yang, X.; Xiao, J. Prediction on rutting decay curves for asphalt pavement based on the pavement-ME and matter element analysis. *Int. J. Pavement Res. Technol.* **2017**, *10*, 466–475. [CrossRef]
4. Lv, S.; Fan, X.; Xia, C.; Zheng, J.; Chen, D.; You, L. Characteristics of Moduli Decay for the Asphalt Mixture under Different Loading Conditions. *Appl. Sci.* **2018**, *8*, 840. [CrossRef]
5. Li, R.; Karki, P.; Hao, P.; Bhasin, A. Rheological and low temperature properties of asphalt composites containing rock asphalts. *Constr. Build. Mater.* **2015**, *96*, 47–54. [CrossRef]
6. Lv, S.; Wang, X.; Liu, C.; Wang, S. Fatigue Damage Characteristics Considering the Difference of Tensile-Compression Modulus for Asphalt Mixture. *J. Test. Eval.* **2018**, *46*, 20170114. [CrossRef]
7. Huang, W. Experimental Investigation into Pavement Performance of Buton Rock Asphalt Mixtures. *J. South China Univ. Technol.* **2012**, *208*, 122–135. [CrossRef]
8. Yin, Y.M.; Zhang, X.N. Research on high temperature rheological characteristics of asphalt mastics with indonesian buton rock asphalt (BRA). *J. Wuhan Univ. Technol.* **2010**, *32*, 85–89. [CrossRef]
9. Ruixia, L.I.; Hao, P.; Wang, C.; Zhang, Q. Modified Mechanism of Buton Rock Asphalt. *J. Highw. Transp. Res. Dev.* **2011**, *12*, 4.
10. Du, S.W. Performance and mechanism of BRA-SBS polymer composite modified asphalt mixture. *J. Build. Mater.* **2012**, *15*, 871–874.
11. Hadiwardoyo, S.P.; Sinaga, E.S.; Fikri, H. The influence of Buton asphalt additive on skid resistance based on penetration index and temperature. *Constr. Build. Mater.* **2013**, *42*, 5–10. [CrossRef]
12. Wang, H.B.; Zhe-Sheng, G.E. Test of Dynamic Rheology Properties of Buton Rock Asphalt Modified Asphalt Cement at High-temperature. *J. Highw. Transp. Res. Dev.* **2008**, *9*, 25.
13. Kocevski, S.; Yagneswaran, S.; Xiao, F.; Punith, V.S.; Smith, D.W.; Amirkhanian, S. Surface modified ground rubber tire by grafting acrylic acid for paving applications. *Constr. Build. Mater.* **2012**, *34*, 83–90. [CrossRef]
14. Wang, M.; Lin, F.; Liu, L. Dynamic Rheological Properties and Microscopic Characteristics of Ash Mastics. *J. Tongji Univ.* **2016**, *44*, 567–571.
15. Nazari, H.; Naderi, K.; Moghadas Nejad, F. Improving aging resistance and fatigue performance of asphalt binders using inorganic nanoparticles. *Constr. Build. Mater.* **2018**, *170*, 591–602. [CrossRef]
16. Zhang, F.; Hu, C. The research for SBS and SBR compound modified asphalts with polyphosphoric acid and sulfur. *Constr. Build. Mater.* **2013**, *43*, 461–468. [CrossRef]
17. You, Z.; Orcid, Q.D.; Xiao, F. Advanced Paving Materials and Technologies. *Appl. Sci.* **2018**, *8*, 588. [CrossRef]
18. Yildirim, Y. Polymer modified asphalt binders. *Constr. Build. Mater.* **2007**, *21*, 66–72. [CrossRef]
19. Fang, C.; Yu, R.; Liu, S.; Li, Y. Nanomaterials Applied in Asphalt Modification: A Review. *J. Mater. Sci. Technol.* **2013**, *29*, 589–594. [CrossRef]
20. Yao, H.; You, Z.; Li, L.; Goh, S.W.; Lee, C.H.; Yap, Y.K.; Shi, X. Rheological properties and chemical analysis of nanoclay and carbon microfiber modified asphalt with Fourier transform infrared spectroscopy. *Constr. Build. Mater.* **2013**, *38*, 327–337. [CrossRef]
21. Jamshidi, A.; Mohd Hasan, M.R.; Yao, H.; You, Z.; Hamzah, M.O. Characterization of the rate of change of rheological properties of nano-modified asphalt. *Constr. Build. Mater.* **2015**, *98*, 437–446. [CrossRef]
22. Li, R.; Xiao, F.; Amirkhanian, S.; You, Z.; Huang, J. Developments of nano materials and technologies on asphalt materials—A review. *Constr. Build. Mater.* **2017**, *143*, 633–648. [CrossRef]
23. Jahromi, S.G.; Khodaii, A. Effects of nanoclay on rheological properties of bitumen binder. *Constr. Build. Mater.* **2009**, *23*, 2894–2904. [CrossRef]
24. Raufi, H.; Topal, A.; Kaya, D.; Sengoz, B. Performance Evaluation of Nano-CaCO<sub>3</sub> Modified Bitumen in Hot Mix Asphalt. In Proceedings of the 18th IRF World Road Meeting, Delhi, India, 14–17 November 2017.
25. Jamal Khattak, M.; Khattab, A.; Rizvi, H.R. Characterization of carbon nano-fiber modified hot mix asphalt mixtures. *Constr. Build. Mater.* **2013**, *40*, 738–745. [CrossRef]
26. Guo, N.; You, Z.; Tan, Y.; Zhao, Y. Performance evaluation of warm mix asphalt containing reclaimed asphalt mixtures. *Int. J. Pavement Eng.* **2016**, *18*, 1–9. [CrossRef]
27. ASTM. *Standard Test Method for Determining the Flexural Creep Stiffness of Asphalt Binder Using the Bending Beam Rheometer (BBR)*; ASTM: West Conshohocken, PA, USA, 2008.
28. Renmin Communication Press. *Specifications and Test Methods of Bitumen and Biminous Mixtures for Highway Engineering*; JTG E20-2011; Renmin Communication Press: Beijing, China, 2011.

29. Renmin Communication Press. *Modifier for Asphalt Mixture Part 5: Natural Asphalt*; JT/T860.5-2014; Renmin Communication Press: Beijing, China, 2014.
30. Renmin Communication Press. *Nanoscale Calcium Carbonate (Powdered Form)*; GB/T19590-2011; Renmin Communication Press: Beijing, China, 2011.
31. Chen, H.; Yan, Z.; Wang, B. Dynamic mechanics performance of aged SBS modified-asphalt. *J. Changan Univ.* **2009**, *29*, 1–5.
32. Liang, H.; Ling, T.; Yu, M.; Zhao, Y.; Tao, M.; Huang, X. High-temperature creep properties of asphalt-rubber and mixture with Sasobit warm mix additives. *J. Changan Univ.* **2015**, *35*, 16–23.
33. Hossain, M.I.; Faisal, H.M.; Tarefder, R.A. Characterisation and modelling of vapour-conditioned asphalt binders using nanoindentation. *Int. J. Pavement Eng.* **2015**, *16*, 382–396. [CrossRef]
34. Gao, D.Y.; Huang, C.S. Viscoelastic Mechanical Model with Five Units and Eight Parameters for Fiber Reinforced Asphalt Concrete. *China J. Highw. Trans.* **2014**, *27*, 1–8, 34.
35. Arabani, M.; Kamboozia, N. The linear visco-elastic behaviour of glasphalt mixture under dynamic loading conditions. *Constr. Build. Mater.* **2013**, *41*, 594–601. [CrossRef]
36. Tsinghua University Press. *Damage Mechanics*; Tsinghua University Press: Beijing, China, 1997.
37. Sharma, H.; Swamy, A.K. Development of probabilistic fatigue curve for asphalt concrete based on viscoelastic continuum damage mechanics. *Int. J. Pavement Res. Technol.* **2016**, *9*, 270–279. [CrossRef]
38. Yi, J.; Shen, S.; Muhunthan, B.; Feng, D. Viscoelastic–plastic damage model for porous asphalt mixtures: Application to uniaxial compression and freeze–thaw damage. *Mech. Mater.* **2014**, *70*, 67–75. [CrossRef]
39. Qian, Z.D.; Wang, J.Y.; Wang, Y.Q. Fatigue Performance of Composite Structure for Perpetual Pavement on Cement Concrete Bridge Deck. *China J. Highw. Trans.* **2012**, *25*, 67–73.
40. Zheng, J.; Lv, S.; Tian, X. Viscoelastic Damage Characteristics of Asphalt Based on Creep Test. *Eng. Mech.* **2008**, *25*, 193–196.
41. Falchetto, A.C.; Moon, K.H. Simple Approach to the Investigation of Asphalt Mixture Strength on Small Beam Specimens at Low Temperature. *J. Mater. Civ. Eng.* **2016**, *29*, 1–11. [CrossRef]




© 2018 by the authors. Licensee MDPI, Basel, Switzerland. This article is an open access article distributed under the terms and conditions of the Creative Commons Attribution (CC BY) license (<http://creativecommons.org/licenses/by/4.0/>).



Article

# Properties Analysis of Oil Shale Waste as Partial Aggregate Replacement in Open Grade Friction Course

Wei Guo <sup>1</sup>, Xuedong Guo <sup>1</sup>, Xing Chen <sup>2</sup> and Wenting Dai <sup>1,\*</sup> 

<sup>1</sup> School of Transportation, Jilin University, Changchun 130022, China; guowei17@mails.jlu.edu.cn (W.G.); guoxd@jlu.edu.cn (X.G.)

<sup>2</sup> Jilin Traffic Planning and Design Institute, Changchun 130000, China; chenxing14@mails.jlu.edu.cn

\* Correspondence: daiwt@jlu.edu.cn; Tel.: +86-130-8681-4298

Received: 2 August 2018; Accepted: 10 September 2018; Published: 12 September 2018

**Featured Application:** This paper developed a new modified open grade friction course. The modified OGFC was prepared by replacing the fine aggregate below 4.75 mm in OGFC with the oil shale waste, and the silane coupling agent modifier was used to assist modification. The technology of the modified OGFC preparation is an effective technique for improving the strength and stiffness of the OGFC and reducing environmental degradation.

**Abstract:** Open graded friction course (OGFC) is a high permeable mixture used to reduce noise, improve friction. However, limitations with the use of OGFC are due to the relatively low strength and stiffness. Therefore, investigating environmental and economic benefits, as well as service life of OGFC technology is the future of the pavement. In this study, a new modified OGFC (SM-OGFC) was prepared by replacing the fine aggregate below 4.75 mm in OGFC with the oil shale waste (OSW), and the silane coupling agent modifier was used to assist modification. The preparation process of SM-OGFC was optimized by central composite design, to obtain an SM-OGFC with the best mechanical properties. The Marshall test, rutting test,  $-15\text{ }^{\circ}\text{C}$  splitting test,  $-10\text{ }^{\circ}\text{C}$  beam bending test, immersion Marshall test, spring-thawing stability test, Cantabro test and permeability test were conducted to evaluate the properties of SM-OGFC. The results prove that SM-OGFC has excellent overall performance in comparison with OGFC and styrene-butadiene-styrene (SBS) modified OGFC. Furthermore, Scanning Electron Microscopy (SEM) observation illustrates that the unique laminar columnar connected structure and cell-like structure antennae of OSW could be the main reasons why SM-OGFC obtained excellent performance. Furthermore, economic analysis indicated that the SM-OGFC mixture had higher cost effectiveness.

**Keywords:** oil shale waste; silane coupling agent; replace fine aggregate; response surface methodology; central composite design

---

## 1. Introduction

The pavement community is actively using sustainable pavement options, such as extending pavement life to reduce life-cycle cost and work zones, increasing usage of recycled material, and industrial by-product, improving pavement surface characteristics for high skid resistance and low noise [1]. Open-graded friction course (OGFC) is a high permeable mixture used as a surface coat for good friction, and splash- and-spray reduction during rain storms. It also decreases the potential for hydroplaning and improve visibility by reducing glare from standing water on pavement [2–5].

However, limitations with the use of such mixtures are much more affected by the relatively low strength and low stiffness. OGFC pavements typically fail by raveling. More specifically, the pavement



fails when the asphalt binder ages and becomes brittle. Draindown, a separation of asphalt mastic from the course skeleton, can occur during storage or transport, which would result in a thin binder coating that is inadequate to prevent particles from being dislodged by traffic. The thin binder film can also age more rapidly, aggravating the raveling problem. Sometimes, the failure occurs when the pavement is only six to eight years old. Such a short life is difficult to accept [6–8].

In order to effectively reduce and prevent the occurrence of raveling damages in OGFC pavements, many researchers all over the world have conducted a large number of fruitful studies. Lyons et al. used different stabilizing additives (cellulose fibers, and styrene-butadiene-styrene (SBS)), and crumb rubber modifier (CRM) in a porous asphalt mixture. The results emphasized the importance of stabilizing additives in porous. Further, the results indicated that CRM or the combination of fibers and SBS were the most effective at increasing the abrasion resistance [9]; Luo et al. investigated a new open-graded asphalt mixture that used epoxy asphalt as binder to improve mix durability. Results showed superior overall performance of the open-graded epoxy asphalt mix compared to conventional open-graded asphalt mix [10]. Yang et al., conducted a material testing system fatigue test to investigate the fatigue performance of open graded friction courses modified with rock asphalt and rubber powder under different stress ratios. The results showed that modifiers, including natural rock asphalt and rubber powder, were added into OGFC could improve its fatigue performance [11]. Shen used rubber aggregate to prepare pavement friction course material. The results indicated that the polymer-rubber aggregate modified porous concrete with the optimum replacing ratio of rubber aggregate to mineral aggregate had higher flexural strength and compressive strength than the ordinary polymer modified porous concrete with mineral aggregate [12].

The technologies of adding the modifier is an effective technique for prolonging the OGFC pavement service life. However, such type of modifier presents high cost that restricts its application in modifying paving asphalt. In the past few years, many studies have been conducted on alternative environmental friendly materials in OGFC to improve its mechanical properties. The use of industrial waste is a promising solution to minimize environmental pollution by sinking the accumulation of waste materials, which results in a reduction of the construction costs [13–15]. Hainin et al. investigated utilization of steel slag as an aggregate replacement in porous asphalt mixtures. It was observed that the use of steel slag could perform admirably during high traffic loading [16]. Cheng et al. used oil shale ash instead of partial mineral powder in the mixture to improve the high- and low-temperature properties of asphalt pavement [17]. In conclusion, investigating environmental and economic benefits, as well as mechanical performance of OGFC technology is the future of the pavement.

However, to the best of our knowledge, no work has been conducted on mechanical performance evaluation of oil shale waste (OSW) as partial aggregate replacement in OGFC. Therefore, this research aimed to evaluate the comprehensive performance of the replacement of 100% of the virgin aggregates with particle sizes below 4.75 mm in OGFC with OSW and explore the optimized conditions for the preparation of the high-strength OGFC.

## **2. Materials and Methods**

### *2.1. Materials*

‘Pan Jin’ base asphalt (90#, F40-2004, Table 1) acquired from China Petrochemical industry was used in this paper. OSW, acquired from oil shale, was produced by a power plant in Jilin province China, as is shown in Figure 1. Properties of OSW are shown in Table 2.



Figure 1. Oil shale waste (OSW) in a power plant in Jilin province China.

Table 1. Technical parameters of ‘Pan Jin’ asphalt.

Technical Parameters	Penetration			25 °C Ductility	Softening Point	Wax Content	Flash Point	Solubility	Density
	15 °C	25 °C	30 °C						
Units		0.1 mm		cm	°C	%≤	°C	%≥	g·cm <sup>-3</sup>
Test results	27.5	81.3	132.6	>130	44.2	18	340	99.9	1.003

Table 2. Physical parameters of OSW.

Physical Property	Apparent Density (g/cm <sup>3</sup> )	Water Absorption (%)	Crushing Value (%)	Cohesion (Kpa)	Internal Friction Angle (°)	Optimum Water Rate (%)
OSW	2.627	18.6	42.2	13.84	33.3	28.3

According to Table 2, it can be seen that the apparent density of the OSW is very close to that of the stone, and the OSW has some characteristics of the rock. However, the OSW generated from the oil shale after extraction has higher crushing value and water absorption. The higher crushing value indicates that the residue cannot bear loads as a skeleton in the asphalt mixture. Higher water absorption may lead to poor water stability of OSW in the pavement material application. So, auxiliary modifiers are needed to improve water stability during application. Silane coupling agent, produced by Shuanglong Chemical Co., Ltd. (Changchun, China), was selected as auxiliary modifiers, since it had been reported to be among the most effective additives for water stability currently available. Silane coupling agent has a special molecular feature, in which it has two different types of functional groups, including organofunctional groups and hydrolysable groups. Silane coupling agent can easily bond silicate material and organic material, due to this molecular feature [18,19].

### 2.2. Oil Shale Waste Preparation

OSW is obtained from combustion of oil shale. Due to the high water absorption of OSW, the OSW stored in open air should be dried in an oven at 120 °C for 4 h. Afterwards, the dried OSW was smashed in the pulverizer, for 3 min, and the used OSW was obtained by sieving the crushed OSW through the 4.75 mm aperture-sized sieve.

### 2.3. SM-OGFC Sample Preparation

SM-OGFC samples are prepared to determine the optimization of SM-OGFC with different asphalt-aggregate ratio, different compaction times, different mixing temperature and different silane coupling agent content. Due to the high specific surface of OSW, the silane coupling agent is not suitable for surface treatment of the OSW directly, so pre-mixing of silane coupling agent and the heated base asphalt is necessary for better mixing. Firstly, the silane coupling agent was mixed into

the base asphalt at 160 °C to stir for 5 min. After pre-mixing, the asphalt with silane coupling agent, granites with grain size greater than 4.75 mm in gradation, OSW with grain size less than 4.75 mm in gradation and mineral powder with particle size less than 0.075 mm were mixed in the vacuum mixing pot. Finally, the SM-OGFC samples are formed through the compaction of mixture. The gradation of OGFC used in this paper is the most commonly used one in China, which is demonstrated in Table 3. The flowchart of preparation of the SM-OGFC is shown in Figure 2. Moreover, two types of OGFC were used for the performance comparison, a conventional OGFC mixture with ‘Pan Jin’ base asphalt (OGFC), and a modified OGFC with SBS modified asphalt (SBS-OGFC). All asphalt mixtures were specified based on Technical Specifications for Construction of Highway Asphalt Pavement in China (JTG F40-2004), and the optimum asphalt content was found to be 4.8% and 4.1% for the control mixture.

**Table 3.** Properties of aggregate and gradation of OGFC-16.

Sieve (mm)	16	13.2	9.5	4.75	2.36	1.18	0.6	0.3	0.15	0.075
Apparent density	2.78	2.78	2.78	2.74	2.74	2.75	2.70	2.70	2.69	2.67
Bulk density	2.77	2.76	2.75	2.68	2.64	2.59	2.60	2.59	2.57	2.55
Gradation (%)	97.5	65	47.5	23.5	11.5	11.5	9	7.5	6.0	4.5

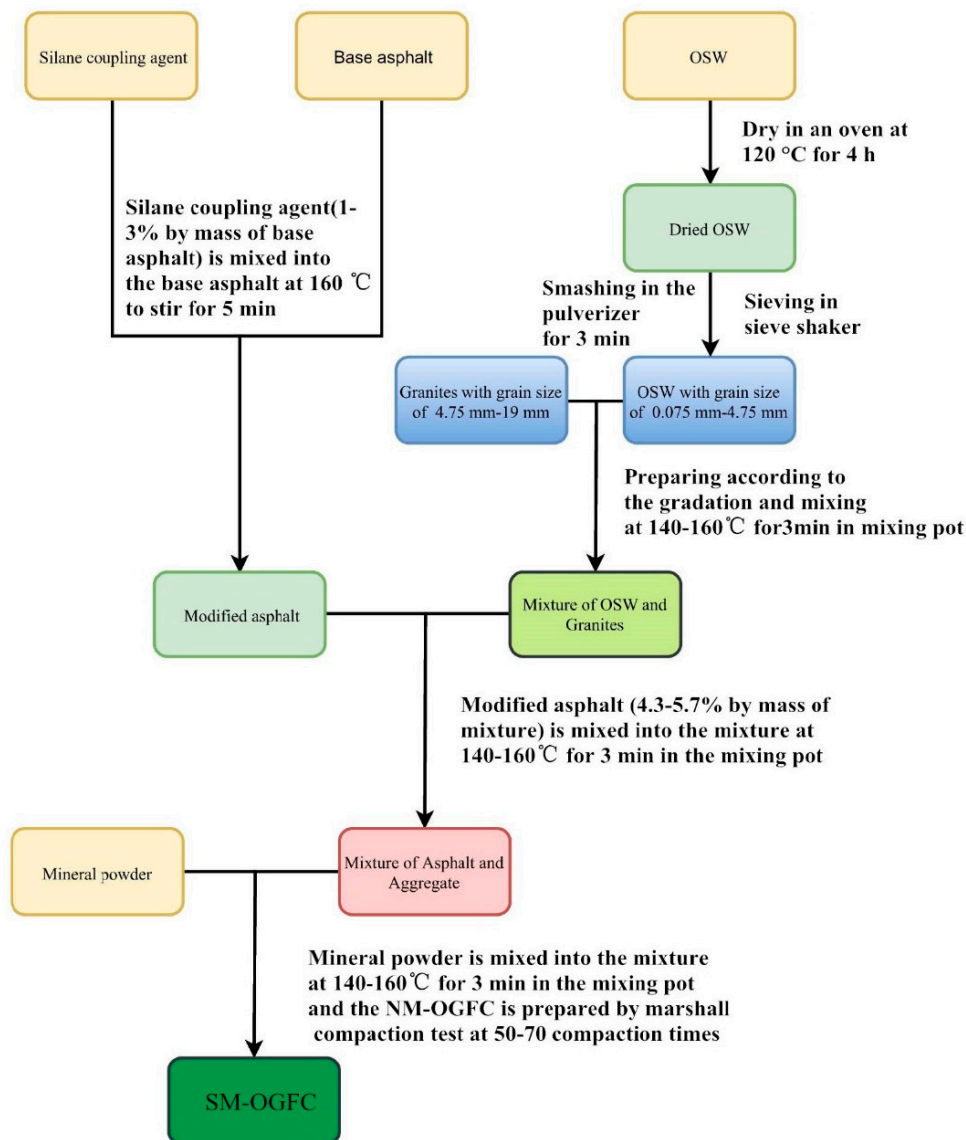


**Figure 2.** The flowchart of preparation of the SM-OGFC.

## 2.4. Performance Evaluation of SM-OGFC

### 2.4.1. High-Temperature Mechanical Performance Test

Marshall test and rutting test are conducted to evaluate the high-temperature performance of SM-OGFC according to Chinese standards GB/T0709-2011 and GB/T0719-2011 in this study. By assessing Marshall stability (MS) and dynamic stability (DS), the resistance of SM-OGFC to pressure, horizontal and shear stress induced from the loading in the high-temperature environment can be predicted.

### 2.4.2. Low-Temperature Mechanical Performance Test

The low-temperature properties of SM-OGFC is observed via Low-temperature splitting test and Low-temperature beam bending test. The splitting strength ( $R_T$ ) of mixtures is obtained by  $-15\text{ }^\circ\text{C}$  splitting test according to Chinese standards GB/T0716-2011. The  $-15\text{ }^\circ\text{C}$  splitting strength is an important factor for assessing the capacity of SM-OGFC to bear dynamic loads at low temperature. The bending-tensile strength ( $R_B$ ), maximum bending strain ( $\epsilon_B$ ) and the bending stiffness modulus ( $S_B$ ) of mixture is acquired through  $-10\text{ }^\circ\text{C}$  beam bending test according to Chinese standards GB/T0715-2011.

### 2.4.3. Water Stability Test

Immersion Marshall test was carried out, to evaluate the water stability of SM-OGFC according to Chinese standards GB/T0709-2011 in this study. Due to the interconnected pores and large porosity of OGFC, most of the water can freely discharge in the interconnected pores. However, there is always a part of the moisture remaining in the mixture, due to the surface tension and capillary action of the water, and the presence of the semi-intersecting void semi-connected pore. The volume of free water has expanded after freezing, which generates the internal temperature stress in the OGFC, and this effect can enlarge the micropore and the original crack in the OGFC. The ice crystalloid is transformed into free water, which caused moisture damage with the increase of temperature.

In order to better evaluate the water stability of OGFC in spring-thawing season, this paper use the spring-thawing stability index to evaluate the water stability of OGFC in spring-thawing season. The specimens were treated by vacuum saturation in 97.3 kPa for 15 min and submerged in a container containing water, then the container with specimens were placed in the precision temp-enclosure at  $-15\text{ }^\circ\text{C}$  and frozen 12 h. Then, the specimens were soaked in water at  $15\text{ }^\circ\text{C}$  for 12 h through controlling the precision temp-enclosure. As described above, a complete freeze-thaw cycle is completed. After 5 freeze-thaw cycles, damaged specimens were collected for Marshall test according to Chinese standards GB/T0709-2011.

### 2.4.4. Cantabro Test

Standard Cantabro Test was conducted to check the raveling resistance of SM-OGFC mixtures. The SM-OGFC mixtures were mixed and compacted in the laboratory using the Marshall compactor for the Cantabro Test (Chinese standards GB/T0733-2011). The specimens were conditioned to  $20\text{ }^\circ\text{C}$  for several hours before testing, and the Los Angeles abrasion drum was conditioned to  $20\text{ }^\circ\text{C} \pm 0.5\text{ }^\circ\text{C}$ . Specimens were weighed, individually subjected to 300 revolutions (30–33 rpm) in the Los Angeles abrasion drum without steel charge, brushed with a soft-bristled brush, and weighed again. The Cantabro losses for each specimen are the mass lost during testing, divided by the specimen initial mass.

### 2.4.5. Permeability Test and Scanning Electronic Microscopy Test

OGFC mixture is a special type of hot mix asphalt characterized by high interconnected air voids and a coarse, granular skeleton, with proper stone-on-stone contact. The presence of a larger

percentage of internal air voids leads to a relatively highly porous structure of OGFC mixes, which helps in quick and effective removal of surface water from the pavement. Thus, the permeability capacity of SM-OGFC determines the performance of permeable pavements. The permeability capacity of SM-OGFC is evaluated via permeability test. The laboratory permeability test is divided into constant head permeability test and falling head permeability test based on Darcy's law. The constant head permeability test is generally applied to measure the permeability coefficient of high permeability material and the falling head permeability test is applicable to low permeability material [20,21]. Therefore, the constant head permeability test was conducted to evaluate the permeability coefficient of SM-OGFC, in accordance with the Specifications for Design of Highway Asphalt Pavement (JTG D50-2006), and the permeability coefficient ( $K$ ) is obtained by the Equation (1):

$$K_{20^{\circ}\text{C}} = \frac{QL}{At\Delta t} \quad (1)$$

$Q$ : The quantity of the water permeating through the specimen during  $t$  time ( $\text{cm}^3$ )

$L$ : Infiltration length (cm)

$A$ : Cross-sectional area of the specimen ( $\text{cm}^2$ )

$t$ : Infiltration time (s)

$\Delta t$ : Water head difference (cm)

Scanning Electron Microscopy test (SEM) was used to magnify the sample and observe its microscopic structure. In this research study, Hitachi SU8000 (Tianmei.co, Tokyo, Japan) scanning electronic microscopy was utilized to observe the micro-structure of OSW particles.

### 3. Optimization of SM-OGFC by Response Surface Methodology (RSM)

#### 3.1. Central Composite Design

In regards to the optimization of SM-OGFC, several factors, such as the asphalt-aggregate ratio, silane coupling agent content, compaction times and mixing temperature, could remarkably influence the compressive strength SM-OGFC. However, if just a single variable of the aforementioned factors is analyzed, cross-impact of the variables would usually be neglected. On the other hand, a complete experimental design to explore the relationships of the exploratory variables is often time-consuming. In this context, response surface methodology (RSM) has been suggested to find the most valuable point, or called optimization to simplify the experimental design and simultaneously, maximize the production, or minimize the cost, side reactions, etc. RSM has been applied in many fields, such as chemical reactions, industry manufacture and many other product optimization. In regards to the RSM, central composite design (CCD) is often used to support the optimization of a two-level factorial or fraction factorial design, which is usually coded as  $-1$  and  $1$  so as to simplify the experimental expression and calculation [22–24]. Nassar et al. applied a central composite design (CCD) with response surface methodology (RSM) to optimize the mix design parameters of cold bitumen emulsion mixture, namely bitumen emulsion content (BEC), pre-wetting water content (PWC) and curing temperature (CT) [25]. Wang et al. designed an experimental scheme to optimize three preparation parameters of styrene-butadiene-styrene (SBS)-modified asphalt mixture reinforced with eco-friendly basalt fiber based on response surface methodology (RSM) [26].

In this study, asphalt-aggregate ratio and silane coupling agent content are considered as key factors in the preparation of SM-OGFC samples; compaction times and mixing temperature are also considered as vital factor in the preparation study. Experiments are designed with six central points. Table 4 shows the range of asphalt-aggregate ratio, silane coupling agent content, compaction times and mixing temperature respectively. The Marshall stability,  $-15^{\circ}\text{C}$  splitting strength, and spring-thawing stability are considered as the response of the software. In this study, CCD approach suggests 30 experiments; six of them are replicated as the central point. Table 5 reveals the proffered experiments and results.

**Table 4.** The coded level of affected variable.

Name	Units	Lower Limit (−1)	Upper Limit (+1)
Asphalt-aggregate ratio	%	4.3	5.7
Silane coupling agent content	%	1	3
Mixing temperature	°C	140	160
Compaction times	n	50	70

**Table 5.** Central composite design.

Run	Asphalt-Aggregate Ratio (A)	Silane Coupling Agent Content (B)	Mixing Tem-Perature (C)	Compaction Times (D)	Marshall Stability (KN)	−15 °C Splitting Strength (Mpa)	Spring-Thawing Stability (KN)
1	1	−1	1	−1	9.01	3.06	7.62
2	−1	1	−1	1	8.49	2.04	7.32
3	1	1	1	−1	9.33	3.4	7.99
4	0	0	2	0	8.98	3.55	7.80
5	1	−1	−1	1	8.98	3.93	7.63
6	−1	−1	1	−1	8.50	2.67	7.30
7	1	1	−1	−1	9.02	3.55	7.73
8	0	−2	0	0	8.78	3.38	7.82
9	1	1	−1	1	8.97	3.42	7.80
10	1	1	1	1	8.67	3.5	7.52
11	1	−1	−1	−1	8.67	3.15	7.63
12	0	0	0	0	9.57	3.89	8.24
13	0	0	0	0	9.64	4.05	8.17
14	−1	1	1	1	8.14	2.41	7.17
15	−1	1	1	−1	8.56	2.45	7.62
16	0	0	−2	0	9.06	3.18	7.93
17	2	0	0	0	7.10	2.54	6.07
18	−1	−1	1	1	8.17	2.93	7.14
19	0	0	0	2	9.30	3.91	8.07
20	0	0	0	0	9.87	3.82	8.66
21	−1	1	−1	−1	8.28	2.48	7.19
22	0	0	0	0	9.22	3.68	8.27
23	0	0	0	−2	9.81	3.48	8.42
24	−1	−1	−1	1	8.06	2.7	7.27
25	−1.429	0	0	0	7.57	1.8	6.52
26	0	2	0	0	9.13	3.09	8.24
27	1	−1	1	1	8.67	3.73	7.28
28	0	0	0	0	9.63	3.57	8.41
29	−1	−1	−1	−1	8.09	2.43	6.91
30	0	0	0	0	9.67	3.82	8.36

### 3.2. Build RSM Model

Model Fit Summary tab is a statistical appraisalment used to suggest the most appropriate model. Take −15 °C splitting strength response model as an example, the details of Model Fit Summary tab are summarized in Table 6. The proposed quadratic model is suggested, due to the *p*-value of the model is less than 0.0001 and the F-value is equal to 44.51.

**Table 6.** Different statistical values form Model Fit Summary tab.

Source	Sequential <i>p</i> -Value	Lack of Fit <i>p</i> -Value	Adjusted R-Squared	Predicted R-Squared
Linear	0.0345	0.0050	0.2225	0.0708
2FI	0.9022	0.0030	0.0783	−0.1258
Quadratic	<0.0001	0.8855	0.9546	0.9240
Cubic	0.7924	0.9204	0.9382	

Based on the experimental data of Table 5, the regression equation of  $-15\text{ }^\circ\text{C}$  splitting strength is calculated by the Equation (2):

$$R_T = 3.79 + 0.49 \times A - 0.08 \times B + 0.05 \times C + 0.097 \times D + 0.084 \times AB - 0.073 \times AC + 0.086 \times AD + 0.006 \times BC - 0.16 \times BD + 0.032 \times CD - 0.56 \times A^2 - 0.13 \times B^2 - 0.1 \times C^2 - 0.018 \times D^2. \tag{2}$$

Moreover, it is found that A, B, D, AB, AC, AD, BD,  $A^2$ ,  $B^2$ , and  $C^2$  terms are significant factors with  $p$ -values less than 0.0500 through ANOVA Analysis. The details of ANOVA Analysis are summarized in Table 7. Based on the analysis above, the original regression is revised. Equation (3) presents the modified regression equation, which deletes the non-significant model terms:

$$R_T = 3.79 + 0.49 \times A - 0.08 \times B + 0.097 \times D + 0.084 \times AB - 0.073 \times AC + 0.086 \times AD - 0.16 \times BD - 0.56 \times A^2 - 0.13 \times B^2 - 0.1 \times C^2. \tag{3}$$

Credibility analysis of modified regression equation is summarized in Table 8. According to Table 8, the value of  $R^2$  is almost one, and therefore the experimental results are in good agreement with the predicted values. In addition, the difference between  $R^2$  and  $R_{Adj}^2$  is 0.02, and there is a good accordance between  $R_{Pred}^2$  and  $R_{Adj}^2$  indicating the accuracy of the proposed model.

**Table 7.** ANOVA Analysis of  $-15\text{ }^\circ\text{C}$  splitting strength response model.

Source	Sum of Squares	df	Mean Square	F-Value	$p$ -Value
Model	10.6	14	0.76	44.51	<0.0001
A-Asphalt-aggregate ratio	5.06	1	5.06	297.6	<0.0001
B-Silane coupling agent content	0.16	1	0.16	9.12	0.0086
C-Mixing temperature	0.059	1	0.059	3.47	0.0823
D-Compaction times	0.23	1	0.23	13.29	0.0024
AB	0.11	1	0.11	6.69	0.0206
AC	0.086	1	0.086	5.03	0.0405
AD	0.12	1	0.12	6.89	0.0191
BC	$5.06 \times 10^{-4}$	1	$5.06 \times 10^{-4}$	0.03	0.8654
BD	0.39	1	0.39	22.77	0.0002
CD	0.016	1	0.016	0.96	0.3439
$A^2$	5.94	1	5.94	349.09	<0.0001
$B^2$	0.49	1	0.49	28.95	<0.0001
$C^2$	0.28	1	0.28	16.54	0.001
$D^2$	$9.14 \times 10^{-3}$	1	$9.14 \times 10^{-3}$	0.54	0.475
Residual	0.26	15	0.017		

**Table 8.** Credibility analysis of modified regression equation.

Std.Dev.	0.13	$R^2$	0.9765
Mean	3.19	$R_{Adj}^2$	0.9546
C.V.%	4.09	$R_{Pred}^2$	0.9240
PRESS	0.82	Adeq Precisor	21.416

### 3.3. RSM Model Validation

The validation of the model can be examined with the diagnostic tab in the design-expert software. The normal plot of the residuals of  $-15\text{ }^\circ\text{C}$  splitting strength is shown in Figure 3. A straight line almost covers all the points, and therefore, there is a normal distribution of errors in the experiments. In addition, there is no abnormal pattern or structure in the residuals plot (Figure 4).

The difference between predicted and actual values of the response is shown in Figure 5. A straight line almost cover all the points, and therefore there are negligible errors between the predicted and actual responses. Thereupon, the proposed mathematical regression is authentic.

Design-Expert?Software  
-15°C splitting strength  
Color points by value of  
-15°C splitting strength:  
4.05  
1.8

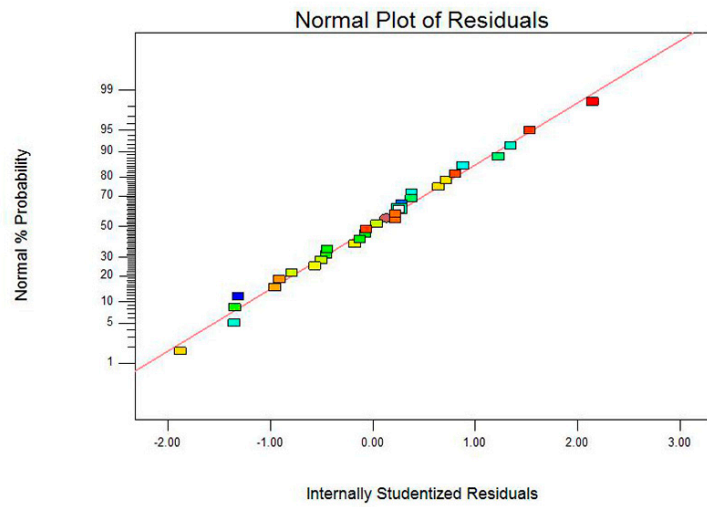


Figure 3. Normal probability plot of residuals of  $-15^{\circ}\text{C}$  splitting strength.

Design-Expert?Software  
-15°C splitting strength  
Color points by value of  
-15°C splitting strength:  
4.05  
1.8

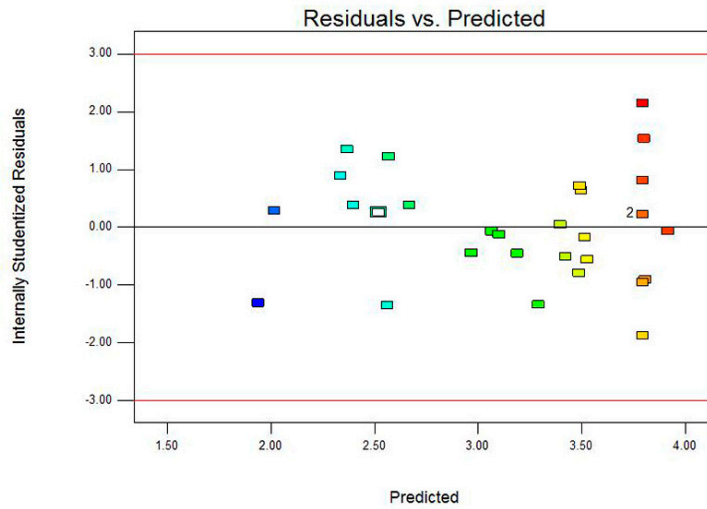


Figure 4. Residual versus predicted values of  $-15^{\circ}\text{C}$  splitting strength.

Design-Expert?Software  
-15°C splitting strength  
Color points by value of  
-15°C splitting strength:  
4.05  
1.8

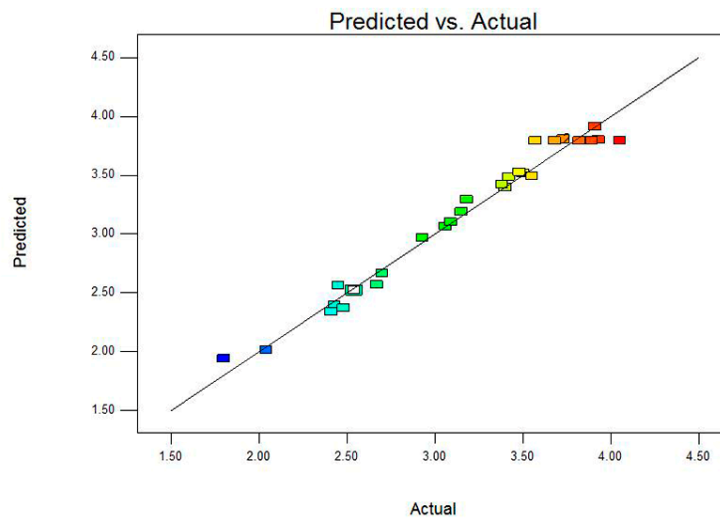


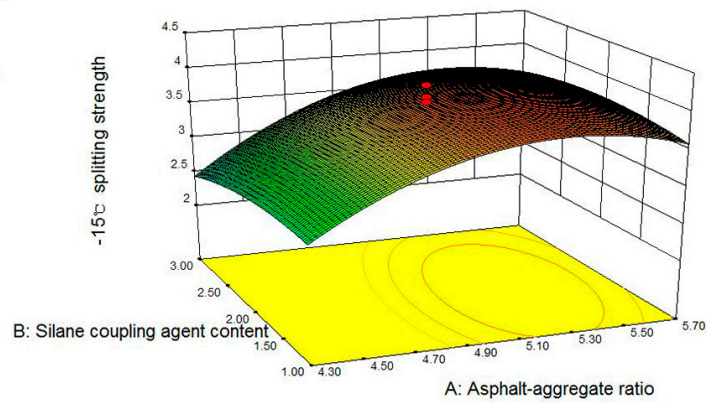
Figure 5. Predicted against actual responses of  $-15^{\circ}\text{C}$  splitting strength.



### 3.4. Response Surface Interaction Analysis

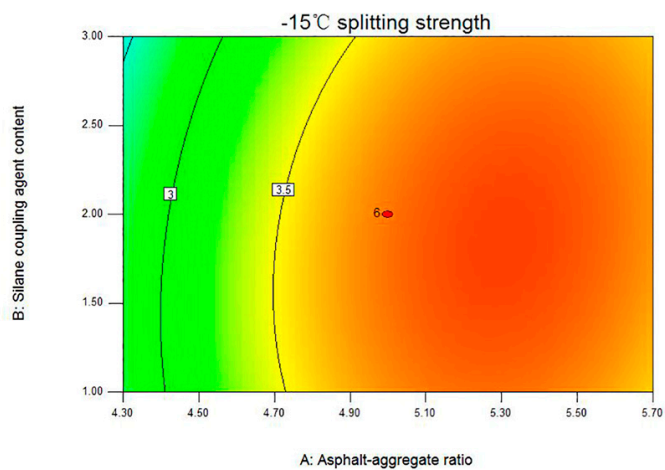
Response surface and Contour plot of regression model is shown in Figure 6A<sub>1</sub>–D<sub>2</sub>.

Design-Expert?Software  
 Factor Coding: Actual  
 -15°C splitting strength  
 ● Design points above predicted value  
 ○ Design points below predicted value  
 4.05  
 1.8  
 X1 = A: Asphalt-aggregate ratio  
 X2 = B: Silane coupling agent content  
 Actual Factors  
 C: Mixing temperature = 150.00  
 D: Compaction times = 60.00



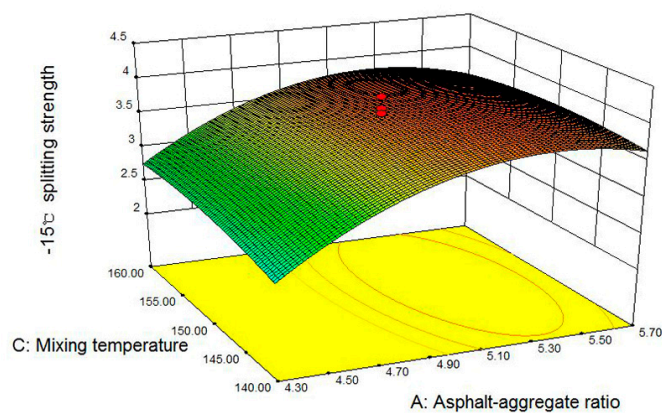
A<sub>1</sub>

Design-Expert?Software  
 Factor Coding: Actual  
 -15°C splitting strength  
 ● Design Points  
 4.05  
 1.8  
 X1 = A: Asphalt-aggregate ratio  
 X2 = B: Silane coupling agent content  
 Actual Factors  
 C: Mixing temperature = 150.00  
 D: Compaction times = 60.00



A<sub>2</sub>

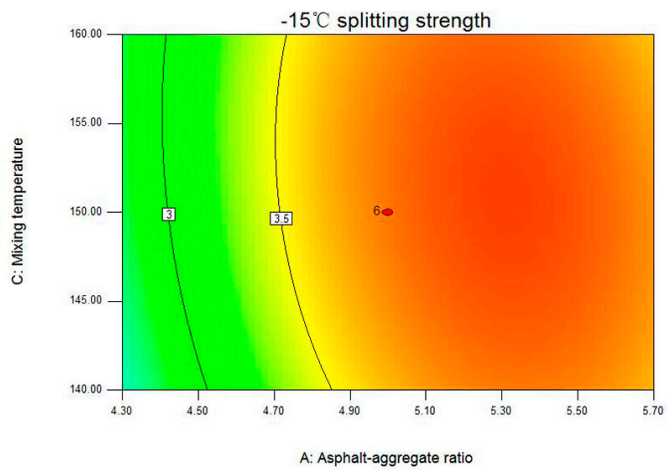
Design-Expert?Software  
 Factor Coding: Actual  
 -15°C splitting strength  
 ● Design points above predicted value  
 ○ Design points below predicted value  
 4.05  
 1.8  
 X1 = A: Asphalt-aggregate ratio  
 X2 = C: Mixing temperature  
 Actual Factors  
 B: Silane coupling agent content = 2.00  
 D: Compaction times = 60.00



B<sub>1</sub>

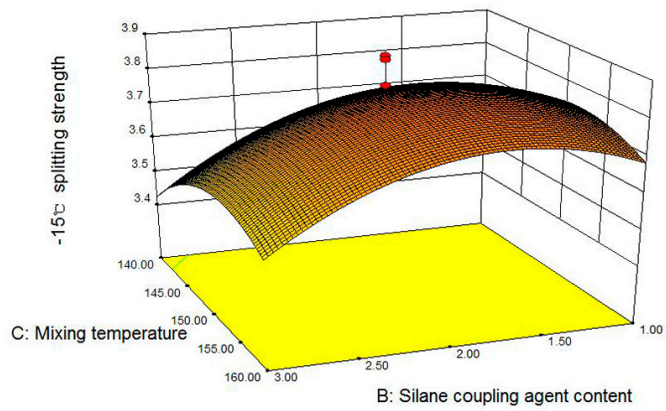
Figure 6. Cont.

Design-Expert?Software  
 Factor Coding: Actual  
 -15°C splitting strength  
 ● Design Points  
 4.05  
 1.8  
 X1 = A: Asphalt-aggregate ratio  
 X2 = C: Mixing temperature  
 Actual Factors  
 B: Silane coupling agent content = 2.00  
 D: Compaction times = 60.00



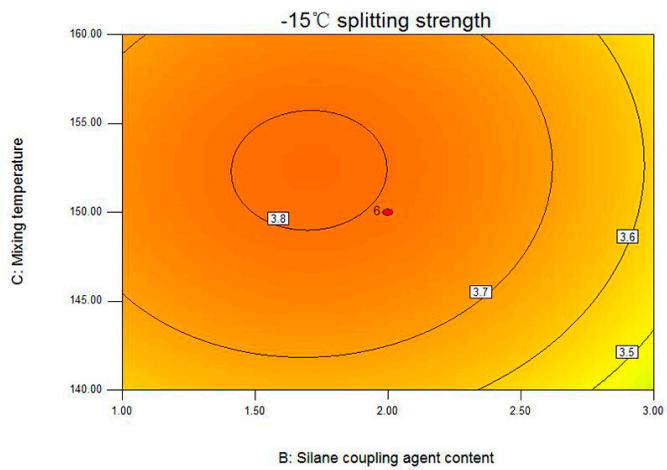
B<sub>2</sub>

Design-Expert?Software  
 Factor Coding: Actual  
 -15°C splitting strength  
 ● Design points above predicted value  
 ○ Design points below predicted value  
 4.05  
 1.8  
 X1 = B: Silane coupling agent content  
 X2 = C: Mixing temperature  
 Actual Factors  
 A: Asphalt-aggregate ratio = 5.00  
 D: Compaction times = 60.00



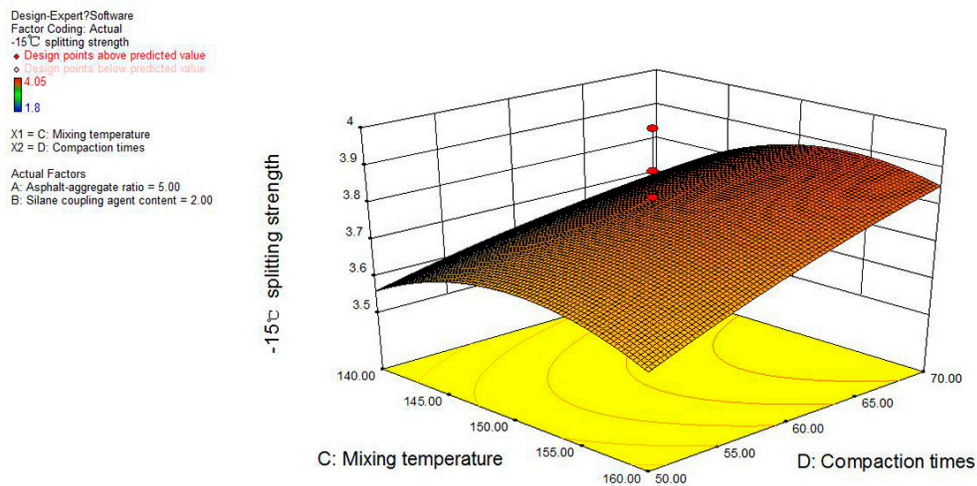
C<sub>1</sub>

Design-Expert?Software  
 Factor Coding: Actual  
 -15°C splitting strength  
 ● Design Points  
 4.05  
 1.8  
 X1 = B: Silane coupling agent content  
 X2 = C: Mixing temperature  
 Actual Factors  
 A: Asphalt-aggregate ratio = 5.00  
 D: Compaction times = 60.00

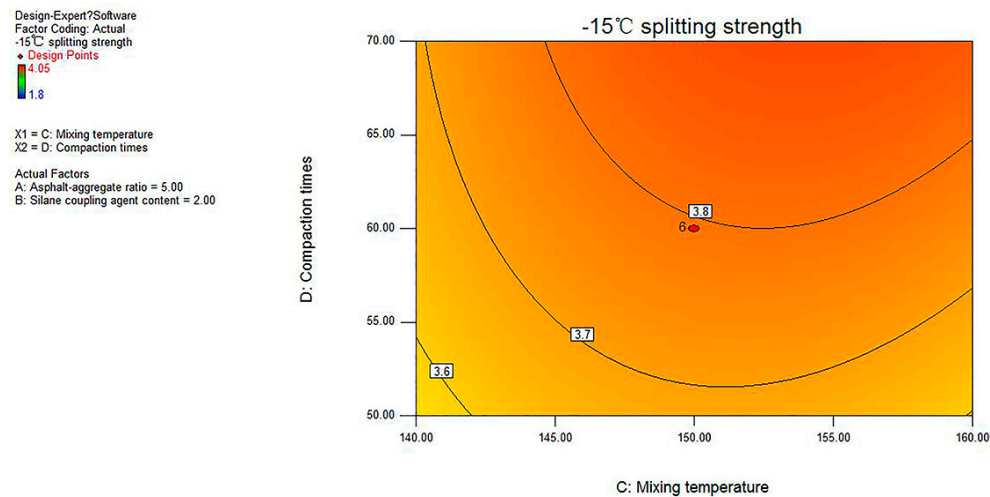


C<sub>2</sub>

Figure 6. Cont.



D<sub>1</sub>



D<sub>2</sub>

**Figure 6.** (A<sub>1</sub>) 3D surface graph of  $-15\text{ }^{\circ}\text{C}$  splitting strength against A and B; (A<sub>2</sub>) contour plot of  $-15\text{ }^{\circ}\text{C}$  splitting strength against A and B; (B<sub>1</sub>) 3D surface graph of  $-15\text{ }^{\circ}\text{C}$  splitting strength against A and C; (B<sub>2</sub>) contour plot of  $-15\text{ }^{\circ}\text{C}$  splitting strength against A and C; (C<sub>1</sub>) 3D surface graph of  $-15\text{ }^{\circ}\text{C}$  splitting strength against B and C; (C<sub>2</sub>) contour plot of  $-15\text{ }^{\circ}\text{C}$  splitting strength against B and C; (D<sub>1</sub>) 3D surface graph of  $-15\text{ }^{\circ}\text{C}$  splitting strength against C and D; (D<sub>2</sub>) contour plot of  $-15\text{ }^{\circ}\text{C}$  splitting strength against C and D.

As shown in the comparison between the four group diagrams, the influence of asphalt-aggregate ratio on  $-15\text{ }^{\circ}\text{C}$  splitting strength is the most significant, which is characterized by the steepness of the surface in Figure 6A<sub>1</sub>,B<sub>1</sub>.

Figure 6B<sub>1</sub> shows a three-dimensional plot of  $-15\text{ }^{\circ}\text{C}$  splitting strength against asphalt-aggregate ratio and mixing temperature when silane coupling agent content is 2% and the compaction times is 60. As can be seen from Figure 6B<sub>1</sub>, with the increase of the asphalt-aggregate,  $-15\text{ }^{\circ}\text{C}$  splitting strength continues to grow until it reaches a stable value. At the mixing temperature of  $140\text{ }^{\circ}\text{C}$ ,  $-15\text{ }^{\circ}\text{C}$  splitting strength rises from 2.52 Mpa to 3.64 Mpa with the increase of asphalt-aggregate ratio from 4.3 to 5%. In addition, with the increasing of asphalt-aggregate ratio within the reasonable range,  $-15\text{ }^{\circ}\text{C}$  splitting strength is maintained at about 3.64 Mpa. This is because the OSW has higher specific surface area compared with stone, thus it can absorb more free asphalt. With the increase of asphalt-aggregate

ratio, the structural asphalt adsorbed on the aggregate surface gradually increased. Therefore, the mechanical properties of SM-OGFC to resist low temperature load are improved.

The shape of contour can reflect the strength of interaction. Oval indicates that the interaction of two factors is significant while circle is the opposite. It can be seen the contour line is oval from Figure 6A<sub>2</sub>, B<sub>2</sub> and D<sub>2</sub>), so the interaction of asphalt-aggregate ratio and silane coupling agent content, asphalt-aggregate ratio and mixing temperature, compaction times and mixing temperature are significant. In comparison, the interaction between silane coupling agent content and mixing temperature is slightly weaker.

### 3.5. Numerical Optimization

Through the discussion of the RSM model, it is found that the process parameters, including asphalt-aggregate ratio, silane coupling agent content, compaction times, and mixing temperature have to confirm in their ranges so that the response factor would be able to reach to its maximum value. The optimal solution to maximin the response factor is shown in Table 9.

**Table 9.** Optimal conditions obtained by Numerical optimization.

Asphalt-aggregate ratio	5.18%
Silane coupling agent content	2.50%
Mixing temperature	153 °C
Compaction times	50
Desirability	0.056

## 4. Results and Discussion

### 4.1. Marshall Test and Rutting Test Results

The Marshall stability of all OGFC mixtures is shown in Figure 7. As shown in Figure 7, the OSW as partial aggregate replacement in OGFC could be effective in enhancing the MS of OGFC mixtures. The higher MS value indicates that the OGFC mixture is stiffer and has better resistance against permanent deformation. The MS value of OGFC, SBS-OGFC, and SM-OGFC were found to be 6.47, 9.12, and 9.63, respectively. It should be noted that the MS value of SM-OGFC was 48.8% higher than OGFC, even 5.6% higher than SBS-OGFC. It is shown that OSW helps to increase the adhesion ability among aggregates of OGFC. The main reason for the increase in adhesion among aggregates in SM-OGFC is that OSW with porous structure has a strong tendency to absorb asphalt binder, which can make the content of the structural asphalt binder increase, and the content of free asphalt binder is decreased as a result. This structural change improves the overall ability of the OGFC to bear loads. Moreover, The RSM predicated the MS value of the optimal SM-OGFC to 9.78, the measured MS value of SM-OGFC was 9.63, and the difference between the two was 1.5%, indicating that the RSM has high prediction accuracy. Figure 8 shows the dynamic stability of all OGFC mixtures. As seen, the DS value of SM-OGFC was 48.9% higher than OGFC, reached 94.7% of SBS-OGFC. This observation indicated that SM-OGFC had better resistance to permanent deformation at high temperature.

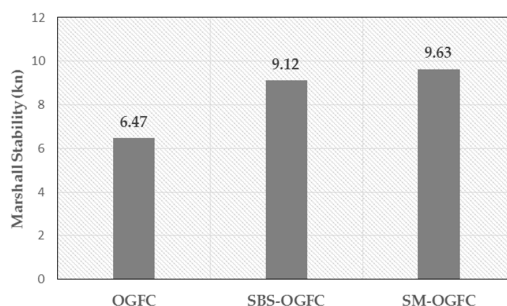


**Figure 7.** Marshall stability for all Open graded friction course (OGFC) mixtures.

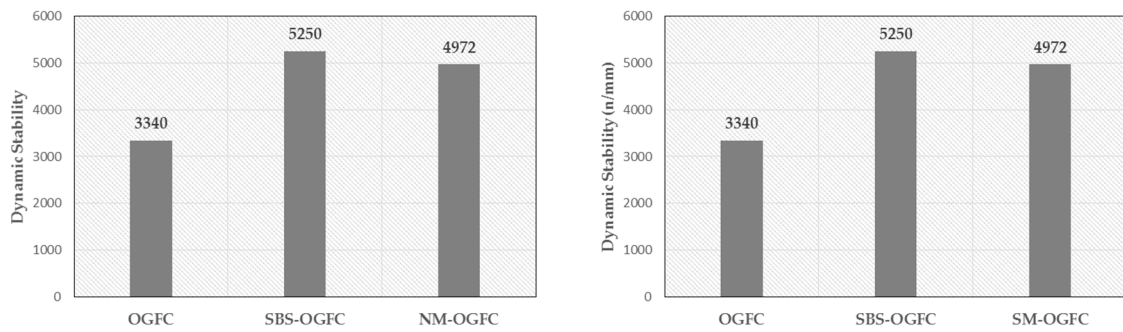


Figure 8. Dynamic stability for all OGFC mixtures.

4.2. Low-Temperature Splitting Test and Low-Temperature Beam Bending Test Results

The low-temperature splitting test results are shown in Figure 9. The  $S_T$  value of OGFC, SBS-OGFC and SM-OGFC were found to be 2.74, 3.87 and 3.71. Furthermore, the  $S_T$  value of SM-OGFC was 35.4% higher than OGFC, and almost equaled to SBS-OGFC. The higher  $S_T$  value indicates that the mixture has better resistance against pressure, horizontal and shear stress induced from the loading in the low-temperature environment. It can be seen that SM-OGFC showed better low-temperature mechanical performance in comparison with OGFC. Moreover, The RSM predicated the  $S_T$  value of the optimal SM-OGFC to 3.75, the measured  $S_T$  value of SM-OGFC is 3.71, and the difference between the two is 0.8%, indicating that the RSM has high prediction in predicting the mechanical properties of SM-OGFC at low temperature.

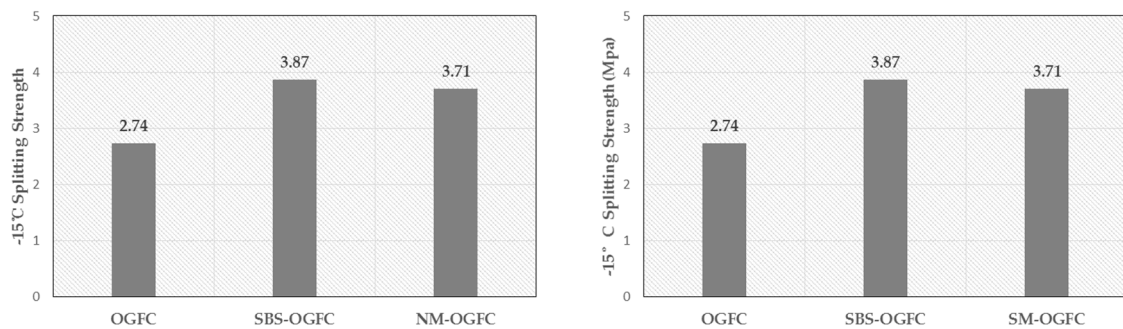


Figure 9. -15 °C Splitting strength for all OGFC mixtures.

Table 10 shows the -10 °C beam bending test results of three OGFC samples. As seen, the  $R_B$  value of SBS-OGFC and SM-OGFC was notably higher than OGFC. However, there are different reasons for the improvement. The main reason for the increase of  $R_B$  value of SBS-OGFC relative to OGFC is, due to the effective modification effect of SBS. The SBS modifier enhances the adhesion and cohesion of asphalt binder, which consequently contribute to the capacity of mixture to bear dynamic loads at low temperature. The main reason for the increase of  $R_B$  value of SM-OGFC is that the OSW with porous structure absorbs the light weight component with less molecular weight of the asphalt, enhances the bond between the asphalt mortar and the aggregate, and improves the mechanical structure of OGFC. In winter, the greater the stiffness modulus of the material, the weaker the stress relaxation performance, the more brittle the material will be, and the more likely the material to produce shrinkage cracks. Therefore, in order to make the OGFC have good low-temperature crack resistance, a smaller bending stiffness modulus is expected. SM-OGFC has the smallest  $S_B$  of the three mixes. The most probable reason for this phenomenon is that the low-temperature bending failure process of the specimen is caused by the tensile failure caused by the internal stress, so the adhesion between the OGFC skeletons mainly play a key role to prevent the damage, while, the added OSW adsorbed asphalt binder to form the OSW-asphalt cement with greater stiffness, and the firm structural asphalt coating on the coarse aggregate enhances the adhesion between the skeletons.



**Table 10.** Low-temperature beam bending test results of all OGFC mixtures.

Types	Bending-Tensile Strength/ $R_B$	Maximum Bending Strain/ $\epsilon_B$	Bending Stiffness Modulus/ $S_B$
OGFC	5.202	2886	1802
SBS-OGFC	7.465	4155	1796
SM-OGFC	6.842	4077	1678

### 4.3. Cantabro Test Results

Figure 10 shows the Cantabro losses of different mixtures after Cantabro test. The Cantabro test was conducted on three replicates of each mixture, so the standard deviation values were shown as the error bar from the averages in the figure. The greater Cantabro losses indicates that the worse raveling resistance. The SBS-OGFC shows the greatest raveling resistance among all OGFC mixtures, which means that the SBS modified asphalt provides a better adhesion and improved raveling resistance of OGFC. SM-OGFC has better raveling resistance than OGFC in this paper. The conclusion drawn here can be confirmed by the result of splitting test and beam bending test.

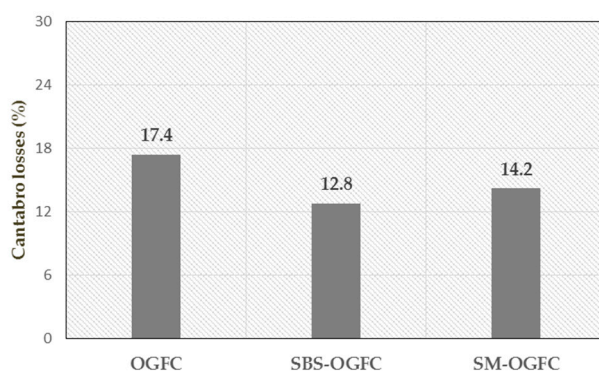


**Figure 10.** Cantabro losses of all OGFC mixtures.

### 4.4. Immersion Marshall Test and Spring-Thawing Stability Test Results

Figures 11 and 12 present the spring-thawing stability (SS), immersion Marshall stability ( $MS_1$ ) and immersion residual stability ( $MS_0$ ) for three mixtures. The  $MS_1$  value is obtained by performing Marshall test after the specimen has been immersed in water at 60 °C for 48 h, and the  $MS_0$  value is obtained by the Equation (4):

$$MS_0 = \frac{MS_1}{MS} \times 100. \tag{4}$$

As shown in Figure 11, the SS value of SM-OGFC was the largest of the three mixtures, and the SS value of SM-OGFC was 42% higher than OGFC, even 1.6% higher than SBS-OGFC. The results indicated that SM-OGFC had excellent performance in resisting moisture damage during spring-thawing season. One reason for the increase of the SS value of SM-OGFC is that silane coupling agent with two different types of functional groups has a strong tendency to bond asphalt and aggregate, which can make the content of moisture that penetrates into the interface between asphalt and aggregate decrease as a result. This improves the performance of SM-OGFC against moisture damage during spring-thawing season. As shown in Figure 12, the  $MS_1$  value of SM-OGFC was 41.4% higher than OGFC, reached 98.7% of SBS-OGFC. The results showed that SM-OGFC had a high Marshall stability after immersion at 60 °C for 48h. However, the  $MS_0$  value of SM-OGFC was the smallest of the three mixtures, which indicated that Marshall stability attenuation of SM-OGFC was the largest among three mixtures after immersion at 60 °C for 48 h. The main reason for this is the high water absorption of OSW. Nevertheless, the higher  $MS_1$  value proved that SM-OGFC had a higher bearing capacity relative to OGFC after immersion at 60 °C for 48 h.

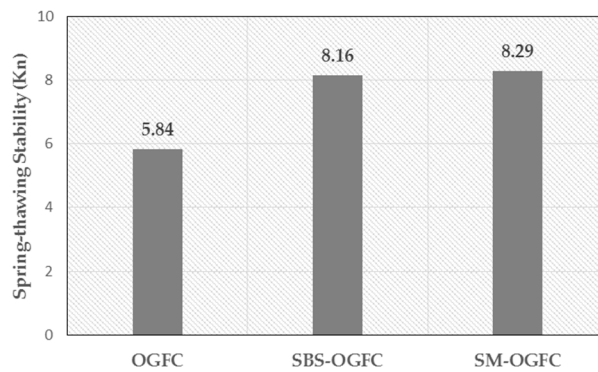


Figure 11. Spring-thawing stability for all OGFC mixtures.

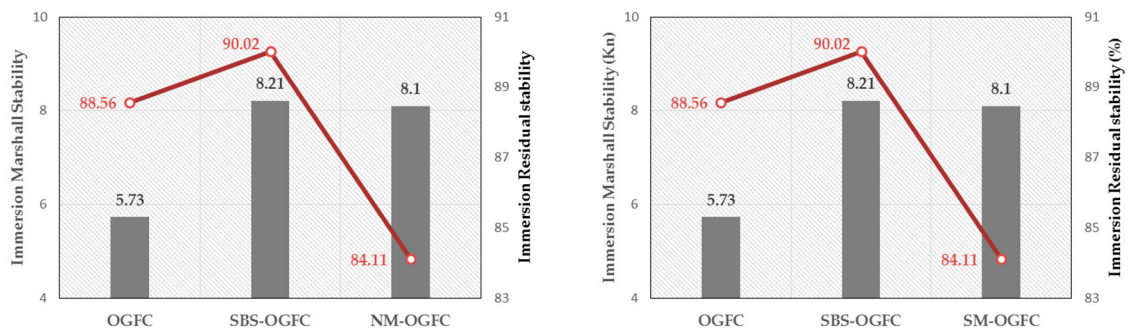


Figure 12. Immersion Marshall stability and Immersion residual stability for all OGFC stability.

#### 4.5. Permeability Test Results

Figure 13 shows the permeability coefficient of three mixtures at temperature of 20 °C. The  $K_{20^{\circ}\text{C}}$  value of OGFC, SBS-OGFC and SM-OGFC were found to 0.19, 0.28 and 0.24. According to the technical requirements of the open grade asphalt mixture in the Specifications for design of Highway Asphalt Pavement in China (JTG D50-2006), It is recommended that the permeability coefficient ( $K_{20^{\circ}\text{C}}$ ) should be greater than 0.01 cm/s, and the  $K_{20^{\circ}\text{C}}$  value of three mixtures meets the specifications. It is well known that asphalt-aggregate ratio plays a key role in permeability performance of OGFC. The lower the asphalt-aggregate ratio, the better the permeability performance of OGFC. Thus, SBS-OGFC shows better permeability performance than OGFC. What is interesting is that SM-OGFC has a higher asphalt-aggregate ratio than OGFC, but has better permeability performance. The main reason for this phenomenon is that SM-OGFC has relatively less free asphalt, which leads to a lower probability of free asphalt blocking the interconnected pores, thus showing better permeability performance.

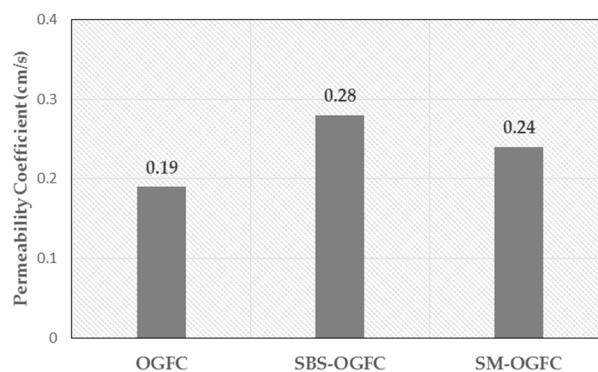
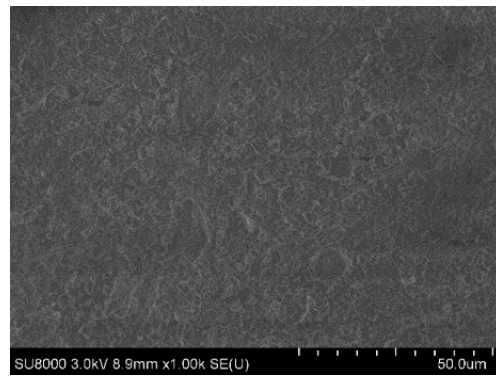


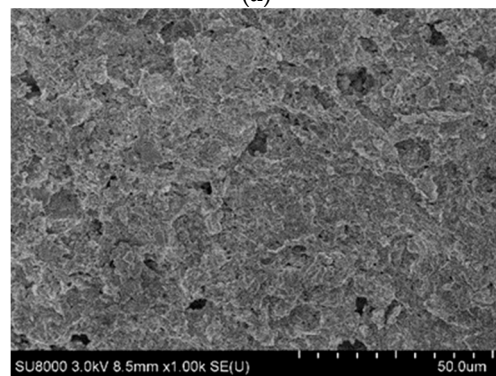
Figure 13. Permeability coefficient for all OGFC mixtures.

#### 4.6. Scanning Electronic Microscopy Test Results

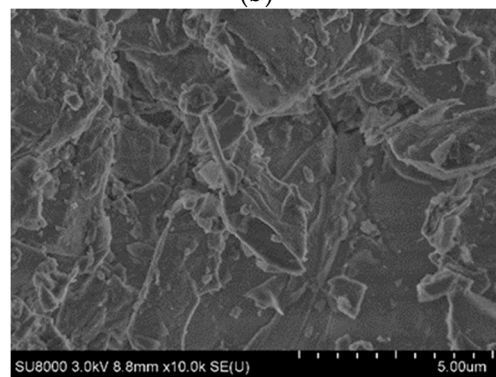
Scanning electron micrographs of granite and OSW with a grain size of 0.6 mm were observed at magnifying power of  $\times 1000$ ,  $\times 10,000$  and  $\times 60,000$ , as are shown in Figure 14a–f.



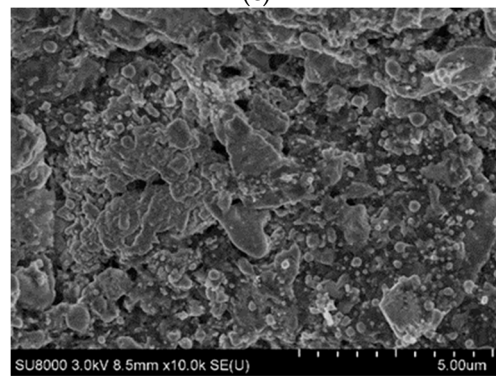
(a)



(b)



(c)



(d)

Figure 14. Cont.



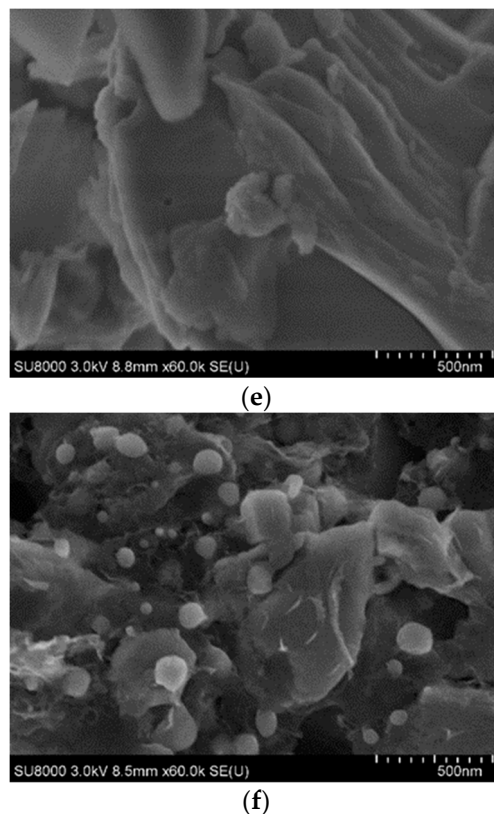


**Figure 14.** (a) Scanning electron microscope image of granite particles ( $\times 1000$ ); (b) Scanning electron microscope image of OSW particles ( $\times 1000$ ); (c) Scanning electron microscope (SEM) image of granite particles ( $\times 10,000$ ); (d) Scanning electron microscope image of OSW particles ( $\times 10,000$ ); (e) Scanning electron microscope image of granite particles ( $\times 60,000$ ); (f) Scanning electron microscope image of OSW particles ( $\times 60,000$ ).

It can be seen from Figure 14 that the surface of OSW is rougher than the granite particles, the micropores of OSW are relatively developed, and the void content of OSW is higher. On the low-magnification scanned image, it was found that the OSW has a large number of micron-sized pores, and the edge of the pores is surrounded by mossy and petal-like protrusions. The micropores with sizes ranging from several microns to about  $30\ \mu\text{m}$  can be seen in the Figure 14b,d. The special structure can provide high specific surface area and adsorption capacity for OSW. On the high-magnification scanned image, the multi-layered cave-like pores are embedded in the micropore, the cavity is embedded with a plurality of cave-like pores, which are connected to each other in the deep micropore, showing an irregular laminar columnar connected structure. On the locally enlarged nano-scale image, many small cell-like structure tentacles appear inside the micropore, this structure has internal surface area provided by the interlayer structure compared with the granite. Due to the unique laminar columnar connected structure and cell-like structure antennae of OSW, it can achieve better bite with asphalt. Compared with granite-asphalt mortar, OSW-asphalt mortar has better structural stability and mechanical properties.

## 5. Economic Analysis

In this section, the economic analysis of SM-OGFC and SBS-OGFC mixture in improving properties is conducted compared normal OGFC mixture. The price ratio PR and performance improvement ration PIR can be calculated by the following equation. The results are listed in Table 10

$$PR = P_m / P_{OGFC} \quad (5)$$

$$PIR = P_{I_m} / P_{I_{OGFC}} \quad (6)$$

where  $P_m$  and  $PI_m$  are the price and properties of SBS-OGFC and SM-OGFC,  $P_{OGFC}$  and  $PI_{OGFC}$  are the price and properties of the normal OGFC mixture [27].

It should be noted that when referring to the marked price in China, the prices of unmodified asphalt binder, SBS and silane coupling agent are 4 CNY/kg, 15 CNY/kg and 6 CNY/kg, respectively. The average price of OGFC-16 unmodified asphalt mixture is 0.380 CNY/kg. It can be calculated that the price of graded broken stone of OGFC-16 is 0.197 (value as 0.20) CNY/kg.

As shown in Table 11, when the 2.5% silane coupling agent is added to the base asphalt and the oil shale waste is used to replace the fine aggregate of the mixtures (SM-OGFC mixture), the pavement performance, including high and low temperature stability, water stability, raveling resistance performance and permeability performance, has an improvement compared to OGFC mixture, while its price is also relatively lower. It is also can be seen that SBS-OGFC mixture has better properties than OGFC mixture, while its price is not rising obviously. Moreover, analyzing the data in Table 11, SM-OGFC has almost the same pavement performance as SBS-OGFC, but has a cheaper price.

Table 11. Economic benefit analysis.

Mixture Type	Marshall Stability (kn)	Dynamic Stability (n/min)	-15 °C Splitting Strength (Mpa)	Bending-Tensile Strength (Mpa)	Cantabro Losses (%)	Immersion Marshall Stability (kn)	Spring-Thawing Stability (kn)	Permeability Coefficient (cm/s)	Asphalt Price (CNH/kg)	Mixture Price (CNH/kg)
SBS-OGFC	9.12	5250	3.71	7.465	12.8	8.21	8.16	0.28	4.52	0.382
SM-OGFC	9.63	4972	3.87	6.842	14.2	8.1	8.29	0.24	4.05	0.363
OGFC	6.47	3340	2.74	5.202	17.4	5.73	5.84	0.19	4.00	0.380
PIR <sub>SBS</sub> -OGFC and PIR <sub>SBS</sub> -OGFC	1.41	1.57	1.35	1.44	0.74	1.43	1.40	1.47	1.13	1.01
PIR <sub>SM</sub> -OGFC and PIR <sub>SM</sub> -OGFC	1.49	1.49	1.41	1.32	0.82	1.41	1.42	1.26	1.01	0.96

## 6. Conclusions

From test results the following conclusions were drawn:

A new modified OGFC (SM-OGFC) was prepared by replacing the fine aggregate below 4.75 mm in OGFC with the oil shale waste, and the silane coupling agent modifier was used to assist modification. The preparation process of SM-OGFC was optimized by CCD to obtain a SM-OGFC with the best mechanical properties. High-temperature mechanical test, low-temperature mechanical test, water stability test, raveling test and permeability test are adopted to evaluate the comprehensive ability of SM-OGFC. The results prove that SM-OGFC has better high temperature mechanical performance, lower temperature mechanical performance, water stability, raveling resistance and permeability performance than OGFC mixture—and even superior to SBS modified OGFC mixture in some aspects. Therefore, it is likely that the development of SM-OGFC could be helpful to make conventional OGFC qualified for complex service ambient, as well as improve the recycling rate of industrial waste to reduce environmental pollution and reduce the cost of asphalt pavement.

SEM analysis are adopted to explore the modification mechanism of oil shale waste. These results indicate that the unique laminar columnar connected structure, and cell-like structure antennae of oil shale waste, could be the main reasons why SM-OGFC obtained excellent comprehensive performance.

**Author Contributions:** Conceptualization, X.G.; Data curation, W.G., X.C. and W.D.; Formal analysis, W.G.; Funding acquisition, X.G.; Investigation, X.G. and W.D.; Project administration, W.D.; Software, W.G. and X.C.; Supervision, X.G.; Writing—original draft, W.G. and X.C.; Writing—review & editing, X.G. and W.D.

**Funding:** This research was funded by the National Nature Science Foundation of China (NSFC) (Grant No. 51178204).

**Acknowledgments:** This research was funded by the National Nature Science Foundation of China (NSFC) (Grant No. 51178204). This financial support is gratefully acknowledged.

**Conflicts of Interest:** The authors declare that there is no conflict of interests regarding the publication of this paper.

## References

1. Chen, J.; Yin, X.J.; Wang, H.; Ding, Y.M. Evaluation of durability and functional performance of porous polyurethane mixture in porous pavement. *J. Clean. Prod.* **2018**, *188*, 12–19. [CrossRef]
2. Punith, V.S.; Suresha, S.N.; Raju, S.; Bose, S.; Veeraragavan, A. Laboratory investigation of open-graded friction-course mixtures containing polymers and cellulose fibers. *J. Trans. Eng.* **2012**, *138*, 67–74. [CrossRef]
3. Alvarez, A.E.; Martin, A.E.; Estakhri, C. A review of mix design and evaluation research for permeable friction course mixtures. *Constr. Build. Mater.* **2011**, *25*, 1159–1166. [CrossRef]
4. Pattanaik, M.L.; Choudhary, R.; Kumar, B. Evaluation of frictional pavement resistance as a function of aggregate physical properties. *J. Trans. Eng. Part B Pavement* **2017**, *143*, 1–8. [CrossRef]
5. Song, W.; Shu, X.; Huang, B.; Woods, M. Laboratory investigation of interlayer shear fatigue performance between open-graded friction course and underlying layer. *Constr. Build. Mater.* **2016**, *115*, 381–389. [CrossRef]
6. Hassan, H.F.; Al-Oraimi, S.; Taha, R. Evaluation of open-graded friction course mixtures containing cellulose fibers and styrene butadiene rubber polymer. *J. Mater. Civ. Eng.* **2015**, *17*, 416–422. [CrossRef]
7. Onyango, M.; Woods, M. Analysis of the Utilization of Open-Graded Friction Course (OGFC) in the United States. In Proceedings of the International Conference on Highway Pavements and Airfield Technology, Philadelphia, PA, USA, 27–30 August 2017; AlQadi, I.L., Ozer, H., VelezVega, E.M., Murrell, S., Eds.; American Society Civil Engineers: New York, NY, USA, 2017.
8. Ouyang, X.Y. Research on moisture damage research in Hunan province expressway pavement. In Proceedings of the International Conference on Automation, Communication, Architectonics and Materials, Wuhan, China, 18–19 June 2011; Zhang, H., Shen, G., Jin, D., Eds.; Trans Tech Publications Inc.: Durnten-Zurich, Switzerland, 2011.
9. Lyons, K.R.; Putman, B.J. Laboratory evaluation of stabilizing methods for porous asphalt mixtures. *Constr. Build. Mater.* **2013**, *49*, 772–780. [CrossRef]

10. Luo, S.; Qian, Z.D.; Xue, Y.C. Performance evaluation of open-graded epoxy asphalt concrete with two nominal maximum aggregate sizes. *J. Cent. South Univ. (Engl. Ed.)* **2015**, *22*, 4483–4489. [CrossRef]
11. Yang, B.; Xiong, B.; Ji, Y.; Ban, G. Experimental study of the fatigue performance of open-graded asphalt mixture friction course. *Mater. Res. Innov.* **2015**, *19*, 464–468. [CrossRef]
12. Shen, W.G.; Shan, L.; Zhang, T.; Ma, H.K.; Cai, Z.; Shi, H. Investigation on polymer-rubber aggregate modified porous concrete. *Constr. Build. Mater.* **2013**, *38*, 667–674. [CrossRef]
13. Fang, F.T.; Chong, Y.C.; Nyunt, T.T.; Loi, S.S. Development of environmentally sustainable pavement mix. *Int. J. Pavement Res. Technol.* **2013**, *6*, 440–446.
14. Li, C.H.; Xiang, X.D.; Zhou, X.Y.; Tu, X.Q. Utilization of Steel Slag as Aggregates for Porous Asphalt Mixture. In Proceedings of the Annual Meetings of Chinese-Society's-Building-Materials, Professional Committees of Stone and Aggregate and Utilization of Solid Waste, Wuhan, China, 28 November–1 December 2013; Wu, S., Chen, M.H., Eds.; Trans Tech Publications Inc.: Durnten-Zurich, Switzerland, 2014.
15. Wang, Y.H.; Wang, G.; Ahn, Y.H. Effects of Using Recycled Asphalt Shingles in Open-Graded Friction Course on Flexible Pavement Performance. *J. Test. Eval.* **2014**, *42*, 1173–1182. [CrossRef]
16. Hainin, M.R.; Rusbintardjo, G.; Hameed, M.A.S.; Hassan, N.A.; Yusoff, N.I.M. Utilisation of steel slag as an aggregate replacement in porous asphalt mixtures. *J. Teknol.* **2014**, *69*, 67–73. [CrossRef]
17. Cheng, Y.C.; Wang, W.S.; Tan, G.J.; Shi, C.L. Assessing High- and Low-Temperature Properties of Asphalt Pavements Incorporating Waste Oil Shale as an Alternative Material in Jilin Province, China. *Sustainability* **2018**, *10*, 2179. [CrossRef]
18. Peng, C.; Chen, P.X.; You, Z.P.; Lv, S.T.; Zhang, R.; Xu, F.; Zhang, H.; Chen, H.L. Effect of silane coupling agent on improving the adhesive properties between asphalt binder and aggregates. *Constr. Build. Mater.* **2018**, *169*, 591–600. [CrossRef]
19. Min, Y.; Fang, Y.; Huang, X.; Zhu, Y.; Li, W.; Yuan, J.; Tan, L.; Wang, S.; Wu, Z. Surface modification of basalt with silane coupling agent on asphalt mixture moisture damage. *Appl. Surf. Sci.* **2015**, *346*, 497–502. [CrossRef]
20. Chen, J.; Sun, P.T.; Li, F.J. Study on permeability coefficient of asphalt mixture. *J. Highw. Transp. Res. Dev.* **2006**, *23*, 5–8. [CrossRef]
21. Woelfl, G.A.; Wei, I.W.; Faulstich, C.N.; Litwack, H.S. Laboratory testing of asphalt concrete for porous pavements. *J. Test. Eval.* **1981**, *9*, 175–181. [CrossRef]
22. Bezerra, M.A.; Santelli, R.E.; Oliveira, E.P.; Villar, L.S.; Escalera, L.A. Response surface methodology (RSM) as a tool for optimization in analytical chemistry. *Talanta* **2008**, *76*, 965–977. [CrossRef] [PubMed]
23. Zhao, W.Z.; Yu, Z.P.; Liu, J.B.; Yu, Y.D.; Yin, Y.G.; Lin, S.Y.; Chen, F. Optimized extraction of polysaccharides from corn silk by pulsed electric field and response surface quadratic design. *J. Sci. Food Agric.* **2011**, *91*, 2201–2209. [CrossRef] [PubMed]
24. Borzoei, M.; Zanjanchi, M.A.; Sadeghi-Aliabadi, H.; Saghale, L. Optimization of a methodology for determination of iron concentration in aqueous samples using a newly synthesized chelating agent in dispersive liquid-liquid microextraction. *Food Chem.* **2018**, *264*, 9–15. [CrossRef] [PubMed]
25. Nassar, A.I.; Thom, N.; Parry, T. Optimizing the mix design of cold bitumen emulsion mixtures using response surface methodology. *Constr. Build. Mater.* **2016**, *104*, 216–229. [CrossRef]
26. Wang, W.S.; Cheng, Y.C.; Tan, G.J. Design Optimization of SBS-Modified Asphalt Mixture Reinforced with Eco-Friendly Basalt Fiber Based on Response Surface Methodology. *Materials* **2018**, *11*. [CrossRef] [PubMed]
27. Cai, L.C.; Shi, X.G.; Xue, J. Laboratory evaluation of composed modified asphalt binder and mixture containing nano-silica/rock asphalt/SBS. *Constr. Build. Mater.* **2018**, *172*, 204–211. [CrossRef]



Article

# Initiation and Propagation of Top-Down Cracking in Asphalt Pavement

Lijun Sun <sup>1,\*</sup>, Gang Wang <sup>2</sup>, Hongchao Zhang <sup>1</sup> and Liping Liu <sup>1</sup>

<sup>1</sup> Key Laboratory of Road and Traffic Engineering of the Ministry of Education, School of Transportation Engineering, Tongji University, 4800 Cao'an Road, Shanghai 201804, China; zhanghc@tongji.edu.cn (H.Z.); llp@tongji.edu.cn (L.L.)

<sup>2</sup> Industry and Asset Management Department, Xi'an JiaoTong University Suzhou Academy, 99 Renai Road, Dushu Lake Higher Education Area, Suzhou Industrial Park, Suzhou 215123, China; wgf2014@xjtusj-sp.com

\* Correspondence: ljsun@tongji.edu.cn; Tel.: +021-6958-3810

Received: 5 April 2018; Accepted: 4 May 2018; Published: 12 May 2018

**Abstract:** Top-down cracking (TDC) alongside the wheel path is one of the commonly seen distress types on asphalt pavements, especially on heavy-duty asphalt pavements. It has been believed that TDC is caused by either tension stress or shear stress in the top asphalt layer(s). In this paper, new initiation and propagation mechanisms of TDC are proposed and validated through both accelerated pavement testing in the field and uniaxial repeated loading penetration tests in the laboratory at different temperatures. The test results clearly show that the uniaxial repeated loading penetration test can simulate both initiation and propagation processes of TDC very closely. Based on these test results, the mechanisms for crack initiation and propagation are further investigated with the finite element (FE) program. The FE analysis results show that under repeated loading, shear damage will occur first in the asphalt layer, then extend horizontally and consequently result in a shear-damaged layer. The damaged layer then led to higher tensile strain in the upper mixture which caused tension cracks and finally propagated upwards to the pavement surface. The whole process of TDC initiation and propagation can be described as “shear damage, then tension propagation”, which is the new mechanism proposed in this paper.

**Keywords:** asphalt pavements; top-down cracking mechanism; shear damage; tension propagation

---

## 1. Introduction

Cracking alongside the wheel path is one of the common distress types seen on asphalt pavements, especially on heavy-duty ones. Different from the traditional bottom-up fatigue cracking, this type of longitudinal cracking, observed within two to six years after opening to traffic [1–4], initiates at the top part of asphalt layer and then propagates downward, and is often called top-down cracking (TDC). There are two different views on TDC mechanisms. Some researchers believe that TDC is caused by the tensile stress/strain initiated at the surface of the pavement. For example, Molenaar [5] used Australian CIRCLY (a computer program for mechanistic pavement design and analysis) elastic analysis program to analyze the effects of the lateral and vertical contact stresses within the pavement and stresses of the tyre on the pavement within the asphalt layers, and concluded that the surface tensile stress at the tyre edge was the cause for top-down cracking. Similar findings were later published by Hugo [4] and Gerritsen [6], respectively. By using a finite element (FE) program CAPA (FE program developed at Delft University of Technology in the Netherlands), Groenendijk [7] analyzed the pavement structure under the measured non-uniform tyre–pavement contact load with the South African Vehicle-Road Pressure Transducer Array (VRSPATA). He found that higher tensile stress at the surface of the layer is

associated with non-uniform tyre–pavement contact pressure and aging of the asphalt mixture, which ultimately led to TDC. Mayer [8] suggested that longitudinal TDC cracks were caused by principal tension stress due to radial ply tyres. Kim and Roque et al. [9] later developed the models for TDC initiation and propagation based on the “tension cracking mechanism assumption”.

The second view on TDC is that it is caused by shear stress/strain. By using the FE method to analyze the pavement stress/strain distributions under tyre loads, Bensalem [10] found that traffic-induced shear strain on the vertical plane at tyre edge was much larger than the lateral tensile strain at same position. Wang [11] computed the stress distributions using the discrete element method (DEM) and bimodal mechanics. The results indicated that the crack was initiated at a depth of 25 mm, and obvious plastic deformation was observed below the cracking zone. He believed that the crack was caused by the shear stress. Based on the calculated octahedral shear strain for three pavement structures, Pellinen et al. [12,13] found that the maximum shear strain location is at the inner side of tyre edge, which indicated that the top-down crack was more likely to occur in the summer time. In recent years, Kim and Roque have shifted their research focuses from the “tension cracking mechanism assumption” to the “shear cracking mechanism assumption” and proposed that TDC was shear-induced or shear-dominant cracking.

This paper, based on the latest findings from TDC-oriented accelerated pavement testing (APT) and laboratory uniaxial repeated penetration tests, develops and validates new TDC initiation and propagation mechanisms. Details are presented in the following sections.

## 2. Field and Laboratory TDC Tests

In order to investigate the TDC mechanisms, both field accelerated pavement testing with MMLS3 (Model Mobile Load Simulator) and laboratory uniaxial repeated loading penetration tests were conducted. The MMLS3 is a mobile loading system developed in South Africa with a maximum load of 2.9 kN, maximum tyre pressure of 850 kPa, maximum loading rate of 7200 pass/h, and tyre that was 80 mm wide inflated to 700 kPa. Since traffic wander was not considered in the test, the wheel track area was 80 mm wide. The test pavement structures for the field APT are listed in Table 1.

**Table 1.** Pavement structures used for field APT.

Pavement Structure		Thickness, Material Type	Asphalt Binder	
			Structure 1	Structure 2
Asphalt Layers	Wearing Course	40 mm SMA13	SBS Modified Asphalt	SBS Modified asphalt
	Binder Course	60 m SUP-19		SBS Modified asphalt + Gilsonite asphalt
	Bottom Layer	80 m SUP-25	Shell70# + Anti-rutting additive	
Base layer		500 mm, 5.0% Cement-treated gravel		
Subbase layer		170 mm, Granular base		

For pavement structure 1, the APT loading was applied under four different temperature conditions: low (Figure 1a), normal (Figure 1b), and two high temperature conditions (Figure 1c). However, pavement structure 2 was tested under the high temperature condition (Figure 1d) only. The number of load repetitions for each test was 1 million. The temperatures at different pavement depth, deformation and cracks on pavement surface were measured during testing. The air temperatures at normal conditions are listed in Table 2.

Table 2. Air temperature when testing (normal temperature).

Load Repetition (×1000)	Maximum Air Temperature, °C	Minimum Air Temperature, °C	Average Air Temperature, °C	Remarks
0~80	27.5	22.0	24.0	Clear Day
80~150	38.5	24.0	31.8	
150~230	28.0	21.0	24.2	
230~300	36.0	23.0	31.4	
300~380	28.0	22.0	24.4	Cloudy Day
380~440	34.0	27.0	30.2	
440~540	27.0	23.0	24.9	
540~630	35.0	25.0	29.9	Little Rain
630~710	31.0	20.0	23.0	
710~860	22.0	16.0	18.5	
860~1000	16.0	11.0	13.2	

Note: The italic data mean the air temperature was taken at night.

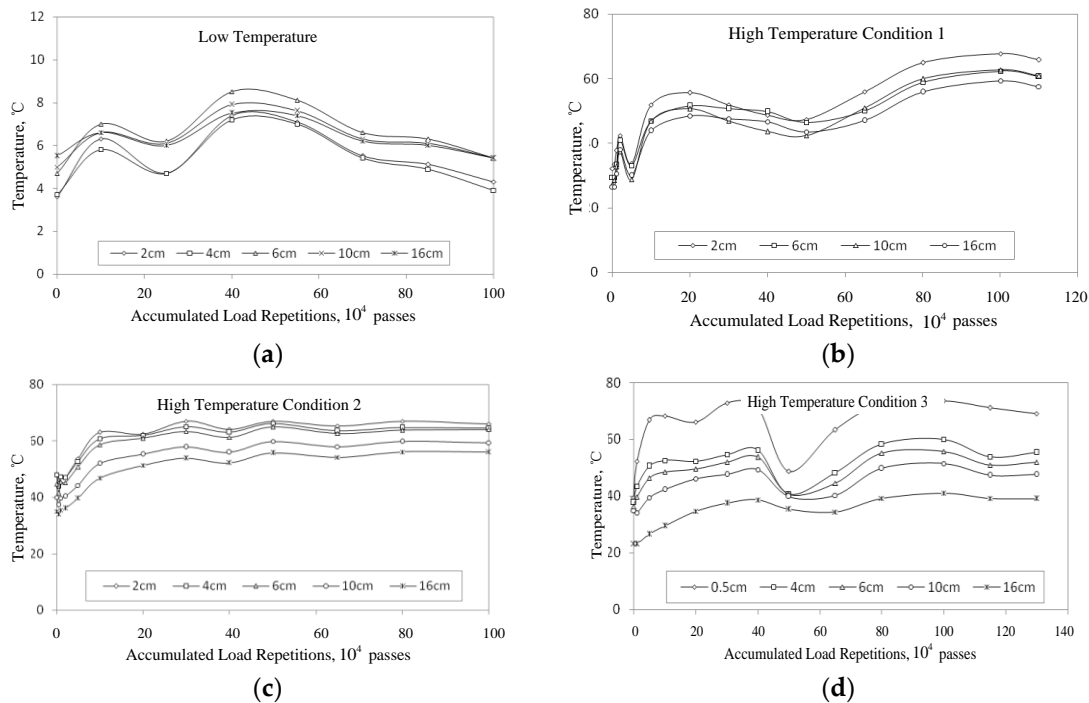


Figure 1. Pavement temperature variations during testing. (a) Low temperature test for structure 1; (b) high temperature test for condition 1; (c) high temperature test for condition 2; (d) high temperature test for condition 3.

Pavement deformation from transverse profiles was automatically measured with a laser profilometer (MLS Profilometer Drive-P2003). The data obtained from the profilometer was accurate to within 0.01 mm. For pavement structure 1, the measured pavement deformation was 2.4 mm after one million load repetitions at normal temperature conditions (Table 2). Neither upheave nor visual crack were observed near the outside of the wheel path. Similar observations were made at the low temperature conditions: there was not any significant deformation nor any cracks after applying one million repetitions of MMLS3 loading. In the case of high temperature conditions (Figure 1b), significant deformation occurred alongside the wheel path, and clearly, longitudinal cracking was found within 2 cm outside of the wheel path. Figure 2 shows the measured rutting profiles at the high temperature conditions (Figure 1c) under different loading repetitions, varying from 0 to 1 million. In Figure 2, there is a “rutting zone” in either side of upheave which is circled in red. It was found



that the deepest position in the either red circle is around 20 mm away from the tyre edge, where the longitudinal cracking is located. To further verify this observation, another test was conducted at high temperature conditions (Figure 1c) at 10 m away from the test site where longitudinal cracking was observed. Again, longitudinal cracks were found within 20 mm from the wheel path.

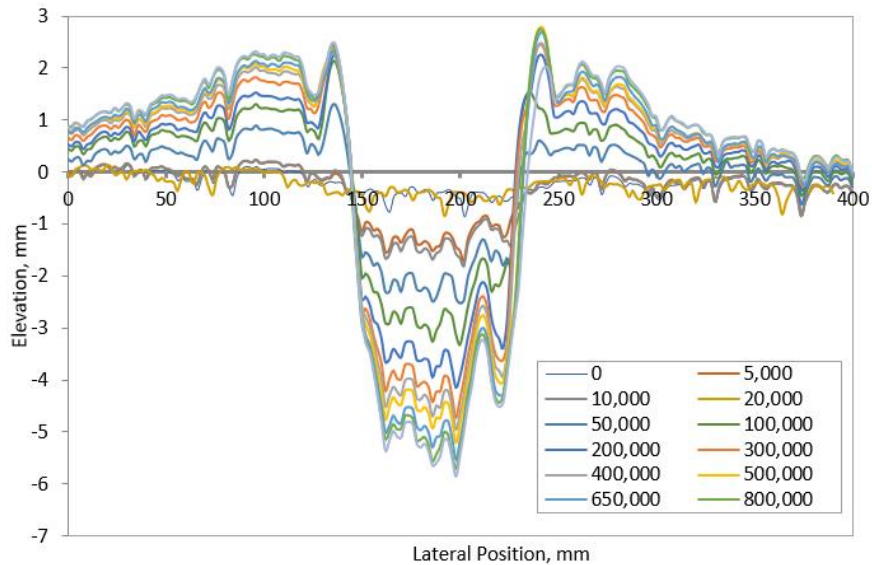


Figure 2. Deformation on pavement surface of high temperature test for structure 2.

Similarly, APT testing was performed on pavement structure 2 at the temperature conditions shown in Figure 1d. Similar deformations (Figure 2) and obvious longitudinal cracking were observed within 20 mm of the wheel path. It can be concluded from the APT test results that longitudinal cracking occurs more often at higher temperature conditions.

Figure 3 shows the observed longitudinal cracking located within 20 mm from the tyre edge with a width of 3 mm. To identify whether or not the longitudinal cracking is TDC, cores were taken and cut in half. It was obvious that the longitudinal cracking observed outside the wheel path was TDC, and that TDC propagated downwards 9 mm from the pavement surface. This observation matches the FE analysis results, which indicates that the maximum shear stresses for pavement structures 1 and 2 at high temperature conditions are located at 10–12 mm below the pavement surface.

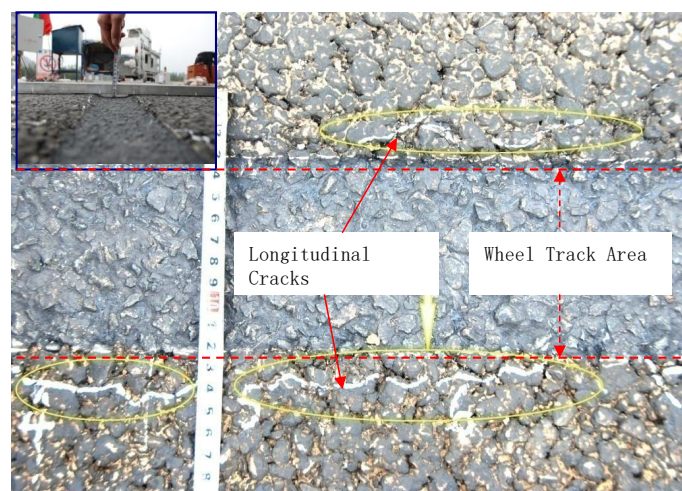


Figure 3. Observed longitudinal cracks outside the wheel path.

In addition to field APT testing, a simple laboratory test—uniaxial repeated penetration test [14]—was developed in Tongji University, as shown in Figure 4, that simulates TDC initiation and propagation. In Figure 4, the specimen diameter is 150 mm, the plunger diameter is 42 mm, test temperature is 60 °C, the loading rate is 1 mm/min, and the loading frequency is 10 Hz.



**Figure 4.** Uniaxial penetration test.

Figure 5 shows a cracked specimen after the uniaxial repeated penetration test. There is downward deformation beneath the plunger in the specimen, and obvious cracks were observed at the edge of the plunger.

Then, the cracked specimen was sliced two times with a diamond saw at Sections A and B, as shown in Figure 5. Cross-Section A was sliced perpendicular to the crack alongside the edge of the plunger; Cross-Section B was sliced around 20 mm away from Section A. The cross-sections of Sections A and B are shown in Figure 6. It can be seen that TDC of Cross-Section A was much more severe than that of Cross-Section B. Therefore, it can be excluded that TDC initiates from outside the specimen (Cross-Section B) and moves inside (Cross-Section A). Compared to the field TDC observed on cores taken from the APT site, the cracks observed in Cross-section A were very similar to the longitudinal cracking seen alongside the wheel path in terms of both the characteristic and the formation of cracks via top to downward propagation.

Additionally, Figure 6 also shows the variations of shear stress (red line) and tangent tension stress (blue line) on the section along its depth. The most severe cracking area occurred at the top part of the specimen (6 mm down from the top surface of specimen)—where the largest shear stress was located—as shown in Figure 6. Meanwhile, tangent stress is compressive stress, rather than tensile stress in this area, and the greatest tangent stress is 40 mm from the top surface, located far away from the severe TDC area. Therefore, it can be concluded that the crack on Cross-Section A was due to shear stress at the edge of the plunger, and initiated at the maximum shear stress area. The uniaxial repeated penetration test result is consistent with the field APT test. Thus, the uniaxial repeated penetration test is a valid test for simulating TDC in the laboratory.

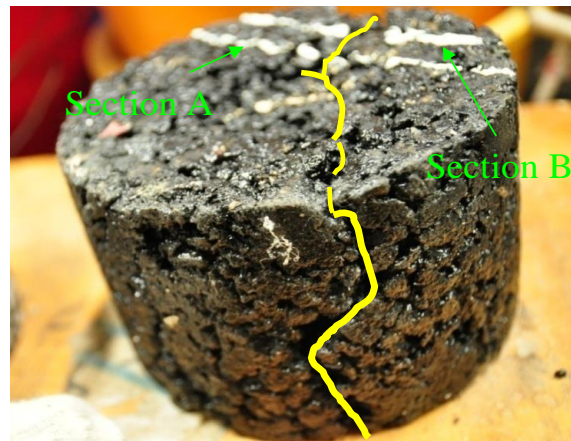


Figure 5. Cracks in penetration specimen.

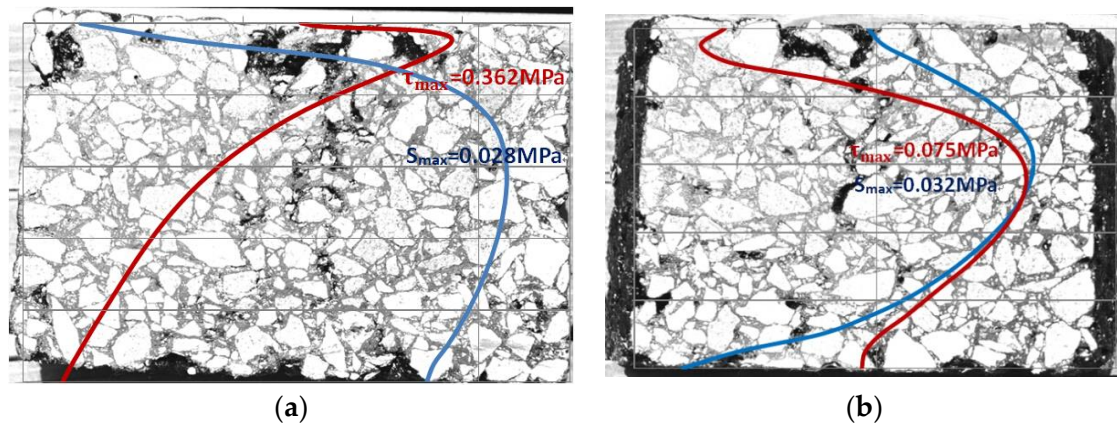


Figure 6. Cracks and stress distribution on cross-sections A and B. (a) Cross-section A; (b) cross-section B.

### 3. Investigation of the TDC Propagation and Material Modulus Decrease under Uniaxial Repeated Penetration Test

#### 3.1. TDC Initiation and Propagation Process under the Uniaxial Repeated Penetration Test

The uniaxial repeated penetration test was performed on specimens with similar volumetric property. The tests were stopped at 30, 50, 70, 90, and 105 thousand load repetitions. Again, each the specimen was sliced at the same Section A as described previously. Figure 7 shows the TDC growing process. It can be seen that the cracks occur first in the area where the maximum shear stress is located, and then gradually grow downward until going through the whole specimen with an increasing number of load repetitions. This process implies that the uniaxial repeated penetration test simulates the TDC initiation and growth process very well.



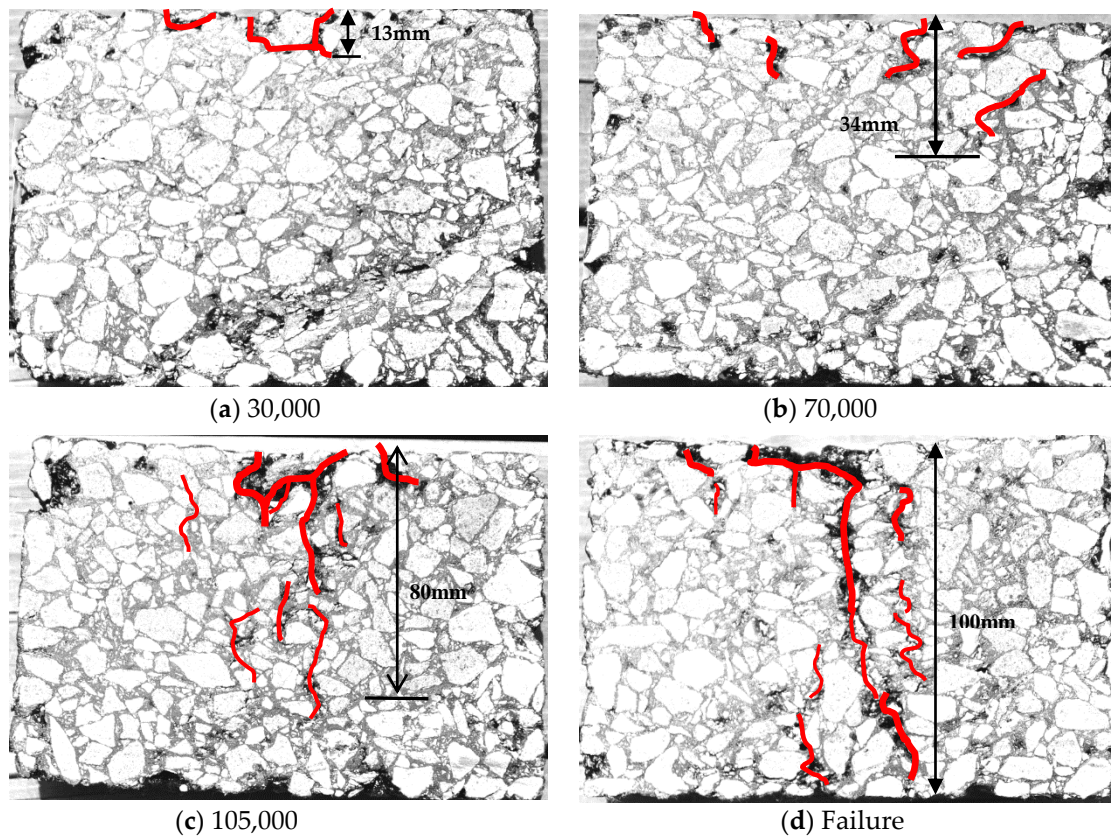


Figure 7. TDC initiation and propagation downward process.

### 3.2. Modulus Decrease Process under the Uniaxial Repeated Penetration Test

During the uniaxial repeated penetration test, the deformation vs. number of load repetitions curve was recorded. Based on the relationship between deformation and number of load repetitions, the penetration modulus (tentatively called the dynamic penetration modulus) can be calculated from Equation (1):

$$|E^{*p}| = \frac{\sigma_0}{\varepsilon_0} \quad (1)$$

where  $|E^{*p}|$  is the dynamic penetration modulus, MPa.  $\sigma_0$  is initial penetration loading intensity,  $\sigma_0 = \frac{P}{A}$ , MPa.  $P$  is penetration load,  $A$  is area of the plunger,  $\text{mm}^2$ .  $\varepsilon_0$  is the initial vertical strain.

Because there is a settling process at the initial loading stage, the dynamic penetration modulus at the 500th load repetition was defined as the initial modulus of the specimen for comparison. The measured relationship between the dynamic penetration modulus and number of load repetitions for 3 different asphalt mixtures (styrene-butadiene-styrene (SBS) Modified asphalt: AC13/AC20/SMA13) under five levels of penetration loading are shown in Figures 8–10, respectively.

It can be seen from Figures 8–10 that the decreasing trends of the dynamic penetration modulus for 3 SBS modified asphalt mixtures are very similar. For example, when the penetration load is 1.3 MPa or higher, the dynamic penetration modulus curves for all 3 asphalt mixtures deteriorate following an S-shape, and keep decreasing towards 0 with an increasing number of load repetitions. When the dynamic penetration modulus decreases to 1/3 of its initial value, the deterioration rate becomes very rapid for all 3 asphalt mixtures.

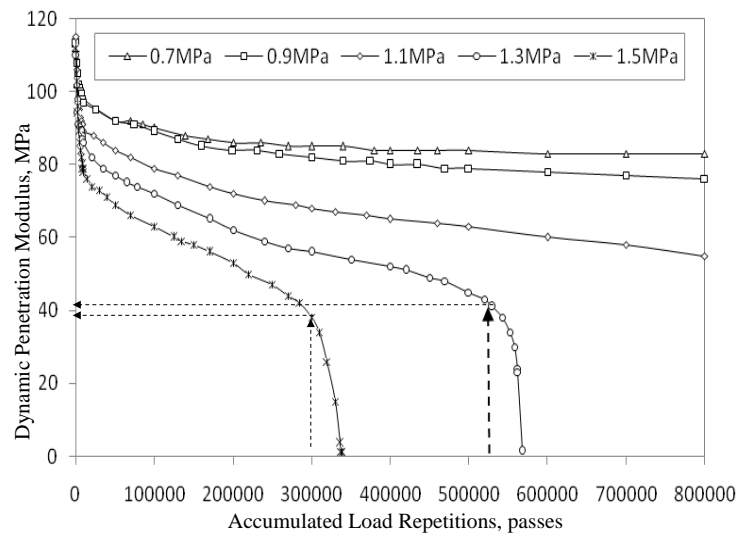


Figure 8. Modulus variation for SBS-AC13.

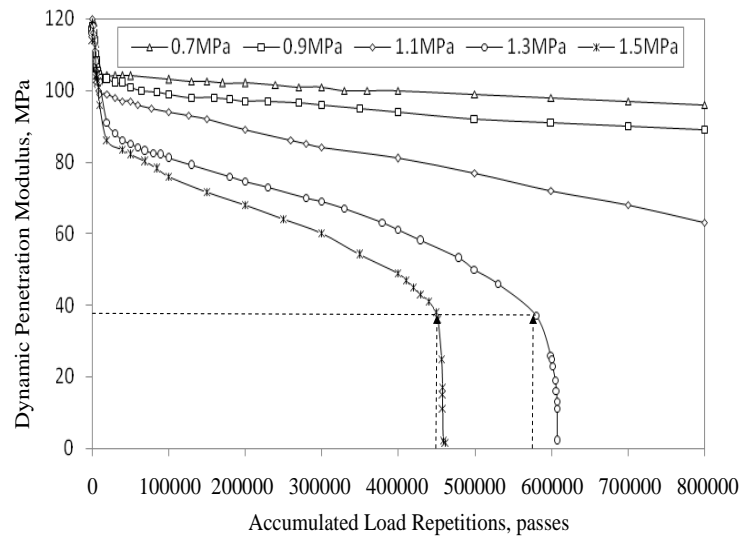


Figure 9. Modulus variation for SBS-AC20.

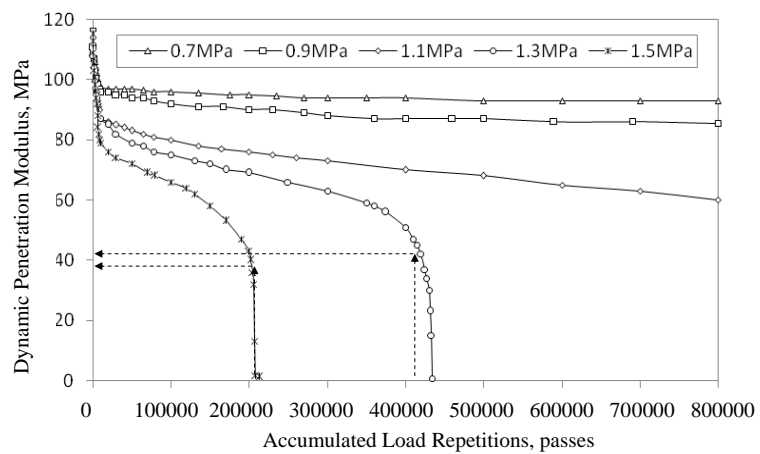


Figure 10. Modulus variation for SBS-SMA13.

### 3.3. Relationship between Dynamic Penetration Modulus Decrease and TDC Growth

Figure 11 shows the relationship between the dynamic penetration modulus deterioration percentage, cracking length percentage (the ratio of cracking length on Cross-Section A to specimen height), and the number of penetration loading repetitions. It can be seen from Figure 11 that there is an obvious consistency between the modulus deterioration percentage and TDC growth ratio. After 80,000 load repetitions, specimens start to show rapid growth in TDC until failure. The threshold for dynamic penetration modulus reduction is about 60–70%, which corresponds to 80,000 load repetitions. The dynamic penetration modulus reduction was found to correlate with the growth of TDC well. The greater the reduction of the dynamic penetration modulus, the more severe the TDC damage.

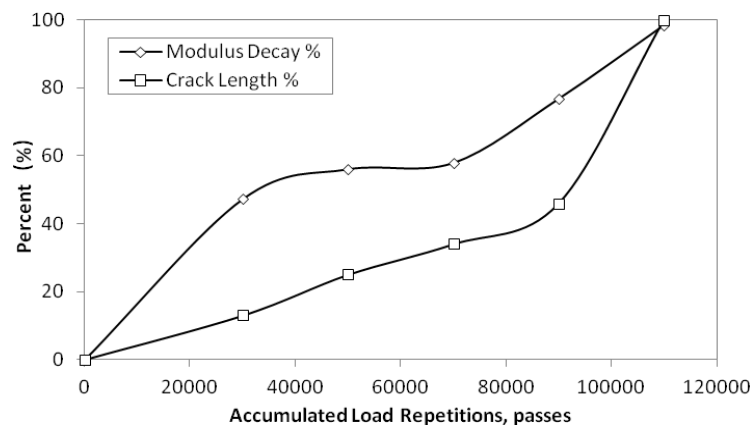


Figure 11. Variation of modulus and crack length.

It can be concluded that the uniaxial repeated penetration test simulates the decreasing process of the dynamic penetration modulus during TDC initiation and growth process very well. The greater the decrease in dynamic penetration modulus, the more severe TDC damage is. The TDC grows rapidly when the dynamic penetration modulus reaches 1/3 of its initial value.

## 4. Proposed New Mechanisms for TDC Initiation and Propagation

Inspired by the laboratory observations (Figures 7–11) and the relationship between TDC initiation and propagation and the dynamic penetration modulus deterioration, the authors explored a new way to view TDC initiation and propagation in asphalt pavements. A pavement structure with a geometry of 6 m × 6 m × 15 m was analyzed by FE method. Traffic loading was represented using a 22 × 16 cm rectangle with uniform distribution pressure of 0.7 MPa.

### 4.1. Simulation of Cracking Initiation and Propagation Process with FE Method

Based on the field and laboratory test results discussed previously, it was concluded that under repeated loading, shear damage occurs first in areas where maximum shear stress is located. Consequently, the modulus in those areas decreases and pavement stresses/strains are re-distributed within the whole pavement structure. When the modulus of the asphalt mixture in this area decreases to around 1/3 of initial value, the crack starts to grow rapidly. This is simulated by FE method, and detailed steps are described as follows:

- Step 1: Establish a set of elements for the shear damage area, named set U.
- Step 2: Compute the shear stress in the original pavement structure, and identify the element (say,  $e_1$ ) with maximum shear stress, then put this element (i.e.,  $e_1$ ) into U.
- Step 3: Assign a reduced modulus value to the elements in U, then reanalyze pavement structure with FE program.

- Step 4: Identify again the element (for example,  $e_2$ ) with the maximum shear stress in the pavement structure, and put element  $e_2$  into U.
- Step 5: Again, assign the discounted modulus value to the elements in U, then reanalyze pavement structure with the FE program.
- Step 6: Find again the element (say,  $e_3$ ) with the maximum shear stress in the pavement structure, and put element  $e_3$  into U.
- Step 7: Repeat above steps.

The element set  $\{e_1 e_2 e_3 \dots e_n\}$  of the shear damage area constitutes the shear damage area in the asphalt pavement structure under repeated loading.

With an assumed 0.7 MPa loading pressure, the numerical simulation of the shear damage process for various pavement structures (see Table 3) was performed. It can be seen from the simulations that maximum shear stress always occurred at the inner side of the tyre edge at a depth of 40 mm. The element with maximum shear stress is believed to damage first, gradually extending to the adjacent elements in a horizontal direction towards the outside of tyre edge. Finally, a “damaged layer” is formed from a damaged element in the pavement structure. Figure 12 shows an example of pavement structure with a damaged layer (DL). The FE method was employed to investigate the impact of the weakened layer on the shear stresses in the layers above (LA) and beneath (LB) the damaged layer. As shown in Figure 13, after shear damage, the maximum shear stresses  $\tau$  in the pavement structures kept a fixed relationship:  $\tau_{DL} > \tau_{LA} > \tau_{LB}$ . Therefore, the maximum shear stress always occurs at the bottom of the damaged layer, 40 mm from the pavement surface. Accordingly, it is anticipated that shear damage in pavements under repeated loading will extend in a horizontal, rather than vertical, direction. Certainly, a shear-damaged layer will be formed. The same conclusion was made when analyzing other types of pavement structures. Horizontal, rather than vertical, extension of shear damage implies that the cause for TDC initiation and propagation may be more complex than initially thought.

**Table 3.** Pavement structures used in finite element method (FEM) simulation.

Structure Parameter	Parameter Value
Asphalt Layer Thickness	10 cm, 18 cm and 30 cm
Modulus Gradient in Asphalt Layer	See Figure 1
Modulus of Base Course	500 MPa, 2000 MPa and 8000 MPa

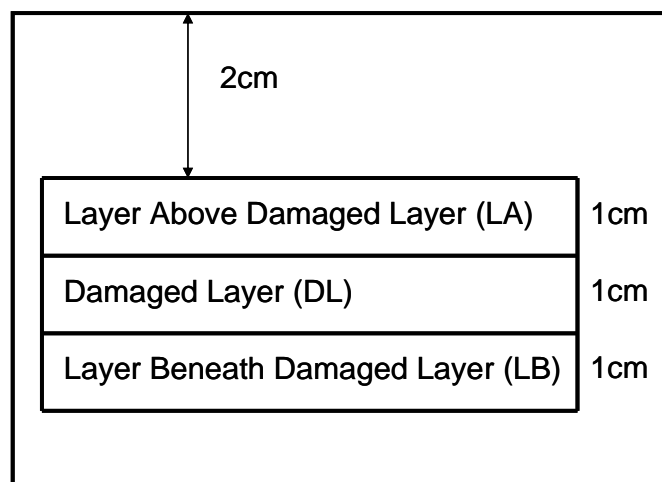


**Figure 12.** Definition of the damaged layer.

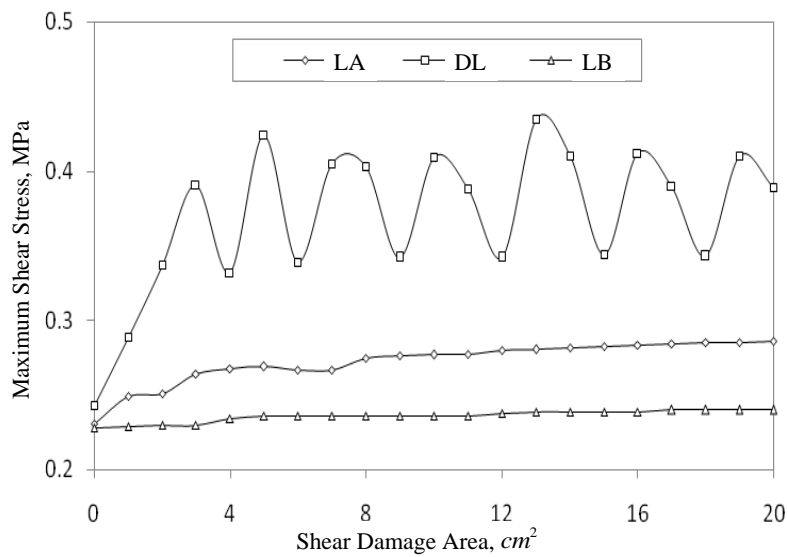


Figure 13. Maximum shear stress variation.

4.2. Effects of Shear Damage Layer on Pavement Tensile Strain Distribution

As discussed above, repeated loading results in a damaged layer in the pavement structure. It is obvious that this damaged layer will influence the tensile stress/strain distribution in nearby layers, including both LA and LB. The maximum tensile strains (at  $x$  direction, which is perpendicular to the traveling direction) in the layers were computed with different assumed shear-damaged areas, as shown in Figure 14.

Figure 14 shows that the maximum tensile strain in LA, DL, and LB at  $x$  direction (i.e.,  $\epsilon_{LA}$ ,  $\epsilon_{DL}$  and  $\epsilon_{LB}$ ) increased by 140.1%, 75.4% and 1.8%, respectively, when the shear damage area increased from 0 to 20  $\text{cm}^2$ . When the shear damage area is larger than 4  $\text{cm}^2$ , the maximum tensile strain at  $x$  direction always kept the same order:  $\epsilon_{DL} > \epsilon_{LA} > \epsilon_{LB}$ . With an increase in the shear damage area, the maximum tensile strain in LA increased rapidly, even exceeding the strain in LB. Therefore, there is a possibility that tension damage can occur in LA, and potentially accelerate the shear damage failure.

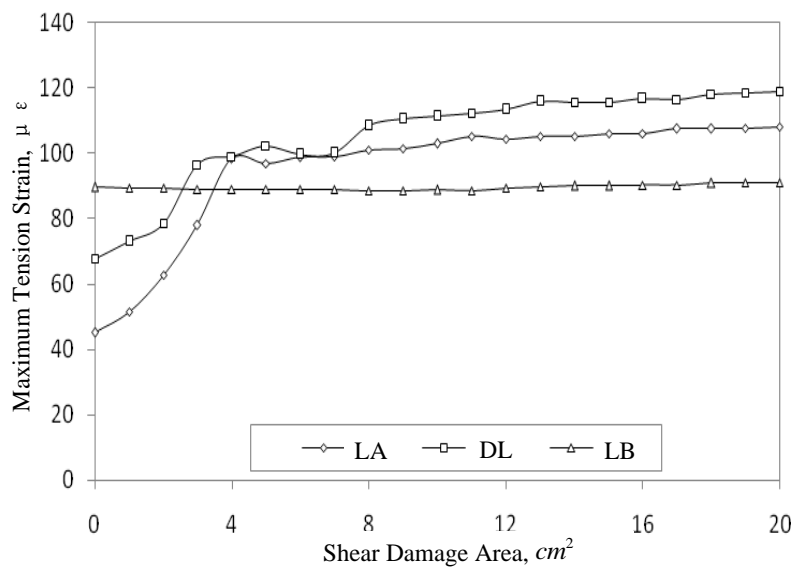


Figure 14. Variation of maximum tensile strain in the  $x$  direction.



Repeated shear stress can damage the layer and result in the DL modulus reduction to almost 1/3 of its initial value, and even to 0 (assumed to be 0.5 MPa in FE model). Consequently, the maximum tensile strain in LA will be more than 120  $\mu\epsilon$ , as shown in Figure 15.

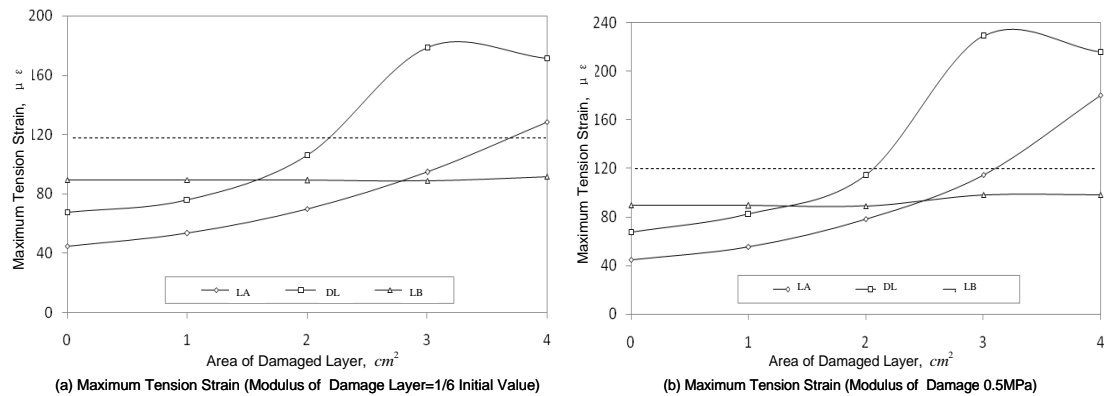


Figure 15. Effects of damaged layer on maximum tensile strain.

As illustrated in Figure 15, when the shear damage area reaches 3~4  $cm^2$ , the maximum tensile strain in LA exceeds 120  $\mu\epsilon$ . Based on the laboratory studies and field survey conducted by Marshall [15], Robert [16], Angela [17], and Xu [18], it can be reasonably assumed that in cases where the tensile strain is above 120  $\mu\epsilon$ , fatigue cracking might occur. The tensile strain in DL is greater than that in LA, and so will accelerate the failure of the layer or the opening of cracks. For the LB, the tensile strain remains at a level of less than 120  $\mu\epsilon$ , indicating a low probability of tension cracking.

#### 4.3. Analysis of TDC Growth Process

It is necessary to take into account the LA modulus reduction and evaluate its impact on the tensile strain in LA. The effects of reduced LA moduli (1, 1/2, 1/4 and 1/6 of its initial value) on the maximum tensile strain in LA are shown in Figure 16.

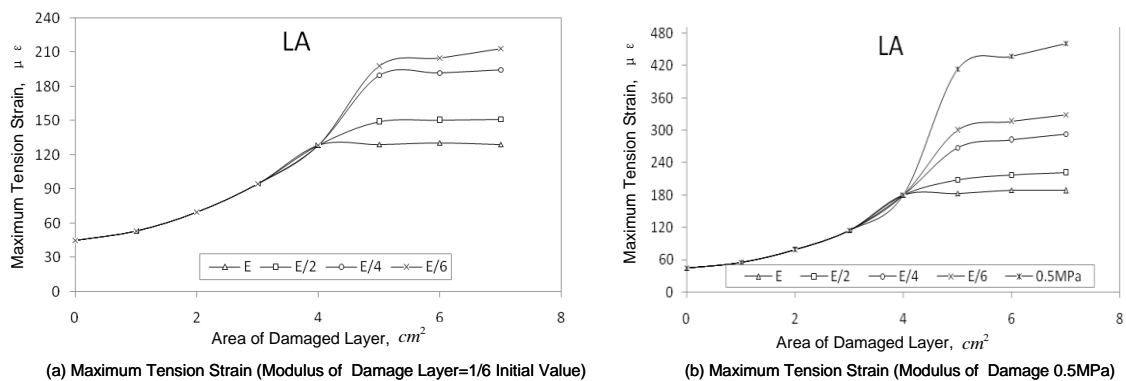


Figure 16. Effects of LA modulus variation on tensile strain.

Figure 16 clearly shows that the tensile strains with discounted moduli are much higher than 120  $\mu\epsilon$ . Thus, longitudinal cracks will occur under repeated loading. It will affect stress and strain responses in the layer above LA, resulting in a strain level higher than 120  $\mu\epsilon$  in the layer above LA. At same time, the maximum shear stress will increase from 0.270 MPa to 0.310 MPa.

In summary, this study proposed a new TDC initiation and propagation mechanism: shear damage in the asphalt layer results in increased tensile strain in the LA, which causes tension cracks; these tension cracks finally propagate upwards to the pavement surface. This new TDC mechanism

can be described as “shear damage, then tension propagation”. After the crack propagates to pavement surface, stresses in the pavement structure will be re-distributed, and the maximum shear stress area will move downwards to the place beneath the crack tip. Then, the process of “shear damage, then tension propagation” will be repeated until it completely goes through the entire asphalt layer. It is worth noting that thermal stress will also accelerate crack propagation, although this was not discussed in detail in this paper.

## 5. Summary and Conclusions

The TDC initiation and propagation process is much more complex than first believed. The field APT test results showed that under repeated loading, TDC occurred first within 20 mm outside of the wheel path and was more easily induced at higher temperatures. The cracking damage characteristics of specimens under laboratory uniaxial repeated penetration test coincided well with the field TDC. Therefore, the uniaxial repeated penetration test can be used to simulate TDC initiation and propagation processes. With increasing load repetitions, the dynamic penetration modulus of the mixture kept decreasing; this decreasing process is consistent with crack length growth.

Based on field and laboratory test data and extensive FE analyses, this paper concluded that top-down cracking is caused by shear stress, although the crack propagation process is not that simple. Maximum shear stress causes damage, which then extends horizontally and forms a damaged layer; the damaged layer will further cause the increased tensile strain in the upper layer. Higher tensile strain will result in crack initiation and propagation upwards to the pavement surface. The whole process can be summarized as “shear damage, then tension extension”. More field, laboratory, and mechanistic analysis is needed to further validate this new TDC mechanism.

**Author Contributions:** Lijun Sun contributed significantly to analysis idea and manuscript preparation; Gang Wang performed the experiments and the data analyses; Hongchao Zhang contributed in mobile APT tests (using MMLS3) and helped revise the manuscript, Liping Liu contributed in APT tests (using MSL66) and helped perform the analysis with constructive discussions.

**Acknowledgments:** The authors gratefully acknowledge financial support from National Natural Science Foundation of China (NSFC) under grant number 51678443.

**Conflicts of Interest:** The authors declare no conflict of interest.

## References

1. Dautzats, R.P. Mechanism of Surface Cracking in Wearing Courses. In Proceedings of the 6th International Conference on the Structural Design of Asphalt Pavements, Ann Arbor, MI, USA, 13–17 July 1987; pp. 232–247.
2. Schorsch, M.; Chang, C.-M.; Gilbert, Y.; Baladi, G.Y. Effects of Segregation on the Initiation and Propagation of Top-Down Cracks. In Proceedings of the 82nd Transportation Research Board Annual Meeting, Washington, DC, USA, 12–16 January 2003.
3. Rowe, G.M.; Saube, R.; Fee, F.; Soliman, N. Development of Lon-Life Overlays for Existing Pavement Infrastructure Projects with Surface Cracking in New Jersey. Ph.D. Thesis, Transportation Research Board/National Research Council, Transportation Research Circular, Number 503, The National Academies of Sciences, Engineering, and Medicine, Washington, DC, USA, December 2001; pp. 96–107.
4. Hugo, F.; Kennedy, T.W. Surface Cracking of Asphalt Mixtures in Southern Africa. *Proc. Assoc. Asph. Paving Technol.* **1985**, *54*, 454–501.
5. Molenaar, A.A.A. Fatigue and Reflection Cracking Due to Traffic Loads. *Proc. Assoc. Asph. Paving Technol.* **1984**, *53*, 440–474.
6. Gerritsen, A.H.; Van Gurp, C.; Van Der Heide, J.; Molenaar, A.A.A.; Pronk, A.C. Prediction and Prevention of Surface Cracking in Asphalt Pavement. In Proceedings of the 8th International Conference on Asphalt Pavement Design, Seattle, WA, USA, 10–14 August 1997; pp. 378–391.
7. Groenendijk, J. *A Review of the Distribution and Conservation Status of the Giant Otter (Pteronurabraziliensis), with Special Emphasis on the Guayana Shield Region*; Netherlands Committee for IUCN: Amsterdam, The Netherlands, 1998.


8. Myers, L.A. Development and Propagation of Surface-Initiated Longitudinal Wheelpath Cracks in Flexible Highway Pavements. Ph.D. Thesis, University of Florida, Gainesville, FL, USA, 2000.
9. Roque, R.; Zou, J.; Kim, R. *Top-Down Cracking of Hot-Mix Asphalt Layers: Models for Initiation and Propagation*; Contractor's Final Report for NCHRP Project 1-42A; NCHRP: Washington, DC, USA, 2010.
10. Bensalem, A.; Broen, A.J.; Nunn, M.E.; Merrill, D.B.; Lloyd, W.G. Finite Element Modeling of Fully Flexible Pavements: Surface Cracking and Wheel Interaction. In Proceedings of the 2nd International Symposium on 3D Finite Element For Pavement Analysis, Design, and Research, Charleston, WV, USA, 11–13 October 2000; pp. 103–121.
11. Wang, L.B.; Myers, L.A.; Mohammad, L.N.; Fu, Y.R. A Micromechanics Study on Top-Down Cracking. In Proceedings of the 2nd Transportation Research Board Annual Meeting, Washington, DC, USA, 12–16 January 2003.
12. Pellinen, T.; Rowe, G.; Biswas, K. *Evaluation of Surface (Top Down) Longitudinal Wheel Path Cracking*; Joint Transportation Research Program: West Lafayette, IN, USA, 2004.
13. Mohammad, F.A.; Collop, A.C.; Brown, S.F. Effects of Surface Cracking on Responses in Flexible Pavements. In Proceedings of the ICE—Transport, London, UK, May 2005; Volume 158, pp. 127–134.
14. Lijun, S.; et al. *Structural Behavior Study for Asphalt Pavements*; Tongji University Press: Shanghai, China, 2003.
15. Marshall, R.T.; Samuel, H.C. Design principles for long lasting HMA pavements. In Proceeding of the 10th International Conference of ISAP for Long Lasting Pavement, Auburn, AL, USA, 7–9 June 2004; pp. 365–384.
16. Peterson, R.L.; Turner, P.; Anderson, M.; Buncher, M. Determination of threshold strain level for fatigue endurance limit in asphalt mixtures. In Proceeding of the 10th International Conference of ISAP for Long Lasting Pavement, Auburn, AL, USA, 7–9 June 2004; pp. 385–398.
17. Angela, L.P.; David, H.T. *Methodology and Calibration of Fatigue Transfer Functions for Mechanistic-Empirical Flexible Pavement Design*; National Center for Asphalt Technology: Auburn, AL, USA, 2006.
18. Xu, O.; Han, S.; Duan, X. Flexible Fatigue Strain Limit for SBS Modified Asphalt Mixture. *J. Constr. Mater.* **2010**, *13*, 193–198.



© 2018 by the authors. Licensee MDPI, Basel, Switzerland. This article is an open access article distributed under the terms and conditions of the Creative Commons Attribution (CC BY) license (<http://creativecommons.org/licenses/by/4.0/>).

Article

# Fatigue Equation of Cement-Treated Aggregate Base Materials under a True Stress Ratio

Songtao Lv <sup>1,3</sup>, Chaochao Liu <sup>1,\*</sup>, Jingting Lan <sup>1</sup>, Hongwei Zhang <sup>2</sup>, Jianlong Zheng <sup>1</sup> and Zhanping You <sup>3</sup> 

<sup>1</sup> National Engineering Laboratory of Highway Maintenance Technology, Changsha University of Science & Technology, Changsha 410004, China; lst@csust.edu.cn (S.L.); lanjingtong@stu.csust.edu.cn (J.L.); zjl@csust.edu.cn (J.Z.)

<sup>2</sup> Inner Mongolia Communications Construction Engineering Quality Supervision Bureau, Hohhot 010051, China; hhhtzhw@163.com

<sup>3</sup> Department of Civil and Environmental Engineering, Michigan Technological University, Houghton, MI 49931, USA; zyou@mtu.edu

\* Correspondence: lcccs@stu.csust.edu.cn

Received: 4 April 2018; Accepted: 26 April 2018; Published: 29 April 2018

**Abstract:** The objective of this article is to establish a fatigue equation based on the true stress ratio for cement-treated aggregate base materials. The true stress ratio herein means the ratio of the stress and the true strength of the cement-treated aggregate base materials related to loading rates and curing times. The unconfined compressive strength tests and compressive resilience modulus tests were carried out under various loading rates and curing times of 3, 7, 14, 28, 60, 90 days, respectively. According to the test results, the relationship between the unconfined compressive strength (a mix design parameter in China) and the compressive resilience modulus (a structural design parameter and the construction quality control parameter in China) of the cement-treated aggregate base material with different curing times was established. However, it was found that the strengths varied with the loading rates, which is not reflected in the existing fatigue equations. Therefore, it is questionable to obtain the stress ratio of fatigue tests with a fixed strength value obtained from the standard strength test where the loading rate is fixed (in China, the fixed loading rate is 1 mm/min for cement-treated aggregate base materials). Thus, in this paper, the four-point bending strength (i.e., flexural strength) test was carried out at different loading rates to resolve such deficiencies. Based on the strength test results at different loading rates, the true stress ratio of the fatigue test corresponding to the fatigue loading rate can be calculated. Then the four-point bending fatigue test was conducted to establish an improved fatigue equation characterized by the true stress ratio. The results show that the patterns of variation for unconfined compressive strength increasing with the curing time were similar to that of the compressive resilience modulus. The fatigue equation curve based on the true stress ratio can be extended to the strength failure point of (1, 1), where both the true stress ratio and the fatigue life value are one. The internal relationship between the strength failure and the fatigue failure was unified. This article provides a theoretical method and basis for unifying the mix design parameters and the construction quality control parameters.

**Keywords:** cement-treated aggregate base; fatigue equation; loading rates; true stress ratio; flexural strength

---

## 1. Introduction

The semi-rigid base asphalt pavement structure has several advantages, such as strong bearing capacity, excellent integrity, and an excellent ability of dispersing upper loads, etc. Meanwhile, the

material can be obtained easily [1,2]. Based on these advantages, semi-rigid base asphalt pavements have been adopted for over 80% of freeways in China. Therefore it is necessary to pay more attention to the design and construction of semi-rigid base asphalt pavements.

The cement-treated aggregate base material is usually defined as a mixture of aggregate, small amounts of cement, and water. When the cement reacts with the water, the hydration products combine the aggregate particles, thereby enhancing the strength and stiffness and improving the durability and impermeability. However, the performance of cement stabilized materials is also affected by many factors, such as aggregate type [3], cement content [4], moisture content [5], fiber content [6], curing time [7], curing condition [8], stress states [9], compaction degree and so on. Therefore many tests on the performance of cement-treated aggregate base materials have been conducted. Deng et al. studied the fatigue attenuation pattern of semi-rigid base materials in laboratory tests. It was noted that the process of fatigue failure can be divided into three stages: the strain stability stage, strain development stage and cracking stage [10]. Chai et al. adopted the falling weight deflectometer (FWD) to measure the performance of a test road in Malaysia's cement-treated aggregate base and found that it is feasible to use the FWD to evaluate the properties of the cement-treated aggregate base structure. The empirical relationship between pavement deformation and stiffness modulus can be established [11]. Danish scholars predicted the resilient modulus of semi-rigid base asphalt pavement through a large amount of experiments, and found that with the increase of the load times, the modulus decreased gradually. The final modulus becomes 3% of its initial modulus [12,13]. It is observed that the fatigue curves of the cement-treated aggregate base material are close to that of the Portland Cement Association (PCA), and the S-N fatigue equation was recommended to predict the fatigue life of semi-rigid materials [14].

Although the performance of cement-treated aggregate base materials has been studied, there are two aspects that have been mostly ignored.

One is the effect of the curing time on the mechanical performance indicator during the construction period. The strength of cement-treated aggregate base material increases with the degree of hydration reaction. If the curing time is insufficient, early fatigue damage occurs easily under the loads of construction trucks. In China, the compressive modulus at the curing time of 90 days is adopted as a structural design parameter, while the design parameter of the mixture proportion design is the unconfined compressive strength at the curing time of seven days. Thus, the curing times are inconsistent with each other.

Another aspect is that the effects of the loading rates on the strength of the cement-treated aggregate base material were not considered when the S-N equation was established. A fixed strength value was used to determine the stress ratio of the fatigue test when the S-N equation was used to evaluate the fatigue properties of the cement-treated aggregate base material. However, it was found that the strength varies with the loading rate [15,16], which is not reflected in the existing fatigue equations [17–20]. Therefore, it is questionable to obtain the stress ratio of the fatigue tests with a fixed strength value obtained from the standard strength test when the loading rate is fixed (in China, the fixed loading rate is 1mm/min). Pell pointed out that the S-N fatigue equation should be applied in the range of  $N_f = 10^4 \sim 10^8$ . If it goes beyond that range, the linear relationship does not necessarily exist. Moreover, when the stress level is larger than the strength obtained by the standard strength test, the stress ratio will be larger than 1, which means that the fatigue life under this stress level will be less than 1, but the actual fatigue life is much greater than 1 [21].

Therefore, in this paper, the analysis was conducted according to the flow chart, as shown in Figure 1. According to the results of the research, the relationship between the unconfined compressive strength (a mixed design parameter) and the compressive resilience modulus (a structural design and construction quality control parameter) of the cement-treated aggregate base material with different curing times was established. Meanwhile, an improved fatigue equation was proposed, which was characterized by the true stress ratio.

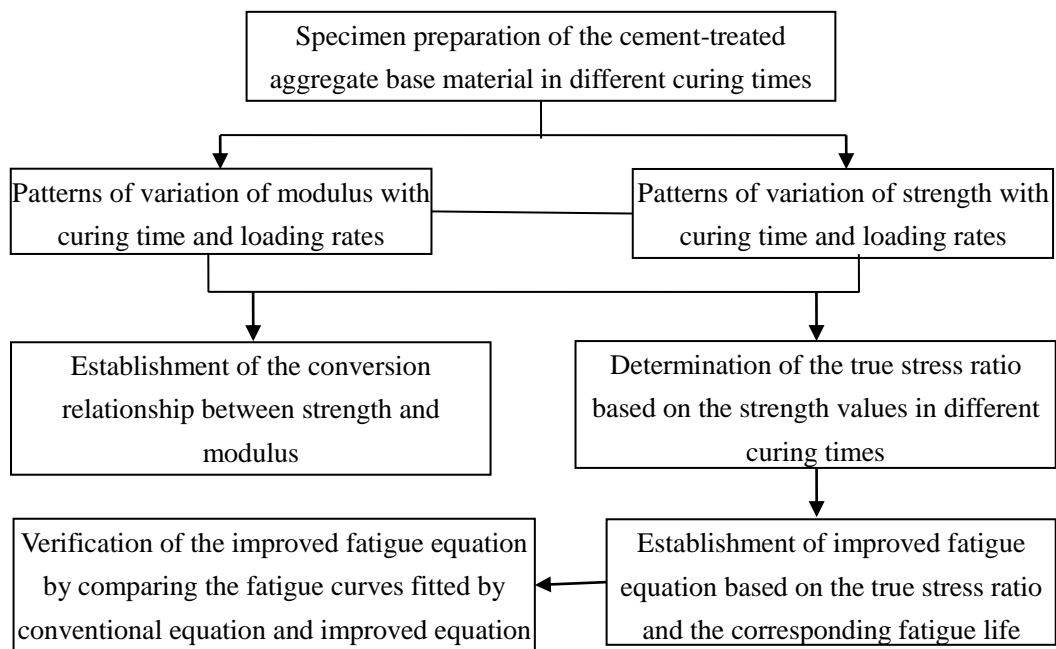


Figure 1. Flow chart of the work.

## 2. Material Properties and Mixture Design

### 2.1. Cement

Portland cement was used as cementitious in the cement-treated aggregate base material and the strength level was 42.5 MPa. Its additives are fly ash and the technical properties are presented in Table 1; the technical requirements are from the Chinese Construction Specifications for Highway Road Bases (JTJ/T F20-2015) [22].

Table 1. The technical indicators of cement.

Test Projects	Test Results	Technical Requirement
Fineness detection	1.8	≤10%
Setting time (min)	initial setting/min	≥180
	final setting/min	≥360
Stability(mm)	3	≤5
Strength of cement mortar (MPa)	3 days flexural strength	≥2.5
	3 days unconfined compressive strength	≥10
MgO content (%)	3.1	≤5%
SO <sub>3</sub> content (%)	1.1	≤3.5%
Loss on ignition	0.9	≤3.0%
Specific surface area (selectivity indicator)	410	300 m <sup>2</sup> /kg~450 m <sup>2</sup> /kg
Initial setting time	110	≥90 min
Final setting time	690	≤720 min

### 2.2. Aggregate

According to the Chinese Construction Specifications for Highway Road Bases (JTJ/T F20-2015) [22], the gradation of cement-treated aggregate base material is shown in Figure 2:

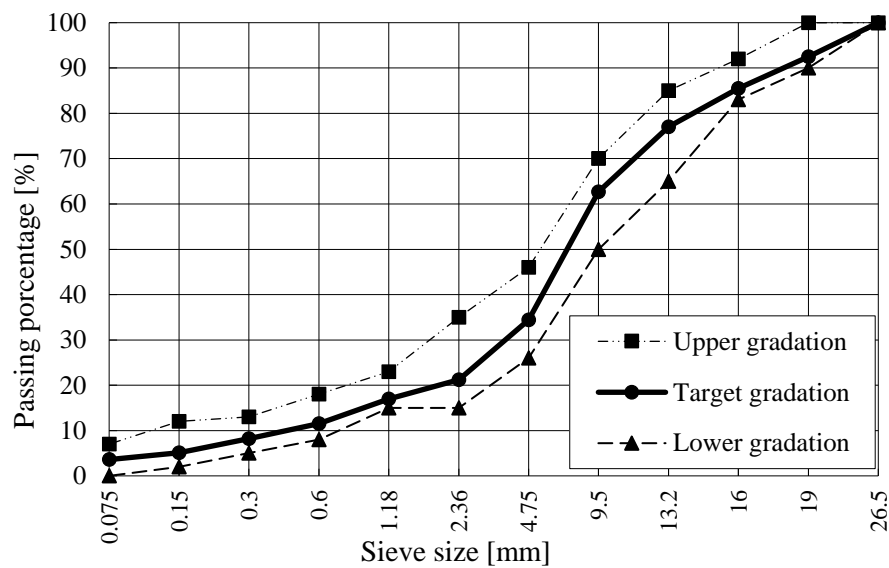


Figure 2. Gradation curve of cement-treated aggregate base material.

The aggregate is limestone and the technical indicators are shown in Table 2.

Table 2. The technical indicators of the aggregate.

Test Projects	Test Results	Technical Requirement [20]
Content of flat and elongated particles in coarse aggregate (%)	11.7%	≤20%
Crushed stone value (%)	19.8%	≤30%
Less than 0.6mm particle Liquid limit/plastic index	26.5%	liquid limit ≤ 28%
	6.2	plastic index ≤ 9
Content of soft stone (%)	0.9	≤3

### 2.3. Mixture Proportion Design

After obtaining the suitable aggregates and determining the synthetic gradation of the mineral aggregate according to Figure 2, the traditional mixture design procedure of the cement-treated aggregate materials was generally as follows: (1) Select the range of the preliminary cement content by weight [22]; (2) Use the preliminary estimated cement content obtained in step (1) to perform the moisture-density testing, and the maximum dry density and the optimum moisture content could be obtained; (3) Prepare the specimens by using the maximum dry density and the optimum moisture content obtained from step (2); (4) Determine the average unconfined compressive strength of the specimens after the seven-day curing time. If the average unconfined compressive strength fulfills the design requirement, the cement content and the water content determined in step (2) are adequate for cement-treated aggregate materials. Otherwise, repeat the above procedure to obtain the required mixture by adjusting the material. Thus, according to the procedure of mixture proportion design, the cement content was determined to be 4.5%, the optimum water content was determined to be 4.6%, and the maximum dry density was determined to be 2.35g/cm<sup>3</sup>.

## 3. Unconfined Compressive Strength Test

### 3.1. Preparation of Specimens for the Unconfined Compressive Strength Test

According to the Chinese Test Methods of Materials Stabilized with Inorganic Binders for Highway Engineering (JTG E51-2009) [23], the static pressure method was employed to prepare the specimens. The cylinder specimen for unconfined compressive strength and resilience modulus tests were fabricated with the static compactor. The compacting rate was 1 mm/min until the top and

bottom heel blocks were pressed into the mold, as shown in Figure 3a, and the diameter and height of the specimens were  $\Phi 150$  mm and 150 mm, respectively. After the molds were released, as shown in Figure 3b, the specimens were wrapped in plastic bags and moved to a standard curing room with a temperature of  $20 \pm 2$  °C and a humidity not less than 95% for the required curing time, as shown in Figure 3c.

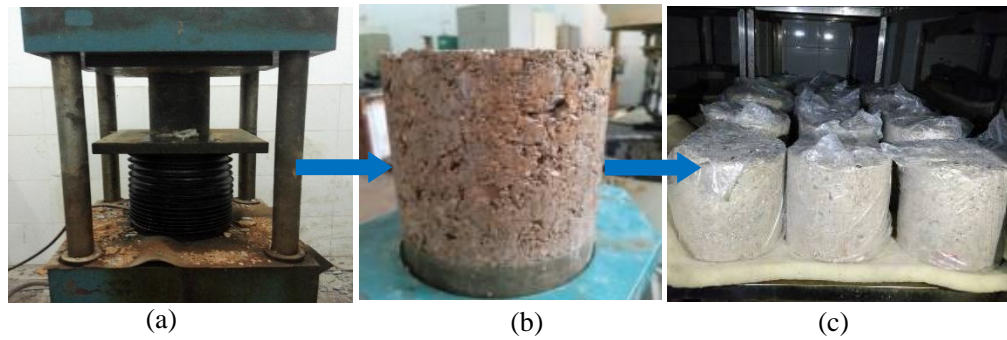


**Figure 3.** Preparation of cement-treated aggregate base material specimens. (a) Hydrostatic molding (b) Specimen demolding (c) Specimen curing.

### 3.2. The Test Process of Unconfined Compressive Strength Test

The cement-treated aggregate base material specimens were prepared with curing times of 3 days, 7 days, 14 days, 28 days, 60 days, 90 days. At the end of a certain curing time, the specimens were put in a sink where they were immersed in water, as shown in Figure 4a, and the water temperature was about  $20 \pm 2$  °C. After being immersed for 24 h, the specimens were taken out of the sink and their height was measured, as shown in Figure 4b. The specimens with a height in the range of  $150 \pm 2$  mm were abandoned as nonstandard specimens. Then, the standard specimens were used to determine the strength of the cement-treated aggregate base material by Material Tests System (MTS), as shown in Figure 4c; the loading rate of the standard strength test was 1mm/min. Furthermore, the cement-treated aggregate base material specimens with a curing time of 28 days were chosen to determine the strength under the loading rates of 0.1, 0.5, 1, 3, 5, 10 mm/min. Figure 4d illustrates the specimen after failure.

According to the Test Methods of Materials Stabilized with Inorganic Binders for Highway Engineering (JTG E51-2009) [23], the ultimate failure load  $P$  could be obtained by the MTS, and the unconfined compressive strength of the specimens were calculated by Equation (1).

$$S_c = \frac{P}{A} \quad (1)$$

where  $S_c$  is the unconfined compressive strength of the specimen (MPa);  $P$  is the ultimate failure load (kN); and  $A$  is the cross sectional area of the specimen ( $\text{mm}^2$ ).



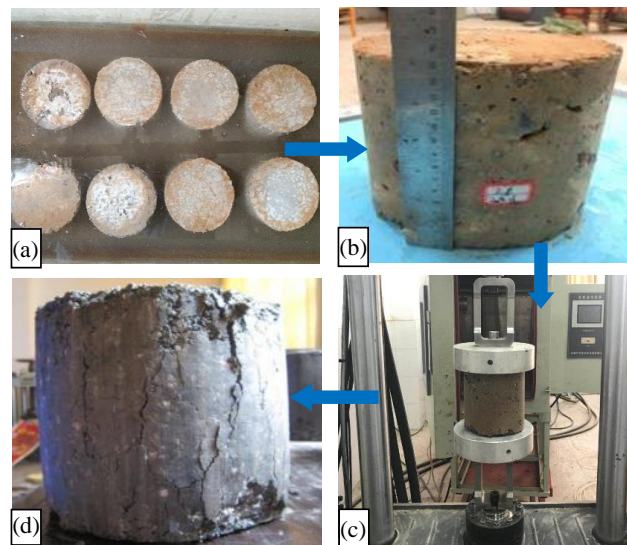


**Figure 4.** The procedure of the unconfined compressive strength test (a) Specimens immersed in water (b) Selection of standard specimens (c) Strength test (d) Failure sample of unconfined compressive strength.

### 3.3. Analysis of Unconfined Compressive Strength Test Results

The specimens were placed in a standard curing room continuously for 3 days, 7 days, 14 days, 28 days, 60 days and 90 days. The unconfined compressive strength test was carried out. The test results of cement-treated aggregate base material with different curing times are shown in Table 3.

**Table 3.** Test results of unconfined compressive strength with different curing times.

Curing Time (t/d)	Loading Rates (mm/min)	Unconfined Compressive Strength of Parallel Specimens $S_c$ (MPa)							Average Value $\bar{S}_c$ (MPa)	$C_v$ (%)	
		1	2	3	4	5	6	7			
3	1	3.1	2.7	2.8	3.2	2.6	3.0	2.8	2.9	7.58	
7		3.4	4.3	3.5	4.0	3.6	3.9	3.4	3.7	9.36	
14		4.7	3.9	4.1	4.2	4.8	4.6	4.3	4.4	7.65	
28		5.1	4.3	4.3	4.7	4.9	4.4	4.6	4.6	6.70	
60		5.5	5.9	5.7	5.4	5.2	5.3	5.5	5.5	4.33	
90		5.9	5.8	5.5	5.6	5.3	6.0	6.2	5.8	5.40	
28		0.1	4.3	4	4.2	4.3	4.5	4	4.2	4.2	6.92
		0.5	4.3	4.2	4.7	4.6	4.6	4.4	4.3	4.4	7.57
		1	4.6	4.3	4.3	4.7	4.9	4.4	4.6	4.5	6.70
		3	5.2	4.8	4.7	5.1	4.9	5.0	5.1	5.0	3.60
	5	5.4	5.3	4.9	5.4	5.2	5.1	4.9	5.2	4.16	
	10	5.3	5.2	5.0	5.6	5.1	5.4	5.2	5.3	7.46	

From the test results for unconfined compressive strength presented in Table 3, it can be noted that the unconfined compressive strength of the cement-treated aggregate base material varied dramatically in both curing times and loading rates. The pattern of variation was described by a logarithmic equation, and the strength test resulted in different curing times and different loading rates, fitted by Equations (2) and (3), respectively. The fitting results are shown in Figure 5, where  $R^2$  is the correlation coefficient of the fitting.

$$S_c = a_1 + b_1 \ln(t + c_1) \tag{2}$$

$$S_c = a_2 + b_2 \ln(t + c_2) \tag{3}$$

where  $S_c$  is the compressive strength;  $t$  is the curing time;  $v$  is the loading rate;  $a_1, a_2, b_1, b_2, c_1,$  and  $c_2$  are the fitting parameters.

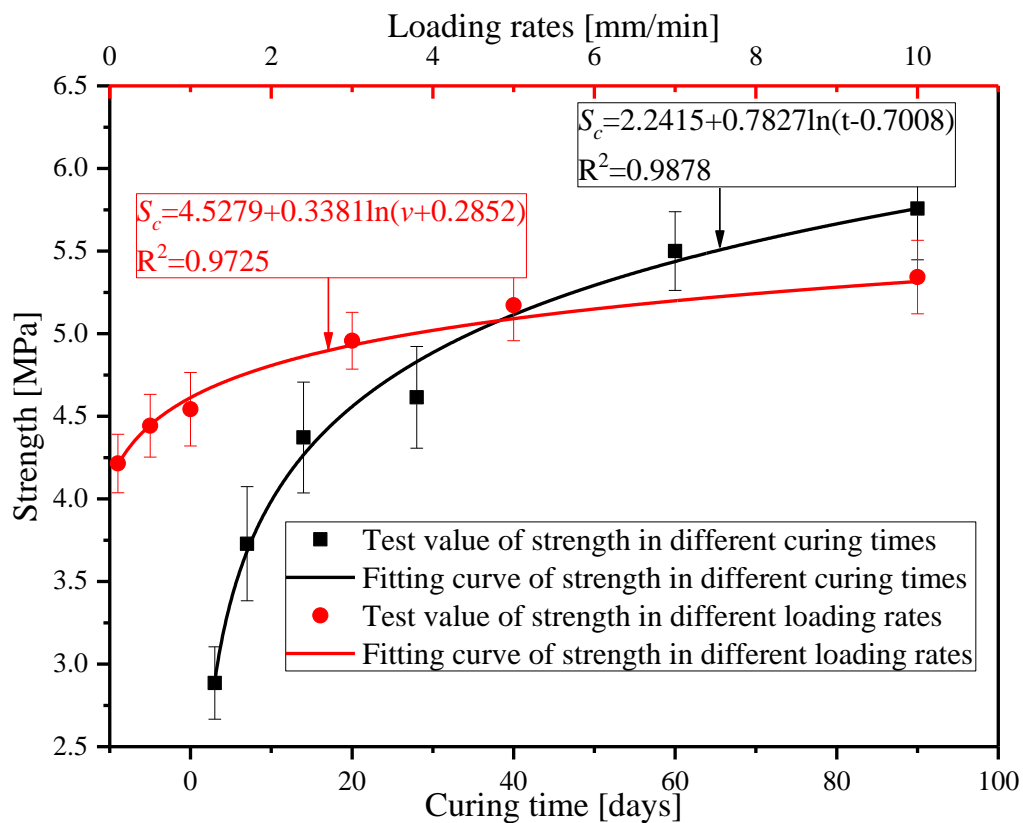


Figure 5. Patterns of variation of unconfined compressive strength with curing time and loading rates.

From the fitting results, it can be noted that:

- (1) The effect of the curing time on the strength of the cement-treated aggregate base material is larger than the loading rate. The strength value increases with an increased curing time. For example, the strength at a curing time of 90 days was two times larger than that of three days. The strength increased quickly with the curing time in the early period, and tended to be stable in the later period. In the first 28 days, the strength value increased by about 58.6% (from 2.9 MPa to 4.6 MPa). This is consistent with the findings in the literature [24,25]. The strength increased slowly in the later period, therefore, the semi-rigid base layer should be maintained for more than 28 days before the upper layers are paved.
- (2) The strength of the cement-treated aggregate base material is affected by the test loading rate significantly, but much less than the curing time. The strength value increased by about 26% (from 4.2 MPa to 5.3 MPa) with the increased loading rate (from 0.1 mm/min to 10 mm/min). Therefore, when the compressive strength was taken as the pavement design parameter, the effect of the loading rate should be considered.

#### 4. Unconfined Compressive Resilient Modulus Test

##### 4.1. Compressive Resilient Modulus Test Process

The preparation of specimens for the modulus test was the same with that for the strength test. The static resilient modulus test method was adopted. The compressive modulus test was carried out in accordance with the Chinese Test Methods of Materials Stabilized with Inorganic Binders for Highway Engineering (JTG E51-2009) [23]. The stress and strain used for static resilient modulus calculations were obtained through seven stages of loading and unloading. According to the strength tests results, the ultimate failure loads corresponding to certain test conditions were determined as  $P$ ,

and then 0.1  $P$ , 0.2  $P$  ..., 0.7  $P$  were employed as the loading level for the seven stages of the loading and unloading procedure. The displacement extensometer was implemented to measure the corresponding strain and placed on both sides of the specimen, as shown in Figure 6.

According to each loading level  $P_i$  and the corresponding deformation  $l_i$ , the resilience modulus could be calculated by Equation (4).

$$E_c = \frac{P_i h}{A l_i} \tag{4}$$

where  $E_c$  is the compressive resilience modulus (MPa);  $P_i$  is the loading level (MPa), and  $i = 1, 2 \dots, 7$ ;  $h$  is the specimen height (mm);  $A$  is the cross sectional area of the specimen (mm<sup>2</sup>); and  $l_i$  is the deformation corresponding to the loading level  $P_i$  (mm).



Figure 6. Device of compression resilience modulus test.

#### 4.2. Patterns of Variation of Compressive Modulus at Different Curing Times and Loading Rates

The modulus of the cement-treated aggregate base material with a curing time of 3 days, 7 days, 14 days, 28 days, 60 days and 90 days was determined under the loading rate of 1mm/min. Then, modulus tests of the cement-treated aggregate base material specimens with a curing time of 28 days were conducted under the loading rates of 0.1 mm/min, 0.5 mm/min, 1 mm/min, 3 mm/min, 5 mm/min, 10 mm/min. The test results are presented in Table 4.

Table 4. Test results of the compressive resilient modulus with different curing times and loading rates.

Curing Times (t/d)	Loading Rates (v/mm/min)	Unconfined Compressive Modulus of Parallel Specimens $E_c$ (MPa)							Average Value $\bar{E}_c$ (MPa)	$C_v$ (%)
		1	2	3	4	5	6	7		
3	1	1830	1515	1573	1370	1518	1578	1365	1536	10.20
7	1	1919	1946	2294	2126	1988	2276	2179	2104	7.37
14	1	2564	2493	2344	2397	2379	2156	2378	2387	5.35
28	1	3004	3243	2806	2793	3286	3049	2935	3017	6.43
60	1	3556	3974	4026	3860	3762	3869	4125	3882	4.82
90	1	4222	4204	4107	4571	4127	3942	4150	4189	4.58
28	0.1	1876	2163	1636	1599	2140	1784	1912	1873	11.86
28	0.5	2424	2296	2351	2189	2634	2306	2405	2372	5.87
28	1	3004	3243	2806	2793	3286	3049	2935	3017	6.43
28	3	3437	3679	3523	3356	3240	3482	3176	3413	5.04
28	5	3628	3827	3741	3976	3664	3792	4006	3805	3.80
28	10	4040	3713	3863	3752	3941	4120	3723	3879	4.16

From the results of the unconfined compressive strength test presented in Table 4, it can be noted that the unconfined compressive modulus of the cement-treated aggregate base material varied significantly with both curing times and loading rates. The patterns of variation might be similar to that of strength, so the average value of the modulus test results with different curing times and loading rates were fitted by Equations (5) and (6), as shown in Figure 7, where  $R^2$  is the correlation coefficient.

$$E_c = m_1 + n_1 \ln(t + p_1) \tag{5}$$

$$E_c = m_2 + n_2 \ln(v + p_2) \tag{6}$$

where  $E_c$  is the compressive modulus,  $t$  is the curing time,  $v$  is the loading rate;  $m_1, m_2, n_1, n_2, p_1,$  and  $p_2$  are the fitting parameters.

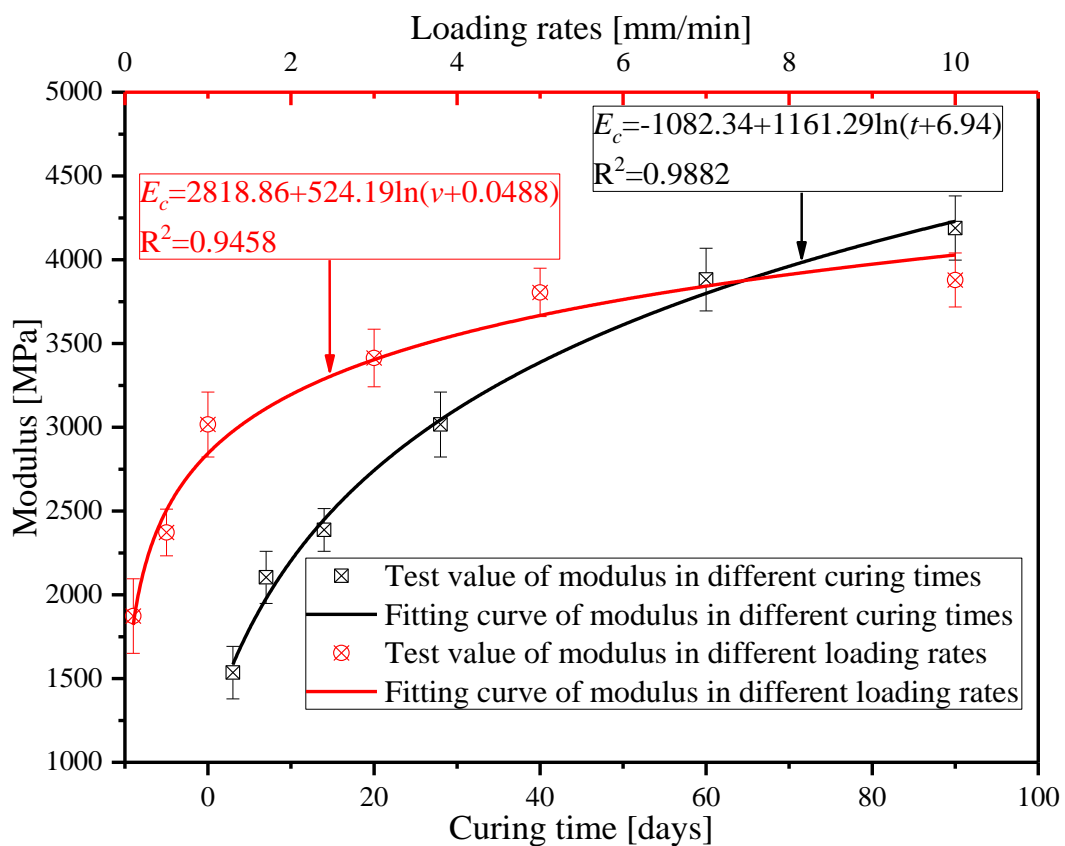


Figure 7. Patterns of variation for compressive resilient modulus with curing times and loading rates.

Based on the fitting results, it can be observed that:

- (1) The effect of the curing times on the modulus of the cement-treated aggregate base material was similar to that for the strength. The modulus varied dramatically with the curing times, especially from 3 days to 28 days, the modulus value increased by 96 % (from 1536 MPa to 3017 MPa). The modulus increased slowly with the later curing times, therefore the cement-treated aggregate base should be maintained for about 28 days after being paved, before paving the upper layer.
- (2) The modulus of the cement-treated aggregate base material is also affected by the loading rates. The modulus value increased by about 107% (from 1873 MPa to 3879 MPa) with the increase of the loading rates (from 0.1 mm/min to 10 mm/min). Therefore, when the compressive resilience modulus is taken as the pavement design parameter, the effect of the loading rates on it should be considered.

### 4.3. The Relationship between Unconfined Compressive Strength and Compressive Modulus

According to the Chinese Specification for Design of Highway Asphalt pavement (JTG D20-2017) [26], the control indicator is the unconfined compressive strength in the mix proportion design of the semi-rigid base material. However, the material design parameters for pavement structure design are the compressive resilient modulus, thus these two parameters are mismatched. In order to bridge the gap between the material design and the structural design, the relationship between the unconfined compression strength and the compression resilient modulus was established. Through comparing the patterns of variation illustrated in Figures 5 and 7, it can be found that the curing time has similar effects on the strength and modulus, as well as the loading rates. This means that a relationship between the strength and modulus could be established.

Under the same test conditions, the patterns of variation for the curing times to the strength and to the modulus were similar. Taking the curing time as an intermediate variable, the relationship between the strength and the modulus was proposed by regression analysis, as shown in Figure 8. Thus, the strength and modulus of the cement-treated aggregate base material could be transformed into each other at the same curing time. This was the same for the loading rates, as shown in Figure 9.

Taking the curing time as an intermediate variable (with the same curing times), the regression analysis equation was obtained as follows.

$$E_c = 0.28S_c^{1.53} R^2 = 0.97 \tag{7}$$

$$E_c = 0.05S_c^{2.61} R^2 = 0.89 \tag{8}$$

Similarly, taking the loading rates as the intermediate variable (with the same loading rates), the regression analysis equation was obtained as follows.

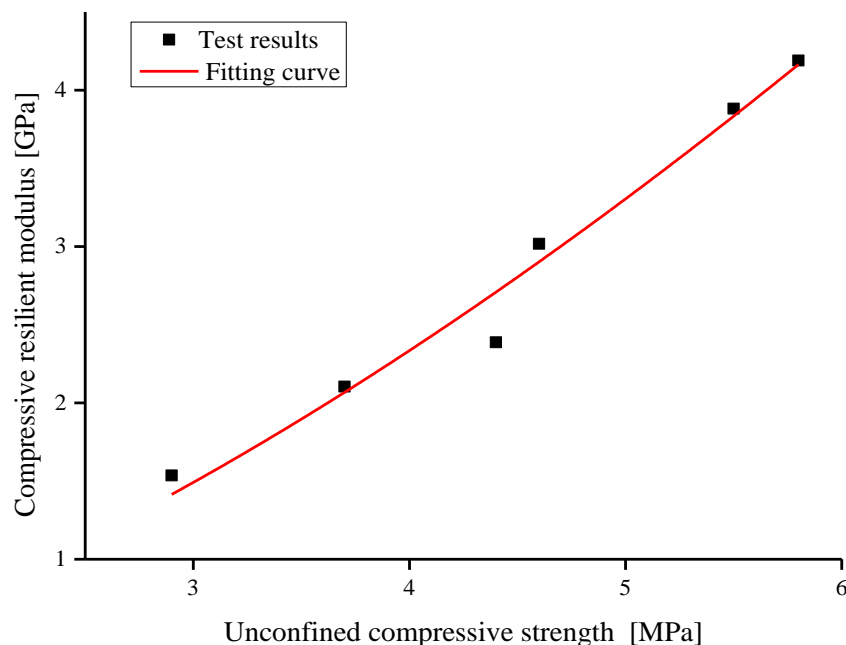


Figure 8. Fitting curve of strength and modulus with the same curing times.

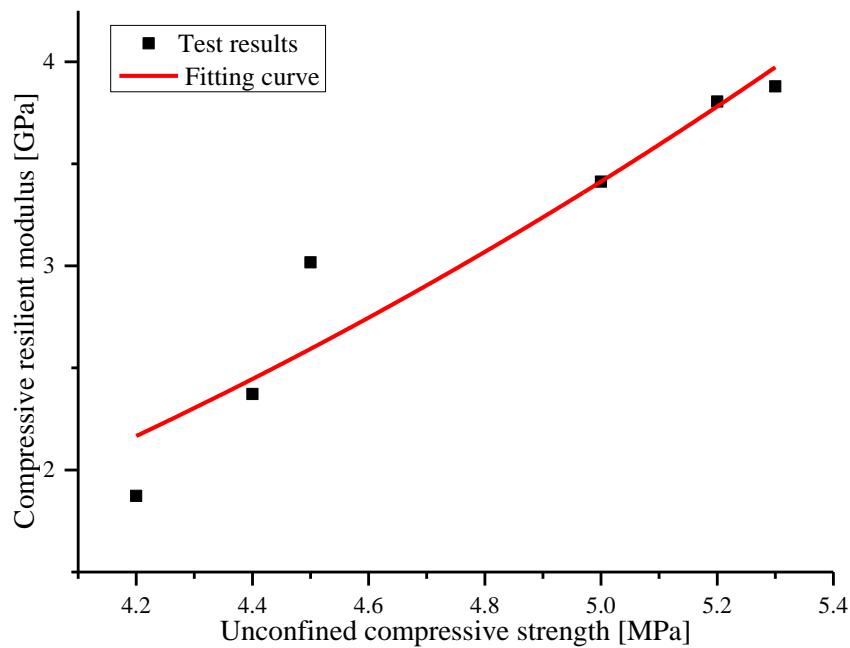


Figure 9. Fitting curve of strength and modulus with the same loading rates.

The regression analysis results bridged the gap between the material design and the structural design. This article provided a theoretical and methodical basis for the unification of the material design parameters and the structural design parameters.

### 5. Fatigue Equation of the Cement-Treated Aggregate Base Material Based on the True Stress Ratio and Nominal Stress Ratio

#### 5.1. S-N Fatigue Equation

The S-N fatigue equation was established by Chaboche [27,28]

$$\frac{dD}{dN} = [1 - (1 - D)^{1+r}]^\alpha \left[ \frac{\sigma}{M(1 - D)} \right]^\gamma \tag{9}$$

where  $D$  is the damage;  $N$  is the cycle number;  $M$ ,  $\alpha$  and  $\gamma$  are the material parameters related to temperature, stress amplitude and average stress; and  $\sigma$  is the stress level.

Through the integration of Equation (9), Equation (10) can be obtained:

$$D(N) = 1 - [1 - (N(1 + \gamma)(1 - \alpha) \left( \frac{\sigma}{M} \right)^\gamma)^{\frac{1}{1-\alpha}}]^{\frac{1}{1+\gamma}} \tag{10}$$

When  $D(N) = 1$ , then  $N = N_f$ , the equation of fatigue life  $N_f$  can be obtained from Equation (10):

$$N_f = \frac{1}{(1 + \gamma)(1 + \alpha)} \left( \frac{\sigma}{M} \right)^{-\gamma} \tag{11}$$

where  $N_f$  is the fatigue life.

Let  $k = \frac{M^\gamma}{(1+\gamma)(1-\alpha)}$ ,  $n = \gamma$ , and Equation (11) can be transformed to:

$$N_f = k \left( \frac{1}{\sigma} \right)^n \tag{12}$$

where  $k$  and  $n$  are the fitting parameters of the fatigue equation;

Let  $k' = \frac{S_t^{-\gamma}}{(1+\gamma)(1-\alpha)(M)^{-\gamma}}$ ,  $n' = \gamma$ , and Equation (11) can be transformed to:

$$N_f = k' \left(\frac{1}{\sigma}\right)^{n'} \quad (13)$$

where  $S_t$  is the strength obtained by the standard strength test; and  $t$  is the nominal stress ratio in fatigue test,  $t = \sigma/S_t$ .

Equations (12) and (13) are the conventional S-N fatigue equations, which have been widely used in characterizing the fatigue performance of pavement materials.

From the definition of the S-N equation, it could be noted that the stress ratios were determined with a certain strength value, obtained by the standard strength test method. The loading rates of the standard strength test are fixed, such as 1 mm/min or 50 mm/min. However, Section 3.1 showed that the strength of the cement-treated aggregate base material varied with the loading rates. Thus, it might bring a large error into the fatigue properties. When the stress level is larger than the failure strength obtained by the standard strength test, the stress ratio calculated by the standard strength was larger than 1, which means that the fatigue life of cement-treated aggregate base material under this stress level will be less than 1. However, the actual fatigue life is much greater than 1, according to the lab test. Therefore it is necessary to establish an improved S-N fatigue equation, which can consider the effects of the loading rates on the strength of the cement-treated aggregate base material.

### 5.2. Establishment of the Fatigue Model Based on the True Stress Ratio

#### (1) Fatigue tests

In this paper, the four-point bending fatigue test was employed to characterize the fatigue properties of the cement-treated aggregate base material. The specimens for the four-point bending fatigue test were prepared using the static compaction method and the size of specimen was 100 mm × 100 mm × 400 mm, as shown in Figure 10.

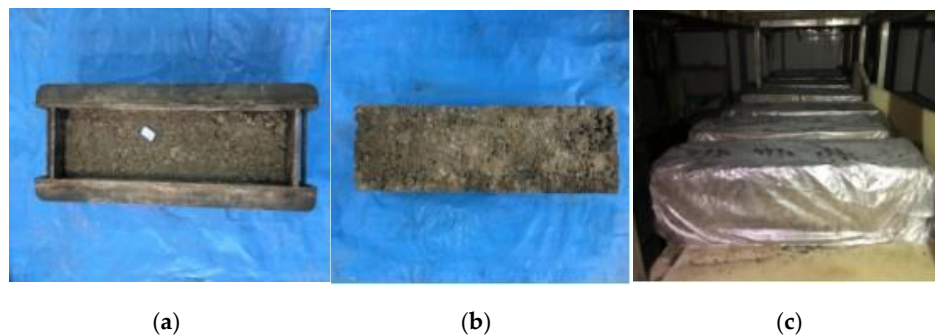


**Figure 10.** Specimen of fatigue test (a) specimen molding (b) specimen after being demolded (c) specimens curing.

Prior the flexural fatigue test, the flexural strength tests were conducted under the standard loading rate of 13 MPa/s, which was calculated by the strength value and the loading time of the strength test. In this way the nominal stress ratio can be determined. Then the strength tests under different loading rates (5 MPa/s, 20 MPa/s, 30 MPa/s, 40 MPa/s, and 50 MPa/s) were conducted to determine the true stress ratio of the fatigue test. The true stress ratio refers to the ratio of fatigue stress level to strength and the strength is related to the loading rates. The procedure of flexural strength tests is the same for the unconfined compressive strength tests described in Section 3.2. The flexural strength of the specimen can be calculated according to Equation (14).

$$S_f = \frac{PL}{b^2h} \quad (14)$$



where  $S_f$  is the flexural strength (MPa);  $P$  is the ultimate failure loads (kN);  $L$  is the distance between two supporting points (mm);  $b$  is the width of the specimen (mm); and  $h$  is the height of the specimen (mm).

The test results are presented in Table 5.

**Table 5.** Flexural strength tests results with different loading rates.

Curing Times (t/d)	Loading Rates $v$ (MPa/s)	Flexural Strength Tests Results of Parallel Specimens							Average Value $\bar{S}_f$ (MPa)	$C_v$ (%)
		$S_f$ (MPa)								
		1	2	3	4	5	6	7		
90	5	1.10	1.11	1.13	1.02	1.17	1.11	1.12	1.11	4.53
	13	1.29	1.31	1.3	1.28	1.36	1.3	1.24	<b>1.30</b>	3.59
	20	1.57	1.68	1.62	1.64	1.6	1.68	1.64	1.63	4.03
	30	2.38	2.35	2.47	2.46	2.44	2.50	2.43	2.43	5.22
	40	2.59	2.66	2.61	2.64	2.57	2.6	2.62	2.61	3.04
	50	2.72	2.62	2.77	2.73	2.74	2.71	2.72	2.72	4.65

As mentioned above, the standard loading rate was 13 MPa/s. From Table 5, it can be observed that the corresponding standard strength was 1.3 MPa when the standard loading rate was 13 MPa/s. The corresponding standard strength of 1.3 MPa was used to calculate the nominal stress ratio.

The fitting result for flexural strength with loading rates is shown in Figure 11;  $R^2$  is the correlation coefficient.

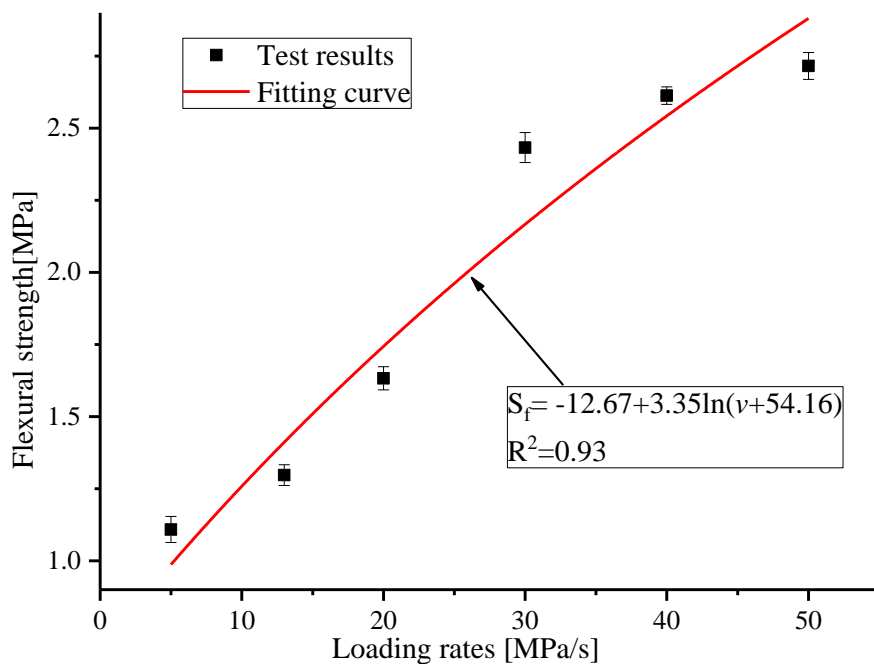


**Figure 11.** Pattern of variation of flexural strength with loading rates.

From the fitting results, it can be noted that the patterns of the variation of flexural strength with loading rates are similar to those of unconfined compressive strength.

(2) S-N fatigue equation characterized by nominal stress ratio and true stress ratio

Generally, the average speed of vehicles on the road is about 60~80 km/s, at which point the pavements receive a loading frequency nearly equivalent to 10 Hz. Thus 10 Hz was taken as the loading frequency of the fatigue tests. The sinusoidal wave illustrated in Figure 12a was implemented as the loading waveform, and  $\sigma$  is the stress level. Based on the result of the flexural strength tests and the loading frequency, the control parameters of the four-point bending fatigue tests, namely



stress level, nominal stress ratio and true stress ratio, could be calculated. The calculated results are presented in Table 6. According to the test setting parameters in Table 6, the four-point bending fatigue tests were carried out as shown in Figure 12b, and the test results are presented in Table 6.

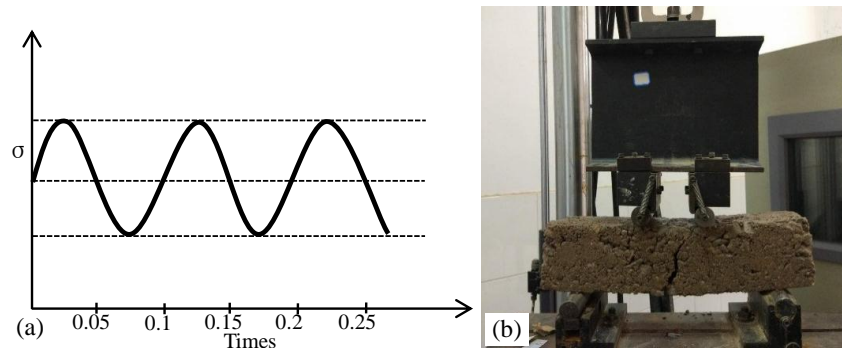


Figure 12. Fatigue test (a) Loading waveform (b) Flexural test.

Table 6. Tests results of flexural fatigue under different stress levels.

$v$ (MPa/s)	$\sigma$ (MPa)	$S_{fv}$ (MPa)	$t_1$ (%)	$t_2$ (%)	Fatigue Life of Parallel Tests $N_f$				Average $N_f$
					1	2	3	4	
5	0.25	1.11	0.19	0.23	12,687,941	12,619,781	12,809,765	12,753,580	12,717,767
13	0.65	1.30	0.50	0.50	2283	2251	2237	2189	2239
20	1.00	1.63	0.77	0.61	567	596	582	603	587
30	1.50	2.43	1.15	0.62	302	317	320	309	312
40	2.00	2.61	1.54	0.77	30	37	33	36	34
50	2.50	2.72	1.69	0.91	6	8	10	8	8

where  $v$  is loading rate;  $\sigma$  is stress level;  $S_f$  is the flexural strength value;  $t_1$  is the nominal stress ratio,  $t_1 = \sigma/1.3$  MPa, 1.3 MPa is the standard strength; and  $t_2$  is the true stress ratio,  $t_2 = \sigma/S_{fv}$ .

The fatigue life of the cement-treated aggregate base material was fitted by S-N fatigue equation with a nominal stress ratio and true stress ratio, respectively. The fitting results are shown in Figure 13.

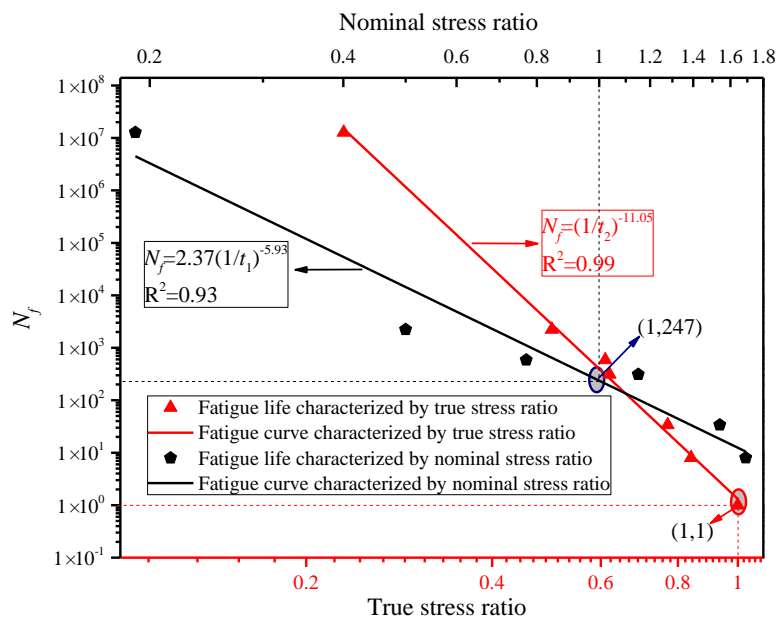


Figure 13. Fatigue curve fitted by nominal stress ratio and true stress ratio.

It can be observed from Figure 13 that:

① When stress levels of 1.5 MPa, 2.0 MPa and 2.5 MPa were exerted on the specimens during the four-point bending fatigue tests, the nominal stress ratios calculated by the standard strength 1.30 MPa were larger than 1. For these stress ratios, the fatigue life should theoretically be less than 1. However, their actual average fatigue lives were 312, 34 and 8, respectively, as shown in Table 6. Meanwhile, when the nominal stress ratio was 1, the actual fatigue life was 247, as shown in Figure 13, which means that the fatigue curve will not go through the point of (1, 1). The reason for this is that the strength of the cement-treated aggregate base material increases with the loading rates. However, the fatigue equation characterized by the nominal stress ratio could not consider it.

② When the true stress ratios were adopted in the *S-N* fatigue equation to reveal the characteristics of the cement-treated aggregate base material, the discrepancy mentioned above was eliminated. Based on the test and fitting results, the fatigue curve characterized by the true stress ratio will pass through the point of (1, 1), as shown in Figure 13. The parameter  $k'$  of the fatigue equation  $N_f = k'(1/t)^{n'}$  was 1, so the equation can be expressed as  $N_f = (1/t)^{n'}$ . This indicates that the fatigue life  $N_f$  will be 1 when the stress ratio  $t$  is 1, which means the fatigue equation curve based on the true stress ratio can be extended to the strength failure point of (1, 1), where both the true stress ratio and the fatigue life are 1. The  $N_f = 1$  represents the strength failure where the fatigue life is 1. Therefore, based on the test and fitting of the results, the fatigue curve reveals the internal relationship between the strength failure and the fatigue failure.

The fatigue equation based on the true stress ratio is more rational than the fatigue equation of the nominal stress ratio. The fatigue test results can be extended in both directions of the fatigue curve. However, if the fatigue curve characterized by the nominal stress extends in the two directions, it will lead to a larger deviation. The greater the scope of the extension, the greater the deviation.

The effect of the loading rates on strength can be considered in the *S-N* fatigue equations characterized by the true stress ratio. It increases the accuracy of the fatigue life prediction for the cement-treated aggregate base material.

## 6. Conclusions

The unconfined compressive strength tests and compressive resilience modulus tests of the cement-treated aggregate base material were carried out under different loading rates and with different curing times. Meanwhile, the fatigue equations characterized by the true stress ratio were established by four-point bending fatigue tests. The following conclusions can be drawn from the above:

- (1) The unconfined compressive strength, compressive resilient modulus and flexural strength of cement-treated aggregate base materials are significantly affected by both the curing times and the loading rates.
- (2) When the nominal stress ratio reaches 1, that is, when the stress level reaches the strength value tested by the traditional strength test method, the theoretical fatigue life is expected to be 1, however, the actual fatigue life based on the conventional fatigue equation is 247. Thus, a large degree of discrimination exists between the theoretical value and the actual value. For the improved fatigue equation, the fatigue life is 1 when the stress ratio is 1 and the actual test result is consistent with the theoretical value expressed by the equation.
- (3) The *S-N* fatigue equation was modified by the true stress ratio, by which the fatigue curve could extend to the point of (1, 1). The relationship between the strength failure and the fatigue failure was established. It is consistent with the actual situation.
- (4) A comparison of the result between the existing and improved fatigue equation will be conducted to find more detailed differences and to develop advanced equations; this research will be conducted in the future with international materials and standards.

**Author Contributions:** S.L. and C.L. conceived the experiments; C.L., J.L. and H.Z. performed the experiments; S.L. and C.L. wrote the paper; J.Z. and Z.Y. outlined and revised the paper.

**Acknowledgments:** This work was supported by National Natural Science Foundation of China (51578081, 51608058), Chinese Academy of Engineering Consulting Research Project(2017-XY-17), The Ministry of Transport Construction Projects of Science and Technology (2015318825120), Key Projects of Hunan Province-Technological Innovation Project in Industry (2016GK2096), National Engineering Laboratory Open Fund Project (kfh160102), Scientific and Technological Innovation Project of Hunan Province for University Graduate Students (CX2017B457), The Guangxi Zhuang Autonomous Region Traffic and Transportation Department Transportation Projects of Science and Technology (2013-32), and The Inner Mongolia Autonomous Region Traffic and Transportation Department Transportation Projects of Science and Technology (NJ-2016-35).

**Conflicts of Interest:** The authors declare no conflict of interest.

## References

1. Judycki, J.; Jaskula, P. Structural Design and Sensitivity Analysis of Semi-Rigid Pavement of a Motorway. *Eng. J.* **2012**, *16*, 117–126. [CrossRef]
2. Sun, J.; Xiao, T.; Dou, Y.; Yang, C. Study on the Rational Thickness of Surface Course on Semi-Rigid Base Asphalt Pavement. *Geohunan Int. Conf.* **2011**, 37–44. [CrossRef]
3. Jiang, Y.; Chen, Z.; Peng, B.; Dai, J. Mixture design method and anti-cracking performance of cement stabilizing crashed rock pavement with dense skeleton type. *J. Xian Highw. Univ.* **2002**, *22*, 9–12.
4. Paige-Green, P.; Netterberg, F. *Cement Stabilization of Road Pavement Materials: Laboratory Testing Programme Phase 1*; Cement & Concrete Institute: Midrand, South African, 2004.
5. Guthrie, W.S.; Young, T.B. Evaluation of Transition Cement for Stabilization of Frost-Susceptible Base Material in Conjunction with Full-Depth Recycling in Weber Canyon, Utah. *Int. Conf. Cold Reg. Eng.* **2006**, 1–13. [CrossRef]
6. Poveda, E.; Ruiz, G.; Cifuentes, H.; Yu, R.; Zhang, X. Influence of the fiber content on the compressive low-cycle fatigue behavior of self-compacting SFRC. *Int. J. Fatig.* **2017**, *101*, 9–17. [CrossRef]
7. Hou, X.; Zhang, P.; Zhang, M. Study on Fracture Toughness of Cement Treated Aggregate. *Adv. Mater. Res.* **2011**, *280*, 76–79. [CrossRef]
8. George, K.P. Shrinkage characteristics of soil-cement mixtures. *Highw. Res. Rec.* **1968**, *225*, 42–48.
9. Lv, S.; Liu, C.; Yao, H.; Zheng, J. Comparisons of synchronous measurement methods on various moduli of asphalt mixtures. *Construct. Build. Mater.* **2018**, *158*. [CrossRef]
10. Deng, X.J.H.; Yang, J. Cyclic test study on fatigue characteristics of semi rigid pavement. *J. Southeast Univ.* **1995**, *25*, 94–99.
11. Chai, G.; Oh, Y.N.E.; Balasubramaniam, A. In-Situ Stabilization of Road Base Using Cement. In Proceedings of the Fifteenth International Offshore and Polar Engineering Conference, Seoul, Korea, 19–24 June 2005.
12. Busch, C.; Thøgersen, F.; Henrichsen, A. Development and Validation of a Mechanistic Recursive-Incremental Deterioration Model for Cement-Stabilized Base Courses. *Transp. Res. Rec. J. Transp. Res. Board* **2006**, *1974*, 128–137. [CrossRef]
13. Judycki, J. Comparison of fatigue criteria for flexible and semi-rigid pavements. In Proceedings of the Conference on Asphalt Pavements—International Society of Asphalt Pavements, Seattle, WA, USA, 10–14 August 1997.
14. Yao, Z. A Review on Design Criteria of Asphalt Pavements. *Highway* **2003**, *2*, 43–49.
15. Kim, J.; West, R.C. Application of the Viscoelastic Continuum Damage Model to the Indirect Tension Test at a Single Temperature. *J. Eng. Mech.* **2010**, *136*, 496–505. [CrossRef]
16. You, Z.; Adhikari, S.; Kutay, M.E. Dynamic modulus simulation of the asphalt concrete using the X-ray computed tomography images. *Mater. Struct.* **2009**, *42*, 617–630. [CrossRef]
17. González, J.M.; Miquel Canet, J.; Oller, S.; Miró, R. A viscoplastic constitutive model with strain rate variables for asphalt mixtures—Numerical simulation. *Comput. Mater. Sci.* **2007**, *38*, 543–560. [CrossRef]
18. Lundström, R.; Isacsson, U.; Ekblad, J. Investigations of stiffness and fatigue properties of asphalt mixtures. *J. Mater. Sci.* **2003**, *38*, 4941–4949. [CrossRef]
19. Lv, S.; Zheng, J. Normalization method for asphalt mixture fatigue equation under different loading frequencies. *J. Cent. South Univ.* **2015**, *22*, 2761–2767. [CrossRef]

20. CEB. *Fatigue of Concrete Structures; State of the Art Report, Bulletin d'Information No. 188*; Comité Euro-International du Béton: Paris, France, 1988.
21. Zheng, J.; Lv, S. Nonlinear fatigue damage model for asphalt mixtures. *China J. Highw. Transp.* **2009**, *22*, 21–28.
22. JTJ/T F20-2015. *The Chinese Construction Specifications for Highway Road Bases*; Renmin Communication Press: Beijing, China, 2015.
23. JTG E51-2009. *The Chinese Test Methods of Materials Stabilized with Inorganic Binders for Highway Engineering*; Renmin Communication Press: Beijing, China, 2009.
24. Zhuang, S.; Liu, P.; Sun, Z. Investigation on deformation and its influencing factors of cement-stabilized macadam base. *J. Build. Mater.* **2003**, *6*, 356–363.
25. Sun, Z.; Wang, T.; Zhi-Hong, X.; Liu, Z.; Qiu, Y.; Xiao, L. Trial Study on Influence Factors of Cement-Stabilized Macadam Strength. *J. Build. Mater.* **2006**, *9*, 285–290.
26. JTG D20-2017. *The Chinese Specification for Design of Highway Asphalt Pavement*; Renmin Communication Press: Beijing, China, 2017.
27. Lv, S.; Luo, Z.; Xie, J. Fatigue performance of aging asphalt mixtures. *Polimery* **2015**, *60*, 126–131. [CrossRef]
28. Lv, S.; Wang, X.; Liu, C.; Wang, S. Fatigue Damage Characteristics Considering the Difference of Tensile-Compression Modulus for Asphalt Mixture. *J. Test. Eval.* **2018**, *46*. [CrossRef]



© 2018 by the authors. Licensee MDPI, Basel, Switzerland. This article is an open access article distributed under the terms and conditions of the Creative Commons Attribution (CC BY) license (<http://creativecommons.org/licenses/by/4.0/>).



Article

# Algorithm for Virtual Aggregates' Reconstitution Based on Image Processing and Discrete-Element Modeling

Danhua Wang <sup>1</sup>, Xunhao Ding <sup>2</sup>, Tao Ma <sup>2,\*</sup>, Weiguang Zhang <sup>2</sup> and Deyu Zhang <sup>3</sup>

<sup>1</sup> School of Computer Engineering, Nanjing Institute of Technology, Nanjing 211167, China; wangdh@njit.edu.cn

<sup>2</sup> School of Transportation, Southeast University, 2 Sipailou, Nanjing 210096, China; 220132397@seu.edu.cn (X.D.); wgzhang@seu.edu.cn (W.Z.)

<sup>3</sup> School of Engineering and Architecture, Nanjing Institute of Technology, Nanjing 211167, China; zhangdy@njit.edu.cn

\* Correspondence: matao@seu.edu.cn; Tel.: +86-158-0516-0021

Received: 15 February 2018; Accepted: 3 May 2018; Published: 7 May 2018

**Abstract:** Based on the Aggregate Imaging Measurement System (AIMS) and the Particle Flow Code in Two Dimensions (PFC2D), an algorithm for modeling two-dimensional virtual aggregates was proposed in this study. To develop the virtual particles precisely, the realistic shapes of the aggregates were captured by the AIMS firstly. The shape images were then processed, and the morphological characteristics of aggregates were quantified by the angularity index. By dividing the particle irregular shape into many triangle areas and adjusting the positions of the generated balls via coordinate systems' conversion within PFC2D, the virtual particles could be reconstructed accurately. By calculating the mapping area, the gradations in two-dimensions could be determined. Controlled by two variables ( $\mu_1$  and  $\mu_2$ ), which were drawn from the uniform distribution (0, 1), the virtual particles forming the specimens could be developed with random sizes and angular shapes. In the end, the rebuilt model of the SMA-13 aggregate skeleton was verified by the virtual penetration tests. The results indicated that the proposed algorithm can not only model the realistic particle shape and gradations precisely, but also predict its mechanical behavior well.

**Keywords:** algorithm; aggregates; reconstitution; image processing; virtual modelling

## 1. Introduction

As the basis materials within the asphalt mixture, coarse aggregates are widely used in asphalt pavements, which form the main skeleton of the total structure. It has been highlighted by many researchers that the aggregates' shape has a significant impact on controlling the mechanical properties of the asphalt mixtures [1–3]. Tests conducted by Campen and Smith [4] showed that the stability of hot-mix asphalt (HMA) concrete could be improved obviously by using crushed aggregates instead of rounded particles. Similar results were shown by Kandhal and Parker [5], that the HMA mixtures consisting of excessive flat and elongated aggregate particles tended to break down, affecting the mix durability. The fatigue performance of the asphalt mixture was also affected by the particles' roundness and angularity, concluded based on Cheung and Dawson's research [6]. In their studies, with the angularity increasing, the ultimate shear strength increased, and permanent deformation decreased, respectively. Thus, it is strongly recommended to use the complex angular particles to improve the grains' interlocking and packing effectively.

However, it is really difficult and time-consuming to reveal the shape influences of coarse aggregates just by laboratory tests due to the appropriate definition of the morphological characteristics and the

following shape acquisition, which is the basis to guarantee the results [7,8]. The discrete-element method (DEM) was proposed by the Cundall [9] firstly, and then, a software program named Particle Flow Code (PFC) was developed to help the mechanical calculation of heterogeneous materials, which has been widely used in many fields [10–12]. As the basic calculation elements, the balls in the software (PFC2D, Itasca Consulting Group: Minneapolis, USA) are all round shaped without any angular shape, which is not consistent with the realistic particles in pavement construction. Therefore, prior to numerical simulation, it is important to rebuild the realistic particle shape, which will influence the simulation results obviously [13–15]. Many modeling methods have been proposed within PFC to characterize the shape features by some researchers. Zhang et al. [16] regarded the aggregate particles as hexahedrons, pentahedrons and tetrahedrons within PFC, respectively. Then, the equal-radius balls were arranged regularly within the particles and were defined as a rigid body. CPA (Computerized Particle Analysis) was utilized to help develop the virtual shape within PFC by Stahl and Konietzky [17]. The input index, known as the grain-shape coefficient, was used to redefine the particle contour. Then, numerical particles were reconstructed by filling the redefined area with balls. Huang [18] reconstructed 3D ballast particles with three images (top, side and front) of the particles with the help of the image processing technology. Similar methods can also be found in the works of Liu and You [19,20], Tutumluer et al. [21] and Dondi and Vignali [22–24], as well. Most of the existing modeling methods can only model the shape roughly with excessive simplification. Although some virtual models were rebuilt precisely by X-ray scanning, the angular shape could not be quantified precisely [25–29]. Liu scanned the particles and rebuilt their virtual shapes according to the acquired images [30,31]. In their studies, the stl-format file were developed, which can reflect the shapes of aggregates precisely. By the designed routine, the virtual particles in three dimensions were developed successfully with enough balls filled. However, their methods can only model the realistic shapes, but cannot evaluate the shape properties of mixtures by a specific index. Therefore, the simulation accuracy mainly depends on the samples' selection and cannot model the material heterogeneity well. Compared to X-ray scanning, the Aggregate Imaging Measurement System (AIMS) apparatus is a promising way for performing particle shape modeling and has been utilized gradually in material analyses [32]. It can capture the morphological characteristics of aggregates and quantifies the shape properties by some design indices such as the angularity index, texture index, size, and so on. However, this apparatus is mainly used for pavement skid resistance measurements nowadays [33–35]. More uses of it should be explored, especially combined with other technologies.

The objective of this study is to propose an algorithm for the virtual aggregates' reconstitution based on the Discrete-Element Method (DEM). To achieve this, the AIMS apparatus with the image processing technology were utilized before the simulations. Then, an innovative method for developing the virtual particles and gradations was proposed precisely. In the end, based on the virtual penetration tests, the precision of the developed models was verified. The relevant issues include: capturing the shape image of particles by AIMS; processing the captured images and measuring their angularity index; modeling the virtual particles with different sizes and shapes; modeling the virtual gradations of specimens; developing the virtual penetration tests to predict and evaluate the performance of coarse aggregates.

## **2. Image Preprocessing and Shape Measurement**

Prior to the virtual particles' reconstitution, several steps were performed that could provide the proposed algorithm with the fundamental data. Firstly, enough aggregate particles were selected and were scanned by the AIMS to obtain their shape image and the angularity index. The particles were put in the turntable of the AIMS and were rotated slowly to go through the scanning area. A digital camera above the particles was utilized to capture the image of the maximum section from the top side. Then, the original images of the particles were converted to the binary ones within the MATLAB routine as shown in Figure 1. As shown, two forms of binary images were acquired via the image processing technology including the shape (Figure 1a) and its contour (Figure 1b).

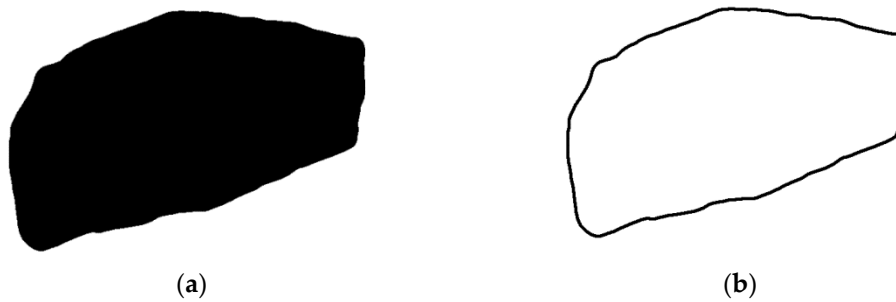


Figure 1. Binary images of aggregate particles: (a) shape; (b) shape contour.

Due to the size differences between the binary images and realistic particles, the processed images should be scaled back based on the actual ones. Because the binary images consisted of pixels only, the sizes were represented by the pixel number at different directions in the images rather than the actual length. In this proposed method, the relationship between the actual length and “pixel length” were quantified by uniform standards as one pixel equal to 0.005 mm. After this standard was developed, based on the actual particle size, the required reduction scale of binary images could be calculated to match the actual size, as shown in Table 1. Furthermore, after the images’ adjustment completed, the actual area of various particles was measured by the ImagePro software. The black area of the shape image in Figure 1a could be distinguished within the software, and the corresponding area was calculated and stored as shown in Table 1, as well.

Table 1. Summaries of the two-dimensional images.

Sample	Angularity	Reduction Scale	Particle Area (m <sup>2</sup> )
1	2864.41	4109.07	0.00033
2	3358.80	2882.90	0.00040
3	1803.25	1692.92	0.00045
4	2354.54	2015.89	0.00053
5	4329.94	2174.40	0.00038
6	3641.75	1925.21	0.00056
7	2192.07	3589.41	0.00036
8	3716.14	3527.46	0.00043
9	2040.78	4591.80	0.00028

Although there was an original coordinate system after image processing, another two coordinate systems were introduced in this proposed method to help the virtual particles’ reconstitution further, including the local coordinate system and global coordinate system. The local one will be introduced in the algorithm part, while the global one is developed as the following. It is necessary to develop a uniform global coordinate system for all particles because the original coordinate system in each image was not the same at all. The central position of each particle was defined firstly as shown in Equation (1):

$$cen_x = \frac{\sum_1^n x_i}{n} \quad cen_y = \frac{\sum_1^n y_i}{n} \tag{1}$$

where  $cen_x$ ,  $cen_y$  are the X- and Y-coordinate values of the particle central position, respectively, in the original coordinate system;  $n$  is the total number of pixels in Figure 1b;  $x_i$ ,  $y_i$  are the X- and Y-coordinate values of the  $i$ -th pixel in Figure 1b in the original coordinate system.

The original coordinate system of each image was converted to the uniform global coordinate system by setting the central positions as the new origin of the coordinates, and the adjustments of the original coordinate are summarized as shown in Table 2. It is noted that the data in Tables 1 and 2 are only a part of the total virtual particles limited by space. The data shown were utilized to illustrate the preparation procedure.



**Table 2.** Adjustments of the image coordinates.

Sample	Adjustments of X-Coordinate	Adjustments of Y-Coordinate
1	-74.53354	-100.6707
2	-75.23496	-103.149
3	-76.80114	-100.0369
4	-74.9621	-104.7988
5	-75.26646	-102.7743
6	-72.68012	-100.83
7	-78.78299	-98.05279
8	-74.50542	-101.9675
9	-80.44268	-105.0318

### 3. Image Preprocessing and Shape Measurement

#### 3.1. Triangle Area Divisions

As the independent element for calculation, the ball within PFC2D should be generated with a specific coordinate value. However, it is very hard to fill the particle shape area with balls directly because of the shape complexity, which prevents precise virtual particle modelling. The proposed algorithm converted the irregular particle shape into several triangles to make it easier to fill the required area with balls. The algorithm is illustrated as follows:

After the shape contour (Figure 1b) was scaled back, its irregular shape was divided into 36 triangle areas firstly, as shown in Figure 2. Measuring lines were drawn every 10 degrees by a user-defined routine based on MATLAB. They were drawn from the central position to the shape contour. Each triangle could represent a part of the shape area approximately. Then, the lengths of 36 lines were measured respectively by the routine. It is noted that the measuring lines in Figure 2 are not true lines, but a routine developed within MATLAB to measure the distance from the central position to the contour along the designed directions. The modelling precision and efficiency are definitely influenced by the number of divided triangles. As shown in Figure 2, with more triangles divided, the boundary of the virtual particle can have better accordance with the realistic one, but needs more complex routines for length measurements, which means more time consumption. To balance the simulation precision and efficiency, 36 triangle divisions were determined finally and were thought as the best after many tries.

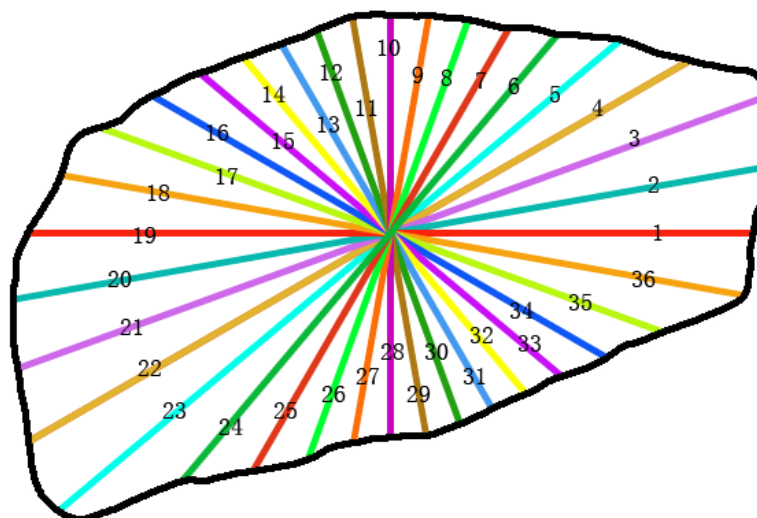


**Figure 2.** Triangle area divisions for measurement.

### 3.2. Filling Area Judgments

By labelling the lines with numbers increasing counter-clockwise as shown in Figure 2, the divided triangles could fall into two categories. One is that the top side of the triangle is longer than the bottom side; another is that the top one is shorter than the bottom one, as shown in Figure 3. The top side is always labelled with a larger number compared to the bottom side in one triangle.  $S_1$  and  $S_2$  are known quantities based on the former measurement in Figure 3, and “ $a$ ” represents the included angle between two adjacent measuring lines with a magnitude of 10 degrees.  $d_1, d_2, d_3, d_4$  and  $d_5$  were calculated as shown in Equation (2).

$$\begin{aligned}
 d_1 &= S_2 \times \cos a \\
 d_2 &= S_1 - d_1 \\
 d_3 &= S_2 \times \sin a \\
 d_4 &= S_2 \times \cos a \\
 d_5 &= d_4 - S_1
 \end{aligned}
 \tag{2}$$

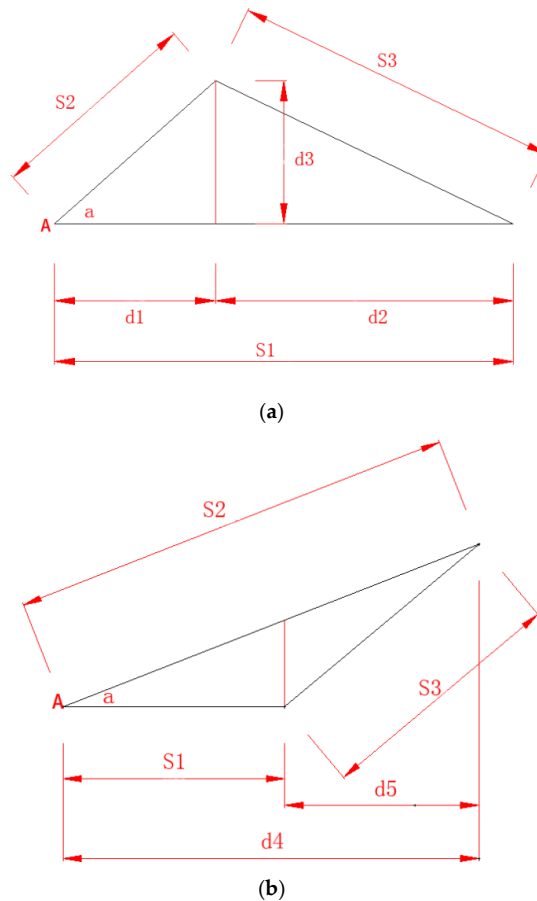


Figure 3. Algorithm for filling the triangle area with discrete balls: (a)  $S_2 \leq S_1$ ; (b)  $S_2 > S_1$ .

When  $S_2 \leq S_1$  (Figure 3a), the algorithm for filling the triangle area with balls by PFC2D was conducted as following:

- ① Start the ball generation from Point A with the coordinate of (0, 0);
- ② Determine the variable  $x_1$ . It is calculated as the following equation:

$$x_1 = x_{1f} + 2 \times rad
 \tag{3}$$

where  $x_1$  is the X-coordinate of the next column of balls that will be generated;  $x_{1f}$  is the X-coordinate of the former column of balls that has been generated;  $rad$  is the radius of the filled balls.

- ③Determine the variable  $h$ , calculated as shown in Equation (4):

$$h = \begin{cases} x_1 \times \tan a & x_1 \leq d_1 \\ \frac{S_1 - x_1}{d_2} \times d_3 & d_1 < x_1 \leq S_1 \end{cases} \quad (4)$$

where  $h$  is the required height of the next column of balls; the others are the same as the former.

- ④Generate uniform balls with coordinates of  $(x_1, 0), (x_1, 2 \times rad), (x_1, 4 \times rad), (x_1, 6 \times rad) \dots$  until the Y-coordinate exceeds  $h$ ;
- ⑤Start to generate the next column of balls by cycling from Steps 2–4 until the X-coordinate exceeds  $S_1$ .

When  $S_2 > S_1$  (Figure 3b), the algorithm is conducted as follows:

- ①Start the ball generation from Point A with the coordinate of  $(0,0)$ ;
- ②Determine the variable  $x_1$ . It is calculated as Equation (3):
- ③Determine the variable  $h_i$ , calculated as shown in Equations (5) and (6):

$$h_1 = x_1 \times \tan a \quad x_1 \leq S_1 \quad (5)$$

where  $h_1$  is the required height of the next column of balls; the others are the same as the former.

$$h_i = \begin{cases} x_1 \times \tan a & i = 1 \\ \frac{x_1 - S_1}{d_5} \times S_2 \times \sin a & i = 2 \end{cases} \quad (6)$$

where  $h_1$  is the required height of the next column of balls;  $h_2$  is the lower limit of the column height when  $x_1$  exceeds  $S_1$ ; the others are the same as the former;

- ④When  $x_1 \leq S_1$ , generate uniform balls with coordinates of  $(x_1, 0), (x_1, 2 \times rad), (x_1, 4 \times rad), (x_1, 6 \times rad) \dots$  until the Y-coordinate exceeds  $h_1$ ; when  $x_1 > S_1$ , generate uniform balls with the coordinates of  $(x_1, h_2), (x_1, h_2 + 2 \times rad), (x_1, h_2 + 4 \times rad), (x_1, h_2 + 6 \times rad) \dots$  until the Y-coordinate exceeds  $h_1$ ;
- ⑤Start to generate the next column of balls by cycling from Step 2–4 until the X-coordinate exceeds  $d_4$ .

### 3.3. Coordinate Systems' Conversion

By the proposed algorithm, the various triangle areas within the particle images could be filled with uniformly-arranged balls successfully. However, when combining all of the triangles to form the whole virtual particle, it is necessary to calibrate the coordinate value from the local coordinate system to the global one. The relationships between the two coordinate systems are shown in Figure 4. The X- and Y-coordinate of each filled ball should be adjusted based on Equation (7).

$$\begin{aligned} x &= x' \times \cos b + y' \times \sin b \\ y &= -x' \times \sin b + y' \times \cos b \end{aligned} \quad (7)$$

where  $x'$  and  $y'$  are the X-, Y-coordinates in the local coordinate system of the triangles, respectively;  $x$  and  $y$  are the X-, Y-coordinates in the global coordinate system of the particles, respectively;  $b$  is the angle between the bottom side of the triangle ( $S_1$ ) and the X-axis.

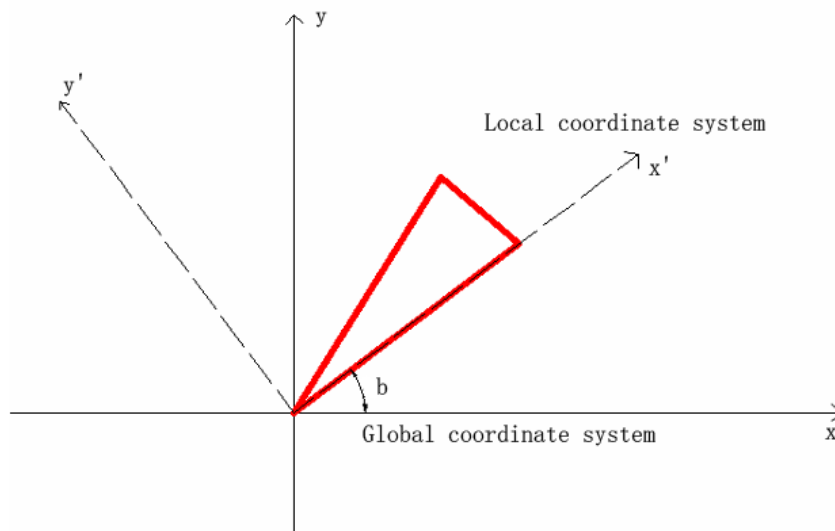


**Figure 4.** Conversions between local and global coordinate systems.

It is noted that two different coordinate systems were used in the modeling process. The local coordinate values represented the relative positions of balls in the virtual particles, while the global coordinate values represented relative positions of balls in the virtual container. When developing the single particle, the local coordinate systems were utilized to fill the irregular area with arranged balls. After that, the positions of all the virtual particles were converted to the global one so that the numerous virtual particles could be distributed within the designed area to form the whole mixtures. After the coordinates were calibrated, the virtual particles could be rebuilt as shown in Figure 5. As shown, the inner area of the virtual particles was filled with balls gradually after each triangle area was processed based on the proposed algorithm. However, although the irregular shapes of the particles were divided into several triangles, the side of  $S_3$  (Figure 3) could only match the actual shape contour similarly. The shape modeling was not precise enough. Therefore, further improvements were made by modeling the shape contour firstly and then filling the inner area of the shape contour with balls by the former algorithm, as shown in Figure 5. The shape contour in Figure 1b was processed by a user-defined routine to read and store the pixel locations of the images. The black pixels were distinguished. Then, a threshold value of 0.005 was selected to filter the redundant black pixels such that the adjacent black pixels within a distance of 0.005 could be ignored and the others retained. By importing the locations of the retained pixels into PFC2D, the balls could be generated in the shape contour, as shown in Figure 5. Then, the whole particle was filled with balls by triangle area filling in the end. Based on the scanning images and with the help of the proposed algorithm, aggregate particles varying in size and shape were reconstructed as shown in Figure 6.



**Figure 5.** Procedure of the virtual particles' modeling.

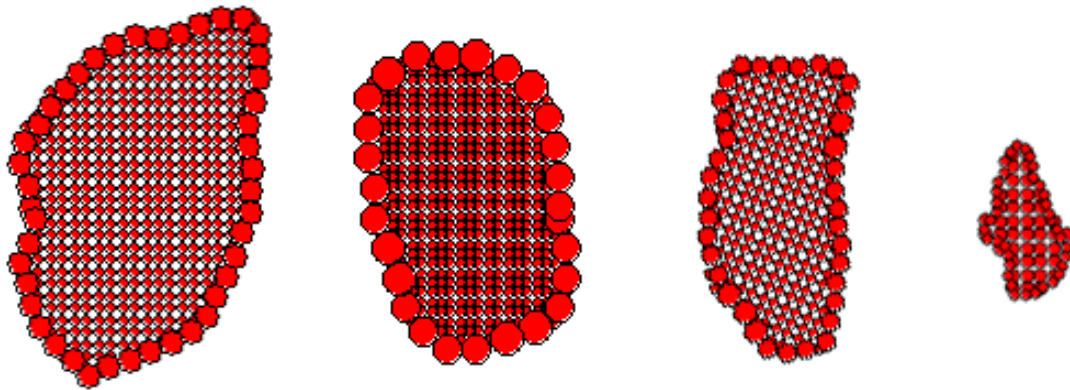


Figure 6. Various virtual particles of different morphological characteristics.

#### 4. Algorithm for Developing Virtual Specimens

##### 4.1. Mapping Area Calculation for Two-Dimensional Specimens

When it comes to the virtual aggregate specimens, several assumptions were made before the simulations as follows:

- ① The differences of the densities among particles were not obvious, so the same density value of  $\rho_1$  can be assigned to all the virtual particles in the simulations;
- ② The virtual specimens consist of particles and voids only without any water.

The virtual specimen of SMA-13 in the penetration test was then developed, and the gradations of SMA-13 are shown in Table 3. To improve the simulation efficiency, only the coarse aggregates were developed despite the fine particles.

Table 3. Gradation for SMA-13.

Gradation	Passing Ratio (%) for Different Sieving Sizes (mm)									
	16	13.2	9.5	4.75	2.36	1.18	0.6	0.3	0.15	0.075
SMA-13	100	95	79.5	48.9	36.7	25.8	16.7	9.7	7.1	6.5

The particle numbers of different grades in the two-dimensional simulation were determined based on the mapping area, as the following equations shown:

$$M = \rho \times \frac{\pi \times D^2}{4} \times h \tag{8}$$

where  $M$  is the total mass of the specimen in three dimensions, g;  $\rho$  is the density of the specimen, g/cm<sup>3</sup>;  $D$  is the diameter of the specimen, cm;  $h$  is the height of the specimen, cm.

When it comes to the two-dimensional specimen, the mass can be converted as follows:

$$m = \frac{M}{V} \times S = \frac{V \times \rho}{V} \times D \times h = Dh\rho \tag{9}$$

where  $m$  is the converted mass of the specimen in two dimensions, g;  $V$  is the total volume of the specimen in three dimensions, cm<sup>3</sup>;  $S$  is the area of the specimen in two dimensions, cm<sup>2</sup>; the others are the same as the former.

Thus, the required area for generating the total virtual particles could be calculated based on Equation (10).

$$S_{total} = \frac{m}{\rho_1} = \frac{Dh\rho}{\rho_1} \tag{10}$$

where  $S_{total}$  is the required area for generating the total virtual particles,  $cm^2$ ;  $\rho_1$  is the density of all the coarse aggregates, which was assumed to be the same value in the simulations,  $g/cm^3$ ; the others are the same as the former.

Based on the assumption that there is no water within the specimen, the following relation can be given:

$$\rho = \frac{\rho_1 \times V \times (1 - K)}{V} = \rho_1 \times (1 - K) \quad (11)$$

where  $K$  is the void content of the total specimen in three dimensions, %; the others are the same as the former.

The mapping area of different grades of particles can be developed in the end as follows:

$$S_{total} = Dh \times (1 - K) \quad (12)$$

$$S_i = S_{total} \times P_i = Dh \times (1 - K) \times P_i \quad i = 4.75, 9.5, 13.2, 16$$

where  $S_{4.75}$ ,  $S_{9.5}$ ,  $S_{13.2}$ ,  $S_{16}$  are the mapping areas of the 4.75-, 9.5-, 13.2-, 16-mm virtual particles, respectively,  $cm^2$ ;  $P_{4.75}$ ,  $P_{9.5}$ ,  $P_{13.2}$ ,  $P_{16}$  are the proportions of the 4.75-, 9.5-, 13.2-, 16-mm virtual particles to the total mass, respectively; the others are the same as the former.

#### 4.2. Generation Process for Virtual Particles with Random Shapes and Sizes

To distribute the virtual particles randomly within the specimen, two parameters ( $\mu_1$  and  $\mu_2$ ) were given to control the generation process better. When generating the next particle,  $\mu_1$  represented the probability of the size, while  $\mu_2$  determined its angular shape. Two random values drawn from the uniform distribution (0, 1) were assigned to  $\mu_1$  and  $\mu_2$  at first. Based on  $\mu_1$  and  $\mu_2$  at the current calculation step, a specific size and shape could be determined. For example, before generating the next virtual particle,  $\mu_1$  would be checked within PFC2D as follows.

- ① If  $\mu_1 \leq \frac{S_{4.75}}{S_{total}}$ , only 4.75-mm particles would be generated;
- ② If  $\frac{S_{4.75}}{S_{total}} < \mu_1 \leq \frac{S_{4.75}+S_{9.5}}{S_{total}}$ , only 9.5-mm particles would be generated;
- ③ If  $\frac{S_{4.75}+S_{9.5}}{S_{total}} < \mu_1 \leq \frac{S_{4.75}+S_{9.5}+S_{13.2}}{S_{total}}$ , only 13.2-mm particles would be generated;
- ④ If  $\frac{S_{4.75}+S_{9.5}+S_{13.2}}{S_{total}} < \mu_1 \leq \frac{S_{4.75}+S_{9.5}+S_{13.2}+S_{16}}{S_{total}}$ , only 16-mm particles would be generated;

After the particle size was determined,  $\mu_2$  would be checked to develop the various angular shapes of the particles based on the angularity index distribution, as shown in Figure 7. For example, for the 4.75-mm particles, the process was conducted as following.

- ① If  $0\% < \mu_2 \leq 6.07\%$ , only 4.75-mm particles with the angularity index ranging from 1500–2000 would be generated;
- ② If  $6.07\% < \mu_2 \leq 21.22\%$ , only 4.75-mm particles with the angularity index ranging from 2000–2500 would be generated;
- ③ If  $21.22\% < \mu_2 \leq 63.64\%$ , only 4.75-mm particles with the angularity index ranging from 2500–3000 would be generated;
- ④ If  $63.64\% < \mu_2 \leq 84.85\%$ , only 4.75-mm particles with the angularity index ranging from 3000–3500 would be generated;
- ⑤ If  $84.85\% < \mu_2 \leq 90.91\%$ , only 4.75-mm particles with the angularity index ranging from 3500–4000 would be generated;
- ⑥ If  $90.91\% < \mu_2 \leq 100\%$ , only 4.75-mm particles with the angularity index ranging from 4000–4500 would be generated;

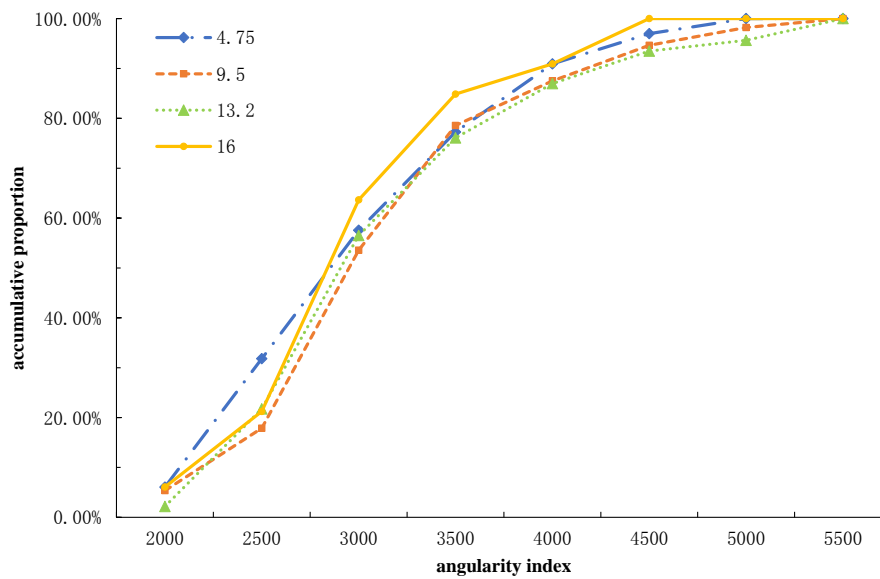


Figure 7. Angularity index distribution of different sizes of particles.

Enough particles were scanned and rebuilt within PFC2D. Thus, when  $\mu_2$  was checked and the angularity index range was determined, corresponding virtual particles with the required shape would be generated by the user-defined routine. By the control of  $\mu_1$  and  $\mu_2$ , the virtual specimen could be developed with random particles obviously.

#### 4.3. Example of Generating a Virtual Specimen

$D$ ,  $h$  and  $K$  were set as 15 cm, 12 cm and 35% during the modeling process, which was in accordance with the laboratory tests. The calculated mapping area is an important parameter to control the particles' generation. The virtual aggregates were generated three times when forming the numerical models, as shown in Figure 8. When simulated, only one third of the mapping area was taken to determine the required number of different grades of aggregates. The virtual particles were generated one by one above the container and then fell down under gravity. Each time the generation completed, the specimen would be compacted by a virtual wall developed within PFC2D. The compacted wall would move downwards until reaching the designed height so as to achieving the required void content. By three cyclical steps, the virtual specimen could be developed as shown in Figure 8.

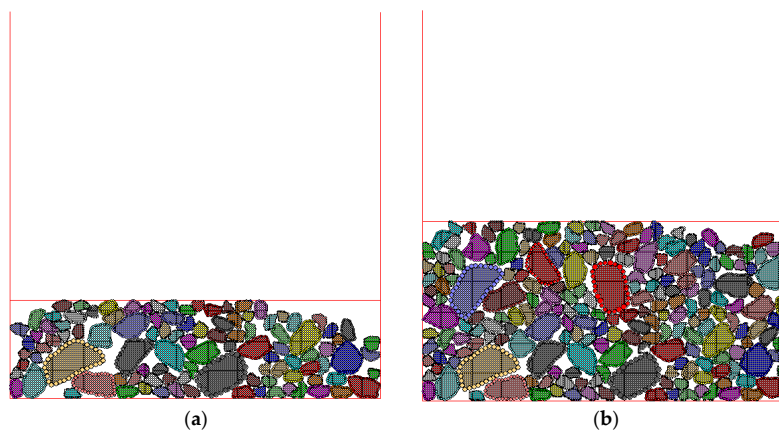
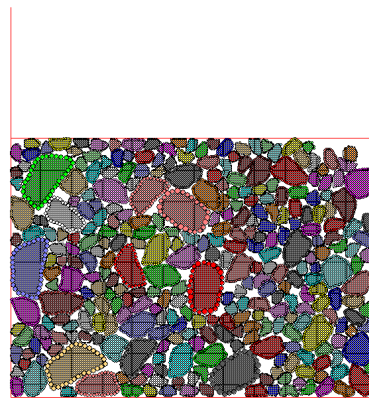


Figure 8. Cont.





(c)

**Figure 8.** Modeling procedure of the virtual specimens: (a) first step of generation; (b) second step of generation; (c) third step of generation.

The generation routine of each grade of aggregate would be carried out until the total area of the generated particles exceeded the requirements. After the modeling completed, the total area of generated particles with different sizes was measured within PFC2D, as shown in Table 4. As shown, the generated virtual specimen was in good accordance with the actual gradations. The error was 5.51%, 3.86% and 3.70% for the 13.2-, 9.5- and 4.75-mm coarse aggregates, respectively. The error was attributed to the last generated particles, which exceeded the required mapping area, and it can be ignored. Thus, it is concluded that the proposed algorithm can well characterize the composition features of the aggregate specimen with precise particle shape reconstitutions and consistent gradation modeling.

**Table 4.** Summaries of the virtual modeling.

Sieving size (mm)	13.2	9.5	4.75
Required mapping area (cm <sup>2</sup> )	11.44	35.21	70.06
Total area of generated particles (cm <sup>2</sup> )	12.07	36.57	72.65
Error (%)	5.51	3.86	3.70

## 5. Performance Prediction of the Rebuilt Models

### 5.1. Experiments

The penetration test using a Universal Testing Machine (UTM: Fuel Instruments & Engineers Pvt. Ltd. Maharashtra, India) was designed to measure the penetration force with the rod depth based on the Chinese test standard (JTG E40-2007: T0134-1993) [36]. A cylinder container with a diameter of 150 mm and a height of 120 mm was adopted during the tests. Then, three specimens with only the particles of 4.5, 9.5 and 13.2 mm were developed and were compacted based on the Chinese test standard (JTG E40-2007: T0131-2007) [36]. When conducting the penetration test, a rod would penetrate into the specimens slowly at a speed of 1.27 mm/min. Then, the force-displacement curves were recorded by the detectors.

To help the reconstitution of the virtual specimens, several data should also be measured before or after the laboratory tests, including the particle density, the density and the void contents of the compacted specimens, as shown in Table 5. The particle density is an input variable in DEM simulations to model the entities' total mass, while the density and void contents of the compacted specimens were utilized to calculate the mapping area of coarse aggregates according to the proposed algorithm. The measurements for the particle density, the density and void contents of the compacted



specimens were carried out based on the Chinese test standard, respectively (JTG E42-2005: T0308-2005, T0309-2005) [37].

**Table 5.** Materials for laboratory penetration tests.

Sieving Size (mm)	Particle Density (g/cm <sup>3</sup> )	Density of Compacted Specimen (g/cm <sup>3</sup> )	Void Contents of Compacted Specimens (%)
13.2	2.744	1.625	39.55
9.5	2.730	1.616	39.66
4.75	2.729	1.594	40.70

### 5.2. Simulations for Performance Prediction

Prior to simulations, several micromechanical models were adopted to characterize the contact behavior between coarse aggregates within PFC2D; including the contact-stiffness model and sliding model [38], as the following equation shows.

Contact-stiffness model:

$$\begin{aligned} F_i^n &= K^n U^n \\ \Delta F_i^s &= -k^s \Delta U^s \end{aligned} \tag{13}$$

where  $F_i^n$  is the normal force at the  $i$ -th contact point;  $\Delta F_i^s$  is the shear contact force increment at the  $i$ -th contact point;  $K^n$  is the normal stiffness at the contact;  $k^s$  is the shear stiffness at the contact;  $U^n$  is the overlap of the two contact entities along the normal direction;  $\Delta U^s$  is the overlap of the two contact entities along the shear direction.

Sliding model:

$$F_{max}^s = \mu |F_i^n| \tag{14}$$

where  $F_{max}^s$  is the maximum allowable shear contact force;  $F_i^n$  is the normal contact force between two entities;  $\mu$  is the friction coefficient in PFC2D.

As shown in Equations (13) and (14), the contact force between two entities (balls) in the normal/shear direction was determined by the contact normal/shear stiffness and their overlap in corresponding directions. As for the normal contact force, the formula is always effective in the simulation, such that the intensity of  $F_i^n$  depends on the value of  $K^n$  and  $U^n$  directly. However, the shear contact force was controlled and calculated based on two different modes for different periods. At the beginning, the shear contact force increment depends on  $k^s$  and  $\Delta U^s$ , when the adjacent entities contact each other. As the accumulative shear force reaches the limiting condition, as shown in Equation (14), the calculation process is converted immediately, in which the intensity of the shear contact force (not the shear force increment) is determined by the friction coefficient and absolute value of the normal contact force currently. As shown, it is significantly important to determine the values of  $K^n$  and  $k^s$  for modeling the micro-contact process in the simulation. According to the PFC2D manual, these two key micro-parameters are calculated by the input value of the balls' normal stiffness  $k_n$  and shear stiffness  $k_s$ , respectively. The appropriate values of  $k_n$  and  $k_s$  can be obtained through a calibration process during the simulation based on the laboratory results. When calibrating the micro-parameters, the size influences should be taken into consideration. This means that the micro-parameters differed from each other for different sizes of particles and should be determined based on the size, respectively.

Thus, the simulations were conducted in two steps. In the first step, the virtual penetration tests of three different compositions were simulated. The three virtual specimens were developed by the proposed algorithm with 4.75-, 9.5- and 13.2-mm particles only, respectively. Then, the calibrated process for the best micro-parameters was done as follows: (1) conduct the laboratory penetration test to get the actual force-displacement curve of the three specimens; (2) conduct the simulations to get the virtual force-displacement curve of the three specimens; (3) obtain the best group of micro-parameters by adjusting their values continuously until the force-displacement curve of the simulation is close to the actual result. By the former process, the calibrated parameters can be obtained as shown in Table 6.

**Table 6.** Calibrated micro-parameters for balls and walls within Particle Flow Code in Two Dimensions (PFC2D).

	Size/mm	$k_n$	$k_s$	$\mu$
ball	4.75	2.2e6	1.5e6	0.6
	9.5	2.5e6	2.5e6	0.55
	13.2	1.2e6	1.2e6	0.5
wall		1e10	1e10	0.6

In the second step, the performance prediction of the SMA13 aggregate skeleton was done by the virtual penetration test. Moreover, the validation of the proposed algorithm was verified by comparing the prediction results with the actual ones. The virtual aggregate skeleton of SMA13 was formed and tested with the rod moving downward at a speed of 1.27 mm/min. Each particle was assigned the best micro-parameters based on Table 6. The prediction results and the actual force-displacement curve are illustrated in Figure 9. Since assumptions were made that there was no breakage or fraction during modeling, only 10-mm penetration depths were simulated. When the depth was less than 10 mm, there was no obvious breakage of the particles in laboratory tests, which can be used for nonlinear mechanical behavior predictions. It is obviously seen that the developed virtual models indeed have a good agreement with the results of the laboratory tests. The proposed algorithm was validated, which can not only model the aggregate shape precisely, but also characterize its mechanical performance well with the calibrated micro-parameters.

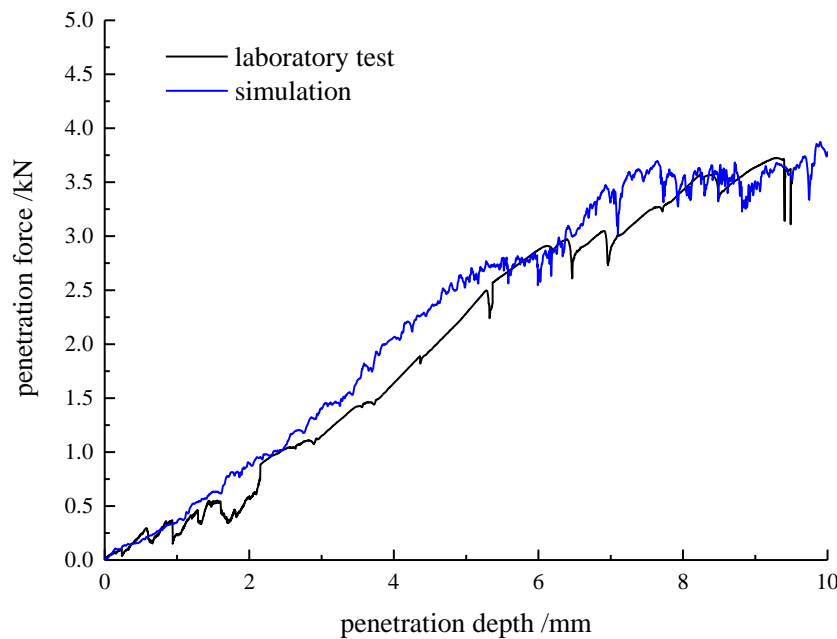


**Figure 9.** Prediction results of SMA-13.

## 6. Conclusions

This paper proposed an algorithm for the reconstitution of the virtual aggregates and specimens based on the DEM methods. By the triangle area's division, the irregular shape of the coarse aggregates can be formed well, and their mechanical performance was validated through the designed simulations. The main conclusions drawn from the study are as follows:

- (1) The scanning images from the AIMS are significant and guarantee the precise modelling of the coarse aggregates. The realistic shapes of the aggregates were captured and quantified through

the inner software within AIMS. By generating the balls in the shape contours and then filling the inner area with balls by the proposed triangle-dividing algorithm, the virtual particles could be rebuilt, which had the same shapes as the realistic ones;

- (2) The mapping area was calculated to convert the three-dimensional volume to a two-dimensional area. Two random variables drawn from the uniform distribution (0, 1) were utilized to control the particles' generation randomly. It was shown that the developed virtual specimen had a good accordance with the required gradations with minor errors of 5.51%, 3.86% and 3.70% for the 13.2-, 9.5- and 4.75-mm coarse aggregates, respectively. Thus, not only the particle shape, but also the heterogeneous composition within the structures could be modelled accurately;
- (3) Based on the calibrated micro-parameters, the mechanical performance of the aggregate skeleton could be well predicted through the proposed algorithm, which was verified by the virtual penetration test of the coarse aggregate skeleton with the SMA-13 gradation.

**Author Contributions:** D.W. and T.M. conceived and designed the experiments; X.D. performed the numerical experiments; W.Z. performed the laboratory experiments; D.Z. contributed analysis tools; D.W. and X.D. wrote the paper.

**Acknowledgments:** The study was financially supported by the Science Foundations of Nanjing Institute of Technology, China (YKJ201423), the National Natural Science Foundation of China (No. 51378006) and the Natural Science Foundation of Jiangsu Province, China (BK20161421).

**Conflicts of Interest:** The authors declare no conflict of interest.

## References

1. Pan, T.; Tutumluer, E.; Carpenter, S.H. Effect of Coarse Aggregate Morphology on Permanent Deformation Behavior of Hot Mix Asphalt. *J. Transp. Eng.* **2015**, *132*, 580–589. [CrossRef]
2. Ramli, I. *Effect of Fine Aggregate Angularity on Rutting Resistance of Asphalt Concrete AC10*; Universiti Teknologi Malaysia: Iskandar Puteri, Malaysia, 2013.
3. Shah, S.M.R.; Abdullah, M.E. Effect of Aggregate Shape on Skid Resistance of Compacted Hot Mix Asphalt (HMA). In Proceedings of the 2010 the 2nd International Conference on Computer and Network Technology (ICCNT), Bangkok, Thailand, 23–25 April 2010; IEEE: Piscataway, NJ, USA, 2010; pp. 421–425.
4. Campen, W.H.; Smith, J.R. A study of the role of angular aggregates in the development of stability in bituminous mixtures. *Proc. AAPT* **1948**, *17*, 114–143.
5. Kandhal, P.S.; Parker, F. *Aggregate Tests Related to Asphalt Concrete Performance in Pavements*; National Cooperative Highway Research Program Report 405; Transportation Research Board: Washington, DC, USA, 1998.
6. Cheung, L.W.; Dawson, A. Effects of particle and mix characteristics on performance of some granular materials. *Transp. Res. Rec. J. Transp. Res. Board* **2002**, *1787*, 90–98. [CrossRef]
7. Hossain, M.; Parker, F., Jr.; Kandhal, P. Tests for evaluating fine aggregate particle shape, angularity, and surface texture. *Transp. Res. Rec. J. Transp. Res. Board* **1999**, *1673*, 64–72. [CrossRef]
8. Hossain, M.S.; Parker, F.; Kandhal, P.S. Comparison and evaluation of tests for coarse aggregate particle shape, angularity, and surface texture. *J. Test. Eval.* **2000**, *28*, 77–87.
9. Cundall, P.A. *Ball-A Program to Model Granular Media Using the Distinct Element Method*; Technical Note; Advanced Technology Group, Dames & Moore: London, UK, 1978.
10. Ma, T.; Wang, H.; Zhang, D.; Zhang, Y. Heterogeneity effect of mechanical property on creep behavior of asphalt mixture based on micromechanical modeling and virtual creep test. *Mech. Mater.* **2017**, *104*, 49–59. [CrossRef]
11. Mishra, B.K.; Rajamani, R.K. The discrete element method for the simulation of ball mills. *Appl. Math. Model.* **1992**, *16*, 598–604. [CrossRef]
12. Su, O.; Akcin, N.A. Numerical simulation of rock cutting using the discrete element method. *Int. J. Rock Mech. Min. Sci.* **2011**, *48*, 434–442. [CrossRef]
13. Lu, M.; McDowell, G.R. The importance of modelling ballast particle shape in the discrete element method. *Granul. Matter* **2007**, *9*, 69. [CrossRef]

14. Das, N.; Thomas, S.; Kopmann, J.; Donovan, C.; Hurt, C.; Daouadji, A.; Ashmawy, A.K.; Sukumaran, B. Modeling Granular Particle Shape Using Discrete Element Method. *Mon. Not. R. Astron. Soc.* **2008**, *420*, 3368–3380.
15. Coetzee, C.J. Calibration of the discrete element method and the effect of particle shape. *Powder Technol.* **2016**, *297*, 50–70. [CrossRef]
16. Zhang, D.; Huang, X.; Zhao, Y. Algorithms for generating three-dimensional aggregates and asphalt mixture samples by the discrete-element method. *J. Comput. Civ. Eng.* **2012**, *27*, 111–117. [CrossRef]
17. Stahl, M.; Konietzky, H. Discrete element simulation of ballast and gravel under special consideration of grain-shape, grain-size and relative density. *Granul. Matter* **2011**, *13*, 417–428. [CrossRef]
18. Huang, H. Discrete Element Modeling of Railroad Ballast Using Imaging Based Aggregate Morphology Characterization. Ph.D. Thesis, University of Illinois at Urbana-Champaign, Urbana, IL, USA, 2010.
19. Liu, Y.; You, Z. Visualization and simulation of asphalt concrete with randomly generated three-dimensional models. *J. Comput. Civ. Eng.* **2009**, *23*, 340–347. [CrossRef]
20. Liu, Y.; You, Z. Accelerated Discrete-Element Modeling of Asphalt-Based Materials with the Frequency-Temperature Superposition Principle. *J. Eng. Mech.* **2011**, *137*, 355–365. [CrossRef]
21. Tutumluer, E.; Qian, Y.; Hashash, Y.M.A.; Davis, D. Field validated discrete element model for railroad ballast. In Proceedings of the Annual Conference of the American Railway Engineering and Maintenance-of-Way Association, Minneapolis, MN, USA, 18–21 September 2011; pp. 18–21.
22. Dondi, G.; Simone, A.; Vignali, V.; Manganelli, G. Numerical and experimental study of granular mixes for asphalts. *Powder Technol.* **2012**, *232*, 31–40. [CrossRef]
23. Dondi, G.; Simone, A.; Vignali, V.; Manganelli, G. Discrete Element Modelling of Influences of Grain Shape and Angularity on Performance of Granular Mixes for Asphalts. *Procedia Soc. Behav. Sci.* **2012**, *53*, 399–409. [CrossRef]
24. Vignali, V. Discrete particle element analysis of aggregate interaction in granular mixes for asphalt: Combined DEM and experimental study. In *7th Rilem International Conference on Cracking in Pavements*; Springer: Berlin, Germany, 2012; pp. 389–398.
25. Fu, Y.; Wang, L.; Tumay, M.T.; Li, Q. Quantification and simulation of particle kinematics and local strains in granular materials using X-ray tomography imaging and discrete-element method. *J. Eng. Mech.* **2008**, *134*, 143–154. [CrossRef]
26. Moreno-Atanasio, R.; Williams, R.A.; Jia, X. Combining X-ray microtomography with computer simulation for analysis of granular and porous materials. *Particuology* **2010**, *8*, 81–99. [CrossRef]
27. Wang, L.; Park, J.Y.; Fu, Y. Representation of real particles for DEM simulation using X-ray tomography. *Constr. Build. Mater.* **2007**, *21*, 338–346. [CrossRef]
28. Hall, S.A.; Bornert, M.; Desrues, J.; Pannier, Y.; Lenoir, N.; Viggiani, G.; Bésuelle, P. Discrete and continuum analysis of localised deformation in sand using X-ray  $\mu$ CT and volumetric digital image correlation. *Géotechnique* **2010**, *60*, 315–322. [CrossRef]
29. Alshibli, K.A.; Reed, A.H. Comparison of X-Ray CT and Discrete Element Method in the Evaluation of Tunnel Face Failure. In *Advances in Computed Tomography for Geomaterials: GeoX 2010*; John Wiley & Sons Inc.: Hoboken, NJ, USA, 2013; pp. 397–405.
30. Liu, Y.; Zhou, X.; You, Z.; Yao, S.; Gong, F.; Wang, H. Discrete element modeling of realistic particle shapes in stone-based mixtures through MATLAB-based imaging process. *Constr. Build. Mater.* **2017**, *143*, 169–178. [CrossRef]
31. Liu, Y.; You, Z.; Zhao, Y. Three-dimensional discrete element modeling of asphalt concrete: Size effects of elements. *Constr. Build. Mater.* **2012**, *37*, 775–782. [CrossRef]
32. Gates, L.L. Experimental Evaluation of New Generation Aggregate Image Measurement System. *Ann. Emerg. Med.* **2010**, *33*, 611.
33. Araujo, V.M.C.; Bessa, I.S.; Branco, V.T.F.C. Measuring skid resistance of hot mix asphalt using the aggregate image measurement system (AIMS). *Constr. Build. Mater.* **2015**, *98*, 476–481. [CrossRef]
34. Rezaei, A.; Hoyt, D.; Martin, A.E. Simple Laboratory Method for Measuring Pavement Macrottexture Pavement Cores and Aggregate Image Measurement System. *Transp. Res. Rec. J. Transp. Res. Board* **2011**, *2227*, 146–152. [CrossRef]
35. Luce, A.D. *Analysis of Aggregate Imaging System (AIMS) Measurements and Their Relationship to Asphalt Pavement Skid Resistance*; Texas A & M. University: College Station, TX, USA, 2009.

36. Ministry of Transport of the People's Republic of China. *Test. Methods of Soils for Highway Engineering*; JTG E40-2007; China Communications Press: Beijing, China, 2007.
37. Ministry of Transport of the People's Republic of China. *Test. Methods of Aggregates for Highway Engineering*; JTG E42-2005; China Communications Press: Beijing, China, 2005.
38. Itasca Consulting Group. *PFC 2D Version 4.0*; Itasca Consulting Group: Minneapolis, MN, USA, 2004.



© 2018 by the authors. Licensee MDPI, Basel, Switzerland. This article is an open access article distributed under the terms and conditions of the Creative Commons Attribution (CC BY) license (<http://creativecommons.org/licenses/by/4.0/>).

Article

# Fatigue Resistance Evaluation of Modified Asphalt Using a Multiple Stress Creep and Recovery (MSCR) Test

Weiguang Zhang <sup>1</sup>, Tao Ma <sup>1,\*</sup>, Gang Xu <sup>1</sup>, Xiaoming Huang <sup>1</sup>, Meng Ling <sup>2</sup>, Xiao Chen <sup>3</sup> and Jiayue Xue <sup>3</sup>

<sup>1</sup> School of Transportation, Southeast University, Nanjing 211189, China; wgzhang@seu.edu.cn (W.Z.); xugang619@hotmail.com (G.X.); huangxm@seu.edu.cn (X.H.)

<sup>2</sup> Texas A&M Transportation Institute, College Station, TX 77843, USA; mengling@tamu.edu

<sup>3</sup> School of Transportation, Southeast University, Nanjing 211189, China; xche0051@163.com (X.C.); xuejiayue\_seu@163.com (J.X.)

\* Correspondence: matao@seu.edu.cn

Received: 23 January 2018; Accepted: 1 March 2018; Published: 12 March 2018

**Abstract:** Fatigue resistance quantification of modified asphalt is typically time consuming and may not correlate well with mixture fatigue test results. In this paper, the applicability of a multiple stress creep and recovery (MSCR) test on asphalt binder's fatigue resistance was evaluated. Six binder types with a variety of modifiers and different modifier contents were characterized. The MSCR test was conducted and its sensitivity to binder type and additive content under different aging durations was evaluated. Mixture fatigue tests including a semi-circular bending- Illinois flexibility index test and indirect tensile strength were conducted using control base asphalt and SBS modified asphalt. A ranking between the binder MSCR and mixture fracture test results was conducted to check if the MSCR result was representative of the mixture's fatigue resistance. Results indicate that the MSCR test at intermediate temperatures (20 °C, 25 °C, and 30 °C) can be performed with good repetitions. It was also found that the MSCR test was sensitive enough to differentiate the fatigue resistance among different binder types and additive contents. The ranking analysis shows that the binder MSCR test at intermediate temperatures showed a similar ranking to the mixture's fatigue tests, indicating that the binder MSCR test could be potentially utilized to represent a mixture's fatigue resistance where binder selection is a major concern. It was also found that the SBS modified binder showed the best crack resistance and was less affected by aging.

**Keywords:** modified asphalt; fatigue resistance; MSCR; intermediate temperature

## 1. Introduction

$G^* \sin \delta$  was developed as a fatigue cracking parameter during the Strategic Highway Research Program (SHRP) for asphalt pavement. Complex shear modulus ( $G^*$ ) is defined as the absolute value of peak shear stress divided by the absolute value of peak shear strain, whereas phase angle ( $\delta$ ) is defined as the lag between strain and stress peak values due to the viscoelastic property of asphalt. The  $G^* \sin \delta$  was proposed to limit the magnitude of  $G^*$  and  $\delta$  to select relative soft asphalt with a high elasticity, and thus to improve the fatigue resistance of asphalt binder. Based on unmodified binder, Anderson et al. [1] found that the  $G^* \sin \delta$  was able to differentiate various asphalt types and contents in resisting fatigue damage in a linear viscoelastic range.

With the increased usage of asphalt modifications (i.e., polymer, warm mix asphalt), researchers started to realize that  $G^* \sin \delta$  cannot successfully be utilized in fatigue characterization, as  $G^* \sin \delta$  has little relation to asphalt mixture fatigue testing results [2,3]. The possible reasons that

caused such discrepancies include: (1) most responses of modified asphalt binder were non-linear, and it was not reasonable to use linear parameters to characterize a non-linear response; (2) one of the assumptions of  $G^*\sin \delta$  was that all the asphalt binders share the same sensitivity to loading rate and testing temperature, whereas this assumption was not applicable to the modified binders [3]; and (3)  $G^*\sin \delta$  was tested at a low strain level with a fixed frequency and no damage was introduced during the test, whereas field traffic was much more complicated and with a higher level of damage severity. Higher strain in asphalt binder may induce significant amounts of viscous flow or yielding, as well as micro-cracking and macrocracking in areas of a high-stress concentration [4].

Both fatigue test and fracture tests were developed to address the above issues. A repeated loading test was used to better simulate the field traffic load, which generates accumulated damage, including the time sweeping test [3], linear amplitude sweep test [5], and dynamic mechanical analyzer test [6]. The fracture test can introduce damage with a high efficiency and is very time efficient. The major fracture tests consist of ductility, crack tip opening displacement, and the monotonic test.

Recently, the multiple stress creep recovery (MSCR) test was applied to quantify the fatigue since the MSCR recovery can be potentially used to evaluate the delayed elastic response of asphalt binder [7]. The MSCR test does not impose the assumption that the material behavior is linear viscoelastic [8]. The test is also sensitive to different binder types at elevated temperatures (i.e., 50 °C or higher). It was found that the MSCR test was able to distinguish modified binders from un-modified binders [9]. The current study using the MSCR on fatigue resistance evaluation was majorly based on correlating MSCR results at a high performance grade (PG) temperature to asphalt fracture test results [7].

In summary, multiple parameters were proposed to quantify the fatigue resistance of both modified and un-modified asphalt to address the limitations of the  $G^*\sin \delta$ . The MSCR test, considering its wide application, is practical to investigate whether it is applicable to evaluate the fatigue performance of modified and unmodified asphalt binders. The current study using MSCR as part of a fatigue study was limited to high testing temperatures, and its correlation with mixture property was not well explored. The research objectives of this study were to (a) examine if the MSCR test was able to distinguish different binder types and additive contents at intermediate temperatures; and (b) evaluate if the MSCR test at intermediate temperatures could correlate well with the fatigue performance of the asphalt mixture. This paper will provide useful information for further implementation of the MSCR test on fatigue evaluations of asphalt pavement.

## 2. Methodology and Scope

Both modified and un-modified binders, including base binder, Styreneic Block Copolymers (SBS) modified binder, rubber modified binder, and warm mix binders (Sasobit, Evotherm M1 and Evotherm 3G), were included. The contents of Sasobit and rubber were 1%, 2%, and 3%, and 5%, 10%, and 15% by weight of asphalt binder, respectively. The ratios of SBS, Evotherm M1m and Evotherm 3G were 4.5%, 0.6%, and 0.6% by weight of asphalt binder, respectively. The aggregate consisting of three stockpiles with basalt was used as the major aggregate source. To better control aggregate gradation, three aggregate stockpiles were further sieved in a laboratory based on each individual sieve size. Mix design was validated in the laboratory to determine the optimum asphalt content using the Superpave method.

Several fatigue tests for both asphalt binders and asphalt mixtures were conducted, consisting of binder MSCR, a mixture semi-circular bending- Illinois flexibility index test (SCB-IFIT), and a mixture indirect tensile test (IDT). Other binder testing, including performance grading, viscosity, and binder monotonic fracture tests were also performed as the reference. Table 1 shows a summary of the all the laboratory mixture and binder tests included in this paper.

**Table 1.** Summary of Laboratory Testing.

Testing	MSCR, Binder	Performance Grading, Binder	Viscosity, Binder	Monotonic Fracture, Binder	SCB, Mixture	IDT, Mixture
Conditions	20, 25, 30 °C	−24 to 100 °C	65, 135 °C	20, 25, 30 °C	30 °C, 50 mm/min	30 °C, 50 mm/min
Parameter	$R_{3,2}$	°C	Viscosity	Fracture Energy	IFIT	Strength, work density
References/standards	AASHTO TP70/M322	AASHTO MP1/M322	AASHTO T316	[7]	[10]	AASHTO T322

The sensitivity of the MSCR test to the binder type and additive content was evaluated. The binder with the best fatigue resistance and the control base asphalt were further chosen to conduct the asphalt mixture fracture test. A ranking between the MSCR test and mixture fatigue test was further compared to evaluate if the MSCR test was well correlated with mixture performance. Short- and long-term aging were applied on both binders and mixtures to address the effect of aging. For all the asphalt binder and mixture tests, three repetitions were used, except for the bending beam rheometer (BBR) test, which includes two test replicates as specified in the AASHTO specification.

### 3. Data Collection

The asphalt binder and aggregate were collected from a local contractor in Nanjing, China. A PG 76-22 binder (without modification) was utilized as the base asphalt. The basalt used is the dominating aggregate type in Jiangsu, China. Basalt is grey to black in color, but rapidly weathers to brown or rust-red due to oxidation of its iron-rich minerals. It has very good characteristics in terms of soundness and abrasion resistance, whereas the major concern is the weak bonding between asphalt and aggregate due to the smooth surfaces of basalt aggregate. Anti-stripping was included to avoid the potential moisture damage.

Mix design was performed in the laboratory to determine the optimum asphalt content based on the Superpave method. A typical local mix with a nominal maximum aggregate size (NMAS) of 13.2 mm was used. Table 2 shows the aggregate gradation and the mix design.

**Table 2.** Aggregate Gradation and Mix Design Parameters.

Aggregate Gradation		Mix Design	
Sieve Size, mm	Percentage Passing, %	Parameter	Value
16.0	100.0	$G_{sb}$	2.854
13.2	94.7	VMA	13.3%
9.5	76.2	VFA	69.8%
4.75	45.7	AC	5.0%
2.36	29.7	$G_{mm}$	2.706
1.18	24.2	$V_{be}$	10.0%
0.6	18.4	$N_{des}$	126 gyrations
0.3	12.7	-	-
0.15	8.7	-	-
0.075	6.1	-	-

Note:  $G_{sb}$ : aggregate bulk specific gravity. VMA: voids in mineral aggregate. VFA: voids filled with asphalt. AC: asphalt content.  $G_{mm}$ : theoretical maximum specific gravity.  $V_{be}$ : volume of effective asphalt.  $N_{des}$ : determined based on 30–100 million design Equivalent Single Axle Load (ESAL).

#### 3.1. Binder and Mixture Aging Test

The asphalt binders were aged by a Thin-Film Oven Test (TFOT) to simulate short-term field aging according to AASHTO T179. The TFOT aged binders were further aged by Pressure Aging Vessel (PAV) to simulate long-term field aging based on AASHTO R28.

Regarding the asphalt mixtures, the short-term aging was conducted by placing loose mixtures in a stainless steel pan, which was then heated for 4 h at 135 °C in a traditional oven. Within the



procedure, mixtures were stirred every 60 min to maintain uniform aging conditioning. In contrast, the long-term mixture aging was performed by utilizing specimens after gyratory compaction and shaping in an oven at 85 °C referring to AASHTO R30. The aging duration was set as two days (48 h), five days (120 h), and eight days (192 h), respectively. To avoid the large deformation or collapsing of specimens, all the specimens were wrapped in foil paper and tied with rubber bands, as seen in Figure 1. The foil paper was stabbed to generate small vents to allow heated air to circulate around the specimens.



**Figure 1.** Specimen Aging (a) Set up in the Oven, and (b) Specimen after Oven Aging on Different Days.

### 3.2. Binder MSCR Test

The MSCR test was used in this study to evaluate the asphalt binder’s resistance to fatigue cracking. The test was performed by a dynamic shear rheometer (DSR) under shear creep and recovery at two stress levels at a specified temperature. The creep portion of the test lasts for 1 s at a constant stress, followed by a 9 recovery. The test was run at a stress level of 0.1 kPa for 20 cycles followed by 10 cycles at a stress level of 3.2 kPa. The test temperatures were 20 °C, 25 °C, and 30 °C. A lower test temperature, such as 15 °C, was also tried, but no smooth time-strain curve can be achieved for rubber and SBS modified binders, and thus the results at 15 °C were not included in this paper.

The MSCR test procedure and results calculation at an intermediate temperature followed AASHTO TP70 and AASHTO M322 exactly. Two parameters, non-recoverable creep compliance ( $J_{nr}$ ), and percent recovery ( $R$ ), could be determined. Only percent recovery ( $R$ ) was analyzed since  $J_{nr}$  and  $R$  was well correlated [10]. Furthermore, this paper focuses on percent recovery at a stress level of 3.2 kPa ( $R_{3.2}$ ) since a high stress level is more critical for cracking performance.

### 3.3. Binder PG Test

A binder high temperature PG and intermediate temperature PG test was performed according to AASHTO MP 1 and AASHTO T315 using (DSR). The binder low temperature PG test was performed in accordance with AASHTO T313 using the BBR method.

### 3.4. Binder Viscosity Test

Viscosity is the ratio between the applied shear stress and the rate of shear and is usually used to measure the resistance of asphalt to flow. The test was conducted following AASHTO T316 using the Rotational Viscometer (RV) method at temperatures of 65 °C and 135 °C. The original asphalt binder (as supplied) and aged residue from the TFOT were both tested. Test results were used to determine laboratory mixing and compaction temperatures based on the binder temperature-viscosity curve.

The determined mixing and compaction temperatures are 175 °C and 170 °C for SBS and rubber modified asphalt, and 160 °C and 145 °C for the rest of the binders.

### 3.5. Binder Fracture Energy Test

Fracture energy was identified to characterize the fracture properties of different asphalt binders at the intermediate temperature based on the stress-strain curve. Previous studies have shown that the fracture energy at intermediate temperatures has a good correlation with the field bottom-up fatigue cracking [11–13]. Binder fracture energy is defined as the area underneath the shear stress-shear strain curve up to the peak stress. The samples were tested in monotonic shear mode by DSR using a constant shear rate to load the samples continuously until shear stress was significantly reduced and approaching zero. The test was performed at 20 °C, 25 °C, and 30 °C using a shear rate of 0.2 s<sup>-1</sup>.

### 3.6. Mixture SCB-IFIT Test

An SCB-IFIT test was adopted to evaluate the fatigue resistance of the asphalt mixture at the intermediate temperature. Although the flexibility index (*FI*) is newly proposed, it is simple and showed potential to match well with field cracking performance [10]. It was reported that the *FI* value was sensitive enough to distinguish various asphalt mixtures and asphalt contents [13]. The test specimen size was 150 mm in diameter and 50 mm in thickness, with a 15-mm notch in depth. The air voids for all the specimens were controlled within 7 ± 0.5%. The specimens were conditioned in a chamber at 25 °C for 2 h before testing. A loading rate of 50 mm/min was applied. Equation (1) shows the equation used to calculate the *FI* value:

$$FI = A \times G_f/m \quad (1)$$

where,

*FI*—is the flexibility index;

*G<sub>f</sub>*—is the fracture energy;

*m*—is the absolute value of *m*-value after peak load in the load-displacement curve; and

*A*—is a unit conversion factor and scaling coefficient (taken as 0.01).

### 3.7. Mixture IDT Test

A mixture fracture test was conducted at room temperature to evaluate fatigue cracking resistance ability according to AASHTO T322 using an indirect (IDT) method. Two parameters were used for material characterization purposes, including IDT strength and fracture work density. Fracture work density is defined as the fracture work divided by the specimen volume; fracture work is defined as the area underneath the tensile stress versus tensile strain curve up to the peak stress. It was found in previous study that the fracture work density could be a good indicator for field fatigue cracking: a higher fracture work density value correlated with a lower field crack amount [11,14]. The test specimen size was 100 mm in diameter and 38 mm in thickness. The air void for all the specimens were controlled within 7 ± 0.5%. The test was conducted at 25 °C at a loading rate of 50 mm/min.

## 4. Asphalt Binder Test Results Analysis

### 4.1. Binder PG and Viscosity

Table 3 shows the test results of binder PG and viscosity at different aging conditions. As shown, the modification of base asphalt was affected more for the high temperature PG compared to the low temperature PG: most modified binders experienced a similarly low PG with base binder, whereas the high temperature PG either increased or decreased to various extents depending on the additive utilized. The Evotherm 3G was the only additive that decreased the high temperature PG

of base asphalt and the reason for this needs further study. Additionally, it is interesting to note that the SBS modification increased both high- and low-temperature PGs, which could be attributed to the crosslinked elastomer network structure of the SBS [15].

In addition,  $\Delta T_c$ , which quantifies the difference in continuous low temperature PG for stiffness and relaxation ( $m$ -value) properties, was also calculated. Results indicate that all the binders exhibited positive  $\Delta T_c$  values (ranged from 0.2 °C to 2.2 °C), except for the modified rubber asphalts (ranged from -0.1 °C to -1.5 °C), indicating that most asphalts were stiffness controlled. It was pointed out that the absolute values of  $\Delta T_c$  smaller than 2.5 °C indicated a low potential of thermal cracking, whereas the threshold value of 2.5 °C was proposed based on a comparison between  $\Delta T_c$  results and field thermal crack amount [16].

Compared to the base binder, the addition of Sasobit and Evotherm reduced viscosity, whereas the addition of SBS and rubber increased viscosity. It is also seen that the viscosity increased after TFOT aging.

**Table 3.** Test Results of Binder PG and Viscosity under Thin-Film Oven Test (TFOT) and Pressure Aging Vessel (PAV) Aging.

Modification	% of Additive	Continues PG, °C TFOT	Continues PG, °C TFOT/PAV	Viscosity, MPa·s Original	Viscosity, MPa·s TFOT
Base	0	78.8–25.6	87.3–25.6	497.5	706.2
Sasobit	1	82.9–23.2	85.8–23.2	474.3	590.8
Sasobit	2	86.7–24.3	88.4–24.3	434.2	553.5
Sasobit	3	90.8–25.7	92.0–25.7	349.2	495.8
Evotherm M1	0.6	79.2–25.6	85.3–25.6	446.7	557.5
Evotherm 3G	0.6	75.4–25.3	83.6–25.3	427.3	533.8
SBS	4.5	92.1–28.5	92.0–28.5	1446.0	1911.3
Rubber	5	85.9–26.8	95.8–26.8	991.8	1166.3
Rubber	10	87.2–27.5	96.5–27.5	1191.7	1554.7
Rubber	15	91.5–27.8	98.3–27.8	1930.0	2297.3

#### 4.2. Binder MSCR Test Results

Figure 2a,b show the ten cycles of creep and data from recovery and test cycle number nine of MSCR testing at 25°C using TFOT/PAV aged base asphalt, respectively. As shown, the curves are fairly smooth with no jagged edges observed, indicating that the application of the MSCR test on fatigue resistance of asphalt binder is technically feasible without sacrificing data accuracy. Figure 2c compares the MSCR  $R_{3,2}$  among all the asphalt types based on the short-term TFOT aged binders. Error bars representing standard deviation of the results are also presented. It can be observed that the error bars are all in small values, representing good repetition of the test.

Additionally, the binders with 15% rubber and SBS hold high  $R_{3,2}$  values and were minorly affected by aging condition and temperature change. Although the asphalt property was very sensitive to the climatic condition, such sensitivity was diminished when SBS or a high content of rubber were applied to reform the base asphalt. In contrast, the Evotherm M1 and Evotherm 3G binders have the lowest  $R_{3,2}$  values and the results are greatly influenced by temperature alternation. The MSCR  $R_{3,2}$  values under TFOT/PAV aging showed exactly the same trend compared to TFOT aged binder with a slight increase of  $R_{3,2}$  values.

Figure 3a,b show the sensitivity of MSCR  $R_{3,2}$  to asphalt binder type and additive content at a testing temperature of 25 °C. By visual observation, the MSCR  $R_{3,2}$  was sensitive enough to distinguish different binder types and additive contents. A statistical t-test was conducted with a significance level of 0.05 between any two binder types in Figure 3a, or between any two additive contents in Figure 3b. Results indicate that except for the rubber-SBS pair (as shown in Figure 3a) and 5% rubber –10% rubber pair (as shown in Figure 3b), all the other pairs were statistically different.

Additionally, Figure 3a shows that the MSCR  $R_{3,2}$  values between TFOT aging and TFOT/PAV aging are almost overlapping except for the Evotherm 3G binder. Such a finding indicates the potential that the Evotherm 3G could experience a fast aging rate, as specified elsewhere [17].

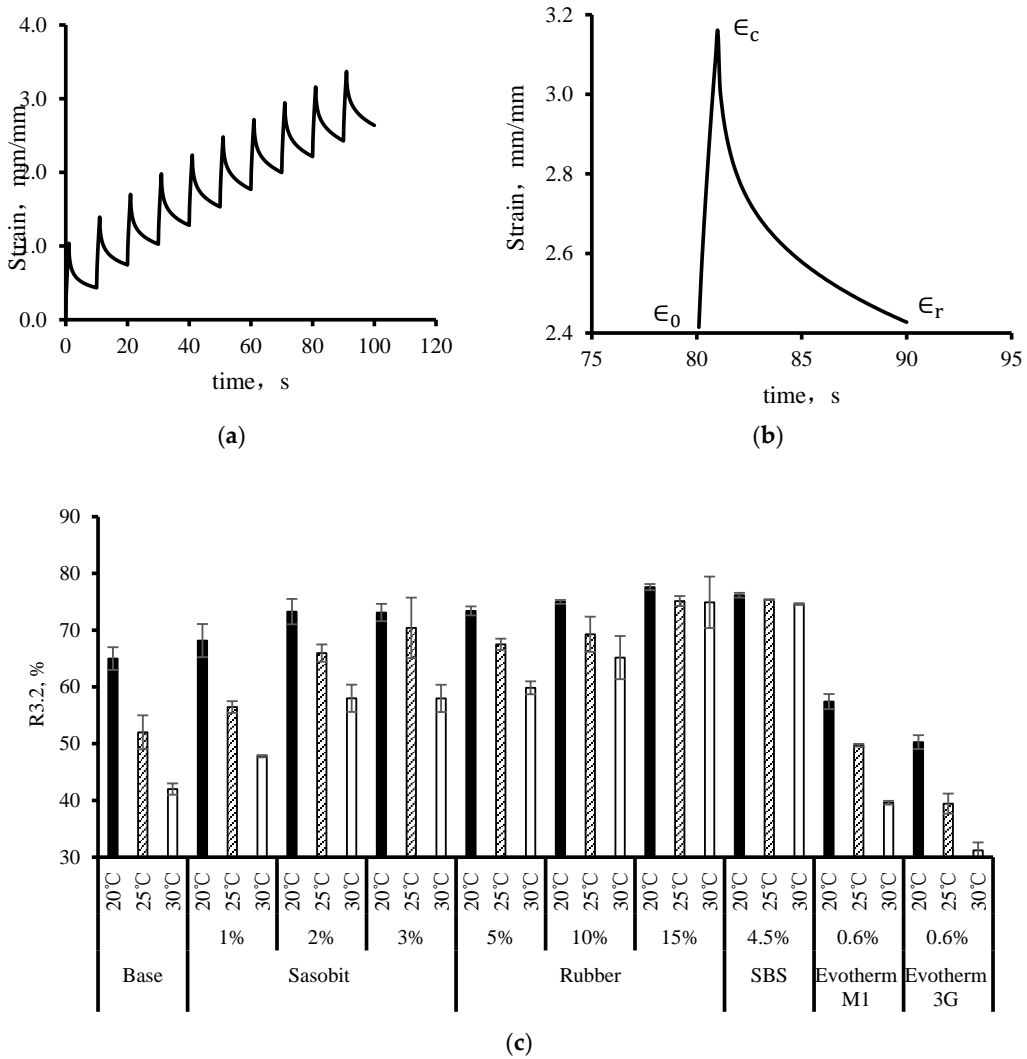


Figure 2. MSCR Test Results (a) Typical 10 Cycles of Creep and Recovery; (b) Test Cycle No. 9 Data Plot Showing Creep and Recovery, and (c)  $R_{3.2}$  Comparison of TFOT Aged Binders.

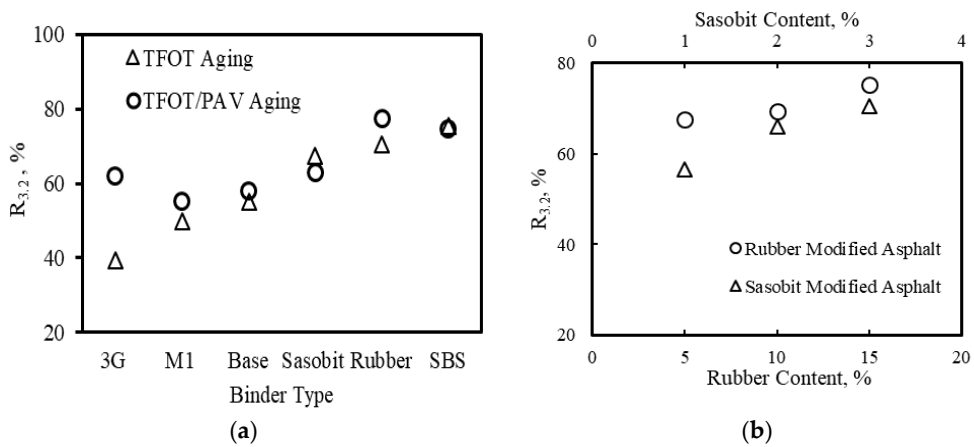
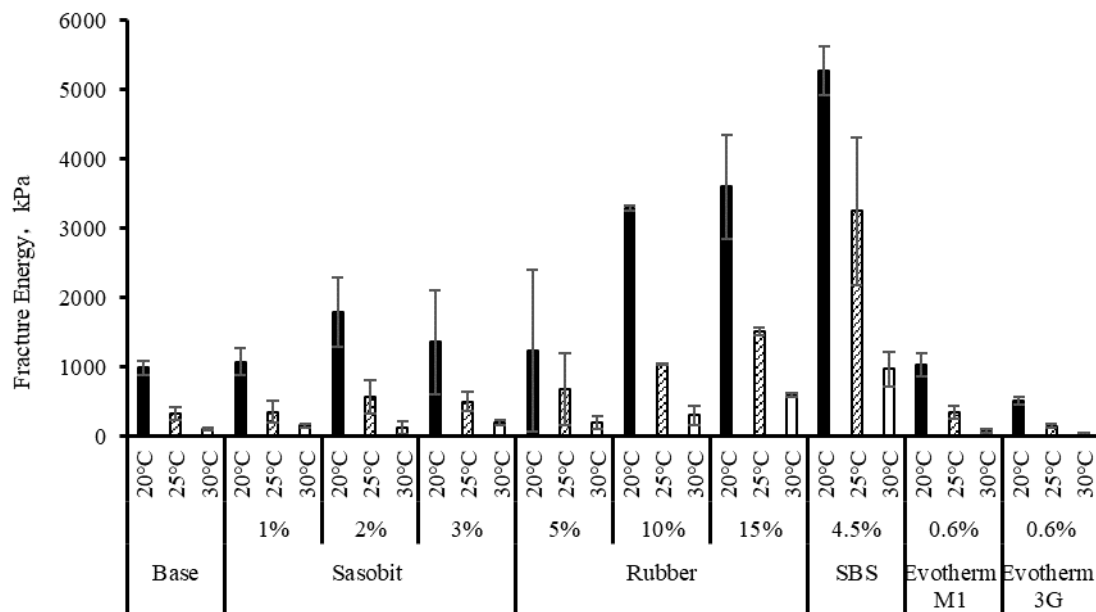


Figure 3. Sensitivity of MSCR  $R_{3.2}$  to (a) Binder Type, and (b) Additive Content.

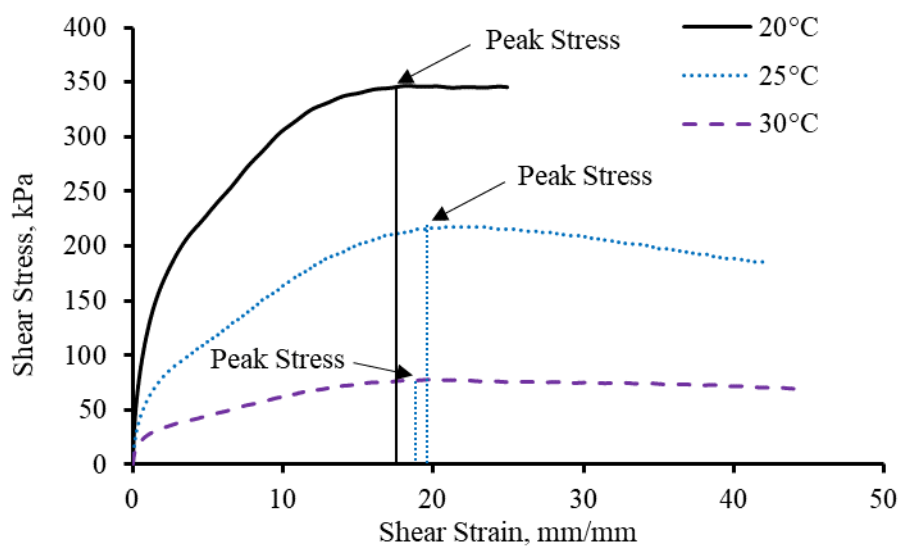
### 4.3. Binder Fracture Energy

The binder fracture energy test results under TFOT aging are shown in Figure 4a. It is seen that the trend between binder MSCR  $R_{3,2}$  and fracture energy matched well. Specifically, the SBS modified binders showed the highest MSCR  $R_{3,2}$  and fracture energy values, whereas the Evotherm M1 and 3G binders displayed the lowest magnitudes.

Additionally, the fracture energy value of the SBS modified binder was obviously altered per temperature change. The plot between shear strain and shear stress that was used to calculate fracture energy was checked, as shown in Figure 4b. It is seen that the shear strains corresponding to the maximum shear stresses are close to each other, whereas the maximum shear stress values decreased with increased temperature. Thus, the reduced fracture energy for SBS modified binders at an elevated temperature was majorly caused by declined maximum shear stress.



(a)



(b)

**Figure 4.** Binder Fracture Energy Test Results for (a) TFOT Aging; and (b) TFOT Aged SBS Binders at Varying Temperatures.

The above analysis shows that the MSCR testing at intermediate temperatures is sensitive enough to differentiate various binder types and additive contents with good repetitions. Next, asphalt mixture SCB-IFIT and IDT testing were conducted to check if the asphalt MSCR test has a similar ranking with a mixture fatigue test. The SBS modified asphalt binder showed the best fracture resistance in the asphalt MSCR and fracture test, and was accordingly selected as the binder used in the mixture tests. Base binder was also selected as the control. Different aging durations of loose mix or compacted specimens were considered to evaluate if the relationship between asphalt MSCR and mixture fracture tests was stable under different oxidative conditions.

### 5. Asphalt Mixture Test Results Analysis

In the laboratory, the testing specimens using both base asphalt and SBS binder were fabricated using gyratory compaction, and were further cut into a proper size for testing. The volumetric information, such as air void and void in mineral aggregate (VMA), were checked. These specimens were aged under both short-term and long-term conditions, as discussed above.

#### 5.1. SCB-IFIT Test

Figure 5 shows an example of the SCB-IFIT results using SBS modified binder based on the aging durations of 4 h and two days. As seen, the fracture energy ( $G_f$ ) in equation (1) is defined as the area underneath the entire curve, and the  $m$ -value is the slope at the inflection point after peak load.

Figure 6 compares the testing results of SCB-IFIT for the asphalt mixtures using #70 and SBS modified binders at various aging durations. The figure shows a clear trend that the  $FI$  values decreased for both binders with a longer aging duration, and thus cracking resistance is reduced. It is also observed that the asphalt mixture using #70 asphalt decreased faster in  $FI$  in contrast to the specimen with SBS modified binders, especially between two aging durations. The fact that the SBS modified asphalt mixture aged less than base asphalt was also found by previous studies [17–19].

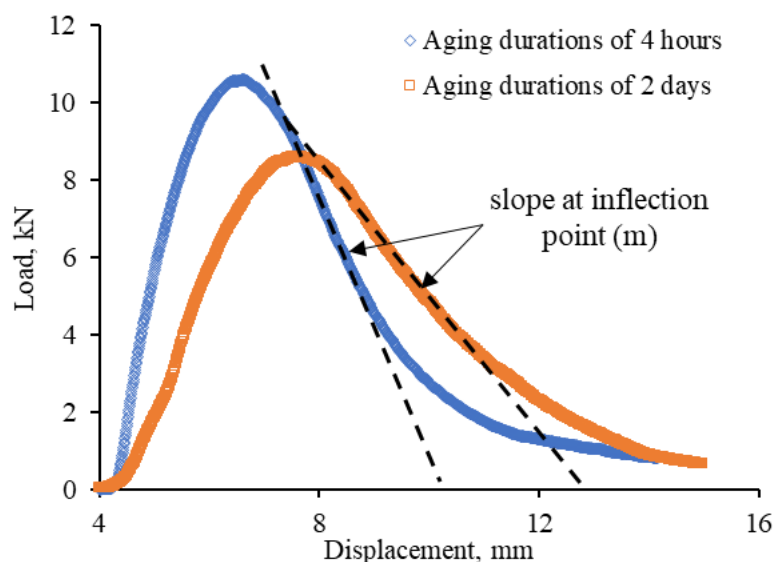


**Figure 5.** Load-displacement curve of semi-circular bending- Illinois flexibility index test (SCB-IFIT) test for mixtures using SBS modified asphalt.

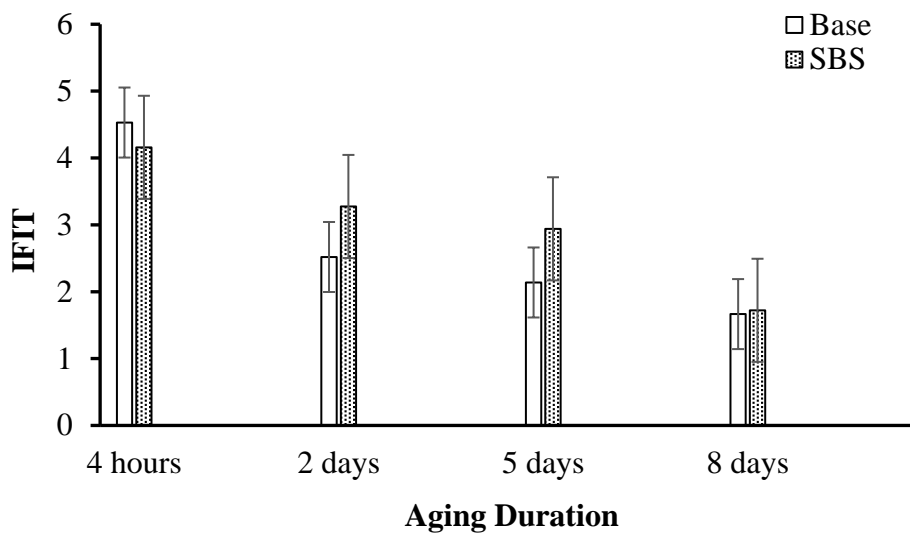


Figure 6. SCB-IFIT test results of unmodified and SBS modified mixtures Flexible index.

### 5.2. IDT Fracture Test

Test results of tensile strength and fracture work density under different aging conditions are shown in Figure 7a,b, respectively. As seen, the IDT strength which only considers peak load was gradually decreased with aging, indicating the decreased cracking resistance. Figure 7b shows that the fracture work density of asphalt mixture using #70 base asphalt decreased with aging time, indicating the reduced cracking resistance. In contrast, the fracture work density of the SBS modified asphalt mixture slightly increased at the end of eight days' aging, which validates the field observation that SBS modified binder was less affected by aging compared to the control asphalt [17]. Fracture work density combines the strength and ductility of a mixture, and since the IDT strength of both mixtures decreased over aging, it is reasonable to assume that the ductility of mixture using SBS modified binders could be higher than the mixture with base asphalt.

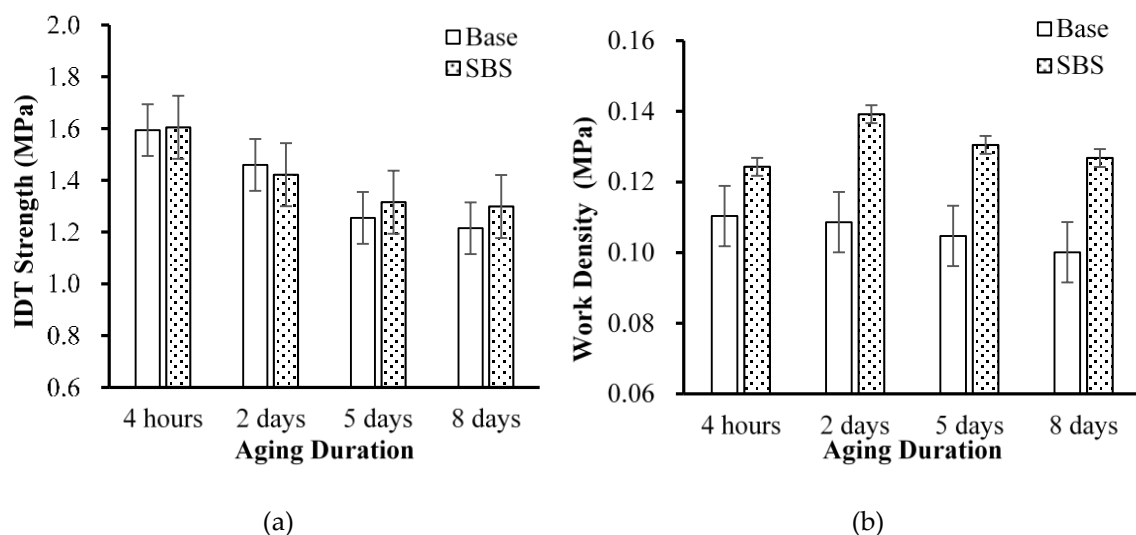


Figure 7. Mixture indirect tensile test (IDT) Fracture test results (a) IDT strength, and (b) fracture work density.

### 6. Ranking between Binder MSCR and Mixture Testing

A paired ranking method was used to determine if the binder MSCR test matched well with the mixture’s fatigue test. The method follows three steps: compare the MSCR results between base asphalt and SBS modified asphalt at different temperature and aging conditions and obtain a ranking (base asphalt  $\geq$  SBS, or base asphalt  $<$  SBS, six comparisons in total); compare mixture testing between base asphalt and SBS modified asphalt at different aging conditions and obtain a ranking (base  $\geq$  SBS, or base  $<$  mixture with SBS modified asphalt base asphalt  $<$  SBS, 12 comparisons in total). Then, the binder and mixture’s ranking results were compared.

The percent difference criterion was used for the ranking purpose. It is suggested based on engineering experience that if the percent difference was within 20%, then there was no significant difference between the pair [20]. Otherwise, whichever mean value was higher indicated more/less crack resistance. Results are shown in Figure 8. As seen, four out of six MSCR pairs showed a percentage difference over 20%, sharing the same trend with mixture ranking in which 11 out of 12 pairs showed a percentage difference over 20%. In contrast, one pair from the MSCR test and two pairs from mixtures’ test experienced a percentage difference less than 20%.

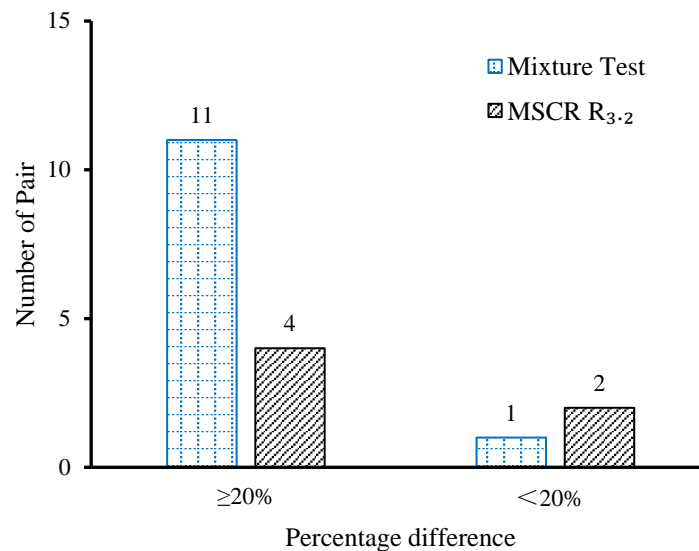


Figure 8. Ranking comparison between MSCR R<sub>3.2</sub> and mixture fatigue test results.

### 7. Summary of Findings

In this study, the applicability of the MSCR test on fatigue resistance of asphalt binder was evaluated. Six binder types with different modifications and additive contents were utilized. Mixture tests were also conducted to evaluate if the MSCR test could represent mixture fatigue performance. Based on the analysis, the following conclusions can be drawn:

- The binder MSCR test can be conducted at intermediate temperatures (20 °C or higher) with a smooth data curve and good repetitions. However, testing temperatures at 15 °C or lower may result in a steep curve and needs to be performed with more caution.
- The binder MSCR test at intermediate temperatures was sensitive enough to differentiate binder type and additive content at different aging durations.
- The binder MSCR test at intermediate temperatures showed a similar ranking to the mixture’s fatigue test, indicating that the binder MSCR test could be potentially utilized to represent a mixture’s fatigue resistance where binder selection is a major concern.



- The binder MSCR test, with binder fracture energy test and mixture's tests, all proved that the SBS modified binder was less affected by aging and showed excellent performance in improving the mixture's durability.
- The above conclusions indicate that the MSCR test could be a promising method to evaluate the fracture properties of asphalt mixture. Further study on the correlation between MSCR and any field test roads could be necessary.

## 8. Clarification

This study focused on one specific aggregate gradation with six different binder types and varying aging conditions. The application of the MSCR test on quantifying the fatigue resistance of other materials such as recycled asphalt pavement (RAP) and porous pavements may need further investigation. This paper provides a framework which can be modified and implemented by local agencies for a variety of material types based on their needs and requirements.

**Acknowledgments:** This study was sponsored by the National Natural Science Foundation of China (project number 51508095). The authors would like to acknowledge the NSFC staff for their assistance.

**Author Contributions:** Weiguang Zhang was in charge of the data analysis and draft paper writing. Tao Ma served as the corresponding author and manuscript revision. Xiaoming Huang provided many valuable suggestions on the data analysis part. Meng Ling revised the manuscript and contributed in data interpretation. Gang Xu, Xiao Chen and Jiayue Xue were responsible for laboratory test and manuscript format.

**Conflicts of Interest:** The authors declare no conflict of interest.

## References

1. Anderson, D.; Hir, Y.; Marasteanu, M.; Planche, J.P.; Martin, D.; Gauthier, G. Evaluation of fatigue criteria for asphalt binders. *Trans. Res. Rec. J. Trans. Res. Board* **2001**, *1766*, 48–56. [CrossRef]
2. Deacon, J.A.; Harvey, J.T.; Tayebali, A.; Monismith, C.L. Influence of binder loss modulus on the fatigue performance of asphalt concrete pavements. *J. Assoc. Asph. Paving Technol.* **1997**, *66*, 633–685.
3. Bahia, U.H.; Hanson, I.D.; Zeng, M.; Zhai, H.; Khatri, A.M.; Anderson, M.R. *Characterization of Modified Asphalt Binders in Superpave Mix Design*; NCHRP Report 459; Transportation Research Board: Washington, DC, USA, 2001.
4. Andriescu, A.; Hesp, S.; Youtcheff, J. Essential and plastic works of ductile fracture in asphalt binders. *Trans. Res. Rec. J. Trans. Res. Board* **2004**, *1875*, 1–8. [CrossRef]
5. Hintz, C.; Velasquez, R.; Johnson, C.; Bahia, H. Modification and Validation of Linear Amplitude Sweep Test for Binder Fatigue Specification. *Trans. Res. Rec. J. Trans. Res. Board* **2011**, *2207*, 99–106. [CrossRef]
6. Kim, Y.; Little, D. *Development of Specification-Type Tests to Assess the Impact of Fine Aggregate and Mineral Filler on Fatigue Damage*; Report 0-1707-10; Texas Department of Transportation: Austin, TX, USA, 2005.
7. Zhou, F.; Mogawer, W.; Li, H.; Andriescu, A.; Copeland, A. Evaluation of fatigue tests for characterizing asphalt binders. *J. Mater. Civ. Eng.* **2013**, *25*, 610–617. [CrossRef]
8. D'Angelo, J.; Kluttz, R.; Dongre, R.N.; Stephens, K.; Zanzotto, L. Revision of the superpave high temperature binder specification: The multiple stress creep recovery test. In Proceedings of the Technical Sessions Asphalt Paving Technology: Association of Asphalt Paving Technologists, Leipzig, Germany, 23–25 May 2007; Volume 76, pp. 123–157.
9. Hossain, Z.; Ghosh, D.; Zaman, M.; Hobson, K. Use of the multiple stress creep recovery (MSCR) test method to characterize polymer-modified asphalt binders. *J. Test. Eval.* **2016**, *44*, 507–520. [CrossRef]
10. Al-Qadi, I.L.; Ozer, H.; Lambros, J.; El Khatib, A.; Singhvi, P.; Khan, T.; Rivera-Perez, J.; Doll, B. *Testing Protocols to Ensure Performance of High Asphalt Binder Replacement Mixes Using RAP and RAS*; Report No. FHWA-ICT-15-017; Illinois Center for Transportation: Rantoul, IL, USA, 2015.
11. Johnson, C.; Bahia, H.; Wen, H. Practical application of viscoelastic continuum damage theory to asphalt binder fatigue characterization. In Proceedings of the Asphalt Paving Technology: Association of Asphalt Paving Technologists-Proceedings of the Technical Sessions, Minneapolis, MN, USA, 15–19 March 2009; Volume 78, pp. 597–638.

12. Shen, S.; Zhang, W.; Shen, L.; Huang, H. A statistical based framework for predicting field cracking performance of asphalt pavements: Application to top-down cracking prediction. *Constr. Build. Mater.* **2016**, *116*, 226–234. [CrossRef]
13. Wu, S.; Wen, H.; Zhang, W.; Shen, S.; Mohammad, L.N.; Faheem, A.; Muhunthan, B. Field performance of top-down fatigue cracking for warm mix asphalt pavements. *Int. J. Pavement Eng.* **2016**, 1–11. [CrossRef]
14. Zhang, W.; Shen, S.; Basak, P.; Wen, H.; Wu, S.; Faheem, A.; Mohammad, L.N. Development of predictive models for initiation and propagation of field transverse cracking. *Transp. Res. Rec. J. Transp. Res. Board* **2015**, *2524*, 92–99. [CrossRef]
15. Xu, O.; Xiao, F.; Han, S.; Amirkhanian, S.N.; Wang, Z. High temperature rheological properties of crumb rubber modified asphalt binders with various modifiers. *Constr. Build. Mater.* **2016**, *112*, 49–58. [CrossRef]
16. Anderson, R.M.; King, G.N.; Hanson, D.I.; Blankenship, P.B. Evaluation of the Relationship between Asphalt Binder Properties and Non-Load Related Cracking. *Meet. Assoc. Asphalt Paving Technol.* **2011**, *80*, 615–663.
17. Zhang, W.G.; Shen, S.H.; Wu, S.H.; Mohammad, L.N. Long-term Field Aging of Warm Mix and Hot Mix Asphalt Binders. *Trans. Res. Rec. J. Trans. Res. Board* **2017**, *2632*, 140–149. [CrossRef]
18. Pasetto, M.; Baldo, N. Unified approach to fatigue study of high performance recycled asphalt concretes. *Mater. Struct.* **2017**, *50*, 113. [CrossRef]
19. Pasetto, M.; Baldo, N. Fatigue performance of recycled hot mix asphalt: A laboratory study. *Adv. Mater. Sci. Eng.* **2017**, *2017*, 4397957. [CrossRef]
20. NCHRP 9-49A. Performance of WMA Technologies: Stage II-Long-Term Field Performance. In Proceedings of the Haifang Wen and Shenghua (Edward) Wu Asphalt Mixture ETG Meeting, Fall Rivers, MA, USA, 8 April 2015. Quarterly Report.



© 2018 by the authors. Licensee MDPI, Basel, Switzerland. This article is an open access article distributed under the terms and conditions of the Creative Commons Attribution (CC BY) license (<http://creativecommons.org/licenses/by/4.0/>).



Article

# Potential of Waste Oyster Shells as a Novel Biofiller for Hot-Mix Asphalt

Nader Nciri , Taesub Shin, Haksoo Lee and Namjun Cho \*

Department of Energy, Materials, and Chemical Engineering, Korea University of Technology and Education, 1600 Chungjeol-ro, Byeongcheon-myeon, Dongnam-gu, Cheonan 330-708, Korea; nader.nciri@koreatech.ac.kr (N.N.); teaja21@koreatech.ac.kr (T.S.); haktop10@koreatech.ac.kr (H.L.)

\* Correspondence: njuncho@koreatech.ac.kr; Tel.: +82-41-560-1342

Received: 6 February 2018; Accepted: 8 March 2018; Published: 11 March 2018

**Abstract:** This paper reports the use of waste oyster shells as a novel biofiller for hot-mix asphalt (HMA) pavement applications. The effects of different fractions (e.g., 0, 5, 10, 15 wt %) of oyster shell powder (OSP) on the bitumen performance were investigated. The chemical properties of unfilled and OSP-filled asphalts were characterized by means of thin layer chromatography-ionization detection (TLC-FID), Fourier transform-infrared spectroscopy (FT-IR), X-ray diffraction (XRD), and scanning electron microscopy (SEM). Thermal characteristics were examined by thermogravimetric analysis (TGA) and differential scanning calorimetry (DSC). Physical and rheological properties were assessed through penetration, softening point, ductility, and dynamic shear rheometer (DSR) tests. Results showed that OSP addition increased the resins content, as well as the stiffness of blends. No obvious reactions have occurred between the filler and the asphalt. A higher dose of OSP altered the morphology of the binder, whereas lower and intermediate doses improved its thermal stability and enhanced its low-temperature, rutting, and fatigue performances with respect to the plain asphalt. Overall, the waste oyster shells could be used as filler substitute, not only to improve the quality of road pavements but also to reduce the cost of their construction and solve the waste disposal problems.

**Keywords:** oyster shell powder; calcite filler; asphalt mastics; rutting; fatigue cracking; thermal stability; glass transition temperature

---

## 1. Introduction

Hot-mix asphalt (HMA) is a heterogeneous multiphase material that consists of aggregates with different sizes and shapes, asphalt cement, and air voids. These components constitute a complex microstructure. While the aggregates act basically as a skeleton, asphalt binder provides an adhesive action (i.e., glue) among aggregate particles and contributes to the viscous-elastic properties of the mixture [1]. Aggregates in HMA can be divided into three types according to their size: coarse aggregates, fine aggregates, and mineral filler. Coarse aggregates are generally defined as those retained on the 2.36-mm sieve. Fine aggregates are those that pass through the 2.36-mm sieve and are retained on the 0.075-mm sieve. Mineral filler is defined as that portion of the aggregate passing the 0.075-mm sieve [2].

Mineral filler is a very fine material with the consistency of flour and is also referred to as mineral dust or rock dust. It can greatly affect the properties of a mixture such as strength, plasticity, voids, resistance to action of water, and the resistance to the forces of weathering. The proper use of filler can improve the asphalt paving mixture through increased density, stability, durability, and skid resistance. On the other hand, excessive quantity of filler tends to increase brittleness and proclivity to cracking, and deficiency of filler tends to increase void content, lower stability, and soften the mix, which leads to

shoving, and rutting of the pavement [3]. Mineral fillers play a dual role in paving mixtures. First, they are part of the mineral aggregate, i.e., they fill the interstices and provide contact points between larger aggregate particles and, thereby, strengthen the mixture. Second, when mixed with asphalt, mineral fillers form a high-consistency binder or matrix that cements larger aggregate particles together. This resulting filler-asphalt mastic is capable of affecting the physical and mechanical properties of the mixture to a large extent [4].

Various studies have shown that there are three primary mechanisms by which fillers reinforce asphalt binder [5–7]: volume filling, particle strutralization, and physicochemical interactions. Volume filling and particle strutralization are both means of mechanical reinforcement. Volume filling increases asphalt mastic stiffness simply as a result of the replacement of asphalt binder volume with rigid particles. Filler particles start to form an interconnected network at a filler volumetric concentration of roughly 40%, leading to a rapid increase in the rate of stiffening with increasing volume fraction [6,8,9]. At lower filler concentrations, particle contact is not established, and the mastic will behave as a dilute suspension, with volume filling constituting the dominant mechanical reinforcement mechanism. The third type of reinforcement, physico-chemical interaction, involves the adsorption of polar fractions (e.g., resins and asphaltenes) of the asphalt binder onto the surface of filler particles through electrostatic, dipole–dipole, or van der Waals forces [7,10,11]. Physiochemical interaction leads to the formation of an interphase adsorbed layer of the polar fractions of asphalt on the surface of filler particles. In addition, loss of certain components of the asphalt to adsorption modifies the chemistry and morphology of the non-adsorbed, “effective” binder matrix [12].

Different types of filler including limestone dust, Portland cement, crushed stone, granite powder, and fine sand are usually used in the asphalt mixtures [3]. Society’s ever-growing concern for protecting the environment has resulted in concentrated attention on the possible reuse of waste materials in road construction [13–17]. Numerous efforts have been made to use waste materials of various origins to partially or fully replace conventional filler in the production of HMA. The wastes that were identified included construction and demolition waste (e.g., crushed bricks and concrete) [18], marble slurry [19], coal waste powder [20], waste glass [21], rice husk ash [22], coconut shells [23], eggshells [24], and seashells [25], etc. It has been found that these materials contain recoverable fractions that are potentially useful in highway related applications. There are numerous examples of successful applications in highway construction for each of these materials. By removing these materials from the waste stream and recycling them in highway applications, demand for virgin raw materials will be reduced, street and highway maintenance costs will be lowered, energy consumption will be reduced, and valuable landfill space will be conserved.

The southeastern coastal sea of South Korea has long been considered one of the most productive oyster growing areas in the world. Shellfish farming makes up a large portion of the local economy. It is estimated that approximately 300,000 tons of oyster shells are produced annually from the shellfish farms, which cover 4100 ha of coastal ocean [26]. The oyster constitutes one of the primary products of shellfish farms, and its industries have greatly contributed to the economic growth, at both national and regional levels [27]. However, disposal of oyster shell waste (OSW) is becoming an increasingly serious problem for the marine aquaculture industry. Huge amounts of OSW are being dumped illegally and constantly into public waters and reclaimed lands, causing a nasty smell as a consequence of the decay of flesh remnants that are attached to the oysters [28]. In an attempt to solve this issue, the government of the Republic of Korea has implemented specific programs and policies to maximize reuse, recycling, and waste reduction [29]. For instances, 10% of OSW is currently recycled as shell meal fertilizer and 50% as catching materials for oyster seedlings (i.e., oyster shells for growing oyster). Unfortunately, and despite all the state efforts made, the remaining part (i.e., 40%) of the OSW is directly dumped in the coastal region, causing environmental problems including pollution of coastal fisheries, the management problem of public water surface, damage of natural landscape, and health/sanitation problems [30]. To cope with this critical situation, new and alternative approaches for recycling OSWs

must urgently be found. The ideal solution would be to convert the calcium carbonate-rich OSW to a product that is both beneficial and economically viable.

The purpose of this preliminary investigation was then to assess, for the first time, the feasibility of using OSW as a performance-enhancing additive for road paving applications. It was undertaken to assist those who have an interest in using or increasing their understanding of the oyster shell materials that may be recovered and used in pavement construction applications. It is intended to provide the potential user or reviewer with sufficient information on the use of oyster shell waste so that he will gain a deeper understanding of the material nature and properties, where other information may be obtained, and what issues need to be evaluated when considering its use in hot-mix asphalt (HMA). However, this research article does not constitute a standard, specification, or regulation.

## 2. Materials and Methods

### 2.1. Preparation of Oyster Shell Powder (OSP)

Specimens of the *Crassostrea gigas* (Figure 1A) were collected from Tongyeong beach, Gyeongsang province, South Korea. First, the oyster shells were properly cleaned by brushes after discarding the fresh remnant to them. Subsequently, they were well washed with deionized water (DI water) to remove the excess of alkalinity and chloride, and dried in a drying oven ( $T = 100\text{ }^{\circ}\text{C}$ ) for ca. 2 days. The dried shells were ground (4 times, 4 h per round) using a dry ball-mill (Oyster Shell Grinding Machine, Zhengzhou Jiangtai Heavy Industrial Machinery Co., Ltd, Weihai, China) to generate a fine powder, which was then sieved in a No. 50 sieve ( $300\text{ }\mu\text{m}$ ). In practical applications, fillers with a granulometry of less than  $75\text{ }\mu\text{m}$  (i.e., passing ASTM standard sieve No. 200) are used to provide the best homogenous asphalt mixtures [31]. However, the asphalt pavement design may not be the greatest scenario for maximizing pavement performance when pavement distresses such as fatigue cracking, rutting, and moisture damage occur. Therefore, the purpose of this investigation was to determine the influence and effects of a wide range of different particle sizes (up to  $300\text{ }\mu\text{m}$ ) on the asphalt-filler mastic performance properties through selected Superpave (i.e., Superior Performance Asphalt Pavement) binder tests. It must be emphasized here that this was done only to learn about the advantages and disadvantages associated with the use of particles larger than the standard. Hence, the aforementioned procedure is not intended to be used in practice. After sieving, the oyster shell powder (labelled as OSP, Figure 1B) was stored at room temperature in a closed container. The particle size and distribution of OSP were performed using a Mastersizer 3000 Smarter Particle Sizing (Malvern Instruments Ltd., Malvern, UK) granulometer. The measurement was carried out at room temperature (ca.  $25\text{ }^{\circ}\text{C}$ ) with an Aero S dry powder disperser ( $P = 1\text{ bar}$ ). The chemical composition was conducted using elemental analyzer (Thermo Scientific™ FLASH 2000 CHNS/O Analyzer, Loughborough, UK), X-ray fluorescence spectrometer (Shimadzu EX-720, Shimadzu Corporation, Chiyoda-ku, Tokyo, Japan), and energy-dispersive spectroscopy (SEM, JSM-6010LA, JEOL Ltd., Akishima, Tokyo, Japan).



Figure 1. Oyster shell waste (A) and its fine powder (B).

## 2.2. Preparation of Filler-Asphalt Mastic Samples

One-base bitumen, denoted as AP-5 asphalt (penetration grading of 60–70 at 25 °C), was used in this study. It was obtained from SK Energy Co. Ltd. Seoul, Republic of Korea. The physicochemical properties of AP-5 asphalt are given in Table 1. The mastics were produced following a standardized experimental protocol, optimized in order to obtain homogeneous OSP-asphalt mastics. The samples were prepared using a high shear L5M-A mixer (Silverson Machines Inc., East Longmeadow, MA, USA) at 180 °C and a speed of 3000 rpm. The OSP contents used were 5, 10, 15 wt % by weight of blend. These percentages were chosen to see closely the impact of a gradual increase in OSP concentration on the attributes of asphalt cement. In preparation, 600 g of the asphalt heated to fluid condition was poured into a 1000 mL stainless steel container. Upon reaching 175 °C, a preweighed amount of OSP was slowly added to the binder in small quantities of approximately half teaspoon. This was done to ease smooth mixing and prevent agglomeration of the additive. The filler also was introduced into the binder about 2.5 cm above the surface of the bitumen, so that the finest part of the filler would not be lost into the air. Mixing was then continued at 180 °C for 2 h to ensure good distribution and dispersion of filler particles. Due to the fact that the preparation procedure will lead to the oxidation of asphalt and changes in its properties, it was also applied on the plain bitumen to achieve the same effect.

After completion, the asphaltic sample was removed from the can and divided into small containers. The blend was cooled to room temperature, sealed with aluminum foil, and stored in a dark chamber thermostated at 25 °C to retain the obtained morphology. Since pretreatment introduces additional cost, the waste of oyster shell powder was intactly mixed with the binder without any prior treatment. This also allows one to study solely the direct effects of filler on the bitumen performance.

**Table 1.** Chemical and physical properties of AP-5 asphalt (PG/60–70).

Elemental Analysis	
C (carbon)	84.62 wt %
H (hydrogen)	10.39 wt %
N (nitrogen)	0.65 wt %
S (sulfur)	3.69 wt %
O (oxygen)	0.65 wt %
SARA Generic Fractions	
Saturates	4.47 wt %
Aromatics	17.45 wt %
Resins	45.18 wt %
Asphaltenes	32.90 wt %
Physical Properties	
Penetration at 25 °C	60.00 dmm
Softening point	50.00 °C
Ductility at 25 °C	110.50 cm

## 2.3. Fourier Transform-Infrared Spectroscopy (FT-IR)

A HYPERION 3000 FT-IR Spectrometer (Bruker Optics, Ettlingen, Germany) was employed to determine whether there were new functional groups that had been generated through OSP additions. The specimen was prepared with the thin KBr disk method. The asphaltic samples were scanned at 32 times with test range from 400 to 4000  $\text{cm}^{-1}$ . All samples were scanned in duplicate.

## 2.4. X-ray Diffraction (XRD)

The XRD data collection was carried out by a Bruker AXS D8 Advance Diffractometer (Bruker AXS GmbH D8 Advance, Karlsruhe, Germany) employing  $\text{CuK}\alpha$  radiation ( $\lambda = 1.54055 \text{ \AA}$ ). The X-ray generator voltage and current were held at 40 kV and 40 mA, respectively. OSP and asphaltaneous

samples were scanned, at room temperature (ca. 25 °C), from 5° to 100° in 2 $\theta$  range with 0.020° step size and 2 s step<sup>-1</sup> counter-time. Ten (10) consecutive measurements were performed and added to each other to increase peak intensities and reduce the signal to noise ratio. A very broad peak between 13° and 30° and a small hump around 42° were detected in X-ray diffractograms of bituminous samples.

#### 2.5. Thin-Layer Chromatography-Flame Ionization Detection (TLC-FID)

Thin-layer chromatography-flame ionization detection (TLC-FID or Iatroscan) allows for the fractionation of asphalt into four generic fractions, namely, saturates, aromatics, resins, and asphaltenes (SARA) [32]. Chemical compositions of the base asphalt and OSP-filled asphalts were measured by the MK-6 analyzer (Iatron Laboratories Inc., Tokyo, Japan). Sample solutions with concentration of 2% (m/v) were prepared by dissolving 80 mg sample in 4 mL dichloromethane. Afterwards, the chromarods were cleaned and activated in FID-flame; 1  $\mu$ L of the solution was spotted on the chromarod using a spotter. The separation of asphalt binder fractions was performed with a three-stage process. The first development was in *n*-hexane (60 mL) and expanded to 100 mm of the chromarods, the second stage in toluene (60 mL) was developed to 70 mm, and the last development was in mixture of dichloromethane/methanol (60 mL, 95/5 by volume) and expanded to 35 mm. The chromarod was dried at 50 °C for 10 min after each development. Then, the chromarods were scanned in the TLC-FID analyzer. A scan rate of 30 s scan<sup>-1</sup> was used. Air and hydrogen flows were 2000 mL min<sup>-1</sup> and 160 mL min<sup>-1</sup>, respectively. SARA analysis was repeated five times at least to ensure reproducibility and accuracy of the results.

#### 2.6. Scanning Electron Microscope (SEM)

The rheological examination was associated with a morphological characterization of asphalt samples, which was conducted by using a Scanning Electron Microscope (JSM-6010LA, JEOL Ltd., Tokyo, Japan). The evaluation was aimed principally at estimating the distribution of OSP particles in the bituminous matrix and determining possible relationships between the microstructure and rheological performance. The analysis was carried out on the surface of samples (ca. 8 mm width and 2 mm thickness). Since the bitumen is nonconductive material, its surface was metalized by applying a thin coating of gold before starting SEM analysis. The images were then scanned in backscattered electron mode with an acceleration tension of electronic beam equal to 5 kV. This was done to prevent irreversible thermal damage to the sample surface. The specimens were photographed at different magnifications (e.g.,  $\times$ 500 and  $\times$ 3000).

#### 2.7. Thermogravimetric Analysis (TGA/DTGA)

The weight loss of OSP, and untreated and OSP-treated asphalt samples, was monitored by thermogravimetric analysis (TGA) using a TA Instruments TGA Q500 thermogravimetric analyzer (TA Instruments, New Castle, DE, USA). Briefly, a piece of approximately 15–20 mg of specimen was cut out and placed in platinum crucible. The analyses were carried out at temperatures between room temperature (ca. 25 °C) and 1000 °C using a nitrogen gas flow of 150 mL min<sup>-1</sup>. The scanning rate was 10 °C min<sup>-1</sup>. Thermogravimetric parameters such as the temperature of initial weight loss ( $T_{\text{onset}}$ ), temperature of final weight loss ( $T_{\text{offset}}$ ), temperature of maximum rate of weight loss ( $T_{\text{max}}$ ), and carbonaceous residue at 1000 °C ( $\Delta W$ , wt %) were determined from the TGA and DTGA curves. All TGA tests were run in triplicate to ensure reproducibility and accuracy.

#### 2.8. Differential Scanning Calorimetry (DSC)

The DSC heat flow as a function of temperature curves was measured for asphalt using a Perkin-Elmer DSC 8000 (PerkinElmer Inc., Waltham, MA, USA) and for oyster shell powder (OSP) using a NETZSCH Simultaneous Thermal Analyzer (STA) 449 F5 Jupiter<sup>®</sup> (NETZSCH-Gerätebau GmbH, Wittelsbacherstraße, Germany). OSP samples of approximately 10–15 mg were held in DSC-TGA Alumina (Al<sub>2</sub>O<sub>3</sub>) crucibles at the heating rate of 10 K min<sup>-1</sup> under an argon flow



rate of 50 mL min<sup>-1</sup> at temperatures ranging from 28 °C to 1000 °C. To perform DSC scans for bituminous specimens, approximately 15–20 mg of base asphalt or OSP-filled asphalt was transferred to a hermetically sealed pan. The pan containing the sample was then placed in the DSC apparatus and maintained at 50 °C for 10 min. Subsequently, the sample was rapidly cooled down to –90 °C at a cooling rate of 20 °C min<sup>-1</sup> followed by a heating from –90 °C to 150 °C. This cooling and heating cycle was executed to eliminate the thermal history of asphalt sample. Finally, the sample was cooled down to –90 °C, held at this temperature for 10 min, then heated to 150 °C at a heating rate of 20 °C min<sup>-1</sup>. DSC heat flow as a function of temperature data was recorded during the heating process of the second cycle. In this work, DSC test was undertaken to determine the glass transition temperature ( $T_{g1}$ ) of the unfilled and OSP-filled asphalts. Each DSC test was repeated three times at least, to ensure the reproducibility and accuracy of results.

### 2.9. Conventional Asphalt Binder Tests (Penetration, Softening Point, and Ductility)

The physical properties of unfilled and OSP-filled asphalts were evaluated by different empirical tests including softening point, ductility, and penetration. The softening point of binder was determined in accordance with ASTM D36 [33], while the ductility was conducted in accordance with ASTM D113 standard [34]. The penetration test, which indicates the binder hardness, was performed in accordance with ASTM D5 [35]. The penetration index (PI) is considered as a measure of temperature susceptibility of asphalt cement. The temperature susceptibility of bituminous samples was calculated using the results obtained from penetration and softening point tests as follows [36,37]:

$$PI = \frac{1952 - 500 \log (\text{Pen } 25) - 20 \times SP}{50 \log (\text{Pen } 25) - SP - 120} \quad (1)$$

in which Pen 25 is the penetration at 25 °C (dmm) and SP is the softening point (°C) of bitumen sample. The PI values vary usually from –3 for high temperature susceptible asphalts to about +7 for highly blown low temperature susceptible asphalt [1]. Each experiment was repeated three times independently, to ensure the reproducibility and accuracy of results.

### 2.10. Dynamic Shear Rheometer (DSR)

A dynamic shear rheometer (DSR, MCR101, Anton Paar Company, Virginia, USA) was used to measure the rheological properties of unfilled and OSP-filled asphalts. DSR test was conducted in accordance with ASTM D7175-15 [38]. The rutting and fatigue cracking performances of bitumen specimens were assessed through  $G^*/\sin \delta$  and  $G^* \cdot \sin \delta$ , respectively. In this research, the test was conducted from 52 °C to 70 °C at an increment of 6 °C for the rutting performance and from 31 to 19 °C at a decrement of 3 °C for the fatigue cracking performance. For the unaged and RTFO- (i.e., rolling thin-film oven) asphalt samples, a 1 mm-thick plate and 25 mm-diameter top plate was employed. On the other hand, a 2 mm-thick plate and 8 mm-diameter top plate was used for PAV- (i.e., pressure aging vessel) binder specimens. The asphalt was sandwiched between two fixed plates. Stress was applied on top of the sample by the oscillating top plate, which oscillated at 1.59 Hz, to measure the maximum stress, maximum strain, and lag of stress and strain. All test results shown in this work represent the average of three replicates.

## 3. Results

### 3.1. Chemical Composition of Oyster Shell Powder (OSP)

CHNS/O analysis, X-ray fluorescence (XRF), and energy-dispersive spectroscopy (EDS) were used to find out the precise values of calcium oxide (CaO), carbon (C), and oxygen (O), respectively, in the oyster shell powder (OSP) of *Crassostrea gigas*. The concentration of chemicals as per the test results is given in Table 2 and Figure 2. Calcium oxide was observed as the largest constituent at 99.033 wt % following by total oxygen at 34.023 wt %. Elemental analysis confirmed that shell powder

is mainly composed of  $\text{CaCO}_3$ , since the measured carbon content (12.072 wt %) is very close to its theoretical content (12.000 wt %). The remaining elements are sulfur trioxide (0.518 wt %), strontium oxide (0.311 wt %), and nitrogen (0.189 wt %). Ferric oxide ( $\text{Fe}_2\text{O}_3$ ), cupric oxide ( $\text{CuO}$ ), magnesium oxide ( $\text{MnO}$ ), hydrogen (H), and sulfur (S) exist only in minor amounts. The raw material used in this experiment is a highly pure calcite, which is expected to influence the physical and rheological properties of asphalt cement when it is introduced into its matrix [3,4,39,40].

**Table 2.** Chemical composition of oyster shell powder (OSP) as raw material used in this work.

Organic Compounds	Concentration (wt %)
C (carbon)	12.072
H (hydrogen)	0.092
N (nitrogen)	0.189
S (sulfur)	0.000
O (oxygen)	34.023
Total	46.376
Inorganic Compounds	Percentage (wt %)
CaO (calcium oxide)	99.033
$\text{SO}_3$ (sulfur trioxide)	0.518
SrO (strontium oxide)	0.311
$\text{Fe}_2\text{O}_3$ (ferric oxide)	0.086
$\text{CuO}$ (cupric oxide)	0.030
$\text{MnO}$ (magnesium oxide)	0.023
Total	100.00

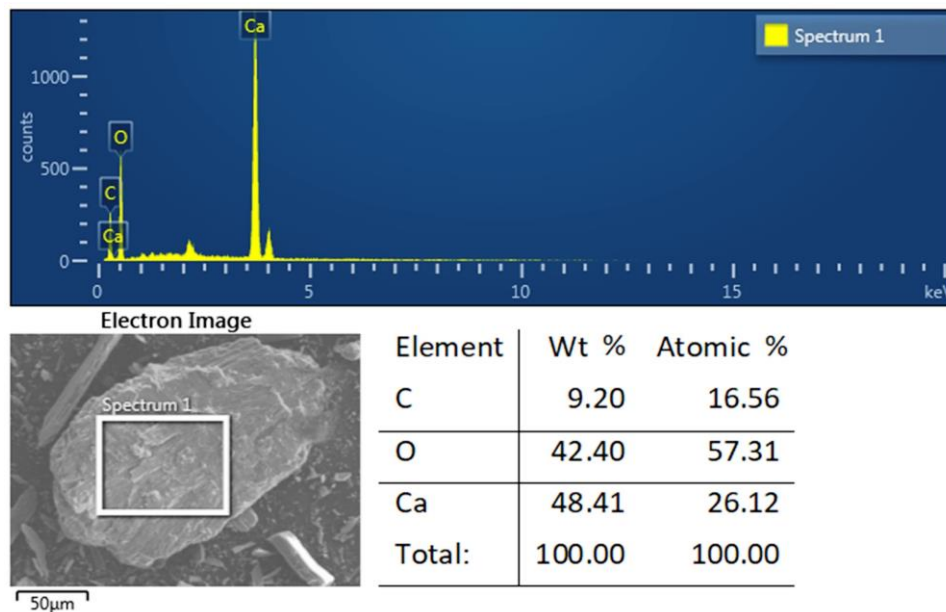


**Figure 2.** Scanning electron microscopy (SEM) with energy-dispersive spectroscopy (EDS) microanalysis for oyster shell powder (OSP).

### 3.2. Particle-Size Distribution (PSD) of Oyster Shell Powder (OSP)

Figure 3 portrays a typical particle size distribution (PSD) histogram of oyster shell powder (OSP) obtained with dry ball grinding. As visualized in this Figure, the sample presents large PSD varying mainly between 111  $\mu\text{m}$  and 211  $\mu\text{m}$ , validating the SEM observation (i.e., powder particles with irregular shapes and different sizes). This behavior could largely be attributed to the higher hardness of the shells, because there is a higher content of calcite in the shells that increases the shell hardness and

strength. Certain characteristic parameters representative of the distribution curve are summarized in Table 3. The size distribution data obtained from a laser diffraction measurement shows that  $D_v(50)$  is  $71.10 \mu\text{m}$ , which represents 50% of particles that are below  $71.10 \mu\text{m}$  (i.e., the median diameter). Similarly,  $D_v(10)$  and  $D_v(90)$  are  $2.98 \mu\text{m}$  and  $307 \mu\text{m}$ , indicating that 10% of particles are below  $2.98 \mu\text{m}$  (i.e., fine fraction) and 90% of particles are below  $307 \mu\text{m}$  (i.e., coarse fraction), respectively. It is generally recognized that the small particles have large, specific surface area (SSA) to interact with asphalt matrix and can be homogeneously dispersed in it, and the opposite is also true [41–43]. Usually, the mineral aggregates of road pavements are suspended throughout a mixture and vary in size from coarse to fine. Adequately compacted asphaltic mixtures generate a structure whose stiffness, stability, and wearing characteristics depend on the cohesiveness of the binder and the interlocking of the aggregates particles. Only the fraction of the mineral filler composed of particles thicker than the asphalt film contributes to the aggregate interlocking. The other fraction of the filler, i.e., the fine particles smaller than the thickness of the asphalt film, is distributed in the asphalt phase and is part of the binder component of the mixture [44].

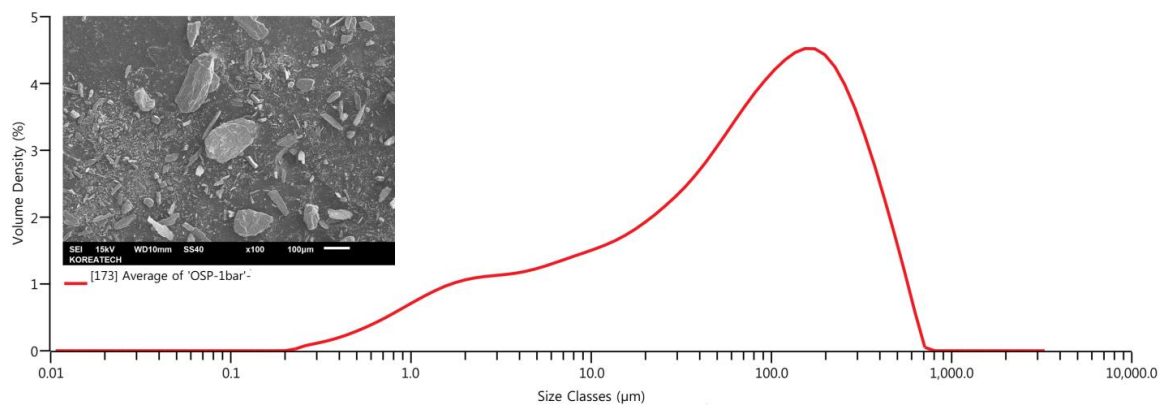


**Figure 3.** Typical particle size distribution for oyster shell powder (OSP) after dry ball milling process.

**Table 3.** Particle-size distribution (PSD) data of oyster shell powder (OSP) achieved using a dispersive air pressure 1 bar.

Parameter	Value
Span	$4.273 \mu\text{m}$
Weighted residual	0.12%
Specific surface area	$0.7582 \text{ m}^2 \text{ g}^{-1}$
D [3,2]	$7.91 \mu\text{m}$
D [4,3]	$117 \mu\text{m}$
$D_v(10)$	$2.98 \mu\text{m}$
$D_v(50)$	$71.10 \mu\text{m}$
$D_v(90)$	$307 \mu\text{m}$
Mode	$162 \mu\text{m}$

Span =  $[D_v(90) - D_v(10)]/D_v(50)$  ( $\mu\text{m}$ ) represents the width or breadth of the distribution based on the 10%, 50%, and 90% quantile. D represents the diameter of powder particles ( $\mu\text{m}$ ). D [3,2]: equivalent surface area mean diameter or the Sauter mean diameter ( $\mu\text{m}$ ). D [4,3]: equivalent volume mean diameter or the De Broncker mean diameter ( $\mu\text{m}$ ).  $D_v(10)$ : 10% of the distribution lies below the  $D_{10}$  ( $\mu\text{m}$ ).  $D_v(50)$ ,  $D_{50}$ , or median, defined as a diameter in which half of the population lies below this value ( $\mu\text{m}$ ).  $D_v(90)$ : 90% of the distribution lies below the  $D_{90}$  ( $\mu\text{m}$ ). Mode, size with highest frequency ( $\mu\text{m}$ ), represents the particle size (or size range) most commonly found in the distribution.

### 3.3. Fourier Transform-Infrared Spectroscopy (FT-IR)

Possible interactions between the oyster shell powder (OSP) and the bitumen matrix were analyzed using FT-IR spectroscopy. The OSP, base asphalt, and OSP-filled asphalts were examined for this purpose. The FT-IR spectra of OSP, and unfilled and OSP-filled asphalts, are given in Figure 4.

As can be seen, all samples are characterized by various bands ranging from 400 to 4000  $\text{cm}^{-1}$ . Referring to the IR spectra of plain bitumen (i.e., AP-5 OSP 0 wt %) and filler-asphalt mastics, the absorption bands at 722  $\text{cm}^{-1}$  correspond to the rocking vibration of the group  $(-\text{CH}_2-\text{CH}-)_n$ . The absorption bands at 1376  $\text{cm}^{-1}$  are assigned to the symmetric bending vibration of  $\text{CH}_3$  functional group, whereas, the absorption bands at 1457  $\text{cm}^{-1}$  are due to the asymmetric bending vibration of  $-\text{CH}_3$  groups and the scissor bending vibration of  $-\text{CH}_2-$  groups. The absorption bands at 2851  $\text{cm}^{-1}$  and 2921  $\text{cm}^{-1}$  result from the symmetric stretching of  $-\text{CH}_3$  and the asymmetric stretching of  $-\text{CH}_2-$ , respectively. In the OSP spectrum, the small peak located at 1794  $\text{cm}^{-1}$  may correspond to the combination vibrations of  $-\text{NH}-$  *in*-plane bending and  $\text{C}=\text{O}$  stretching. The shoulder of carbonate compounds (e.g., bicarbonate ion,  $\text{HCO}_3^-$ ) occurs at 2513  $\text{cm}^{-1}$ . On the other hand, the intensities of the  $\text{C}-\text{O}$  bands of oyster shell powder between 500  $\text{cm}^{-1}$  and 1500  $\text{cm}^{-1}$  are the strongest. The multiple bands observed at 712, 874, 1159, and 1396  $\text{cm}^{-1}$  are ascribed to the *in*-plane bending vibration, the *out*-of-plane bending vibration, the symmetric stretching, and the asymmetric stretching of carbonate ion (i.e.,  $\text{CO}_3^{2-}$ ), respectively [45,46]. From the foregoing data, it is evident that no new characteristic absorption bands of OSP/asphalt blends was generated, thereby demonstrating that no chemical reaction took place between the oyster shell powder and the asphalt cement.

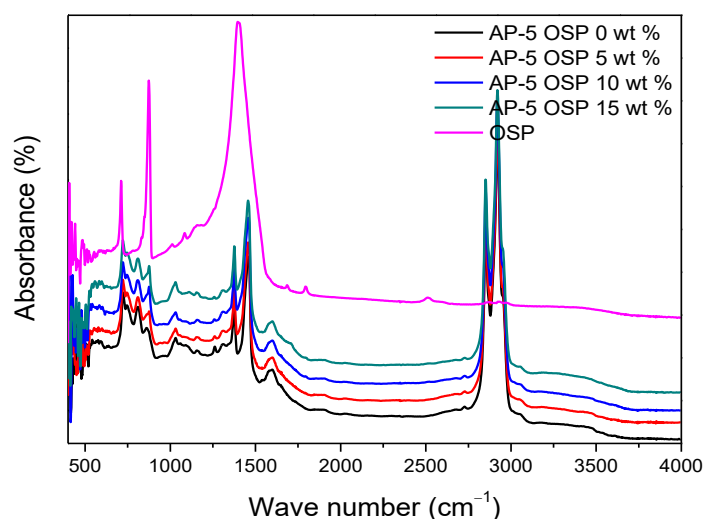


Figure 4. FT-IR spectra of OSP, neat asphalt, and OSP-filled asphalts.

### 3.4. X-ray Diffraction (XRD)

X-ray diffraction (XRD) patterns of OSP, neat asphalt, and OSP-filled asphalts are shown in Figure 5. Oyster shells are biological wastes, which are mainly made up of calcium carbonate ( $\geq 96$  wt %) and minor amounts of other minerals. It can clearly be seen that the major crystalline phase of oyster shell waste is calcite (i.e.,  $\text{CaCO}_3$ ). No peaks due to other phases were detected, indicating the high purity of raw material under study. X-ray diffraction of neat asphalt sample (AP-5 OSP 0 wt %) was analyzed and the diffractogram is presented in Figure 5. Figure 5 shows that most of the peaks appear at around  $2\theta$  value of  $20^\circ$  and  $25^\circ$ . The  $\gamma$ -peak, which occurs at approximately  $2\theta = 20^\circ$ , mirrors the packing distance of saturated structure that comes from the X-rays scattered by the aliphatic chains or the condensed naphthenic rings. It has been reported that this band arises principally from paraffins order [47]. The (002) peak or graphene peak, which appears at about  $2\theta = 25^\circ$ , is due to the diffraction of X-rays from the stacks of aromatic sheets. The (10) and (11) peaks, or (100) and (110) reflections, originate from the *in*-plane structure of the aromatic molecules. They refer to the first and second nearest neighbors in the ring compounds. Generally, the size of an aromatic sheet is often determined from the (10) peak ( $2\theta = 40^\circ$ ), and not from (11) peak, due to its very weak intensity [48]. It is widely known that when the peaks in the XRD patterns are broader, the more short range exists in that

structure type. This case comprises the unfilled and OSP-filled asphalts. On the other hand, when the XRD pattern peaks are sharper and narrower, the more highly crystalline phase with high degree of long-range order exists. The oyster shell powder meets this criterion. As demonstrated by XRD patterns, with the increase in OSP dosage from 5 to 15 wt %, the intensity of the  $\text{CaCO}_3$  peaks gradually increased without affecting the XRD profile of the base bitumen. This suggests that OSP exists stably in the binder structure, which means that its addition did not cause any change in the crystalline phase of bitumen (governed chiefly by asphaltene compound). Accordingly, it can be assumed that the OSP has no chemical reaction in the asphalt system and exists independently with only filling effect.

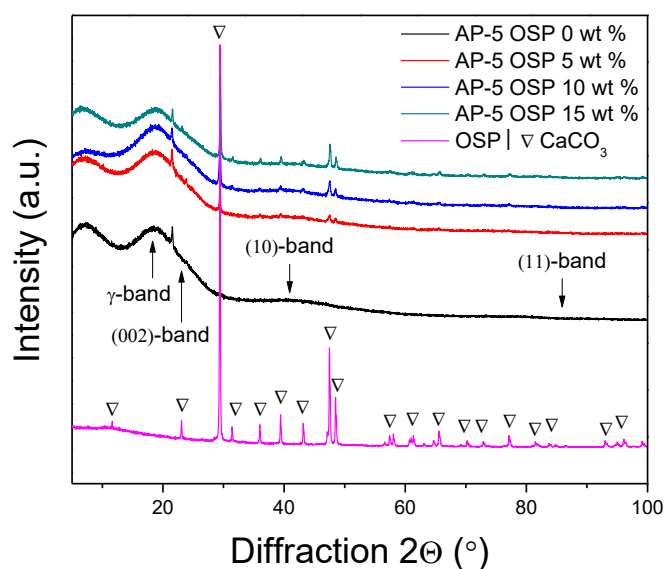


Figure 5. XRD patterns of OSP, neat asphalt, and OSP-filled asphalts.

### 3.5. Thin-Layer Chromatography-Flame Ionization Detection (TLC-FID)

To gain deeper insight into the impact of oyster shell powder (OSP) on the composition of asphalt cement, this latter was divided into SARA (i.e., saturates, aromatics, resins, and asphaltenes) fractions by using standard procedure based on adsorption chromatography (e.g., TLC-FID) [32]. Figure 6 pinpoints the distribution of SARA type hydrocarbons in the base asphalt (i.e., AP-5 OSP 0 wt %) and asphalt treated with different proportions (e.g., 5, 10, and 15 wt %) of OSP. Curiously, it shows that the composition of asphalt changed after the addition of OSP. The fraction of aromatics components decreased; meanwhile, the fraction of resins increased. The remaining species such as saturates and asphaltenes did not undergo any significant changes. The changing of such composition fraction implies that the aromatics in lighter fractions of asphalt were more probably changed to resins. In other terms, it seems that the aromatics were selectively interacted with OSP surface [49,50] and readily converted into resin-like structures (see Figure 7). The oyster shell powder (i.e.,  $\text{CaCO}_3$ ) with high calcium content is naturally hydrophilic material and tends to create strong bonds with hydrophobic organic compounds such as bitumen. The strong bonding between the calcite (mainly calcium sites) and adsorbate aromatic molecules most likely involved the carboxylic, hydroxylic, and amines groups; some van der Waals and electrostatic interactions may have also occurred [49,50]. This is a very interesting finding that necessitates further in-depth investigation.

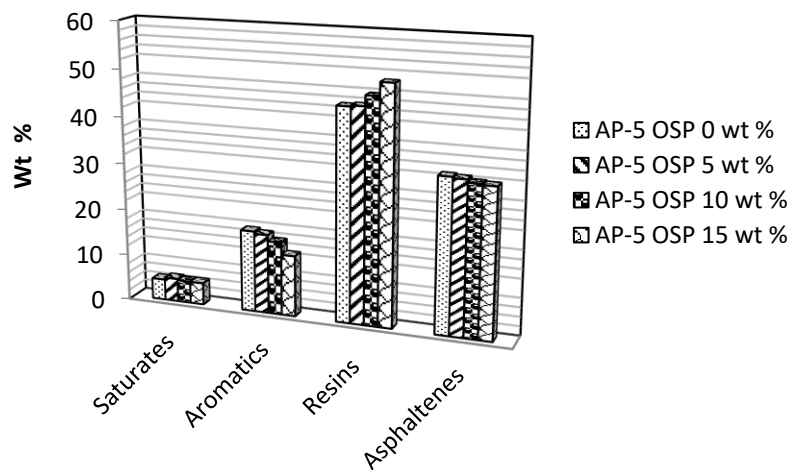


Figure 6. Chemical composition of unfilled and OSP-filled asphalts.

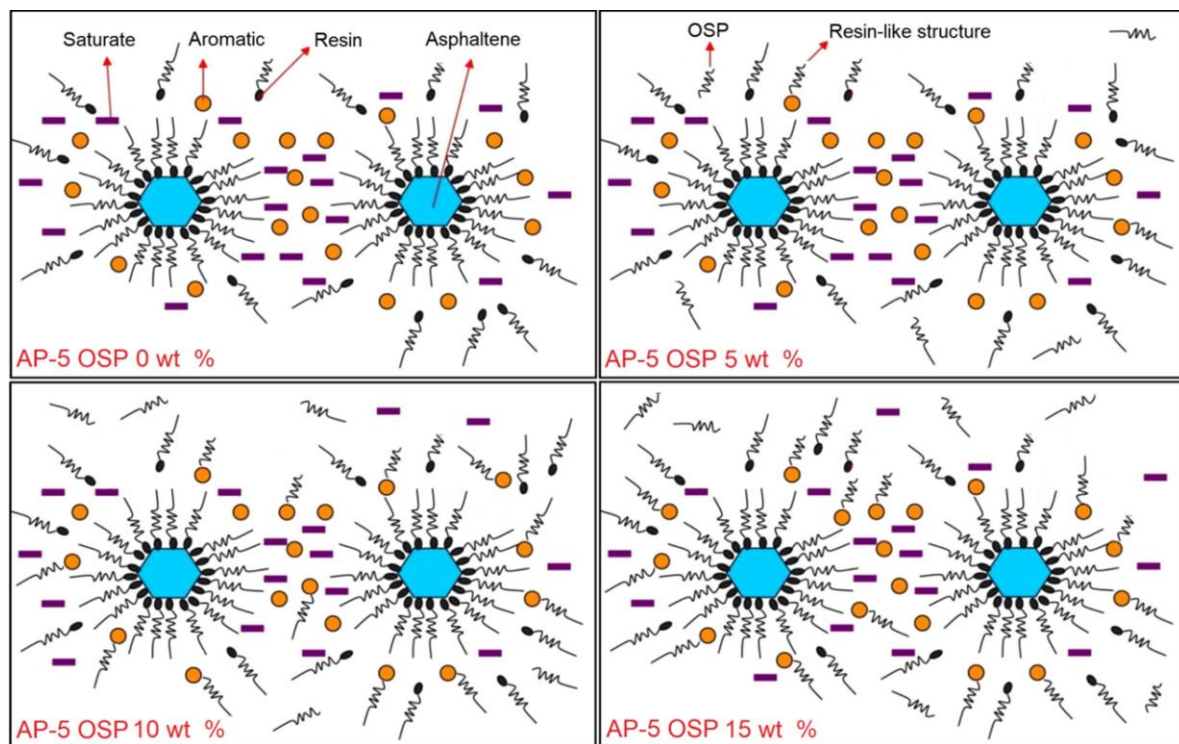


Figure 7. Adsorption of aromatic components on oyster shell powder surface at different doses (e.g., 0, 5, 10, 15 wt %) and creation of resin-like structures.

### 3.6. Conventional Asphalt Binder Tests (Penetration, Softening Point, and Ductility)

The results of empirical tests such as penetration, softening point, and ductility for unfilled and OSP-filled asphalts are given in Table 4. It is readily seen by reference to this Table that the physical properties of asphalt were greatly affected following the addition of OSP. The penetration and ductility of filled asphalt were decreased, whereas its softening point was increased.

The OSP essentially stiffens the binder due to three major reinforcement mechanisms:

- (1) Volumetric-filling reinforcement: the stiffening caused by the presence of rigid inclusions (e.g., mineral filler) in a less rigid matrix (e.g., viscoelastic binder).



- (2) Physicochemical reinforcement: the stiffening caused by the interfacial effects between filler particles and asphalt, including adsorption, absorption, and selective sorption. Here, the treated asphalt efficiently creates a rigid layer, which leads to a higher net volume concentration of rigid matter, increasing thereby the mastic stiffness.
- (3) Particle-interaction reinforcement: the stiffening beyond physicochemical reinforcement and volume filling. This effect increases with increasing filler dosage, as rigid matter accumulates a skeletal framework form [51].

Too much OSP could over-stiffen the road surface, making it more susceptible to cracking or raveling. Therefore, special caution should be taken when using this biofiller. The increase in softening point is desired, as the binder with high softening point is less susceptible to permanent deformation. Therefore, asphaltic mixtures prepared with oyster shell powder (OSP) are initially expected to have better rutting performance. Also, the softening point variation is quietly similar to viscosity variation. Actually, these two physical properties are firmly linked, since it is logical to assume that asphalts with high softening point are also more viscous than those that have low softening point. The OSP does not form a homogenous liquid with asphalt, but remains a solid, which has an impact on the increase in viscosity, which is an indicator of fluid resistance against shear [52,53]. By increasing the addition of a solid that is insoluble in asphalt, one should expect the increase of mixture viscosity, regardless of the asphaltene content in the base asphalt.

This prediction was also made based on direct observation taken during the mixing process. Astonishingly, it was noticed that the blends were becoming overly viscous, with further OSP incorporation (particularly with 15 wt %). This increase in viscosity is attributed essentially to the higher asphaltene content of the base AP-5 asphalt (ca. 32.90 wt %). It has been reported that the asphalt with greater asphaltene content, when compounded with basic filler (e.g.,  $\text{CaCO}_3$ ), will result in higher viscosity, while acid filler (e.g., granite) will result in lower viscosity [54]. If a large quantity of biofiller is added, the HMA (i.e., hot-mix asphalt) blend will become difficult to dump, spread, and compact. Accordingly, special attention should be bestowed on the selected OSP dose in order to achieve an adequate consistency.

Table 4 also illustrates that, in all cases, as the mineral filler content increased in the asphalt cement, the ductility (at 25 °C) decreased very rapidly. These results revealed that the mastics tend to crack due to the asphalt elongation, which decreased as the OSP content increased. Low ductility indicates that the bitumen is brittle and will fracture before deforming much under a tensile load. Owing to its high surface area, the OSP formed strong bonds with the binder matrix, promoting the bitumen cohesion.

For a great numerous technical applications, the changes in consistency between 0 °C and the temperature of softening point form a highly important and much-discussed quality consideration in judging the utility of an asphaltic bitumen. This property of temperature susceptibility as reflected by penetration index (PI) proposed by Pfeiffer and van Doormaal has been related to various mastic properties and OSP contents. According to Table 4, the PI values of asphalt binder were increased as the OSP content increased in the mastic. Therefore, the temperature susceptibility of binders was decreased by increasing the quantity of OSP. The PI varies generally from  $-3$  to  $+7$  [1]. Asphalt with high thermal susceptibility has PI of  $-3$  (e.g., most sol-asphalts and those extracted from cracking processes), and asphalt binder with PI of  $+7$  (e.g., most gel-asphalts, blown asphalts) is insusceptible to variations in temperature [55]. Asphalt binder with higher PI yields less temperature susceptibility that leads to an improvement in rutting resistance and reduction in low temperature cracking [56]. In light of information available from conventional test methods, it can be reasonably assumed that the mixing of asphalt binder with OSP could have a positive impact on improving temperature susceptibility, rutting performance, and low temperature cracking.

**Table 4.** Physical properties of unfilled and OSP-filled asphalts.

Sample	Penetration at 25 °C (dmm)	Penetration Index (PI)	Softening Point (°C)	Ductility at 25 °C (cm)
AP-5 OSP 0 wt %	60.00	−0.77	50.00	110.50
AP-5 OSP 5 wt %	58.20	−0.11	53.00	103.33
AP-5 OSP 10 wt %	55.10	+0.80	57.70	95.10
AP-5 OSP 15 wt %	52.50	+1.24	60.50	89.50

### 3.7. Dynamic Shear Rheometer (DSR) Test

#### 3.7.1. Rutting Performance ( $G^*/\sin \delta$ )

The high temperature performance grade of each bitumen sample was determined using DSR (i.e., dynamic shear rheometer) test results ( $G^*/\sin \delta$ ) and the Superpave (i.e., Superior Performance Asphalt Pavement) binder specification. Based on the specification to minimize rutting,  $G^*/\sin \delta$  at  $10 \text{ rad s}^{-1}$  must have a minimum of 1 kPa for unaged bitumen sample and 2.2 kPa for rolling thin-film oven (RTFO)-aged bitumen sample [38]. The Superpave rutting parameter  $G^*/\sin \delta$  is inversely proportional to the dissipated energy, and thus higher  $G^*/\sin \delta$  will have lesser dissipated energy, and thus higher rut resistant. Figure 8 shows the DSR results, at various temperatures (e.g., 52, 58, 64, and 70 °C), for the unaged base asphalt (i.e., AP-5 OSP 0 wt %) and unaged asphalt containing different fractions of OSP (e.g., 5, 10, 15 wt %). The performance grade of neat asphalt (i.e., AP-5 OSP 0 wt %) was 64 °C prior to failure at 70 °C. Whereas, the 5 and 10 wt % OSP-filled asphalt samples can resist rutting until 70 °C. Their rutting parameters ( $G^*/\sin \delta$ ) were higher than those of the neat asphalt sample. The  $G^*/\sin \delta$  values recorded at 70 °C for 5, 10, and 15 wt % OSP, were 1175, 1484, and 832 Pa, respectively. The most outstanding value of rutting resistance was observed with 10 wt % OSP. High rutting parameter was observed from 52 °C to 70 °C. The rutting resistance increased as the OSP content increased up to 10 wt % OSP, followed by a decrease with 15 wt % OSP. This may be due to the agglomeration among the OSP particles with further increment of additive in asphalt cement blends. Generally, this finding showed that the OSP increased the stiffness of the virgin bitumen. The mineral particles (i.e.,  $\text{CaCO}_3$ ) seemingly reinforced the bitumen matrix by increasing the bond strength between the filler and binder combinations, improving thereby the cohesion of the bitumen. Consequently, the bitumen properties were enhanced by increasing the stiffness and improving rutting performance.

The RTFO-asphaltic samples shown in Figure 9 demonstrate clearly that both the unfilled and 15 wt % OSP-filled asphalt samples resisted rutting until 64 °C before failing at 70 °C. After short-term aging, all the samples obviously became markedly stiff, thereby increasing the rutting resistance. The asphalt mixtures containing 5 and 10 wt % OSP showed higher performance compared to the neat asphalt and asphalt treated with 15 wt % OSP at all the tested temperatures practically. These results are in tune with those obtained from unaged OSP-asphalt mastic samples. The rutting resistance values of the asphalt filled with 10 wt % OSP at 52 °C were 17,250 Pa and 2794 Pa at 70 °C, which were the highest of all aged asphalt samples. Furthermore, rutting performance showed significant differences between the OSP contents. The 15 wt % OSP obtained the lowest rutting parameters at 64 °C and 70 °C with  $G^*/\sin \delta$  of 2960 and 1886 Pa, respectively. This asphalt exhibited a lower stiffness than the OSP-filled asphalt samples during short-term aging. The large surface area of the OSP absorbs and distributes the heat rapidly relative to the unfilled asphalt, which stands alone at distributing the heat in the slow rate and causing the bitumen to age swiftly. Therefore, 10 wt % OSP was the optimum dose that could retard the aging of the bitumen at higher temperature compared with other OSP fractions (e.g., 5 and 15 wt %). The results of penetration and softening point tests shown in Table 4 confirm the positive impact of OSP on high temperature of filled bitumens.



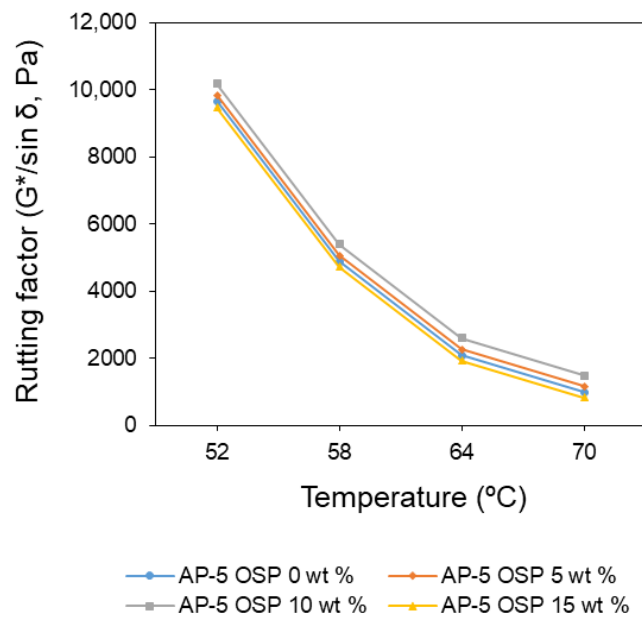


**Figure 8.** Effect of temperature on the rutting parameter of unfilled and OSP-filled asphalts under unaged condition.

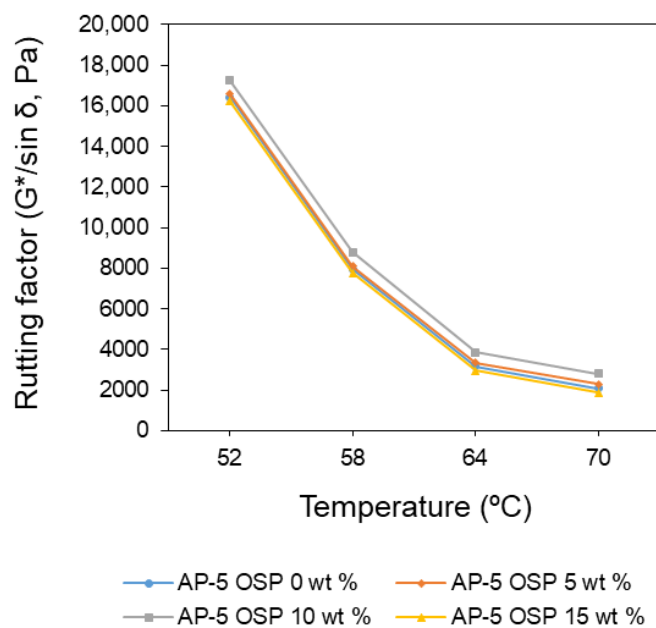


**Figure 9.** Effect of temperature on the rutting parameter of unfilled and OSP-filled asphalts under short-term aging condition (RTFO: rolling thin-film oven).

### 3.7.2. Fatigue Cracking Performance ( $G^* \cdot \sin \delta$ )

$G^* \cdot \sin \delta$  is the fatigue cracking factor in the Superpave (i.e., Superior Performance Asphalt Pavement) binder Specification. Requirement to address fatigue cracking in Superpave binder specification is that  $G^* \cdot \sin \delta$  at  $10 \text{ rad s}^{-1}$  shall not exceed 5000 kPa [38]. Thus, low values of  $G^*$  and  $\delta$  are considered desirable attributes from the standpoint of resistance to fatigue cracking. The higher  $G^* \cdot \sin \delta$  value, the more fatigue cracking is susceptible the bitumen. Figure 10 displays the fatigue cracking performance of the base asphalt (i.e., AP5 OSP 0 wt %) and asphalts treated with different concentrations of OSP (e.g., 5, 10, and 15 wt %) under the PAV (i.e., pressure aging vessel) condition.

The increasing trend of the master curve highlighted that the treated samples resist fatigue cracking from intermediate to lower temperatures (e.g., 31, 28, 25, 22, and 19 °C). The failure temperature was reached when the fatigue cracking parameter ( $G^* \cdot \sin \delta$ ) exceeded 5000 kPa. From the foregoing data it is obvious that 15 wt % OSP exhibited  $G^* \cdot \sin \delta$  value of 5325 kPa, which failed at temperature of 19 °C. Also, the failure temperature of the base asphalt sample was attained at 19 °C, with  $G^* \cdot \sin \delta$  value of 5225 kPa. Similarly, failure temperature was observed on 5 wt % OSP-filled asphalt with a recorded  $G^* \cdot \sin \delta$  value of 5125 kPa. The optimum was reached only with 10 wt % OSP-filled asphalt sample, because it showed lower  $G^* \cdot \sin \delta$  value than the base asphalt and met the Superpave minimum requirement at 19 °C ( $G^* \cdot \sin \delta = 4925$  kPa). It becomes clear that 10 wt % OSP exhibits higher resistance to fatigue cracking as compared with other OSP contents.

The higher geometric irregularity of the OSP yields higher adsorption intensity. This effect will result in a strengthening of the filler-binder bonds and a relative increase in the fixed binder amount, while the mastic will get higher consistency and strength (i.e., stiffness) than the control specimen. However, during the service life of the road pavement, bitumen tends to stiffen due to oxidation phenomenon, leading to fatigue cracking. In this investigation, the absorbed heat in the OSP-filled asphalts during high temperatures was stored longer than that in the neat asphalt. Thus, during the decrement of test temperature, the OSP slowly released the heat and the heat loss under equilibrium condition, which helped to maintain the viscoelasticity of the bitumen instead of rapidly releasing the heat and stiffening its matrix. Overall, an intermediate dose of OSP (i.e., 10 wt %) can retard the aging process effectively as compared with 5 and 15 wt % OSP-asphalt mastic samples. The large surface area of the OSP particles delayed the heat loss, especially, when more appropriate amounts were added. With the viscoelasticity of the bitumen and its capacity to resist rutting and cracking under consideration, 10 wt % OSP was considered as the optimum filler dose for bitumen because of its superior performance compared to that of the control binder.

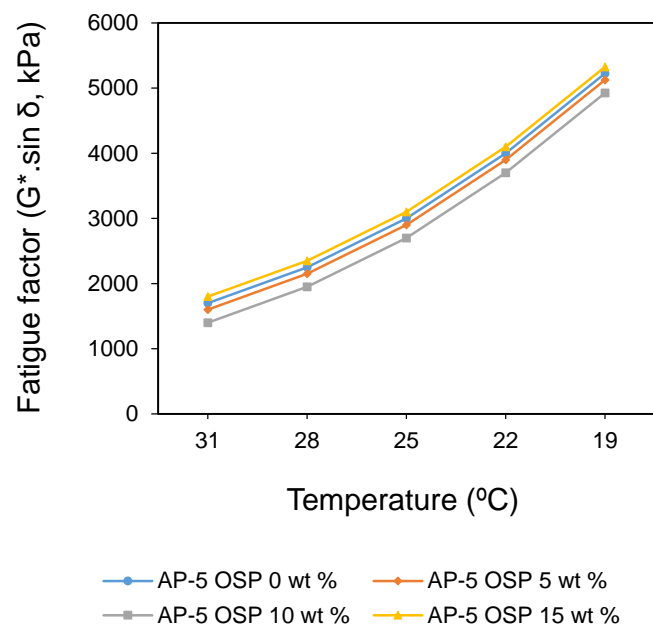


**Figure 10.** Effect of temperature on the fatigue cracking parameter of unfilled and OSP-filled asphalts under long-term aging condition (PAV: pressure aging vessel).

### 3.8. Scanning Electron Microscope (SEM)

The possible interaction between OSP particles and asphalt binder was further assessed by SEM imaging analysis for a better understanding of the rheological findings. This approach permitted the identification of inorganic filler distribution inside the bituminous matrix, thus helping to explain

the differences detected in fatigue and rutting behaviors between unfilled and OSP-filled asphalts. Figures 11 and 12(A1,2–D1,2) display the SEM patterns of OSP, base asphalt (i.e., AP-5 OSP 0 wt %), and asphalt treated with different concentrations of OSP (e.g., 5, 10, 15 wt %). The SEM micrographs were taken at different levels of magnification (e.g.,  $\times 100$ ,  $\times 500$ , and  $\times 3000$ ). In the low magnification SEM images (Figure 11,  $\times 100$ ), it can clearly be seen that the OSP comprises some large particles and high fraction of fine particles, which resulted in a more heterogeneous distribution. The comminuted powder exhibits an irregular crystal structure of densely attached fine grains (e.g., width 1–130  $\mu\text{m}$ , length 1–246  $\mu\text{m}$ ) caused probably by the mechanical effect during dry grinding. These results are also being well observed in particle size distribution curves in Figure 3. The filler is detectable as angular and rough particles with schistous structure and low propensity to agglomerate.

By examining the SEM images of AP-5 asphalt treated with 5 and 10 wt % OSP, the presence of filler in the asphaltic matrix can be easily detected in the form of uneven distributed aggregates. On the contrary, it is worth mentioning that in the case of neat asphalt (i.e., AP-5 OSP 0 wt %), the SEM image reveals the existence of a continuous network that is characterized by a uniform, smooth, and homogeneous surface. As seen in Figure 12 (B1,2,C1,2), the OSP in different shapes (i.e., mainly in flat shapes) could be obviously identified in the asphalt bulk. Generally, it can be found that the oyster shell powder (i.e., dispersed phase) and asphaltic material (i.e., viscoelastic matrix) exist independently, establishing that there is perhaps no chemical reaction between them. Hence, as one mineral admixture, OSP mainly plays its role through “micro-aggregate filling effect” and “morphological effect” in the bituminous material. The micro-aggregate filling effect means that the micro-particles of mineral admixture spread evenly across the basic phase of asphalt with the consolidation and filling effects. On the other side, the morphological effect arises from the effect caused by grain composition, surface property, internal structure, external morphology, and other physical features of the particles. These two effects supplement each other and are interrelated.

The oyster shell powder obtained with dry ball grinding is finer and barely homogeneous, and thus its addition made the particle stacking in the asphalt much closer. It can be assumed that there is fairly better interface binding among particles, so the asphalt strength is improved, especially for early strength (generated particularly with 5 and 10 wt % of filler). Therefore, when the content of added OSP is increased to 15 wt %, the asphalt strength (i.e., stiffness and hardness) shows an increased trend. This tendency to rise is largely dictated by the physical properties of oyster shell powder such as gradation, specific surface area, shape, and porosity. Oyster shell powder is an amorphous material that agglomerates at higher concentration and can significantly affect the mechanical properties of resultant composite.

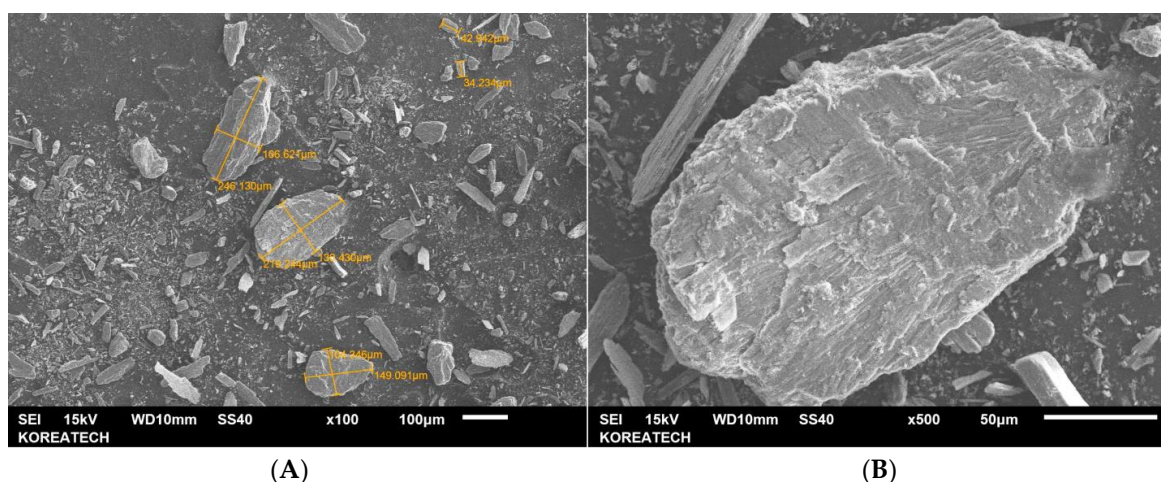


**Figure 11.** Scanning electron microscope (SEM) micrographs of oyster shell powder (OSP) obtained with dry ball grinding at different magnifications  $\times 100$  (A) and  $\times 500$  (B).

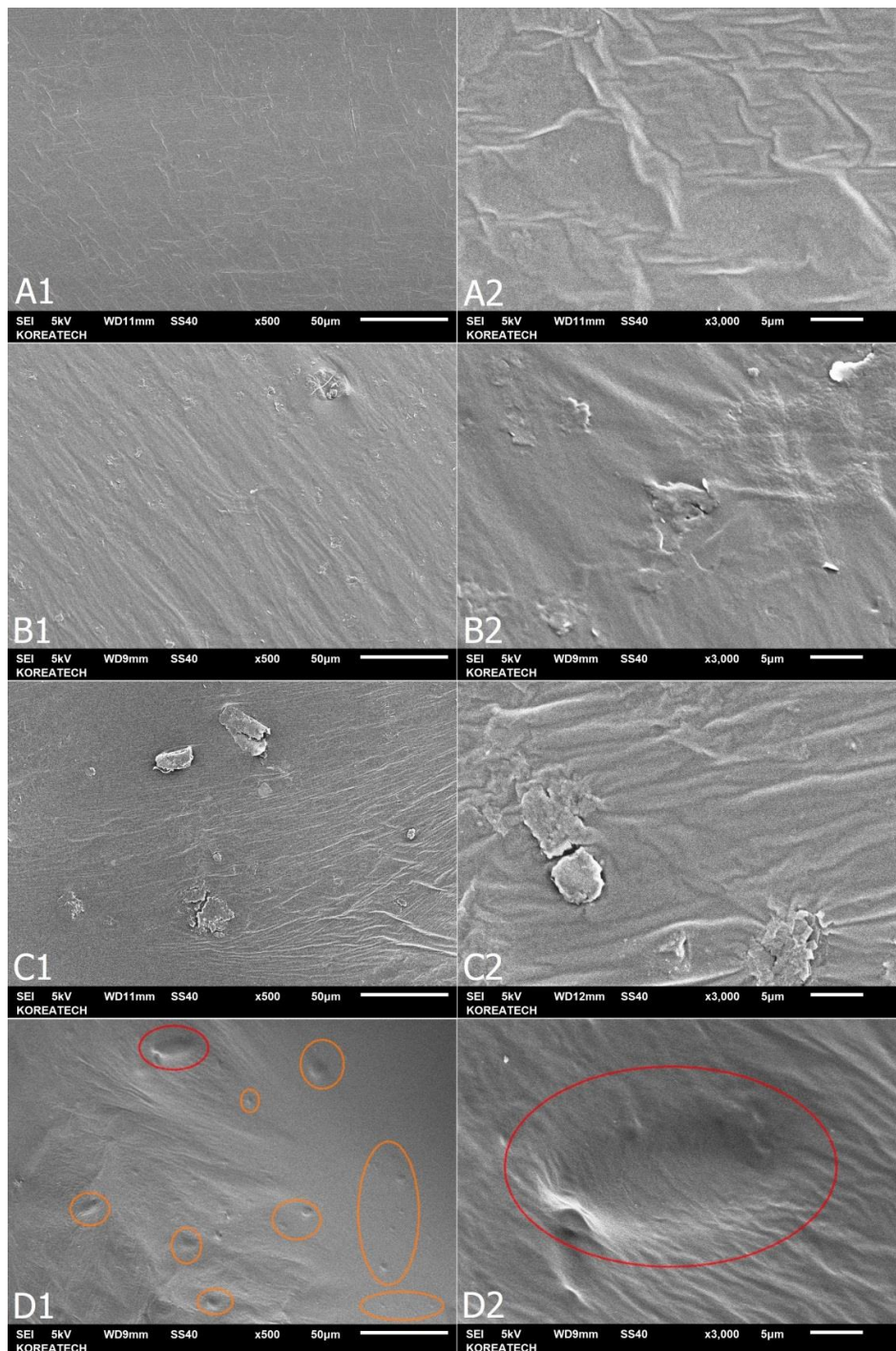


**Figure 12.** Scanning electron microscope (SEM) micrographs of unfilled and OSP-filled asphalts taken at  $\times 500$  [denoted with number 1] and  $\times 3000$  [denoted with number 2] magnifications. (A) AP-5 OSP 0 wt %; (B) AP-5 OSP 5 wt %; (C) AP-5 OSP 10 wt %; (D) AP-5 OSP 15 wt %.

The SEM micrographs of 5 and 10 wt % OSP-filled asphalts (Figure 12(B1,2,C1,2)) display a more uniform material, since filler particles are well embedded in the bituminous phase, creating a more efficiently collaborative morphological structure between bitumen and filler. Nevertheless, in the case of the 15 wt % OSP-filled asphalt (Figure 12(D1,2)), it can be seen that there are certain number of holes or large amount of voids (highlighted with orange and red circles) due to detachment of OSP grains. This is most likely due to the poor bonded interfacial area between filler and binder matrix, which



causes brittle deformation of the bio-composite. In turn, this implies the formation of agglomerate structures (i.e., irregular particle clusters or flocs) in the bituminous phase, thereby creating an internal discontinuous network that is unable to properly englobe the filler particles. Contrarily, with regard to the 5 and 10 wt % OSP-filled binders, the bitumen is able to entirely coat the filler particles. This finding further supports the results obtained in terms of rutting and fatigue performances of the 15 wt % OSP-treated asphalts as compared to those of the 5 and 10 wt % OSP-treated ones.

### 3.9. Thermogravimetric Analysis (TGA/DTGA)

Response of the bio-composite specimens to thermal loads was assessed using TGA/DTGA (i.e., thermogravimetric and derivative thermogravimetric). The percentage of weight loss (i.e., degradation, wt %) versus temperature increase is displayed in Figure 13. TGA analysis was performed under an inert atmosphere of nitrogen (i.e., N<sub>2</sub>) and from 25 °C to 1000 °C. This temperature range was chosen, not only to simulate the temperature at which the HMA (i.e., hot mix asphalt) is produced (150–190 °C) but also to gain some insight into the material stability when it is subjected to higher temperatures. The TGA/DTGA curves of OSP, and unfilled and OSP-filled asphalts, are depicted in Figures 13 and 14, respectively. Table 5 lists the different events that occurred during the experiment. As shown in Figure 13, it is apparent that there are three typical decomposition stages for neat asphalt (i.e., AP-5 OSP 0 wt %): (1) The first phase of mass loss happened in the temperature up to around 362.23 °C, corresponding to release of oil content from the asphaltic samples (i.e., mainly saturates and aromatics). (2) Afterwards, there was a minor variation in weight, and then substantial weight loss occurred again in the second stage from approximately 362.23 °C to 457.56 °C, which was primarily caused by the thermal degradation of hydrocarbonaceous materials (i.e., resins and some portion of asphaltene fraction). (3) The last stage occurred, corresponding to the combustion of the remaining asphaltenes and the formation of char residues (ca. 14.29 wt %) [57].

TGA was conducted also to determine the calcination characteristics of the oyster shell powder. The TGA profile of OSP is shown in Figure 13. It is evident that in the first stage, the humidity was removed from OSP (i.e., CaCO<sub>3</sub>), i.e., only 1.33 wt %. According to European Standards UNE-EN 13043 [58], the moisture content of filler for bituminous mixtures should be below 1 wt %. However, OSP was found to contain 1.33 wt % of humidity, which may cause stripping in HMA (i.e., hot mix asphalt) pavements and ultimately result in premature failure. Accordingly, the water should be removed to ensure proper adhesion between bitumen and the aggregate surface, thus providing the mixture with adequate resistance to moisture, the most deleterious factor affecting road pavement quality [59]. On the other hand, like many other additives (e.g., natural and synthetic zeolites) [60–62], the water-containing OSP could be used in the production of WMA (i.e., warm mix asphalt). The most common WMA technology utilizes asphalt foaming by adding a small amount of water into the hot binder or directly to the aggregate and asphalt mixer [60]. This process allows the asphalt mixture to have good workability during laying and compaction, and durability during traffic exposure [63].

At the second stage from 641.31 °C to 710.76 °C, the total weight loss referred to loss of carbon dioxide (CO<sub>2</sub>) as 42.78 wt %. Theoretical weight loss is known to be 44 wt %. In the third stage at 710.76–999.98 °C, the total weight loss was 45.09 wt %. There was a considerable change in the weight of the oyster shell powder as the temperature was raised from 25.21 °C to 999.98 °C due to calcination reactions, which commenced at 641.31 °C; however, the complete calcination of OSP resulting in a phase-change of the sample was only achieved at 999.98 °C. A major component of the oyster shell powder was identified as pure CaCO<sub>3</sub> at the temperature of 641.31 °C. The moisture and organic content removal was achieved below 641.31 °C. When temperature was raised from 641.31 °C to 710.76 °C, CaCO<sub>3</sub> (i.e., calcite, calcium carbonate) and CaO (i.e., lime, calcium oxide) were identified as the main components of the OSP. The calcination under inert atmosphere led to a mass loss of 45.09 wt %. A major component of the oyster shell powder at temperatures above 710.76 °C was identified as pure crystalline CaO. It can be admitted that most of the oyster shell was transformed

to CaO by final pyrolysis at temperatures higher than 710.76 °C. Hence, this infers that the optimum temperature of calcination of oyster shell was reached at a temperature range of around 641.31 °C.

The initial degradation temperatures ( $T_{onset}$ ) of unfilled and OSP-filled asphalts were determined by the bi-tangent method and presented in Table 5. Owing to the addition of 5 and 10 wt % OSP, the thermal stability of the mastics was well developed, but not with 15 wt %. The oyster shell powder is a sort of inorganic material, which is difficult to degrade like organic material. When it interacts with the asphalt matrix, it can obviously improve the thermal stability of resultant composite. This is similar to the physical properties mentioned previously, and OSP not only strengthens the physical properties (i.e., stiffness) but also increases the thermal stability.

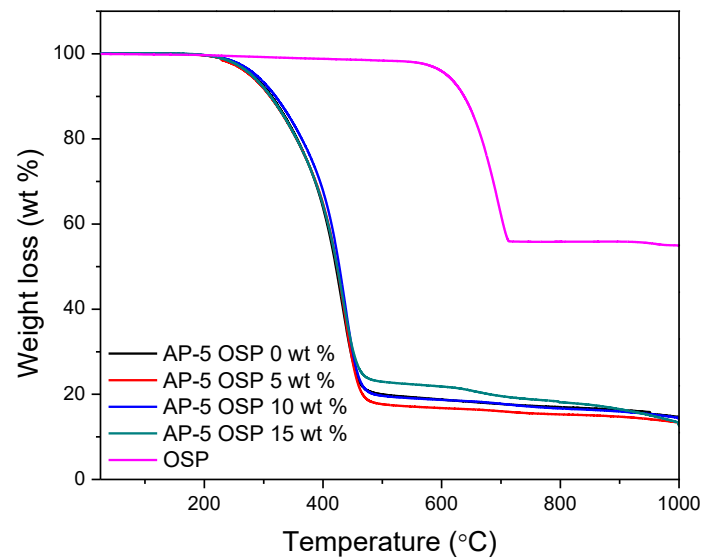


Figure 13. TGA thermograms of OSP, neat asphalt, and OSP-filled asphalts.

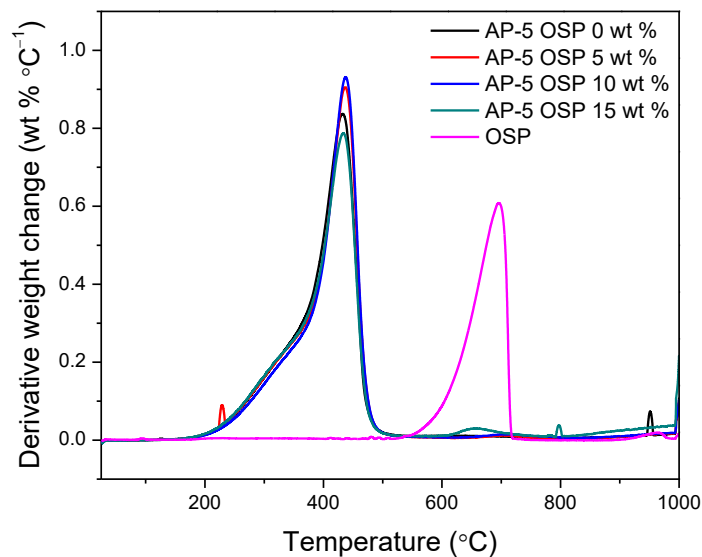


Figure 14. DTGA thermograms of OSP, neat asphalt, and OSP-filled asphalts.

**Table 5.** TGA and DTGA thermogram data of OSP, neat asphalt, and OSP/asphalt blends containing 5, 10, and 15 wt % OSP loading at heating rate of 10 °C min<sup>-1</sup>.

Sample	TGA/DTGA (°C)						−ΔW (wt %)
	Stage 1	Stage 2	Stage 3	T <sub>onset</sub>	T <sub>offset</sub>	T <sub>max</sub>	
OSP	25.21–641.31	641.31–710.76	710.76–999.98	641.31	710.76	695.89	54.91
AP-5 OSP 0 wt %	25.39–362.23	362.23–457.56	457.56–999.97	362.23	457.56	432.27	14.29
AP-5 OSP 5 wt %	25.25–369.64	369.64–460.60	460.60–999.98	369.64	460.60	437.14	13.01
AP-5 OSP 10 wt %	25.14–374.47	347.47–460.72	460.72–999.98	374.47	460.72	437.80	14.11
AP-5 OSP 15 wt %	25.15–362.42	362.42–458.33	458.33–999.98	362.42	458.33	433.65	12.56

T<sub>onset</sub>: onset of thermal degradation (°C). T<sub>offset</sub>: offset of temperature of final loss (°C). T<sub>max</sub>: maximum decomposition temperature (°C). ΔW: carbonaceous residue at 1000 °C (wt %).

### 3.10. Differential Scanning Calorimetry (DSC)

The differential scanning calorimetry (DSC) was carried out to elucidate the impact oyster shell powder (OSP) on the thermal transitions of asphalt cement. The effect of OSP content (e.g., 0, 5, 10, and 15 wt %) on the glass transition temperature ( $T_g$ ) of binders obtained from Figure 15 is illustrated in Table 6. Figure 15 demonstrates several thermal effects of the base asphalt (i.e., AP-5 OSP 0 wt %): (a) At very low temperatures (from −34 °C to −15 °C), the increase in heat capacity can be attributed to the first glass transition temperature ( $T_{g1}$ ) within the hydrocarbon matrix. It arises mainly from the maltene phase (i.e., a mixture of saturates, aromatics, and resins components) and is the most prominent transition. (b) Above  $T_{g1}$ , a second glass transition temperature ( $T_{g2}$ ) occurs. It comes from a maltene-asphaltene interfacial zone, which is most likely rich in resins. For convenience's sake, it can be defined as “an interphase”, even though it may not be a strictly separate phase [64,65]. It becomes clear that the pure AP-5 asphalt is a mixture, and this mixture is not completely homogenous, since it shows more than one  $T_g$ . Surprisingly, no obvious endothermic or exothermic effects have been shown in the DSC thermograms. This may be because the AP-5 asphalt contains inconsiderable amount of saturates (ca. 4.47 wt %; *n*-alkanes (waxes/paraffins), *iso*-alkanes, and cyclo-alkanes), which will bring a possible positive impact on crack susceptibility due to the absence of wax. The DSC curve for OSP, given in Figure 16, exhibits only a sharp endothermic peak located at 820.50 °C that can be ascribed to the decomposition of CaCO<sub>3</sub> and possible removal of absorbed water molecules that occur according to the following dissociation equation: CaCO<sub>3</sub> (s) + Heat → CaO (s) + CO<sub>2</sub> (g) (1). This reaction is also confirmed by TGA/DTGA analysis.

In inert atmosphere, some differences stand out. Figure 16 indicates that there is change in glass transition temperature ( $T_g$ ) between unfilled and OSP-filled asphalt samples. This fact implies that the presence of OSP affected the  $T_g$  of asphalt to some extent. The DSC data of neat asphalt and OSP-asphalt mastics filled with various contents of OSP (e.g., 5, 10, and 15 wt %) are outlined in Table 6. The first glass transition peak temperature ( $T_{g1}$ ) of OSP/asphalt composites was smaller than that of neat asphalt. As the filler content increased to 10 and 15 wt %, the  $T_{g1}$  dropped from −26.70 (for neat asphalt: AP-5 OSP 0 wt %) to −28.91 °C and to −28.12 °C, respectively. However, the OSP/asphalt composite was also found to have a slightly higher glass transition peak temperature than the base asphalt. The temperature slightly rose from −26.70 °C to −25.61 °C with a filler dose of 5 wt %. The  $T_g$ , though, changed irregularly with the OSP content.

This probably happened because when incorporating filler into a viscoelastic matrix, the binder will adsorb on the filler surface, creating a monomolecular layer, which causes an increase in  $T_g$ , but with higher concentration; the filler will form a superstructure (i.e., chains), which changes the whole inner structure of the binder system, thereby lowering  $T_g$ . Also, this could be related to the physicochemical interaction effect, which originates from the adsorption of polar groups in asphalt (mainly resins and asphaltenes) onto the surface of OSP particles. This adsorption is partially responsible for the observed changes in thermal properties (e.g., glass transition temperature,  $T_g$ ) and the rheological properties (e.g., stiffness and viscosity) of OSP/asphalt blends. The amount of polar

groups adsorbed is seemingly found to be dependent on the Braunauer-Emmett-Teller (BET) surface area of the filler but not on the chemical composition of the filler or bitumen [66]. The higher the BET surface area (e.g., 10 and 15 wt % OSP), the greater the amount of polar groups adsorbed and the lower the glass transition temperature, and vice-versa (with 5 wt % OSP) [66]. The reduction in the glass transition temperature indicates that this adsorption phenomenon results in asphalt softening. The data deduced from DSC studies indicates that higher content of OSP will worsen the low-temperature performance of bitumen; however, lower content ( $\leq 5$  wt %) will improve it [67,68]. Further BBR (i.e., bending beam rheometer) and DMA (i.e., dynamic mechanical analysis) studies are absolutely necessary to prove this assumption.

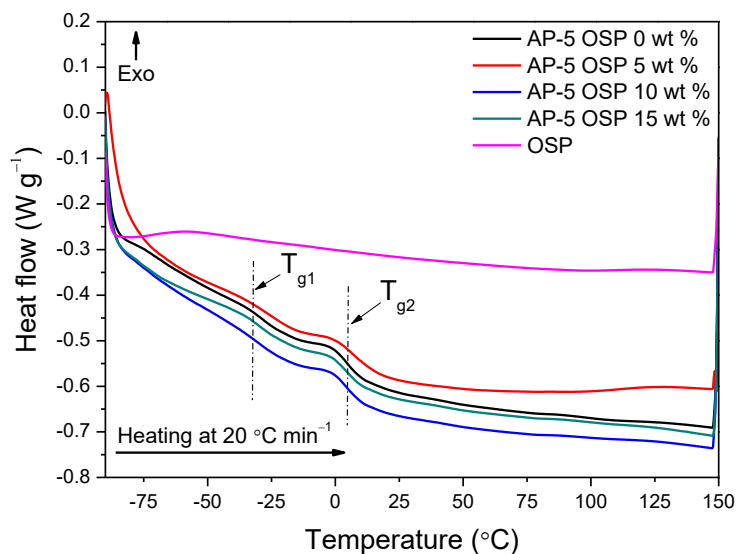


Figure 15. DSC thermograms of OSP, neat asphalt, and OSP-filled asphalts.

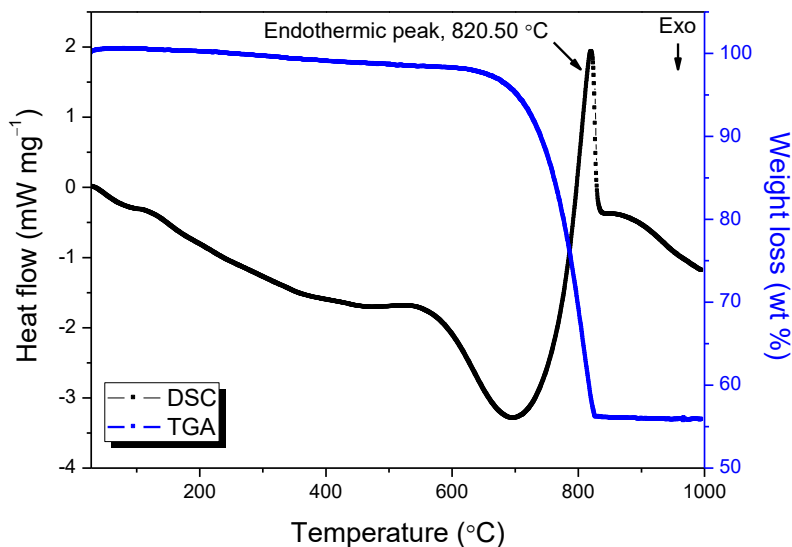


Figure 16. STA (TGA/DSC) measurement of OSP (sample mass 11.151 mg) in Alumina crucibles at a heating rate of  $10 \text{ K min}^{-1}$  in argon atmosphere ( $50 \text{ mL min}^{-1}$ ).



**Table 6.** DSC thermogram data of OSP, neat asphalt, and OSP/asphalt blends containing 5, 10, and 15 wt % OSP loading at heating rate of 20 °C min<sup>-1</sup>.

Sample	Thermal Parameter			
	$T_{g1}$ (°C)	$\Delta Cp_1$ (J g <sup>-1</sup> °C <sup>-1</sup> )	$T_{g2}$ (°C)	$\Delta Cp_2$ (J g <sup>-1</sup> °C <sup>-1</sup> )
OSP	†	†	†	†
AP-5 OSP 0 wt %	-26.70	0.1946	5.17	0.2360
AP-5 OSP 5 wt %	-25.61	0.2083	9.37	0.2554
AP-5 OSP 10 wt %	-28.91	0.2343	6.08	0.2559
AP-5 OSP 15 wt %	-28.12	0.2077	5.74	0.2469

$T_{g1}$ : glass transition of maltenic phase (°C).  $T_{g2}$ : glass transition of maltenic–asphaltene interphase region (°C). †: absence of glass transition temperature in DSC thermogram of OSP.

#### 4. Conclusions

To recover the oyster shell waste (OSW) for potential use, engineers, researchers, generators, and regulators need to be aware of the properties of these materials, how they can be used, and what limitations may be associated with their use. This preliminary study was conducted mainly to develop a means of converting WOS into useful filler in road pavement construction. The effect of different concentrations (e.g., 0, 5, 10, 15 wt %) of oyster shell powder (OSP) on the bitumen performance was examined. FT-IR and XRD data demonstrated that no apparent reactions have occurred between the inorganic filler and the asphalt cement. In response to filler treatment, TLC-FID revealed that the resin content increased at the expense of aromatic content. Due to the good distribution of OSP particles in the bituminous matrix, the thermal stability of bio-composites was achieved only with 5 and 10 wt %, as compared to plain bitumen. On the other hand, SEM analysis disclosed that a higher concentration (i.e., 15 wt %) of filler provoked an agglomeration and affected the bitumen morphology and microstructure. DSC results indicated that a lower content of natural CaCO<sub>3</sub> reduced the glass transition temperature ( $T_{g1}$ ) of binder; however, intermediate and higher contents increased it. The increase in hardness and stiffness, following the addition of mineral filler, was reflected by a decrease in penetration and ductility, and an increase in softening point of blends. The incorporation of OSP also enhanced the fatigue and rutting resistance of filler-asphalt mastics in comparison to control sample. The results of incremental increases in filler content up to 10 wt % were shown to be beneficial in all respects. In short, it can be concluded that OSP could be used as alternative filler in hot-mix asphalt (HMA). However, further comparative investigations with conventional mineral filler are required before integrating effectively this biofiller into practice. Future work may involve the inclusion of additional rheological techniques such as bending beam rheometer (BBR) test, rotational viscometer test, direct tension tester (DTT), etc.

**Acknowledgments:** We gratefully acknowledge helpful technical support of Center for Research and Facility in KOREATECH. This work was supported by “Korea-Tunisia joint research Programme” grant funded by the Korea government (Ministry of Science, ICT & Future Planning) in 2016 (NRF-2016K1A3A1A09919130).

**Author Contributions:** Nader Nciri performed the research, analyzed, and interpreted the data, and wrote the paper. Taesub Shin and Haksoo Lee conceived and designed the experiments. Namjun Cho supervised the project.

**Conflicts of Interest:** The authors declare no conflict of interest.

#### References

1. Read, J.; Whiteoak, D. *The Shell Bitumen Handbook*, 5th ed.; Thomas Telford Publishing: London, UK, 2003; p. 464, ISBN 13:978-0727732200.
2. Transportation Research Board of the National Academies. Chapter 4. Aggregates. In *NCHRP (National Cooperative Highway Research Program) REPORT 673—A Manual for Design of Hot Mix Asphalt with Commentary*; National Academy of Sciences: Washington, DC, USA, 2011; pp. 28–45, ISBN 978-0-309-15564-9.
3. Lee, D.Y. The Effect of Filler on Asphalt Cement Mastics. Ph.D. Thesis, Iowa State University of Science and Technology, Ames Iowa, USA, 1964.

4. Chen, J.S. Rheological Properties of Asphalt-Mineral Filler Mastics. *J. Jpn. Soc. Civil Eng.* **1997**, *36*, 269–277. [CrossRef]
5. Kim, M.; Buttlar, W. Stiffening Mechanisms of Asphalt-Aggregate Mixtures. *Transp. Res. Rec. J. Transp. Res. Board* **2010**, *2181*, 98–108. [CrossRef]
6. Underwood, B.S.; Kim, Y.R. Experimental investigation into the multiscale behavior of asphalt concrete. *Int. J. Pavement Eng.* **2011**, *12*, 357–370. [CrossRef]
7. Clopotel, C.; Velasquez, R.; Bahia, H. Measuring physico-chemical interaction in mastics using glass transition. *Road Mater. Pavement* **2012**, *13*, 304–320. [CrossRef]
8. Rigden, P.J. The use of fillers in bituminous road surfacings. A study of filler-binder systems in relation to filler characteristics. *J. Chem. Technol. Biot.* **1947**, *66*, 299–309. [CrossRef]
9. Heukelom, W. The role of filler in bituminous mixes. *J. Assoc. Asph. Paving Technol.* **1965**, *34*, 396–429.
10. Anderson, D.A. Mechanical Behavior and Reinforcement of Mineral Filler-Asphalt Mixtures. *J. Assoc. Asph. Paving Technol.* **1973**, *42*, 37–66.
11. Craus, J.; Ishai, I.; Sides, A. Some physico-chemical aspects of the effect and the role of the filler in bituminous paving mixtures. *J. Assoc. Asph. Paving Technol.* **1978**, *46*, 558–588.
12. Davis, C.; Castorena, C. Implications of physico-chemical interactions in asphalt mastics on asphalt microstructure. *Constr. Build. Mater.* **2015**, *94*, 83–89. [CrossRef]
13. Fini, E.H.; Al-Qadi, I.L.; You, Z.; Zada, B.; Mills-Beale, J. Partial replacement of asphalt binder with bio-binder: Characterization and modification. *Int. J. Pavement Eng.* **2012**, *13*, 515–522. [CrossRef]
14. Dhasmana, H.; Ozer, H.; Al-Qadi, I.L.; Zhang, Y.; Schideman, L.; Sharma, B.K.; Chen, W.T.; Minarick, M.J.; Zhang, P. Rheological and Chemical Characterization of Biobinders from Different Biomass Resources. *Transp. Res. Rec. J. Transp. Res. Board* **2015**, *2505*, 121–129. [CrossRef]
15. Guarin, A.; Khan, A.; Butt, A.A.; Birgisson, B.; Kringos, N. An extensive laboratory investigation of the use of bio-oil modified bitumen in road construction. *Constr. Build. Mater.* **2016**, *106*, 133–139. [CrossRef]
16. Kowalski, K.J.; Król, J.B.; Bańkowski, W.; Radziszewski, P.; Sarnowski, M. Thermal and Fatigue Evaluation of Asphalt Mixtures Containing RAP Treated with a Bio-Agent. *Appl. Sci-Basel* **2017**, *7*, 216. [CrossRef]
17. Król, J.B.; Niczke, Ł.; Kowalski, K.J. Towards Understanding the Polymerization Process in Bitumen Bio-Fluxes. *Materials* **2017**, *10*, 1058. [CrossRef] [PubMed]
18. Chen, M.; Lin, J.; Wu, S. Potential of recycled fine aggregates powder as filler in asphalt mixture. *Constr. Build. Mater.* **2011**, *25*, 3909–3914. [CrossRef]
19. Chandra, S.; Kumar, P.; Feyissa, B.A. Use of Marble Dust in Road Construction. *Road Mater. Pavement* **2002**, *3*, 317–330. [CrossRef]
20. Modarres, A.; Rahmanzadeh, M. Application of coal waste powder as filler in hot mix asphalt. *Constr. Build. Mater.* **2014**, *66*, 476–483. [CrossRef]
21. Saltan, M.; Öksüz, B.; Uz, V.E. Use of glass waste as mineral filler in hot mix asphalt. *Sci. Eng. Compos. Mater.* **2015**, *22*, 271–277. [CrossRef]
22. Sargin, Ş.; Saltan, M.; Morova, N.; Serin, S.; Terzi, S. Evaluation of rice hush ash as filler in hot mix asphalt concrete. *Constr. Build. Mater.* **2013**, *48*, 390–397. [CrossRef]
23. Jeffry, S.N.; Jaya, R.P.; Hassan, N.A.; Yaacob, H.; Mirza, J.; Drahman, S.H. Effect of nanocharcoal coconut-shell ash on the physical and rheological properties of bitumen. *Constr. Build. Mater.* **2018**, *158*, 1–10. [CrossRef]
24. Kiruthiha, K.; Loshini, G.; Thivya, M. Strengthening of Flexible Pavement using Egg Shell as a Filler. *Int. J. Eng. Trends Technol. (IJETT)* **2015**, *21*, 483–486. [CrossRef]
25. Arabani, M.; Babamohammadi, S.; Azarhoosh, A.R. Experimental investigation of seashells used as filler in hot mix asphalt. *Int. J. Pavement Eng.* **2014**, *16*, 502–509. [CrossRef]
26. KDI (Korea Development Institute). *Report of Economic Policy (in Korean)*; KDI (Korea Development Institute): Seoul, Korea, 2002.
27. Yoon, G.L.; Kim, B.T.; Kim, B.O.; Han, S.H. Chemical–mechanical characteristics of crushed oyster-shell. *Waste Manag.* **2003**, *23*, 825–834. [CrossRef]
28. Lee, J.Y.; Lee, C.H.; Ha, B.H.; Kim, S.C.; Lee, D.K.; Kim, P.J. Effect of Oyster Shell Meal on Improving Soil Microbiological Activity. *Korean J. Soil Sci. Fertil.* **2005**, *38*, 281–286.
29. Yang, E.I.; Yi, S.T.; Leem, Y.M. Effect of oyster shell substituted for fine aggregate on concrete characteristics: Part I. Fundamental properties. *Cement Concr. Res.* **2005**, *35*, 2175–2182. [CrossRef]

30. Lee, C.H.; Lee, J.Y.; Ha, B.H.; Kim, P.J. Increased Available Phosphate by Shell Meal Fertilizer Application in Upland Soil. *Korean J. Soil Sci. Fertil.* **2005**, *38*, 52–57.
31. American Association of State Highway and Transportation Officials. *AASHTO T-37, Sieve Analysis of Mineral Filler for Hot Mix Asphalt (HMA)*; American Association of State Highway and Transportation Officials: Washington, DC, USA, 2011.
32. Masson, J.F.; Price, T.; Collins, P. Dynamics of Bitumen Fractions by Thin-Layer Chromatography/Flame Ionization Detection. *Energy Fuels* **2001**, *15*, 955–960. [CrossRef]
33. American Society of Testing Materials (ASTM) International. *ASTM D36/D36M-14e1, Standard Test Method for Softening Point of Bitumen (Ring-and-Ball Apparatus)*; American Society of Testing Materials (ASTM) International: West Conshohocken, PA, USA, 2014.
34. American Society of Testing Materials (ASTM) International. *ASTM D113-07, Standard Test Method for Ductility of Bituminous Materials*; American Society of Testing Materials (ASTM) International: West Conshohocken, PA, USA, 2007.
35. American Society of Testing Materials (ASTM) International. *ASTM D5/D5M-13, Standard Test Method for Penetration of Bituminous Materials*; American Society of Testing Materials (ASTM) International: West Conshohocken, PA, USA, 2013.
36. Zhang, J.; Wang, J.; Wu, Y.; Wang, Y.; Wang, Y. Evaluation of the improved properties of SBR/weathered coal modified bitumen containing carbon back. *Constr. Build. Mater.* **2009**, *23*, 2678–2687. [CrossRef]
37. Karmakar, S.; Roy, T.K. Effect of Waste Plastic and Waste Tires Ash on Mechanical Behavior of Bitumen. *J. Mater. Civil Eng.* **2016**, *28*. [CrossRef]
38. American Society of Testing Materials (ASTM) International. *ASTM D7175-15, Standard Test Method for Determining the Rheological Properties of Asphalt Binder Using a Dynamic Shear Rheometer*; American Society of Testing Materials (ASTM) International: West Conshohocken, PA, USA, 2015.
39. Tan, Y.; Li, X.; Wu, J. Internal Influence Factors of Asphalt-Aggregate Filler Interactions Based on Rheological Characteristics. *J. Mater. Civil Eng.* **2012**, *24*, 1520–1528.
40. Zhang, J.; Li, X.; Liu, G.; Pei, J. Effects of material characteristics on asphalt and filler interaction ability. *Int. J. Pavement Eng.* **2017**, 1–10. [CrossRef]
41. Zaniewski, J.P.; Reyes, C.H. *Evaluation of the Effect of Fines on Asphalt Concrete*; Technical Report; West Virginia University: Morgantown, WV, USA, 2003.
42. Muniandy, R.; Aburkaba, E.; Yunus, R.; Hamid, H.; Salihudin, H. Influence of Mineral Filler Particle Size and Type on Rheological and Performance Properties of SMA Asphalt-filler Mastics. *Asian J. Appl. Sci.* **2012**, *5*, 522–537.
43. Wen, H.; Zhang, K.; Hobbs, A.; Edburg, S.L. Microstructural characterization and micromechanics of asphaltic materials–II: Simulation of drying aggregate in asphalt plants. In *Asphalt Pavements*, 2nd ed.; Kim, R.Y., Ed.; CRC Press Taylor & Francis Group: London, UK; New York, NY, USA, 2014; Volume 1, pp. 963–970, ISBN 978-1-138-02693-3.
44. Dukatz, E.L.; Anderson, D.A. The Effect of Various Fillers on the Mechanical Behavior of Asphalt and Asphaltic Concrete. *J. Assoc. Asph. Pavements* **1980**, *49*, 530–549.
45. Naemchan, K.; Meejoo, S.; Onreabroy, W.; Limsuwan, P. Temperature Effect on Chicken Egg Shell Investigated by XRD, TGA, and FTIR. *Adv. Mater. Res.* **2008**, *55–57*, 333–336. [CrossRef]
46. Jazie, A.A.; Pramanik, H.; Shinha, A.S.K.; Jazie, A.A. Egg Shell as Eco-friendly Catalyst for Transesterification of Rapeseed Oil: Optimization for Biodiesel Production. *Int. J. Sustain. Dev. Green Econ.* **2013**, *2*, 27–32.
47. Siddiqui, M.N.; Ali, M.F.; Shirokoff, J. Use of X-ray diffraction in assessing the aging pattern of asphalt fractions. *Fuel* **2002**, *81*, 51–58. [CrossRef]
48. AlHumaidan, F.S.; Hauser, A.; Rana, M.S.; Lababidi, H.M.S.; Behbehani, M. Changes in asphaltene structure during thermal cracking of residual oils: XRD study. *Fuel* **2015**, *150*, 558–564. [CrossRef]
49. Rigo, V.A.; Metin, C.O.; Nguyen, Q.P.; Miranda, C.R. Hydrocarbon Adsorption on Carbonate Mineral Surfaces: A First Principles Study with van der Waals Interactions. *J. Phys. Chem. C* **2012**, *116*, 24538–24548. [CrossRef]
50. Wang, H.; Grant, D.J.; Burns, P.C.; Na, C. Infrared Signature of the Cation- $\pi$  Interaction between Calcite and Aromatic Hydrocarbons. *Langmuir* **2015**, *31*, 5820–5826. [CrossRef] [PubMed]
51. Buttlar, W.G.; Bozkurt, D.; Al-Khateeb, G.G.; Waldhoff, A.S. Understanding Asphalt Mastic Behavior through Micromechanics. *Transp. Res. Rec. J. Transp. Res. Board* **1999**, *1681*, 157–169. [CrossRef]

52. Al-Qadi, I.; Fini, E.; Elseifi, M.; Masson, J.F.; McGhee, K. Viscosity Determination of Hot-Poured Bituminous Sealants. *Transp. Res. Rec. J. Transp. Res. Board* **2006**, *1958*, 74–81. [CrossRef]
53. Al-Qadi, I.L.; Fini, E.H.; Elseifi, M.A.; Masson, J.F.; McGhee, K.M. Development of a Viscosity Specification for Hot-Poured Bituminous Sealants. *J. Test. Eval.* **2007**, *35*, 395–403.
54. Winniford, R.S. The rheology of asphalt-filler systems as shown by the microviscometer. *Am. Soc. Test. Mater.* **1961**, *STP309*, 109–120.
55. Zapién-Castillo, S.; Rivera-Armenta, J.L.; Chávez-Cinco, M.Y.; Salazar-Cruz, B.A.; Mendoza-Martínez, A.M. Physical and rheological properties of asphalt modified with SEBS/montmorillonite nanocomposite. *Constr. Build. Mater.* **2016**, *106*, 349–356. [CrossRef]
56. Shafabakhsh, G.H.; Ani, O.J. Experimental investigation of effect of Nano TiO<sub>2</sub>/SiO<sub>2</sub> modified bitumen on the rutting and fatigue performance of asphalt mixtures containing steel slag aggregates. *Constr. Build. Mater.* **2015**, *98*, 692–702. [CrossRef]
57. Nciri, N.; Kim, J.; Kim, N.; Cho, N. An In-Depth Investigation into the Physicochemical, Thermal, Microstructural, and Rheological Properties of Petroleum and Natural Asphalts. *Materials* **2016**, *9*, 859. [CrossRef] [PubMed]
58. Asociación Española de Normalización y Certificación (AENOR). *UNE-EN 13043, Aggregates for Bituminous Mixtures and Surface Treatments for Roads, Airfields and Other Trafficked Areas*; Asociación Española de Normalización y Certificación (AENOR): Madrid, Spain, 2004. (In Spanish)
59. Jahromi, S.G. Estimation of resistance to moisture destruction in asphalt mixtures. *Constr. Build. Mater.* **2009**, *23*, 2324–2331. [CrossRef]
60. Wozuk, A.; Zofka, A.; Bandura, L.; Franus, W. Effect of zeolite properties on asphalt foaming. *Constr. Build. Mater.* **2017**, *139*, 247–255. [CrossRef]
61. Wozuk, A.; Franus, W. A Review of the Application of Zeolite Materials in Warm Mix Asphalt Technologies. *Appl. Sci-Basel* **2017**, *7*, 293. [CrossRef]
62. Zhang, Y.; Leng, Z.; Zou, F.; Wang, L.; Chen, S.S.; Tsang, D.C.W. Synthesis of zeolite A using sewage sludge ash for application in warm mix asphalt. *J. Clean. Prod.* **2018**, *172*, 686–695. [CrossRef]
63. Oner, J.; Sengoz, B. Utilization of Recycled Asphalt Concrete with Warm Mix Asphalt and Cost-Benefit Analysis. *PLoS ONE* **2015**, *10*, e116180. [CrossRef] [PubMed]
64. Masson, J.F.; Polomark, G.; Collins, P. Glass transitions and amorphous phases in SBS-bitumen blends. *Thermochim. Acta* **2005**, *436*, 96–100. [CrossRef]
65. Nciri, N.; Kim, N.; Cho, N. New insights into the effects of styrene-butadiene-styrene polymer modifier on the structure, properties, and performance of asphalt binder: The case of AP-5 asphalt and solvent deasphalting pitch. *Mater. Chem. Phys.* **2017**, *193*, 477–495. [CrossRef]
66. Clopotel, C.; Bahia, H. The effect of bitumen polar groups adsorption on mastics properties at low temperatures. *Road Mater. Pavement* **2013**, *14*, 38–51. [CrossRef]
67. Guo, M.; Tan, Y.Q.; Zhang, L. Effect of Filler on Glass Transition of Asphalt Mastics. *Adv. Eng. Forum* **2012**, *5*, 376–381. [CrossRef]
68. Tan, Y.; Guo, M. Study on the phase behavior of asphalt mastic. *Constr. Build. Mater.* **2013**, *47*, 311–317. [CrossRef]



© 2018 by the authors. Licensee MDPI, Basel, Switzerland. This article is an open access article distributed under the terms and conditions of the Creative Commons Attribution (CC BY) license (<http://creativecommons.org/licenses/by/4.0/>).



MDPI  
St. Alban-Anlage 66  
4052 Basel  
Switzerland  
Tel. +41 61 683 77 34  
Fax +41 61 302 89 18  
[www.mdpi.com](http://www.mdpi.com)

*Applied Sciences* Editorial Office  
E-mail: [applsci@mdpi.com](mailto:applsci@mdpi.com)  
[www.mdpi.com/journal/applsci](http://www.mdpi.com/journal/applsci)





MDPI  
St. Alban-Anlage 66  
4052 Basel  
Switzerland  
Tel: +41 61 683 77 34  
[www.mdpi.com](http://www.mdpi.com)



ISBN 978-3-0365-5541-6